Reliable Grid Condition Detection and Control of Single-Phase Distributed Power Generation Systems

Ciobotaru, Mihai

Link to publication from Aalborg University

Reliable Grid Condition Detection and Control of Single-Phase Distributed Power Generation Systems

by

Mihai Ciobotaru

Dissertation submitted to the Faculty of Engineering, Science & Medicine at Aalborg University
in partial fulfillment of the requirements for the degree of
Doctor of Philosophy in Electrical Engineering

Aalborg University
Institute of Energy Technology
Denmark, January, 2009

Preface

This thesis is written under the research project 2058-03-0003 entitled "*Reliable grid conditions detection and control in distributed power generation systems (DPGS)*" financially supported by the Danish Council for Independent Research, Risø National Laboratory, Energinet.dk and Aalborg University. This project was divided into two sub-projects, one entitled "*Reliable grid condition detection and control of single-phase DPGS*" which is presented in this thesis and deals with single-phase systems and the second one entitled "*Grid monitoring and advanced control of DPGS*" which treats three-phase systems.

The research project was carried out under the supervision of Prof. Remus Teodorescu (main supervisor) and Prof. Frede Blaabjerg (co-supervisor), both from Institute of Energy Technology, Aalborg University, Denmark. My deepest gratefulness goes to my supervisors for their guidance and professional support during the project period. Additionally, many thanks to the steering committee composed of Uffe Borup from Danfoss Solar, Poul Sørensen from Risø National Laboratory, Kim Larsen from Vestas and Kent Søbrink from Energinet.dk, for their comments and helpful suggestions during the steering meetings.

I would like to express my gratitude to Prof. Vassilios Agelidis and Prof. Emil Ceanga for their kindness and professional guidance during my stays abroad at School of Electrical and Process Engineering, Murdoch University, Australia and at "Dunarea de Jos" University of Galati, Romania.

I want to thank to all my colleagues from Institute of Energy Technology for their friendly companion which guided me through the lifestyle of Aalborg University. Special thanks go to Assoc. Prof. Florin Iov for his help and moral support. Also, many thanks to all my fellow PhD students, who assisted me many times and gave me support in different ways. In particular, I thank to Adrian Timbus, Dezso Sera, Tamas Kerekes, Uffe Jakobsen and Laszlo Mathe.

I would also like to thank to Assoc. Prof. Pedro Rodriguez and Luna Alvaro, from Universitat Politecnica de Catalunya, Spain, for sharing their experience and time with me during their visits at Institute of Energy Technology.

Finally, but not least, I want to express my appreciation to Loredana Tanaselea and to my entire family in Romania for their generous and continuous moral support.

Mihai Ciobotaru,
Aalborg, January 2009

Dedicated
to my mother Tudosia for her exceptional dedication to the family
and
to the memory of my father Paraschiv.

Abstract

The constant growth of Distributed Power Generation Systems (DPGS) presents an efficient and economic way of generating electricity closer to the load(s). The DPGS can contribute to an efficient and renewable electricity future by potentially: increasing the use of renewable sources of energy; improving the efficiency of the electricity system by reducing transmission and distribution losses; improving the security of the electricity supply through increased diversity of supply and reduced vulnerability to simultaneous system failures. However, the new trend of using DPGS comes also with a suite of new challenges. One of the challenges is the interaction between the DPGS and the utility grid. As a consequence, grid interconnection requirements applying to distributed generation are continuously updated in order to maintain the quality and the stability of the utility grid.

The new upcoming standards addressed to the grid-connected systems will harmonize the combination of the DPGS and the classical power plants. Consequently, the major tasks of this thesis were to develop new grid condition detection techniques and intelligent control in order to allow the DPGS not only to deliver power to the utility grid but also to sustain it.

This thesis was divided into two main parts, namely "Grid Condition Detection" and "Control of Single-Phase DPGS". In the first part, the main focus was on reliable Phase Locked Loop (PLL) techniques for monitoring the grid voltage and on grid impedance estimation techniques. Additionally, a new technique for detecting the islanding mode has been developed and successfully tested. In the second part, the main reported research was concentrated around adaptive current controllers based on the information provided by the grid condition detection techniques.

To guarantee the correct generation of the reference signals and to meet the demands regarding the operation boundaries with respect to voltage amplitude and frequency values required by standards, the grid-connected converters need an accurate and fast detection of the phase angle, amplitude and frequency of the utility voltage. As a consequence, a new voltage monitoring algorithm including an offset rejection technique was proposed in this thesis. Additionally, the discrete implementation of the algorithm was given.

The estimation of the grid impedance can be used by the control of numerous grid-connected systems, such as active filters, islanding detection techniques, non-linear

current controllers including hysteresis and predictive control, detection of the operation mode (on-grid or off-grid) of a DPGS, etc. Therefore, estimating the grid impedance can add extra functions into the operation of the grid-connected converters. Hence, three different methods have been developed with relation to the grid impedance estimation. The first method uses the harmonic injection technique; the second method is based on active and reactive power variations and the third proposed method is based on identification techniques.

The islanding detection is an important and necessary safety future of the grid-connected systems to comply with. The islanding should be detected fast in conformity with the standard requirements for the grid interconnection. Accordingly, an accurate and less-disturbing islanding detection algorithm based on PLL technique was developed and tested successfully in this thesis.

The control of a DPGS is mainly designed in accordance with the electrical grid condition at the Point of Common Coupling (PCC). Usually, the parameters of the controllers are tuned for some assumed values of the electrical grid parameters. However, the parameters of the electrical grid such as grid impedance or grid frequency can change. Therefore, the control should be able to follow these changes by using the data provided by the grid condition detection techniques in order to maintain the performance and the robustness of the entire system. Regarding the advance control of DPGS, an active damping technique for grid-connected systems using inductor-capacitor-inductor (LCL) filters was proposed in the thesis. The method is based on a notch filter, whose stopband can be automatically adjusted in relation with an estimated value of the grid impedance.

Table of contents

Nomenclature

List of Abbreviations

A/D	-	Analogue to Digital
AC	-	Alternating Current
APF	-	All-Pass Filter
CHP	-	Combined Heat and Power
cof	-	Cut-off frequency
DC	-	Direct Current
DFT	-	Discrete Fourier Transform
DPGS	-	Distributed Power Generation System
DQ	-	synchronous reference frame
DSP	-	Digital Signal Processor
FC	-	Fuel Cell
FIFO	-	First-In First-Out
FIR	-	Finite Impulse Response
HC	-	Harmonic Compensator
IIR	-	Infinite Impulse Response
LCL	-	inductor(L)-capacitor(C)-inductor(L)
LPF	-	Low-Pass Filter
MPPT	-	Maximum Power Point Tracker
NDZ	-	Non-Detection Zones
NF	-	Notch Filter
OFP	-	Over-Frequency Protection
OSG	-	Orthogonal Signal Generator
OSG-SOGI	-	OSG based on SOGI
OVP	-	Over-Voltage Protection
PCC	-	Point of Common Coupling
PI	-	Proportional Integral
PLL	-	Phase-Locked Loop
PQ	-	active(P) and reactive(Q) power
PR	-	Proportional Resonant
PR+HC	-	PR controller with HC

p.u.	-	Per unit
PV	-	Photovoltaic
PWM	-	Pulse-Width Modulation
RL	-	resistor(R)-inductor(L)
RLC	-	resistor(R)-inductor(L)-capacitor(C)
RMS	-	Root Mean Square
SOGI	-	Second Order Generalized Integrator
STQ	-	Statistic technique
THD	-	Total Harmonic Distortion
UFP	-	Under-Frequency Protection
UPS	-	Uninterruptible Power Supply
UVP	-	Under-Voltage Protection
VSI	-	Voltage Source Inverter
WT	-	Wind Turbines
ZCD	-	Zero-Crossing Detection

List of symbols

ω	-	angular frequency
t	-	time
θ	-	phase angle
$v(t), v$	-	instantaneous voltage
$i(t), i$	-	instantaneous current
V	-	root mean square value of voltage
I	-	root mean square value of current
$\tan^{-1}(...)$	-	arctangent function
T	-	time period
$f, freq.$	-	frequency
u_k	-	clock signal
s	-	complex variable in Laplace domain
$\mod(...)$	-	modulo function
ε_θ	-	phase angle error
ε_v	-	voltage error
ε_i	-	current error
ε_{dc}	-	DC voltage error
qv	-	quadrature voltage component
ζ	-	damping ratio
ω_n	-	undamped natural frequency
v', qv'	-	orthogonal voltage system produced by OSG-SOGI
$H_{...}(...)$	-	transfer function
$u[...], u(...)$	-	input variable

$y[...], y(...)$	-	output variable
T_s	-	sampling time
k	-	gain value
qv'_i	-	quadrature voltage component of OSG-SOGI before removing the offset value
z	-	complex variable in discrete domain
n	-	actual sample
$est.$	-	estimated value
$ampl.$	-	amplitude
v_{dc}	-	DC link voltage
i_{dc}	-	DC link current
T_{set}	-	settling time
j	-	square root of -1
Im	-	imaginary part
Re	-	real part
Z	-	impedance
R	-	resistance
L	-	inductance
C	-	capacitance
P	-	active power
Q	-	reactive power
Δv	-	voltage drop
e_g	-	grid equivalent generator
$\overrightarrow{\Lambda_h}$	-	complex Fourier vector
h_v	-	voltage harmonics
h_i	-	current harmonics
Δt_P	-	variation period of active power
Δt_Q	-	variation period of reactive power
I_{err}	-	criterion function
σ_{inj}	-	injected signal
f_r	-	resonant frequency
K_P	-	plant gain
K_C	-	control gain
Subscripts	-	
$\cdots_h$	-	harmonic order
$\cdots_{IC}$	-	initial condition
$\cdots_{\alpha,\beta}$		components in the stationary coordinates
$\cdots_{d,q}$		components in the synchronous coordinates

$\cdots_{\text{min,max}}$	minimum, maximum
$\cdots_g$	grid signal component
$\cdots_f$	filter signal component
$\cdots_{PCC}$	PCC signal component
$\cdots_{inv}$	inverter signal component
$\cdots_{meas}$	measured value
$\cdots_{ref}$	reference value

Superscripts

$\widehat{\cdots}$	-	estimated value
$\hat{\cdots}$	-	peak value
$\overset{*}{\cdots}$	-	reference value
$\overrightarrow{\cdots}$	-	vector

Chapter 1

Introduction

This chapter starts by describing the background and the motivation of the thesis and includes a short overview about single-phase Distributed Power Generation Systems (DPGS). Next, the objectives and the limitations of the PhD research project are given. Subsequently, the main contributions of the thesis are presented. Next, a list of scientific publications derived from this thesis thus far is given. Finally, the outline of the thesis is presented.

1.1 Background and motivation

The continuous increasing importance of small-scale electricity generation, also known as DPGS, enabled by the advancement of power electronics, presents significant opportunities to utilities and customers alike. New, efficient and economic ways of generating electricity closer to the load(s) as part of a deregulated industry environment are possible nowadays. For instance, the single-phase systems present opportunities for micro DPGS to be connected to the electrical grid through roof-top Photovoltaic (PV) systems, thus being easily accessible in the residential areas. A short overview about single-phase DPGS is given in the coming section.

1.1.1 Overview of single-phase DPGS

In classical power systems, most of electricity is generated in large, centralized power stations which can be a long way from where the electricity is used. The electricity is transported over long distance transmission lines, and then carried through local distribution networks to where it is needed. Then, the system control centers continuously monitor the voltage frequency and amplitude [XI]. On the opposite, the distributed generation is different, meaning that the electricity is generated from small-scale systems and is used on-site or nearby. It can be used to generate electricity for homes, farms, businesses and industries. As a consequence, the overall structure of the

power system has started nowadays to be changed due to the increased penetration of DPGS [1], [2], [XI].

The DPGS are usually connected to the local distribution network. This means that when there is not enough electricity being generated by the local distributed generation units, the users can still get electricity from the national electricity grid. It also means that if the electricity is generated in excess, the electricity surplus can be exported into the national electrical grid.

The electricity from the DPGS can be generated using different systems including both renewable and non-renewable sources such as Wind Turbines (WT), PV generators, wave generators, small hydro, Fuel Cells (FC) and gas/steam powered Combined Heat and Power (CHP) stations. However, only the small power level DPGS (below 5 kW) such as PV and FC systems can be connected to the electrical grid through single-phase power converters. Consequently, only the DPGS based on PV and FC systems will be described.

The PV systems represent an emerging energy technology which is environmentally friendly and easy to use inside and outside populated areas. At the beginning, the PV technology was very expensive and it was only used as power supply for special stand-alone applications such as communication satellites. However, the continuous progress of the semiconductor technology allowed the development of commercial less expensive PV cells, thus making the PV systems an important alternative energy source.

PV systems can be used for homes, offices, public buildings or remote sites where grid connection is either unavailable or too expensive. PV systems can be mounted on roofs or on building facades or can operate as standalone systems. The innovative PV array technology and mounting systems means that PV can be retrofitted on existing roofs or easily incorporated as part of the building envelope at construction stage. Modern PV technology has advanced rapidly and PV is no longer restricted to square and flat panel arrays but can be curved and shaped to the building design.

There are four primary applications for PV power systems such as off-grid domestic, off-grid non-domestic, grid-connected distributed and grid-connected centralized. In the last few years, an exponential increase in grid-connected PV applications has been observed. As reported in [3], about 2,26 GW of PV capacity was installed during 2007 (an increase of more than 50 % over the previous year) which brought the total installed capacity to 7,8 GW. The cumulative installed grid-connected and off-grid PV power is given in Figure 1.1 [3].

Another alternative resource is represented by FCs. Historically, the FC was first invented in 1839, but the technology largely remained dormant until the late 1950s. During the 1960s, NASA used precursors to today's FC technology as power sources in spacecraft [4]. The FC is an interesting technology due to its high conversion efficiency (around 70%) which is superior when compared to different classical conversion systems such as Otto motors, Diesel engine, steam and gas turbines or to renewable conversion systems such as WTs (around 40%) and PV systems (around 20-25 % with the new PV cell technology).
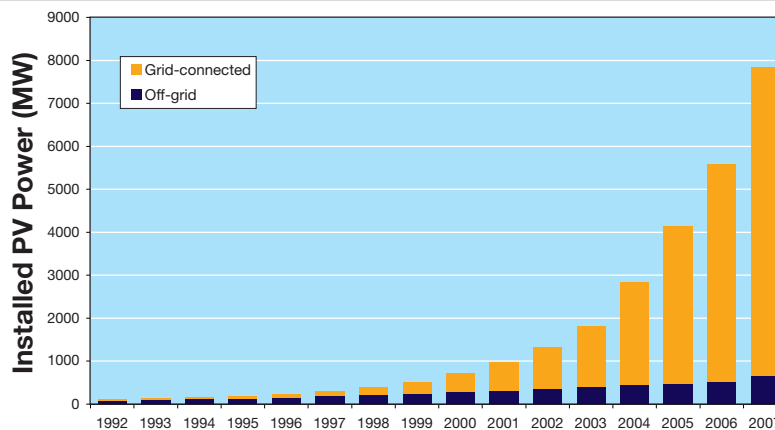
Figure 1.1. Cumulative installed grid-connected and off-grid PV power in the reporting countries [3].

The FCs are unique in terms of the variety of their potential applications; they can provide energy for systems as large as a utility power station, as small as a laptop computer, and just about everything in between, including light cars and trucks. Fuel cells have also the potential to provide distributed power generation [4].

While they currently face market barriers due to their high prices, fuel cells have the potential to be more economically viable in the near future. An environmental benefit of this technology may be enhanced if fuel cells can eventually use hydrogen produced by electrolysis from renewable energy sources. Thus, the main disadvantage of the renewable energy sources, which is their high uncertainty in the availability, can be alleviated. Therefore, hybrid systems using different combinations such as PV - FC or wind - FC will become more important in near future of the distributed generation.

1.1.2 Project Motivation

The distributed generation can contribute to an efficient and renewable electricity future by potentially: increasing the use of renewable sources of energy; improving the efficiency of the electricity system by reducing transmission and distribution losses; improving the security of the electricity supply through increased diversity of supply and reduced vulnerability to simultaneous system failures (the impact of simultaneous failure may be less with a high number of small generation units than a few large power stations) [5].

Besides the advantages, the new trend of using distributed generation comes also with a suite of new challenges. One of the new issues which increasingly attracts the attention of researchers is the interaction between the DPGSs and the utility grid. A harmonic interaction between a large number of distributed power inverters and the distribution network has been reported in [6]. As a consequence, grid interconnection requirements applying to distributed generation are continuously updated in order to maintain the quality and the stability of the utility grid [7-11].

1.2 Objectives and Limitations

In the past, people have thought mostly about how to get the energy from wind, solar, waves, tide, etc. With the continuous increase of the distributed generation the problem has moved now to the delivery of this energy to the electrical grid in the most efficient way possible. At the same time, the new upcoming standards addressed to the grid-connected systems will harmonize the combination of the classical power plants and the DPGSs. Therefore, the two main objectives of this thesis are focused on the new grid condition detection techniques and on the intelligent control which will allow the DPGS not only to deliver power to the utility grid but also to sustain it. The objectives and the limitations of this research project are described in the following.

1.2.1 Objectives

Based on the new introduced standard requirements for DPGS [7-11], the primary goal of this thesis is to report new and reliable grid condition detection techniques for single-phase grid-connected systems in order to meet these stringent requirements. This main goal regarding the detection of the grid condition contains three main objectives, namely the grid voltage monitoring, grid impedance estimation and islanding detection. Additionally, a secondary goal is to document advanced control algorithms which will make use of the grid condition detection techniques. The main objectives of this thesis are described in the coming paragraphs.

Grid voltage monitoring – To guarantee the correct generation of the reference signals and to meet the demands regarding the operation boundaries with respect to voltage amplitude and frequency values required by standards, the grid-connected converters need an accurate and fast detection of the phase angle, amplitude and frequency of the utility voltage. The grid voltage monitoring can be easily influenced by the grid disturbances, thus providing inaccurate values to the control. This can lead to poor performances or undesired disconnections of the DPGS. Consequently, new reliable algorithms for monitoring the grid voltage have been investigated in order to provide accurate values for the voltage phase, amplitude and frequency. Moreover, the elaborated algorithms have to have a fast detection rate and to be robust under grid disturbances.

Grid impedance estimation – The grid impedance value can be used by the control of numerous grid-connected systems. Some of the applications which rely on the grid impedance value can be enumerated as follows: current controllers with improved stability and dynamic performance; active filter control; detection of grid faults and grid unbalances; compliance with certain stringent standards for islanding detection; non-linear current controllers including hysteresis and predictive control; detection of the operation mode (on-grid or off-grid) of a DPGS.

Many applications mentioned above assume a fixed value for the grid impedance. However, the grid impedance value can experience fluctuations which can compromise the assumption of constant grid impedance made by the control. Therefore, estimating

the grid impedance can add extra functions into the operation of the grid-connected converters. Thus, the grid power converters can become more intelligent and they will sustain a better integration of DPGSs into the utility grid.

Islanding detection – This is an important and necessary safety future of the grid-connected systems to comply with. The islanding phenomenon can occur when the electrical grid is disconnected and the grid-connected converter continues to operate on local loads. The islanding should be detected fast in conformity with the standard requirements for the grid interconnection. Even though, numerous anti-islanding detection methods exist already, most of the passive methods are not accurate enough and a large part of the active methods are too invasive thus affecting the output power quality of the grid-connected converters. Therefore, the development of an accurate and less-disturbing islanding detection algorithm becomes a necessity.

Advanced control – The control of a DPGS is mainly designed in accordance with the electrical grid condition at the Point of Common Coupling (PCC). The parameters of the controllers are tuned for some assumed values of the electrical grid parameters. However, the parameters of the electrical grid such as grid impedance or grid frequency can change. Therefore, the control should be able to follow these changes by using the data provided by the grid condition detection techniques in order to maintain the performance and the robustness of the entire system.

1.2.2 Tools used

The control algorithms developed along this thesis were created using a simulation platform based on MATLAB®/Simulink [12]. Additionally, either transfer functions or PLECS® toolbox [13] for Simulink were used in order to simulate electrical circuits. The PLECS® toolbox was preferred when compared to other electrical circuit simulators due to its MATLAB®/Simulink integration. The dSPACE - DS1103 controller board [14] was used for the experimental implementation of the developed algorithms due to its power processing capabilities and the interconnectivity with Simulink. The Voltage Source Inverter (VSI) used for the test setup was a commercial product provided by Danfoss A/S [15]. Finally, a programmable AC load from California Instruments A/S [16] was used to emulate the electrical grid in order to test some algorithms under special grid conditions.

1.2.3 Project Limitations

In the technical literature there are many ways to configure a distributed generation system. As presented in §1.1, there are many energy sources (using either renewable or conventional energy) to be used. In many applications, the conversion of the power is performed by the power electronic equipment using a large variety of topologies. In spite of the fact that this thesis is focused mostly on single-phase grid connected PV systems, most of the methods described in this thesis can be applied to a large variety of DPGS, including the three-phase systems.

All the experimental tests along this research project were done using only a single-stage converter supplied by either a DC power source or a string of sixteen PV panels connected in series. The power converter represented by a VSI was connected to the low voltage grid (230 V) through an inductor(L)-capacitor(C)-inductor(L) (LCL) filter.

One of the key issues of the grid impedance estimation is the assumed grid model. The grid model gives the relationship between the voltage and the current measured at the PCC. Different grid models have been used in the technical literature using different levels of complexity. However, the grid impedance is mainly inductive and therefore the grid impedance was considered having a resistor(R)-inductor(L) (RL) model.

1.3 Main contributions

In the opinion of the author, the main contributions of this PhD research project are enumerated in the following, in the order they appear presented in the thesis.

Chapter 2 presents a comprehensive review about grid voltage monitoring techniques used for single-phase systems in order to give a clear classification of the existent methods presented in the technical literature.

- **New voltage monitoring method**

A single-phase Phase-Locked Loop (PLL) algorithm using an Orthogonal Signal Generator (OSG) based on the Second Order Generalized Integrator (SOGI) and including an offset rejection technique was proposed in Chapter 2. Additionally, the discrete implementation of the algorithm was given in order to avoid any possible challenges faced by implementing a discrete system. The proposed algorithm proved to be robust and able to handle all types of grid voltage distortions giving great results.

- **New grid impedance estimation methods**

Three different methods have been developed with relation to the grid impedance estimation. These methods are presented along Chapter 3. The first method using harmonic injection technique was developed based on similar existent methods. However, a new calculation algorithm has been proposed to ease the computation of the grid impedance, thus avoiding the heavy computation algorithm based on Discrete Fourier Transform (DFT). A second grid impedance estimation method based on active (P) and reactive (Q) power variations was proposed. The major benefit of this method is that it can use the natural active power variations of the input power sources such as WTs or PVs. A deliberate active power variation is produced only when necessary, thus minimizing the distortion of the output power. However, the reactive power variation has to be produced deliberately at every disturbance cycle. The third proposed grid impedance estimation method is based on identification techniques. This method has the merit to combine the advantages of both active and passive grid impedance estimation methods.

- **New islanding detection method**

Even though numerous anti-islanding detection methods exist already, most of the passive methods are not accurate enough and a large part of the active methods are too

invasive thus affecting the output power quality of the grid-connected converters. Consequently, an accurate and less-disturbing islanding detection algorithm has been developed and tested successfully, as presented in Chapter 4. It is worth mentioning here that the proposed anti-islanding algorithm is under patent pending. Moreover, a non-exclusive license was bought by a PV inverters manufacturer.

- **New active damping method**

Regarding the advanced control of DPGS, an active damping technique for grid-connected systems using LCL filters is presented in §6.2.2. The proposed method is based on a notch filter, whose stopband can be automatically adjusted in relation with an estimated value of the grid impedance.

1.4 List of scientific publications derived from this thesis

The results of the research project documented in this thesis have been published in international conference proceedings and journals. The list of these publications is as follows.

I. M. Ciobotaru, R. Teodorescu, and F. Blaabjerg, "Control of single-stage single-phase PV inverter," *Proc. of EPE*, 2005, pp. P1-P10.

II. M. Ciobotaru, R. Teodorescu, and F. Blaabjerg, "Improved PLL structures for single-phase grid inverters," *Proc. of PELINCEC,* 2005, pp. 6.

III. A. V. Timbus, M. Ciobotaru, R. Teodorescu, and F. Blaabjerg, "Adaptive resonant controller for grid-connected converters in distributed power generation systems," *Proc. of APEC*, 2006, pp. 6.

IV. M. Ciobotaru, R. Teodorescu, and F. Blaabjerg, "A new single-phase PLL structure based on second order generalized integrator," *Proc. of PESC*, 2006, pp. 1-6.

V. M. Ciobotaru, T. Kerekes, R. Teodorescu, and A. Bouscayrol, "PV inverter simulation using MATLAB/Simulink graphical environment and PLECS blockset," *Proc. of IECON*, 2006, pp. 5313-5318.

VI. P. Rodriguez, A. Luna, M. Ciobotaru, R. Teodorescu, and F. Blaabjerg, "Advanced grid synchronization system for power converters under unbalanced and distorted operating conditions," *Proc. of IECON*, 2006, pp. 5173-5178.

VII. M. Ciobotaru, R. Teodorescu, and F. Blaabjerg, "Control of single-stage single-phase PV inverter," *EPE Journal*, 2006, vol. 16, no. 3, pp. 20-26.

VIII. M. Ciobotaru, R. Teodorescu, and F. Blaabjerg, "On-line grid impedance estimation based on harmonic injection for grid-connected PV inverter," *Proc. of ISIE*, 2007, pp. 2437-2442.

IX. M. Ciobotaru, R. Teodorescu, P. Rodriguez, A. Timbus, and F. Blaabjerg, "Online grid impedance estimation for single-phase grid-connected systems using PQ variations," *Proc. of PESC*, 2007, pp. 2306-2312.

X. A. V. Timbus, P. Rodriguez, R. Teodorescu, and M. Ciobotaru, "Line impedance estimation using active and reactive power variations," *Proc. of PESC*, 2007, pp. 1273-1279.

XI. F. Iov, M. Ciobotaru, D. Sera, R. Teodorescu, and F. Blaabjerg, "Power electronics and control of renewable energy systems," keynote paper, *Proc. of PEDS*, 2007, pp. P-6-P-28.

XII. M. Ciobotaru, R. Teodorescu, and V. G. Agelidis, "Offset rejection for PLL based synchronization in grid-connected converters," *Proc. of APEC*, 2008, pp. 1611-1617.

XIII. M. Ciobotaru, V. G. Agelidis, and R. Teodorescu, "Accurate and less-disturbing active anti-islanding method based on PLL for grid-connected PV inverters," *Proc. of PESC*, 2008, pp. 4569 – 4576.

XIV. M. Ciobotaru and R. Teodorescu, "Software active anti-islanding method based on phase modulation for photovoltaic grid-connected inverters," *Patent pending*, Aalborg University, 2007.

The relation between the chapters of this thesis and the publications mentioned above is given in Table 1.1.

Chapter number	Publications
Chapter 2	[II], [IV], [VI], [XII]
Chapter 3	[VIII], [IX], [X]
Chapter 4	[XIII], [XIV]
Chapter 5	[I], [V], [VII], [XI]
Chapter 6	[III]

Table 1.1. Relation between the scientific publications and the thesis chapters.

The results of this thesis have also contributed to other projects related with grid-connected converters and selected output has been published in the following papers and reports. However, these papers will not be included in this thesis.

1. M. Ciobotaru, F. Iov, P. Zanchetta, Y. De Novaes, and F. Blaabjerg, "Study and analysis of a natural reference frame current controller for a multi-level H-bridge power converter," *Proc. of PESC 2008*, pp. 2914-2920.

2. M. Ciobotaru, F. Iov, P. Zanchetta, Y. De Novaes, and J. Clare, "A stationary reference frame current control for a multi-level H-bridge power converter for universal and flexible power management in future electricity network," *Proc. of PESC 2008*, pp. 3943-3949.

3. F. Iov, M. Ciobotaru, and F. Blaabjerg, "Power electronics control of wind energy in distributed power systems," keynote paper, *Proc. of OPTIM 2008*, pp. XXIX-XLIV.

4. M. Ciobotaru, F. Iov, Y. Fan, S. Biffaretti, and P. Zanchetta, "Advanced power converters for universal and flexible power management in future electricity network," Report for EU Research Project on Control Strategies for UNIFLEX, Nottingham - School of Electrical and Electronic Engineering, University Park, 2008, 162 pages.

1.5 Outline of the thesis

The thesis is divided into three main parts. The **Part I** contains Chapter 2, Chapter 3 and Chapter 4 and is called "Grid Condition Detection". The **Part II** includes Chapter 5 and Chapter 6 and is called "Control of Single-Phase DPGS". Finally, **Part III**, called "List of Publications", presents the papers published thus far from this research project.

The first two parts of the thesis including the "Introduction" and the "Conclusions" were structured in seven chapters.

Chapter 2 starts with an overview about grid voltage monitoring techniques. Next, a classification of different OSG techniques used by the single-phase PLLs is given. A complete algorithm based on SOGI for monitoring the grid voltage is proposed and described in detail. Next, the offset rejection capabilities as well as the discrete implementation of the proposed algorithm are presented. Finally, simulation and experimental results are given to prove the effectiveness of the proposed algorithm.

Chapter 3 begins with an overview about grid impedance estimation techniques. The overview is then followed by a short presentation of the applications well suited for grid impedance estimation. Next, three methods of grid impedance estimation are presented. The first method uses the harmonic injection; the second method is based on active and reactive output power variations of the grid-connected converter and the third method is based on identification techniques. The simulation and selected experimental results are presented after each proposed method.

Chapter 4 introduces an islanding detection technique. The chapter starts with an overview of the existent anti-islanding methods. Then, an accurate and less-disturbing active islanding detection method is proposed and described in detail. Selected results are given to demonstrate the effectiveness of the proposed algorithm.

Chapter 5 gives in the first part an overview about the general control structure of a single-phase DPGS. The second part of this chapter presents an improved DC voltage controller which is able to remove the 100 Hz typical ripple from the measured DC voltage. The last part of the chapter introduces a comparison between the classical Proportional Integral (PI) and the Proportional Resonant (PR) current controllers.

Chapter 6 describes methods of how to make the grid-connected converters more flexible using advanced control techniques. The main focus is to increase the performances and the robustness of the current controller. The chapter is divided into two main parts. In the first part, a frequency adaptive PR controller has been developed and tested. The second part presents an adaptive current controller based on the estimation of the grid impedance.

Chapter 7 starts summarizing the work presented along this thesis. The main conclusions are deduced based on the achieved results. Finally, the directions for future work are outlined.

Part I

Grid Condition Detection

Chapter 2

Grid Voltage Monitoring

This chapter begins with an overview about grid voltage monitoring techniques. Next, a classification of different OSG techniques used by the single-phase PLLs is given. A complete algorithm based on SOGI for monitoring the grid voltage is proposed and described in detail. Next, the offset rejection capabilities as well as the discrete implementation of the proposed algorithm are presented. Finally, simulation and experimental results are given to prove the effectiveness of the proposed algorithm.

2.1 Introduction

A DPGS require a high degree of grid condition detection in order to meet standard specifications in terms of power quality and safety [7-11].

An accurate and fast detection of the phase angle, amplitude and frequency of the utility voltage is required by the grid-connected converters in order to guarantee the correct generation of the reference signals and to meet the demands regarding the operation boundaries with respect to voltage amplitude and frequency values required by standards. The standard IEC61727-2002 [9] is given as an example in this regard. This standard applies to the utility-interconnected PV power systems utilizing static (solid-state) non-islanding inverters for the conversion of DC to AC.

According to IEC61727-2002 [9], the boundaries of operation with respect to grid voltage amplitude and frequency are shown in Figure 2.1. A continuous operation area between 0.85 and 1.10 *p.u.* and ± 1 Hz around the nominal frequency is defined. Abnormal conditions can arise on the utility grid which requires a response from the grid-connected PV system. This response is to ensure the safety of utility maintenance personnel and the general public, as well as to avoid damage to connected equipment, including the PV system. The abnormal utility conditions of concern are the grid voltage amplitude and frequency excursions above or below the values stated in Figure 2.1. The grid-connected PV system has to cease to energize the utility line within the specified time interval if the voltage amplitude or frequency exceeds the predefined

limits. The most restrictive requirement is when the maximum trip time is 0.05 seconds for a grid voltage amplitude excursion above 1.35 *p.u.* (Figure 2.1). An accurate and fast grid voltage monitoring algorithm is required in order to comply with these requirements.

The principle of the grid voltage monitoring, which consists in getting the parameters of the voltage at the PCC, is presented in Figure 2.2 and (2.1). The voltage equation is divided in two main parts: the fundamental and the harmonics. The grid phase angle $(\omega \cdot t)$ is mostly used for synchronization. Additionally, the detection of the grid phase angle can also be used for anti-islanding detection algorithms [17]. The angular frequency of the grid voltage (ω) is used for over/under frequency detection algorithms but also to provide information to the control system (such as resonant controllers or filters which need to adjust their resonance frequency). The amplitude of the grid voltage $(\widehat{V})$ is required for over/under voltage and to provide information to the control system (such as power feed forward loop). Additional information such as harmonic content of the grid voltage can be required for some algorithms (e.g. harmonics monitoring for the passive anti-islanding methods [17] or active power filters applications [18, 19]).

$$v(t) = \underbrace{\widehat{V} \cdot \sin\left(\omega \cdot t\right)}_{Fundamental} + \underbrace{\sum \widehat{V_h} \cdot \sin\left(\omega_h \cdot t + \theta_h\right)}_{Harmonics} \tag{2.1}$$

This chapter focuses on the phase angle, frequency and amplitude estimation of the grid voltage. A short overview about methods used for monitoring the grid voltage is presented next.
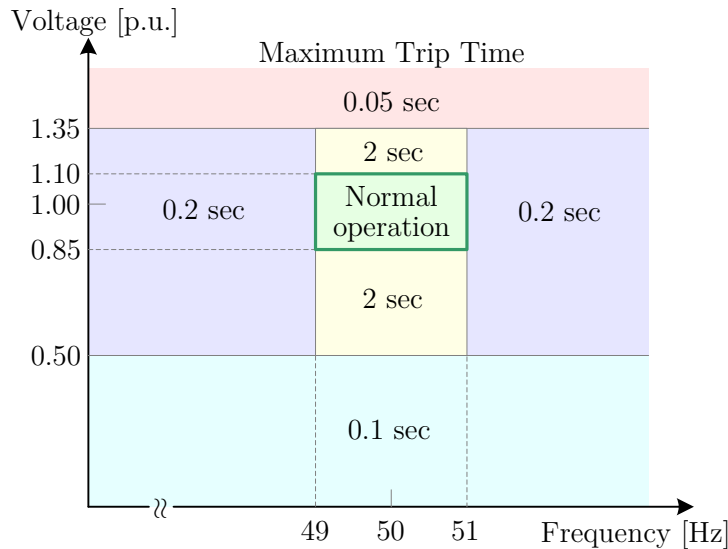
Figure 2.1. Maximum trip times for both voltage amplitude and frequency according to the standard IEC61727-2002 [9].
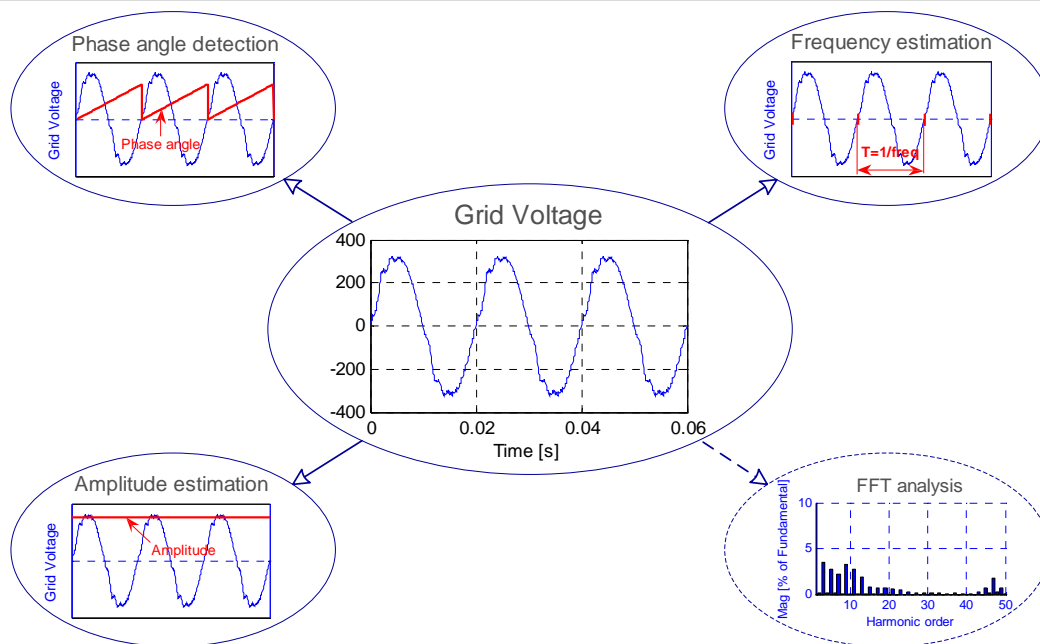
Figure 2.2. The principle of the grid voltage monitoring.

2.2 Overview of the grid voltage monitoring techniques

Numerous methods using different techniques for monitoring the grid voltage are presented in the technical literature about DPGS. However, some of the methods are not always categorized properly, thus leading to confusion. Therefore, to bring clarity in this regard, the techniques used for monitoring the grid voltage can be organized as presented in Figure 2.3.

The grid voltage monitoring techniques can be split into two main categories, namely methods based on Zero-Crossing Detection (ZCD) which does not involve a phase controller and methods based on PLL which includes a phase controller. Furthermore, the methods based on a PLL can also be split into three other categories, namely PLL based on the ZCD, on the arctangent function ($\tan^{-1}$) and on the Park Transform. All these techniques are presented in more details in the coming sections.
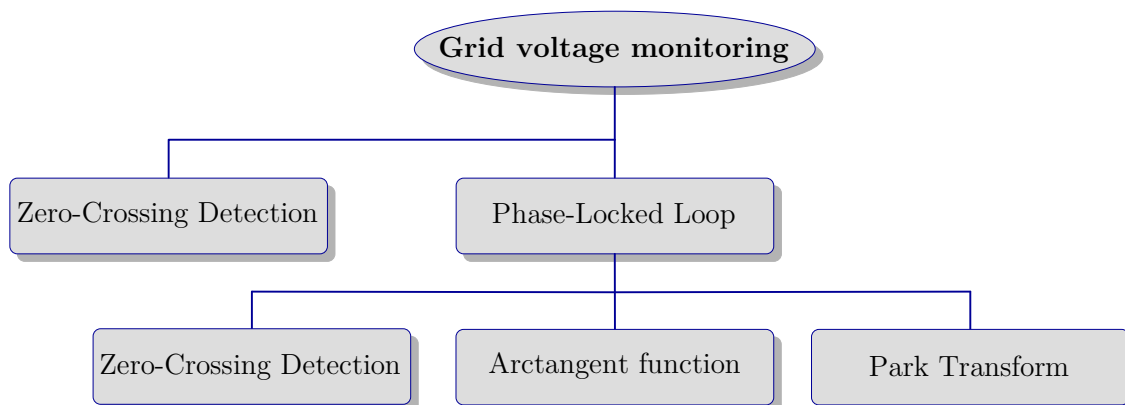
Figure 2.3. Classification of the grid voltage monitoring techniques for DPGS.

2.2.1 Grid voltage monitoring based on ZCD

A simple method of obtaining the phase and frequency information is to detect the zero-crossing point of the grid voltage [20-22]. The method, as presented in Figure 2.4, is based on counting the zero-crossings of the grid voltage, thus the frequency of the fundamental is estimated. Then, the phase-angle of the grid voltage is obtained by integrating the estimated frequency and no phase controller is involved.

This method has two major drawbacks. Since the zero-crossing point can be detected only at every half cycle of the utility frequency, the phase tracking action is impossible between the detecting points and thus a fast dynamic performance cannot be obtained [23]. Some work has been done in order to alleviate this problem using multiple level crossing detection as presented in [24]. However, this method increases the complexity of the ZCD technique.

Significant line voltage distortion due to notches caused by power device switching and/or low frequency harmonic content can easily corrupt the output of a conventional ZCD [25]. Therefore, the zero-crossing detection of the grid voltage needs to obtain its fundamental component at the line frequency. This task is usually made by a filter. To avoid the delay introduced by this filter, numerous techniques are used in the technical literature. Methods based on advanced filtering techniques are presented in [25-29]. Other methods use neural networks for detection of the true zero-crossing of the grid voltage waveform [30-32]. Furthermore, an improved accuracy in the integrity of the zero-crossing can also be obtained by reconstructing a voltage representing the grid voltage [33-36].

However, starting from its simplicity, when the two major drawbacks are alleviated by using advanced techniques, the zero-crossing method proves to be rather complex and unsuitable for applications which require accurate and fast tracking of the grid voltage vector.
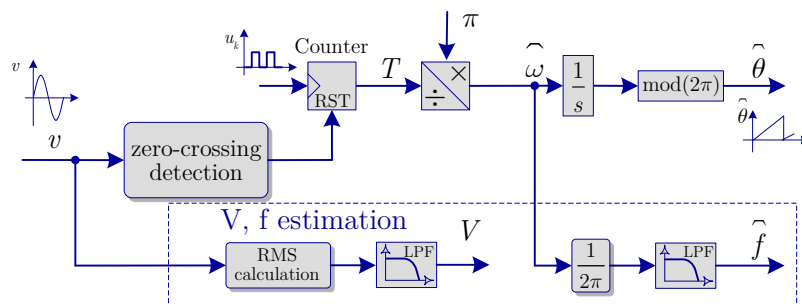
Figure 2.4. Grid voltage monitoring based on Zero-Crossing Detection without including a phase controller.

2.2.2 Grid voltage monitoring based on PLL

Recently, there has been an increasing interest in PLL techniques for grid-connected converter systems [37]. Typically, the PLL technique is applied in communication technologies. Though, it has been proven that its application to the grid-connected converter systems was a success [22, 23, 37-54], [II], [IV], [VI]. Used for such systems,

the PLL is a grid voltage phase detection algorithm. The main task of the PLL algorithm is to provide the phase angle of the grid voltage which is mostly used to synchronize the output current of the converter with the voltage at the PCC for the cases when no reactive power is required. Moreover, using the PLL algorithm, the grid voltage parameters such as amplitude and frequency, can be easily monitored.

The PLL is composed of a phase comparator which provides an error signal (ε_θ) to a PI controller, as it can be seen in Figure 2.5. An initial frequency value (ω_{IC}) is then added to the output of the PI controller resulting the estimated frequency ($\hat{\omega}$) of the grid voltage. The advantage of adding ω_{IC} to the output of the PI controller is a better dynamic performance every time the PLL is reset. Then, the estimated phase-angle ($\hat{\theta}$) of the grid voltage is obtained by integrating the estimated frequency. To provide the phase-angle reference to the phase comparator, the following three techniques can be used: the ZCD, the arctangent function ($\tan^{-1}$) or the Park Transform.

2.2.2.1 ZCD based PLL

The ZCD technique can also be used to provide the phase-angle reference for a PLL [22] (Figure 2.5). The integrator is reset to 0 every time the positive slope zero-crossing is reached and to π every time the negative slope zero-crossing is reached, thus providing the phase-angle reference for the PLL. The shortcomings of this method are similar to the methods presented in §2.2.1.
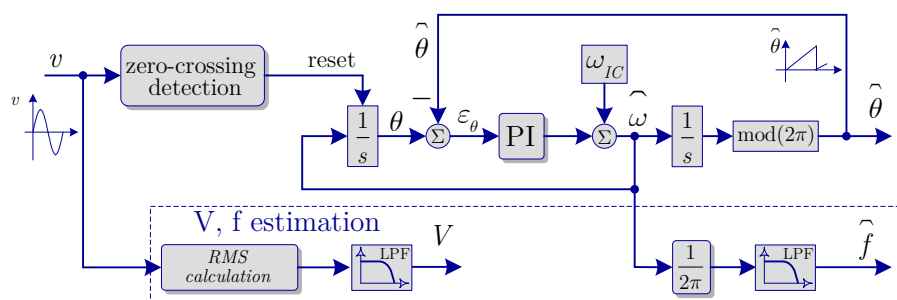
Figure 2.5. PLL structure based on the ZCD.

2.2.2.2 Arctangent function based PLL

The arctangent function technique (Figure 2.6) is another solution for detecting the phase-angle and the frequency of the grid voltage [22, 45]. An orthogonal voltage system is required to implement this technique. This method is used in motor drives applications to transform the feedback signals to a reference frame suitable for control purposes [55]. However, this method has the drawback that it requires advanced filters to obtain an accurate detection of the phase angle and frequency in the case of a distorted grid voltage [53]. Even though, the method using the arctangent function is easy to understand, it has implementation difficulties related with the avoidance of divisions by zero. Therefore, this technique is not well suited for grid-connected converter applications.
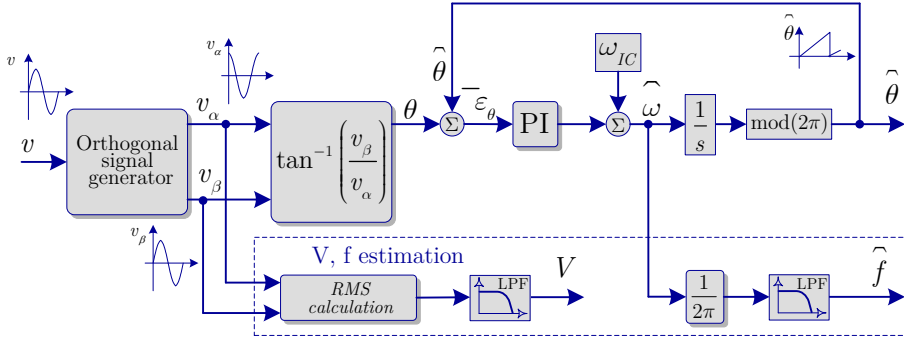
Figure 2.6. PLL structure based on the arctangent function.

2.2.2.3 Park Transform based on PLL

The most widely used PLL is based on the Park Transform, as presented in Figure 2.7 [IV], [V]. Like in the case of the arctangent function technique, an orthogonal voltage system is required for the PLL based on the Park Transform.

A more detailed structure of the PLL based on the Park Transform is given in Figure 2.8 for a better understanding of how the phase comparator is obtained through the use of the Park Transform. The input of the PI controller (ε_θ) is defined by (2.2). The result is not the difference between the angles but it depends on it. The grid voltage (v) is considered normalized.

$$\varepsilon_\theta = v_q = -\sin\hat{\theta} \cdot \cos\theta + \cos\hat{\theta} \cdot \sin\theta = \sin(\theta - \hat{\theta}) \tag{2.2}$$
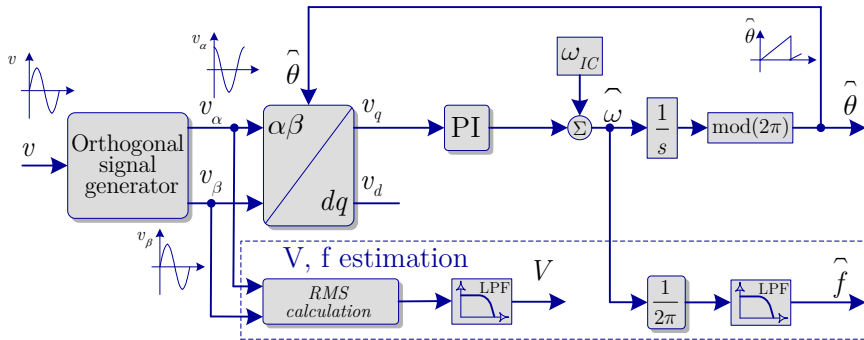
Figure 2.7. PLL structure based on the Park Transform.
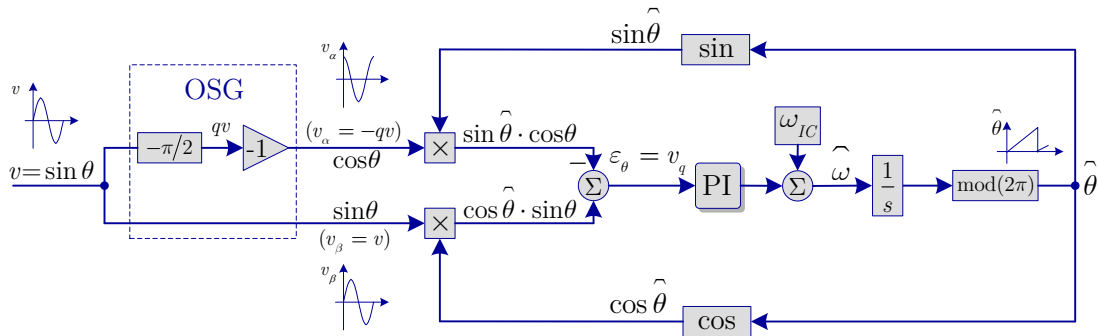
Figure 2.8. PLL structure based on the Park Transform in detail.

The sine function is nonlinear, and for small values of $\sin(\theta - \hat{\theta})$ (when θ and $\hat{\theta}$ are almost equal), (2.2) can be expressed as (2.3). Thus, the phase comparator is obtained through the use of the Park Transform.

$$\varepsilon_\theta = v_q = \sin(\theta - \hat{\theta}) \approx \theta - \hat{\theta} \tag{2.3}$$

In a three-phase system, the orthogonal voltage system is obtained through the Clarke Transform. However, for a single-phase system, the orthogonal voltage system has to be artificially generated [22]. Therefore, more attention is to be paid for the orthogonal voltage system techniques.

Next section discusses about techniques used for generating the orthogonal voltage system. The structure responsible for generating the orthogonal voltage system is called Orthogonal Signal Generator (OSG).

2.3 Overview of the OSG techniques

In the technical literature, several techniques for generating the orthogonal voltage components from a single-phase system are described, some of which are compared in [22, 37, 56].

The OSG provides the quadrature (qv) of the input signal (v), as it can be seen from Figure 2.9. In order to have an analogy with the voltage components in the stationary coordinates (v_α and v_β), the convention presented in (2.4) is used through the entire thesis. For instance, v_α and v_β are required by the arctangent and the Park Transform techniques used by a PLL structure.

$$\begin{cases} v_\alpha = -qv = \widehat{V}\cos(\omega t) \\ v_\beta = v = \widehat{V}\sin(\omega t) \end{cases} \tag{2.4}$$

- $\widehat{V}$ represents the amplitude and ωt represents the phase-angle of the input voltage signal.

Figure 2.9. a) Orthogonal voltage system; b) Stationary reference frame.

As it can be noticed from Figure 2.9 and (2.4), the input signal (v) is a function of $\sin(\omega t)$ while its quadrature (qv), generated by the OSG, is a function of $\cos(\omega t)$. However, most OSGs cannot provide directly v_α, of which phase-angle leads t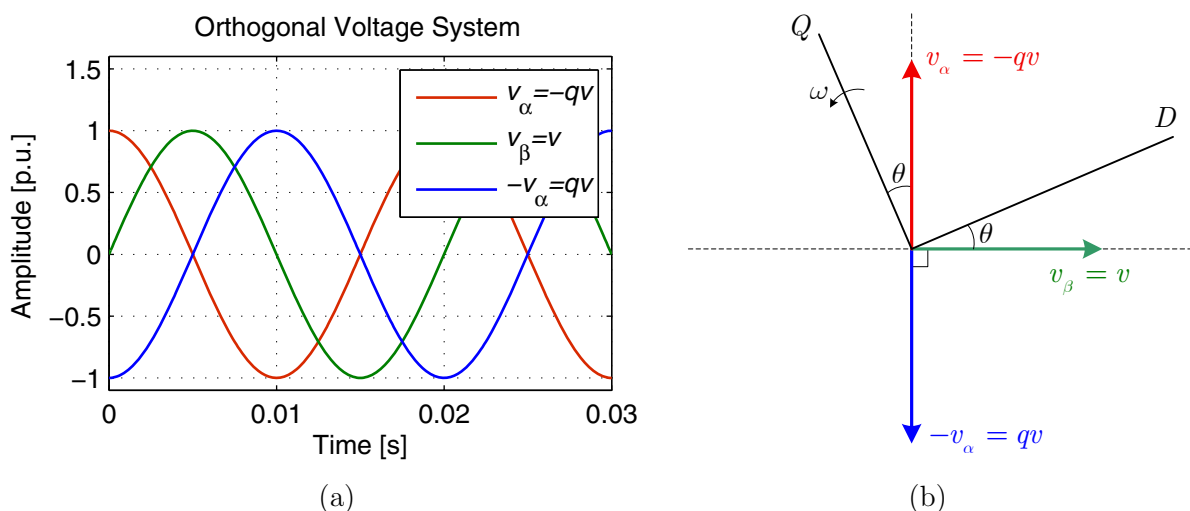he input signal phase-angle by $\pi/2$. Instead, it generates a quadrature signal (qv), of which phase-angle lags the input signal phase-angle by $\pi/2$. Therefore, to obtain v_α, a minus sign should be considered, as presented in (2.4). For example, the Park Transform from (2.5) will be equivalent to the one presented in (2.6).

$$\begin{cases} v_d = v_\alpha \cdot \cos\hat{\theta} + v_\beta \cdot \sin\hat{\theta} \\ v_q = -v_\alpha \cdot \sin\hat{\theta} + v_\beta \cdot \cos\hat{\theta} \end{cases} \tag{2.5}$$

$$\begin{cases} v_d = -qv \cdot \cos\theta + v \cdot \sin\theta \\ v_q = qv \cdot \sin\theta + v \cdot \cos\theta \end{cases} \tag{2.6}$$

An easy technique of generating the orthogonal voltage system for a single-phase system incorporates a transport delay function, which is responsible for introducing a phase shift of $\pi/2$ with respect to the fundamental frequency of the input signal [II]. A related method, but more complex of creating a phase shift of $\pi/2$, uses the Hilbert Transform [37, 40].

Another different method of generating the orthogonal voltage system is based on inverse Park Transform [37, 50, 54], [II]. In [22], a method using estimated phase and amplitude is presented. Other methods used as orthogonal signal generators are based on filters, namely second order filter, first order filter and all pass filter [22].

Other methods use a Kalman estimator-based filter [42] or a resonant structure based on SOGI [57], [IV], which is derived from Kalman estimator-based filter, being a simplified form of this. There are several techniques for generating the orthogonal voltage system and six OSG techniques are presented.

2.3.1 Transport delay based OSG

The transport delay method is easy to implement through the use of a First-In First-Out (FIFO) buffer. The buffer size is set to one-quarter of the number of samples contained in one cycle of the fundamental. The general structure of the OSG based on the transport delay technique is presented in Figure 2.10.
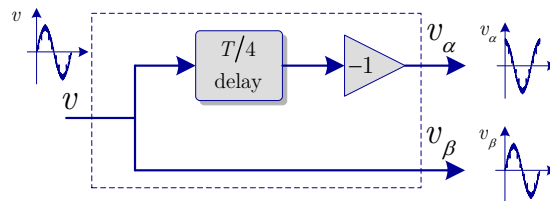

Figure 2.10. OSG based on transport delay.

Generally speaking, the algorithm is easy to use and the tuning process does not pose special difficulties. Though, the transport delay technique has two major draw-

backs: 1) it is not frequency adaptive, thus errors can occur when the grid frequency experience fluctuations, due to its fixed delay, and 2) it creates an unfiltered orthogonal voltage system. However, some work has been done to alleviate these shortcomings as presented in [58], [II]. In order to eliminate the errors caused by the grid frequency variations, the cosine-component of the PLL output $(\cos\hat{\theta})$ used in the Park Transform, as shown in Figure 2.8, is produced using the same delay procedure used to obtain the cosine-component of the grid voltage (v_α), thus the errors cancel each other [II].

2.3.2 Hilbert Transform based OSG

A related but more complex method compared to the transport delay technique, is to generate the quadrature signal through the use of Hilbert Transform [37, 40], as presented in Figure 2.11. For a real signal *f(t)*, the Hilbert Transform (*H*) is defined as shown in (2.7).

$$f(t) = H(f) = \frac{1}{\pi} P \int_{-\infty}^{\infty} \frac{f(\tau)}{t - \tau} d\tau \tag{2.7}$$

- where P is Cauchy principal value.

By means of the Hilbert Transform, it is possible to generate a signal which is orthogonal with the input signal. As a drawback, the ideal Hilbert Transform, as defined in (2.7), leads to a non-causal system and it is not practically realizable. However, the Hilbert Transform can be approximated with a high-order Finite Impulse Response (FIR) filter. The main difference of the transport delay technique when compared with the Hilbert Transform is that, all the harmonic content of the input signal is subjected to the same time delay. As concluded in [37], the Hilbert Transform does not represent a good solution for creating an orthogonal voltage system due to its complexity, increased computational time and poor performances.
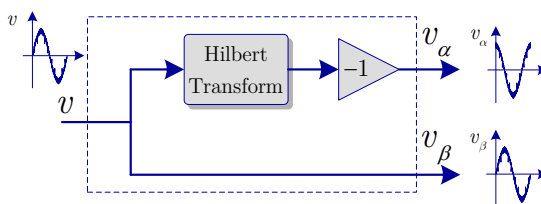
Figure 2.11. OSG based on Hilbert Transform.

2.3.3 Estimated phase angle and amplitude based OSG

A simple OSG technique is presented in Figure 2.12 [22]. The method is based on the estimated amplitude $(\widehat{V})$ and phase-angle $(\hat{\theta})$, as provided by the PLL structure. The estimated amplitude $(\widehat{V})$ can be multiplied by $\cos\hat{\theta}$ resulting:

$$v_\alpha = \widehat{V} \cos\hat{\theta} \cong \widehat{V} \cos\theta \tag{2.8}$$
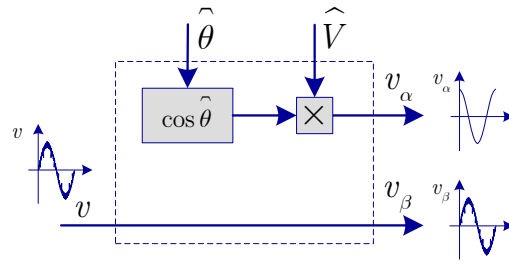
Figure 2.12. OSG based on estimated phase angle and amplitude.

Therefore, the quadrature of the input signal is obtained in a very simple way. However, this method has the drawback that it is highly dependent on the settling time of the PLL, thus resulting in poor overall dynamics. Moreover, the PI controller of the PLL is difficult to tune, due to the interdependent loops created by using the estimated amplitude and phase-angle. The poor performances of this method are concluded in [22].

2.3.4 Inverse Park Transform based OSG

A different method to generate the orthogonal system uses the inverse Park Transform, presented in Figure 2.13 [54].

As it can be seen from Figure 2.13, a single phase voltage (v) and an internally generated signal (v_α) are used as input to a Park Transform block ($\alpha\beta - dq$). The signal v_α is obtained through the use of an inverse Park Transform, where the inputs are the d and q-axis outputs of the Park Transform, fed through first order pole blocks. The two first order lag blocks added to the structure must be adequately tuned in order to guarantee the performance of the single-phase PLL [50]. The inner loop (the α-axis voltage loop) must be fast enough so that the outer loop performs the tracking function with the α-axis voltage stabilized. The stationary frame is seen by the outer loop as if it was obtained from a three phase system and thus the tracking of the "virtual" utility voltage vector can be performed.
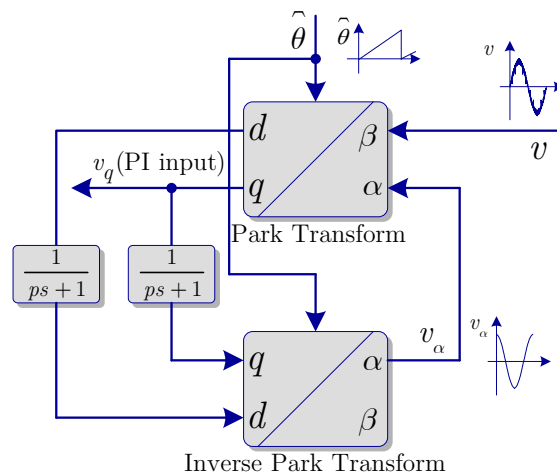
Figure 2.13. OSG based on inverse Park Transform.

The tuning of the two first order lag blocks is performed using a methodology presented in [50].

Although the algorithm of the inverse Park Transform is easy to implement, requiring only an inverse Park and two first-order low-pass filters, the tuning of the PI controller and the choice of the time constant of the filters are difficult processes, as compared with the other PLL algorithms. This is due to the presence of the two interdependent nonlinear loops, which makes linearization and use of linear system analysis tools more troublesome [37].

2.3.5 Filter based OSG

Another way of creating an orthogonal voltage system is through the use of a Low-Pass Filter (LPF) or an All-Pass Filter (APF). In [22], three of such methods are presented. The methods are based on the second order LPF, first order LPF and on the APF.

2.3.5.1 Second order filter based OSG

The OSG method based on the second order filter is shown in Figure 2.14 [22]. The damping ratio is $\zeta = 1/\sqrt{2}$ and the undamped natural frequency ω_n has the same value as the estimated frequency $\widehat{\omega}$. Having as input the voltage signal $(v = \widehat{V}\sin(\omega t))$, the second order filter produces an output signal with a $-\pi/2$ phase-angle shift and an amplitude of $\widehat{V}/\sqrt{2}$. Therefore, v_α is calculated by (2.9).

$$v_\alpha \cong \left\{ \left(-\sqrt{2}\right)\left[\frac{\widehat{V}}{\sqrt{2}}\sin\left(\omega t - \frac{\pi}{2}\right)\right]\right\} = \widehat{V}\cos\left(\omega t\right) \tag{2.9}$$

The second order filter, as presented in Figure 2.14, is frequency dependent, thus the estimated frequency $(\widehat{\omega})$ of the PLL can be used for adjusting the value of the undamped natural frequency (ω_n). By doing so, the second-order filter based OSG is not affected by the grid frequency variations. As a drawback, the OSG based on the second order filter is not able to filter both of the orthogonal voltages $(v_\alpha$ and $v_\beta)$. Thus, the advantage of the filtered v_α is minimized.
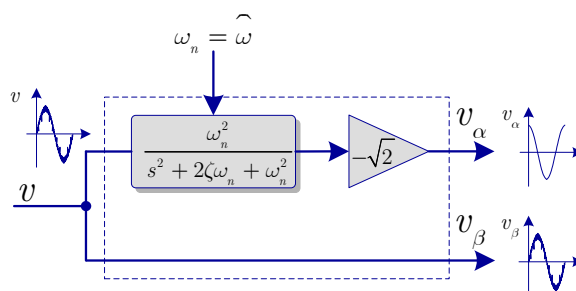
Figure 2.14. OSG based on second-order low-pass filter.

2.3.5.2 First order filter based OSG

Figure 2.15 shows another filter based OSG which uses a first order filter [22]. The cutoff frequency (ω_n) has the same value as the estimated frequency $(\widehat{\omega})$. Having the voltage signal $(v = \widehat{V}\sin(\omega t))$ as input, the first order filter produces an output signal equal to $\left(\widehat{V}/\sqrt{2}\right)\sin\left(\omega t - \pi/4\right)$. Therefore, v_α is calculated by (2.10).

$$v_\alpha = v - 2\cdot\frac{\widehat{V}}{\sqrt{2}}\sin\left(\omega t - \frac{\pi}{4}\right) = \widehat{V}\sin\left(\omega t\right) - 2\cdot\frac{\widehat{V}}{\sqrt{2}}\sin\left(\omega t - \frac{\pi}{4}\right) = \widehat{V}\cos\left(\omega t\right) \quad (2.10)$$

Similar to the second order filter based OSG, the first order based OSG can use the estimated frequency $(\widehat{\omega})$ of the PLL to calculate the undamped natural frequency $(\omega_n = \widehat{\omega})$, thus it is not affected by the grid frequency variations. However, as concluded in [22], the steady state performance of the first order filter based OSG is worse than the second order filter based OSG. As a drawback, the OSG based on the first order filter is not able to filter both of the orthogonal voltages (v_α and v_β). Thus, the advantage of the filtered v_α is minimized.

Figure 2.15. OSG based on first-order low-pass filter.

2.3.5.3 All-pass filter based OSG

Figure 2.16 presents an OSG based on the all-pass filter [22]. The damping ratio is $\zeta = 1$ and the undamped natural frequency is $\omega_n = \left(\sqrt{2} - 1\right)\cdot\widehat{\omega}$. Having as input the grid voltage $(v = \widehat{V}\sin(\omega t))$, the all-pass filter produces an output signal with a $-\pi/2$ phase-angle shift and an amplitude of $\widehat{V}$. Therefore, v_α is calculated by (2.11).

$$v_\alpha = \widehat{V}\cos\widehat{\theta} \cong \widehat{V}\cos\theta \quad (2.11)$$
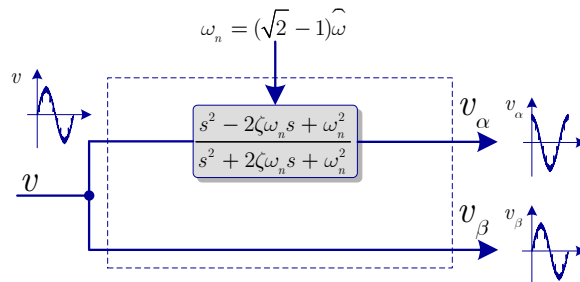
Figure 2.16. OSG based on all-pass filter.

Unlike the other OSG techniques previously presented, the all-pass filter based OSG is able to directly produce the component v_α. This is due to the fact that the all-pass filter (Figure 2.16) is able to produce an output signal whose phase-angle leads the input voltage phase-angle by $\pi/2$. Similar to the second order filter and first order filter based OSG, the all-pass filter based OSG can use the estimated frequency ($\widehat{\omega}$) of the PLL to calculate the undamped natural frequency ($\omega_n = \left(\sqrt{2} - 1\right) \cdot \widehat{\omega}$), thus it is not affected by the grid frequency variations. However, as concluded in [22], the steady state performances of the all-pass filter based OSG are worse than second order filter based OSG. Moreover, the OSG based on the all-pass filter is not able to filter any of the orthogonal voltages (v_α and v_β).

2.3.6 SOGI based OSG

All of the OSG methods described thus far present at least one of the following shortcomings: sensitivity to frequency variations, poor dynamic performance, poor or nonfiltering, high sensitivity to offset, high complexity and implementation difficulties. In order to overcome most of these shortcomings, another OSG technique based on the SOGI has been proposed in [IV]. The approach has been used before in order to compute the instantaneous active and reactive power [57]. After more investigations turns out that the OSG based on SOGI (OSG-SOGI) is a simplified form derived from adaptive Kalman filtering theory [42]. Through the investigations, the OSG-SOGI proved to be the most promising candidate out off all OSG techniques presented above.

2.4 OSG-SOGI based PLL using the Park Transform

The PLL structure using Park Transform and the OSG-SOGI has been chosen as the most promising candidate for the grid voltage monitoring. The theory, the design, the implementation and the operation of the OSG-SOGI are presented and verified in this section by both simulations and experiments.

2.4.1 OSG-SOGI structure

The structure of the OSG-SOGI is shown in Figure 2.17. The input signal v is the voltage signal measured at the PCC. As output signals, two sine waves (v' and qv') with a phase shift of $\pi/2$ are generated. The component v' has the same phase and amplitude as the fundamental of the input voltage signal (v).

Figure 2.17. OSG-SOGI structure.

The SOGI acts like an infinite gain band-pass filter whose transfer function is defined in (2.12) [42, 45, 57], [IV]. The closed-loop transfer functions ($H_d = v'/v$ and $H_q = qv'/v$) of the OSG-SOGI, as presented in Figure 2.17, are defined in (2.13) and (2.14) respectively.

$$H_{SOGI}(s) = \frac{\omega_n s}{s^2 + \omega_n^2} \tag{2.12}$$

$$H_d(s) = \frac{v'}{v}(s) = \frac{k\omega_n s}{s^2 + k\omega_n s + \omega_n^2} \tag{2.13}$$

$$H_q(s) = \frac{qv'}{v}(s) = \frac{k\omega_n^2}{s^2 + k\omega_n s + \omega_n^2} \tag{2.14}$$

- where ω_n represents the undamped natural frequency of the SOGI which is equal to the estimated frequency ($\omega_n = \widehat{\omega}$);
- k is the gain which affects the bandwidth of the OSG-SOGI and is equal to the double of the damping ratio ($k = 2\zeta$).

The Bode representations of the closed-loop transfer functions $H_d = v'/v$ and $H_q = qv'/v$, for the proposed OSG-SOGI at different values of gain k, are shown in Figure 2.18a and Figure 2.18b. The tuning of the proposed structure is frequency dependent, thus problems can occur when grid frequency has fluctuations. As a consequence, an adaptive tuning of the structure with respect to its resonance frequency is required. Therefore, the resonance frequency of the SOGI is adjusted online using the estimated voltage frequency ($\widehat{\omega}$) as provided by the PLL.

Using the OSG-SOGI, the input voltage signal (v) is filtered resulting two clean orthogonal voltage waveforms (v' and qv'), due to the resonance frequency of the SOGI at $\widehat{\omega}$.
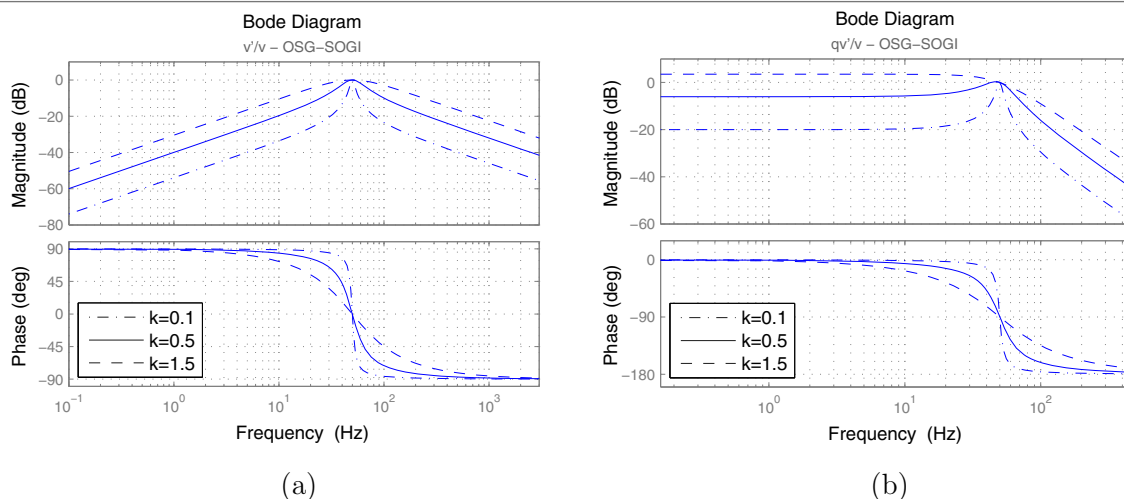
Figure 2.18. Bode plots of the closed-loop transfer functions: a)$H_d = v'/v$ and b) $H_q = qv'/v$ for different values of the gain k.

The OSG-SOGI combines all the advantages of the OSG methods presented in §2.3. Specifically, by using the OSG-SOGI (Figure 2.17), the following three main tasks can be accomplished: - generation of the orthogonal voltage system; - filtering of the orthogonal voltage system without delay; - making the OSG structure frequency adaptive. However, the OSG-SOGI (Figure 2.17), has a common drawback specific to all OSG methods presented in §2.3. Namely, all OSG methods are sensible to voltage offset. As it can be seen from Figure 2.18, the OSG-SOGI rejects the DC component only for the component v'. The orthogonal component qv' is directly affected by the presence of any voltage offset. Therefore, an improved OSG-SOGI is proposed in [XII]. This improvement is presented and analyzed in the next section.

2.4.2 Offset rejection using OSG-SOGI

An important issue associated with accurate grid voltage monitoring is the presence of an offset in the measured voltage signal. This inherent voltage offset is typically introduced by the measurements or data conversion processes, and causes errors for the estimated parameters of the voltage signal. For instance, the grid-connected converters based on fixed-point Digital Signal Processor (DSP) require a manual setting of an offset before the Analogue to Digital (A/D) conversion in order to deliver a positive signal (e.g. 0 to +3V signal) to the A/D converter input of the fixed-point DSP. After the A/D conversion the signal data type is `uint` (unsigned integer) and has to be converted to `int` (integer) in accordance with the offset applied before the A/D conversion. Therefore, a perfect matching between the offset value (applied before the A/D conversion) and the signal data type conversion from `uint` to `int` is difficult to obtain.

As concluded in [47], the error caused by the voltage offset has the same frequency as the utility voltage. Since the frequency of the error is relatively low, the low pass filtering effect of the loop filter cannot be expected. The extremely low band-width can

provide the filtering effect. However, this degrades the dynamic performance and is not acceptable. Therefore, more attention has to be considered for the voltage offset.

The OSG-SOGI including offset rejection is shown in Figure 2.19. As it can be seen from Figure 2.18a, the component v' does not contain any DC component. In the case of any offset in the voltage signal v, the signal ε_v will contain that offset due to the subtraction $v - v' = \varepsilon_v$. Therefore, the improvement over the structure presented in Figure 2.17 consists in subtracting $k\varepsilon_v$ from qv_i' (red structure from Figure 2.19). Furthermore, a LPF is required to filter out the harmonics which can be present in the voltage signal (v).

From Figure 2.20a and Figure 2.20b, the effectiveness of the proposed method for the offset rejection can be noticed. The solid lines are obtained using the OSG-SOGI presented in Figure 2.17, while the dashed, dotted and dashdot lines are obtained for three different cut-off frequencies of the LPF using the OSG-SOGI with offset rejection (Figure 2.19). A gain k of 0.7 has been used for the plots presented in Figure 2.20.
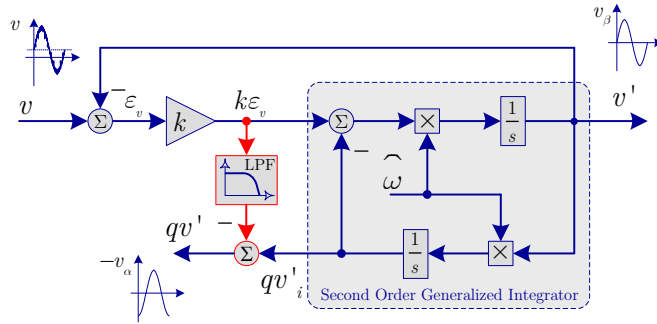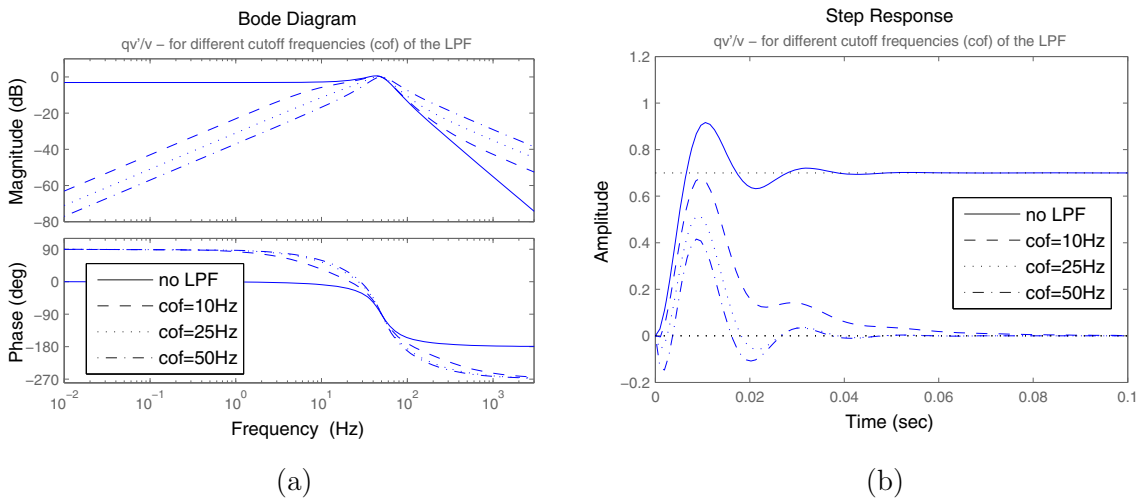

Figure 2.19. Offset rejection using OSG-SOGI.

| (a) | (b) |

Figure 2.20. a) Bode diagram and b) Step response of the closed-loop transfer function $H_q = qv'/v$ for k=0.7.

2.4.3 Discrete implementation of OSG-SOGI

As presented above, the OSG-SOGI proved to be a very promising candidate for providing the orthogonal voltage system to a PLL. However, its discrete implementation needs special attention as described in the coming sections.

2.4.3.1 Euler method

The Euler method is the most commonly used method to obtain a discrete-time integrator. The equations of this method are presented below [59]:

- *Forward Euler method:*

$$y[n] = y[n-1] + T_s u[n-1] \tag{2.15}$$

For this method, $\dfrac{1}{s}$ is approximated by:

$$T_s \frac{z^{-1}}{1 - z^{-1}} \tag{2.16}$$

- *Backward Euler method:*

$$y[n] = y[n-1] + T_s u[n] \tag{2.17}$$

For this method, $\dfrac{1}{s}$ is approximated by:

$$T_s \frac{1}{1 - z^{-1}} \tag{2.18}$$

The OSG-SOGI structure, as presented in Figure 2.17 and Figure 2.19, can be easily implemented in a discrete form using the Forward Euler method for the first integrator (whose output is v') and the Backward Euler method for the second integrator (whose output is qv') to avoid an algebraic loop. It is also known that the discrete-time integrator using the Euler method does not have an ideal phase of -90 degrees throughout the whole spectrum of frequencies.

The Bode phase plot for the discrete-time integrators using Forward Euler, Backward Euler and Trapezoidal methods are shown in Figure 2.21. The sampling time (T_s) was set to 10^{-4}s. It can be noticed that at 50 Hz the Forward and Backward Euler methods are not able to provide an exact phase of -90 degrees. Therefore, the two outputs (v' and qv') of the OSG-SOGI will not be exactly orthogonal.

However, the solution for this inconvenience is to make use of more advanced numerical methods for the discrete-time integrator. Thus, three different methods are described in the following:

- *Trapezoidal method*;
- *Second order integrator*;
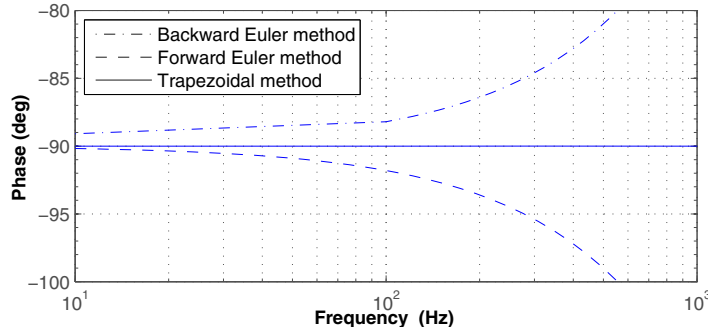- *Third order integrator.*

Figure 2.21. Phase Bode plot of a discrete-time integrator using Forward Euler, Backward Euler and Trapezoidal methods.

2.4.3.2 Trapezoidal method

The equation of the integrator using the Trapezoidal method is presented below [59]:

$$y[n] = y[n-1] + \frac{T_s}{2}\Big(u[n] + u[n-1]\Big) \tag{2.19}$$

For this method, $\dfrac{1}{s}$ is approximated by:

$$\frac{T_s}{2}\frac{1+z^{-1}}{1-z^{-1}} \tag{2.20}$$

As it can be seen from Figure 2.21, a phase of -90 degrees can be obtained using the Trapezoidal method for the whole spectrum of frequencies. The Trapezoidal method cannot be applied by just replacing $\dfrac{1}{s}$ (from Figure 2.17 or Figure 2.19) by (2.20), because it will create an algebraic loop. Therefore, the solution is to use the Trapezoidal method for the close-loop transfer function $H_d = \dfrac{v'}{v}$ (2.13) of the OSG-SOGI. By doing so, the algebraic loops are avoided.

Replacing s by $\dfrac{2}{T_s}\dfrac{z-1}{z+1}$, in (2.13) will result:

$$H_0\big(z\big) = \frac{k\omega\,\dfrac{2}{T_s}\dfrac{z-1}{z+1}}{\left(\dfrac{2}{T_s}\dfrac{z-1}{z+1}\right)^2 + k\omega\,\dfrac{2}{T_s}\dfrac{z-1}{z+1} + \omega^2} \tag{2.21}$$

Solving further the equation it results:

$$H_0\big(z\big) = \frac{\big(2k\omega T_s\big)\big(z^2-1\big)}{4\big(z-1\big)^2 + \big(2k\omega T_s\big)\big(z^2-1\big) + \big(\omega T_s\big)^2\big(z+1\big)^2} \tag{2.22}$$

Making the following substitutions, as presented in (2.23), and bringing the equation to a canonical form results in:

$$\begin{cases} x = 2k\omega T_s \\ y = \left(\omega T_s\right)^2 \end{cases} \tag{2.23}$$

$$H_0\left(z\right) = \frac{\left(\dfrac{x}{x+y+4}\right) + \left(\dfrac{-x}{x+y+4}\right)z^{-2}}{1 - \left(\dfrac{2\left(4-y\right)}{x+y+4}\right)z^{-1} - \left(\dfrac{x-y-4}{x+y+4}\right)z^{-2}} \tag{2.24}$$

Substituting $\begin{cases} b_0 = \dfrac{x}{x+y+4} \\ b_2 = \dfrac{-x}{x+y+4} = -b_0 \end{cases}$ and $\begin{cases} a_1 = \dfrac{2(4-y)}{x+y+4} \\ a_2 = \dfrac{x-y-4}{x+y+4} \end{cases}$, a simple discrete form of

(2.13) is obtained:

$$H_d\left(z\right) = \frac{b_0 + b_2 z^{-2}}{1 - a_1 z^{-1} - a_2 z^{-2}} \tag{2.25}$$

Furthermore, (2.25) can be represented as follows:

$$H_d\left(z\right) = b_0 \cdot \frac{1 - z^{-2}}{1 - a_1 z^{-1} - a_2 z^{-2}} \tag{2.26}$$

The implementation of the Trapezoidal method using (2.26) is depicted in Figure 2.22, where $w = 2T_s\omega$.
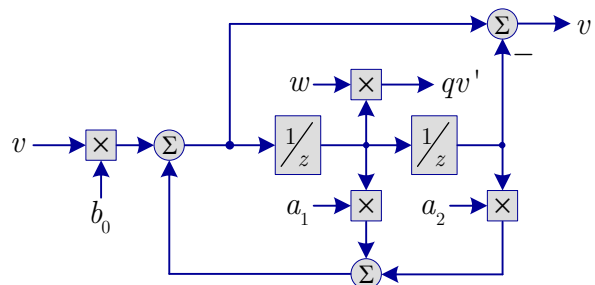

Figure 2.22. Trapezoidal method implementation of the OSG-SOGI.

2.4.3.3 Second order integrator

The equation of the second order integrator is [59]:

$$y[n] = y[n-1] + \frac{T_s}{2}\left(3u[n-1] - u[n-2]\right) \tag{2.27}$$

For this method, $\dfrac{1}{s}$ is approximated by:

$$\frac{T_s}{2}\frac{3z^{-1} - z^{-2}}{1 - z^{-1}} \tag{2.28}$$

The implementation of the second order using (2.28) is presented in Figure 2.23.
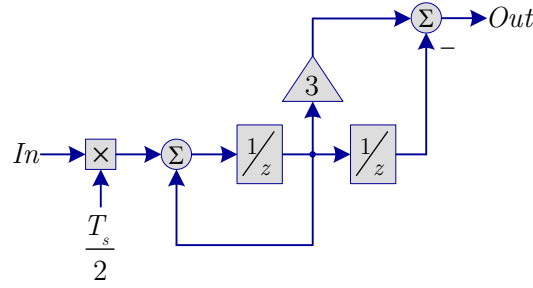
Figure 2.23. Canonic form of the discrete second order integrator.

2.4.3.4 Third order integrator

The equation of the third order integrator is [59]:

$$y[n] = y[n-1] + \frac{T_s}{12}\Big(23u[n-1] - 16u[n-2] + 5u[n-3]\Big) \tag{2.29}$$

For this method, $\frac{1}{s}$ is approximated by:

$$\frac{T_s}{12} \frac{23z^{-1} - 16z^{-2} + 5z^{-3}}{1 - z^{-1}} \tag{2.30}$$

Figure 2.24 shows the implementation of the third order integrator.
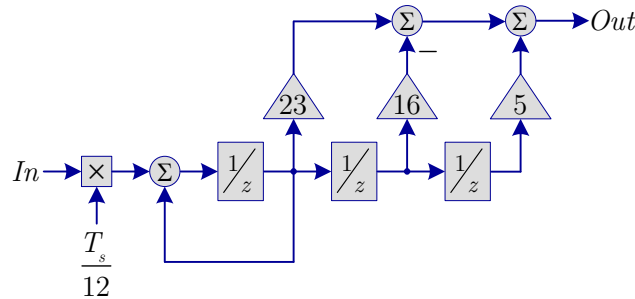

Figure 2.24. Canonic form of the discrete third order integrator.

2.4.3.5 Simulation results of the discrete implementation of OSG-SOGI

In order to test the performance of the discrete OSG-SOGI using the Euler method, the PLL structure presented in Figure 2.7 has been used. Due to the fact that qv' is not exactly 90 degrees phase shifted with respect to v', a ripple of 100 Hz will appear in the estimated amplitude and frequency of the input signal, as it can be seen from Figure 2.25. The input voltage signal was an ideal sinusoid with a fundamental frequency of 50 Hz and amplitude of 325.3 V.

In Figure 2.26, a comparison between the Trapezoidal method *(T)*, second order integrator *(2)* and third order integrator *(3)* is made. The input signal was the same signal as presented in Figure 2.25. As it can be noticed, the best results are obtained when the third order integrator is used. It is confirmed however, that all three proposed solutions give significantly better results when compared to the Euler method. However, the most promising candidate in terms of performances and less complexity is the Trapezoidal method, which gives better performances than the second order integrator and is less complex than the third order integrator.
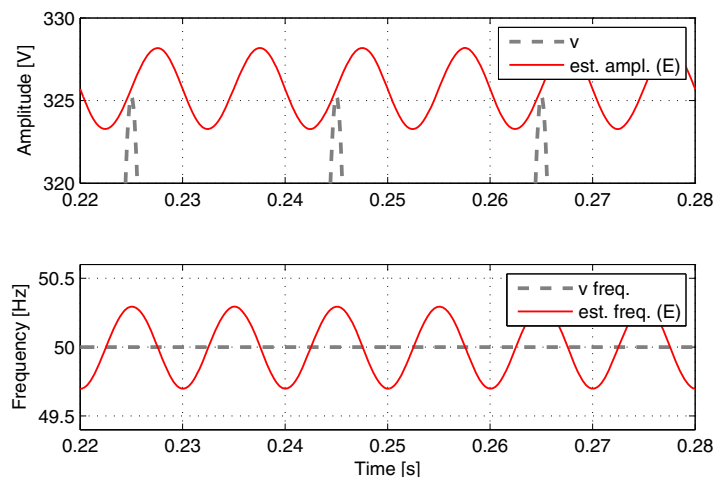
Figure 2.25. Estimated amplitude and frequency of the input signal when Euler (E) method is used.
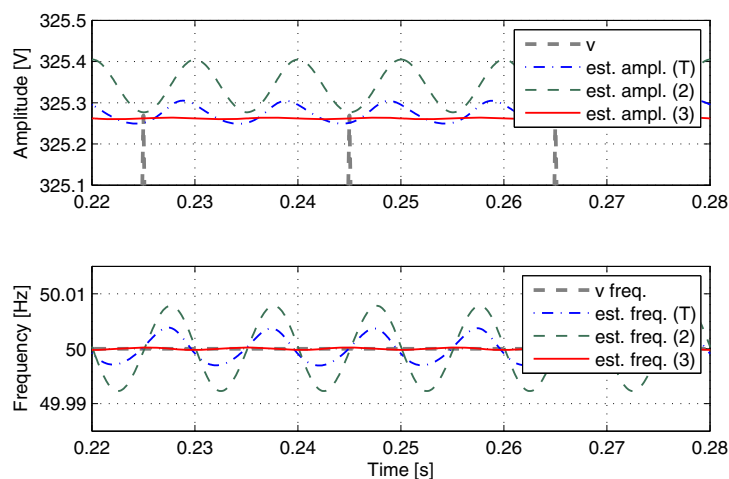
Figure 2.26. Estimated amplitude and frequency of the input voltage signal when Trapezoidal Method (T), second order integrator (2) and third order integrator (3) are used.

2.4.4 Selected results

A single-phase DPGS has been considered in order to test the chosen candidates for the single-phase PLL including the OSG. The technique based on the Park Transform (Figure 2.7) has been chosen for the PLL, while the SOGI technique including the offset rejection (Figure 2.19) has been chosen for the OSG. The discrete implementation of the OSG-SOGI was based on the Trapezoidal implementation, as presented in Figure 2.22. The general structure of the single-phase DPGS including the power circuit and the control structure is presented in Figure 2.27.

Figure 2.27. Single-phase DPGS based on PLL technique.

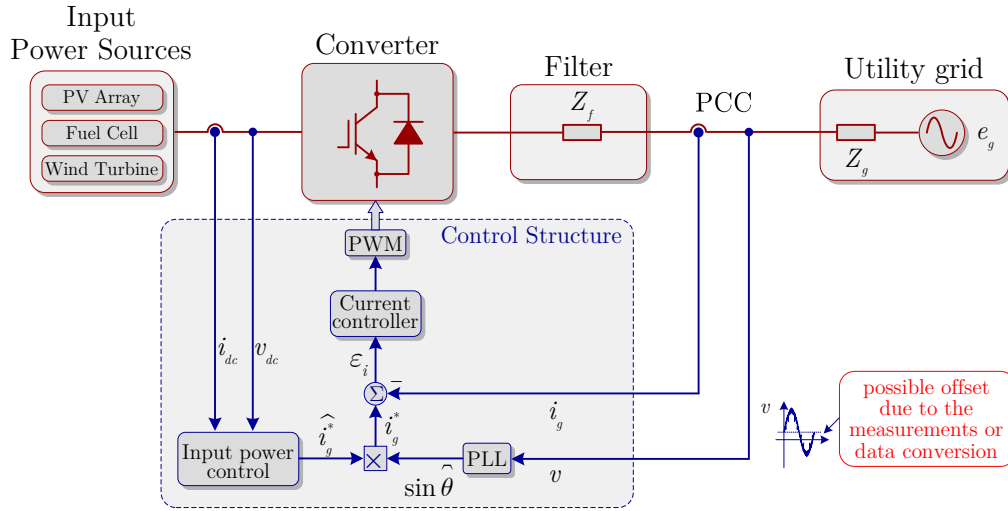Figure 2.28 shows how the OSG-SOGI structure is able to generate a clean orthogonal voltage system (represented by v' and qv') using a highly distorted grid voltage waveform (v) containing notches.

For all experimental results presented in this section, the PI controller parameters of the PLL structure were set as follows: - the settling time $T_{set} = 0.06 \text{ s}$; - damping ratio $\zeta = 1$. All the measurements have been done without using additional filters.

The behavior of the PLL based on OSG-SOGI under a grid voltage sag of 50% is shown in Figure 2.29 and Figure 2.30. The results of using two different values of the gain k (from Figure 2.19) are depicted in Figure 2.29a (for k=0.8) and in Figure 2.29b (for k=0.4) for a grid voltage Total Harmonic Distortion (THD) of 10%. It can be noticed that a smaller value of the gain gives a better filtering but slows the dynamic response of the system. In Figure 2.30 the PLL structure is tested under a high content of notches in the grid voltage.
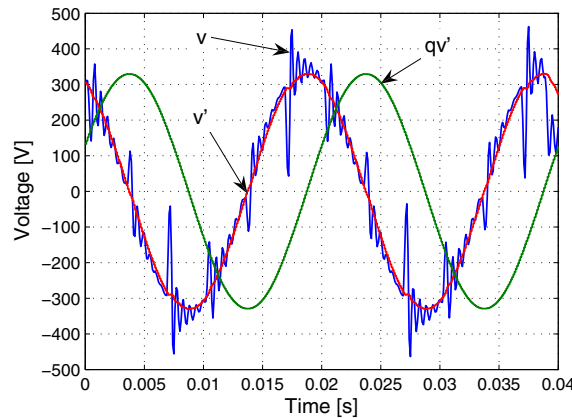
Figure 2.28. Distorted voltage signal (v) and the generated orthogonal voltage system (v' and its quadrature qv').

(a)   (b)
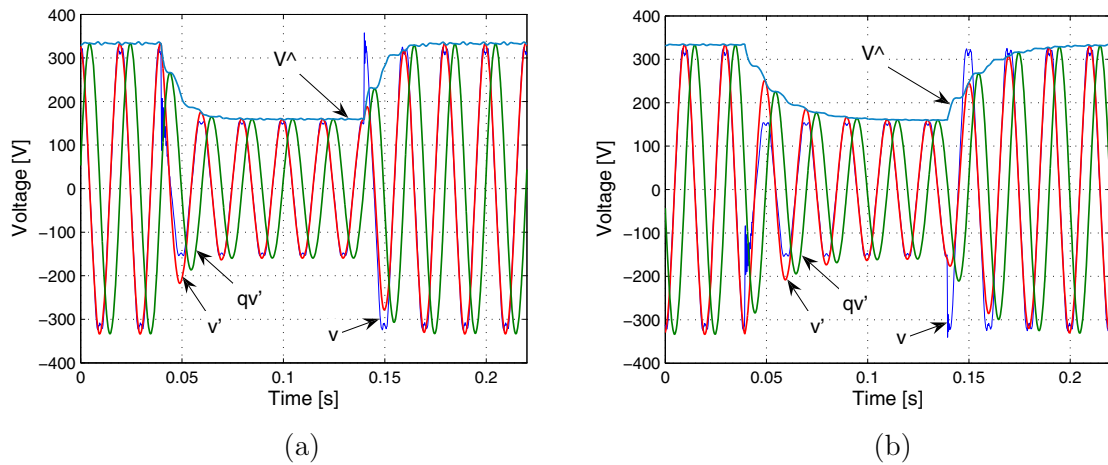
Figure 2.29. Voltage sag of 50% and 10% voltage THD: a) for k=0.8 and b) k=0.4.
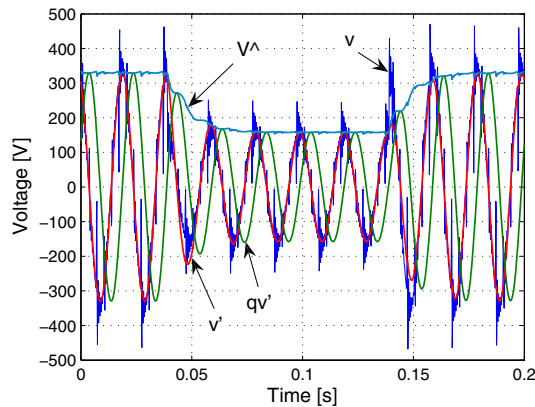
Figure 2.30. Voltage sag of 50% including notches (for k=0.8).

Figure 2.31 shows a frequency step *(a)* and sweep *(b)* response from 50Hz up to 51Hz. A fast estimation of the grid frequency can be observed. The grid voltage THD was set to 3% for this experiment.

The PLL behavior under a phase jump of 60 degrees and voltage sag of 25% is presented in Figure 2.32. It can be noticed that the PLL system responds according to its settling time (T_{set} = 0.06 s).

(a)   (b)
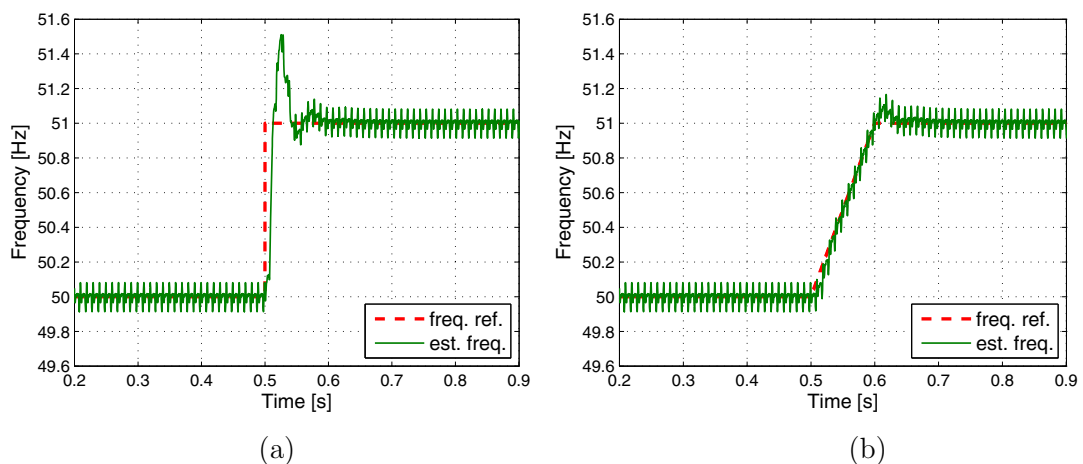
Figure 2.31. a) Voltage frequency step from 50 up to 51 Hz (for k=0.8); b) Voltage frequency sweep from 50 up to 51 Hz (for k=0.8).

Figure 2.32. Phase jump of 60 degrees and voltage sag of 25%.

Two cases have been analyzed in order to test the effectiveness of the OSG-SOGI including the offset rejection, as presented in Figure 2.19. In the first case a 5% (of the voltage amplitude) offset has been introduced in the measured voltage at PCC (Figure 2.33). For the second case a 25% offset has been introduced in order to test the robustness of the proposed method (Figure 2.34). The plots *(a-b)* from Figure 2.33 and Figure 2.34 show the voltage waveform and its amplitude, as estimated by the OSG-SOGI. The plots *(c-d)* fro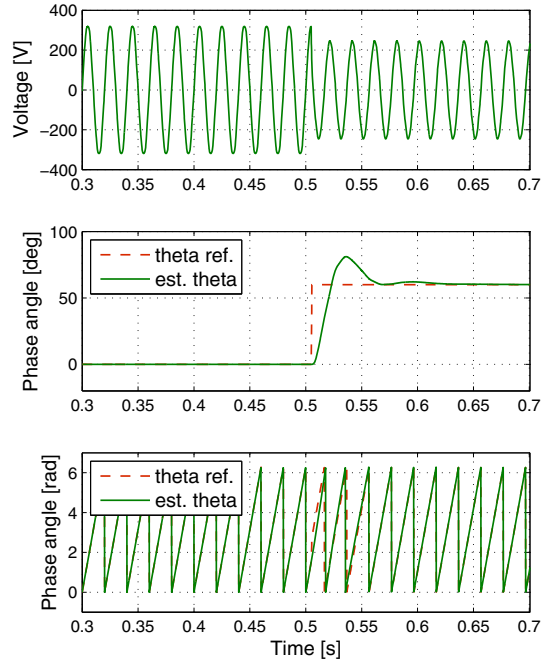m Figure 2.33 and Figure 2.34 contain the orthogonal voltage system (v' and qv'), generated by the OSG-SOGI. The plots *(e-f)* from Figure 2.33 and Figure 2.34 represent the estimated frequency of the voltage using the PLL based on OSG-SOGI.

The Figure 2.33*(a-c-e)* and Figure 2.34*(a-c-e)* show the results obtained using the OSG-SOGI structure without offset rejection (Figure 2.17), while the Figure 2.33*(b-d-f)* and Figure 2.34*(b-d-f)* show the results obtained using the improved OSG-SOGI structure with offset rejection (Figure 2.19). As it can be noticed from Figure 2.33*(a-c-e)* (OSG-SOGI without offset rejection), a 5% offset in the voltage highly affects the estimation of the frequency and amplitude of the voltage (2 Hz ripple in the estimated frequency and 25 V ripple in the estimated amplitude is noticed). On the contrary, using the offset rejection method, as presented in Figure 2.19, the estimated frequency and amplitude of the voltage are not affected by the 5% voltage offset Figure 2.33*(b-d-f)*. Moreover, the offset rejection method proved to be very efficient and robust even when using a 25% offset in the voltage as shown in Figure 2.34*(b-d-f)*.

Figure 2.33. Obtained results using the OSG-SOGI without offset rejection (Figure 2.17) and the improved OSG-SOGI with offset rejection (Figure 2.19) under a 5% voltage offset: a-b) estimation of the voltage amplitude; c-d) generated orthogonal voltage system; e-f) estimation of the voltage frequency.
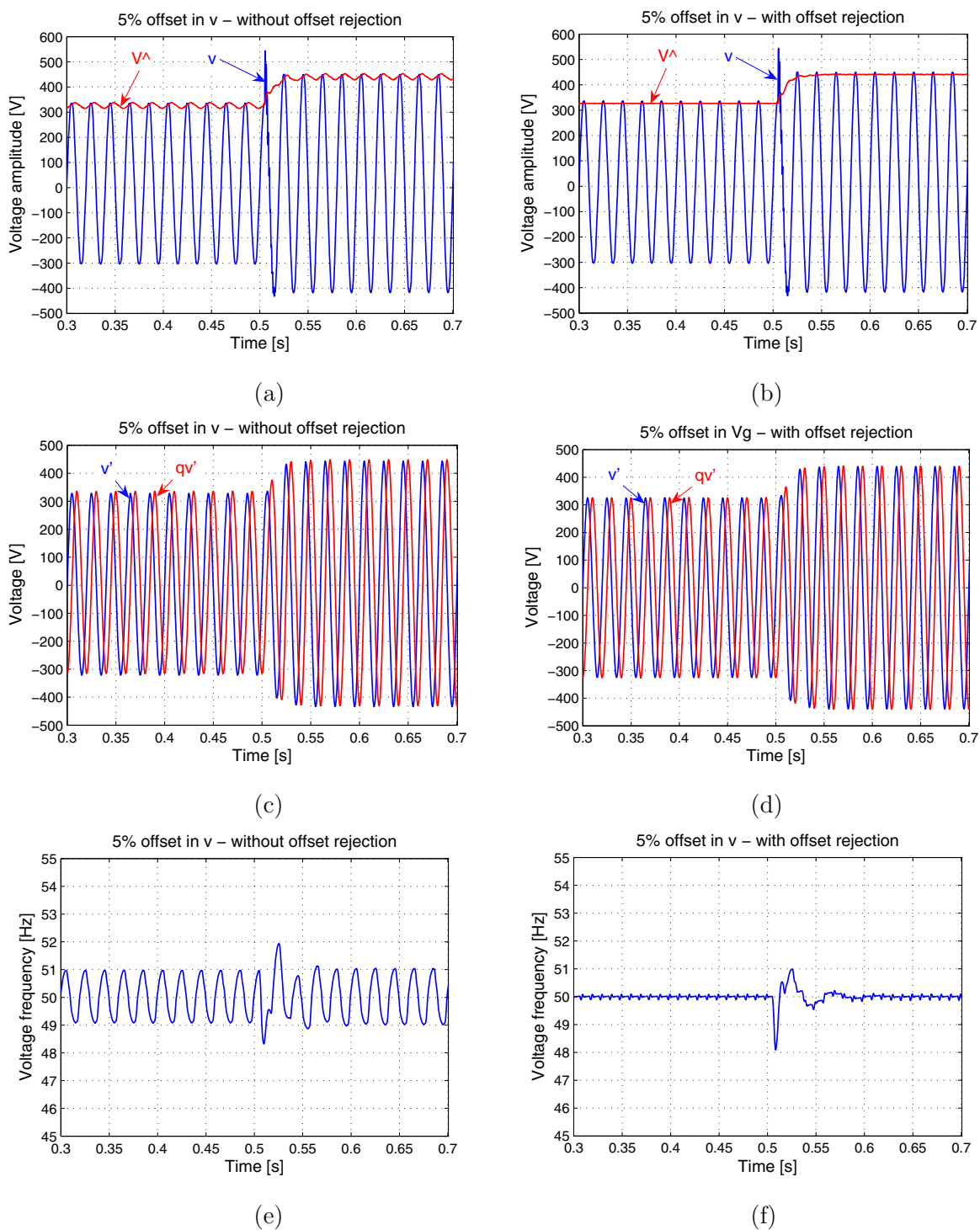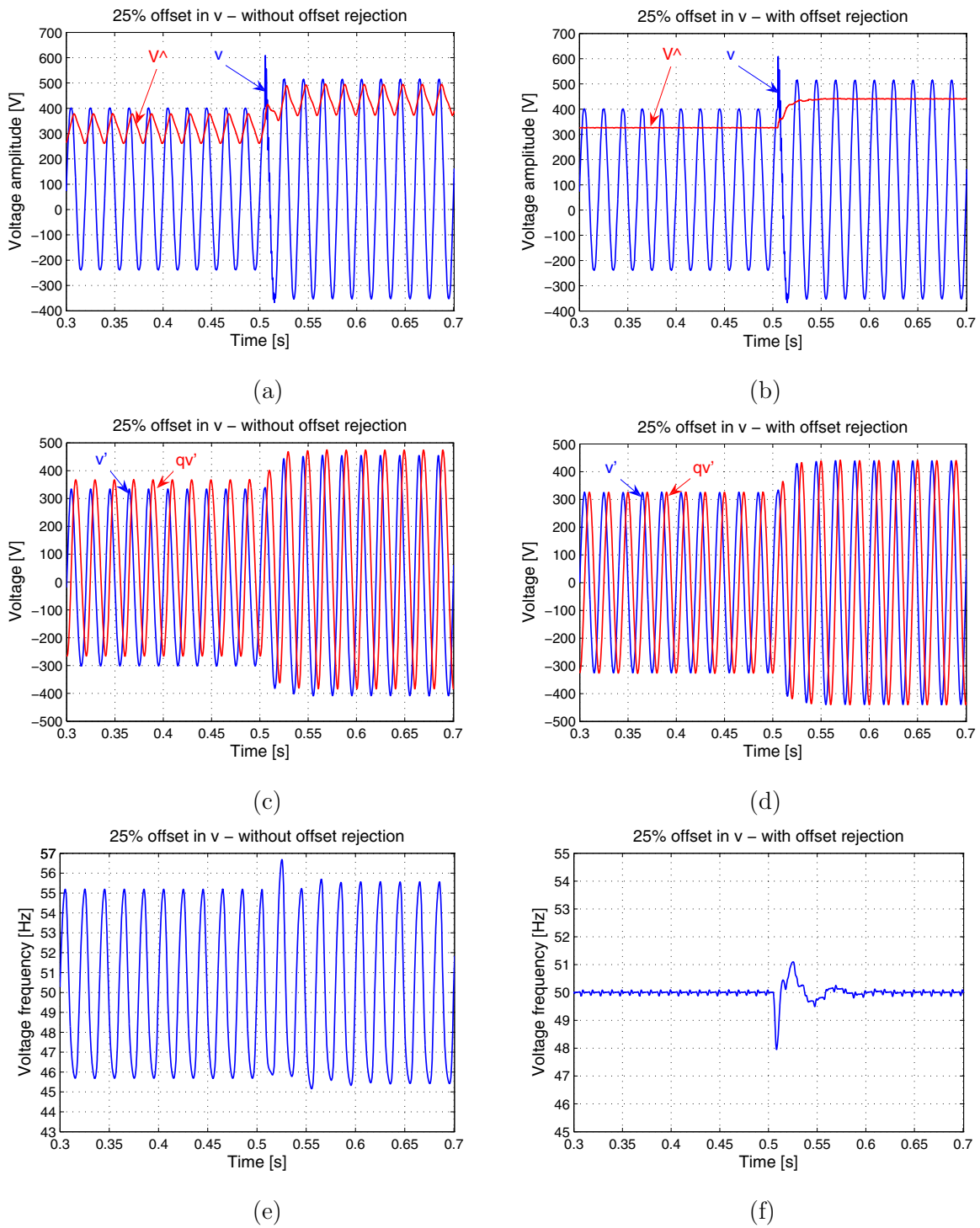
Figure 2.34. Obtained results using the OSG-SOGI without offset rejection (Figure 2.17) and the improved OSG-SOGI with offset rejection (Figure 2.19) under a 25% voltage offset: a-b) estimation of the voltage amplitude; c-d) generated orthogonal voltage system; e-f) estimation of the voltage frequency.

2.5 Summary

A comprehensive overview about grid voltage monitoring techniques for single-phase systems is presented in this chapter.

Unlike the three-phase systems where the orthogonal voltage system is easily obtained through the Clarke Transform, the orthogonal voltage system for the single-phase systems has to be artificially generated. This represents the main challenge for monitoring the grid voltage of a single-phase system. An analysis of the existent orthogonal signal generators up to date is given in this chapter in order to emphasize their advantages and disadvantages. Next, a voltage monitoring technique to combine all the advantages of the existent methods in one single structure is proposed.

A new algorithm for single-phase systems was derived using the well-known vector approach associated with the three phase systems. The proposed structure is based on OSG-SOGI and it has the following advantages:

- the orthogonal voltage system is filtered without delay;
- good dynamics;
- frequency adaptive;
- offset rejection capabilities;
- robust under grid voltage disturbances;
- relatively simple to implement.

An important issue associated with accurate grid voltage monitoring is the presence of an offset in the measured grid voltage. The majority of the PLL based synchronization systems are not able to reject the voltage offset which is typically introduced by the measurements or data conversion processes. Therefore, the proposed method presents also an effective offset rejection capability for grid-connected converters based on a PLL technique. The proposed method is suitable for both, grid-connected systems (e.g. PV, WT) and power condition equipments (e.g. Uninterruptible Power Supply (UPS), active filters) which rely on PLL based synchronization.

The presented results proved the performances and robustness of the proposed method based on OSG-SOGI for monitoring the grid voltage of a single-phase system.

Chapter 3

Grid Impedance Estimation

This chapter starts with an overview of grid impedance estimation techniques. The overview is then followed by a short presentation of the applications well suited for grid impedance estimation. Next, three methods of grid impedance estimation are presented. The first method uses the harmonic injection; the second method is based on active and reactive output power variations of the grid-connected converter and the third method is based on identification techniques. The simulation and selected experimental results are presented after each proposed method of grid impedance estimation.

3.1 Introduction

A large penetration of DPGSs affects the impedance value of the electrical grid, as presented in Chapter 1. It is also known that the performance of the grid-connected converter depends on the grid impedance [IX]. Additionally, the stability of the controllers depends upon the grid impedance as the grid impedance is an addition in series to the output filter impedance of the converter. Furthermore, improved quality of delivered power can be achieved if the grid impedance value is used in conjunction with active filter control [60, 61]. Moreover, the detection of grid faults and grid unbalance can be achieved based on the grid impedance information. Furthermore, the grid impedance estimation is required to comply with certain stringent standards for islanding detection such as the German standard VDE 0126 for grid-connected (PV) systems [7]. Also, the non-linear current controllers including hysteresis and predictive control rely on a good knowledge of the grid impedance. Additionally, the estimated value of the grid impedance can be used by the DPGS to decide if it runs in grid connected or stand alone (intentional islanding) mode [62]. Therefore, it is obvious that estimating the grid impedance can add extra functions into the operation of the grid-connected converters. Thus, the grid power converters can become more intelligent and they will sustain a better integration of DPGS into the utility grid.

3.2 Grid impedance estimation techniques – An overview

According to [63-69], different techniques can be used for the estimation of the line impedance. It is noticeable that, usually, these methods use special hardware dedicated devices. Once the inputs are acquired by voltage and current measurement, the processing part follows, typically involving large mathematical calculations in order to obtain the impedance value.

Commonly, the methods for estimating the grid impedance can be classified into two main categories, namely passive and active methods, as shown in Figure 3.1.

The passive methods are based on the measurements of present grid distortions [70, 71]. The value of the grid impedance is estimated by means of the information given by the usual operation of the converter. A major drawback of the passive methods is that the distortion has neither the amplitude nor the repetition rate to be properly measured, thus failing to give a proper estimation of the grid impedance.

On the other side, the active methods require a deliberate perturbation of the grid followed by acquisition and signal processing in order to extract the information needed to estimate the grid equivalent impedance [62, 63, 66, 67, 69, 72, 73], [VIII], [IX], [X]. The active methods can also be split into two main categories, namely hardware methods and software methods.
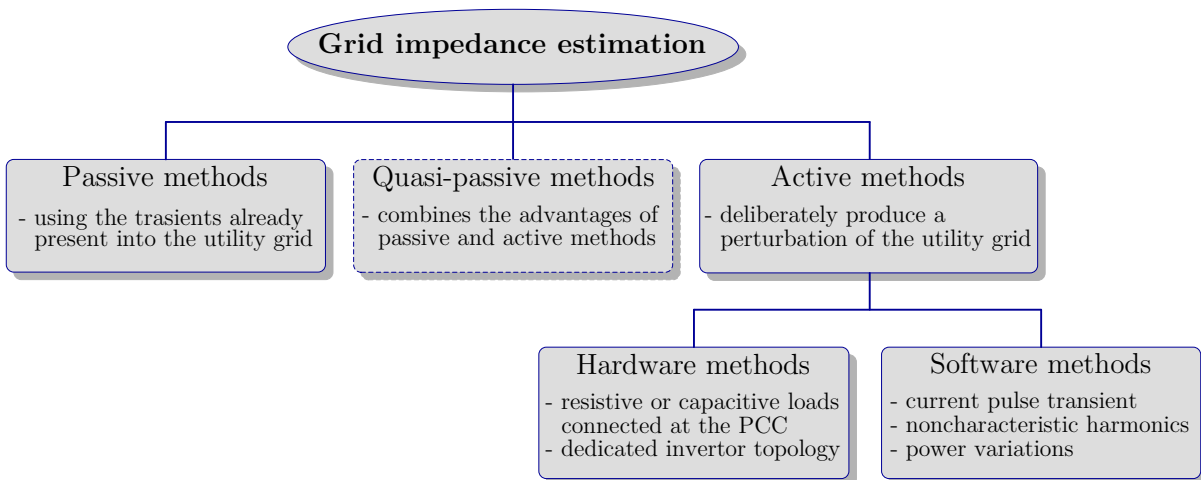
Figure 3.1. Classification of the grid impedance estimation methods.

The hardware methods are based on external devices (e.g. resistive or capacitive loads [74]) which are usually connected at PCC creating short transients to the electrical grid and then acquisitions and data processing are followed in order to estimate the equivalent grid impedance. It is worth mentioning that these methods are well suited for obtaining fast results, due to the limited time of the disturbing effect on the utility grid. One of the hardware methods generates a transient current in the grid (e.g. a resistive short circuit) and then measures the grid voltage and current at two different time instants, before and after the impulse occurs. The impulse will bring in a large harmonic spectrum that afterwards should be analyzed. The obtained results show the grid response over a large frequency domain, making this method well suited in applications where the impedance must be known at different frequencies. However, this method may involve high performance A/D conversion devices and must also use special numerical techniques to eliminate noise and random errors [72].

Another hardware method proposes the development of a dedicated inverter topology [64], where the computation of grid impedance is done by measuring the phase difference between supply and inverter voltage. Yet another technique [75] repetitively connects a capacitive load to the network and then measures the difference in phase shift of the voltage to the current.

The software methods make use of the grid power converter itself by using its control to deliberately produce the grid disturbance, thus no extra hardware components are required. The most common disturbances can be summarized as follows [X]:

- **Non-characteristic harmonics** – injected into the grid which give the possibility of calculating the grid impedance at a particular frequency [69, 73, 76, 77], [VIII]. Usually, this method is followed by an extrapolation in order to get the grid impedance at fundamental frequency;
- **Current pulse transient** – usually applied at zero crossing of the voltage and produces a voltage transient in the grid based on which the grid impedance can be estimated [61, 63, 66, 67, 71, 72];
- **Power variations** (of both active and reactive power) – produce grid voltage variations based on which the grid impedance can be estimated [62, 78], [IX], [X].

Compared to the passive methods, the active methods can estimate with a better accuracy the equivalent grid impedance due to the extra information gained by the perturbation they produce.

However, the active methods can decrease the quality of the delivered power to the utility grid. Therefore, in order to combine the non-intrusive advantage of the passive methods with the accuracy of the active methods, quasi-passive methods have been proposed in the literature [79, 80]. These quasi-passive methods are based on parametric identification using recursive least squares technique or model based technique.

3.3 Equivalent model of the grid impedance

In order to estimate the grid impedance, it is good to know in advance the typical impedance limits (Z_{min} and Z_{max}, see Figure 3.2) of the grid to be investigated. Depending on the value of the grid impedance, the grid can be stiff (low grid impedance) or weak (high grid impedance). As defined in Figure 3.2, the grid impedance can be either inductive ($Z_{g(L)}$) or capacitive ($Z_{g(C)}$). One of the key issues of the grid impedance estimation is the assumed grid model. The grid model gives the relationship between the voltage and the current measured at the PCC.
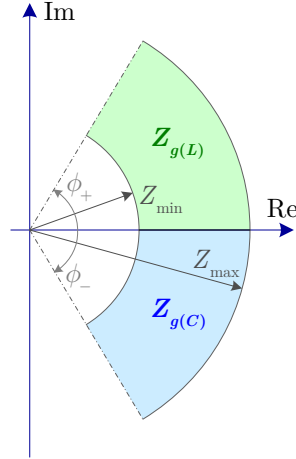
Figure 3.2. Typical grid impedance limits.

Grid models have been used in the technical literature [6, 81] using different levels of complexity. Usually, the grid impedance is mainly inductive (green area in Figure 3.2) and therefore the grid impedance is mostly considered as:

$$Z_g = R_g + j \cdot \omega L_g \tag{3.1}$$

Moreover, the recent grid codes [80] consider the equivalent grid impedance model as presented in (3.1). The equivalent grid model considered along this thesis is presented in Figure 3.3. The grid model consists of a grid equivalent generator (e_g) (capable to reproduce different harmonics and disturbances) and an equivalent impedance (Z_g) composed of a resistive (R_g) and an inductive (L_g) part.

According to Figure 3.3, the voltage at the PCC can be expressed as:

$$v_{PCC} = v_g + \Delta v_g = v_g + i_g \cdot Z_g \tag{3.2}$$

Figure 3.3. Equivalent grid impedance model.

3.4 Application suited for grid impedance estimation

In this thesis, two applications requiring online grid impedance estimation have been investigated and they are briefly presented in the coming sections. One of the applications is about the islanding detection for the German standard VDE0126 [7], while the other one relates to adaptive control for grid converters.
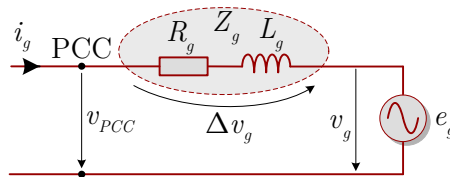
3.4.1 Anti-islanding standard compliance

The VDE0126 requirement is to isolate the supply within 5 seconds after an impedance change of 1 ohm. Therefore, the PV inverters should make use of an online impedance estimation technique [IX]. The test setup for this standard is presented in Figure 3.4. More details about islanding detection are presented in Chapter 4.
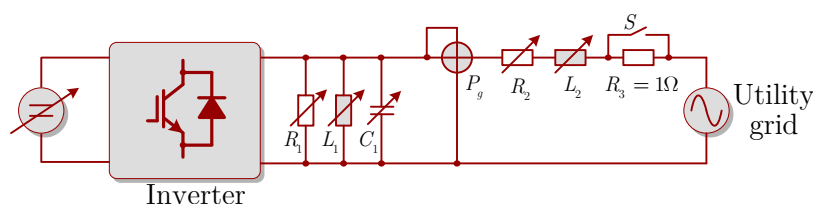
Figure 3.4. Test setup for the German standard VDE0126.

3.4.2 Adaptive control for grid converters

The estimation of the grid impedance can also be used in order to increase the stability and the performances of the current controller by adjusting its parameters online (Figure 3.5). If the variation of the grid impedance is mainly resistive, then the damping of the line filter changes, thus affecting the stability of the grid-connected converter control. If the variation is mainly inductive, then the bandwidth of the controller changes [82], thus affecting the performances of the grid-connected converter control. Also, in this case, due to the additional inductance of the grid, the tuning order of the line filter becomes lower and the filter will not fulfill the initial design purpose. Therefore, besides the islanding detection standard requirement, the knowledge about the grid impedance value is an added feature for the grid-connected converters [69]. More details about adaptive control based on grid impedance estimation are presented in §6.2.2.

Figure 3.5. Adaptive control of the grid-connected inverter.

3.5 Grid impedance estimation based on harmonic injection

The grid impedance estimation method described below is based on producing a perturbation on the output of the power converter that is in the form of periodical injection of one or two harmonic signals. The single harmonic injection uses a 400 Hz (*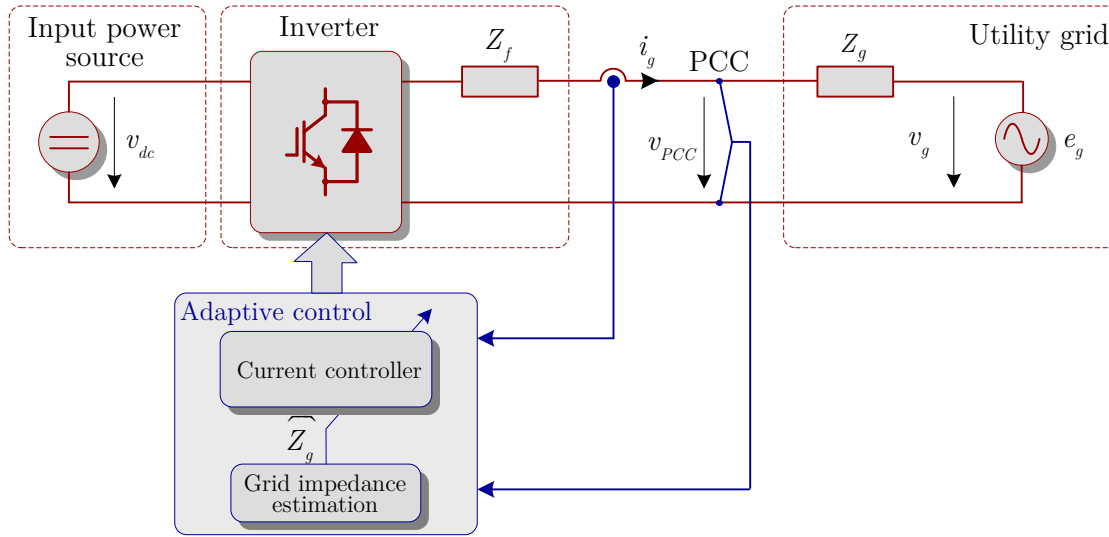h1*) signal, while the double harmonic injection uses 400 Hz (*h1*) and 600 Hz (*h2*) signals, respectively. The reason for choosing these specific frequencies is explained later on in this chapter. During the perturbation, the current response(s) at the same frequency as the injected signal(s) is/are measured. The value of the grid impedance is estimated using two different signal processing algorithms. The DFT technique is used for the single harmonic injection and the statistic technique (STQ) is used for the double harmonic injection.

The method based on harmonics injection is related to the referenced patent US 6,933,714 [76] where two different frequency signals (e.g. 40Hz and 60 Hz) are injected into the grid for a period of 3 fundamental cycles and based on DFT algorithm, the frequency components for these frequencies are extracted from the measured grid voltage and current and by dividing the voltage to the current the equivalent grid impedance at these frequencies is determined. By linear interpolation, the grid impedance at 50 Hz is determined.

A similar method but using a single harmonic injection of 75 Hz is presented in [69, 73, 77]. The measurements are processed by Fourier analysis for the specific injected harmonic and, finally, the injected harmonic voltage and current are obtained.

An important drawback of these methods is that the disturbance in the current is rather important leading to power quality degradation to some extent, taking into account that the harmonic signals are injected every second for a period of 3 fundamental cycles. Therefore, the proposed method will have the advantage with respect to [69, 73, 76, 77] of a reduced disturbance at the output of the grid converter by using higher frequencies for a shorter period of time. However, this method is limited by the

assumption that the grid impedance is usually linear for a frequency range up to the injected harmonics (e.g. 400 or 600 Hz).

3.5.1 Single harmonic injection

The proposed single harmonic injection method is based on the injection of a harmonic signal of 400 Hz (*h1*) followed by acquisitions of current and voltage at the PCC. Next, the equivalent grid impedance is obtained through the use of a DFT algorithm.

3.5.1.1 Perturbation

Figure 3.6 presents the principle of single harmonic signal injection. Figure 3.6a shows the injected harmonic signal (*h1*). The inverter voltage reference after injecting the harmonic signal (*h1*) is presented in Figure 3.6b. The effect of the signal injection is seen in the voltage and current at the PCC as presented in Figure 3.6c. A small disturbance of the grid current can be noticed compared to some similar known methods that make use of a low frequency harmonic injection (e.g. 40, 60, 75 Hz) [69, 76, 77].
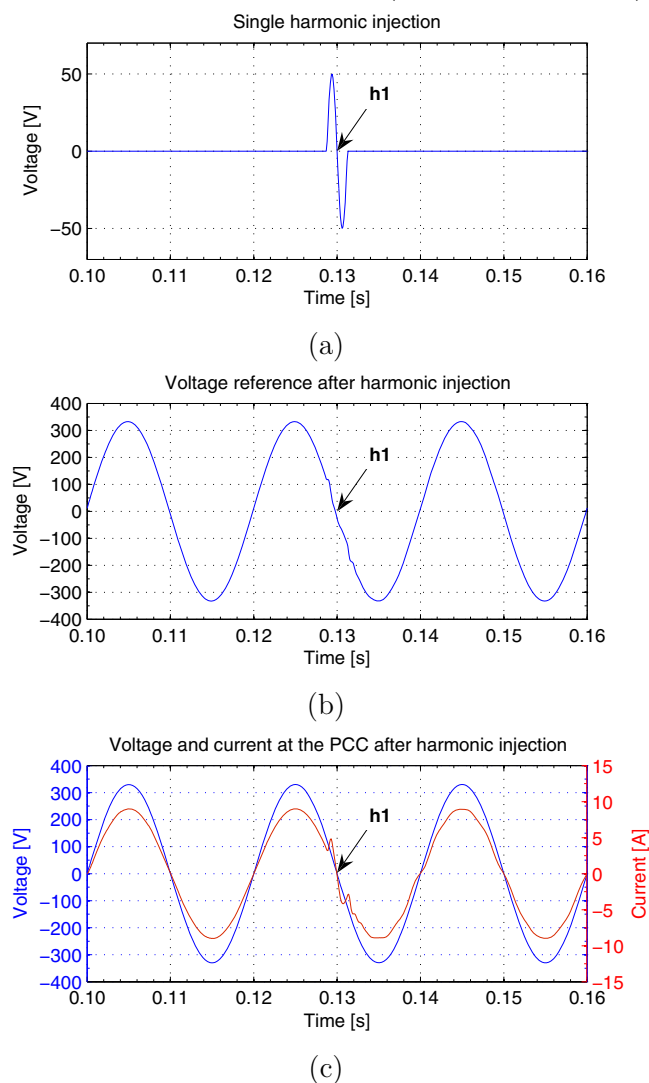

(a)

(b)

(c)

Figure 3.6. Principle of single harmonic signal injection: a) injected harmonic signal (h1), b) inverter voltage reference, c) voltage and current at the PCC.

The grid-connected inverter is used directly to inject the harmonic current by adding a harmonic voltage to the inverter voltage reference as it can be seen in Figure 3.7. The harmonic can be injected at the zero voltage crossing moment. Thus, the active power produced by the grid-connected inverter will be less affected compared to already known methods. However, some of the inverter topologies use special techniques like no switching near the zero crossing voltage, in order to increase their overall efficiency. Therefore, the harmonic injection should avoid the zone near the zero crossing in this particular case.

The single harmonic injection uses a 400 Hz periodical signal as presented in Figure 3.7, where:

- $\widehat{\theta}$ – represents the grid phase angle as provided by the PLL structure. It is used to synchronize the injection signal with the zero crossing of the grid voltage, as shown in Figure 3.6;
- i_g – actual grid current;
- i_g^* – grid current reference;
- v_{h1} – injected voltage harmonic;
- v_{inv}^* – inverter voltage reference.

There are some limitations by choosing the harmonic signal frequency. The chosen frequency should not interact with the resonance of the current controller in the case when the proportional resonant current controller with harmonics compensation is used (see Figure 3.8). Another limitation is that the chosen frequency should not be near the output filter resonance frequency as presented in [6], which can negatively affect the final result. Also, a higher harmonic signal frequency requires a higher sampling time to be used to keep a good resolution of the signal processing.
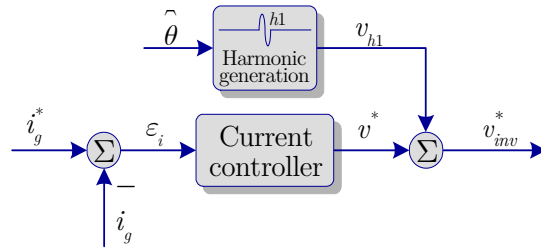

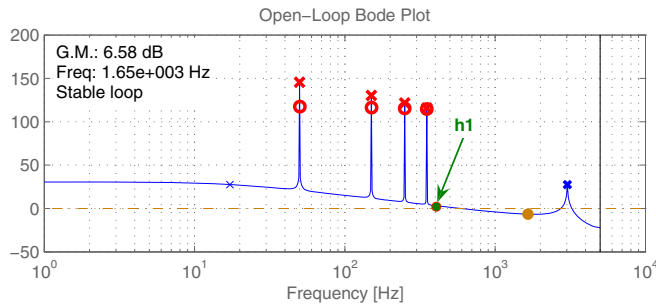*Figure 3.7. Single harmonic injection.*

Figure 3.8. Single harmonic (h1) injection frequency range.

By using a higher frequency injection (e.g. 400 Hz) compared to [69, 76, 77] (e.g. 40, 60, 75 Hz) implies an assumption that the grid impedance is linear on that frequency range. However, the error caused by this assumption does not affect significantly the estimation of the grid impedance, as it can be noticed from the results presented in §3.5.3. Finally, by linear interpolation, the grid impedance at fundamental frequency can be estimated.

3.5.1.2 Calculations

The single harmonic injection method consists in the injection into the grid of a single frequency harmonic having one period time in a cycle (Figure 3.7). The cycle time can be half or one second. In this case, the grid-connected inverter injects the single harmonic into the grid and measures the response of the injection using the current and voltage sensors. The signals are further derived in the way of DFT analysis and finally the amplitude and phase are obtained. The DFT algorithm uses (3.3) for coefficients calculation of the voltage and current harmonic.

$$\overrightarrow{\Lambda_h} = \sum_{n=0}^{N-1} v(n) \cdot \cos\left(\frac{2\pi \cdot h \cdot n}{N}\right) - j \cdot \sum_{n=0}^{N-1} v(n) \cdot \sin\left(\frac{2\pi \cdot h \cdot n}{N}\right) \tag{3.3}$$

$$\overrightarrow{\Lambda_h} = \lambda_{hr} + j \cdot \lambda_{hi} \tag{3.4}$$

where:

- N is the number of samples per fundamental period;
- $v(n)$ is the input signal (voltage or current) at point n;
- $\overrightarrow{\Lambda_h}$ is the complex Fourier vector of the hth harmonic of the input signal;
- λ_{hr} is the real part of $\overrightarrow{\Lambda_h}$;
- λ_{hi} is the imaginary part of $\overrightarrow{\Lambda_h}$.

In the following, using the relations (3.5), (3.6) and (3.7) it is possible to estimate the grid impedance Z_h and the resistive (R_g) and inductive (L_g) part of it. Figure 3.9 shows the estimation structure used for this method.

$$\overrightarrow{Z_h} = R_g + j \cdot \omega_h \cdot L_g \tag{3.5}$$

$$\overrightarrow{Z_h} = \left|\frac{\overrightarrow{v_h}}{\overrightarrow{i_h}}\right| \tag{3.6}$$

$$\widehat{R_g} = \mathrm{Re}\left\{\overrightarrow{Z_h}\right\}$$
$$\widehat{L_g} = \frac{\mathrm{Im}\left\{\overrightarrow{Z_h}\right\}}{\omega_h} \tag{3.7}$$

Figure 3.10a illustrates the waveforms of the voltage harmonics (h_v) and current harmonics (h_i) (see Figure 3.9) after the fundamental frequency was removed, while Figure 3.10b shows only the part of the signals to be processed by the DFT algorithm.
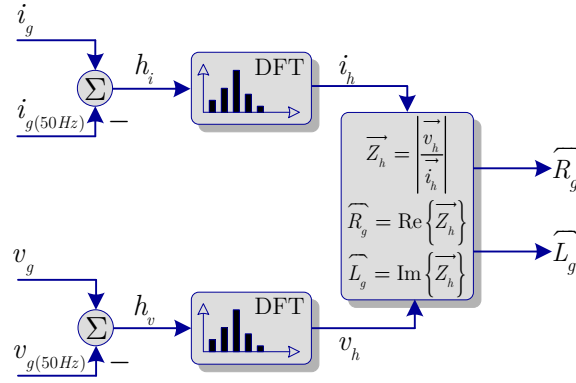
Figure 3.9. Grid impedance estimation algorithms for single harmonic injection.

| (a) | (b) |
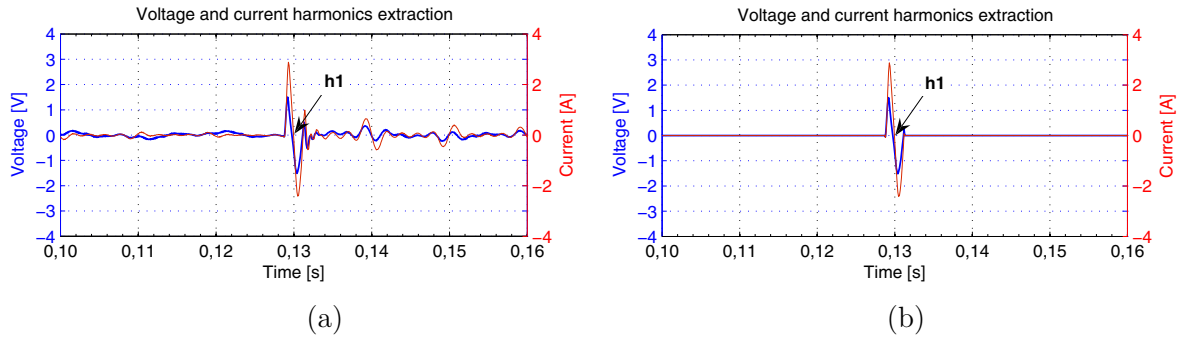
Figure 3.10. Voltage and current harmonics extraction: a) Removing the fundamental frequency; b) Signals to be processed by the DFT.

3.5.2 Double harmonic injection

Due to the complexity of the DFT algorithm for estimating the grid impedance, another method based on harmonic injection is proposed. Instead of using a single harmonic injection followed by the DFT algorithm, a double harmonic injection followed by a STQ method is proposed. The double harmonic injection method is based on the injection of two harmonic signals of 400 Hz (*h1*) and 600Hz (*h2*) respectively, followed by acquisitions of current and voltage at the PCC. Next, the equivalent grid impedance is obtained through the use of a STQ algorithm.

3.5.2.1 Perturbation

The principle of double harmonic injection is presented in Figure 3.11. The only difference compared to the single harmonic injection consists of making use of two harmonics at different frequencies injected alternatively. Figure 3.11a shows the injected harmonic signals (*h1* and *h2*). The inverter voltage reference after injecting the harmonic signals (*h1* and *h2*) is presented in Figure 3.11b. The effect of the signals injection is seen in the voltage and current at the PCC as presented in Figure 3.11c.
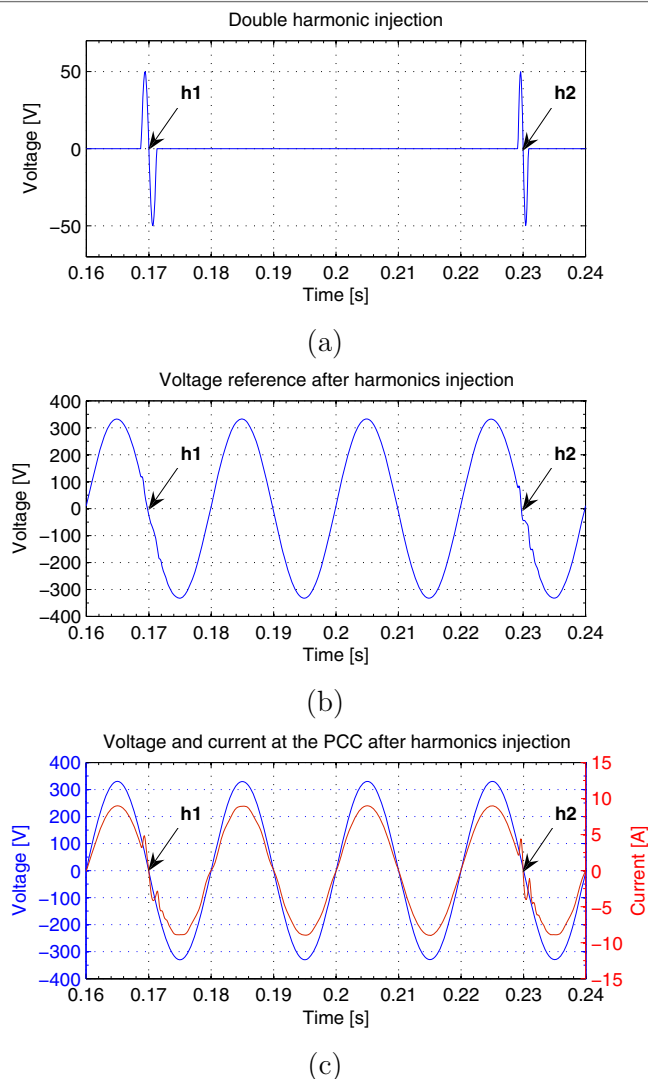
Figure 3.11. Principle of double harmonic signal injection: a) injected harmonic signals (h1,h2), b) inverter voltage reference, c) voltage and current at the PCC.

Similar to the single harmonic injection, a small disturbance of the grid current can be noticed compare to some similar known methods that make use of a low frequency harmonic injection (e.g. 40, 60, 75 Hz) [69, 76, 77].

Like for the single harmonic injection method, the grid-connected inverter is used directly to inject the harmonic current by adding a harmonic voltage to the inverter voltage reference, as it can be seen in Figure 3.12. The harmonic can be injected at the zero voltage crossing moment. Thus, the active power produced by the grid-connected inverter will be less affected compared to already known methods.
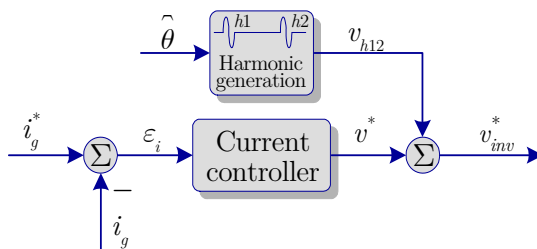
Figure 3.12. Double harmonic injection.

However, some of the inverter topologies use special techniques like no switching near the zero crossing voltage, in order to increase their overall efficiency. Therefore, the harmonic injection should avoid the zone near the zero crossing in this particular case.

The double harmonic injection uses 400 Hz (*h1*) and 600Hz (*h2*) periodical signals, as presented in Figure 3.12.

There are some limitations for choosing the harmonic frequencies of the injected signal. The chosen frequency should not interact with the resonance of the current controller in the case when a PR current controller with Harmonics Compensator (HC) is used (see Figure 3.13). Another limitation is that the chosen frequency should not be near the output filter resonance frequency as presented in [6], which can negatively affect the final result. Also, a higher harmonic signal frequency requires a higher sampling time to be used in order to keep a good resolution of the signal processing.

Moreover, the interval between the two chosen frequencies should be enough in order to keep low the errors generated by the interpolation technique used for obtaining the grid impedance at the fundamental frequency.

By using a higher frequency injection (e.g. 400 and 600 Hz) compared to [69, 76, 77] (e.g. 40, 60, 75 Hz) implies an assumption that the grid impedance is linear on that frequency range. However, the error caused by this assumption does not affect significantly the estimation of the grid impedance. Finally, by linear interpolation, the grid impedance at fundamental frequency can be estimated.
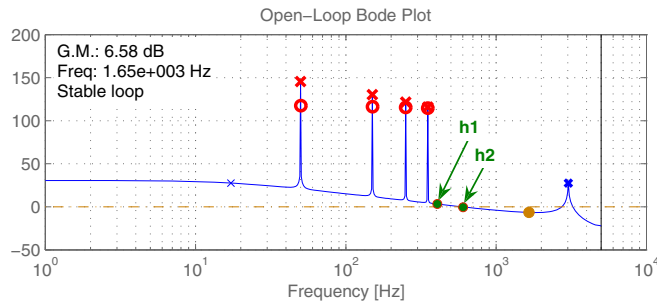
Figure 3.13. Double harmonic injection frequency range.

3.5.2.2 Calculations

The double injection method is explained as injecting two harmonic signals at different frequencies followed by harmonic response amplitude analyses for those two particular injected harmonics (see Figure 3.12). This approach provides an alternative of being involved with phase angle calculation (e.g. DFT technique), which could be difficult to implement on a DSP which operates in fixed-point numerical format. This method uses the maximum absolute values mean of the current and voltage harmonic response at the frequency of the injected harmonics (see Figure 3.14). Thus, by computing the grid impedance in two different points (meaning two injected harmonics at different frequencies) the grid parameters are calculated by solving the following set of equations:

$$\begin{cases} Z_{h1}^2 = R_g^2 + \omega_{h1}^2 \cdot L_g^2 \\ Z_{h2}^2 = R_g^2 + \omega_{h2}^2 \cdot L_g^2 \end{cases} \tag{3.8}$$

$$\widehat{L_g} = \sqrt{\frac{Z_{h1}^2 - Z_{h2}^2}{\omega_{h1}^2 - \omega_{h2}^2}} \tag{3.9}$$

$$\widehat{R_g} = \sqrt{\frac{\omega_{h1}^2 \cdot Z_{h2}^2 - \omega_{h2}^2 \cdot Z_{h1}^2}{\omega_{h1}^2 - \omega_{h2}^2}} \tag{3.10}$$

where:

- ω_{h1}, ω_{h2} denote injected harmonic frequencies;
- Z_{h1}, Z_{h2} are the impedances calculated for ω_{h1}, ω_{h2};
- $\widehat{R_g}$, $\widehat{L_g}$ are the estimated resistive and inductive parts of the grid impedance.

Figure 3.15a illustrates the waveforms of the voltage harmonics (h_v) and current harmonics (h_i) (see Figure 3.14) after the fundamental frequency was removed, while Figure 3.15b shows only the part of the signals to be processed by the STQ algorithm.
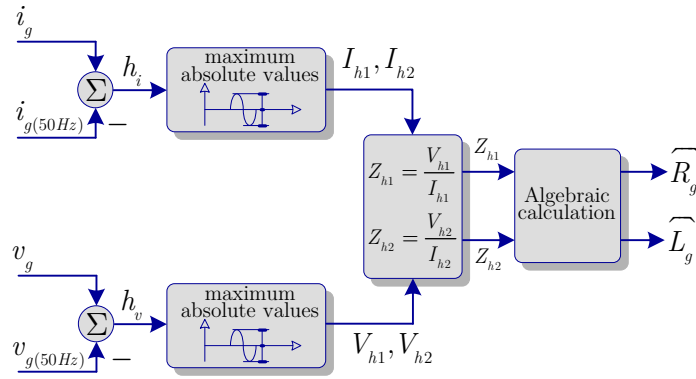
Figure 3.14. Grid impedance estimation algorithm for double harmonic injection.
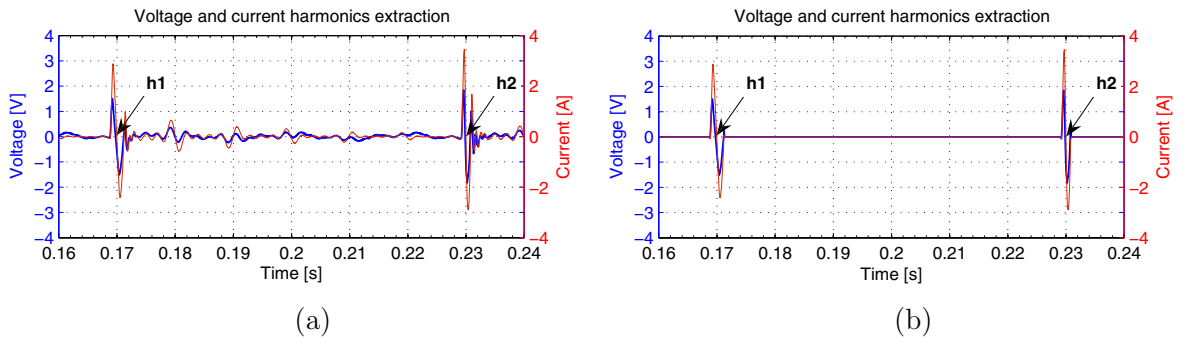
Figure 3.15. Voltage and current harmonics extraction: a) Removing the fundamental frequency; b) Signals to be processed by the STQ algorithm.

3.5.3 Selected results

In order to validate the working principle of the single harmonic injection method, a simulation model has been created in Matlab/Simulink. The model consists of two main parts, namely the power circuit (hardware part) and the control structure (soft-

ware part), as shown in Figure 2.27. The power circuit is represented by a single-phase DPGS and it includes the grid connected power converter, an output filter attached to the power converter, the equivalent grid impedance and the voltage source of the grid. The control structure is composed of an input power control unit (e.g. Maximum Power Point Tracker (MPPT) algorithms, DC voltage controller, etc), a single-phase PLL, a current controller (e.g. PR controller) and a PWM generator.

Figure 3.16 presents the grid impedance estimations for ten different values (between 0.05 mH and 2.5 mH) of the grid inductance L_g on a grid resistance R_g of 0.5 Ω. The blue line represents the actual grid impedances Z_{h1} and Z_{h2} at the harmonic frequencies (where *h1* is the first injected harmonic having the frequency equal with 400 Hz and *h2* is the second injected harmonic having the frequency equal with 600 Hz). The red line represents the estimated grid impedance using (3.3) and (3.6) of the DFT algorithm (Figure 3.9). The estimated grid impedance, using the STQ method (Figure 3.14), is represented by the green line. It can be seen that both methods based on harmonic injection give good results in terms of real grid impedance estimation, providing less than 15% error at all times. Moreover, the harmonic injection method based on STQ performs similar to the method based on DFT. This means that using a less complicated algorithm for estimating the grid impedance is possible to obtain similar results compare to a complex algorithm like DFT which is difficult to implement on a real time platform based on a DSP. Therefore, the harmonic injection method based on STQ algorithm can be a better candidate for a low cost system used to estimate the grid impedance.

The grid impedance estimation (at the frequency of the injected harmonic) on step variation in both grid inductance and resistance are presented in Figure 3.17 (R_g step from 0.5 to 1 Ω and L_g step from 0.25 and 0.5 mH). The blue line represents the actual grid impedance at the harmonic frequencies. The red line represents the estimated grid impedance using DFT algorithm, and the green line represents the estimated grid impedance using the STQ method. The grid inductance and resistance are finally obtained using (3.7), (3.9) and (3.10), as shown in Figure 3.18.

As it can be seen from Figure 3.17 and Figure 3.18, the harmonic injection method based on STQ algorithm performs similar to the DFT algorithm under grid impedance variations such as resistive and inductive steps. However, the grid impedance estimation method based on harmonic injection using either DFT or STQ algorithm suffers due to the assumption of the grid impedance linearity over a broad range of frequencies (e.g. 50 to 400 Hz or 50 to 600 Hz). Therefore, the grid impedance estimation method based on harmonic injection is not the best candidate in the case of highly nonlinear grid impedance.

(a)   (b)

Figure 3.16. Grid impedance estimation (at the frequency of the injected harmonic) a) h1 – 400Hz; b) h2 – 600Hz (Rg = 0.5 Ω and Lg – varies between 0.05 and 2.5 mH).

(a)   (b)

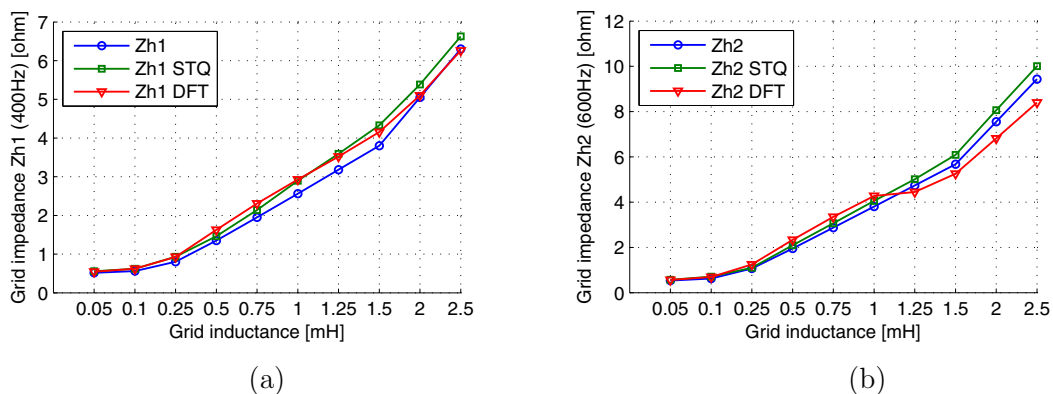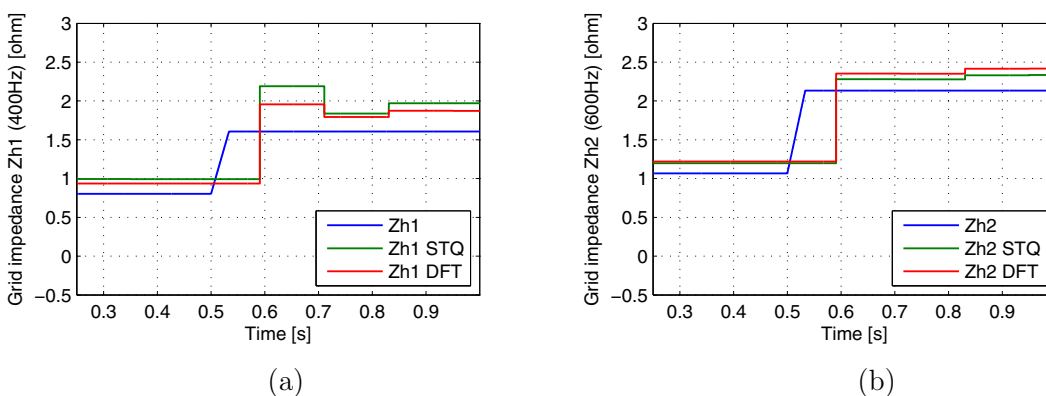*Figure 3.17. Grid impedance estimation (at the frequency of the injected harmonic) a) h1 – 400Hz; b) h2 – 600Hz (Rg step from 0.5 to 1 Ω and Lg step from 0.25 and 0.5 mH).*
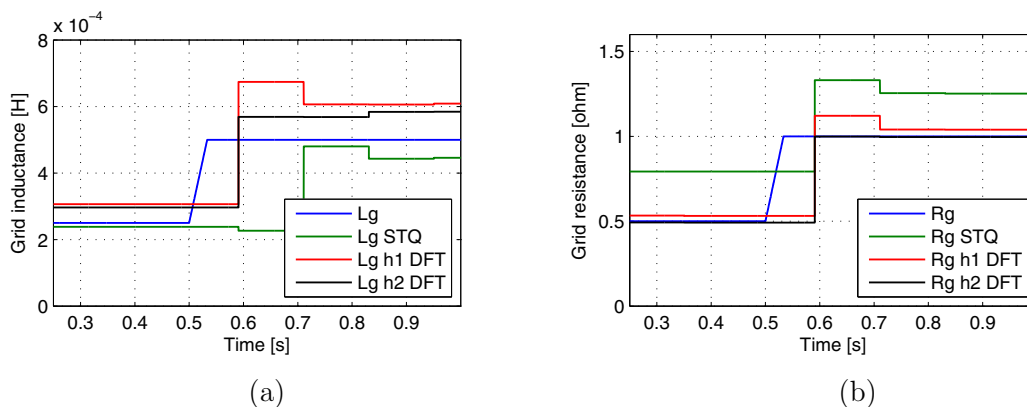

(a)   (b)

Figure 3.18. a) Grid inductance estimation (Lg step from 0.25 and 0.5 mH); b) Grid resistance estimation (Rg step from 0.5 to 1 Ω).

3.6 Grid impedance estimation based on PQ variations

An alternative solution to the grid impedance estimation based on harmonic injection is proposed. The proposed method is based on active and reactive power (PQ) variations. This method is proposed to avoid the assumption made for the harmonic injection technique which is to consider the grid impedance linear over a broad range of frequencies.

3.6.1 Method description

3.6.1.1 Perturbation

The method relies on the variation of active and reactive output power of the grid-connected converter. The principle of the active and reactive power variations is presented in Figure 3.19. A PQ control strategy is required to implement this method for a single-phase grid-connected system, as presented in [57].

The PQ control structure is depicted in Figure 3.19a. The OSG block is required to implement a PQ control in single-phase systems. The orthogonal voltage system is generated by a SOGI structure, as described in Chapter 2. For three-phase systems, this is not longer required, being replaced by the Clarke transformation block (abc-$\alpha\beta$).

The accuracy of this method depends on the values of the PQ variations (ΔP – variation value of active power P and ΔQ – variation value of reactive power Q) and the duration of the perturbations (Δt_P – variation period of active power P and Δt_Q – variation period of reactive power Q), as shown in Figure 3.19b.

The PQ control principle is based on the relations presented in (3.11) and (3.12) according to [57].

$$
\begin{cases}
P = \dfrac{1}{2}\left(v_\alpha \cdot i_\alpha + v_\beta \cdot i_\beta\right) \\[2mm]
Q = \dfrac{1}{2}\left(v_\beta \cdot i_\alpha - v_\alpha \cdot i_\beta\right)
\end{cases}
\tag{3.11}
$$

$$
\begin{cases}
i_\alpha^* = \dfrac{2\cdot\left(v_\beta \cdot Q^* + v_\alpha \cdot P^*\right)}{v_\alpha^2 + v_\beta^2} \\[4mm]
i_\beta^* = \dfrac{2\cdot\left(v_\beta \cdot P^* - v_\alpha \cdot Q^*\right)}{v_\alpha^2 + v_\beta^2}
\end{cases}
\tag{3.12}
$$

(a)

(b)
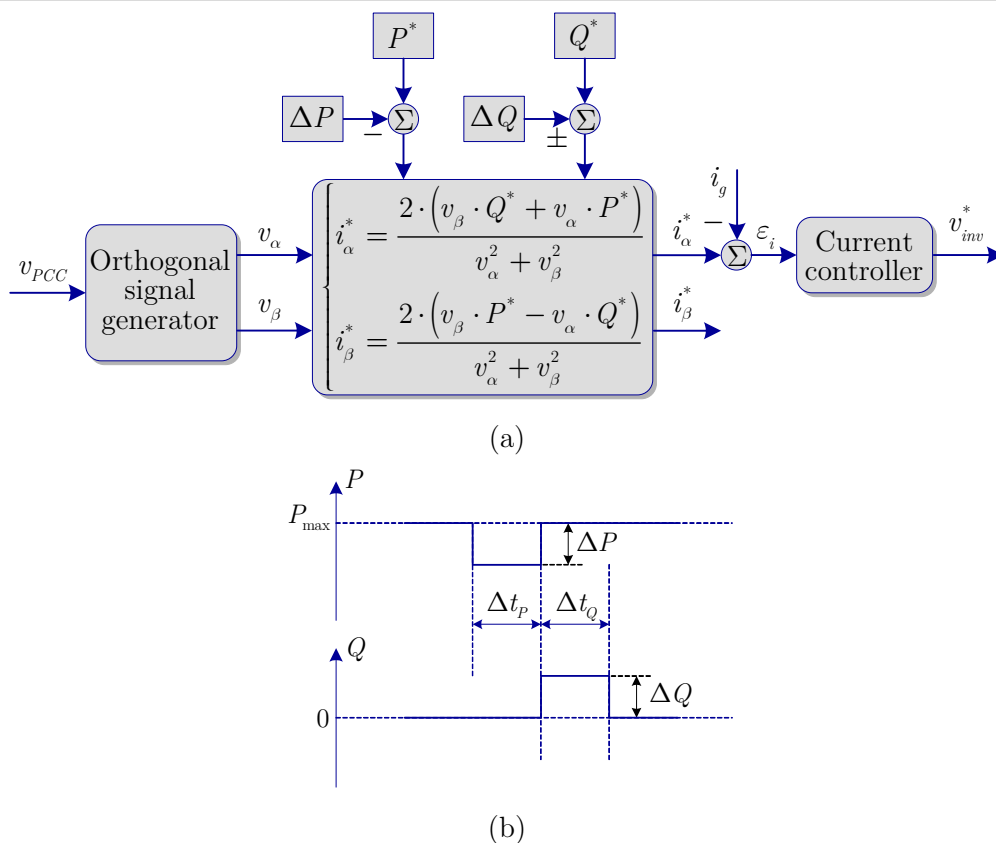
Figure 3.19. a) Structure for single-phase PQ control; b) Principle of PQ variations.

3.6.1.2 Calculations

Figure 3.20 shows the principle of how the method using PQ variations works. The estimation of the grid impedance using PQ variations is explained in the following.

The main idea of the PQ variations method is based on making the power converter to work in two operating points (see Figure 3.20) to avoid the unknown variable v_g from (3.2). The equations of the voltage in these two working points are presented in (3.13). It is considered that the grid impedance is linear between these two nearby working points. The voltages V_1 and V_2 represent the voltage at the PCC for the working points 1 and 2. By subtracting V_2 from V_1 (3.14), the unknown variable $\overrightarrow{V_g}$ is avoided.
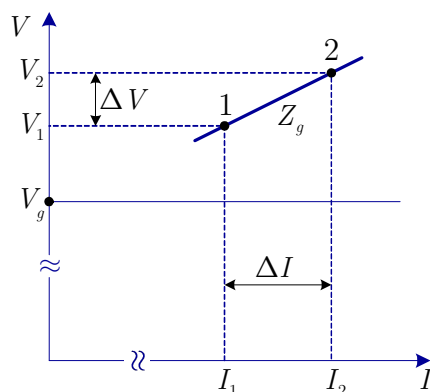
Figure 3.20. Power converter working in two operating points.

$$\begin{cases} \vec{V}_1 = \vec{I}_1 \cdot \vec{Z}_g + \vec{V}_g \\ \vec{V}_2 = \vec{I}_2 \cdot \vec{Z}_g + \vec{V}_g \end{cases} \tag{3.13}$$

$$\vec{V}_1 - \vec{V}_2 = \vec{Z}_g \left(\vec{I}_1 - \vec{I}_2 \right) \Leftrightarrow \Delta \vec{V} = \vec{Z}_g \cdot \Delta \vec{I} \tag{3.14}$$

The relation of the grid impedance Z_g can be written as shown in (3.15).

$$\vec{Z}_g = R_g + j \cdot \omega L_g = \frac{\vec{V}_1 - \vec{V}_2}{\vec{I}_1 - \vec{I}_2} \tag{3.15}$$

Furthermore, the expressions of the estimated resistance $\widehat{R}_g$ and inductance $\widehat{L}_g$ are given in (3.16) and (3.17).

$$\begin{cases} \widehat{R}_g = \mathrm{Re}\left(\dfrac{\vec{V}_1 - \vec{V}_2}{\vec{I}_1 - \vec{I}_2} \right) \\[4mm] \widehat{L}_g = \dfrac{1}{\omega} \cdot \mathrm{Im}\left(\dfrac{\vec{V}_1 - \vec{V}_2}{\vec{I}_1 - \vec{I}_2} \right) \end{cases} \tag{3.16}$$

$$\begin{cases} \widehat{R}_g = \dfrac{\Delta V_d \cdot \Delta I_d + \Delta V_q \cdot \Delta I_q}{\Delta I_d^2 + \Delta I_q^2} \\[4mm] \widehat{L}_g = \dfrac{\Delta V_q \cdot \Delta I_d - \Delta V_d \cdot \Delta I_q}{\left[\Delta I_d^2 + \Delta I_q^2 \right] \cdot \omega} \end{cases} \tag{3.17}$$

The term ΔV_q from (3.17) is considered equal to 0, as the orthogonal voltage system is created artificially for a single-phase system.

As it can be seen from (3.17), the calculation algorithm for the grid impedance is less complicated in contrast with some of the known algorithms based on more advanced mathematics such as DFT method [69, 76, 77] or Prony estimation [66].

3.6.2 Selected results

The following parameters were used for the PQ variations: ΔP=100 W (6.6 % of nominal P), ΔQ=100 VAr, $\Delta t_P = \Delta t_Q = 60$ ms.

A LPF having a transfer function as shown in (3.18), has been used (to filter the V_d, I_d and I_q components) to get accurate values for $\widehat{R}_g$ and $\widehat{L}_g$ according to (3.17). The Bode diagram and the step response of the LPF are presented in Figure 3.21a and Figure 3.21b. The LPF has been designed as a tradeoff between good filtering and good dynamic.

$$H_{LPF}(s) = \sum_{n=2h,4h,8h\ldots} \frac{s^2 + 2\xi_2 \omega_n s + \omega_n^2}{s^2 + 2\xi_1 \omega_n s + \omega_n^2}, \text{ where } \xi_2 \ll \xi_1 \tag{3.18}$$

In the following, selected results are presented to validate the grid impedance estimation method based on PQ variations.

The first set of results is obtained for a simultaneous resistive step of 0.1 ohm and an inductive step of 100 μH, in the case of a grid voltage THD equal to 0% (Figure 3.22, Figure 3.23, Figure 3.24 and Figure 3.25).

Figure 3.22 shows the behavior of the grid voltage (V_{PCC}) and the grid current (I_g) under PQ variations. The references and the measured values of the active and reactive power are shown in Figure 3.23a and Figure 3.23b. The filtered values of V_d, I_d, and I_q, as shown in Figure 3.24, are used for solving (3.17). The estimated values of the resistive (R_{est}) and inductive (L_{est}) part of the grid impedance for simultaneous R_g and L_g steps (R_g step from 0.1 to 0.2 ohm and L_g step from 100 to 200 μH, for a grid voltage THD of 0%) are presented in Figure 3.25a and Figure 3.25b.

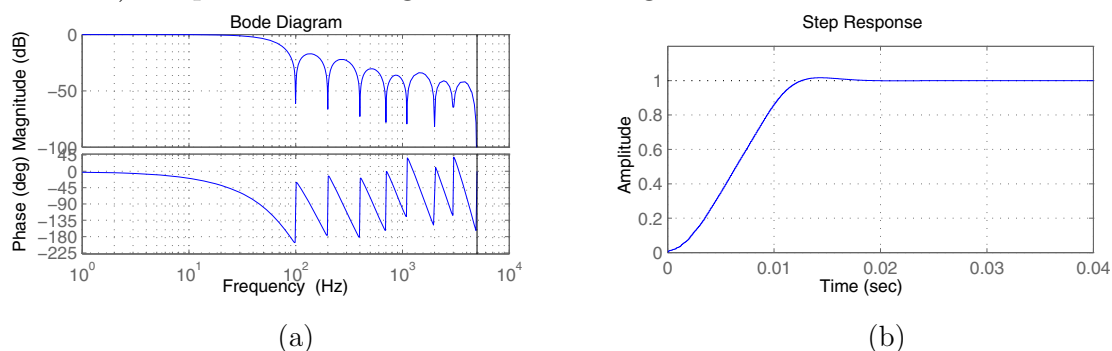(a)   (b)

Figure 3.21. LPF used by the PQ variation method: a) Bode diagram and b) Step response.
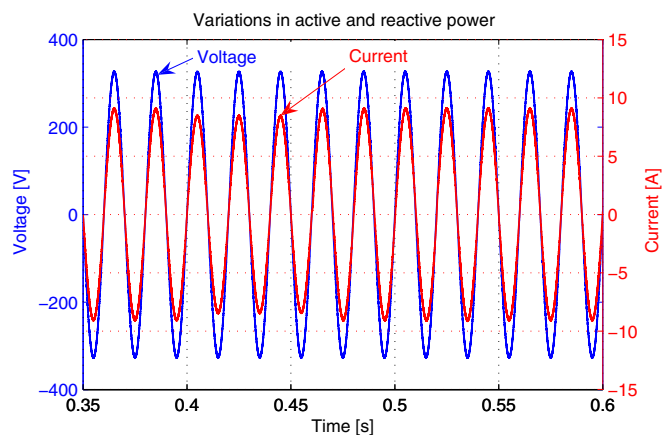

Figure 3.22. Grid voltage (V_{PCC}) and the grid current (I_g) under PQ variations.

(a)   (b)

Figure 3.23. Reference and measured values of: a) active and b) reactive power during PQ variations under a grid voltage THD of 0%.

(a)

(b)

(c)

Figure 3.24. Measured and filtered values of: a) V_d, b) I_d and c) I_q during PQ variations for a grid voltage THD of 0%.

(a)

(b)

Figure 3.25. Estimated values of: a) resistive (R_{est}) and b) inductive (L_{est}) part of the grid impedance for simultaneous R_g and L_g steps (R_g step from 0.1 to 0.2 Ω and L_g step from 100 to 200 μH, grid voltage THD = 0%).

The second set of results is obtained for a simultaneous resistive step of 0.1 Ω and an inductive step of 100 μH, in the case of a grid voltage THD equal to 2.5% (Figure 3.26, Figure 3.27 and Figure 3.28). This is to show that the harmonics have a minimal impact on the obtained results using the proposed method based on PQ variations.

Figure 3.26a and Figure 3.26b show the references and the measured values of the active and reactive power. The filtered values of V_d, I_d, and I_q, as shown in Figure 3.27, are used for solving (3.17). The estimated values of the resistive (R_{est}) and inductive (L_{est}) part of the grid impedance for simultaneous R_g and L_g steps (R_g step from 0.1 to 0.2 ohm and L_g step from 100 to 200 μH, for a grid voltage THD of 2.5%) are presented in Figure 3.28a and Figure 3.28b. As it can be noticed, similar results are obtained when comparing Figure 3.25a with Figure 3.28a, and Figure 3.25b with Figure 3.28b. Thus, it is proved that the presence of harmonics has a minimal impact on the effectiveness of the grid impedance method based on PQ variations.

Figure 3.29 shows the results for the case when the grid converter is connected to the grid through an AC transformer. For this particular case, the following test has been performed: - simultaneous R_g and L_g steps (R_g step from 1 to 2 Ω and L_g step from 2.5 to 5 mH, for a grid voltage THD of 2.5%).

For the compliance with VDE0126, a resistive step of 1 Ω has been performed in both cases, without (L_g=100 μH) and with (L_g=2.5 mH) an AC isolation transformer. As it can be seen from Figure 3.30, the proposed method using PQ variations successfully fulfills the requirement of VDE0126.
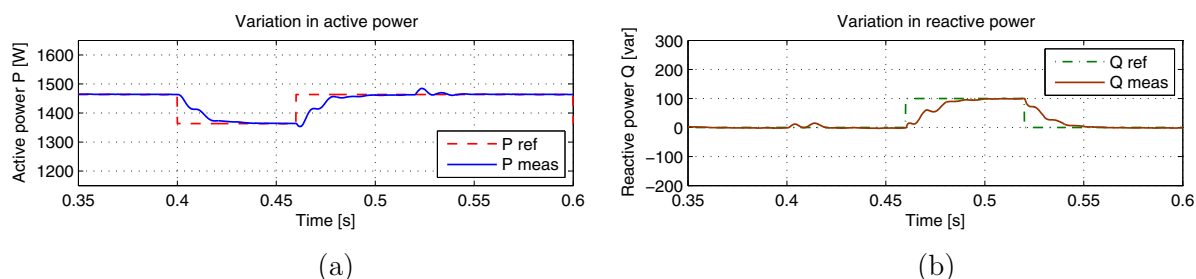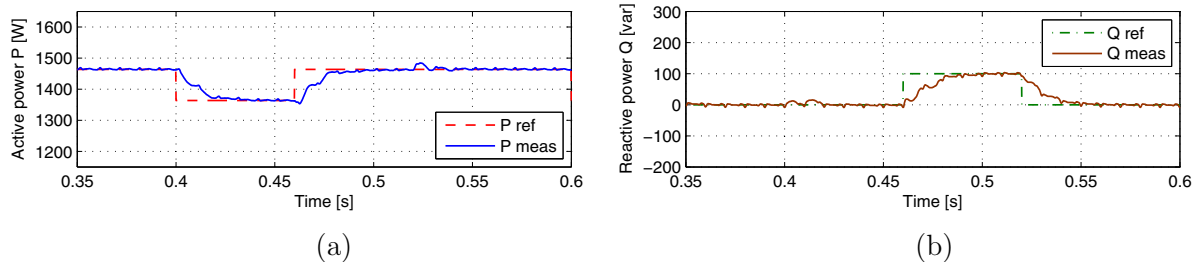

Figure 3.26. Reference and measured values of: a) active and b) reactive power during PQ variations under a grid voltage THD of 2.5%.
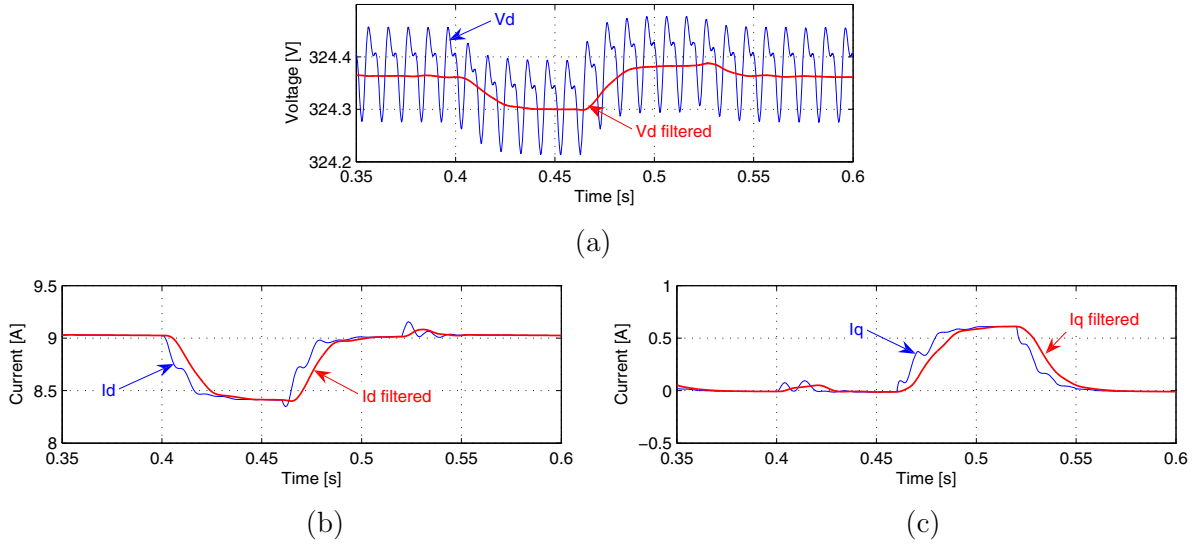

Figure 3.27. Measured and filtered values of: a) V_d, b) I_d and c) I_q during PQ variations for a grid voltage THD of 2.5%.
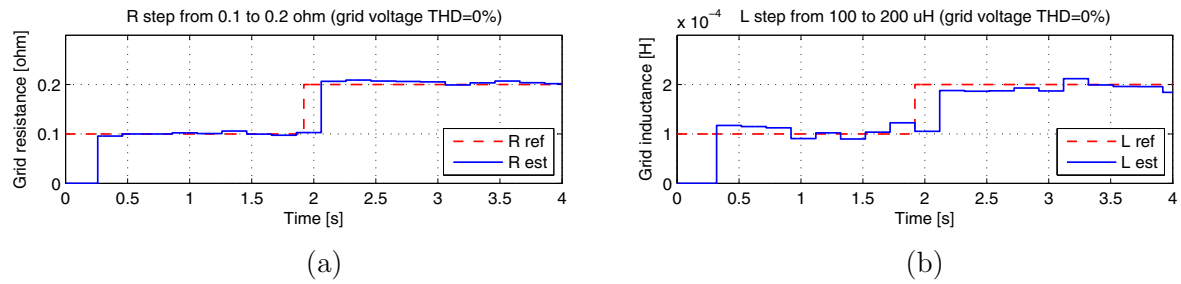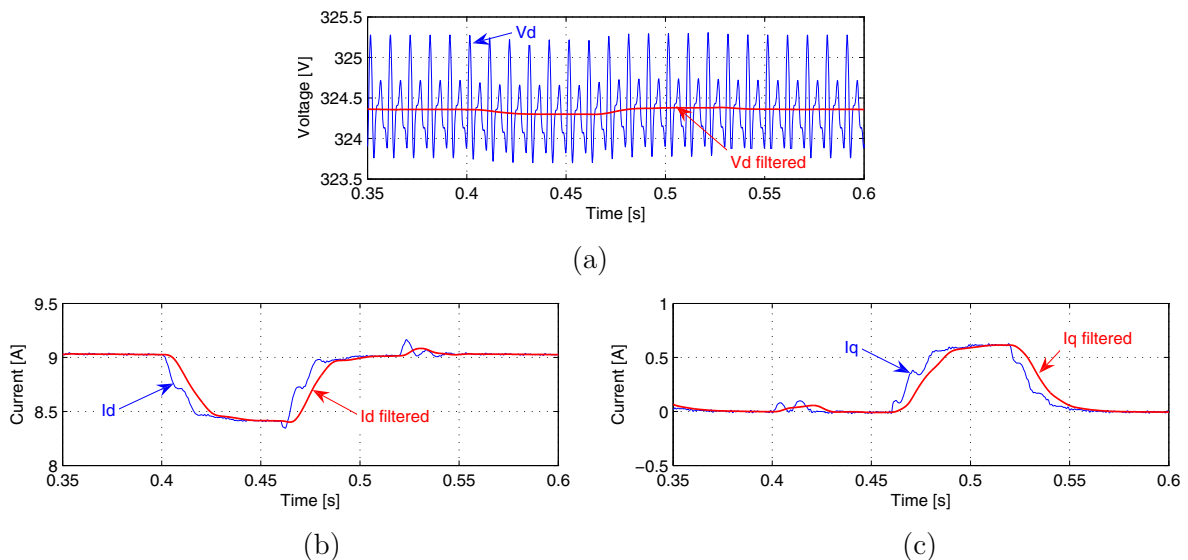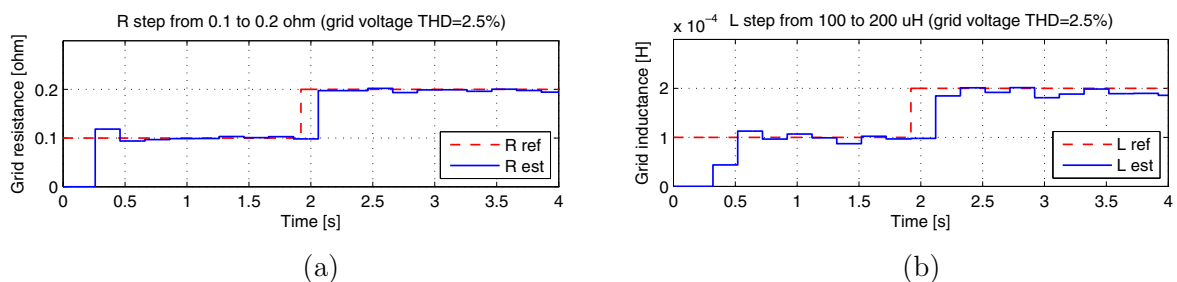

Figure 3.28. Estimated values of: a) resistive (R_{est}) and b) inductive (L_{est}) part of the grid impedance for simultaneous R_g and L_g steps (R_g step from 0.1 to 0.2 Ω and L_g step from 100 to 200 μH, grid voltage THD = 2.5%).

(a)   (b)
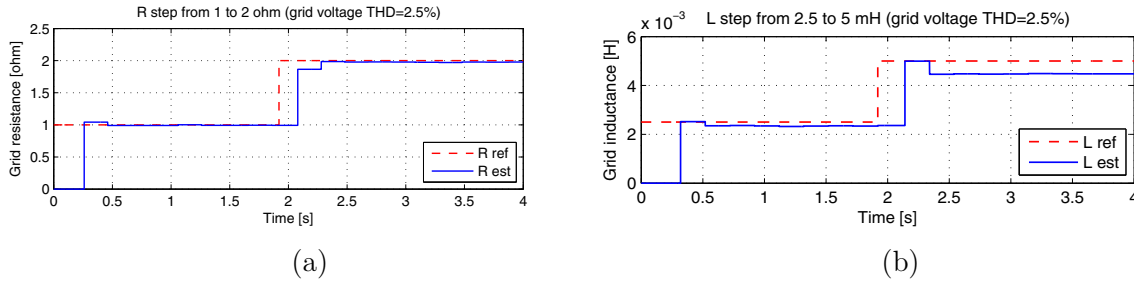
Figure 3.29. Simultaneous R and L steps: a) R step from 1 to 2 Ω and b) L step from 2.5 to 5mH (grid voltage THD = 2.5%).

(a)   (b)
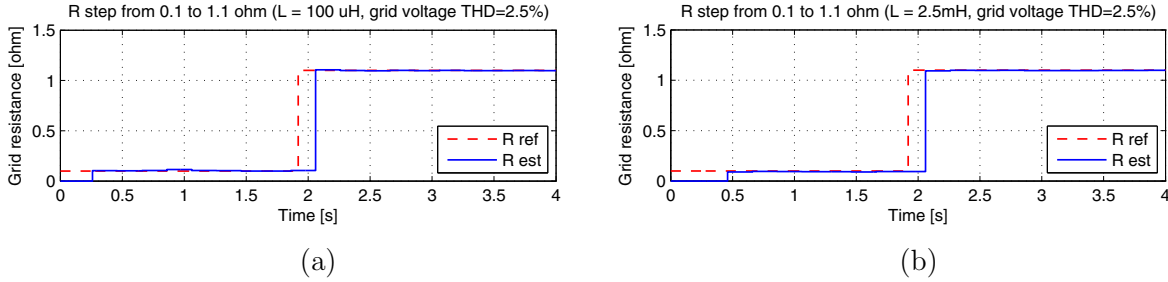
Figure 3.30. Resistive step of 1ohm (R step from 0.1 to 1.1 Ω, grid voltage THD = 2.5%): a) L=100 μH and b) L=2.5mH.

As it can be noticed from the presented results, the grid impedance estimation based on PQ variations performs better than the grid impedance estimation methods based on harmonic injection. Moreover, the PQ variations method can use the natural active power variations of a single-phase DPGS such as a PV inverter system where the input power varies according to the solar irradiation. However, varying the active power of a DPGS could create flickers in the case when the grid is weak and the output power of the DPGS is significant. Nevertheless, the proposed PQ variations method is focused for the single-phase DPGS which does not have significant power to create flickers.

3.7 Grid impedance estimation using model based identification

In §3.2 it has been mentioned that the active methods of the grid impedance estimation come with extra information about the electrical grid compared to the passive methods. This is due to the use of different perturbations which are deliberately produced by the active methods. However, in some of the cases (e.g. weak electrical grid) the active methods can decrease the quality of the delivered power to the utility grid when the perturbations are used too often. Therefore, a quasi-passive method (a tradeoff between active and passive methods) is proposed to combine the non-intrusive advantage of the passive methods with a better accuracy of the active methods.

The quasi-passive method is based on parametric identification using the model based identification. This method behaves like a passive method most of the time. The active behavior of the quasi-passive method comes in order to overcome the assumption that the voltage source of the electrical grid (v_g) (Figure 3.3) is time invariant. Usually,

the equivalent voltage source v_g of the electrical grid can be easily obtained at zero current, according to (3.2). For instance, before starting an inverter, the voltage at PCC (v_{PCC}) is measured at zero current and then this voltage value is kept as v_g in order to solve (3.2). However, v_g can change its value in time depending on the grid conditions. Therefore, the PCC voltage at zero current should be measured from time to time in order to get the actual value of v_g. Nevertheless, the equivalent voltage source of the electrical grid changes its value very little and slowly according to the technical literature about low voltage distribution grids. Hence, it is enough if the PCC voltage at zero current is measured every few minutes. To conclude, the measurements of the PCC voltage at zero current repeated every few minutes give the active behavior of the so called quasi-passive method.

There are several techniques to perform the identification process of a physical system. All these techniques can be classified according to the amount of prior knowledge that is available from the system [83]. The identification algorithms can be based on parametric or non-parametric identification.

Non-parametric identification tries to obtain an expression for the system transfer function of the estimated model based only on the relationship between output and input signals obtained from experimental testing (on-line or off-line).

On the other hand, the parametric identification claims to obtain the parameters for the transfer function based on prior system structure knowledge [83]. This is the case to be explored further.

3.7.1 Model based identification using parametric identification

The proposed identification algorithm follows the block diagram showed in Figure 3.31. The estimated model of the process $\underline{p}$ is a function of two parameters of the electrical grid (R_g and L_g):

$$\underline{p} = \begin{bmatrix} R_g \\ L_g \end{bmatrix} \tag{3.19}$$

The model of the process $\underline{p}$, which represents the impedance of the electrical grid, is considered as a function of resistance (R_g) and inductance (L_g).
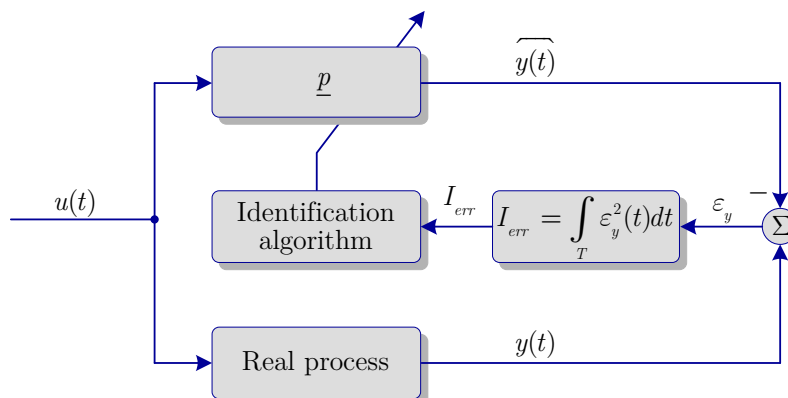
Figure 3.31. General structure of model-based identification.

The block $\underline{p}$ represents the model of the real process and its output $\widehat{y(t)}$ represents the estimated grid current, as shown in Figure 3.31. The output $\widehat{y(t)}$ is then compared with the output of the real process $y(t)$, resulting the error ε_y. Based on the criterion function I_{err} having the expression given in (3.20), the identification algorithm modifies the parameters of the modeled process in order to minimize the error ε_y.

$$I_{err} = \int_T \varepsilon_y^2(t)dt \tag{3.20}$$

Figure 3.32 shows the grid impedance estimation technique using model based identification. The model of the equivalent grid impedance is defined by the transfer function as described in (3.21):

$$\underline{p} = \frac{1}{\widehat{L_g}s + \widehat{R_g}} \tag{3.21}$$

The voltage drop (Δv_g) on the grid impedance (Z_g) (see Figure 3.3) is obtained after subtracting the voltage source of the electrical grid (v_g) from the voltage at the PCC (v_{PCC}). As mentioned before, the voltage v_g is considered equal to the PCC voltage at zero current.

The identification algorithm is a minimum searching algorithm and is presented next.
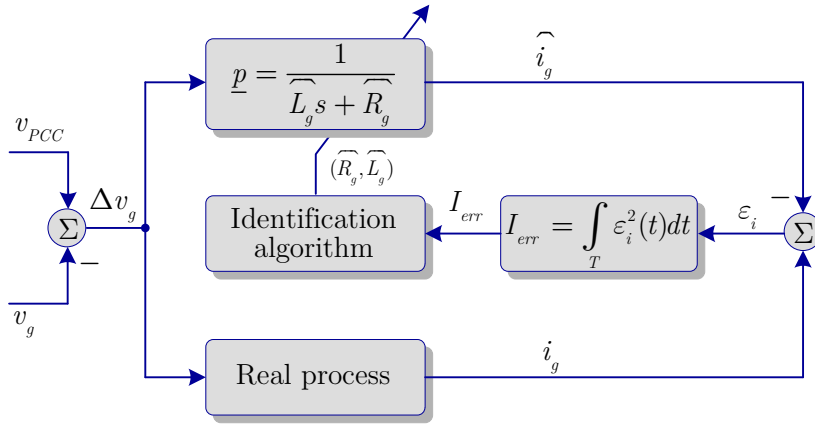
Figure 3.32. Grid impedance estimation using model based identification.

3.7.2 Minimum searching algorithm

The identification algorithm has to find the right values for the parameters of the process $\underline{p}$. When the parameters $\widehat{R_g}$ and $\widehat{L_g}$ match the values of the real process a minimum value of I_{err} is obtained.

A 3D representation of I_{err}, which is function of R_g and L_g, is presented in Figure 3.33. A logarithmic scale has been used to emphasize the minimum of the function I_{err}. For this representation, the parameters of the modeled process $\underline{p}$ have been varied as

follows: the resistance $\widehat{R_g}$ was varied from 0.1 to 1 Ω with an increment of 0.1 Ω and the inductance $\widehat{L_g}$ was varied from 0.1 to 1 mH with an increment of 0.1 mH. As a result, 100 values of I_{err} were obtained as it can be seen from Figure 3.33. The parameters of the real process were set as follows: $R_g=0.5$ Ω and $L_g=0.5$ mH. The criterion function I_{err} has a single minimum which is reached when the values set for $\widehat{R_g}$ and $\widehat{L_g}$ match the values of the real process parameters. Therefore, a 2D searching algorithm can be used in order to find the minimum of I_{err}.

Five conditions have to be set in order to perform a 2D searching. The first condition is to set the initial values for $\widehat{R_g}$ and $\widehat{L_g}$ before the searching algorithm starts. The best way to start the searching is to set $\widehat{R_g}$ and $\widehat{L_g}$ to the smallest values possible for a real electrical grid.

The second condition is to find which parameter has to be modified first in order to reach a partial minimum of I_{err} and then switch to modify the other parameter so as to find the absolute minimum of I_{err}. As it can be seen from Figure 3.34 and Figure 3.35, the most predominant parameter to be changed is $\widehat{R_g}$. The variation of the resistance affects the most the criterion function I_{err}. Figure 3.34 shows that the partial minima for the whole range of the inductance values are obtained at 0.5 Ω which was set for the real process, unlike Figure 3.35 which shows that the partial minima for the whole range of the resistive values are not obtained only at 0.5 mH which was set for the real process. Therefore, the searching algorithm has to start looking for the right value of $\widehat{R_g}$ and then should switch to look for the right value of $\widehat{L_g}$. Once the minimum of I_{err} is found, the searching moves alternatively from $\widehat{R_g}$ to $\widehat{L_g}$ in order to see if there is any change in any of them.
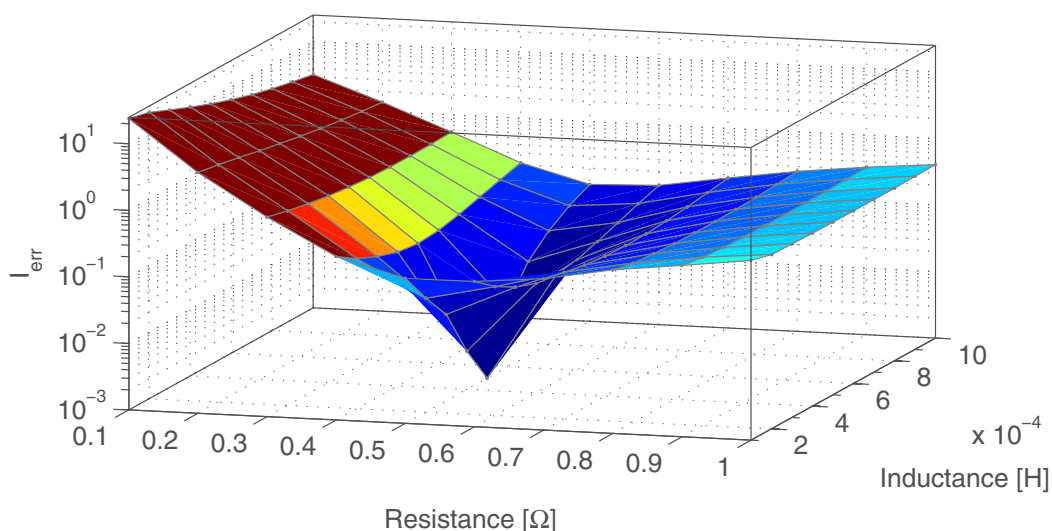
Figure 3.33. Relief of the criterion function I_{err}.
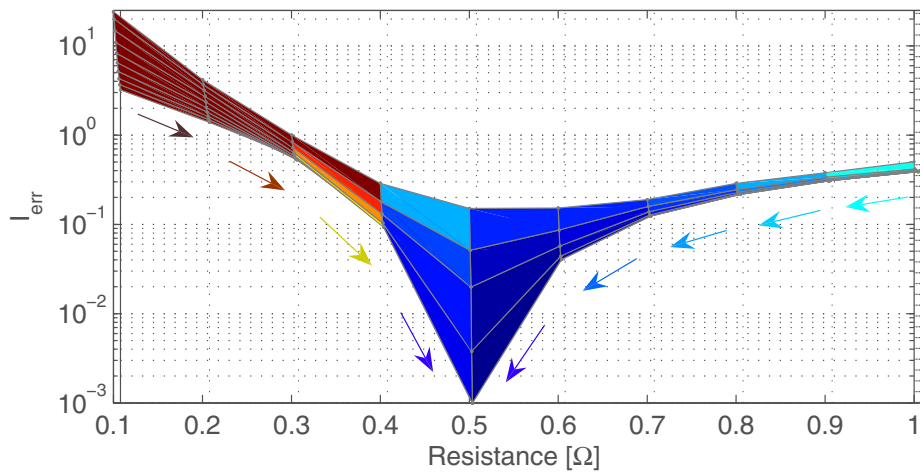
Figure 3.34. Searching the minimum of the grid resistance R_g.
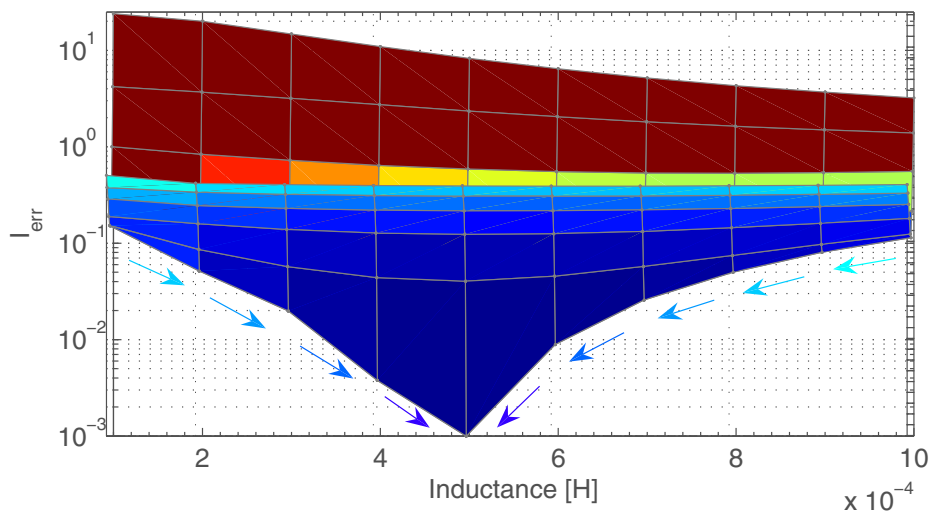
Figure 3.35. Searching the minimum of the grid inductance L_g.

The third condition is to set the boundaries of the searching algorithm for $\widehat{R_g}$ and $\widehat{L_g}$. The boundaries should be in accordance with the physical limits of the electrical grid. This is to limit the range of the searching algorithm, thus reducing the necessary steps for reaching minimum of I_{err}.

The fourth condition is to choose an adequate increment for the variation of $\widehat{R_g}$ and $\widehat{L_g}$. If the increment is small the estimation of R_g and L_g runs smoother but it takes more time to rich the right values. On the opposite, if the increment is large it takes less time to rich the right values but could compromise the resolution of the estimated values.

Finally, the fifth condition is to chose an appropriate time between the variation of $\widehat{R_g}$ and $\widehat{L_g}$. One period of the fundamental proved to be the optimal time between the variation of $\widehat{R_g}$ and $\widehat{L_g}$.

Figure 3.36 presents the canonical form of the modeled process $\underline{p}$ whose transfer function is expressed in (3.21). The canonical form is used in order to be able to change the parameters of the transfer function in real time. The reset signal (RST) is used to reset the integrator every time the values of $\widehat{R_g}$ and $\widehat{L_g}$ are changed. As it can be seen, the reset signal is synchronized with the zero crossings of the grid voltage.
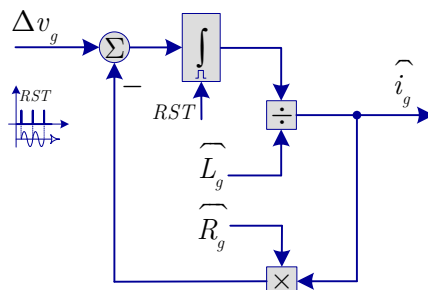
Figure 3.36. Canonical form of the transfer function presented in (3.21).

3.7.3 Selected results

The periodical measurement of the PCC voltage at zero current can be avoided by waiting first for a change in the grid impedance and then the PCC voltage is measured at zero current in order to validate the change of the grid impedance.

A simulation model based on the structure presented in Figure 2.27 was used to validate the proposed identification technique based on the searching algorithm. Figure 3.37 and Figure 3.38 show the estimation of the resistive and the inductive part of the grid impedance.
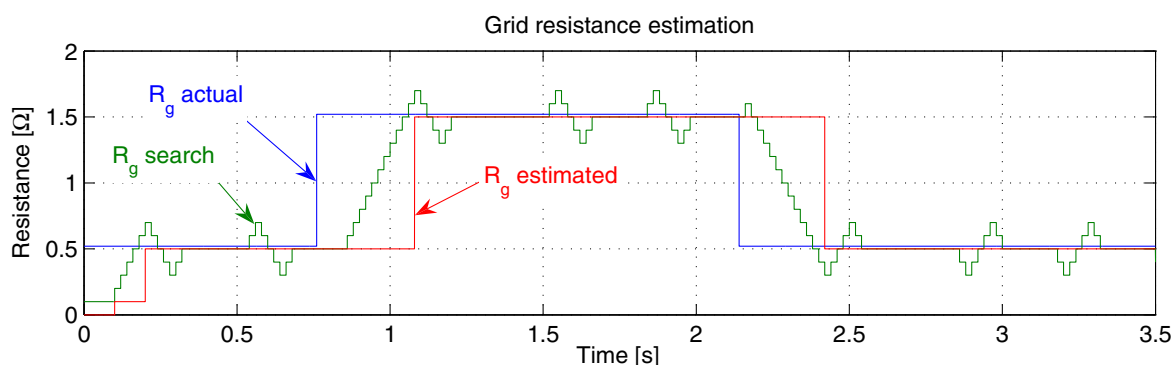
Figure 3.37. Estimation of the grid resistance R_g.
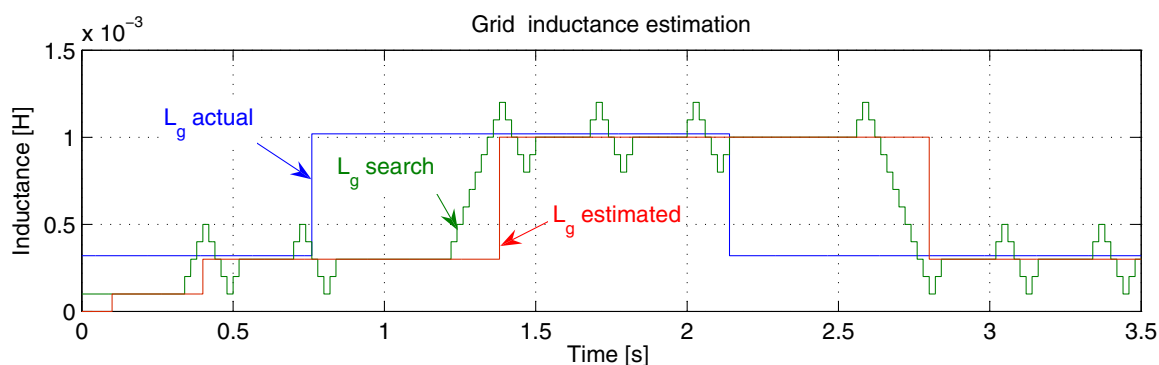
Figure 3.38. Estimation of the grid inductance L_g.

The initial real value of the grid resistance (R_g actual) was set to 0.52 Ω and the initial real value of the grid inductance (L_g actual) was set to 0.32 mH. As it can be noticed, it takes about 0.6 second to find the closest values of R_g and L_g.

Two steps were performed in R_g and L_g in order to test the dynamic performance of the identification technique. The steps consist of adding 1 Ω to R_g and 0.7 mH to L_g for a period of time from 0.76 to 2.14 seconds. It can be noticed that both estimated values for R_g and L_g are close to the real values. The error between the real value and the estimated value can be maximum the half of the increment value used for changing $\widehat{R_g}$ and $\widehat{L_g}$. The increment for $\widehat{R_g}$ was set to 0.1 Ω and the increment for $\widehat{L_g}$ was set to 0.1 mH, which give enough accuracy to the estimated values of R_g and L_g.

Figure 3.39 shows the actual (i_g) and estimated (i_g est) grid current during the steps of R_g and L_g. The figure includes also the evolution of the error between the actual and the estimated grid current. Two steady state areas of the first subplot are zoomed out in order to show how the estimated signal and the error signal are reset every fundamental cycle.

The evolution of I_{err} during the steps of R_g and L_g is presented in Figure 3.40. The representation of I_{err} is shown on a logarithmic scale for a better visualization. The signal I_{err} max represents the maximum of the criterion function I_{err} accumulated during one fundamental cycle. This signal is further used by the searching algorithm in order to determine the right values for the resistive and inductive part of the grid impedance.
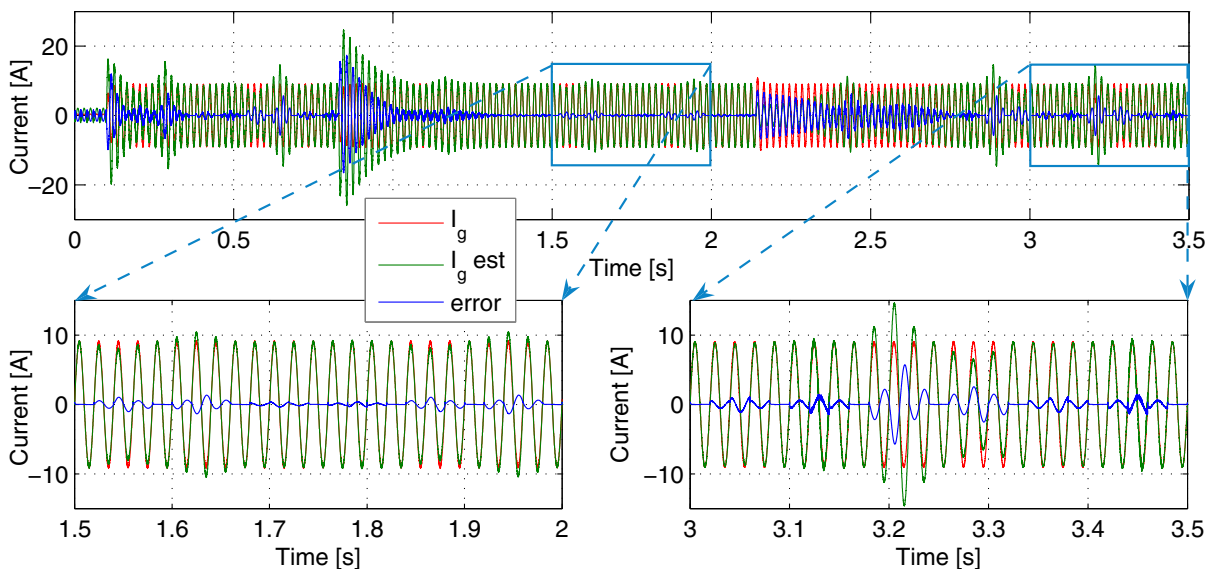
Figure 3.39. Actual and estimated grid current including the evolution of the error between the currents during the steps of R_g and L_g.
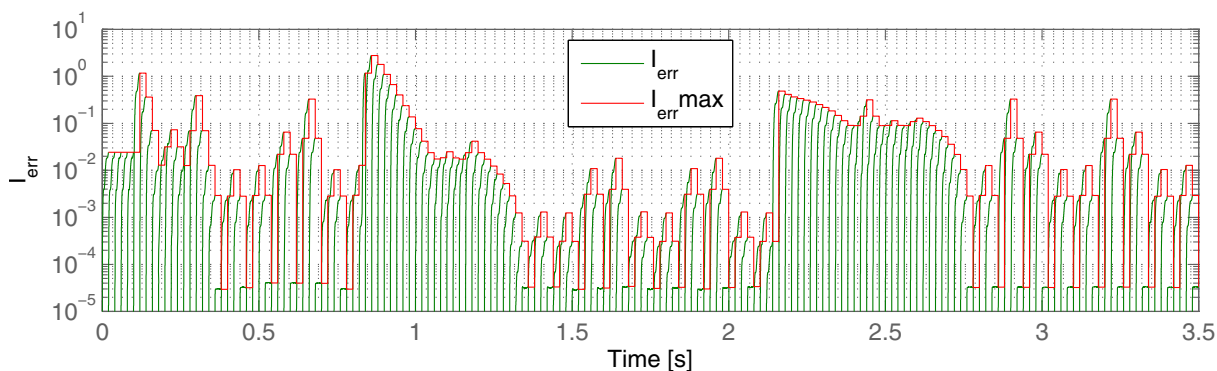
Figure 3.40. Evolution of I_{err} during the steps of R_g and L_g.

3.8 Summary

The estimation of the grid impedance is very useful for a better interaction between the DPGSs and the utility network. The information about the grid impedance can be used in many applications. However, in this thesis the estimation of the grid impedance was focused only on two well suited applications such as anti-islanding standard requirements (such as VDE0126) and adaptive control for DPGSs. In this chapter two active methods of grid impedance estimation were proposed.

One of the methods is based on single or double harmonic injection using two different algorithms such as DFT or STQ in order to estimate the grid impedance. It was shown that using a harmonic signal injection at a higher frequency (e.g. 400 - 600Hz) the output power of the inverter is less disturbed when compared to known similar methods. Moreover, the calculation algorithm based on STQ method is less complicated in contrast with some of the known algorithms based on more advanced mathematics such as DFT method or Prony extrapolation, thus being suitable for low cost systems. However, the use of a higher frequency injection implies an assumption that the grid impedance is linear on this frequency range. Nevertheless, the error caused by this assumption does not affect significantly the estimation of the grid impedance.

The second active method is based on the variations of the active and reactive output power of a DPGS. The calculation algorithm for the grid impedance based on PQ variations is less complicated in contrast with some of the known algorithms based on DFT method or Prony extrapolation. Also, the PQ variations method proved to be robust under the presence of harmonics. However, the implementation of the proposed method necessitates the usage of the PQ control for a single-phase system which can be troublesome in the case of using an inappropriate method to generate the orthogonal systems of the voltage and current.

In order to choose the most promising candidate for estimating the grid impedance it was noticed that the grid impedance estimation based on PQ variations performs better than the case of harmonic injection. Moreover, the PQ variations method can use the natural active power variations of a single-phase DPGS such as a PV inverter system where the input power varies according to the solar irradiation. However,

varying the active power of a DPGS could create flickers if the grid is weak and the output power of the DPGS is significant. Nevertheless, the proposed PQ variations method is focused for the single-phase DPGS which does not have significant power to create flickers.

A grid impedance estimation method using the model based identification was finally proposed as a tradeoff between the active and passive grid impedance estimation methods in order to get most of the advantages of both mentioned methods.

The quasi-passive method using the model based identification proved to be very effective. The method is more accurate compared to the active methods based on harmonic injection or PQ variations methods. Moreover, this method does not affect the power quality due to its passive behavior. However, the active behavior of the quasi-passive method comes in order to overcome the assumption that the voltage source of the electrical grid is time invariant. Therefore, the equivalent voltage source of the electrical grid can be obtained by periodical measurements of the PCC voltage at zero current. Nevertheless, the periodical measurement of the PCC voltage at zero current can be avoided by waiting first for a change in the grid impedance and then the PCC voltage is measured at zero current in order to validate the change of the grid impedance.

Chapter 4

Islanding Detection

This chapter presents an islanding detection technique. The chapter starts with an overview of the existent anti-islanding methods. Then, an accurate and less-disturbing active islanding detection method is proposed and described in detail. Selected results are given to demonstrate the effectiveness of the proposed algorithm.

4.1 Introduction

In the last few years the penetration of the DPGS with the electrical grid has increased and this was possible due to the inverter technology developments [84]. The evolution of the recommended guidelines and standards has streamed manufacturing and shaped inverter design and control [8, 10, 11, 85]. However, this necessitates continuous harmonization of standards at international level [86].

One important standard requirement for grid-connected systems is about island detection. Islanding phenomenon for a DPGS is defined when the inverter continues to operate with local loads when the electrical grid is disconnected [10]. Islanding can be intentional or unintentional [10]. For an unintentional island in which the DPGS energizes a portion of the electrical grid through the PCC, the DPGS shall detect the island and cease to energize the electrical grid within two seconds of the formation of an island [10, 11, 86]. As an issue, it applies for all DPGS including PV systems [8]. Although the probability of islanding occurrence is extremely low [87], standards dealing with the interconnection of inverter based photovoltaic system with the electrical grid require that an effective anti-islanding method is incorporated into the operation of the inverter [8, 11, 86].

4.2 Islanding detection techniques – An overview

There are numerous islanding detection methods reported for grid-connected PV systems in the technical literature [88-103] and their development has been summarized in a number of recent technical papers [17, 95, 104] and reports [88, 101]. They can be classified into two broad categories, namely, passive and active which can be inverter built or utility supported. The passive methods use the information already available about the electrical grid (e.g. voltage and current at the PCC) and are based on the monitoring of the following:

- Over-voltage/under-voltage protection (OVP / UVP) [88, 93];
- Over-frequency/under-frequency protection (OFP / UFP) [88, 93];
- Voltage phase jump [88, 93, 95];
- Voltage harmonic monitoring [93, 95];
- Current harmonic monitoring [17].

Although the passive methods have a nonintrusive character, they have a number of weaknesses and inability to detect islanding. The use of non-detection zones (NDZ) is used as a measure of performance for both these techniques as well as the active ones in a number of papers [91, 97]. An evaluation of different but most widely-used passive anti-islanding methods is offered for passive methods in [17, 103] and an excellent overview report for both passive and active methods is given in [88].

Active methods have been developed in order to overcome the limitations of the passive methods. In simple terms, active methods introduce perturbations into the inverter output power for a number of parameters as follows:

- Active and reactive power variation [93, 94];
- Active frequency drift or frequency shift up/down [88, 95, 96, 98, 99, 102];
- Sliding mode or slip-mode frequency shift [88, 95, 99];
- Sandia frequency shift or accelerated frequency drift or active frequency drift with positive feedback [95, 98];
- Impedance measurement [69, 77, 88, 93, 95], [VIII], [IX];
- Detection of impedance at a specific frequency or monitoring of harmonic distortion [69, 77, 88, 100], [VIII];
- Sandia voltage shift [88];
- Frequency jump [88].

In a recent paper [103], it has been shown that although the effectiveness of passive methods can be established by non-detection zones as represented by the power mismatch space (ΔP vs. ΔQ), in active frequency drifting methods their performance can be evaluated by using load parameter space based on the values of the quality factor (Q_f) and resonant frequency of the local load (f_0) [91].

Although most of the papers have been concentrated on PV inverters, islanding detection is also needed for all other inverter based systems using different sources such as FC [10, 94].

Many papers have concentrated on single-phase inverters and others also address three-phase technology [101], using DQ implementation [90]. Recently, the power mismatch for the 3rd and 5th harmonics and the implementation of an active anti-islanding method using resonant controllers was reported in [100].

Although numerous techniques exist and their implementation varies, it is important to note that a recommendation for software based algorithms would simplify matters for the easier adoption of the most robust and simplest techniques of all, and this should be kept as a guide for further development of the anti-islanding technology [87]. Moreover, there is a little technical information available for anti-islanding methods operating with controllers based on PLL for single-phase systems as most of them rely on the zero-crossing of the voltage to get information in order for the anti-islanding method to operate.

4.3 Active islanding detection technique based on PLL

This chapter proposes a simple non-invasive active anti-islanding method suitable for single-phase grid-connected inverter systems. The method relies on the current angle being the monitored variable which is derived from a PLL structure based on a OSG-SOGI [IV], [XII]. Prior to deriving the angle reference signal for the current controller, this angle signal is slightly distorted by a sinusoidal signal having a very low amplitude and the same frequency as the one obtained from the PLL fully synchronized at the same time. Every cycle this distortion is corrected as long as the grid voltage is available. When the grid is disconnected, the distortion through a loop of either positive or negative injection will continue to distort the angle reference eventually pushing the feedback signal from the inverter to cross the selected boundary and therefore causing the inverter to trip and prevent islanding.

4.3.1 Method description

The proposed anti-islanding method and the PLL implementation are both shown in Figure 4.1 [XIII]. The main task of a PLL is to provide unity power factor operation, which involves synchronization of the inverter output current with the grid voltage, and to give a pure sinusoidal current reference. The OSG and the PLL structure for a single-phase system have been described in detail in [IV], [XII].
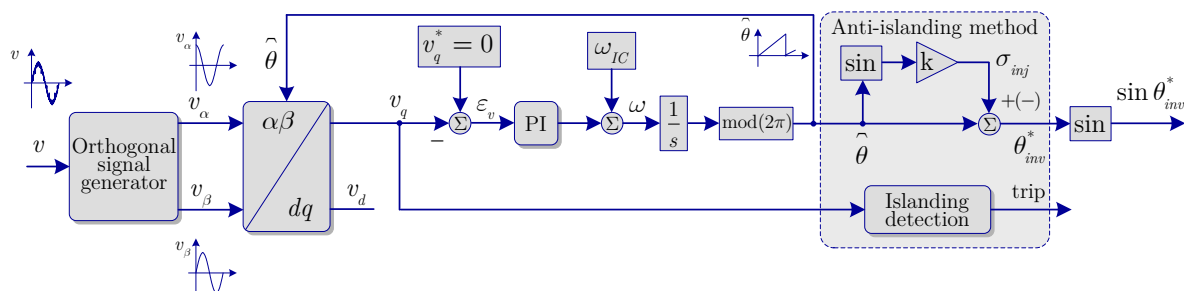

Figure 4.1. Proposed anti-islanding method using OSG-SOGI based PLL.

The method is based on the modification of the derived angle from the PLL ($\widehat{\theta}$). In particular, a sinusoidal signal (σ_{inj}) synchronized with the cycle is injected to slightly modify $\widehat{\theta}$. A feedback signal is then extracted from the voltage in the q axis (v_q), as a consequence of the injected signal σ_{inj}. The signal injection can be done with either positive or negative sign as shown in Figure 4.1.

The injected signal is defined by (4.1):

$$\sigma_{inj} = k \cdot \sin\widehat{\theta} \tag{4.1}$$

- where the gain k is used to choose the amount of disturbance needed for the islanding detection.

The resulting phase angle reference of the inverter (Figure 4.1) becomes:

$$\sin\theta^*_{inv} = \sin(\widehat{\theta} + \sigma_{inj}) = \sin(\widehat{\theta} + k \cdot \sin\widehat{\theta}) \tag{4.2}$$

Since:

$$\sin(a + b) = \sin a \cdot \cos b + \cos a \cdot \sin b \tag{4.3}$$

From (4.2) and (4.3) by replacing $a = \widehat{\theta}$ and $b = k \cdot \sin\widehat{\theta}$ results:

$$\sin\theta^*_{inv} = \sin\widehat{\theta} \cdot \cos(k \cdot \sin\widehat{\theta}) + \cos\widehat{\theta} \cdot \sin(k \cdot \sin\widehat{\theta}) \tag{4.4}$$

The approximations presented in (4.5) are made in order to show the analogy of the proposed method compare to a second-harmonic signal injection.

$$\begin{cases} \sin(k \cdot \sin\widehat{\theta}) \simeq k \cdot \sin\widehat{\theta}, \text{ for } 0 < k \ll 1 \\ \cos(k \cdot \sin\widehat{\theta}) \simeq 1, \text{ for } 0 < k \ll 1 \end{cases} \tag{4.5}$$

Applying the approximations from (4.5) to (4.4) results:

$$\sin\theta^*_{inv} \simeq \sin\widehat{\theta} + k \cdot \sin\widehat{\theta} \cdot \cos\widehat{\theta} \tag{4.6}$$

Being known that:

$$\sin 2\theta = 2 \cdot \sin\theta \cdot \cos\theta \tag{4.7}$$

and writing (4.6) as:

$$\sin\theta^*_{inv} \simeq \sin\widehat{\theta} + \frac{k}{2} \cdot (2 \cdot \sin\widehat{\theta} \cdot \cos\widehat{\theta}) \tag{4.8}$$

It yields:

$$\sin\theta^*_{inv} \simeq \sin\widehat{\theta} + \frac{k}{2} \cdot \sin 2\widehat{\theta} \tag{4.9}$$

For small values of k (e.g. for $k<0.05$), the addition of $k \cdot \sin\widehat{\theta}$ to $\widehat{\theta}$, as provided by the PLL, is similar to the addition of a second-harmonic signal ($\widehat{A} \cdot \sin 2\widehat{\theta}$) to $\sin\widehat{\theta}$. The only difference being that the amplitude of the signal as expressed in (4.9) can be slightly different (app. 0.05%) than the amplitude of the signal as expressed in (4.2).

The addition of $k \cdot \sin\widehat{\theta}$ to $\widehat{\theta}$ has been chosen over the addition of a second-harmonic signal due to the fact that the signal expressed in (4.2) is unitary unlike the signal expressed in (4.9), thus not affecting the current reference amplitude. In other

words, by adding $k \cdot \sin \widehat{\theta}$ to $\widehat{\theta}$, the current reference will contain a small sinusoidal signal with a frequency twice the fundamental frequency, according to (4.9).

When the inverter supplies power to the grid, the consequence of adding $k \cdot \sin \widehat{\theta}$ to $\widehat{\theta}$ is observed as a feedback signal in the voltage (in the q axis) measured at the PCC. The feedback signal has the double of the fundamental frequency and its amplitude is related to the grid impedance value. The feedback signal can be extracted from the voltage at PCC after the Park Transform (from v_q). After the transformation, the feedback signal frequency will become half of the frequency, as it is demonstrated below.

The Park Transform is presented as:

$$v_q = -\sin \theta \cdot v_\beta + \cos \theta \cdot v_\alpha \tag{4.10}$$

Considering the orthogonal voltage system of the feedback voltage ($v_\alpha^{'}$ and $v_\beta^{'}$) due to the signal injection as shown in (4.2) and removing the fundamental components, the expression shown in (4.10) becomes:

$$v_q^{'} = -\sin \theta \cdot v_\beta^{'} + \cos \theta \cdot v_\alpha^{'} \tag{4.11}$$

- where $v_\alpha^{'}$ and $v_\beta^{'}$ are considered normalized and represented as:

$$\begin{cases} v_\alpha^{'} = \sin\left(2\theta\right) \\ v_\beta^{'} = \sin\left(2\theta + \pi\big/2\right) = \cos\left(2\theta\right) \end{cases} \tag{4.12}$$

From (4.11) and (4.12) it results:

$$v_q^{'} = -\sin \theta \cdot \cos\left(2\theta\right) + \cos \theta \cdot \sin\left(2\theta\right) \tag{4.13}$$

Knowing that:

$$\begin{cases} \sin\left(2\theta\right) = 2 \cdot \sin \theta \cdot \cos \theta \\ \cos\left(2\theta\right) = \cos^2 \theta - \sin^2 \theta \end{cases} \tag{4.14}$$

It results:

$$v_q^{'} = -\sin \theta \cdot \left(\cos^2 \theta - \sin^2 \theta\right) + \cos \theta \cdot 2 \cdot \sin \theta \cdot \cos \theta \tag{4.15}$$

Solving the expression shown in (4.15), it yields:

$$v_q^{'} = \sin \theta \cdot \left[-\left(\cos^2 \theta - \sin^2 \theta\right) + 2 \cdot \cos^2 \theta\right] = \sin \theta \cdot \underbrace{\left[\sin^2 \theta + \cos^2 \theta\right]}_{=1} = \sin \theta \tag{4.16}$$

Thus, the feedback voltage signal can by easily extracted after the Park Transform by using a resonant filter tuned on the fundamental frequency.

The proposed islanding detection method is based on the detection of the grid impedance changes. The relation between the feedback signal due to the injection and the grid resistance is nonlinear (Figure 4.2a), while the relation with the grid inductance is linear (Figure 4.2b).

One of the main advantages of the proposed anti-islanding method is that it does not affect the zero crossing of the current. A very small amplitude of the injected signal

(σ_{inj}) is required to be injected at all times for the method to be successful when needed.

The structure presented in Figure 4.3 assists with the monitoring of the anti-islanding condition, where:

- λ_{Amp} is the amplitude of the feedback signal extracted from v_q;
- $\lambda_{AmpAvg50}$ is the 50 Hz average of the signal λ_{Amp};
- $\lambda_{AmpAvg5}$ is the 5 Hz average of the signal $\lambda_{AmpAvg50}$;
- δ represents the difference between the actual value of $\lambda_{AmpAvg50}$ and the delayed value of $\lambda_{AmpAvg5}$.

When the islanding occurs, this is also reflected in the grid impedance value. The change in the grid impedance value is then detected in the feedback signal in the form of δ. Then, following the algorithm shown in Figure 4.4, a trip signal is generated.

The flowchart of the islanding detection algorithm (the "Logic" block from Figure 4.3) is presented in Figure 4.4. The algorithm is described as follows:

- the component δ is compared to a threshold value;
- when δ is bigger than the threshold value a timer is started.

(a)   (b)
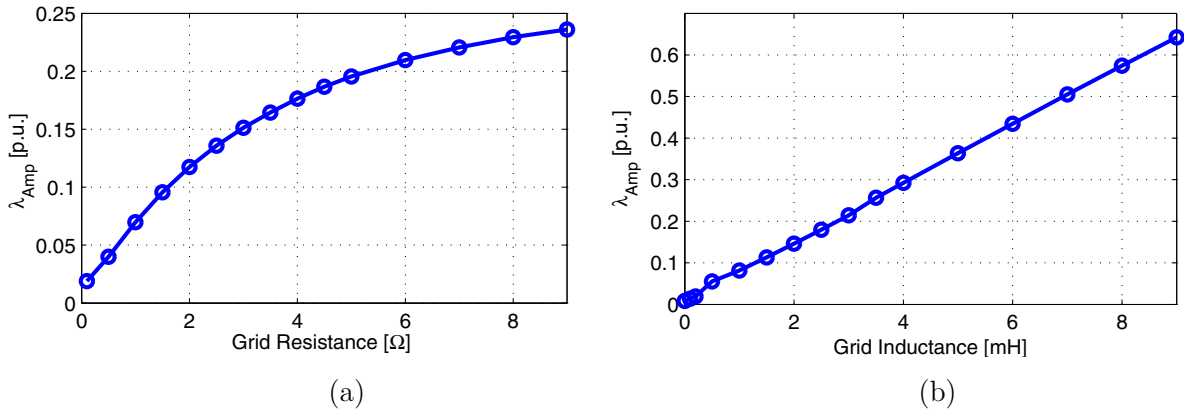
Figure 4.2. The relation between the feedback signal and the grid impedance: a) grid resistance R_g; b) grid inductance L_g.
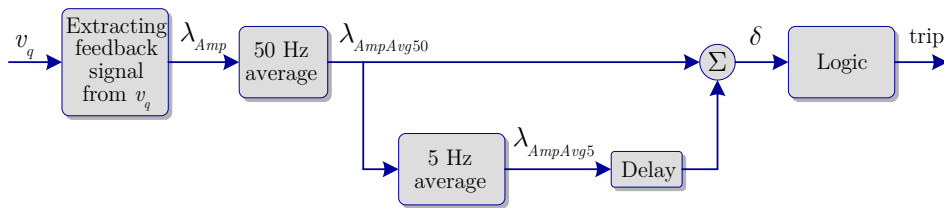
Figure 4.3. Signal processing for islanding detection.
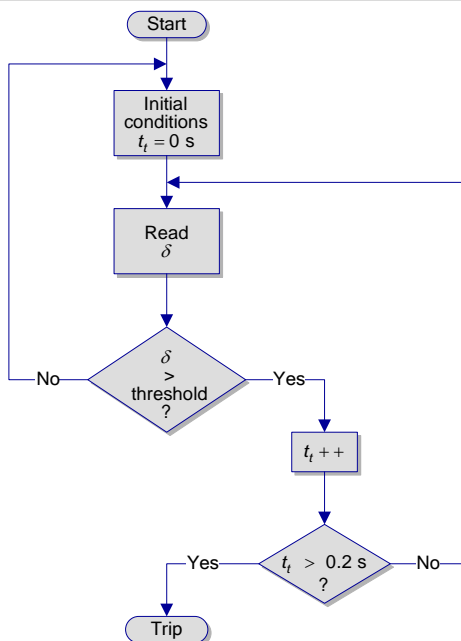
Figure 4.4. The islanding detection algorithm.

The time value of the timer is named t_t and its initial condition is 0 s. If the δ remains larger than the threshold value for more than 0.2 s the inverter is tripped. Otherwise, if δ becomes smaller than the threshold value within 0.2 s, the timer is reset to 0 s. The threshold value and the tripping time can be chosen in accordance with one of the standards IEEE 929-2000 [8], IEEE 1547.1-2005 [11] and VDE 0126.1.1 [7].

Figure 4.5b and Figure 4.6b show the effect of the injected signal (σ_{inj}) for the inverter phase angle reference (θ_{inv}^*) and for the grid current reference in p.u. ($\sin\theta_{inv}^*$) respectively, when the amplitude of the injected signal is 10 times larger than necessary for clarity purposes. The zero crossings of the grid current reference are not affected (Figure 4.6b).

(a)   (b)
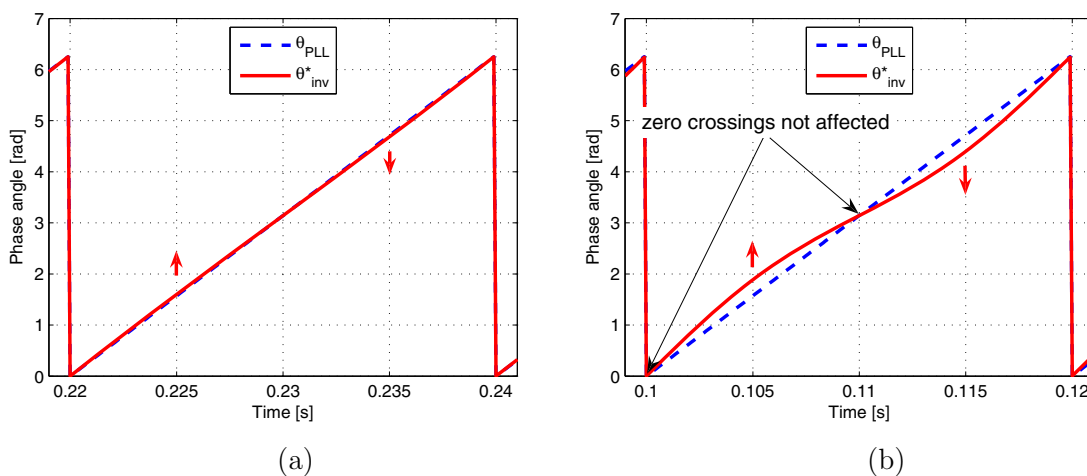
Figure 4.5. The effect of the injected signal (σ_{inj}) for the inverter phase angle reference (θ_{inv}^*) at: a) normal operation and b) when the amplitude of the injected signal is 10 times larger than necessary; where $\theta_{PLL} = \hat{\theta}$.

77

(a)   (b)
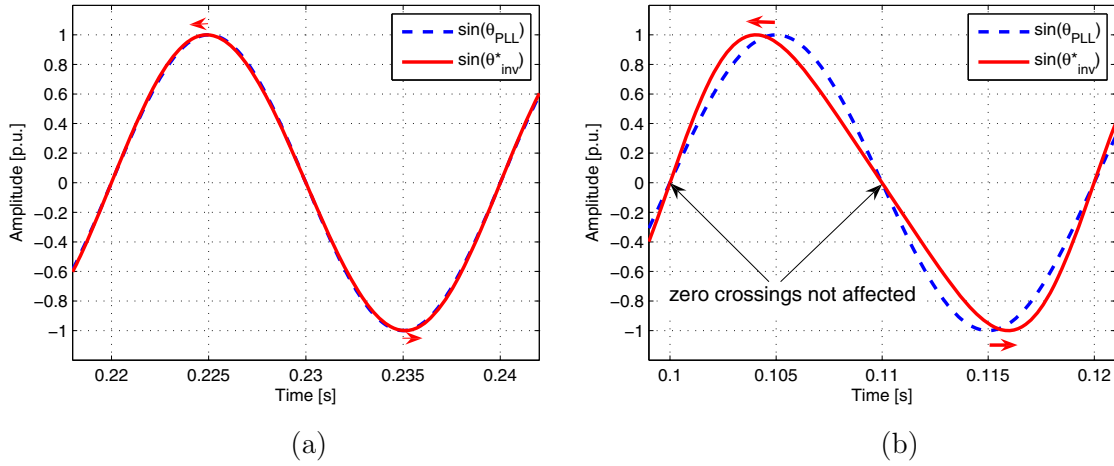
Figure 4.6. The effect of the injected signal (σ_{inj}) for the grid current reference in p.u. ($\sin\theta_{inv}^*$) at: a) normal operation and b) when the amplitude of the injected signal is 10 times larger than necessary; where $\theta_{PLL} = \hat{\theta}$.

4.3.2 Selected results

The proposed method has been implemented on a setup as shown in Figure 4.7 for validation purposes. The setup consists of two main parts, namely the power circuit (hardware part) and the control structure (software part). The power circuit is represented by a single-phase DPGS which includes an input power source, a grid connected power converter, an output filter attached to the power converter, an RLC local load connected at the PCC, the equivalent grid impedance and the voltage source of the grid. The control structure is composed of an input power control unit (e.g. MPPT algorithms, DC voltage controller, etc), a single-phase PLL, a current controller (e.g. PR controller) and a PWM generator.

Based on the requirements of the IEEE Standard 929-2000, it is imperative that any method of anti-islanding is tested to establish its performance when a parallel resistor(R)-inductor(L)-capacitor(C) (RLC) load with a specific quality factor (Q) is used.
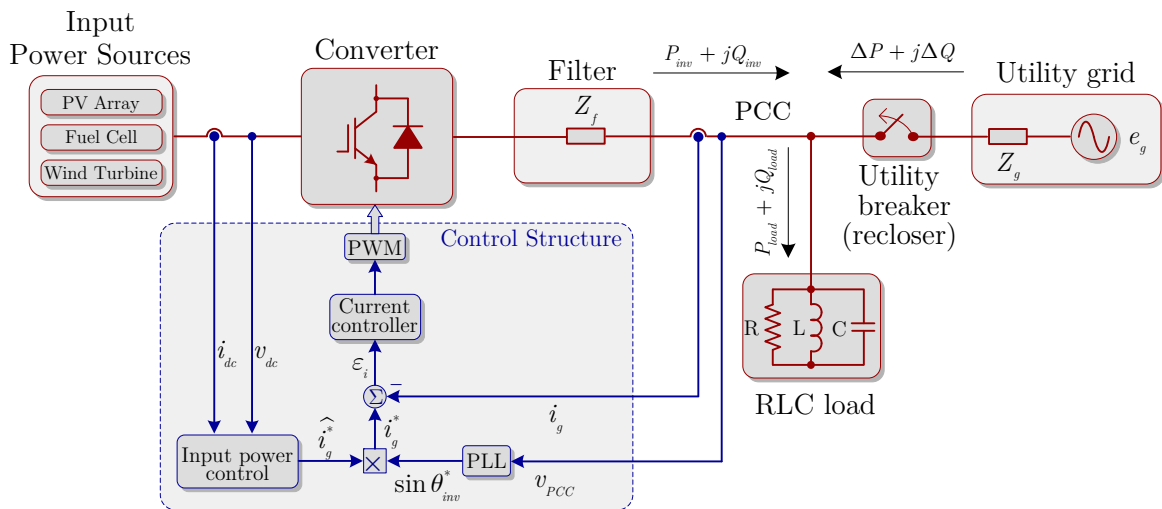
Figure 4.7. Power circuit and control structure of a grid connected system having an RLC load connected at the PCC.

Figure 4.8 shows a comparison of the grid current and the inverter phase angle reference with and without signal injection. As it can be seen, the grid current is not affected significantly by the injected signal (σ_{inj}). The gain k (see Figure 4.1) represents the injection ratio and it was set to 0.03 for all of the results presented here. Very small amplitude of the injected signal (σ_{inj}) was required to be injected at all times in order to detect the islanding even for an RLC load with a quality factor of 10. The grid voltage THD was about 2.5% for all of the results.

Four cases were investigated in order to validate the proposed method. In the Case 1 only a parallel resistive load of 36.14 Ω was used. The islanding detection and the grid current and the voltage in the PCC for the Case 1 are presented in Figure 4.9 which confirms that the islanding is detected within the time frame required by the standards [8, 11].
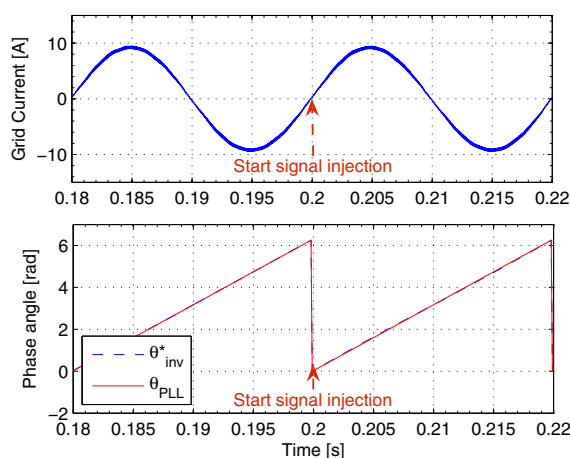
Figure 4.8. Comparison of the grid current and the phase angle reference with/without signal injection.
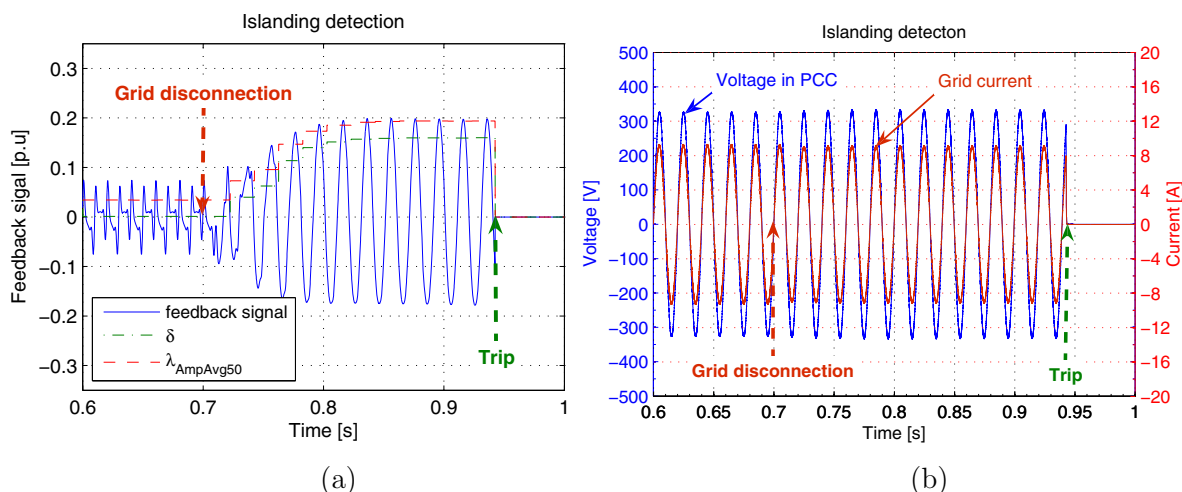
Figure 4.9. Islanding detection in the case of a parallel R load only: a) islanding detection based on the feedback signal; b) grid current and voltage at the PCC.

Figure 4.10 represents the Case 2 where a parallel RLC load with a quality factor of 2.5 and a resonance frequency (f_r) equal to the fundamental frequency was used in accordance with the IEEE Standard 929-2000 [8]. As it can be noticed, the islanding detection does not pose any difficulties. The currents through the RLC load are shown in Figure 4.10c. A significant change in the harmonic content can be seen when the grid is disconnected. This is due to the harmonic background of the electric grid.

Figure 4.11 shows the Case 3 where a parallel RLC load with a quality factor of 1 in accordance with the IEEE Standard 1547.1 [11] was used. As it can be seen, the islanding detection performs very well.

Figure 4.12 presents the Case 4 where a parallel RLC load with a quality factor of 10 was used. This was to show that the proposed method can perform well even under higher quality factors (e.g. $Q=10$). The proposed method proved to be robust and effective even under such extreme scenarios.

(a)

(b)

(c)
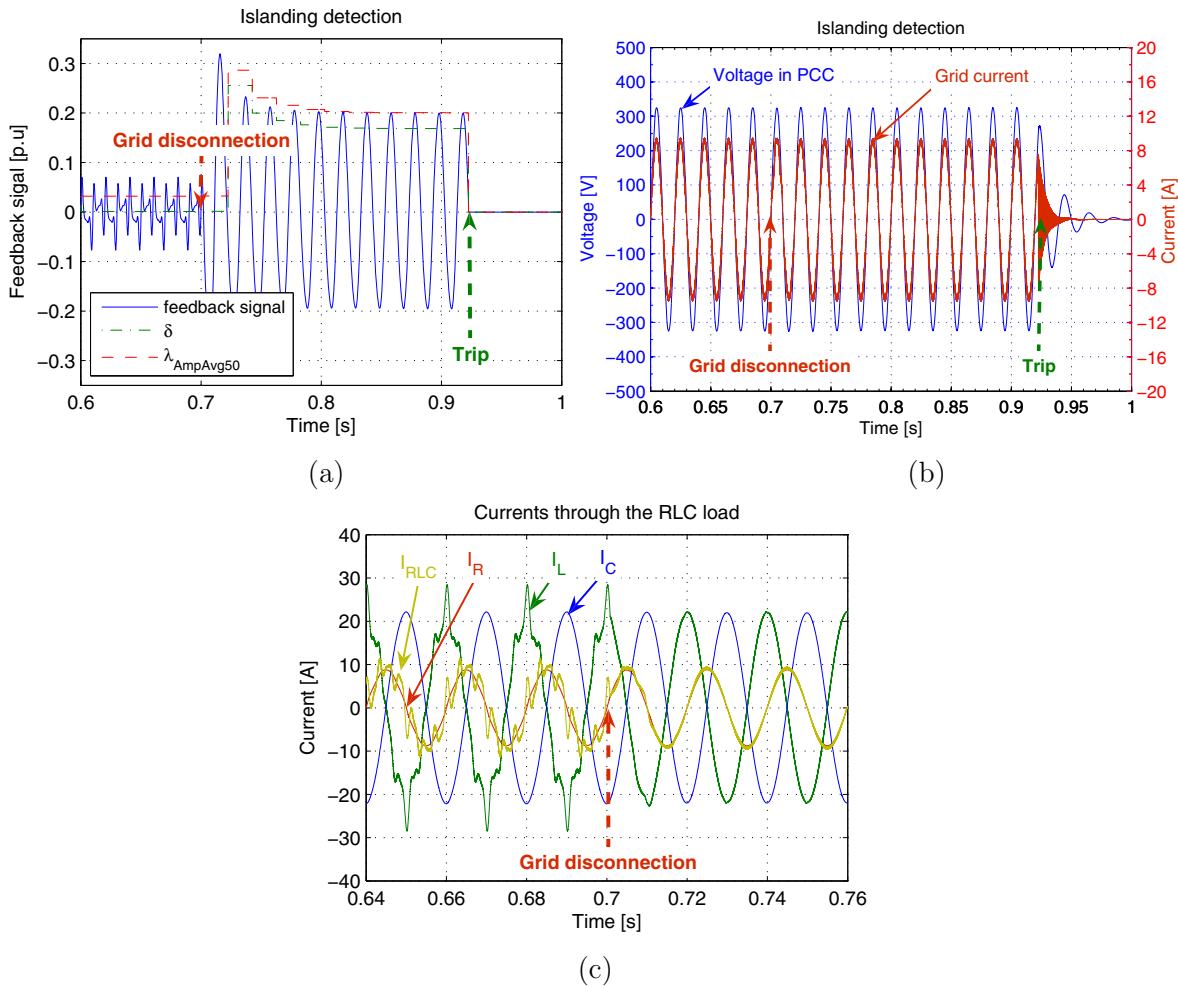
Figure 4.10. Islanding detection in the case of a parallel RLC load with a Q=2.5 and f_r=50Hz: a) islanding detection; b) grid current and voltage at the PCC; c) currents through the RLC load.
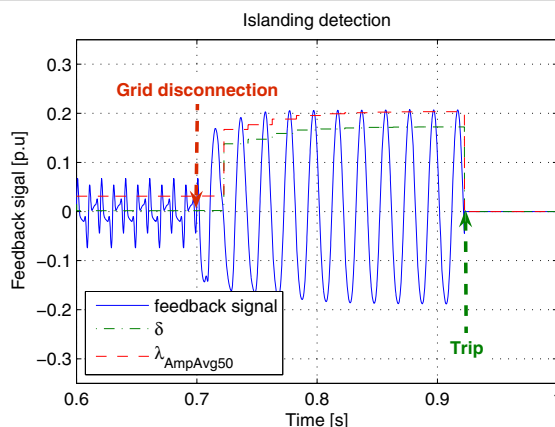
Figure 4.11. Islanding detection in the case of a parallel RLC load with Q=1.
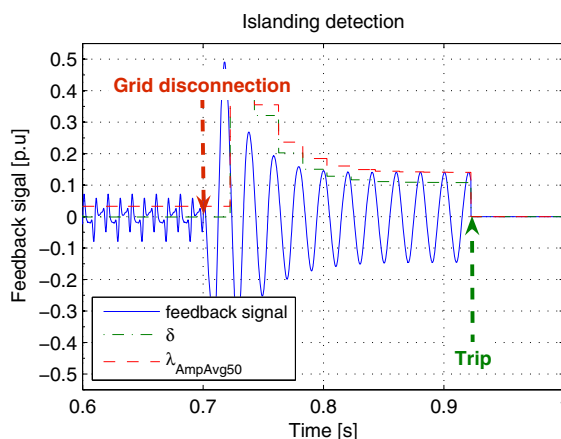
Figure 4.12. Islanding detection in the case of a parallel RLC load with a Q=10.

4.4 Summary

This chapter proposed an accurate and less-disturbing active anti-islanding method based on PLL for single-phase grid connected inverter systems. The method is based on the detection of the grid impedance changes. The proposed method relies on a continuous injection of a signal to the inverter angle being used as a modified reference for the inverter current to be generated. This affects the inverter in a negligible way when the grid is available. However, the method is able to detect grid failure by detecting the changes in the grid impedance. Namely, the feedback signal extracted from the voltage gives the information about the grid impedance changes, thus resulting in an effective islanding detection.

Four different scenarios using different local loads were investigated in order to test the effectiveness and the robustness of the proposed method. As noticed from experimental results, the method proved to be effective even under extreme scenarios, such as a parallel RLC load with a quality factor equal to ten and the resonant frequency equal to the fundamental frequency.

Part II

Control of Single-Phase DPGS

Chapter 5

Control Review of DPGS

This chapter gives in the first part an overview about the general control structure of a single-phase DPGS. The second part of this chapter presents an improved DC voltage controller which is able to remove the 100 Hz typical ripple from the measured DC voltage. The last part of the chapter introduces a comparison between the classical PI and the PR current controllers.

5.1 Overview of general control structure

As it has been presented in Chapter 1, efficient and economic ways of generating electricity closer to the load(s) are possible nowadays. However, this is valid only for low power three-phase systems or for single-phase systems such as PV, small wind turbine, FC, etc. The single-phase system presents opportunities for micro DPGS to be connected to the grid (e.g. roof-top PV systems).

A general structure of a DPGS is presented in Figure 5.1. The DPGS consists of a power circuit and a control unit.
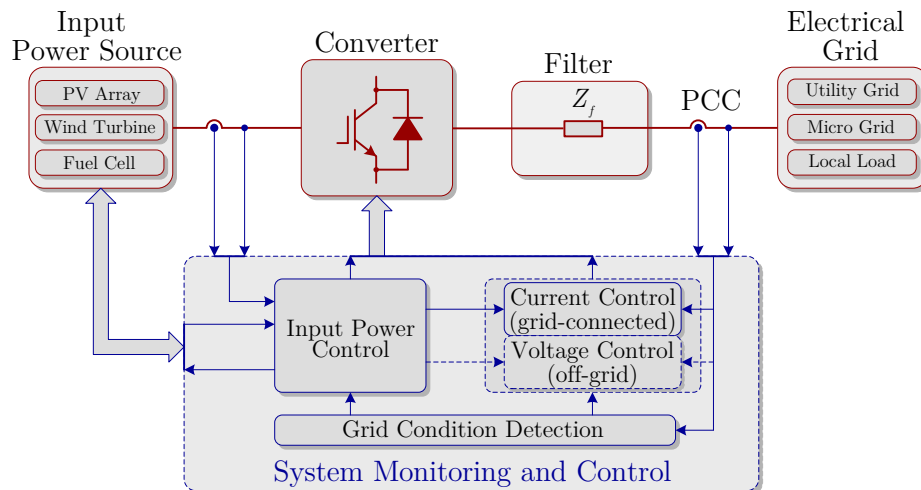
Figure 5.1. General structure of a DPGS.

The power circuit contains the input power source (e.g. photovoltaic, fuel cell, small wind turbine, etc), the converter which can be a single-stage converter (e.g. DC-AC converter) or a double stage converter (e.g DC-DC and DC-AC converter with or without galvanic isolation), an output filter in order to cut-off the switching frequency and the load system which can consist of grid impedance or local loads.

A solution using a single-stage converter (DC to AC) for a 1.5kW single-phase PV inverter has been developed and successfully tested in [I], [VII]. The advantages of the single-stage converters are: good efficiency, a lower price and easier implementation. The disadvantage is that requires a high DC voltage (typically higher than 350 V).

The control part is composed of three main control elements, namely: - the grid condition detection; - the input power control and - the control of the AC current (for grid-connected systems) or AC voltage (for off-grid systems).

The grid condition detection deals in general with the grid voltage monitoring which provides information about the amplitude, phase and frequency of the grid voltage (Chapter 2). The grid condition detection can also be used to provide other functions such as: - protections for the grid connected converter in the case of under/over voltage or under/over frequency; - islanding detection or - grid impedance estimation.

The input power control structure differs depending on the input power source used. For instance, in the case when a PV system is used, the input power control is composed of a MPPT, a DC voltage controller and a power feed-forward in order to improve the slow dynamic of the MPPT (Figure 5.2). In the case of a double stage converter with a DC-DC converter and a DC-AC converter, the MPPT is typically implemented for the DC-DC converter [VII].

There are different techniques for controlling the AC voltage in the case of off-grid generation systems such as voltage droop or frequency droop control [57]. However, the control of off-grid applications is not discussed in this thesis.

In the technical literature there are several strategies for the control of the AC current in the case of distributed generation systems. A very common technique used for both motor drives and grid connected systems is the well known *dq* control (synchronous rotating *dq* reference frame). However, the *dq* control strategy cannot be implemented for single-phase systems. Therefore, other strategies are considered for such systems. Most of the single-phase distributed generation systems use only the control of the active power which is based on the stationary reference frame. Nevertheless, the control of active and reactive power is also possible for single-phase systems as is presented in [57]. The PQ control for a single-phase grid-connected system is described in §3.6, where the $\alpha\beta$ approach of the three-phase systems is used for a method to estimate the grid impedance.
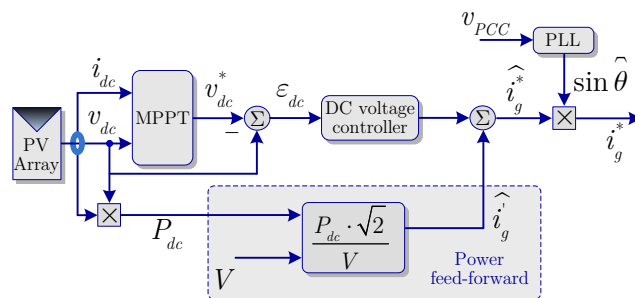
Figure 5.2. Typical input power control structure for a PV system.

Several controllers, such as PI, PR, dead-beat, hysteresis or predictive controllers, can be used to control the current in the case of distributed generation systems. In the situation when the control strategy is implemented in stationary reference frames, the use of the classical PI controller leads to unsatisfactory current regulation due to its drawbacks [VII]. Therefore, the PR, dead-beat and hysteresis controller become a good alternative in such situation. A comparison between the PI controller versus the PR controller is given in §5.3.

5.2 Improved DC voltage controller

An important problem when controlling the DC voltage is represented by the presence of the 100 Hz typical ripple in the measured DC voltage. This ripple is due to the fact that the DC power in a single-phase grid connected system is a function of squared sinus of the fundamental frequency (e.g. 50 Hz). Thus, the ripple becomes double (e.g. 100 Hz) of the fundamental frequency. The amplitude of the DC voltage ripple is directly related to the value of the DC capacitor used for the DC bus. Therefore, if the DC capacitance decreases, the amplitude of the ripple becomes bigger. However, the converter manufacturers tend to decrease the value of the DC capacitance in order to keep the production costs low, thus leading to a higher DC voltage ripple. The propagation of this low frequency ripple to the reference of the converter output current is undesirable.

Usually, the measured DC voltage is filtered before it is used for a DC controller in a grid-connected inverter system, as shown in Figure 5.3. The most commonly used filters are the LPF or the running average filter. However, these filters introduce a significant delay. The delay could affect the stability of the DC voltage controller in the case when the band-width of the filter is not chosen properly. The filter has to have a faster dynamic compared to the DC voltage controller to not affect the stability. A slower response time of a filter means also a slower DC voltage controller leading to a sluggish control of the DC voltage. Therefore, a notch filter tuned at double the fundamental frequency has been used as an alternative filter to the classical LPF or the running average filter. A comparison between the notch filter and the running average filter is given next.
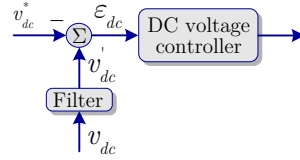
Figure 5.3. DC voltage controller using a filtered measured DC voltage.

The transfer function of the notch filter (H_{NF}) is presented in (5.1).

$$H_{NF}(s) = \frac{s^2 + 2\zeta_2 \omega_n s + \omega_n^2}{s^2 + 2\zeta_1 \omega_n s + \omega_n^2}, \text{ where } \zeta_2 \ll \zeta_1 \tag{5.1}$$

Figure 5.4 shows the Bode plot of the transfer function presented in (5.1). As it can be noticed, the notch filter cuts only the frequency of the DC voltage ripple.

The parameters used for the running average filter are given as follows: the sampling frequency was 10 kHz; the number of samples for the average was 100 with an overlap of 99 samples.

A comparison between the step responses of the running average filter and the notch filter, both set at 100 Hz, is given in Figure 5.5. The notch filter responds faster than the running average filter. Nevertheless, in the case of a noisy measured DC voltage, an average running filter is preferred to the notch filter due to the fact that it filters out all the harmonics above the frequency of the DC voltage ripple.

Three cases were considered in order to test the dynamics of the DC voltage loop under a step of 10 % in the DC voltage reference. The parameters of the DC voltage controller were the same for all of the three cases ($K_p = 0.5$ and $K_i = 50$).
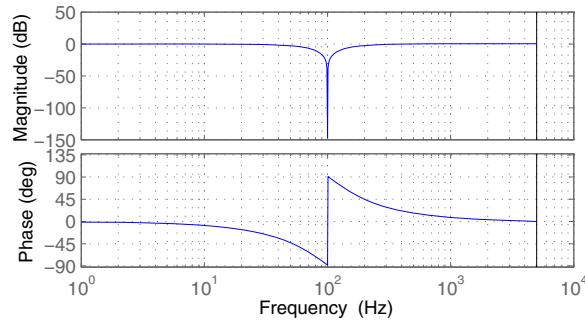
Figure 5.4. Bode diagram of the notch filter.
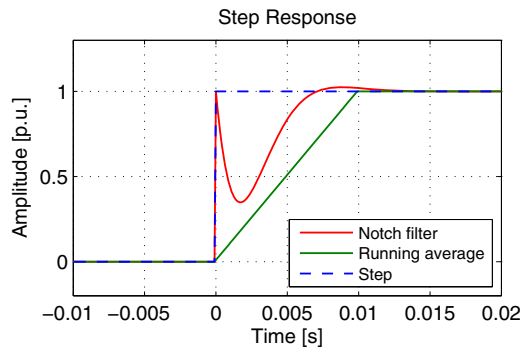
Figure 5.5. Step response of the filters using running average or notch filter.

The first case uses a DC voltage loop without filtering the measured DC voltage. The response of the system in this case is presented in Figure 5.6a and the converter output current is shown in Figure 5.6b. It is noticeable the negative influence of the DC voltage ripple on the converter output current in the case when the measured DC voltage is not filtered. Figure 5.6a shows also the filtered DC voltage using the running average filter ("*Vdc Avg*") and the notch filter ("*Vdc Notch*"). The reference and the measured DC voltage are represented by "*Vdc Ref*" and "*Vdc Meas*" respectively.

The second analyzed case uses a DC voltage loop including a running average filter for the measured DC voltage. The response of the system in this case is presented in Figure 5.7a and the converter output current is shown in Figure 5.7b. As it can be seen, a poor dynamic response is obtained compared to the first case. The influence of the higher delay introduced by the running average filter is seen in a considerable big overshoot. A slower DC voltage controller is recommended in this case.

The third case uses a DC voltage loop including a notch filter for the measured DC voltage. The response of the system in this case is presented in Figure 5.8a and the converter output current is shown in Figure 5.8b. As it can be noticed, a similar dynamic response is obtained compared to the first case when no filter is used for the measured DC voltage. The influence of the lag introduced by the notch filter is less significant compared with the second case when a running average filter is used. The DC voltage loop is not significantly affected by the presence of the notch filter.

A comparison between the harmonic current spectra for all three cases presented above is presented in Figure 5.9. As it can be seen, the presence of the filters for the DC voltage loop makes a big difference compared with the case when no filtering is present. The current THD drops significantly in the case when filters are used. The difference in the current THD between the running average filter and the notch filter is very small and is due to the fact that the running average filter cuts off all the harmonics above 100 Hz, while the notch filter cuts off only the DC voltage ripple of 100 Hz, as shown in Figure 5.4.
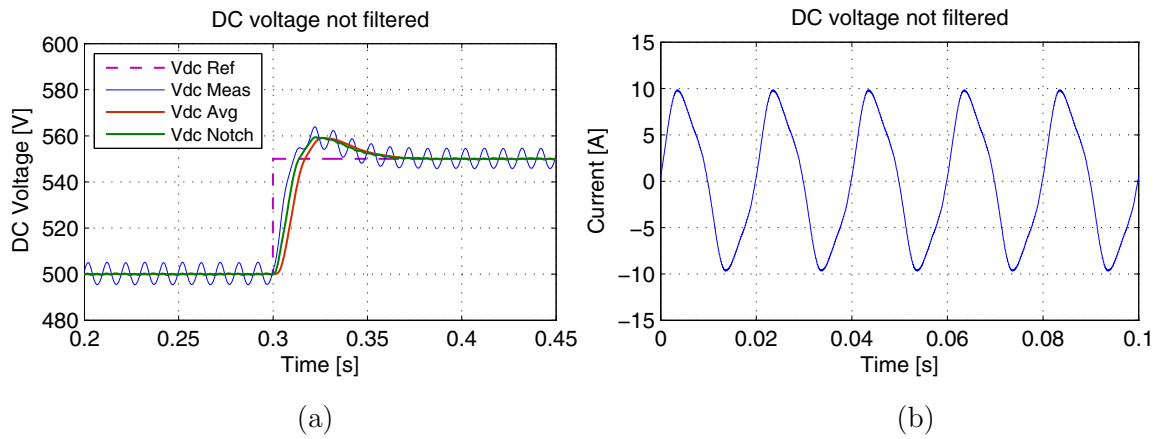
Figure 5.6. a) Step response of the DC voltage controller and b) converter output current using no filter for the measured DC voltage.
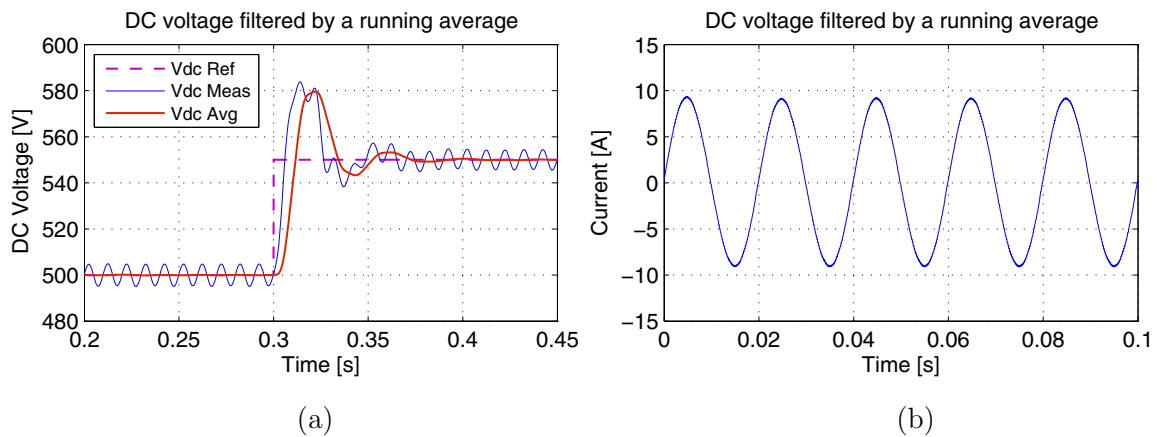
Figure 5.7. a) Step response of the DC voltage controller and b) converter output current using running average filter for the measured DC voltage.
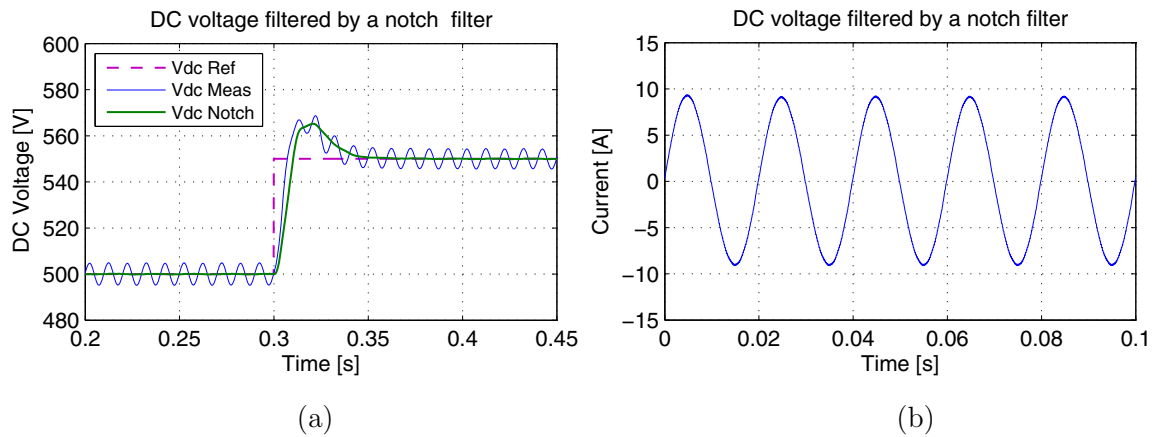
Figure 5.8. a) Step response of the DC voltage controller and b) the converter output current using notch filter for the measured DC voltage.
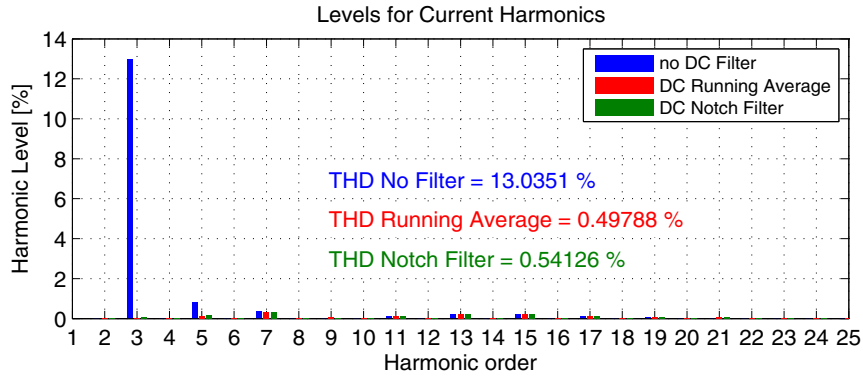
Figure 5.9. The currents spectrums for three different cases: no DC filter, running average filter and notch filter.

The high level of the third harmonic in the case when no filter is used for the DC voltage loop is due to the propagation of the 100 Hz DC voltage ripple to the output current amplitude reference ($\widehat{i_g^*}$), as shown in (5.2). $\widehat{i_{ct}}$ is the constant value of $\widehat{i_g^*}$ and $\widehat{A_{dcR}}$ is the amplitude of the propagated 100 Hz ripple through the DC voltage controller.

$$\widehat{i_g^*} = \widehat{i_{ct}} + \widehat{A_{dcR}} \cdot \sin(2\omega_{50}t) \tag{5.2}$$

This reference is then multiplied with the sinus of the grid phase angle as provided by the PLL to yield (5.3).

$$i_g^* = \left(\widehat{i_{ct}} + \widehat{A_{dcR}} \cdot \sin(2\omega_{50}t)\right) \cdot \sin(\omega_{50}t) \tag{5.3}$$

Doing the multiplications results:

$$i_g^* = \widehat{i_{ct}} \cdot \sin(\omega_{50}t) + \widehat{A_{dcR}} \cdot \sin(2\omega_{50}t) \cdot \sin(\omega_{50}t) \tag{5.4}$$

Using the trigonometric identity:

$$\sin\alpha \cdot \sin\beta = \frac{1}{2}\cos(\alpha - \beta) - \frac{1}{2}\cos(\alpha + \beta) \tag{5.5}$$

(5.4) becomes:

$$i_g^* = \widehat{i_{ct}} \cdot \sin(\omega_{50}t) + \widehat{A_{dcR}} \cdot \left(\frac{1}{2}\cos(\omega_{50}t) - \frac{1}{2}\cos(3\omega_{50}t)\right) \tag{5.6}$$

and finally:

$$i_g^* = \underbrace{\widehat{i_{ct}} \cdot \sin(\omega_{50}t)}_{\text{Fundamental}} + \underbrace{\frac{\widehat{A_{dcR}}}{2}\cos(\omega_{50}t)}_{\text{Reactive current}} - \underbrace{\frac{\widehat{A_{dcR}}}{2}\cos(3\omega_{50}t)}_{\text{Third harmonic}} \tag{5.7}$$

Each term can be easily identified as the fundamental current and two undesirable components: a reactive current and a third harmonic current which are directly related with the amplitude of the 100 Hz ripple signal ($\widehat{A_{dcR}}$).

5.3 Current control loop using PI or PR controllers

The vector control or the field oriented control is well known for its fast and precise control in three-phase systems. Their set values are DC-quantities in spite of the fact that AC-quantities are controlled [57]. PI controllers are used in order to control the DC-quantities which are in the rotating reference frame. Usually, the control algorithm of a three-phase system is based on the Park Transform and space vectors. However, in single-phase systems only one space vector exists. Therefore, the three-phase control strategy can be converted into a new control structure applicable for single-phase systems, as presented in [57]. The new derived controller is called PR controller and it is based on a double integrator whose poles resonate to a chosen frequency.

An analysis of the classical PI versus PR controllers is given in the following in order to emphasize their advantages and disadvantages. First, a calculus of the steady-state error for a current control loop is performed to highlight the need of a double integrator controller in the case when AC-quantities are controlled.

5.3.1 Calculus of the steady-state error for a current control loop

The current control loop of a grid connected system is considered in Figure 5.10 in order to analyze the steady-state error caused by the control of AC-quantities [59].

The variables shown in Figure 5.10 are presented as follows:

- $v_g(s)$ is the perturbation of system which is represented by the equivalent source voltage of the grid;
- $\varepsilon_i(s)$ is the error obtained by subtracting the measured grid current from the current reference;
- $v_{inv}(s)$ is the voltage produced by the inverter;
- $i_g(s)$ is the measured grid current;
- $i_g^*(s)$ is the current reference for the current control loop;
- $H_C(s)$ is the transfer function in Laplace domain of the current controller;
- $H_P(s)$ is the transfer function in Laplace domain of the plant which is usually composed of the output filter of the converter and the grid impedance;
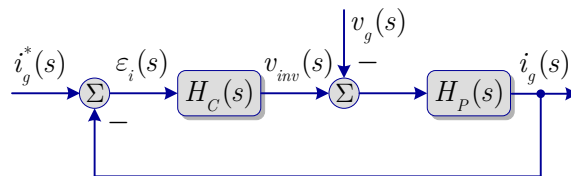
Figure 5.10. Current control loop.

The expression of the error produced by the perturbation $v_g(s)$ is:

$$\varepsilon_i(s) = \frac{H_P(s)}{1 + H_C(s) \cdot H_P(s)} \cdot v_g(s) \tag{5.8}$$

Replacing the transfer functions of $H_C(s)$ and $H_P(s)$ with the expressions shown in (5.9) and (5.10):

$$H_C(s) = \frac{K_C}{s^{\alpha_C}} \cdot H_C^{'}(s), \tag{5.9}$$

$$H_P(s) = \frac{K_P}{s^{\alpha_P}} \cdot H_P^{'}(s) \tag{5.10}$$

(where $H_C^{'}(0) = 1$ and $H_P^{'}(0) = 1$), the expression of the error from (5.8) becomes:

$$\varepsilon_i(s) = \frac{s^{\alpha_C} \cdot K_P \cdot H_P^{'}(s)}{s^{\alpha_C + \alpha_P} + K_C \cdot K_P \cdot H_C^{'}(s) \cdot H_P^{'}(s)} \cdot v_g(s) \tag{5.11}$$

The steady-state error ε_s becomes:

$$\varepsilon_s = \lim_{t \to \infty} \varepsilon(t) = \lim_{s \to 0} s\varepsilon(s) = \lim_{s \to 0} s \frac{s^{\alpha_C} K_P H_P^{'}(s)}{s^{\alpha_C + \alpha_P} + K_C K_P H_C^{'}(s) H_P^{'}(s)} v_g(s) \tag{5.12}$$

Considering the perturbation $v_g(s)$ as a ramp signal for small intervals of time, $v_g(s)$ can be approximated as $v_g(s) = 1/s^2$. Replacing $v_g(s)$ in (5.12) it results:

$$\varepsilon_s = \lim_{s \to 0} \frac{1}{s} \cdot \frac{s^{\alpha_C} K_P H_P^{'}(s)}{s^{\alpha_C + \alpha_P} + K_C K_P H_C^{'}(s) H_P^{'}(s)} \tag{5.13}$$

Three different cases are possible (α_C) as presented in Figure 5.11.

- if $\alpha_C = 0$, the steady-state error tends to infinity ($\varepsilon_s \to \infty$);

- if $\alpha_C = 1$, the steady-state error is $\varepsilon_s = \dfrac{1}{K_C}$;

- if $\alpha_C = 2$, the steady-state error becomes 0 ($\varepsilon_s = 0$).
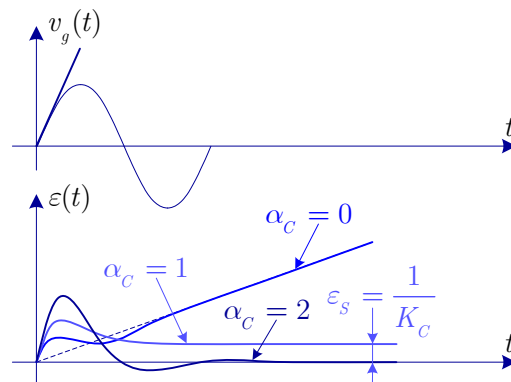
Figure 5.11. Current control loop responses for three different values of α_C.

These three possibilities can be easily identified as follows:

- $\alpha_C = 0$ for a Proportional (P) controller;
- $\alpha_C = 1$ for a PI controller;
- $\alpha_C = 2$ for a Proportional double Integrator (PI²) controller which is also called PR controller.

As it can be noticed, only the double integrator of the PR controller is able to completely eliminate the steady-state error. In the case of a PI controller, the steady-state error becomes inverse proportional with the proportional gain of the controller (K_C). Therefore, a voltage feed-forward is used in order to remove the steady-state error of a PI controller in the case of grid connected systems.

It is worth mentioning that all the conclusions concerning the steady-state error of the current control loop in the continuous time are also valid for discrete time systems.

A comparison between the classical PI versus PR controller follows.

5.3.2 PI versus PR controller comparison

The classical PI controller including the voltage feed-forward (v_{ff}) is commonly used for single-phase grid-connected converters (Figure 5.12a).

The PI current controller $H_{PI}(s)$ is simply defined as:

$$H_{PI}(s) = K_P + \frac{K_I}{s} \tag{5.14}$$

A voltage feed-forward is used in order to remove the steady-state error of the PI controller and to improve the dynamic response. The voltage feed-forward signal is obtained by filtering the measured voltage at PCC. Using the voltage feed-forward can lead to stability problems related to the delay introduced in the system by the voltage filter. Therefore, in order to alleviate this problem an advanced filtering method for the voltage should be considered.
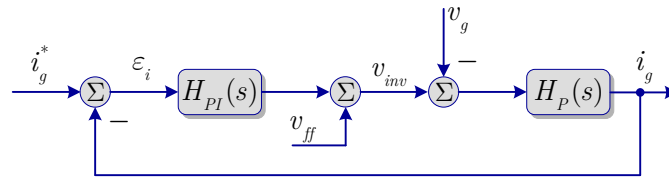
(a)
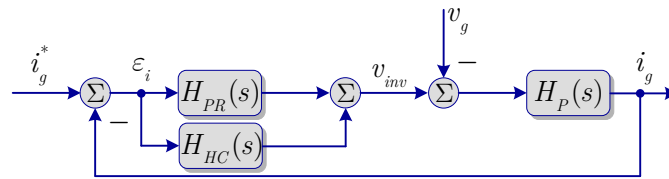
(b)

Figure 5.12. Current control loop of a grid connected converter: a) with PI controller; b) with PR controller.

The Root-locus and the Bode diagram analysis of the PI controller are presented in Figure 5.13. The PI controller was set to give standard stability margins (a gain margin bigger than 7dB and a phase margin bigger than 60 degrees for a standard damping factor of 0.7).

An LCL filter was used as the output filter of the converter. The parameters of the LCL filter were: L_{fi}=1426 μH, C_f=2.2 μH, L_{fg}=713 μH, where L_{fi} is the filter inductor on the inverter side, C_f is the filter capacitor and L_{fg} is the filter inductor on the grid side. The LCL filter was further connected to the electrical grid through an AC transformer with a series inductance of 2.1 mH. The parameters used for both PI and PR controller were K_p=30 and K_i=1500.

As it has been mentioned before, an alternative solution for the poor performances of the PI controller when controlling AC-quantities is the PR controller. The current control loop using the PR controller including the HC is shown in Figure 5.12b.

The PR controller $H_{PR}(s)$ is defined as [57, 105-107]:

$$H_{PR}(s) = K_P + K_I \frac{s}{s^2 + \omega_o^2} \tag{5.15}$$

The HC $H_{HC}(s)$ is defined as [105], [VII]:

$$H_{HC}(s) = \sum_{h=3,5,7\dots} K_{Ih} \frac{s}{s^2 + \left(\omega_o h\right)^2} \tag{5.16}$$

The HC is designed to compensate the selected harmonics which are the most predominant in the current spectrum. The addition of the HC to the PR controller does not affect the bandwidth of the controller.
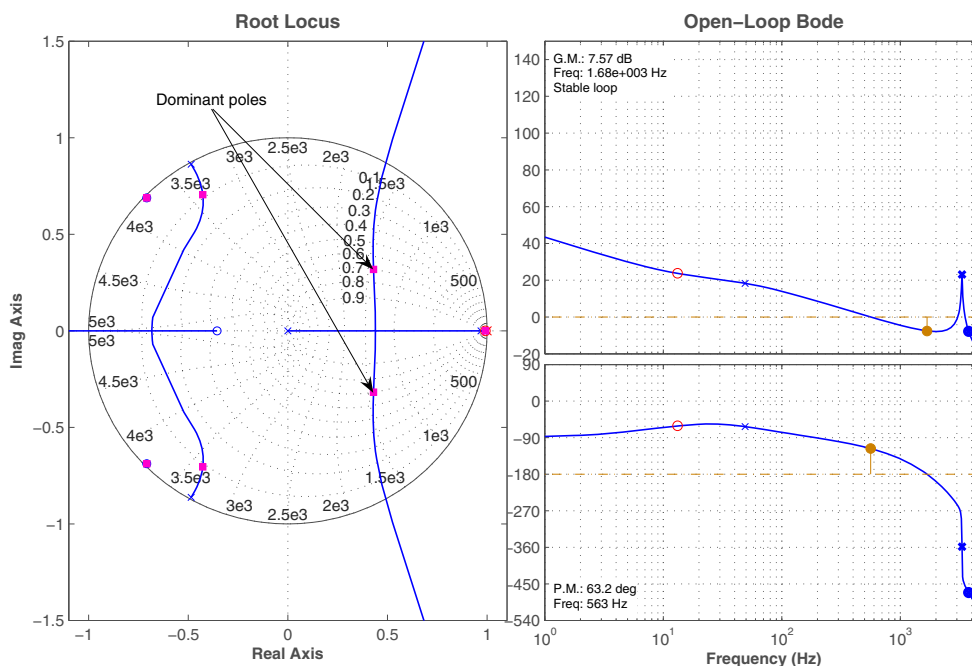
Figure 5.13. PI current controller – Root-locus and Bode diagram analysis.

95

The Root-locus and Bode diagram analysis of the PR+HC controller are presented in Figure 5.14. The 3rd, 5th and 7th harmonics were selected to be compensated by the current controller. The size of the proportional gain K_p from PR controller determines the bandwidth and the stability margins [106], in the same way as the PI controller. As for the PI controller, it can be observed from the open-loop Bode diagram (Figure 5.14) that the PR controller was tuned to give the standard stability margins (a gain margin bigger than 7dB and a phase margin bigger than 60 degrees for a standard damping factor of 0.7).

The output current and the voltage at PCC for a power level of 1.5 kW are presented in Figure 5.15 in order to show both, the steady-state and the dynamic performances of the PI, PR and PR+HC controllers.

Figure 5.15(a, b and c) shows the steady-state performances of the analyzed controllers for the current control loop. As it can be seen, the PR+HC controller gives the best results.

In order to test the dynamic performances of the investigated controllers a transient in the form of a 5 amps step in the current reference is performed. The grid current response to the transient is presented in Figure 5.15d for the PI controller, in Figure 5.15e for the PR controller and in Figure 5.15f for the PR+HC controller. As it can be observed, the PR/PR+HC controller gives better transient response when compared to the PI controller. Both, the steady-state and the transient tests are performed using the same parameters (in terms of proportional and integral gain) for the PI and PR/PR+HC controllers.
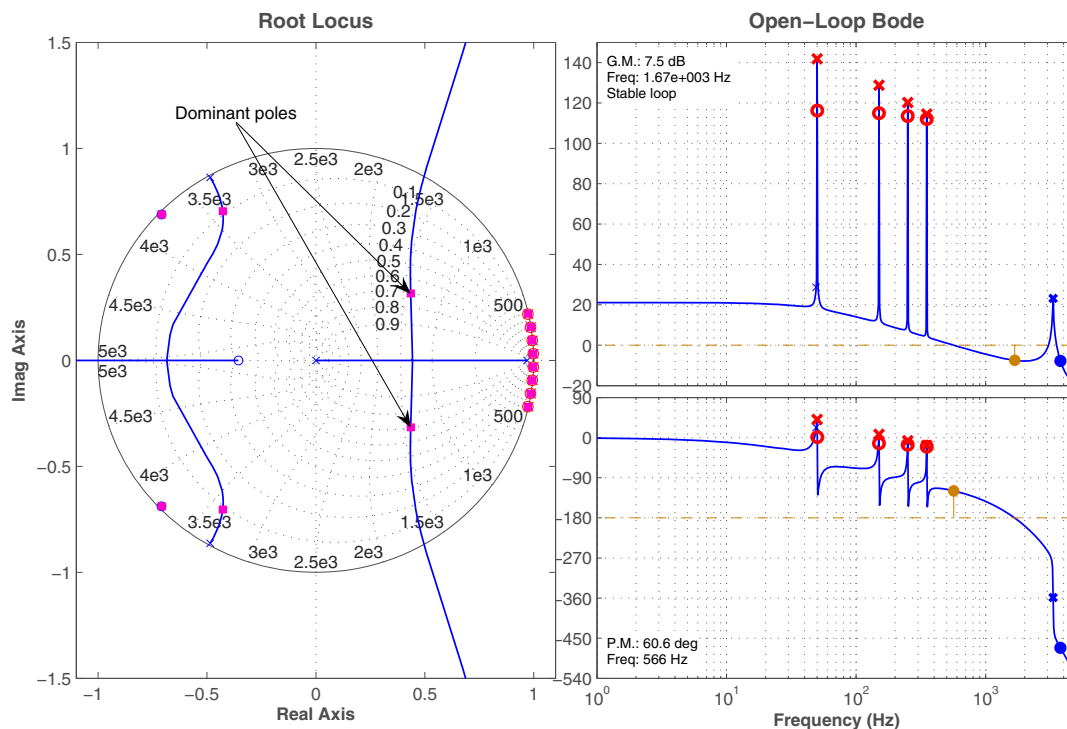
Figure 5.14. PR current controller – Root-locus and Bode diagram analysis.
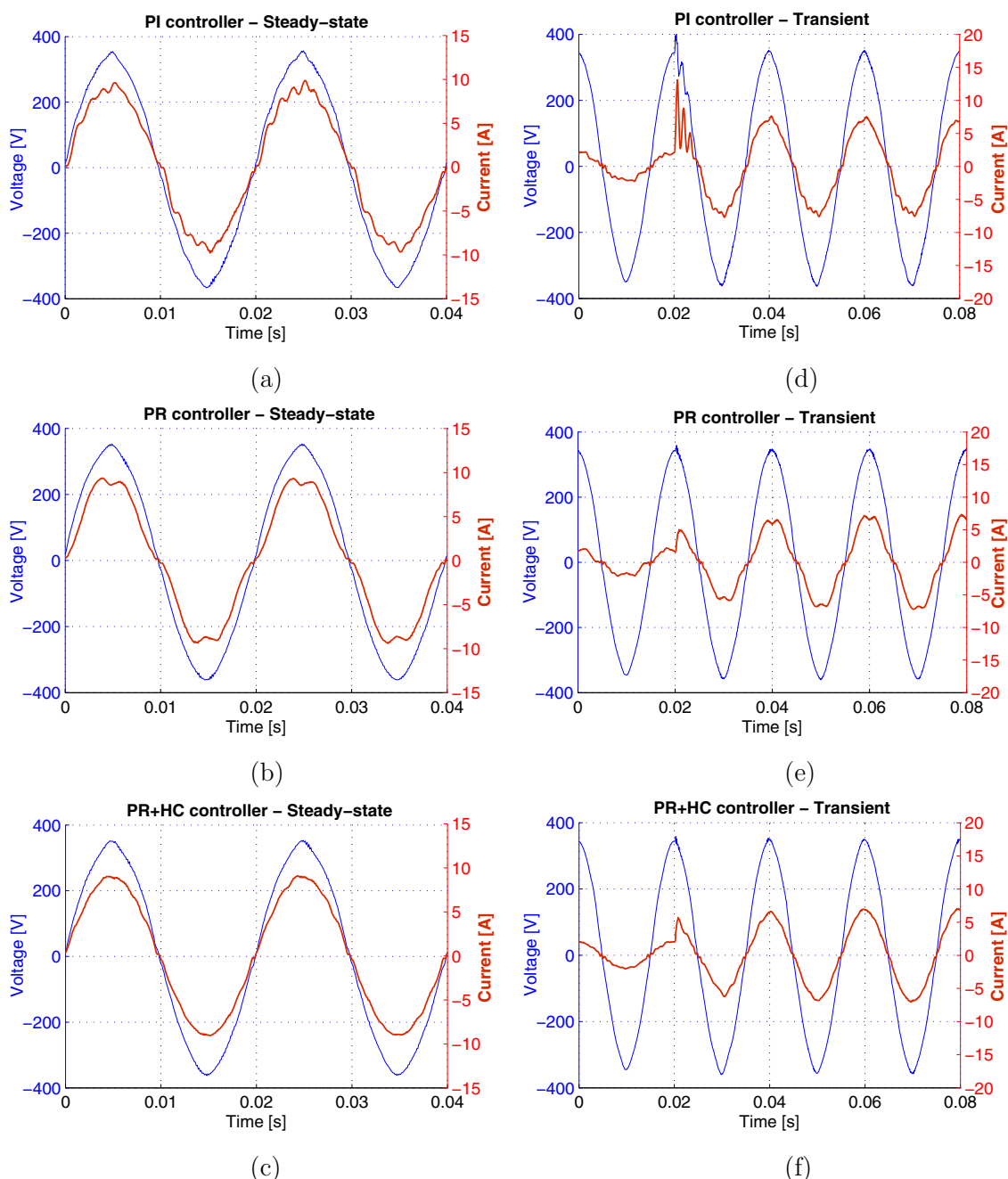
Figure 5.15. Grid current (red) and grid voltage (blue) at 1.5 kW for: a) PI, b) PR and c) PR+HC controllers. Grid current response (red) at a 5 A step in the current reference for: d) PI, e) PR and f) PR+HC controllers.

Figure 5.16 presents a comparison of the output current spectrum in the lower frequency region for the case of using PI, PR/PR+HC controllers. Using the PI controller with voltage feed-forward a current THD of 5.8% has been obtained while in the case of the PR controller the measured current THD was 9.7%. Adding the HC for the PR controller a drastic attenuation of the current THD can be observed, decreasing to 0.5%.
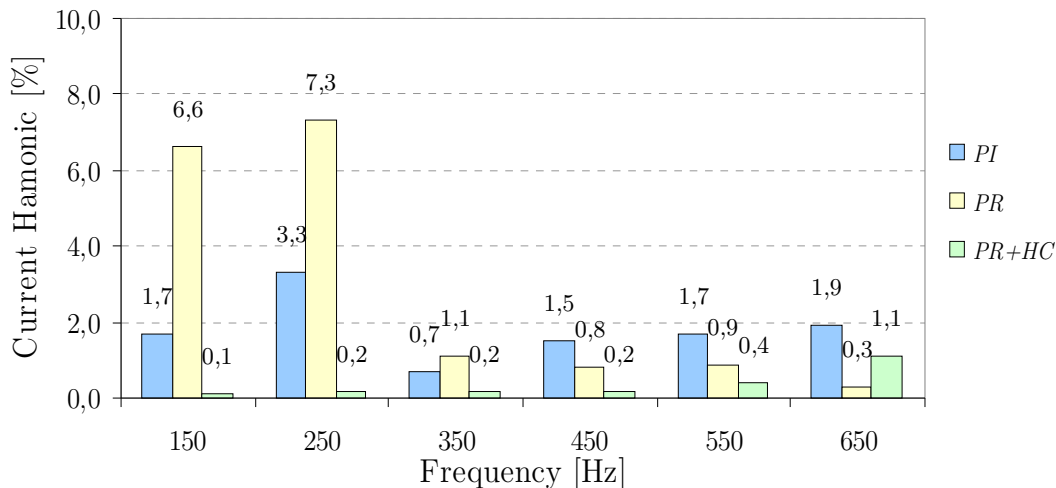
Figure 5.16. Measured grid current harmonics normalized to the fundamental for PI, PR and PR+HC controllers.

5.4 Summary

A general control structure for a single-phase DPGS including the interactions between its main parts has been given in this chapter.

A solution for improving the DC voltage controller has been proposed. The improvement consists in removing the 100 Hz typical ripple from the measured DC voltage by means of a notch filter tuned to the ripple frequency. A comparison between the classical solution using a running average and the solution using a notch filter has been given. It has been shown that better dynamics are obtained for the DC voltage control loop in the case when the notch filter is used. However, in the case of a noisy measured DC voltage, an average running filter is preferred to the notch filter due to the fact that it filters out all the harmonics above the frequency of the DC voltage ripple.

The current control loop has been analyzed and a comparison between the classical PI controller and the PR/PR+HC controller has been given finally. It has been demonstrated that the PR+HC controller gives better steady-state and dynamic performance when compared to the classical PI controller for the current control loop. The two well known drawbacks of the PI controller (steady-state error and poor harmonics rejection capability) have been alleviated by the PR+HC controller. The PR controller is able to remove the steady-state error without using a voltage feed-forward, which makes it more reliable. By adding the selective HC to the PR controller, a very good rejection for the dominant harmonics can be obtained.

Chapter 6

Advanced Control of DPGS

This chapter describes methods of how to make the grid-connected converters more flexible using advanced control techniques. The main focus is to increase the performances and the robustness of the current controller. The chapter is divided into two main parts. In the first part, a frequency adaptive PR controller has been developed and tested. The second part presents an adaptive current controller based on the estimation of the grid impedance.

6.1 Introduction

The control of a DPGS is mainly designed in accordance with the electrical grid conditions at the PCC. The controllers are tuned for some assumed values of the electrical grid parameters. However, the parameters of the electrical grid such as grid impedance or grid frequency can change. Therefore, the control should be able to sense and follow these changes in order to maintain the performance and the robustness of the system.

Figure 6.1 presents the boundaries for ensuring the performance and the robustness of a control system [59].
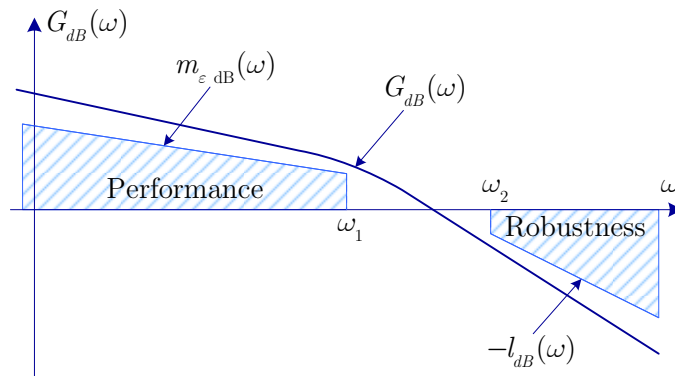
Figure 6.1. Margins for ensuring the performance and the robustness of a control system.

The term $m_{\varepsilon\ \mathrm{dB}}(\omega)$ represents the permissible margin of the error while $l_{dB}(\omega)$ is the upper bound which gives the upper limit of uncertainty. The frequency ω_1 is chosen in such a way (6.1) as to give a sufficient bandwidth in order to ensure a good response time, thus maintaining good performances.

$$G_{dB}(\omega) \geq m_{\varepsilon\ dB}(\omega); \text{ where } \omega \in [0,\omega_1] \tag{6.1}$$

The frequency ω_2 is chosen in such a way (6.2) as to give a sufficient stability margin in order to maintain the robustness.

$$G_{dB}(\omega) < -l_{dB}(\omega); \text{ where } \omega > \omega_2 \tag{6.2}$$

The estimation of the grid conditions such as impedance and frequency can help the control by providing additional information about the grid parameters variations. The development of an adaptive PR current controller regarding the grid frequency has been published in [III] and is addressed in §6.2.1. Another adaptive method for the current controller concerning the proportional gain is described in §6.2.2. Also, §6.2.2 presents a method based on a notch filter of how to improve the robustness of the PR current controller when using LCL output filter.

6.2 Adaptive Current Controller

6.2.1 Frequency Adaptive PR Controller

As presented in §5.3, the PR controller offers good performance when compared to the classical PI controller. However, the PR and PR+HC controllers necessitate the resonant frequency value (ω_0) inside their transfer functions, as seen in (5.15) and (5.16). Usually, the nominal value of the grid frequency and its multiples for the HC are used, but in the case when the grid frequency experiences fluctuations, the performance of both PR and HC is diminished. Therefore, the frequency information of the PR controller has to be provided by the PLL [III] which is already used in most of DPGS today, as shown in Figure 6.2 (dashed line) and then detailed in Figure 6.3.
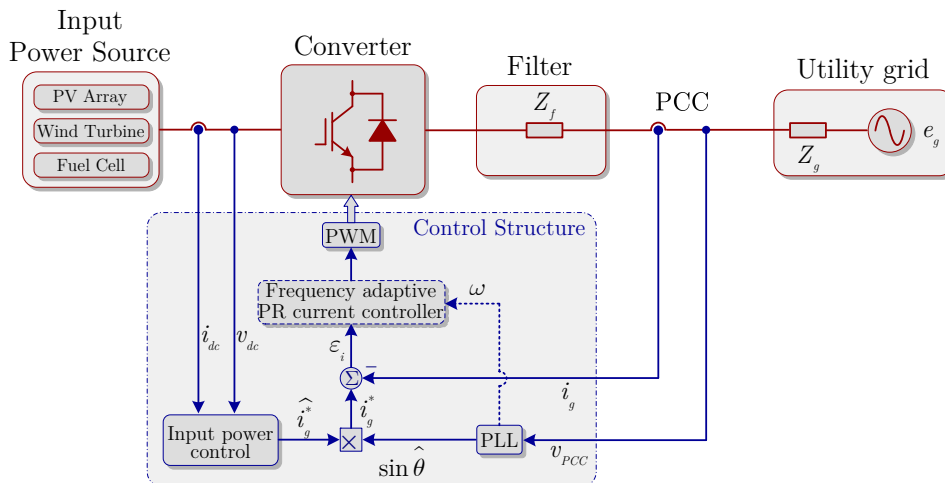
Figure 6.2. DPGS control using frequency adaptive PR current controller.
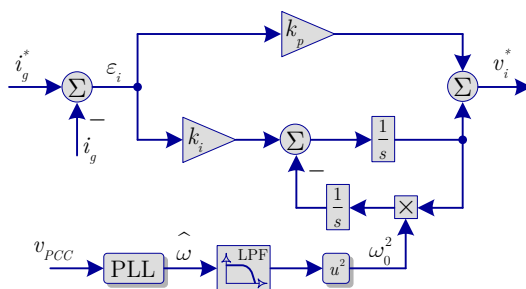
Figure 6.3. Frequency adaptive PR controller.

The Bode diagram of the PR controller for different integral gains (K_i) and its resonance frequency (ω_0) set to 50 Hz is shown in Figure 6.4. As it can be noticed, the PR controller achieves a very high gain in a narrower frequency band centered around the resonance frequency. The width of this frequency band depends on the integral time constant K_i. A low K_i leads to a very narrow band while a high value of K_i leads to a wider band. However, as presented in [III], some of DPGS should be able to run on grid frequency deviation from 47 Hz up to 55 Hz. In the case when the grid frequency changes its value to 47 Hz or to 55 Hz, (like the arrows point out in Figure 6.4b), the performance of PR controller is drastically reduced due to the low gain at that frequency. Therefore, the PR controller using fixed resonant frequency will not be able to eliminate the steady state errors in such operation condition. Moreover, the harmonic compensation associated with the PR controller is also based on the fundamental frequency. The HC is more sensible to a change in the grid frequency due to the fact that it contains multiples of the fundamental frequency, thus the frequency deviation increase faster in correlation with the harmonic order to be compensated.

(a)   (b)
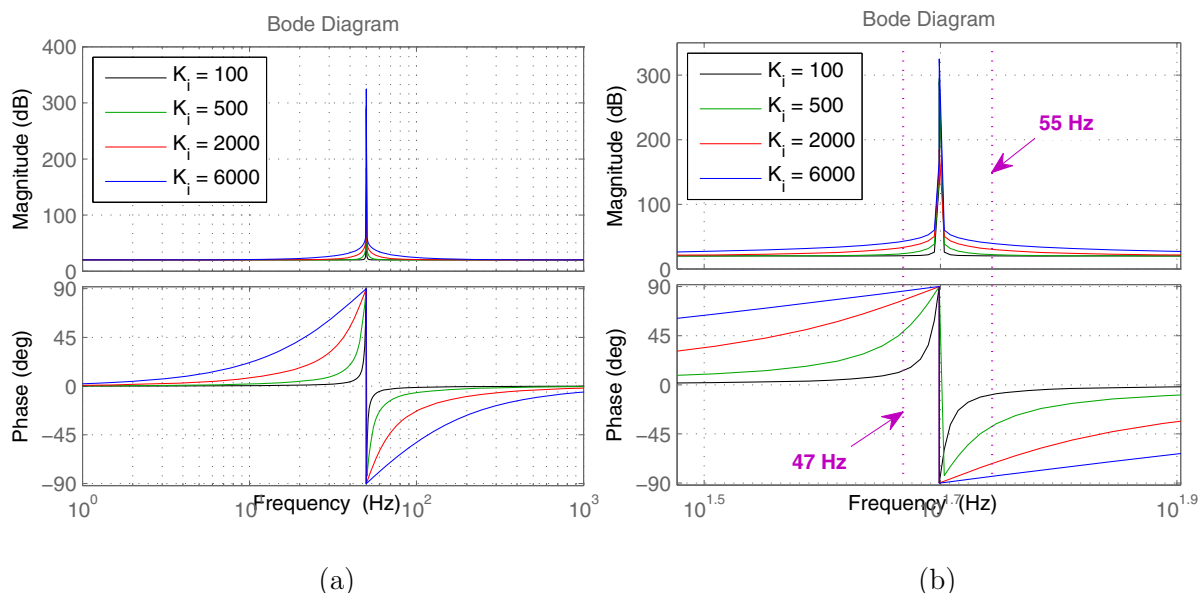
Figure 6.4. Bode diagram of the PR controller (tuned at 50 Hz) for: a) four different integral gains (K_i) and b) a zoom in the proximity of 50 Hz.

A test system represented by the schematic in Figure 6.2 was used to test the adaptive PR current controller. Four frequency steps (from 50 to 49, 51, 47 and 55 Hz) were performed using a grid simulator in order to test the performances of the frequency adaptive PR controller. However, the grid frequency will never experience a step change, but a ramp characteristic instead. According to most of the grid codes, the grid frequency has a slope variation of maximum 10 Hz in a second. Secondly, the settling time of the PLL should be fast enough in order to provide the frequency information in time. Additionally, in the case of a fast PLL controller, filtering of the frequency signal may be necessary in order to obtain a steady value. In this case, the time constant of the filter should be chosen carefully to not introduce too much delay to the actual grid frequency value.

The experimental results in the case of ± 1 Hz frequency variation are presented in Figure 6.5 and Figure 6.6. First, the PLL response for the frequency step is shown in Figure 6.5a and Figure 6.6a. It can be noticed that the PLL responds according to its settling time which was set to 50 ms. The grid frequency estimated by the PLL is further used by the PR controller in order to match its resonance frequency with the actual grid frequency.

(a)	(b)	(c)
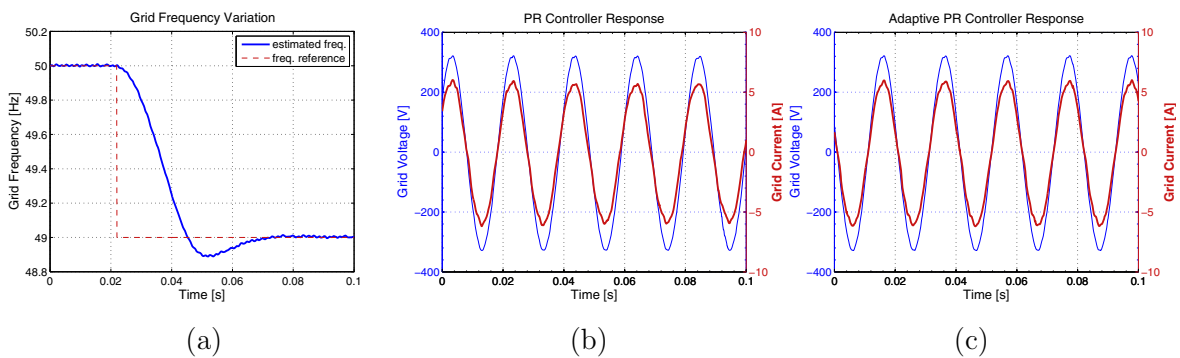
Figure 6.5. Experimental results for a frequency step from 50 Hz down to 49 Hz: a) PLL frequency response, b) voltage at PCC (blue) and output current (red) using PR controller and c) voltage at PCC (blue) and output current (red) using frequency adaptive PR controller.

(a)	(b)	(c)
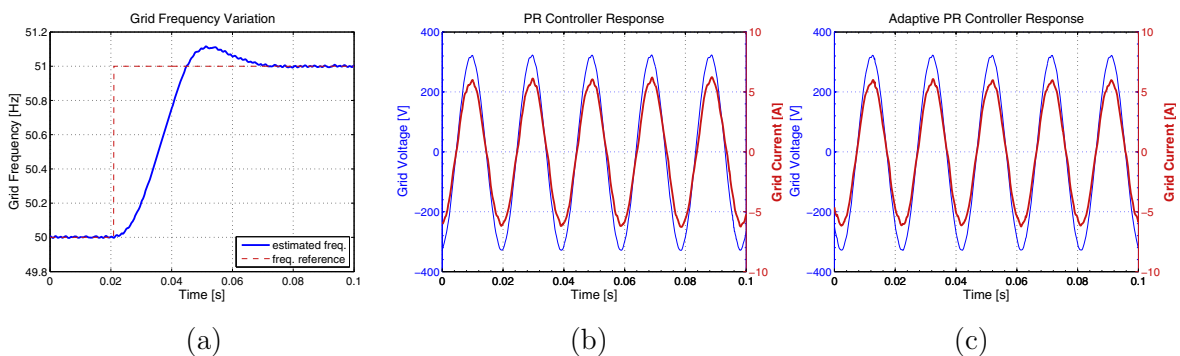
Figure 6.6. Experimental results for a frequency step from 50 Hz up to 51 Hz: a) PLL frequency response, b) voltage at PCC (blue) and output current (red) using PR controller and c) voltage at PCC (blue) and output current (red) using frequency adaptive PR controller.

Figure 6.5b and Figure 6.6b show the voltage at PCC and the output current of the converter in the case of PR controller. As it can be noticed, there is a small phase lead/lag in the two situations when the frequency decreases/increases 1 Hz. The results for the frequency adaptive PR controller are presented in Figure 6.5c and Figure 6.6c. Almost no change in the output current is observed after the frequency step change of ± 1 Hz.

Figure 6.7 shows a frequency step from the normal grid value of 50 Hz down to 47 Hz. The behavior of the PLL in terms of estimated frequency is shown in Figure 6.7a. As it can be seen from Figure 6.7b, without grid frequency information, the PR controller exhibits stationary errors in the current control. Steady state errors in terms of amplitude and phase lead/lag are easily noticed when the grid frequency changes its value. Anyway, when the information about the grid frequency is provided, the PR controller has no problem to regulate the current and to maintain unity power factor of the DPGS (Figure 6.7c). However, a short transient error can be observed right after the step frequency is applied. This is due to the delay of the estimated frequency which is directly related with the settling time of the PLL. A similar situation is noticed for a frequency step from 50 Hz up to 55 Hz (Figure 6.8).
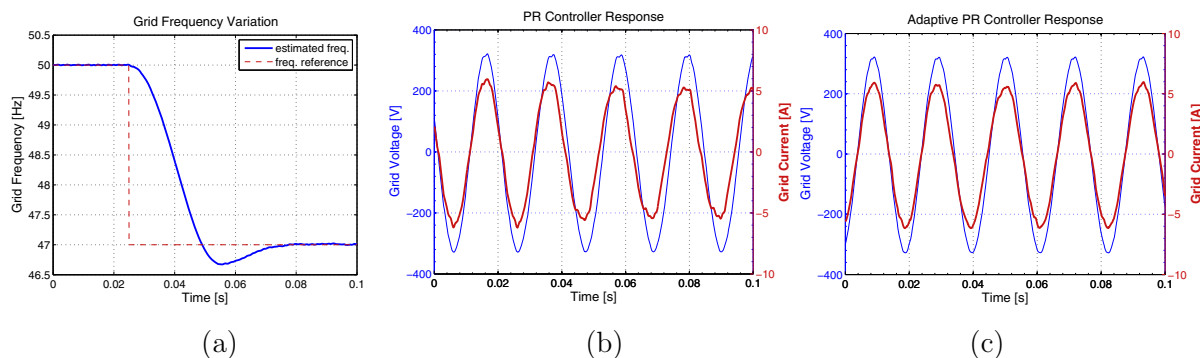
Figure 6.7. Experimental results for a frequency step from 50 Hz down to 47 Hz: a) PLL frequency response, b) voltage at PCC (blue) and output current (red) using PR controller and c) voltage at PCC (blue) and output current (red) using frequency adaptive PR controller.
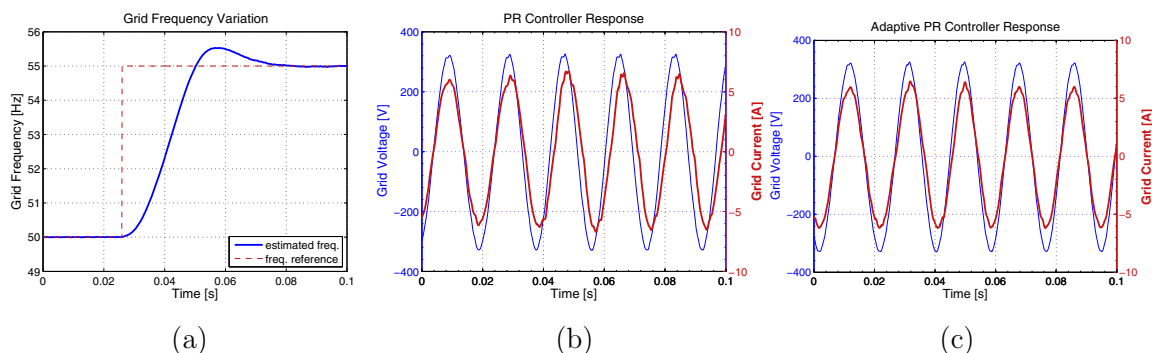
Figure 6.8. Experimental results for a frequency step from 50 Hz up to 55 Hz: a) PLL frequency response, b) voltage at PCC (blue) and output current (red) using PR controller and c) voltage at PCC (blue) and output current (red) using frequency adaptive PR controller.

The DPGSs, especially the wind turbines, should be able to run on grid frequency deviation from 47 Hz up to 55 Hz [105]. In the case when the grid frequency moves outside of the 50±1 Hz, the performance of the PR controller is highly reduced due to the low gain at that frequency, hence will not be able to eliminate the steady state errors in such operation condition. Therefore, the PR current controllers should be associated with an adaptive frequency control.

6.2.2 Adaptive Current Controller using the estimated grid impedance

It is known that the grid impedance has impact on the control of the grid converters. A large variation on the grid impedance highly decreases the stability and the performance of the current controller. Usually, the current controller parameters are tuned in accordance with the output filter impedance of the converter and some assumed value of the grid impedance. A linear current controller for AC reference tracking with zero steady state errors (zero phase shift and zero amplitude error) can be constructed either by transforming the control system into an equivalent DC system and using a DC controller or by using an AC controller (e.g. the PR controller).

In both cases the stability of the controllers depends upon the grid impedance value as the grid impedance is in series with the output filter of the converter. If the variation of the grid impedance is mainly resistive, then the damping of the line filter changes, affecting the stability of the grid-connected converter control. If the variation is mainly inductive, then the bandwidth of the controller changes (Figure 6.9). Thus, the performance of the current loop controller could decrease significantly for higher values of the grid inductance. The estimation of the grid impedance can be used in order to alleviate this problem. Therefore, the current controller parameters can be automatically adjusted using the impedance information provided by a grid impedance estimation method (Chapter 3).
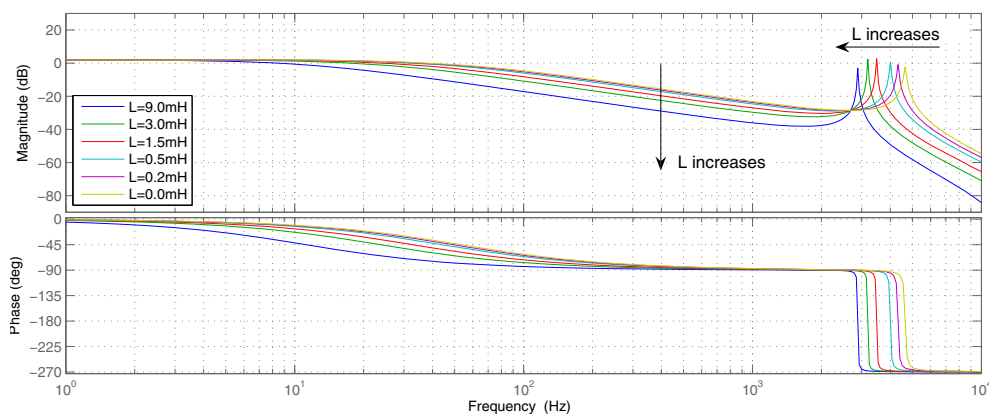
Figure 6.9. Bode plot of a grid model for different values of the grid inductance (L_g) in case of using an LCL filter.

(a)   (b)
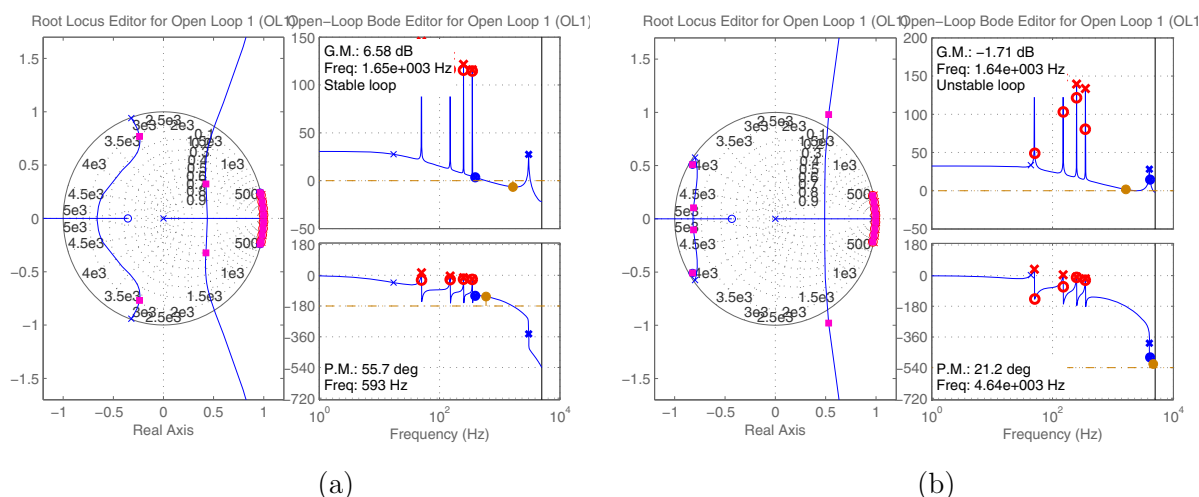
Figure 6.10. Root-Locus diagrams and open-loop Bode plots for a current loop using PR controller (Kp=25) for: a) a grid inductance Lg=3 mH, and b) a grid inductance Lg=0.3 mH.

Figure 6.10 shows two analyses, namely, the Root-loci and the Bode diagrams of the same current loop using the same controller parameters. The plant is composed of the output LCL filter and the equivalent grid impedance circuit (Figure 6.13). The only difference between the two analyses is that the grid inductance has been changed from 3 mH in the first case to 0.3 mH in the second case. As it can be observed from Figure 6.10b, the current loop becomes unstable if the controller parameters (especially the proportional gain) are kept constant. In this case, the proportional gain (K_p) was set to 25. This case can happen when grid-connected converters made by the same manufacturer are connected in different places of a distribution network or in the case when the distribution network itself suffers modifications. In these situations, a manual configuration of the current controller parameters has to be carried out by the maintenance team. In order to avoid this situation, an adaptive proportional gain controller based on gain scheduling method can be used. The general structure of an adaptive current controller using gain scheduling technique is presented in Figure 6.11.

The structure of the Gain scheduling technique used for adjusting the proportional gain of the current controller is shown in Figure 6.12. The proportional gains can be used from a lookup table, where each proportional gain corresponds to certain interval of the estimated grid inductance. The control design is made for different operating conditions in order to obtain the schedules. An interval of a current controller damping between 0.6 and 0.8 can be chosen for the instance as an increment for the gain schedules. However, the use of the gain scheduling technique requires good models of the system to be controlled. Therefore, an important factor is the effectiveness of the grid impedance estimation method.

The transition between the gains could create bumps. Therefore, an interpolation method has to be considered in order to smooth the transitions between the gains.
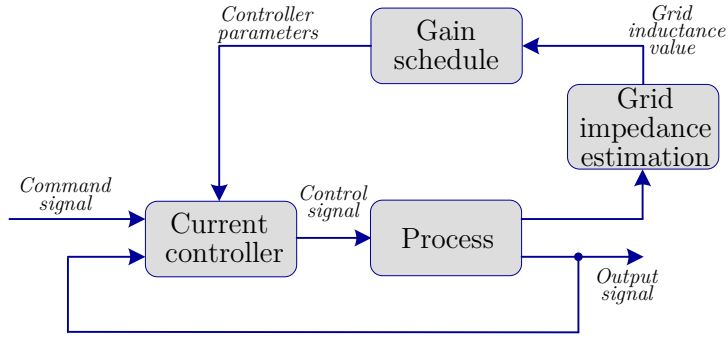
Figure 6.11. Adaptive current controller using gain scheduling technique.
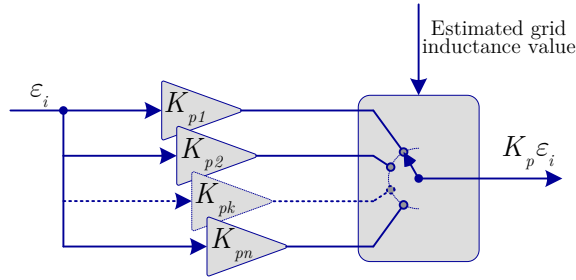
Figure 6.12. Gain scheduling technique.

As pointed out in [82], the use of an output LCL filter for a distributed generation system is widely used in industrial products. The schematic of the LCL filter including the equivalent grid impedance is shown in Figure 6.13. The advantage of the LCL filter when compared to the L filter is to reduce the harmonics caused by the converter switching while minimizing the inductance values due to its higher order [106]. In general, the use of an LCL filter makes the current controller less stable in the case when a proper damping strategy is not adopted [82]. This is due to the resonance frequency of the LCL filter, as expressed in (6.3), which introduces two resonant poles to the current loop.

$$\omega_{res} = \sqrt{\frac{L_{fi} + L_{fg}}{C_f L_{fi} L_{fg}}} \tag{6.3}$$

The damping methods, used to improve the stability of the current loop when using LCL filters, are classified in passive and active methods. In the case of passive damping, a resistor is usually added in series with the capacitor or in parallel with the grid side inductor of the LCL filter; the second case using active damping seems more attractive for particular applications above several kilowatts, where the use of a damping resistor becomes an inconvenient and the losses could require active cooling. Thus the efficiency decrement becomes a key point [82].
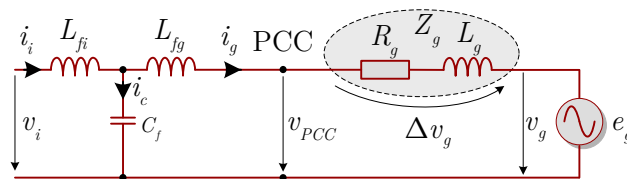
Figure 6.13. Output LCL filter and the equivalent grid impedance.

Some work has been published in the technical literature about active damping solutions. An active damping method of the LCL resonance based on a digital Infinite Impulse Response (IIR) filter is proposed in [107]. A control loop for damping the filter capacitor voltage is proposed in [108]. An alternative solution consists of adopting a controller in cascade to the main controller [109, 110].

Another solution to damp the resonance peak introduced by the LCL filter is to make use of a notch filter having a transfer function (H_{nf}) as presented in (6.4). This filter is attached to the current loop (Figure 6.14) and is tuned at the resonance frequency of the LCL filter which is easily obtainable knowing the parameters of the LCL filter (6.3). However, the grid inductance comes in series with the grid side inductor of the LCL filter, thus changing the resonance frequency of the LCL filter (Figure 6.9). Therefore, an estimated value of the grid inductance (Chapter 3) can add more value to the active damping method using a tunable notch filter.

$$H_{nf}(s) = \frac{s^2 + 2\zeta_2\omega_0 s + \omega_0^2}{s^2 + 2\zeta_1\omega_0 s + \omega_0^2} \tag{6.4}$$

- where the dependencies of the terms ζ_1 and ζ_2 are described in (6.5).

$$\begin{cases} \zeta_2 \ll \zeta_1 \\ \zeta_2 = \dfrac{\zeta_1}{\alpha} \end{cases} \tag{6.5}$$

The notch filter having the transfer function as presented in (6.4) can be tuned online using the grid impedance information. The cutoff frequency (ω_0) of the notch filter is calculated by (6.6) which is related with the resonance frequency of the LCL filter (6.3). The only difference is made by the grid inductance (L_g) connected in series with the grid side inductance (L_{fg}). The term α from (6.5) is directly related to the grid resistance (R_g) and can be expressed as $\alpha = k \cdot R_g$, where k is a constant.

$$\omega_0 = \sqrt{\frac{L_{fi} + L_{fg} + L_g}{C_f L_{fi}(L_{fg} + L_g)}} \tag{6.6}$$

The Bode diagram and the step response of the expression presented in (6.4) for three different damping values ($\zeta_1 = 0.707, 0.353$ and 1.414) are shown in Figure 6.15. As it can be noticed, the damping factor ζ_1 can be varied to obtain a wider or a narrower stopband of the notch filter. From Figure 6.15b it can be seen that the step response is fast enough to not affect the current loop dynamics.
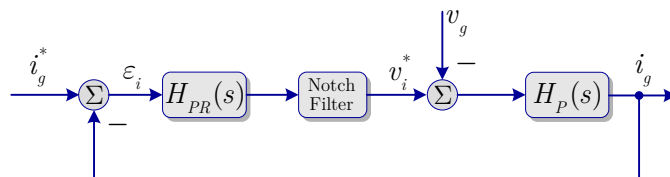
Figure 6.14. Active damping method based on a notch filter.

Figure 6.16a show the Bode diagrams of the LCL filter plus the grid inductance, the notch filter (NF) and the two combined. As it can be observed, the resonance peak introduced by the LCL filter is almost completely damped by the notch filter whose cutoff frequency was tuned using (6.6). Figure 6.16b gives the Bode diagrams of the LCL filter combined with the notch filter for three different grid inductances (L_g). This is to show that the active damping method based on the notch filter is not very sensitive to the grid inductance changes. However, the use of a grid impedance estimation method with a decent accuracy can increase the effectiveness of the active damping method.

The Root loci and the open-loop Bode diagrams of the current loop with and without including the notch filter are depicted in Figure 6.17. The poles introduced by the notch filter can be seen in Figure 6.17b.
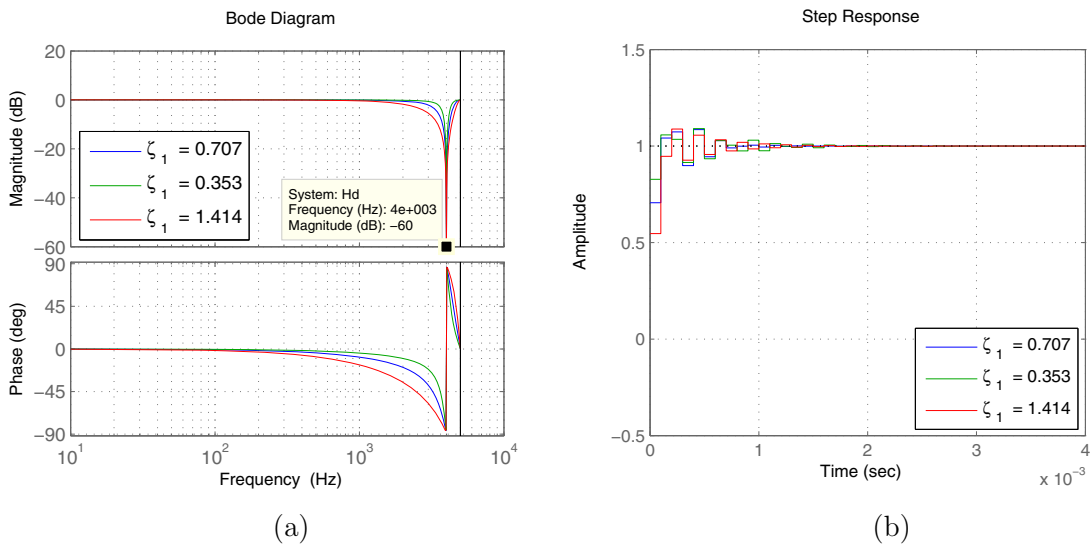
Figure 6.15. a) Bode diagram and b) Step response of the notch filter for three different values of the damping factor ζ_1.
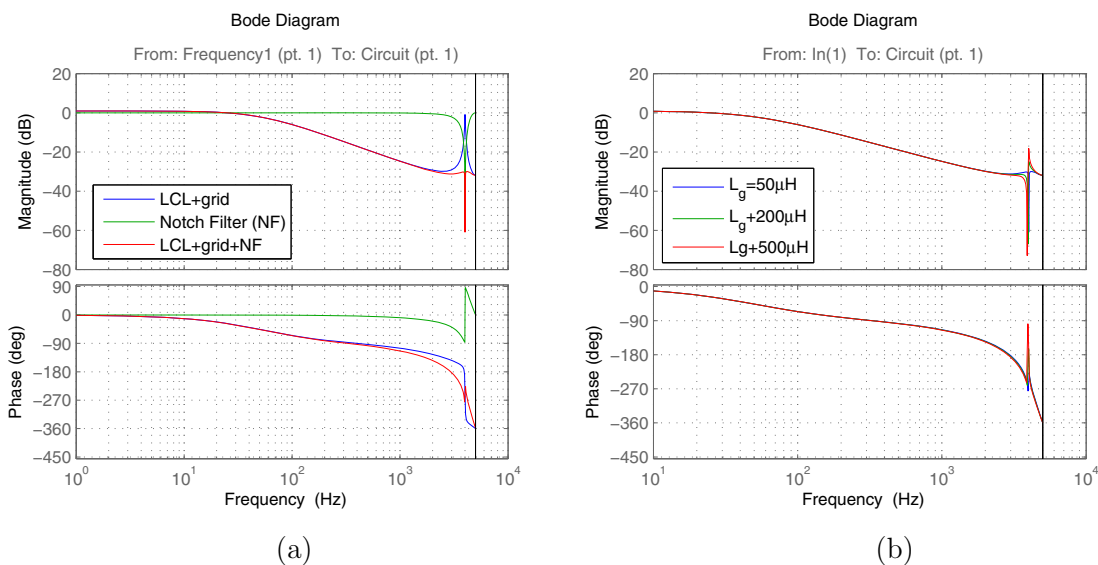
Figure 6.16. a) Bode diagrams of the LCL filter plus the grid inductance, the notch filter (NF) and the two combined; b) Bode diagrams of the LCL filter combined with the notch filter for three different grid inductances (L_g).

(a)

(b)
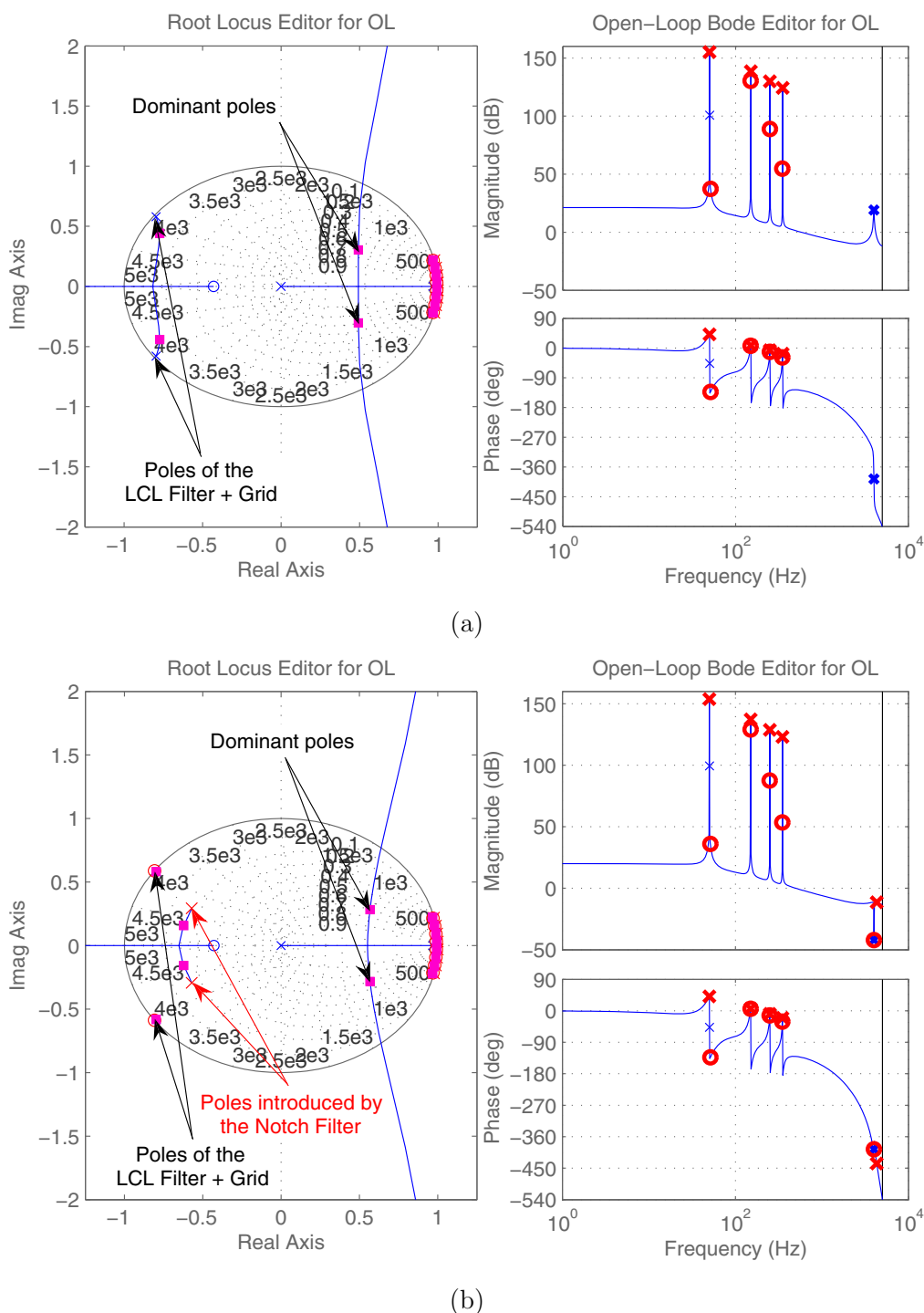
Figure 6.17. Root loci and open-loop Bode diagrams of the current loop: a) without and b) with the notch filter included.

Two cases were considered in order to test the effectiveness of the active damping method based on a notch filter. In the first case, the current loop was tested under steps (between 5 and 10 amps peak) in the current reference. For the second case, the current loop was tested under grid voltage swells of 5%. For both cases, two variations of the current controller proportional gain (K_p) were performed from 0.5 to 1.9 (Figure 6.18) and from 0.5 to 10.1 (Figure 6.21) in order to find the stability margins of the current loop using or not a notch filter. The simulated results are shown and described next.

In the first case, the current loop dynamic performance was tested under current reference steps (between 5 and 10 amps peak) and the results are presented in Figure 6.19, Figure 6.20 and Figure 6.22. The current reference and the output current of the current loop with or without a notch filter are presented in Figure 6.19 and Figure 6.20 respectively. As it can be seen, the current loop without a notch filter gets to instability very fast (for a K_p around 1.5) while the current loop including a notch filter stays stable even when the K_p is equal to 10 (Figure 6.22). Therefore, both the performance and the robustness of the current controller are increased by using a notch filter, as expressed in (6.4).
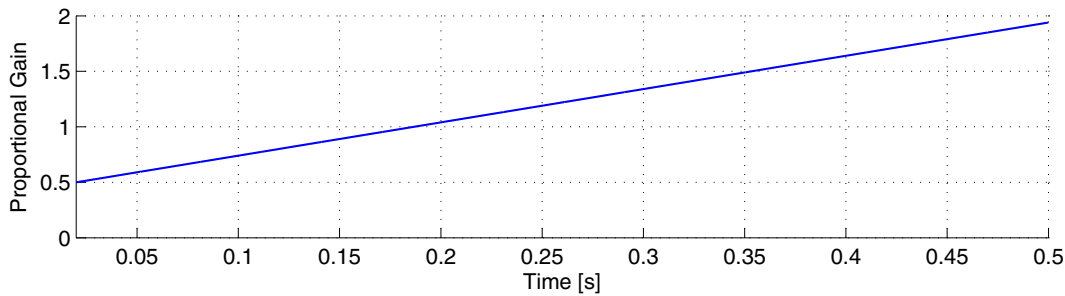
Figure 6.18. Variation of the current controller proportional gain (K_p) from 0.5 to 1.9.
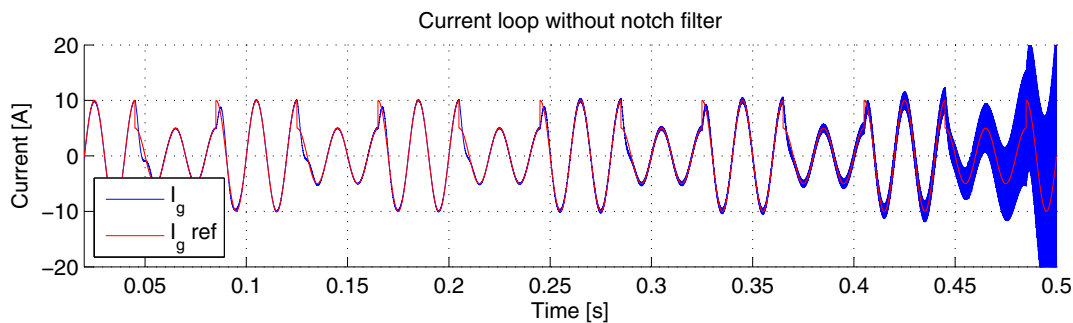
Figure 6.19. Steps (between 5 and 10 amps peak) of the current reference and the output current response for a current loop without the notch filter, where a Kp variation between 0.5 and 1.9 was performed.
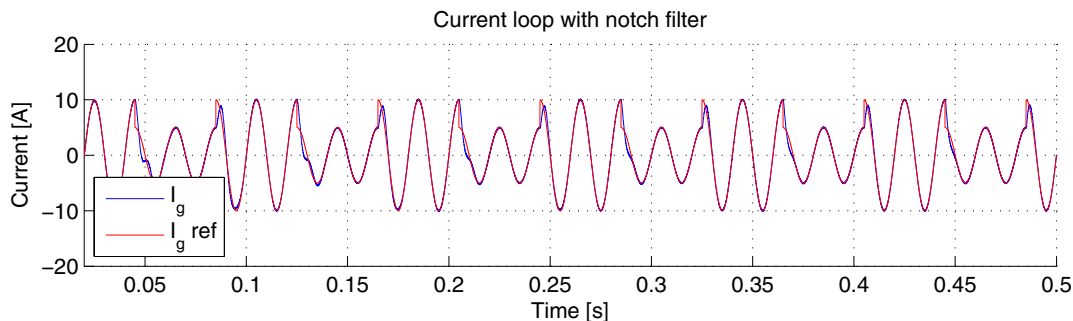
Figure 6.20. Steps (between 5 and 10 amps peak) of the current reference and the output current response for a current loop with the notch filter, where a Kp variation between 0.5 and 1.9 was performed.

In the second case, the current loop dynamic performance was tested under grid voltage swells of 5% (Figure 6.23) and the results are presented in Figure 6.24, Figure 6.25 and Figure 6.26. The current reference and the output current of the current loop including or not a notch filter are presented in Figure 6.24 and Figure 6.25 respectively. Alike the first case, the current loop without a notch filter gets to instability for a K_p around 1.5 while the current loop with the notch filter stays stable even when the K_p is equal to 10 (Figure 6.26). As it can be noticed, very good performance was obtained for the current loop under grid voltage swells when a notch filter was used.
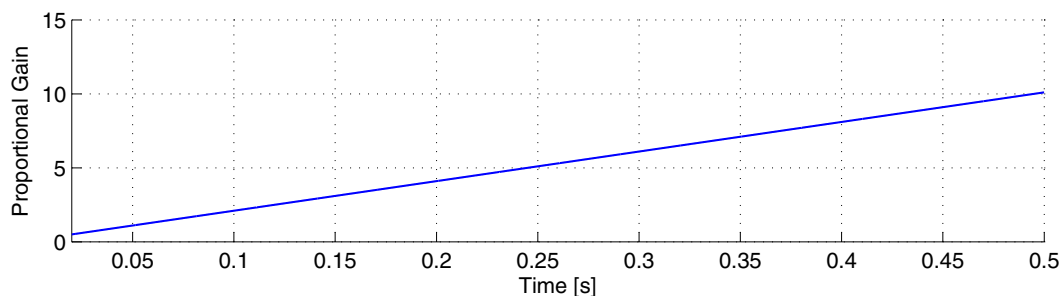
Figure 6.21. Variation of the current controller proportional gain from 0.5 to 10.1.
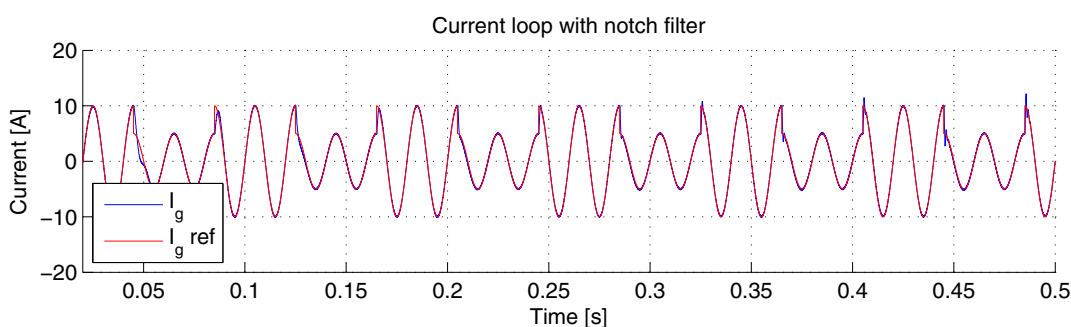
Figure 6.22. Steps (between 5 and 10 amps peak) of the current reference and the output current response for a current loop with the notch filter, where a Kp variation between 0.5 and 10.1 was performed.
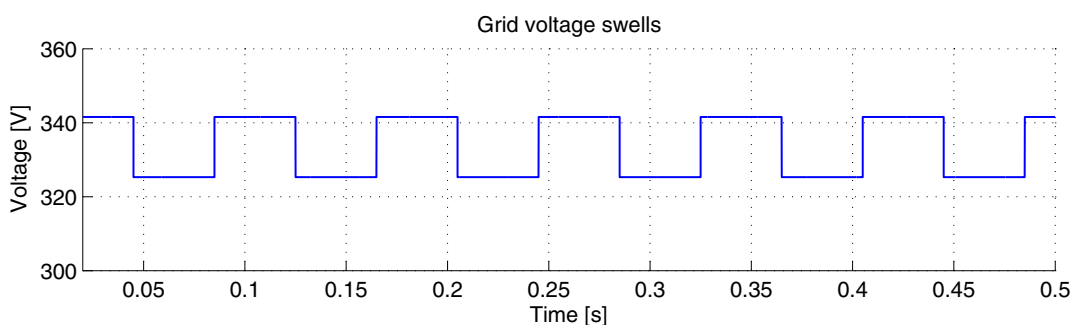
Figure 6.23. Grid voltage amplitude for grid voltage swells of 5%.
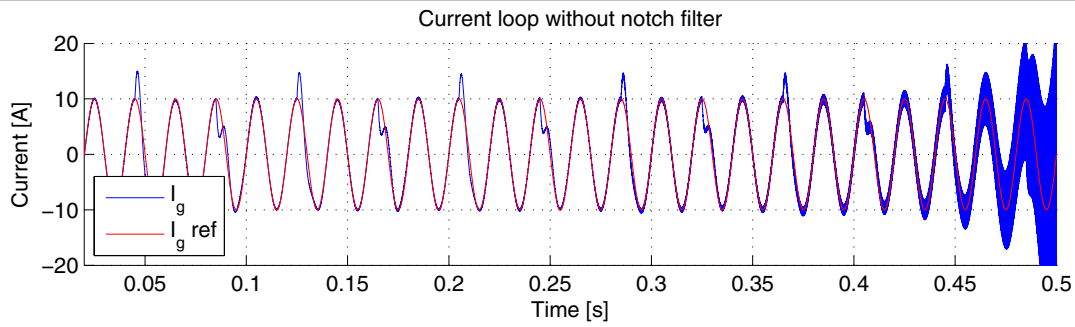
Figure 6.24. The current reference and the output current response in the case of grid voltage swells of 5% for a current loop without the notch filter, where a Kp variation between 0.5 and 1.9 was performed.
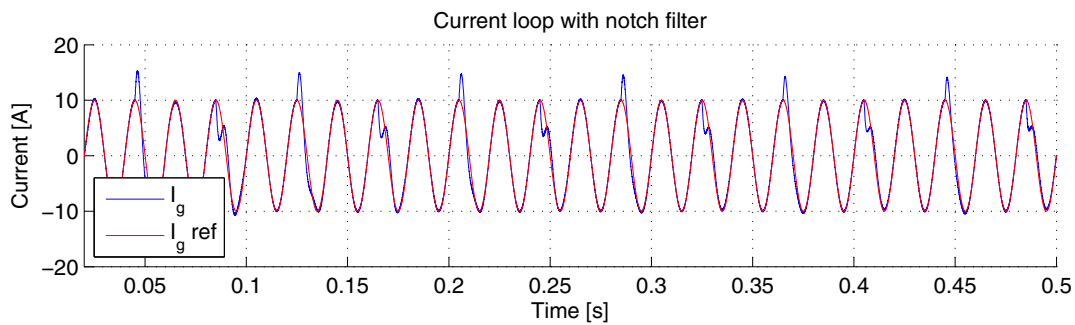
Figure 6.25. The current reference and the output current response in the case of grid voltage swells of 5% for a current loop with the notch filter, where a Kp variation between 0.5 and 1.9 was performed.
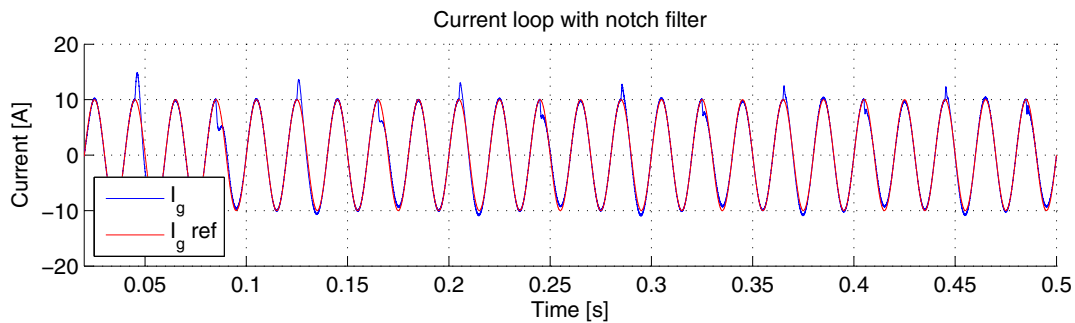
Figure 6.26. The current reference and the output current response in the case of grid voltage swells of 5% for a current loop with the notch filter, where a Kp variation between 0.5 and 10.1 was performed.

From the results presented here, it is confirmed that the active damping method based on a notch filter can significantly improve the robustness of a current loop when using LCL filters.

6.3 Summary

This chapter presented some techniques of improving the control of the grid-connected converters. First, an introduction about how to improve the control in terms of performance and robustness has been given.

Second, the need of using a frequency adaptive PR controller has been emphasized. It has been demonstrated that in the case of grid frequency fluctuations, problems in regulating the grid current and keeping unity power factor occur. As a solution to these problems, a proposal consisting of using the grid frequency information provided by the PLL, inside the PR controller model has been made. In this way, an adaptive tuning of the PR controller with respect to the grid frequency has been obtained. Experimental results showing the controller running over a large band of frequency variations have been presented for validating the proposed method.

Finally, the use of the grid impedance estimation for improving the performance and the stability of the current controller has been presented, being known that large variations of the grid impedance highly decrease the stability and the performance of the current controller. In order to make the current controller more intelligent, the gain scheduling technique can be used to automatically adjust the parameters of the current controller in accordance with the grid impedance value. Moreover, an active damping method based on a notch filter can be used in order to increase the stability of a grid-connected converter when using an LCL output filter. The presented results have confirmed that the active damping method based on a notch filter can significantly improve the robustness and the performance of a current control loop when using LCL filters.

Chapter 7

Conclusions

This chapter starts summarizing the work presented along this thesis. The main conclusions are deduced based on the achieved results. Finally, the directions for future work are outlined.

7.1 Summary

This thesis has been divided into two main parts, namely "Grid Condition Detection" and "Control of Single-Phase DPGS". In the first part, the main focus was on reliable PLL techniques for monitoring the grid voltage and on grid impedance estimation techniques. Additionally, a new technique for detecting the islanding mode have been developed and successfully tested. In the second part, the main reported research was concentrated around adaptive current controllers based on the information provided by the grid condition detection techniques.

In Chapter 2, after an initial investigation of the voltage monitoring techniques a major challenge has been identified for the single-phase DPGS. Unlike the three-phase systems where the orthogonal voltage system is easily obtained through the Clarke transform, the orthogonal voltage system for the single-phase systems has to be artificially generated. An analysis of the existent orthogonal signal generators up to date was given in order to emphasize their advantages and disadvantages. The PLL based on an OSG-SOGI came as a solution to combine all the advantages of the existent methods in one single structure. Therefore, the new developed algorithm for monitoring the grid voltage has the following benefits: the orthogonal voltage system is filtered without delay; it presents good dynamics; it is frequency adaptive, thus not being affected by the grid frequency fluctuations; it has offset rejection capabilities; it is robust under grid voltage disturbances. In addition, although the algorithm has the above presented advantages it is rather simple to implement. It is worth to be mentioned that the offset rejection capability is a feature almost inexistent for the majority of the PLL based synchronization systems which are not able to reject the voltage

offset which is typically introduced by the measurements and data conversion processes. The proposed method based on SOGI-OSG is suitable for both, distributed generation systems (e.g. PV, WT) as well as power condition equipments (e.g. UPS, active filters) which rely on PLL based synchronization.

As mentioned in the introduction of Chapter 3, the estimation of the grid impedance is very useful for a better interaction between the DPGS and the utility network. The information about the grid impedance can be used in many applications. However, in this thesis the estimation of the grid impedance was focused only on two well suited applications such as anti-islanding standard requirements (such as VDE0126) and adaptive control for DPGS.

Two active methods and one quasi-passive method have been developed regarding the estimation of the grid impedance. The first active method is based on the harmonic injection technique which uses a less complicated calculation algorithm in contrast with some of the known used algorithms based on more advanced mathematics such as DFT method or Prony extrapolation, thus being suitable for low cost systems. The second active method is based on the PQ variations of a DPGS. One of the major advantages of this technique is that it can use the natural active power variations of the input power sources such as WT or PV. Furthermore, the PQ variations method proved to be very robust under harmonics conditions. However, the implementation of this technique necessitates the usage of the PQ control for a single-phase system which can be troublesome in the case of using an inappropriate method to generate the orthogonal systems of the voltage and current.

Comparing the two proposed active grid impedance estimation methods it was noticed that the grid impedance estimation based on PQ variations performs better than the grid impedance estimation methods based on harmonic injection. However, both of the active methods are able to comply with the requirements of the anti-islanding standard VDE0126. Nevertheless, all the active methods for estimating the grid impedance come with the drawback that the output power quality of the grid-connected converter is more or less affected by the deliberate disturbances. Therefore, a quasi-passive grid impedance estimation method using the model based identification was proposed as a trade off between the active and passive grid impedance estimation methods in order to get most of the advantages of both mentioned methods.

The proposed quasi-passive method using the model based identification proved to be very effective. Moreover, this method does not affect the power quality due to its passive behavior. However, the active behavior of the quasi-passive method comes in order to overcome the assumption that the voltage source of the electrical grid is time invariant.

Chapter 4 introduced an accurate and less-disturbing active anti-islanding method based on PLL for grid connected inverter systems. The islanding detection method is based on the detection of the grid impedance changes. The disturbance produced by this method affects the inverter in a negligible way when the grid is available. The obtained results have proved the effectiveness of the proposed method even under

extreme scenario such as a parallel RLC load with a quality factor equal to ten and the resonant frequency equal to the fundamental frequency.

A general control structure for a single-phase DPGS including the interactions between its main parts was given in Chapter 5. The most important control elements were identified and summary described. In addition, an improvement of the DC voltage control loop was proposed consisting in the elimination of the 100 Hz typical ripple from the measured DC voltage by means of a notch filter tuned at the ripple frequency. It was proven by the results that the proposed solution performs better then the classical solution using running average filter.

An analysis of the current control loop followed by a comparison between the classical PI and the PR+HC controllers was given in the last part of Chapter 5. It has been demonstrated that the PR+HC controller gives better steady-state and dynamic performance when compared to the classical PI controller for the current control loop.

Chapter 6 introduced new techniques for improving the control of the grid-connected converters. First, a frequency adaptive PR controller has been presented in order to make the current controller immune to grid frequency fluctuations. The proposed method was validated by the experimental results showing a good behavior of the current controller over a large band of frequency variations. Finally, the use of grid impedance estimation for improving the performances and the stability of the current controller is presented. Consequently, the gain scheduling technique was presented as a solution to automatically adjust the parameters of the current controller in accordance with the grid impedance value. Furthermore, an active damping method based on a notch filter was used in order to increase the stability of a grid-connected converter when using an LCL output filter. The presented results proved that the active damping method based on a notch filter significantly improved the robustness of a current loop when using LCL filters.

7.2 Future work

The research work reported in this thesis has laid the groundwork for many interesting directions to increase its impact.

An interesting research point is the study of the parallel operation of the grid-connected converters concerning the grid impedance estimation and the islanding detection techniques, as the parallel operation could be already motivated by the increased penetration of the DPGS.

Even though, three grid impedance methods were developed and tested under various conditions, the considered model of the grid impedance was a simple equivalent RL model, as the grid impedance is mainly inductive in most of the cases. However, an interesting topic is to study the influence of an RLC grid model over the estimation of the grid impedance.

Next, it is important to investigate further the grid impedance estimation based on identification technique and to test it on an experimental setup, as it presents very

promising simulation results. Moreover, an interesting idea is to closely study the differences introduced by using an inverse model in Laplace domain or in discrete time domain.

Another interesting research topic is to develop a complete model combining a grid impedance estimation method together with an adaptive current controller. Therefore, the estimated grid impedance value can be provided in real time to the current controller in order to make it adaptive.

Bibliography

[1]   F. Iov, M. Ciobotaru, and F. Blaabjerg, "Power electronics control of wind energy in distributed power systems," in *Proc. of OPTIM*, 2008, pp. XXIX-XLIV.

[2]   F. Blaabjerg and S. Munk-Nielsen, "European Power Electronic conference in Aalborg, Denmark - 1000 participants discussing the future energy technologies," *IEEE Power Electronics Society Newsletter,* vol. 18, pp. 8-10, 2007.

[3]   Report, "PV Trends 2008," *IEA Photovoltaic Power Systems Programme, http://www.iea-pvps.org/,* 2008.

[4]   Report-193-1, "Fuel cells for distributed generation, a technology and marketing summary," *Energy Center of Wisconsin,* March 2000.

[5]   Distributed-Generation, "Energy Efficiency and Conservation Authority (EECA) , New Zeeland," *[Online], http://www.eeca.govt.nz.*

[6]   J. H. R. Enslin and P. J. M. Heskes, "Harmonic interaction between a large number of distributed power inverters and the distribution network," *Power Electronics, IEEE Transactions on,* vol. 19, pp. 1586-1593, 2004.

[7]   "Automatic disconnection device between a generator and the public low-voltage grid," *German Standard, DIN VDE 0126-1-1.*

[8]   "IEEE recommended practice for utility interface of photovoltaic (PV) systems," *IEEE Std 929-2000,* 2000.

[9]   "Characteristics of the utility interface for photovoltaic (pv) systems," *IEC 61727-2002,* 2002.

[10] "IEEE standard for interconnecting distributed resources with electric power systems," *IEEE Std 1547-2003,* pp. 0_1-16, 2003.

[11] "IEEE standard conformance test procedures for equipment interconnecting distributed resources with electric power systems," *IEEE Std 1547.1-2005,* pp. 0_1-54, 2005.

[12] Mathworks-Inc., "Matlab/Simulink," [Online], http://www.mathworks.com/, 2008.

[13] Plexim-GmbH, "PLECS Toolbox," [Online], http://www.plexim.com/, 2008.

[14] dSPACE-GmbH, "dSPACE - DS1103 controller board," [Online], http://www.dspace.com/, 2008.

[15] Danfoss, "Danfoss 5000 series converter," [Online], http://www.danfoss.com/, 2008.

[16] California-Instruments, "California Instruments - programmable AC load," [Online], http://www.calinst.com/, 2008.

[17] M. Francesco De, L. Marco, D. A. Antonio, and P. Alberto, "Overview of anti-islanding algorithms for PV systems. Part I: Passive methods," in *Proc. of PEMCC*, 2006, pp. 1878-1883.

[18] L. Asiminoaei, F. Blaabjerg, and S. Hansen, "Detection is key - Harmonic detection methods for active power filter applications," *Industry Applications Magazine, IEEE,* vol. 13, pp. 22-33, 2007.

[19] C. Lascu, L. Asiminoaei, I. Boldea, and F. Blaabjerg, "High performance current controller for selective harmonic compensation in active power filters," *Power Electronics, IEEE Transactions on,* vol. 22, pp. 1826-1835, 2007.

[20] F. M. Gardner, "Phaselock Techniques," *Publisher: Wiley-Interscience,* vol. 2nd edition, ISBN-10: 0471042943, 304 pages, 1979.

[21] F. Mur, V. Cardenas, J. Vaquero, and S. Martinez, "Phase synchronization and measurement digital systems of AC mains for power converters," in *Proc. of CIEP*, 1998, pp. 188-194.

[22] J. W. Choi, Y. K. Kim, and H. G. Kim, "Digital PLL control for single-phase photovoltaic system," *Electric Power Applications, IEE Proceedings,* vol. 153, pp. 40-46, 2006.

[23] S.-K. Chung, "A phase tracking system for three phase utility interface inverters," *Power Electronics, IEEE Transactions on,* vol. 15, pp. 431-438, 2000.

[24] C. T. Nguyen and K. Srinivasan, "A new technique for rapid tracking of frequency deviations based on level crossings," *Power Apparatus and Systems, IEEE Transactions on,* vol. PAS-103, pp. 2230-2236, 1984.

[25] B. P. McGrath, D. G. Holmes, and J. J. H. Galloway, "Power converter line synchronization using a discrete Fourier transform (DFT) based on a variable sample rate," *Power Electronics, IEEE Transactions on,* vol. 20, pp. 877-884, 2005.

[26] O. Vainio, S. J. Ovaska, and M. Polla, "Adaptive filtering using multiplicative general parameters for zero-crossing detection," *Industrial Electronics, IEEE Transactions on,* vol. 50, pp. 1340-1342, 2003.

[27] S. Valiviita, S. J. Ovaska, and J. Kyyra, "Adaptive signal processing system for accurate zero-crossing detection of cycloconverter phase currents," in *Proc. of PCC*, 1997, pp. 467-472, vol.1.

[28] O. Vainio and S. J. Ovaska, "Noise reduction in zero crossing detection by predictive digital filtering," *Industrial Electronics, IEEE Transactions on,* vol. 42, pp. 58-62, 1995.

[29] R. W. Wall, "Simple methods for detecting zero crossing," in *Proc. of IECON*, 2003, pp. 2477-2481, vol. 3.

[30] S. Valiviita, "Neural network for zero-crossing detection of distorted line voltages in weak AC-systems," in *Proc. of IMTC*, 1998, pp. 280-285, vol. 1.

[31] S. Das, P. Syam, G. Bandyopadhyay, and A. K. Chattopadhyay, "Wavelet transform application for zero-crossing detection of distorted line voltages in weak AC-systems," in *Proc. of INDICON*, 2004, pp. 464-467.

[32] S. Valiviita, "Zero-crossing detection of distorted line voltages using 1-b measurements," *Industrial Electronics, IEEE Transactions on,* vol. 46, pp. 917-922, 1999.

[33] R. Weidenbrug, F. P. Dawson, and R. Bonert, "New synchronization method for thyristor power converters to weak," *Industrial Electronics, IEEE Transactions on,* vol. 40, pp. 505-511, 1993.

[34] D. M. Baker and V. G. Agelidis, "Phase-locked loop for microprocessor with reduced complexity voltage controlled oscillator suitable for inverters," in *Proc. of PEDES*, 1998, pp. 464-469, vol. 1.

[35] D. Nedeljkovic, J. Nastran, D. Voncina, and V. Ambrozic, "Synchronization of active power filter current reference to the network," *Industrial Electronics, IEEE Transactions on,* vol. 46, pp. 333-339, 1999.

[36] D. Nedeljkovic, V. Ambrozic, J. Nastran, and D. Hudnik, "Synchronization to the network without voltage zero-cross detection," in *Proc. of MELECON*, 1998, pp. 1228-1232, vol. 2.

[37] S. M. Silva, B. M. Lopes, B. J. C. Filho, R. P. Campana, and W. C. Bosventura, "Performance evaluation of PLL algorithms for single-phase grid-connected systems," in *Proc. of IAS*, 2004, pp. 2259-2263, vol. 4.

[38] W. Tsai-Fu, S. Chih-Lung, N. Hung-Shou, and L. Guang-Feng, "A 1phi-3W inverter with grid connection and active power filtering based on nonlinear programming and fast-zero-phase detection algorithm," *Power Electronics, IEEE Transactions on,* vol. 20, pp. 218-226, 2005.

[39] L. R. Limongi, R. Bojoi, C. Pica, F. Profumo, and A. Tenconi, "Analysis and comparison of phase-locked loop techniques for grid utility applications," in *Proc. of PCC*, 2007, pp. 674-681.

[40] M. Saitou, N. Matsui, and T. Shimizu, "A control strategy of single-phase active filter using a novel d-q transformation," in *Proc. of IAS*, 2003, pp. 1222-1227, vol. 2.

[41] P. Rodriguez, J. Pou, J. Bergas, J. I. Candela, R. P. Burgos, and D. Boroyevich, "Decoupled double synchronous reference frame PLL for power converters control," *Power Electronics, IEEE Transactions on,* vol. 22, pp. 584-592, 2007.

[42] K. De Brabandere, T. Loix, K. Engelen, B. Bolsens, J. Van den Keybus, J. Driesen, and R. Belmans, "Design and operation of a phase-locked loop with Kalman estimator-based filter for single-phase applications," in *Proc. of IECON*, 2006, pp. 525-530.

[43] P. Rodriguez, J. Pou, J. Bergas, I. Candela, R. Burgos, and D. Boroyevic, "Double synchronous reference frame PLL for power converters control," in *Proc. of PESC*, 2005, pp. 1415-1421.

[44] T. Ostrem, W. Sulkowski, L. E. Norum, and C. Wang, "Grid connected photovoltaic (PV) inverter with robust phase-locked loop (PLL)," in *Proc. of TDC*, 2006, pp. 1-7.

[45] S. Shinnaka, "A new frequency-adaptive phase-estimation method based on a new PLL structure for single-phase signals," in *Proc. of PCC*, 2007, pp. 191-198.

[46] V. Kaura and V. Blasko, "Operation of a phase locked loop system under distorted utility conditions," in *Proc. of APEC*, 1996, pp. 703-708, vol. 2.

[47] S. K. Chung, "Phase-locked loop for grid-connected three-phase power conversion systems," *Electric Power Applications, IEE Proceedings,* vol. 147, pp. 213-219, 2000.

[48] A. W. Krieger and J. C. Salmon, "Phase-locked loop synchronization with gated control," in *Proc. of ECE*, 2005, pp. 523-526.

[49] A. V. Timbus, R. Teodorescu, F. Blaabjerg, M. Liserre, and P. Rodriguez, "PLL algorithm for power generation systems robust to grid voltage faults," in *Proc. of PESC*, 2006, pp. 1-7.

[50] L. N. Arruda, S. M. Silva, and B. J. C. Filho, "PLL structures for utility connected systems," in *Proc. of IAS*, 2001, pp. 2655-2660, vol. 4.

[51] E. S. Sreeraj and K. Chatterjee, "Power factor improvement in one cycle controlled converter," in *Industrial Electronics, IEEE International Symposium on*, 2006, pp. 1454-1460.

[52] S. K. Chung, H. B. Shin, and H. W. Lee, "Precision control of single-phase PWM inverter using PLL compensation," *Electric Power Applications, IEE Proceedings,* vol. 152, pp. 429-436, 2005.

[53] A. Timbus, M. Liserre, R. Teodorescu, and F. Blaabjerg, "Synchronization methods for three-phase distributed power generation systems. An overview and evaluation," in *Proc. of PESC*, 2005, pp. 2474-2481.

[54] L. N. Arruda, B. J. Cardoso Filho, S. M. Silva, S. R. Silva, and A. S. A. C. Diniz, "Wide bandwidth single and three-phase PLL structures for grid-tied," in *Proc. of PSC*, 2000, pp. 1660-1663.

[55] M. Kazmierkowski, R. Krishnan, and F. Blaabjerg, "Control in Power Electronics – Selected Problems," *Academic Press,* 2002.

[56] J. Salaet, S. Alepuz, A. Gilabert, and J. Bordonau, "Comparison between two methods of DQ transformation for single phase converters control. Application to a 3-level boost rectifier," in *Proc. of PESC*, 2004, pp. 214-220, vol. 1.

[57] B. Burger and A. Engler, "Fast signal conditioning in single-phase systems," *Proc. of EPE,* pp. P1-P10, 2001.

[58] S. B. Kjaer, "Design and control of an inverter for photovoltaic applications," *PhD Thesis, Aalborg University, ISBN: 87-89179-53-6,* 2005.

[59] E. Ceanga, C. Nichita, L. Protin, and N. A. Cutululis, "Théorie de la commande des systèmes," *Editura Tehnicã Bucharest,* ISBN 973- 31-2103-7, 2001.

[60] A. Tarkiainen, R. Pollanen, M. Niemela, and J. A. Pyrhonen, "Identification of grid impedance for purposes of voltage feedback active filtering," *Power Electronics Letters, IEEE,* vol. 2, pp. 6-10, 2004.

[61] M. Sumner, A. Abusorrah, D. Thomas, and P. Zanchetta, "Improved power quality control and intelligent protection for grid connected power electronic con-

verters, using real time parameter estimation," in *Proc. of IAS*, 2006, pp. 1709-1715.

[62] A. V. Timbus, R. Teodorescu, and P. Rodriguez, "Grid impedance identification based on active power variations and grid voltage control," in *Proc. of IAS*, 2007, pp. 949-954.

[63] M. C. Di Piazza, P. Zanchetta, M. Sumner, and D. W. P. Thomas, "Estimation of load impedance in a power system," in *Proc. of HQP*, 2000, pp. 520-525, vol. 2.

[64] N. Ishigure, K. Matsui, and F. Ueda, "Development of an on-line impedance meter to measure the impedance of a distribution line," in *Proc. of ISIE*, 2001, pp. 549-554, vol. 1.

[65] J. P. Rhode, A. W. Kelley, and M. E. Baran, "Line impedance measurement: a nondisruptive wideband technique," in *Proc. of IAS*, 1995, pp. 2233-2240, vol. 3.

[66] M. Sumner, B. Palethorpe, D. Thomas, P. Zanchetta, and M. C. Di Piazza, "Estimation of power supply harmonic impedance using a controlled voltage disturbance," in *Proc. of PESC*, 2001, pp. 522-527, vol. 2.

[67] M. Sumner, B. Palethorpe, D. W. P. Thomas, P. Zanchetta, and M. C. Di Piazza, "A technique for power supply harmonic impedance estimation using a controlled voltage disturbance," *Power Electronics, IEEE Transactions on,* vol. 17, pp. 207-215, 2002.

[68] M. Tsukamoto, S. Ogawa, Y. Natsuda, Y. Minowa, and S. Nishimura, "Advanced technology to identify harmonics characteristics and results of measuring," in *Proc. of HQP*, 2000, pp. 341-346, vol. 1.

[69] L. Asiminoaei, R. Teodorescu, F. Blaabjerg, and U. Borup, "Implementation and test of an online embedded grid impedance estimation technique for PV inverters," *Industrial Electronics, IEEE Transactions on,* vol. 52, pp. 1136-1144, 2005.

[70] K. O. H. Pedersen, A. H. Nielsen, and N. K. Poulsen, "Short-circuit impedance measurement," *Generation, Transmission and Distribution, IEE Proceedings,* vol. 150, pp. 169-174, 2003.

[71] A. Bien, D. Borkowski, and A. Wetula, "Estimation of power system parameters based on load variance observations - laboratory studies," in *Proc. of EPQU*, 2007, pp. 1-6.

[72] B. Palethorpe, M. Sumner, and D. W. P. Thomas, "Power system impedance measurement using a power electronic converter," in *Proc. of HQP*, 2000, pp. 208-213, vol. 1.

[73] A. V. Timbus, R. Teodorescu, F. Blaabjerg, and U. Borup, "Online grid impedance measurement suitable for multiple PV inverters running in parallel," in *Proc. of APEC*, 2006, p. 5.

[74] D. Crevier and A. Mercier, "Estimation of higher frequency network equivalent impedances by harmonic analysis natural waveforms," *Power Apparatus and Systems, IEEE Transactions on,* vol. PAS-97, pp. 424-431, 1978.

[75] K. Klaus-Wilhelm, "Process and device for impedance measuring in AC networks as well as process and device for prevention of separate networks," *German Patent DE19504271 C1,* 1996.

[76] H. Fasshauer and M. Viotto, "Method and apparatus for measuring the impedance of an electrical energy supply system," *US Patent 6933714,* 2005.

[77] L. Asiminoaei, R. Teodorescu, F. Blaabjerg, and U. Borup, "A digital controlled PV-inverter with grid impedance estimation for ENS detection," *Power Electronics, IEEE Transactions on,* vol. 20, pp. 1480-1490, 2005.

[78] L. S. Czarnecki and Z. Staroszczyk, "On-line measurement of equivalent parameters for harmonic frequencies of a power distribution system and load," *Instrumentation and Measurement, IEEE Transactions on,* vol. 45, pp. 467-472, 1996.

[79] S. Cobreces, F. Huerta, D. Pizarro, F. J. Rodrguez, and E. J. Bueno, "Threephase power system parametric identification based on complex-space recursive least squares," in *Proc. of WISP*, 2007, pp. 1-6.

[80] S. Cobreces, P. Rodriguez, D. Pizarro, F. J. Rodriguez, and E. J. Bueno, "Complex-space recursive least squares power system identification," in *Proc. of PESC*, 2007, pp. 2478-2484.

[81] A. A. Girgis and R. B. McManis, "Frequency domain techniques for modeling distribution or transmission networks using capacitor switching induced transients," *Power Delivery, IEEE Transactions on,* vol. 4, pp. 1882-1890, 1989.

[82] M. Liserre, F. Blaabjerg, and R. Teodorescu, "Grid impedance estimation via excitation of LCL-filter resonance," *Industry Applications, IEEE Transactions on,* vol. 43, pp. 1401-1407, 2007.

[83] L. Ljung, *System Identification: Theory for the User*, Second ed.: Prentice Hall PTR, 1999.

[84] F. Blaabjerg, C. Zhe, and S. B. Kjaer, "Power electronics as efficient interface in dispersed power generation systems," *Power Electronics, IEEE Transactions on,* vol. 19, pp. 1184-1194, 2004.

[85] M. Calais, J. Myrzik, T. Spooner, and V. G. Agelidis, "Inverters for single-phase grid connected photovoltaic systems-an overview," in *Proc. of PESC*, 2002, pp. 1995-2000, vol. 4.

[86] A. Woyte, K. De Brabandere, D. Van Dommelen, R. Belmans, and J. Nijs, "International harmonization of grid connection guidelines: adequate requirements for the prevention of unintentional islanding," *Progress in Photovoltaics: Research and Applications,* vol. 11, pp. 407-424, 2003.

[87] N. Cullen, J. Thornycroft, and A. Collinson, "Risk analysis of islanding of photovoltaic power systems within low voltage distribution networks," *IEA Report PVPS, T5-08,* March 2002.

[88] W. Bower and M. Ropp, "Evaluation of islanding detection methods for photovoltaic utility-interactive power systems," *IEA Task V Report IEA-PVPS, T5-09,* March 2002.

[89] H. Guo-Kiang, C. Chih-Chang, and C. Chern-Lin, "Automatic phase-shift method for islanding detection of grid-connected photovoltaic inverters," *Energy Conversion, IEEE Transaction on,* vol. 18, pp. 169-173, 2003.

[90] C. Jeraputra and P. N. Enjeti, "Development of a robust anti-islanding algorithm for utility interconnection of distributed fuel cell powered generation," *Power Electronics, IEEE Transactions on,* vol. 19, pp. 1163-1170, 2004.

[91] V. John, Y. Zhihong, and A. Kolwalkar, "Investigation of anti-islanding protection of power converter based distributed generators using frequency domain analysis," *Power Electronics, IEEE Transactions on,* vol. 19, pp. 1177-1183, 2004.

[92] A. Kitamura, M. Okamoto, F. Yamamoto, K. Nakaji, H. Matsuda, and K. Hotta, "Islanding phenomenon elimination study at Rokko test center," in *Proc. of PVSC*, 1994, pp. 759-762, vol. 1.

[93] H. Kobayashi, K. Takigawa, E. Hashimoto, A. Kitamura, and H. Matsuda, "Method for preventing islanding phenomenon on utility grid with a number of small scale PV systems," in *Proc. of PVSC*, 1991, pp. 695-700, vol. 1.

[94] L. A. C. Lopes and S. Huili, "Performance assessment of active frequency drifting islanding detection methods," *Energy Conversion, IEEE Transactions on,* vol. 21, pp. 171-180, 2006.

[95] M. E. Ropp, M. Begovic, and A. Rohatgi, "Prevention of islanding in grid-connected photovoltaic systems," *Progress in Photovoltaics: Research and Applications,* vol. 7, pp. 39-59, 1999.

[96] M. E. Ropp, M. Begovic, and A. Rohatgi, "Analysis and performance assessment of the active frequency drift method of islanding prevention," *Energy Conversion, IEEE Transactions on,* vol. 14, pp. 810-816, 1999.

[97] M. E. Ropp, M. Begovic, A. Rohatgi, G. A. Kern, R. H. Bonn, Sr., and S. Gonzalez, "Determining the relative effectiveness of islanding detection methods using phase criteria and nondetection zones," *Energy Conversion, IEEE Transactions on,* vol. 15, pp. 290-296, 2000.

[98] P. Sanchis, L. Marroyo, and J. Coloma, "Design methodology for the frequency shift method of islanding prevention and analysis of its detection capability," *Progress in Photovoltaics: Research and Applications,* vol. 13, pp. 409-428, 2005.

[99] G. A. Smith, P. A. Onions, and D. G. Infield, "Predicting islanding operation of grid connected PV inverters," *Electric Power Applications, IEE Proceedings,* vol. 147, pp. 1-6, 2000.

[100] Z. Ye, L. Li, L. Garces, C. Wang, R. Zhang, M. Dame, R. Walling, and N. Miller, "A new family of active antiislanding schemes based on DQ implementation for grid-connected inverters," in *Proc. of PESC*, 2004, pp. 235-241, vol. 1.

[101] Z. Ye, R. Walling, L. Garces, R. Zhou, L. Li, and T. Wang, "Study and development of anti-islanding control for grid-connected inverters," *National Renewable Energy Laboratory, NREL/SR-560-36243,* May 2004.

[102] S. Yuyama, T. Ichinose, K. Kimoto, T. Itami, T. Ambo, C. Okado, K. Nakajima, S. Hojo, H. Shinohara, S. Ioka, and M. Kuniyoshi, "High speed frequency shift method as a protection for islanding phenomena of utility interactive PV systems," *Solar Energy Materials and Solar Cells,* vol. 35, pp. 477-486, 1994.

[103] Y. Zhihong, A. Kolwalkar, Z. Yu, D. Pengwei, and W. Reigh, "Evaluation of anti-islanding schemes based on nondetection zone concept," *Power Electronics, IEEE Transactions on,* vol. 19, pp. 1171-1176, 2004.

[104] M. Francesco De, L. Marco, and D. A. Antonio, "Overview of anti-islanding algorithms for PV systems. Part II: Active methods," in *Proc. of IPEMC*, 2006, pp. 1884-1889.

[105] Eltra&Elkraft, "Wind turbines connected to grids with voltage below 100 kV," http://www.eltra.dk, 2004.

[106] R. Teodorescu, F. Blaabjerg, M. Liserre, and A. Dell'Aquila, "A stable three-phase LCL-filter based active rectifier without damping," in *Proc. of IAS*, 2003, pp. 1552-1557, vol. 3.

[107] C. P. Dick, S. Richter, M. Rosekeit, J. Rolink, and R. W. De Doncker, "Active damping of LCL resonance with minimum sensor effort by means of a digital infinite impulse response filter," in *Proc. of EPE*, 2007, pp. 1-8.

[108] V. Blasko and V. Kaura, "A novel control to actively damp resonance in input LC filter of a three-phase voltage source converter," *Industry Applications, IEEE Transactions on,* vol. 33, pp. 542-550, 1997.

[109] M. Liserre, A. Dell'Aquila, and F. Blaabjerg, "Genetic algorithm based design of the active damping for a LCL-filter three-phase active rectifier," in *Proc. of APEC*, 2003, pp. 234-240, vol. 1.

[110] M. Liserre, R. Teodorescu, and F. Blaabjerg, "Stability of photovoltaic and wind turbine grid-connected inverters for a large set of grid impedance values," *Power Electronics, IEEE Transactions on,* vol. 21, pp. 263-272, 2006.

Part III

List of Publications

[I]   Control of single-stage single-phase PV inverter

by M. Ciobotaru, R. Teodorescu, and F. Blaabjerg,
Article published in Proceedings of EPE, 2005, pp. P1-P10

Control of single-stage single-phase PV inverter

Mihai Ciobotaru, Remus Teodorescu and Frede Blaabjerg
Institute of Energy Technology
Aalborg University
Pontoppidanstraede 101
DK-9220, Aalborg, Denmark
Tel.: +45 / 9635 9252
Fax: +45 / 2539 4182
E-Mail: mpc@iet.aau.com, ret@iet.aau.com, fbl@iet.aau.com
URL: http://www.iet.aau.dk

Keywords

«Distributed power», «Harmonics», «Photovoltaic», «Single phase system», «Solar Cell System»

Abstract

In this paper the issue of control strategies for single-stage photovoltaic (PV) inverter is addressed. Two different current controllers have been implemented and an experimental comparison between them has been made. A complete control structure for the single-phase PV system is also presented. The main elements of the PV control structure are: - a maximum power point tracker (MPPT) algorithm using the incremental conductance method; - a synchronization method using the phase-locked-loop (PLL), based on delay; - the input power control using the dc voltage controller and power feed-forward; - and the grid current controller implemented in two different ways, using the classical proportional integral (PI) and the novel proportional resonant (PR) controllers. The control strategy was tested experimentally on 1.5 kW PV inverter.

Introduction

The market for PV power applications continues to develop at a high rate. Between 2002 and 2003 the total installed capacity in the International Energy Agency (IEA) Photovoltaic Power Systems (PVPS) countries grew by 36 %, reaching 1 809 MW. Moreover, the price level of the PV modules and the system costs (inverter included) has decreased significantly. The use to PV systems connected in parallel with the mains was simplified and is often supported by incentives from utilities and/or governmental bodies. Before connecting a PV system to the power network, the dc voltage of the solar modules must be converted into an ac voltage. Some protection systems are required to prevent damage in the PV system caused by the utility network and vice versa. The PV systems require standards addressing the use and the performance of grid-connected PV inverters, thus ensuring the safety and quality of the manufacture.

The purpose of the power electronics in PVPS is to convert the dc current from the PV panels into ac current to the grid, with the highest possible efficiency, the lowest cost and to keep a superior performance. The basic interfacing is shown in Fig. 1.

A controversial issue for PV inverters is the harmonics level. The IEEE 929 standard permits a limit of 5% for the current total harmonic distortion (THD) factor with individual limits of 4% for each odd harmonic from 3rd to 9th and 2% for 11th to 15th while a recent draft of European IEC61727 suggests almost the same thing as previously mentioned. These levels are far more stringent than other domestic appliances, like

IE61000-3-2, as PV systems are viewed as generation sources and so are subject to higher standards than load systems.
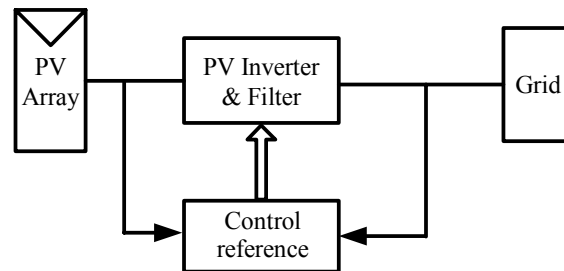
Fig. 1: Power electronic system with the grid, source (PV array), power converter and control

For current-controlled PV inverters in most of the cases we make use of PI controller with grid voltage feed-forward (VFF) [1], [2], but this solution exhibits two well known drawbacks (due to the poor performance of the integral action): inability of the PI controller to track a sinusoidal reference without steady-state error and poor disturbance rejection capability. An alternative solution in order to alleviate the PI's drawbacks is presented in [3], where a second order generalized integrator (GI) can be used. The GI is a double integrator that achieves an "infinite" gain at a certain frequency (resonance frequency), and almost no attenuation exists outside this frequency. Thus, it can be used as a notch filter in order to compensate the harmonics in a very selective way. Another approach reported in [4] where a new type of stationary-frame regulators called Proportional Resonant (PR) is introduced. In this approach the classical PI dc-compensator is transformed into an equivalent ac-compensator having the same frequency response characteristics in the bandwidth of concern.

This paper is aimed at presenting a single-stage converter for single-phase PV systems. Two different current controllers have been implemented and an experimental comparison between them has been made. A complete control structure for the single-phase PV system is also presented. An incremental conductance method has been used in order to track the MPPT of the PV characteristic. In order to get a clean sinusoidal current reference (synchronized with the grid voltage) it is used a PLL, a based on delay structure. The conclusions are presented in the final part of the paper.

System description

Usually the power converter interface from the dc source to the load and/or to the grid consists of a two-stage converter: the dc-dc converter and the dc-ac converter. An interesting alternative solution could be the use of a single-stage converter where the dc-dc converter is avoided and in order to ensure the necessary dc voltage level the PV array can be a string of PV panels or a multitude of parallel strings of PV panels. In the classical solution with two-stage converter, the dc-dc converter requires several additional devices producing a large amount of conduction losses, sluggish transient response and high cost while the advantages of the single-stage converters are: good efficiency, a lower price and easier implementation. The disadvantages of the single-stage converter are the fact that the PV panels are in series and if the shading occurs on one or several PV panels then the efficiency of the whole system is reduced.

As shown in Fig. 2, the PV inverter system consists of a solar panel string and a dc link capacitor C_{dc} on the dc side with an output ac filter (LCL), insulation transformer and grid connection on the ac side. The number of panels in the string has to ensure a dc voltage higher then the ac voltage peak at all time. The energy conversion from dc to ac side is made by a single-phase voltage source inverter. The used solar-panel string consists of sixteen uniserial PV panels (120 W for each panel).
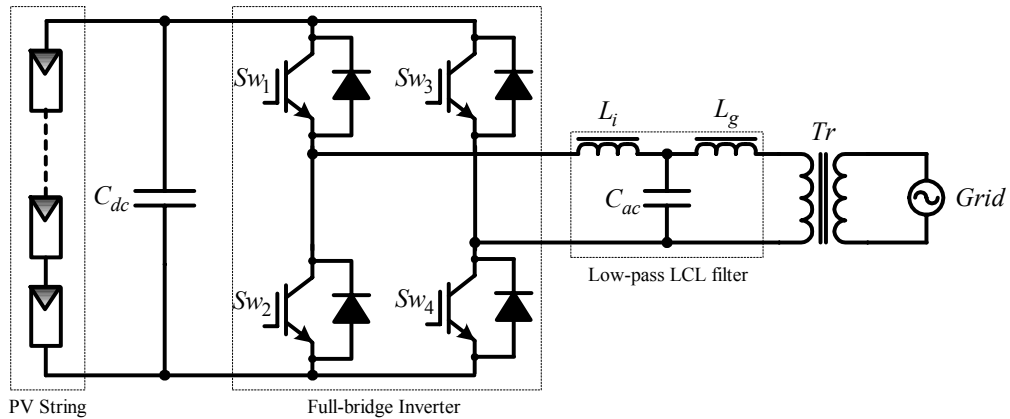
Fig. 2: The voltage source PV inverter connected to the grid through an LCL filter

Control strategy

For the grid-connected PV inverters in the power range of 1-5 kW, the most common control structure for the dc-ac grid converter is a current-controlled H-bridge PWM inverter having a low-pass output filter. Typically L filters are used but the new trend is to use LCL filters that have a higher order (3rd) which leads to more compact design. The drawback is its resonance frequency which can produce stability problems and special control design is required [5]. The control structure of the PV energy conversion system is shown in Fig. 3.
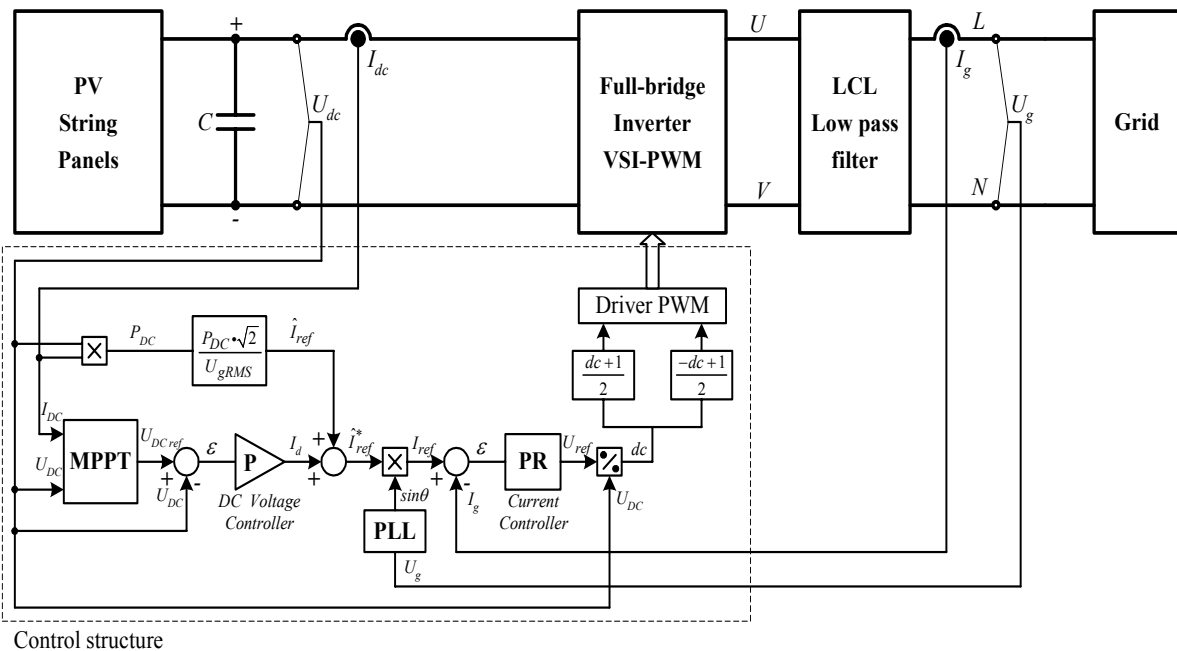
Fig. 3: Control diagram of the PV energy conversion system

The main elements of the control structure are the synchronization algorithm based on PLL, the MPPT, the input power control and the grid current controller.

PLL structure

The PLL is used to provide a unity power factor operation which involves synchronization of the inverter output current with the grid voltage and to give a clean sinusoidal current reference. The PI controller parameters of the PLL structure are calculated in such a way that we can set directly the settling time and the damping factor of this PLL structure. The PLL structure is also used for grid voltage monitoring in order to get the amplitude and the frequency values of the grid voltage. The general form of the PLL structure is presented in Fig. 4.
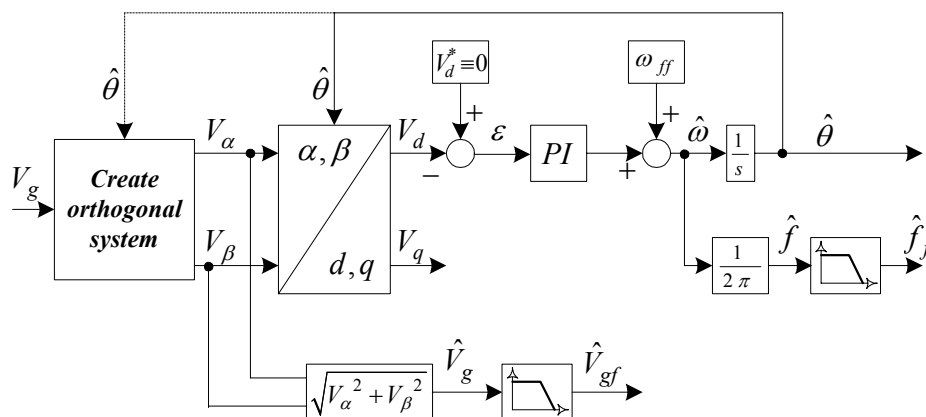
Fig. 4: General structure of a single phase PLL

MPPT algorithm

The task of the MPPT in a PV energy conversion system is to tune continuously the system so that it draws maximum power from the solar array regardless of weather or load conditions. Since the solar array has non ideal voltage-current characteristics and the conditions such as irradiance, ambient temperature, and wind that affect the output of the solar array are unpredictable, the tracker should deal with a nonlinear and time-varying system. The conventional MPPT algorithms are using $dP/dV = 0$ to obtain the maximum power point output. Several algorithms can be used in order to implement the MPPT as follows [6]: perturb and observe, incremental conductance, parasitic capacitance and constant voltage, but only the first two are the most frequently used.

The incremental conductance algorithm has been chosen as a MPPT strategy in this paper. This algorithm has advantages compared to perturb and observe as it can determine when the MPPT has reached the MPP, where perturb and observe oscillates around the MPP. Also, incremental conductance can track rapidly the increase and decrease of irradiance conditions with higher accuracy than perturb and observe.

One disadvantage of this algorithm is the increased complexity when compared to perturb and observe. This increases the computational time and slows down the sampling frequency of the array voltage and current. The flowchart of the incremental conductance algorithm is shown in Fig. 5 [7] where the V_k and I_k are the momentary voltage and current of the PV array and V_{k-1} and I_{k-1} are the previous voltage and current, respectively. The dP/dV term can be replaced by $I + \left(\Delta I / \Delta V \right) \cdot V$. The output of the MPPT is the dc voltage reference (V^*_{pv}).
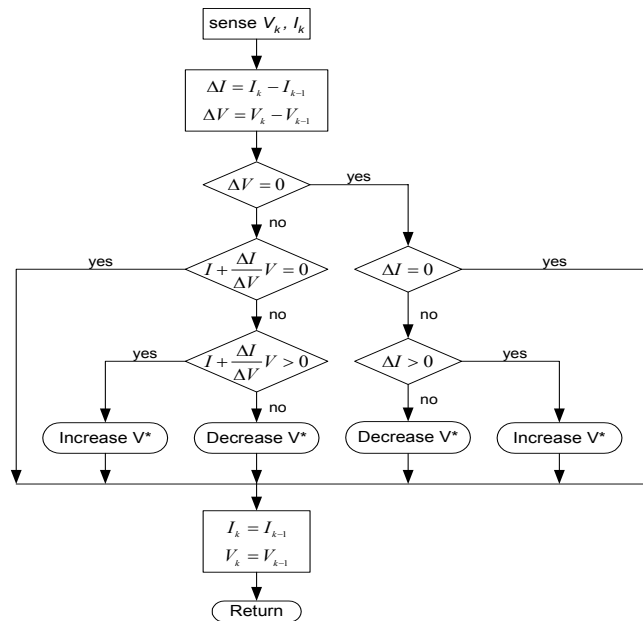
Fig. 5: Flowchart of the incremental conductance algorithm

Input power control

The control strategies of input power in the case of a power configuration of PV system without dc-dc converter are presented in the following section. In Fig. 6 a new control strategy of input power is proposed. The new element introduced is the power feed-forward. The computed value of the current amplitude reference using the PV power (P_{PV}) and the RMS value of the ac voltage ($V_{ac\,RMS}$) is added to the output value of the dc voltage controller ($\hat{I}_r$) resulting in the ac current amplitude reference ($\hat{I}_{ref}$).

Using the input power feed-forward the dynamic of the PV system is improved being known the fact that the MPPT is rather slow. The dc voltage controller ensures a quick response of the PV system at a sudden change of the input power.

Fig. 6: New control structure of controlling the input power. A feed-forward of input power is used

Grid current controller

Classical PI control with grid voltage feed-forward (U_g) as depicted in Fig. 7a, is commonly used for current-controlled PV inverters.

a)   b)
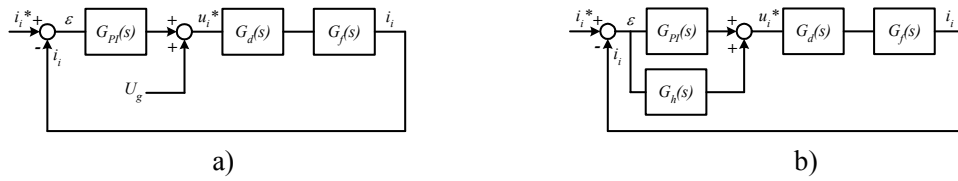
Fig. 7: The current loop of PV inverter: a) with PI controller; b) with PR controller

The PI current controller $G_{PI}(s)$ is defined as:

$$G_{PI}(s) = K_P + \frac{K_I}{s}$$
(1)

In order to get a good dynamic response, a grid voltage feed-forward is used, as depicted in Fig. 7a. This leads in turn to stability problems related to the delay introduced in the system by the voltage feedback filter (U_g). In order to alleviate this problem an advanced filtering method for the grid voltage feed-forward should be considered. A Bode diagram analysis of the PI controller is presented in Fig. 8.
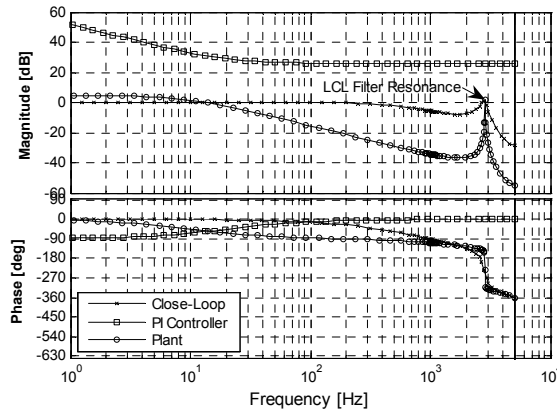
Fig. 8: PI current controller – Bode diagram analysis

As it has been mentioned in the introduction of this paper, an alternative solution for the poor performances of the PI controller is the PR controller. The current loop of the PV inverter with PR controller is shown in Fig. 7b.

The PR current controller $G_c(s)$ is defined as [3], [5]:

$$G_c(s) = K_P + K_I \frac{s}{s^2 + \omega_o^2}$$
(2)

The harmonic compensator (HC) $G_h(s)$ as defined in [5]:

$$G_h(s) = \sum_{h=3,5,7} K_{Ih} \frac{s}{s^2 + (\omega_o h)^2}$$
(3)

is designed to compensate the selected harmonics 3rd, 5th and 7th as they are the most predominant harmonics in the current spectrum.

A processing delay, usually equal to T_s for the PWM inverters [2], is introduced in $G_d(s)$. The filter transfer function $G_f(s)$ is expressed in (4) [8].

$$G_f(s) = \frac{i_i(s)}{u_i(s)} = \frac{1}{L_i s} \frac{\left(s^2 + z_{LC}^2\right)}{\left(s^2 + \omega_{res}^2\right)} \tag{4}$$

- where $z_{LC}^2 = \left[L_g C_f\right]^{-1}$ and $\omega_{res}^2 = \frac{\left(L_i + L_g\right) \cdot z_{LC}^2}{L_i}$

The current error - disturbance ratio rejection capability at null reference is defined as:

$$\left.\frac{\varepsilon(s)}{u_g(s)}\right|_{i_i^* = 0} = \frac{G_f(s)}{1 + \left(G_c(s) + G_c(s)\right) \cdot G_d(s) \cdot G_f(s)} \tag{5}$$

where: ε is current error and the grid voltage u_g is considered as the disturbance for the system.
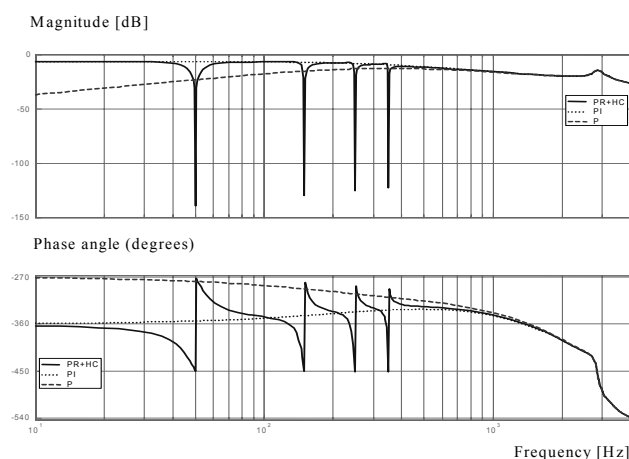
Fig. 9: Bode diagram of the disturbance rejection (current error ratio disturbance) of the PR+HC (3rd, 5th and 7th), PI and P current controllers

In Fig. 9 is presented the Bode diagram of the disturbance rejection for the P, PI and PR controllers. It can be very easily noticed that the PI rejection capability is worse in comparison with the PR and from Fig. 9 it can be observed that the PI rejection capability at 5th and 7th harmonics is comparable with that one of a simple proportion controller, the integral action being irrelevant. Thus, it is demonstrated the superiority of the PR controller respect to the PI in terms of harmonic current rejection.

The close-loop frequency response of the system and also the Bode plots of the PR + HC and the plant are presented in Fig. 10a The Fig. 10b presets the root-locus of the close-loop current control system and the open-loop frequency response of the system.

The size of the proportional gain K_p from PR controller determines the bandwidth and stability phase margin [3], in the same way as for the PI controller. As it can be observed from the open-loop Bode diagram (Fig. 10b) the phase margin (PM) is determined to be equal with 42 deg, indicating a good stability of the system. Also, the dominant poles of the controller are well damped as it can be seen in Fig. 10b exhibiting a damping factor equal with 0.7.

a)   b)
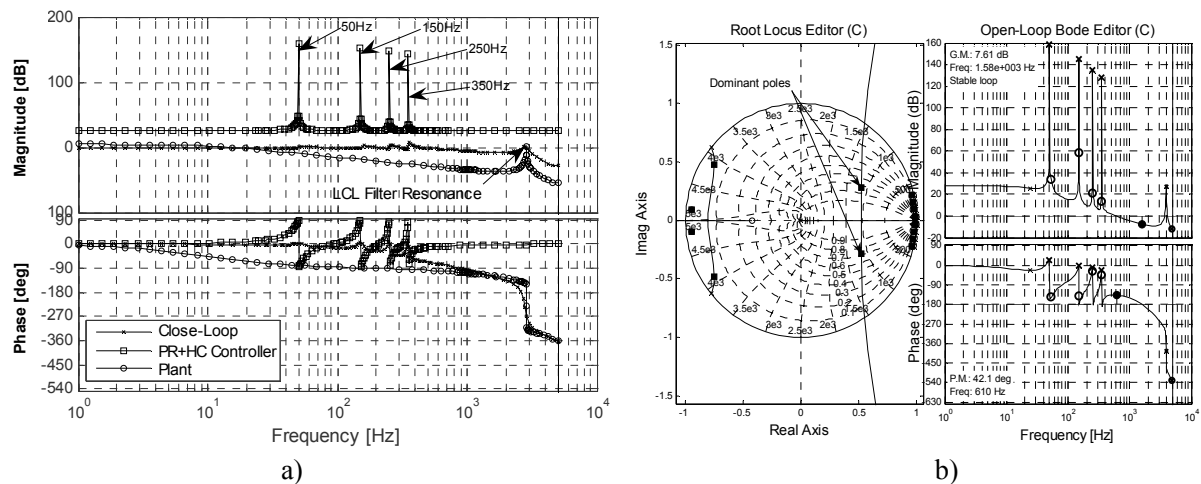
Fig. 10: PR current controller – Bode diagrams a) and root-locus b) analysis

Experimental results

A single-stage grid-connected PV inverter (1.5 kW power range) was built in order to analyze the PV systems performance, as depicted in Fig. 11a. The system is dSPACE based and voltage source inverter (VSI) is controlled using a unipolar PWM to place the harmonics on the high frequency side making them easier to filter. The parameters of the LCL filter were: L_i=1426 µH, C_{ac}=2.2 µF, L_g=713 µH. The power stage of a Danfoss VLT 5004 rated 400V/10A was used. The switching frequency of the inverter was 10 kHz. The control algorithm shown in Fig. 3 was implemented using dSPACE DS1103 platform.

The system was tested in the following condition: - the open circuit dc voltage provided by the uniserial sixteen PV panels was around 660 V, the RMS value of the grid voltage was U_g = 225 V with a THD of 2.2 % background distortion. The grid impedance was measured to 1.2 ohms with a series inductance of 2.1 mH because of a insulation transformer using in order to connect the PV system to the grid.

The plotted results have been captured using the graphical interface of the dSPACE system (Control Desk) and then exported to Matlab workspace for plotting.

a)   b)
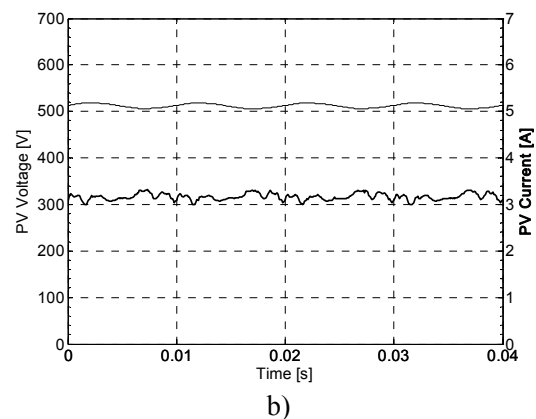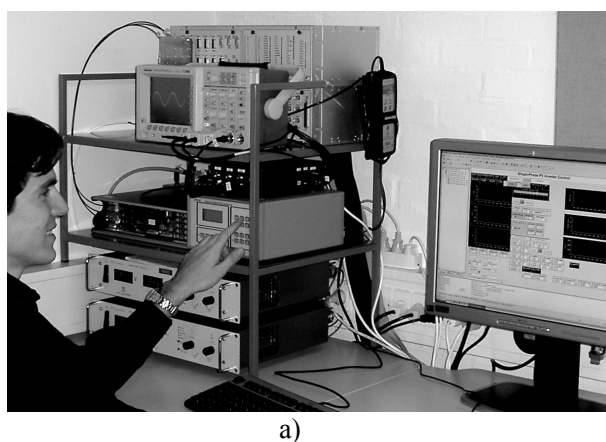
Fig. 11: a) Experimental test setup of the 1.5 kW PV inverter; b) PV voltage and current (marked) at 1.5 kW injected power to the grid

The voltage and current of the PV panels at 1.5 kW power on the ac side, are presented in the Fig. 11b.

The grid current and grid voltage at 1.5 kW for PI, PR and PR+HC controllers are presented in Fig. 12 a), b) and c). As it can be seen a much lower THD is obtained with the PR+HC controller. The grid current response at a 5 A step in the current reference is presented for the PI (Fig. 12d), PR (Fig. 12e) and PR+HC (Fig. 12f). As it can be observed the PR and PR+HC controller yields a smaller overshoot than the PI controller.

Fig. 12: Grid current (marked) and grid voltage at 1.5 kW for PI a), PR b) and PR+HC c) controllers. Grid current response (marked) at a 5 A step in the current reference for PI d), PR e) and PR+HC f) controllers

In Fig. 13, a comparison of the spectrum for PI, PR and PR+HC in the lower frequency region is presented.
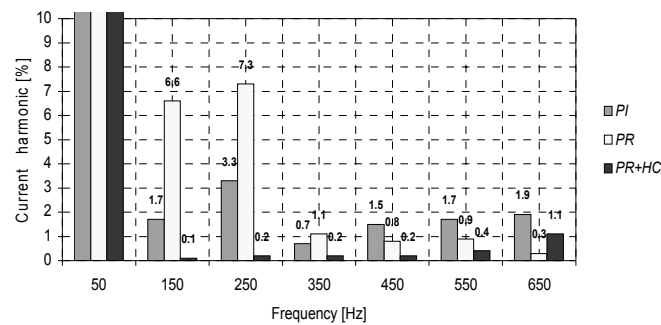
Fig. 13: Measured grid current harmonic spectrum for PI, PR and PR+HC controllers

Using PI controller with VFF has been obtained a current THD of 5.8% while in case of the PR controller the measured current THD was 9.7%. Adding the HC for the PR controller a drastic attenuation of the current THD can be observed, decreasing to 0.5%.

Conclusion

An interesting alternative solution using a single-stage converter, where the dc-dc converter is avoided, has been developed and successfully tested on a dSPACE controlled 1.5kW single-phase PV inverter. The advantages of the single-stage converters are: good efficiency, a lower price and easier implementation, while the main disadvantage is the fact that the PV panels are in series and if the shading occurs on one or several PV panels then the efficiency of the whole system is reduced.

It has been demonstrated that the PR+HC controller gives better performances then the classical PI controller for the grid current loop. The two well known drawbacks of the PI controller are: - steady-state error; and - poor harmonics rejection capability. The steady-state error can be overcame by the PR controller. The PR controller is able to remove the steady-state error without using VFF, which makes it more reliable. By adding the selective HC to the PR controller, a very good rejection for the dominant harmonics can be obtained.

References

[1]. M. Kazmierkovski, R. Krishnan, F. Blaabjerg. Control in Power Electronics, Selected Problems, Academic Press 2002, ISBN 0-12-402772-5.
[2]. C. Cecati, A. Dell'Aquila, M. Liserre and V. G. Monopoli. Design of H-bridge multilevel active rectifier for traction systems, IEEE Trans. on Ind. App., Vol. 39, Sept./Oct. 2003, pp. 1541-1550.
[3]. X. Yuan, W. Merk, H. Stemmler, J. Allmeling. Stationary-Frame Generalized Integrators for Current Control of Active Power Filters with Zero Steady-State Error for Current Harmonics of Concern Under Unbalanced and Distorted Operating Conditions, IEEE Trans. on Ind. App., Vol. 38, No. 2, Mar./Apr. 2002, pp. 523 – 532.
[4]. D. N. Zmood and D. G. Holmes. Stationary Frame Current Regulation of PWM Inverters with Zero Steady-State Error, IEEE Trans. on Power Electronics, Vol. 18, No. 3, May 2003, pp. 814 – 822.
[5]. R. Teodorescu, F. Blaabjerg, M. Liserre, U. Borup. A New Control Structure for Grid-Connected PV Inverters with Zero Steady-State Error and Selective Harmonic Compensation, Proc. of APEC'04, Vol. 1, pp. 580-586.
[6]. D.P. Hohm and M.E. Ropp. Comparative Study of Maximum Power Point Tracking Algorithms Using an Experimental, Programmable, Maximum Power Point Tracking Test Bed, Proc. of Photovoltaic Specialists Conference, 2000, pp.1699 – 1702.
[7]. Y.C. Kuo and T.J. Liang. Novel Maximum-Power-Point-Tracking Controller For Photovoltaic Energy Conversion System, IEEE Transactions on Industrial Electronics, Vol. 48, No. 3 , 2001 pp. 594 – 601.
[8] M. Liserre, F. Blaabjerg and S. Hansen. Design and Control of an LCL-filter Based Active Rectifier, Proc. of IAS'01, Vol. 1, pp. 299-307.

[II]   Improved PLL structures for single-phase grid inverters

by M. Ciobotaru, R. Teodorescu, and F. Blaabjerg,
Article published in Proceedings of PELINCEC, 2005, pp. 6.

Improved PLL structures for single-phase grid inverters

Mihai Ciobotaru, Remus Teodorescu and Frede Blaabjerg
Institute of Energy Technology
Aalborg University
Pontoppidanstraede 101
DK-9220, Aalborg, Denmark
Tel.: +45 / 9635 9252
Fax: +45 / 2539 4182
E-Mail: mpc@iet.aau.dk, ret@iet.aau.dk, fbl@iet.aau.dk
URL: http://www.iet.aau.dk

Abstract — **Phase, amplitude and frequency of the utility grid are critical information for the operation of the grid-connected power conditioning equipments. In such applications, an accurate and fast detection of the phase angle of the utility voltage is essential to assure a correct generation of the reference signals. This paper presents two improved phase-locked-loop (PLL) methods for single-phase grid connected systems. The investigated PLL methods are based on a transport delay method and an inverse Park transformation method. The improvements in the case of using the delay-based PLL are: non-frequency dependent and better filtering of the harmonics. For the other investigated PLL method based on inverse Park transformation the improvement consists of better filtering of the harmonics. Experimental results validate the effectiveness of the two proposed methods.**

Index Terms — **Phase-Locked-Loop (PLL), single-phase distributed generation system, grid connected power converter.**

I. INTRODUCTION

PHASE, amplitude and frequency of the utility voltage are critical information for the operation of the grid-connected power conditioning and power generating equipments. In such applications, an accurate and fast detection of the phase angle of the utility voltage is essential to assure the correct generation of the reference signals.

The phase-locked loop (PLL) [1], [2] structure is a feedback control system that automatically adjusts the phase of a locally generated signal to match the phase of an input signal. The purpose of the PLL in a grid connected system is to synchronize the inverter current angle, θ_{inv}, with the angle of the grid voltage, θ_{grid}, in order to obtain a power factor as close to unity as possible. The angle θ_{inv} is used to calculate the reference current that is compared to the actual output current of the inverter. The main idea in the PLL is that it changes the inverter current frequency, ω_{inv}, if the inverter current and the grid voltage are out of phase. If the inverter current lags the grid voltage the PLL will decrease ω_{inv} until

the inverter current is in phase with the grid voltage. On the other hand, if the inverter current leads the grid voltage, ω_{inv} is increased until they are in phase. In order to be able to synchronize θ_{inv} with θ_{grid} it is necessary somehow to measure θ_{grid}. This has been done by detecting the zero crossing on the grid voltage as shown in Fig. 1. Instead of the zero crossing detection method another solution are used in nowadays [3]-[7].

Fig. 1. Zero crossing detection structure including voltage monitoring

Most recently, there has been an increasing interest in Phase-Locked-Loop (PLL) topologies for grid-connected systems [3]. In order to use a PLL method in single-phase systems an artificial orthogonal voltage system should be created [4]. It is well known that in single-phase systems there are less informations than in three-phase systems regarding the grid condition, so more advanced methods should be considered in order to create an orthogonal voltage system [3]-[6].

Also using a PLL structure the grid voltage parameters can be monitored such as grid voltage amplitude and frequency. This grid voltage monitoring is used to ensure that the performances of the investigated methods comply with the standard requirements for operation under common utility distortions such as line notching/harmonics, voltage sags/swells/loss, frequency variations and phase jumps.

This paper presents two different improved methods for single-phase PLL structures.

II. THE SINGLE PHASE PLL STRUCTURE

The general structure of a single-phase PLL is shown in Fig. 2.

Fig. 2. General structure of a single-phase PLL including voltage monitoring.

An easy way to generate a quadrature signal in a single-phase system is through the use of a transport delay block, which is responsible for introducing a phase shift of 90 degrees with respect to the fundamental frequency of the input signal (grid voltage) [3]. A related method, but more complex is to generate the quadrature signal through the use of Hilbert transformation [5]. Due to its noncausality, it is not practically realizable, but it is possible to be approximated with a high order Finite Impulse Response (FIR) filter. The two mentioned methods are presented in Fig. 3a and Fig. 3b, respectively.

Fig. 3. Orthogonal signal generation based on: a) transport delay, b) Hilbert transformation.

The basic difference of the transport delay method, compared with the Hilbert transformation method is that, all the harmonic content of the input signal is subjected to the same time delay. For the Hilbert transformation method, all the harmonic content is phase-shifted 90 degrees. Therefore, the Hilbert transformation method will not be further investigated in this paper due to its complexity and poor behavior compared with the delay method [3].

The transport delay method is easily implemented through the use of a first-in, first-out (FIFO) buffer, with size set to one-fourth of the number of samples contained in one cycle of the fundamental frequency. Generally speaking, the algorithm is easily implemented and the tuning process does not pose special difficulties. Anyway, the transport delay method has also two drawbacks: it is frequency dependent due to its fixed delay, therefore problems can occur when the grid frequency experience fluctuations, and create an unfiltered orthogonal system.

A different method to generate the orthogonal system is using the inverse Park Transformation, introduced in [4]. The inverse Park method is presented in Fig. 4.

Fig. 4. Orthogonal system generation based on inverse Park transformation.

As it can be seen, a single phase voltage (V_g) and an internally generated signal (V_β) are used as input to a Park transformation block ($\alpha\beta$-dq). V_β is obtained through the use of an inverse Park transformation, where the inputs are the d- and q-axis output of the Park transformation, fed through first order low pass filters (LPF). The two first order lag blocks added to the structure must be adequately tuned in order to guarantee the performance of the single-phase PLL [6]. The inner loop (the β-axis voltage loop) must be fast enough so that the outer loop performs the tracking function with the β-axis voltage stabilized. The stationary frame is seen by the outer loop as if it was obtained from a three phase system and thus the tracking of the "virtual" utility voltage vector can be performed. The tuning of the two first order lag blocks is performed using the following method [6]:

- Set the location of the poles for suitable bandwidth and robustness, considering the continuous variation of this parameters with the phase angle of the input signal;
- Evaluate the disturbance rejection characteristic.

Although the algorithm of the inverse Park transformation is easily implemented, requiring only an inverse Park and two first-order low-pass filters, the tuning of the PI controller and the choice of the time constant of the filters are a more difficult process, as compared with other PLL algorithms. This is due to the presence of the two interdependent nonlinear loops, which make linearization and use of linear system analysis tools more trouble some [3].

III. IMPROVED PLL STRUCTURES

A. Transport delay method

One of the improved single-phase PLL structure methods uses the transport delay block. Due to the fact that this method uses a constant delay in order to generate the quadrature signal of the grid voltage, when the grid frequency experiences fluctuations, the single-phase PLL behavior will be negatively affected. When the grid frequency changes its value, the transport delay block is not able to modify its fixed value and the produced signal will not be in a quadrature with the input signal (V_g). This issue will generate errors in the grid voltage phase angle, frequency and amplitude measurement. The proposed method using the transport delay-based PLL structure is presented in the following.

In order to eliminate this drawback of the transport delay method, a small change in the initial Park transformation is proposed.
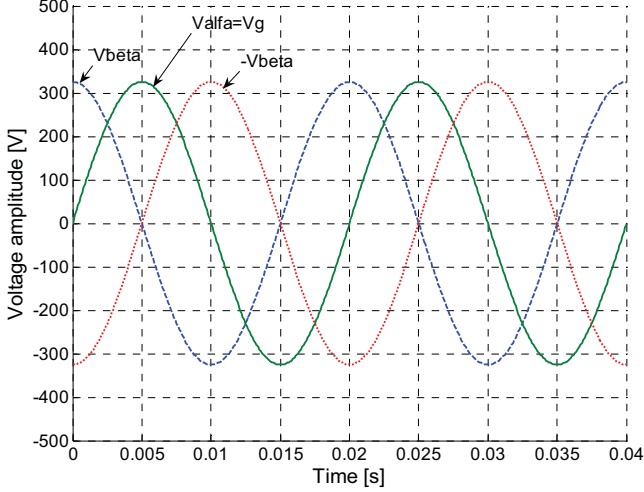

Fig. 5. Orthogonal voltage system.

Fig. 5 shows an orthogonal voltage system where the grid voltage represents the α-signal. The reference frames considered in the transformations is depicted in Fig. 6. Eq. (1) shows the direct Park transformation utilized in Fig. 2.
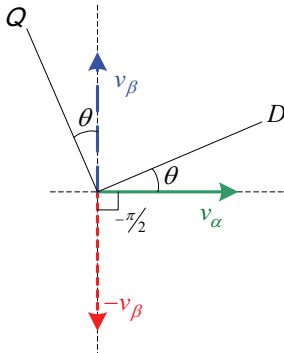

Fig. 6. Reference frames of the orthogonal voltage system.

$$\begin{cases} v_d = v_\alpha \cdot \sin\hat{\theta} + v_\beta \cdot \cos\hat{\theta} \\ v_q = -v_\alpha \cdot \cos\hat{\theta} + v_\beta \cdot \sin\hat{\theta} \end{cases} \quad (1)$$

- where $\hat{\theta}$ represents the estimated grid voltage angle provided by the PLL structure.

When a transport delay block is used, a quadrature signal of the input is created. If the grid voltage represents the α-signal, the obtained quadrature signal provided by the transport delay block will be $-v_\beta$ as presented in Fig. 5 and Fig. 6. The orthogonal voltage system created by using transport delay method is presented as follows:

$$\begin{cases} \sin(\omega_{50} \cdot t) \rightarrow \boxed{delay \ {}^{T_{50}}\!/_4} \rightarrow \sin\left(\omega_{50} \cdot t - {}^{T_{50}}\!/_4\right) = -\cos(\omega_{50} \cdot t) \\ v_\alpha = V_g \cdot \sin\theta \\ -v_\beta = V_g \cdot \sin\left(\theta - {}^{T_{50}}\!/_2\right) \end{cases} \quad (2)$$

Therefore, the transport delay block provides a quadrature signal equal with $-v_\beta$ instead of v_β, which should be taken

into consideration when the Park transformation is used.

Thus, (1) will become as presented in (3):

$$\begin{cases} v_d = v_\alpha \cdot \sin\hat{\theta} - (-v_\beta) \cdot \cos\hat{\theta} \\ v_q = -v_\alpha \cdot \cos\hat{\theta} - (-v_\beta) \cdot \sin\hat{\theta} \end{cases} \quad (3)$$

Substituting v_α and $-v_\beta$ from (2) into (3) results in:

$$\begin{cases} v_d = V_g \cdot \sin\theta \cdot \sin\hat{\theta} - V_g \cdot \sin(\theta - {}^{T_{50}}\!/_4) \cdot \cos\hat{\theta} \\ v_q = -V_g \cdot \sin\theta \cdot \cos\hat{\theta} - V_g \cdot \sin(\theta - {}^{T_{50}}\!/_4) \cdot \sin\hat{\theta} \end{cases} \quad (4)$$

The second term of (4) (v_q), used in the control loop of the PLL structure as input, becomes as follows:

$$v_q = V_g \cdot \left[-\sin(\omega_{50} \cdot t) \cdot \cos(\widehat{\omega_{50} \cdot t}) - \sin\left(\omega_{50} \cdot t - {}^{T_{50}}\!/_4\right) \cdot \sin(\widehat{\omega_{50} \cdot t}) \right] \quad (5)$$

Substituting $\sin\left(\omega_{50} \cdot t - {}^{T_{50}}\!/_4\right) = -\cos(\omega_{50} \cdot t)$ (5) will become:

$$v_q = V_g \cdot \underbrace{\left[\sin(\widehat{\omega_{50} \cdot t}) \cdot \cos(\omega_{50} \cdot t) - \sin(\omega_{50} \cdot t) \cdot \cos(\widehat{\omega_{50} \cdot t}) \right]}_{\equiv 0, \ when \ \hat{\theta}=\theta} \quad (6)$$

When the frequency changes its value from ω_{50} to ω_n, the constant delay will generate a phase shift error (φ_{er}) in the quadrature signal as presented in (5):

$$\sin(\omega_n \cdot t) \rightarrow \boxed{delay \ {}^{T_{50}}\!/_4} \rightarrow \sin\left(\omega_n \cdot t - {}^{T_{50}}\!/_4 + \varphi_{er}\right) \quad (7)$$

If the grid frequency changes its value from ω_{50} to ω_n, (5) becomes:

$$v_q = V_g \cdot \underbrace{\left[-\sin(\omega_n \cdot t) \cdot \cos(\widehat{\omega_n \cdot t}) - \sin\left(\omega_n \cdot t - {}^{T_{50}}\!/_4 + \varphi_{er}\right) \cdot \sin(\widehat{\omega_n \cdot t}) \right]}_{\neq 0, \ when \ \hat{\theta}=\theta} \quad (8)$$

In order to eliminate the errors introduced by φ_{er}, a change in the Park transformation is proposed. The change consists in the substitution of $\cos\hat{\theta}$ of the Park transformation presented in (1) with the quadrature signal of $\sin\hat{\theta}$ using the same transport delay block as in case when $-v_\beta$ is created:

$$\sin(\widehat{\omega_n \cdot t}) \rightarrow \boxed{delay \ {}^{T_{50}}\!/_4} \rightarrow \sin\left(\widehat{\omega_n \cdot t} - {}^{T_{50}}\!/_4 + \varphi_{er}\right) = -\cos(\widehat{\omega_n \cdot t}) \quad (9)$$

resulting:

$$\cos(\widehat{\omega_n \cdot t}) = -\sin\left(\widehat{\omega_n \cdot t} - {}^{T_{50}}\!/_4 + \varphi_{er}\right) \quad (10)$$

The substitution presented in (10) will produce the same phase shift error (φ_{er}) as in the case of generating $-v_\beta$ using the transport delay block.

Using (10) in (8) results in:

$$v_q = V_g \cdot \underbrace{\left[\begin{array}{l} \sin\left(\widehat{\omega_n \cdot t} - {}^{T_{50}}\!/_4 + \varphi_{er}\right) \cdot \sin(\omega_n \cdot t) \\ \\ -\sin\left(\omega_n \cdot t - {}^{T_{50}}\!/_4 + \varphi_{er}\right) \cdot \sin(\widehat{\omega_n \cdot t}) \end{array} \right]}_{\equiv 0, \ when \ \hat{\theta}=\theta} \quad (11)$$

As it can be seen from (11), if the grid frequency changes

its value from ω_{50} to ω_n, the v_q term will not be affected (at $\hat{\theta} = \theta$).

Another improvement for the transport delay method consists in using a first-order LPF in order to get a clean v_q as presented in Fig. 7. The dynamics of the PLL will be slightly affected in this case, while the harmonic content from v_q will decrease considerably.
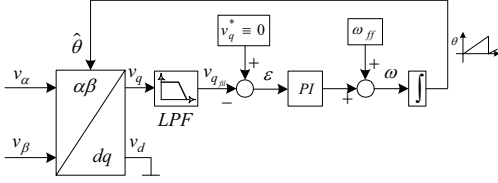

Fig. 7. PLL with v_q filtering using a first-order low-pass filter.

B. Park transformation method

As it can be seen from Fig. 4, the v_q output of the Park transformation is used directly as input for the PLL structure to obtain phase and frequency information of the input signal (grid voltage) [3]. In the case of high harmonic content in the grid voltage, the v_q output of the Park transformation will be affected due to the fact that one of the two inputs of the Park transformation ($v_\alpha = v_g$) is not filtered.

In order to avoid the harmonic propagation into the PLL control loop a new Park transformation can be used, as presented in Fig. 8. The inputs of this new Park transformation will be the outputs (v_α and v_β) of the inverse Park transformation. Therefore, instead of using the v_q signal directly as input for the PLL control loop (see Fig. 4), a new Park transformation using two clean outputs (v_α and v_β) of the inverse Park transformation is used (see Fig. 8). The harmonic content from v_q will be significantly decreased in this case, while the dynamic of the PLL will be slightly affected.
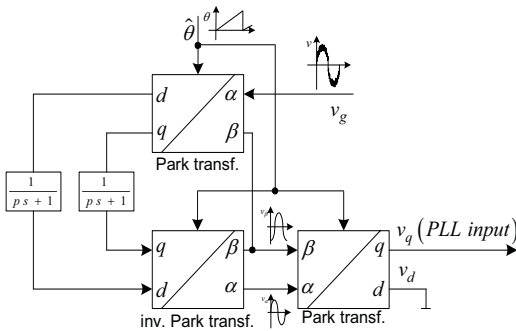
Fig. 8. Improved Park transformation PLL method.

IV. EXPERIMENTAL RESULTS

The single-phase PLL topologies were implemented in a dSPACE DS1103 based system [7]. In order to test the PLL structures and to observe their behavior under different grid conditions, an experimental system connected to a grid simulator (California Instruments) has been used.

A. Transport delay method

Three types of disturbances were used to evaluate the behavior of the transport delay based PLL.

The parameters of the PLL structure have been set as follows: - settling time t_{set}= 0.05 seconds and damping factor ξ=1. The sampling frequency was equal to 10 kHz.

A frequency sweep from 50 to 51 Hz was created, in order to test the improved transport delay based PLL at frequency variations. Fig. 9 presents the estimated grid frequency of a PLL structure using the classical delay method. The estimated grid frequency of the improved delay method, presented in § III.A, is shown in Fig. 10. It can be seen that the improved method is not frequency dependent as the classical method is.
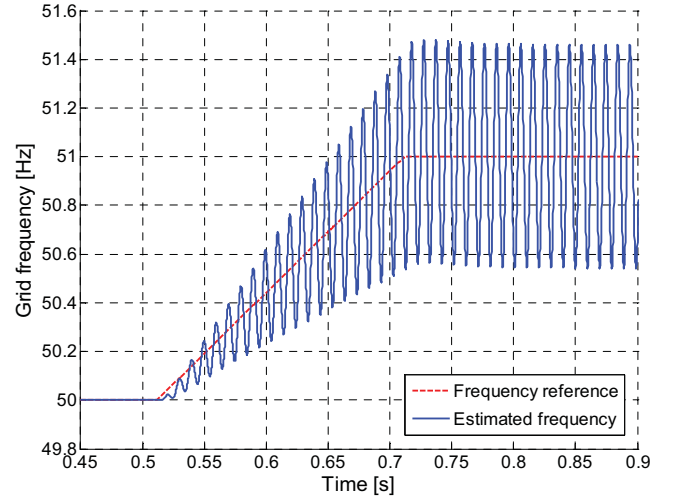
Fig. 9. Frequency sweep response of the classical delay based PLL.
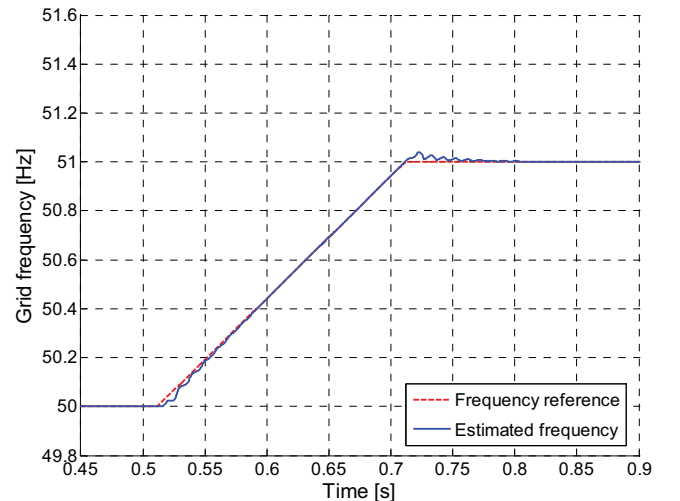
Fig. 10. Frequency sweep response of the improved delay based PLL.

The behavior of the classical delay and improved delay methods under a sudden phase jump of 45 degrees is presented in Fig. 11. A non significant difference between the responses of the two methods can be observed.
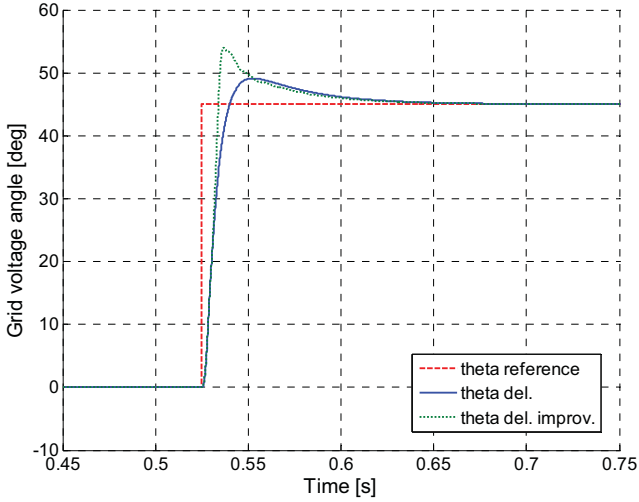
Fig. 11. Operation of the delay based PLL under a 45° phase angle jump.

Fig. 12 and Fig. 13 illustrate the behavior of the improved delay based PLL (without and with LPF on v_q) under a frequency step from 50 to 51 Hz. An abnormal high harmonic content of the input voltage signal (THD=12%) was also considered in these measurements.
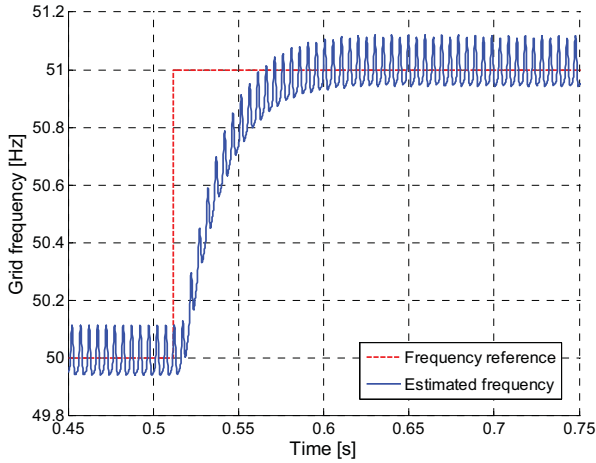
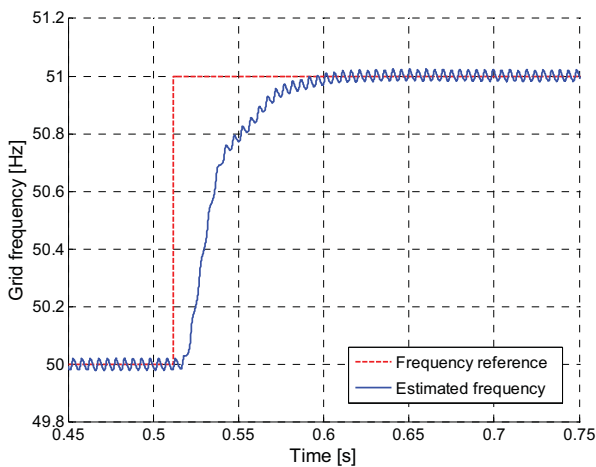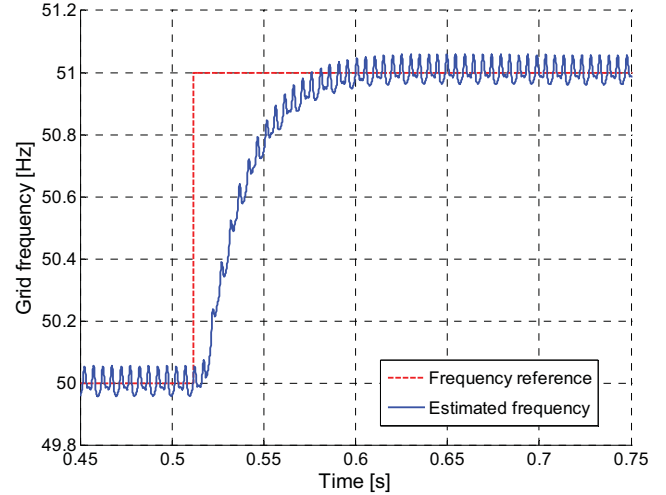Fig. 12. Estimated frequency by the delay based PLL without LPF.

Fig. 13. Estimated frequency by the delay based PLL with LPF.

The estimated grid frequency provided by the PLL structure was filtered in the both cases, using another first-order LPF with a cut-off frequency equal to 6 Hz.

A clean estimated grid frequency is obtained when a LPF is used on v_q, as shown in Fig. 13. The cut-off frequency of the LPF was set to 70 Hz. The ripple in the phase angle of the improved delay based PLL is decreased and the response time is preserved, as presented in Fig. 14.
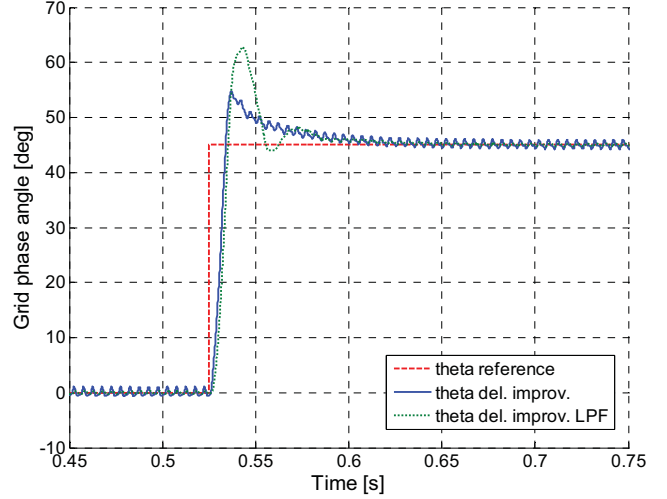
Fig. 14. Operation of the improved delay based PLL under a 45° phase angle jump, with and without a LPF.

B. Park transformation method

Fig. 15 and Fig. 16 illustrate the behavior of the inverse Park based PLL (without and with a new Park transformation as presented in § III.B) under a frequency step from 50 to 51 Hz. An abnormal high harmonic content of the input voltage signal (THD=12%) was also considered in these measurements.

Fig. 15. Estimated frequency by the inverse Park based PLL.

The estimated grid frequency provided by the inverse Park based PLL was filtered in the both cases, using a first-order LPF with a cut-off frequency equal to 6 Hz.
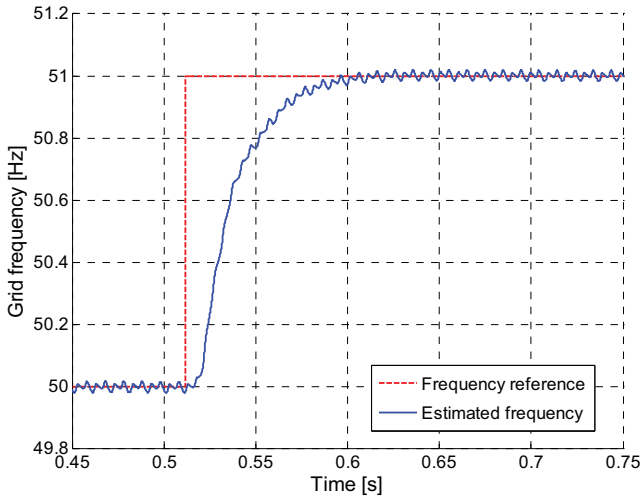
Fig. 16. Estimated frequency by the improved inverse Park based PLL.
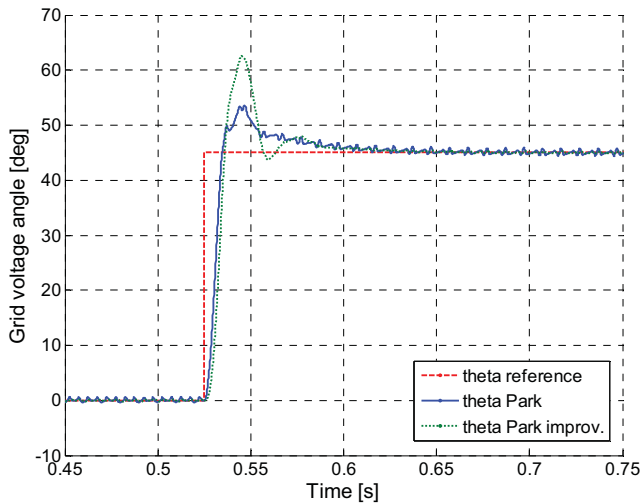
Fig. 17. Operation of the inverse Park based PLL under a 45° phase angle jump.

The behavior of the inverse Park based PLL (without and with a new Park transformation) under a sudden phase jump of 45 degrees is presented in Fig. 17. The ripple in the phase angle of the improved inverse Park based PLL is decreased and the response time is preserved.

V. CONCLUSION

In this paper two improved PLL methods for single-phase systems have been presented. The investigated PLL methods are based on transport delay block and inverse Park transformation.

The improvements in the case of using the delay-based PLL are: non frequency dependent and better filtering of the harmonics.

For the inverse Park transformation based PLL the improvement consists of better filtering of the orthogonal voltage system.

Experimental results validate the effectiveness of the proposed methods.

REFERENCES

[1] S.K. Chung, "*Phase-Locked Loop for Grid-Connected Three-Phase power conversion systems*", IEE Proc. – Electr. Power Appl., Vol. 147, No. 3, 2000, pp. 213-219.
[2] G. Hsieh, and J.C. Hung, "Phase-locked loop techniques – a survey," *IEEE Trans. on Industrial Electronics*, 1996, vol. 43, no. 6, pp. 609-615.
[3] S.M. Silva, B.M. Lopes, B.C. Filho, R.P. Campana and W.C. Boaventura, "*Performance evaluation of PLL algorithms for single-phase grid-connected systems*", Proc.of IAS'04, vol. 4, pp. 2259 - 2263.
[4] S.M. Silva, M. Sidelmo, L.N. Arruda and B.C. Filho, "*Wide Bandwidth Single and Three-Phase PLL Structures for Utility Connected Systems*", Proc. of EPE'01, pp. 1660-1663.
[5] M. Saitou, N. Matsui and T. Shimizu, "*A Control Strategy of Single-phase Active Filter using a Novel d-q Transformation*", proc. of IAS'03, vol. 2, pp.1222-1227.
[6] L.N. Arruda, S.M. Silva and B.C. Filho, "*PLL Structures for Utility Connected Systems*", Proc. of IAS'04, vol. 4, pp. 2655–2660.
[7] M. Ciobotaru, R. Teodorescu and F. Blaabjerg, "*Control of Single-Stage Single-Phase PV Inverter*", Proc. of EPE'05, ISBN: 90-75815-08-5.

[III]   Adaptive resonant controller for grid-connected converters in distributed power generation systems

by A. V. Timbus, M. Ciobotaru, R. Teodorescu, and F. Blaabjerg,
Article published in Proceedings of APEC, 2006, pp. 1601-1606.

Adaptive Resonant Controller for Grid-Connected Converters in Distributed Power Generation Systems

Adrian V. Timbus, Mihai Ciobotaru, Remus Teodorescu and Frede Blaabjerg

Aalborg University, Institute of Energy Technology

DK-9220 Aalborg East, Denmark

avt@iet.aau.dk, mpc@iet.aau.dk, ret@iet.aau.dk, fbl@iet.aau.dk

Abstract—Due to its superior performance when regulating sinusoidal waveforms and the possibility to compensate for low order harmonics by means of Harmonic Compensator (HC), Proportional Resonant (PR) controller is a real alternative to the conventional Proportional Integral (PI) controller, when implemented in a grid connected system like Distributed Power Generation Systems (DPGS).

Anyway, both PR and HC necessitate the resonant frequency value inside their internal model. Normally, the nominal value of the grid frequency and its multiples are used, but in the case when the grid frequency experiences fluctuations, the performance of both PR and HC is diminished.

This paper discuss the possibility of improving the behavior of resonant controller and harmonic compensator in the case of grid frequency variations. The proposed solution makes use of the frequency information provided by the Phase-Locked Loop (PLL) system already used in most of DPGS today. Experimental results are presented in order to validate the proposed solution and it shows to work very well.

Index Terms—Inverter control, adaptive resonant controller, PLL, power generation systems, grid codes

I. INTRODUCTION

WORLD WIDE energy consumption is predicted to increase considerably due to more and more appliances that are using electricity. Among the energy sources, wind and solar energy are receiving higher interest due to their potential. Nowadays, wind turbine (WT) systems are widely used in countries with high wind potential like Germany, Denmark, Spain, etc. Moreover, development of large projects are ongoing for India, China and other countries. The installation of photovoltaic (PV) systems registers also an exponential increase, with Germany and Japan leading the list of the countries having the largest capacity installed.

Unconditional availability of the power source and the environmental friendliness of these systems are their major advantages over the traditional energy sources such as oil and natural gas, but their efficiency and controllability stand as the major drawbacks. In addition to this, the Transmission System Operators (TSOs) are imposing tough standards [1]–[4] when both WT and PV systems are interconnecting the utility network. Among many other demands, power system stability and power quality are primary requests but lately, ride-through capabilities for short grid disturbances, in the case of WT systems should also be provided. As a consequence, large research efforts are put into the control of these systems in order to improve their behavior.

Except a few wind turbine topologies, almost all WT and PV systems are interfacing the utility grid through a PWM driven Voltage Source Inverter (VSI) [5]. In this situation, the control strategy of the inverter deals with the grid integration of the distributed system. Due to the similarities in hardware, initially the control strategies applied to drives applications were also ported to DPGS. Anyway, due to more restrictive standard demands for power quality, other control strategies and controller types [6]–[9] have also been investigated. One of the most common control structures applied to DPGS is based on Voltage Oriented Control (VOC) employing a controller for the dc-link voltage and a controller to regulate the injected current into the utility network [10].

Recently, Proportional Resonant (PR) controller attracted an increased interest due to its superior behavior over the traditional PI controllers, when regulating sinusoidal signals. Removal of the steady state error in single phase systems, no need for coupling or voltage feedforward and easy tuning stand as its main advantages. As already highlighted, the resonant frequency information is necessary in their internal model. This issue may be regarded as a drawback when implemented in a grid tied system, due to frequency variations of the utility network.

This paper, discusses the improvement of the PR

controller used in a VOC control structure for current regulation, in the case of grid frequency variations. Since the grid frequency may experience fluctuations, it is reasonable to use its value as input in the PR controller. This paper proposes to use the frequency estimation provided by a Phase-Looked Loop (PLL) algorithm [11] in order to obtain adaptiveness of the controller in respect to grid frequency.

A description and main characteristics of the PR controller is firstly given. This is followed by the standard demands in respect to frequency boundaries for both PV and WT systems. Further on, the control strategy and the proposed solution are described. Considerations about how the PLL system should be designed are also given. Finally, experimental results validate the effectiveness of the proposed solution.

II. Resonant controller in DPGS

The resonant controller structure arises due to the known drawbacks of PI controllers such as the difficulty in removing the steady-state error in stationary reference frame for single-phase systems, the need of decoupling and voltage feed-forward in three-phase systems and, in general the limitations in compensating for the low order harmonics for complying with the power quality standards [9], [12]–[15].

The typical resonant current controller is defined as [13]:

$$G_c(s) = K_p + K_i \frac{s}{s^2 + \omega^2} \quad (1)$$

where: K_p – proportional gain, K_i – integral gain, ω – the resonance frequency.

The Bode-plots of the resonant controller for different integral gains K_i and ω set to 50 Hz are shown in Fig. 1(a). As it can be seen, this type of controller can achieve very high gain in a narrow frequency band centered around the resonance frequency. The width of this frequency band depends on the integral time constant K_i. A low K_i leads to a very narrow band while a high K_i leads to a wider band. Anyway, if the grid frequency changes to 55 Hz, (like the arrow shows in Fig. 1(b)), the controller performance will not be high and it will not be able to regulate the current at this frequency as it behaves only as a proportional gain.

Selective harmonic compensation can also be included in the structure by cascading several generalized integrators tuned to resonate at the desired frequency. In [9] the transfer function of a typical harmonic compensator designed to compensate for the 3rd, 5th and 7th harmonics, as they are the most prominent harmonics in the current spectrum, is given as:

$$G_h(s) = \sum_{h=3,5,7} K_{ih} \frac{s}{s^2 + (\omega \cdot h)^2} \quad (2)$$

where h is the harmonic order.
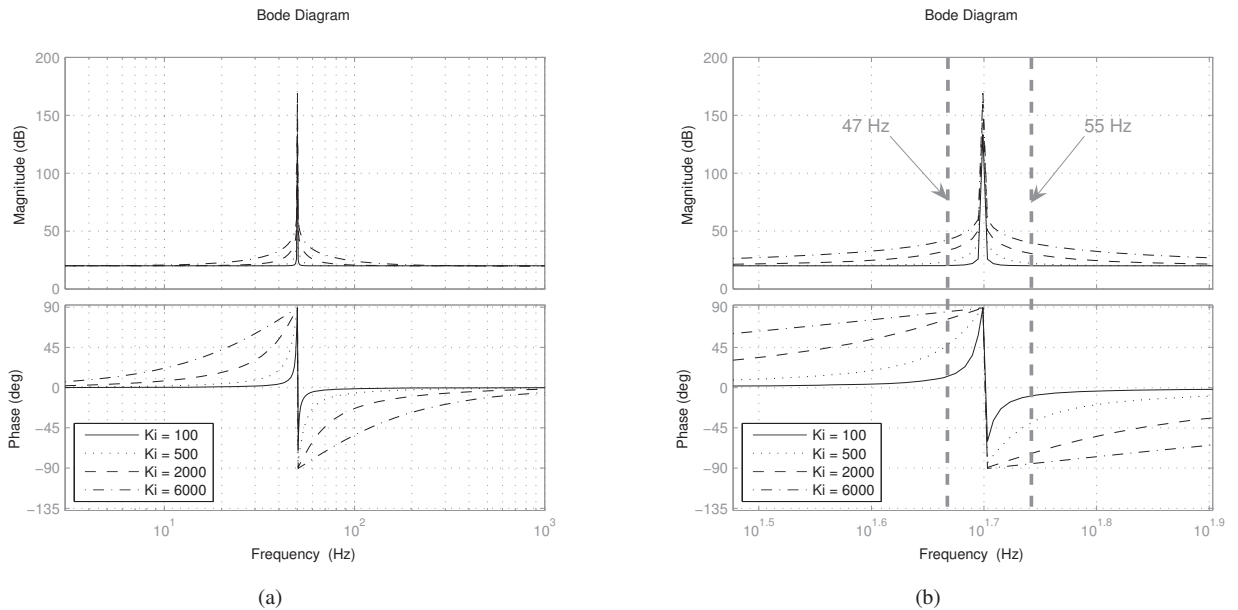
Fig. 1. Bode-plot of resonant controller tuned for 50 Hz (a) having different integral gains and (b) zoom in around 50 Hz frequency.

As a consequence, also compensation for the lower harmonics can be achieved and their content in the power system can be minimized.

Anyway, it is important to notice that both the resonant controller and the harmonic compensator are frequency dependent. This may be a problem as the standards for DPGS demand to overcome grid frequency variation. Even though almost all power systems are well regulated in respect to both voltage and frequency, deviations from the normal values may happen. As a consequence, if the resonant controller is tuned for 50 Hz and grid frequency varies, problems in current regulation will occur. Therefore, the necessity of automatic adaptation of the resonant frequency for both the controller and the harmonic compensator arises.

III. Grid demands for DPGS

The demands for interconnecting distributed generation systems are different in the case of photovoltaic systems and wind turbine systems. Normally the demands for WT systems are more severe compared to those applying to PV systems. For example, both voltage and frequency ranges of operation are much larger in the case of wind turbines, thus such systems should have a control strategy that allows them to ride-through when larger grid variations occur.

A. Photovoltaic system demands

As stated in [1], [2], [16], the frequency variations that a PV system should ride-through are as large as $\pm$ 1Hz in Europe [2], $\pm$ 0.5 Hz in North America [1] and $\pm$ 0.2 Hz in Germany, Austria and Switzerland [16].

Looking closer at Fig. 1(b), it can be noticed that on small frequency variations, the resonant controller is expected to work properly due to the high enough integral gain on this frequency interval.

In order to see if the PR controller can handle such small frequency oscillations without grid frequency information, experimental results are presented further in § V.

B. Wind turbine system demands

When interfacing the utility network, the wind turbine systems have to fulfill the imposed demands by the Transmission System Operators (TSOs). These demands are given in the so called *grid codes* and they are country or TSO specific. The grid codes are referring to different issues, such as voltage and frequency limits, active and reactive power generation/consumption, etc.

Most interesting for this work is the frequency boundaries under which the wind turbine systems have to run.

Frequency range	Clearing time
< 47.0 Hz	0.3 s
47 – 47.5 Hz	10 s
47.5 – 48.0 Hz	5 min
48 – 49.0 Hz	25 min
49 – 50.2 Hz	continuous
50.2 – 53.0 Hz	1 min
> 53.0 Hz	0.3 s

According to the grid codes in Denmark [3], the working range for the wind turbine systems is from 47 Hz up to 53 Hz. Corresponding codes can also be seen for other countries [17]. There are different clearing times of the turbines depending on the frequency value, as it is stated in Table I. According to [17], the largest frequency interval on which a WT system should run is the one specified by the Swedish grid operator, SVK. In this case, the lower limit is 47 Hz but the upper limit goes up to 55 Hz.

IV. Proposed method

The proposed method makes use of the frequency estimation provided by a Phase Locked Loop (PLL) algorithm already existent in almost all DPGS and inputs this into the resonant controller. In this way, if the grid frequency varies from the its nominal value, the PLL will sense that. Moreover, this information will be transmitted to the current controller, which will adapt its resonant frequency to the new value.

A. Control strategy and experimental setup

Fig. 2 shows the proposed control strategy including the hardware setup. The system comprises the PWM inverter supplied by a DC power source which ensures
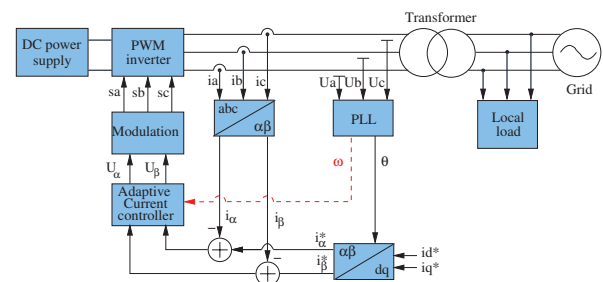

Fig. 2.   Proposed control system including the hardware.

K_p	K_i	K_{i3}	K_{i5}	K_{i7}
40	6000	6000	6000	6000

The parameters for the controller are stated in Table II, where K_i is the integral gain of the fundamental, K_{i3} is the integral gain for the 3rd harmonic, K_{i5} for the 5th and K_{i7} for the 7th harmonic.

B. PLL system

The PLL system implemented in synchronous reference frame [11] is employed to keep synchronization with the grid voltage. This type of PLL is able additionally to provide the grid frequency information. This information is used as input into the resonant controller in order to have an adaptive tuning in respect to the grid frequency.

the dc-link voltage necessary for the application. The connection to the grid is made through an isolation transformer. The three phase voltages are sampled and used by the synchronization algorithm which provides the grid voltage vector angle. Using this angle, the reference currents in the stationary reference frame are constructed using a $dq \rightarrow \alpha\beta$ transformation module. In this way, the control of active and reactive current reference is ensured. The sampled phase currents are also transformed into $\alpha\beta$ reference frame and subtracted from their reference. The resonant current controller implemented in stationary reference frame controls the input error to zero and sets the reference voltage for the modulator.

The PLL controller plays an important role in this situation. Firstly, the controller should be designed to respond with minimum of overshoot to the grid frequency variations, otherwise a value that generates tripping may be detected. In [11], a design method using a compensator to damp the overshoot of the controller is described. However the grid frequency will never experience a step change, but a ramp characteristic instead. According to most of the grid codes, this frequency variation has a
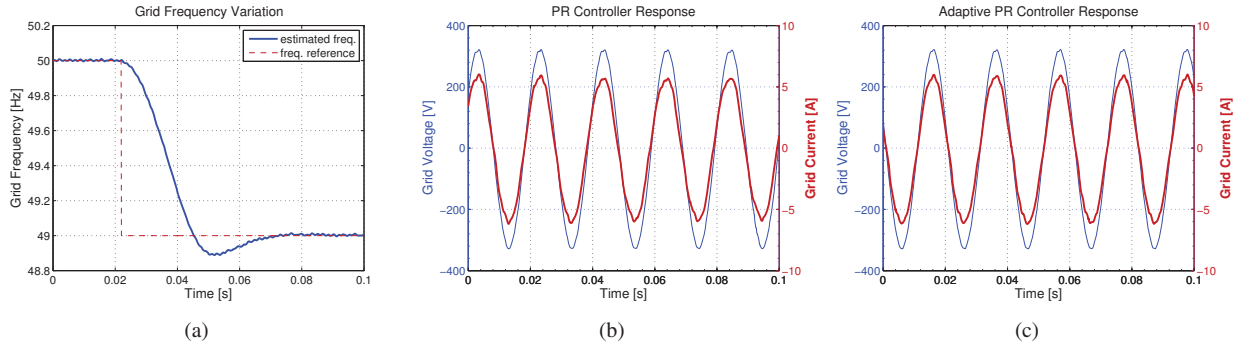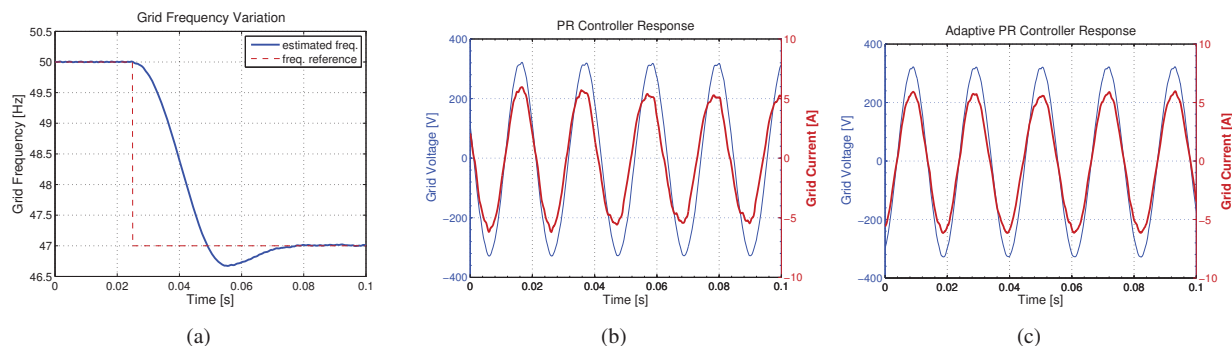

Fig. 3. Experimental results for a frequency step: (a) frequency step from 50 Hz down to 49 Hz, (b) resonant controller results (grid voltage and current (ticker)) and (c) adaptive resonant controller results (grid voltage and current (ticker)).
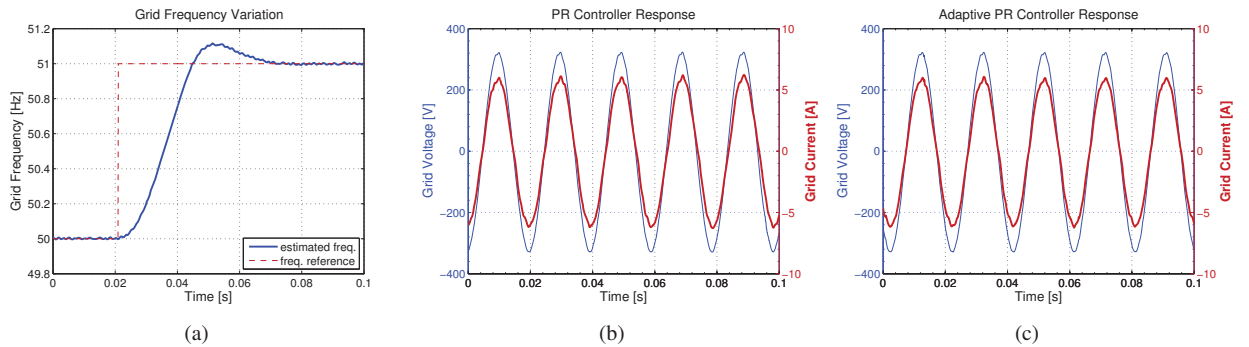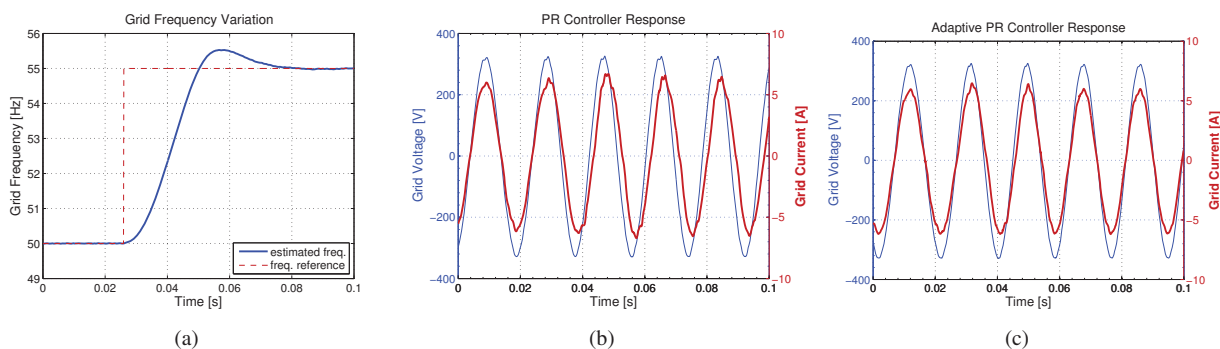

Fig. 4. Experimental results for a frequency step: (a) frequency step from 50 Hz up to 51 Hz, (b) resonant controller results (grid voltage and current (ticker)) and (c) adaptive resonant controller results (grid voltage and current (ticker)).

1604

slope of 1 Hz/s, thus the overshoot may not be a practical problem. Secondly, the locking time of the PLL should be fast enough, to provide the frequency information in time so that the system can cease energizing the network as the clearing times request. In addition, in the case of a fast PLL controller, filtering of the frequency signal may be necessary in order to have a steady value. Again, the time constant of the filter should be carefully chosen not to delay too much the actual grid frequency value.

V. EXPERIMENTAL RESULTS

A test system represented by the schematic in Fig. 2 is built to test the proposed structure. The frequency variations for both PV and WT systems are created using a grid simulator. In the case of PV systems, ± 1 Hz variations is used while in the case of WT a step from 50 Hz down to 47 Hz and from 50 Hz up to 55 Hz is created as these values are the highest stated in the grid codes [17]. Even though the situation of step change is not likely to happen in the grid, from the control point of view, it is the worst case for the PR controller, hence

this is considered here.

A. Results in the case of PV systems

The results in the case of ± 1 Hz frequency variation are presented in Fig. 3 and Fig. 4. In Fig. 3(a), the grid frequency experiences -1 Hz deviation from the nominal value of 50 Hz. The dotted curve depicts the command send to the grid simulator which is used to create the frequency variation. The continuous line represents the frequency estimation of the PLL system which is further used by the resonant controller in order to obtain adaptiveness to the grid frequency. As it might be noticed in Fig. 3(b) and Fig. 4(b), there is a very small phase leading/lagging in the two situations when the frequency decreases/increases one Hz. Moreover, there is almost no steady state error in the regulated current in the two cases, being nearly similar with the plots in Fig. 3(c) and Fig. 4(c) where the frequency information is used to make the PR adaptive. This makes the adaptiveness of the PR controller an optional feature in case of PV systems.

Fig. 5. Experimental results for a frequency step: (a) frequency step from 50 Hz down to 47 Hz, (b) resonant controller results (grid voltage and current (ticker)) and (c) adaptive resonant controller results (grid voltage and current (ticker)).

Fig. 6. Experimental results for a frequency step: (a) frequency step from 50 Hz up to 55 Hz, (b) resonant controller results (grid voltage and current (ticker)) and (c) adaptive resonant controller results (grid voltage and current (ticker)).

B. Results in the case of WT systems

Fig. 5(a) shows a frequency step from the normal grid value of 50 Hz down to 47 Hz. Again, the dotted line represents the command for the grid simulator, while the normal line is the PLL output which is actually used by the resonant controller. As it can be seen in Fig. 5(b), without grid frequency information, the resonant controller encounters problems in the current regulation. A steady state error is noticed when the frequency changes (the amplitude of the current drops) and the power factor is not unity anymore. Anyway, when the information about the grid frequency is provided, the proposed controller has no problem to regulate the current and maintain unity power factor of the distributed generation system, as reported in Fig. 5(c). A similar situation is noticed for a frequency step from 50 Hz up to 55 Hz, as shown in Fig. 6.

As a consequence, the adaptiveness of the PR controller is a must when it is used in WT applications.

VI. CONCLUSION

The paper treats the issue of Proportional Resonant (PR) controller used for current regulation in grid tied systems and the utility frequency experiences deviation from its nominal value. It has been demonstrated that in the case of grid frequency fluctuations, problems in regulating the grid current and keeping unity power factor occur.

As a solution to this, a proposal consisting in using the grid frequency information provided by the PLL, inside the PR model has been made. In this way, an adaptive tuning of the resonant controller in respect to the grid frequency is obtained. Experimental results showing the controller running over a large band of frequency variations are presented for validating the proposed method.

Due to the small allowed frequency deviation in the case of PV systems, the adaptiveness of PR controller has a minor impact on the current regulation. On the other hand, in the case of WT systems, adaptive resonant controller is a must in order to provide a good quality of the injected current and unity power factor during grid frequency variation.

REFERENCES

[1] IEEE15471, "IEEE standard for interconnecting distributed resources with electric power systems," July 2003.

[2] IEC1727, "Characteristic of the utility interface for photovoltaic (PV) systems," November 2002.

[3] Eltra and Elkraft, "Wind turbines connected to grids with voltage below 100 kV," http://www.eltra.dk, 2004.

[4] E.ON-Netz, "Grid code – high and extra high voltage," E.ON Netz GmbH, Tech. Rep., 2003. [Online]. Available: http://www.eon-netz.com/EONNETZ$_$eng.jsp

[5] F. Blaabjerg, Z. Chen, and S. Kjaer, "Power electronics as efficient interface in dispersed power generation systems," *IEEE Trans. on Power Electronics*, vol. 19, no. 5, pp. 1184–1194, 2004.

[6] J. Liang, T. Green, G. Weiss, and Q.-C. Zhong, "Evaluation of repetitive control for power quality improvement of distributed generation," in *Proc. of PESC'02*, vol. 4, Cairns, Qld., 2002, pp. 1803–1808.

[7] P. Mattavelli and F. Marafao, "Repetitive-base control for selective harmonic compensation in active power filters," *IEEE Trans. on Industrial Electronics*, vol. 51, no. 5, pp. 1018–1024, 2004.

[8] F. Kanellos and N. Hatziargyriou, "A new control scheme for variable speed wind turbines using neural networks," *IEEE Power Engineering Society Winter Meeting*, vol. 1, pp. 360–365, 2002.

[9] R. Teodorescu and F. Blaabjerg, "Proportional-resonant controllers. A new breed of controllers suitable for grid-connected voltage-source converters," in *Proc. of OPTIM'04*, vol. 3, 2004, pp. 9–14.

[10] M. Kazmierkowski, R. Krishnan, and F. Blaabjerg, *Control in Power Electronics – Selected Problems*. Academic Press, 2002.

[11] A. V. Timbus, M. Liserre, R. Teodorescu, and F. Blaabjerg, "Synchronization methods for three phase distributed power generation systems. An overview and evaluation," in *Proc. of PESC'05*, 2005, pp. 2474–2481.

[12] S. Fukuda and T. Yoda, "A novel current-tracking method for active filters based on a sinusoidal internal model," *IEEE Trans. on Industrial Electronics*, vol. 37, no. 3, pp. 888–895, 2001.

[13] X. Yuan, W. Merk, H. Stemmler, and J. Allmeling, "Stationary-frame generalized integrators for current control of active power filters with zero steady-state error for current harmonics of concern under unbalanced and distorted operating conditions," *IEEE Trans. on Industry Applications*, vol. 38, no. 2, pp. 523–532, 2002.

[14] R. Teodorescu, F. Blaabjerg, U. Borup, and M. Liserre, "A new control structure for grid-connected LCL PV inverters with zero steady-state error and selective harmonic compensation," in *Proc. of APEC'04*, vol. 1, 2004, pp. 580–586.

[15] D. Zmood and D. G. Holmes, "Stationary frame current regulation of PWM inverters with zero steady-state error," *IEEE Trans. on Power Electronics*, vol. 18, no. 3, pp. 814–822, 2003.

[16] OVO/ONORM, "Photovoltaic semiconductor converters - Part 1: Utility interactive fail save protective interface for PV-line commutated converters," 1999.

[17] T. Ackermann, *Wind Power in Power Systems*. John Wiley & Sons, Ltd., 2005, iSBN: 0-470-85508-8.

[IV] **A new single-phase PLL structure based on second order generalized integrator**

by M. Ciobotaru, R. Teodorescu, and F. Blaabjerg,
Article published in Proceedings of PESC, 2006, pp. 1511-1516.

A New Single-Phase PLL Structure Based on Second Order Generalized Integrator

Mihai Ciobotaru, Remus Teodorescu and Frede Blaabjerg

Aalborg University
Institute of Energy Technology
Pontoppidanstraede 101, 9220 Aalborg
DENMARK
mpc@iet.aau.dk, *ret@iet.aau.dk*, *fbl@iet.aau.dk*

Abstract – **Phase, amplitude and frequency of the utility voltage are critical information for the operation of the grid-connected inverter systems. In such applications, an accurate and fast detection of the phase angle, amplitude and frequency of the utility voltage is essential to assure the correct generation of the reference signals and to cope with the new upcoming standards. This paper presents a new phase-locked-loop (PLL) method for single-phase systems. The novelty consists in generating the orthogonal voltage system using a structure based on second order generalized integrator (SOGI). The proposed structure has the following advantages: - it has a simple implementation; - the generated orthogonal system is filtered without delay by the same structure due to its resonance at the fundamental frequency, - the proposed structure is not affected by the frequency changes. The solutions for the discrete implementation of the new proposed structure are also presented. Experimental results validate the effectiveness of the proposed method.**

I. INTRODUCTION

Phase, amplitude and frequency of the utility voltage are critical information for the operation of the grid-connected inverter systems. In such applications, an accurate and fast detection of the phase angle, amplitude and frequency of the utility voltage is essential to assure the correct generation of the reference signals and to cope with the new upcoming standards.

Most recently, there has been an increasing interest in Phase-Locked-Loop (PLL) topologies for grid-connected systems. The PLL is a grid voltage phase detection structure. In order to detect this phase an orthogonal voltage system is required. In single-phase systems there is less information than in three-phase systems regarding the grid condition, so more advanced methods should be considered in order to create an orthogonal voltage system [1]-[6].

The main task of a PLL structure is to provide a unitary power factor operation, which involves synchronization of the inverter output current with the grid voltage, and to give a clean sinusoidal current reference. Also using a PLL structure the grid voltage parameters, such as grid voltage amplitude and frequency, can be monitored. The grid voltage monitoring is used to ensure that the performances of a grid-connected system comply with the standard requirements for operation under common utility distortions as line harmonics /notches, voltage sags/swells/loss, frequency variations and phase jumps.

The general structure of a single-phase PLL including the grid voltage monitoring is shown in Fig.1. Usually, the main difference among divers single-phase PLL methods is the orthogonal voltage system generation structure.
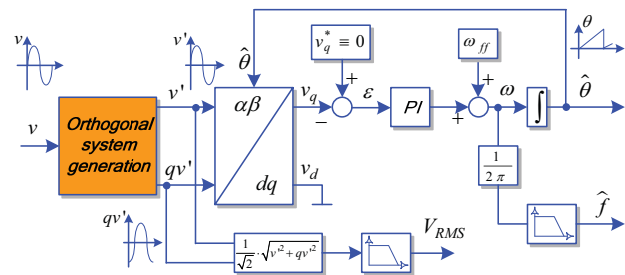
Fig. 1. General structure of a single-phase PLL

An easy way of generating the orthogonal voltage system in a single-phase structure is using a transport delay block, which is responsible for introducing a phase shift of 90 degrees with respect to the fundamental frequency of the input signal (grid voltage). A related method, but more complex of creating a quadrature signal is using the Hilbert transformation [3]. Another different method of generating the orthogonal voltage system is using an inverse Park Transformation as presented in [1], [3], [4] and [5]. All this methods has some shortcomings as follows: frequency dependency, high complexity, nonlinearity, poor or none filtering. Thus, further attention should be paid on single-phase PLL systems.

This paper presents a new method of single-phase PLL structure based on second order Generalized Integrator (GI). The proposed method is a good alternative for creating an orthogonal system in single-phase systems compared to known method [1]-[5]. This method is further presented and experimentally validated.

II. ORTHOGONAL SYSTEM GENERATION

The proposed method of creating an orthogonal system is depicted in Fig. 2. As output signals, two sine waves (v' and qv') with a phase shift of 90° are generated. The component v' has the same phase and magnitude as the fundamental of the input signal (v) [7].
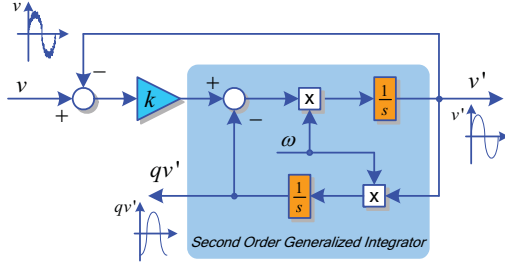

Fig. 2. General structure of a single-phase PLL

The presented structure is based on second order generalised integrator (SOGI), which is defined as [7]-[11]:

$$GI = \frac{\omega s}{s^2 + \omega^2} \qquad (1)$$

- where ω represents the resonance frequency of the SOGI.

The closed-loop transfer functions ($H_d = \dfrac{v'}{v}$ and $H_q = \dfrac{qv'}{v}$) of the structure presented in Fig. 2 are defined as:

$$H_d(s) = \frac{v'}{v}(s) = \frac{k\omega s}{s^2 + k\omega s + \omega^2} \qquad (2)$$

$$H_q(s) = \frac{qv'}{v}(s) = \frac{k\omega^2}{s^2 + k\omega s + \omega^2} \qquad (3)$$

- where k affects the bandwidth of the closed-loop system.

The Bode representation and the step response of the closed-loop transfer function ($H_d = \dfrac{v'}{v}$) for the proposed structure at different values of gain k are shown in Fig. 3(a) and (b).

(a)

(b)
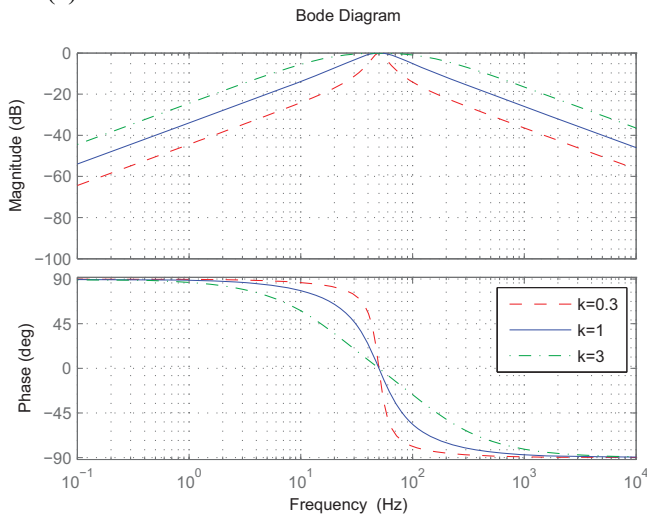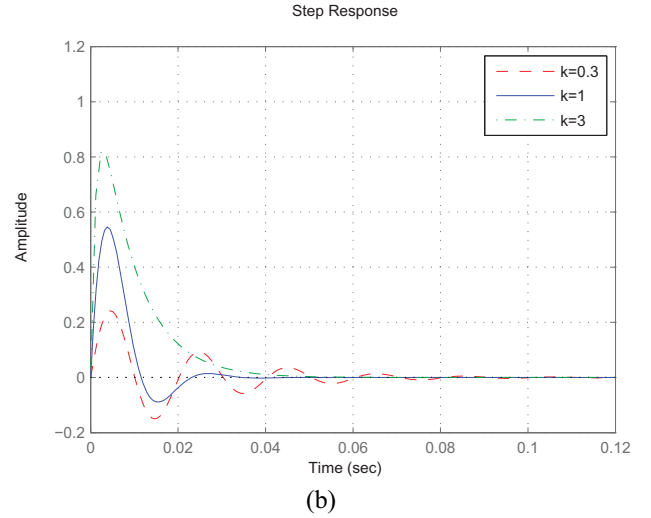
Fig. 3. Bode Plot *(a)* and Step Response *(b)* of the close-loop transfer function (H_d) at different values of gain k

The tuning of the proposed structure is frequency dependent, thus problems can occur when grid frequency has fluctuations. As a consequence, an adaptive tuning of the structure in respect to its resonance frequency is required. Therefore, the resonance frequency value of the SOGI is adjusted by the provided frequency of the PLL structure.

The proposed method for creating the orthogonal system has a main advantage compared to known methods (i.e. Transport-Delay, Hilbert Transformation, and Inverse Park Transformation) [1]-[5]. Only using a simple structure, as it can be seen from Fig. 2, three main tasks are performed: - generating the orthogonal voltage system; - filtering the orthogonal voltage system without delay; - the structure is frequency adaptive.

Using the proposed method the input signal v (grid voltage) is filtered resulting two clean orthogonal voltages waveforms v' and qv', due to the resonance frequency of the SOGI at ω (grid frequency). The level of filtering can be set from gain k as follows: - if k decreases the bandpass of the filter becomes narrower resulting a heavy filtering, but in the same time the dynamic response of the system will become slower as it can be observed from Fig. 3(b). As it can be seen from Fig. 3(a), at resonance frequency there is no attenuation compared to a quite large attenuation outside this frequency.

An example about how it works this method is presented in Fig. 4. The effect of the filter is depicted with a distorted grid voltage waveform (Vg) containing notches. The created orthogonal system is represented of v' and qv'. For this experimental result the gain k was equal to 0.8.
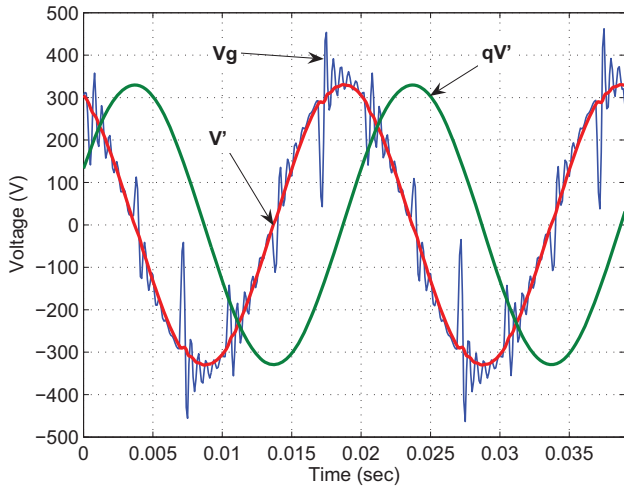
Fig. 4. Distorted grid voltage Vg and generated orthogonal voltage system (V' and its quadrature qV')

III. DISCRETISATION OF THE SOGI

The discrete implementation of the orthogonal system generation structure based on SOGI is described in the following.

The Euler method is the most used common method in order to obtain a Discrete-Time Integrator. The equations of this method are presented below:

Forward Euler method:

$$y(n) = y(n-1) + T_s u(n-1)$$

For this method, $\frac{1}{s}$ is approximated by:

$$T_s \frac{z^{-1}}{1-z^{-1}} \tag{4}$$

Backward Euler method:

$$y(n) = y(n-1) + T_s u(n)$$

For this method, $\frac{1}{s}$ is approximated by:

$$T_s \frac{1}{1-z^{-1}} \tag{5}$$

The structure presented in Fig. 2 can be easily implemented in a discrete form using the Forward Euler method for the first integrator (its output is v') and the Backward Euler method for the second integrator (its output is qv') in order to avoid an algebraic loop. It is also known that the Discrete-Time Integrator using Euler method does not have an ideal phase of -90 degrees.

The phases for the Forward Euler, Backward Euler and Trapezoidal methods at different frequencies are shown in Fig. 5. The sampling time (T_s) was set to 10^{-4}. It can be noticed that at 50 Hz the Forward and Backward Euler methods do not provide a phase of -90 degrees. Therefore, the two outputs (v' and qv') of the orthogonal system generation structure presented in Fig. 2 will not be exactly in quadrature.
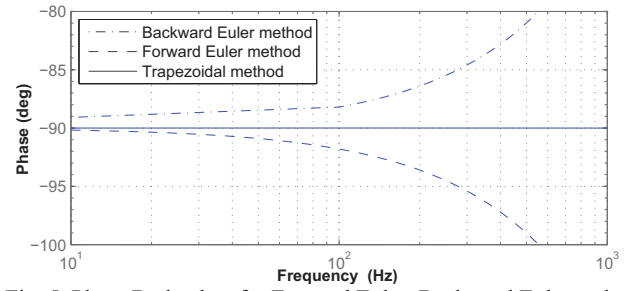
Fig. 5. Phase Bode plots for Forward Euler, Backward Euler and Trapezoidal methods

Due to the fact that qv' is not 90 degrees phase shifted by v', a ripple of 100 Hz will appear in the estimated amplitude and frequency of the input signal as it can be seen form Fig. 6. The input signal was a clean sinusoid with a frequency of 50 Hz and 325 units amplitude.
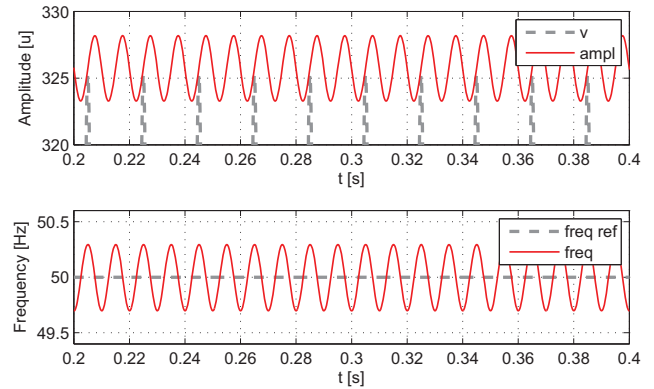
Fig. 6. Estimated amplitude and frequency of the input signal when Euler method is used

However, the solution for this inconvenience is to make use of more advanced numerical methods for the Discrete-Time Integrator. Thus, three different methods are described in the following:

- *Trapezoidal method*;
- *Second order integrator*;
- *Third order integrator*;

A. Trapezoidal method

The equation of the integrator using this method is presented below:

$$y(n) = y(n-1) + \frac{T_s}{2}\left[u(n)+u(n-1)\right]$$

For this method, $\frac{1}{s}$ is approximated by:

$$\frac{T_s}{2}\frac{1+z^{-1}}{1-z^{-1}} \tag{6}$$

As it can be seen from Fig. 5 a phase of -90 degrees can be obtained using Trapezoidal method for the whole spectrum of frequencies. Anyway, the Trapezoidal method can not be applied just replacing $\frac{1}{s}$ from Fig. 2 with (6), because an

algebraic loop will issue. Therefore, the solution is to use the Trapezoidal method for the close-loop transfer function ($H_d = \dfrac{v'}{v}$) presented in (2) in order to avoid any other algebraic loops.

Replacing s by $\dfrac{2}{T_s}\dfrac{z-1}{z+1}$, in (2) will result:

$$H_0(z) = \frac{k\omega\dfrac{2}{T_s}\dfrac{z-1}{z+1}}{\left(\dfrac{2}{T_s}\dfrac{z-1}{z+1}\right)^2 + k\omega\dfrac{2}{T_s}\dfrac{z-1}{z+1}+\omega^2} \qquad (7)$$

Solving further the equation it results:

$$H_0(z) = \frac{(2k\omega T_s)(z^2-1)}{4(z-1)^2 + (2k\omega T_s)(z^2-1)+(\omega T_s)^2(z+1)^2} \qquad (8)$$

Making the following substitutions $\begin{cases} x = 2k\omega T_s \\ y = (\omega T_s)^2 \end{cases}$ and bringing the equation to a canonical form it will result:

$$H_0(z) = \frac{\left(\dfrac{x}{x+y+4}\right)+\left(\dfrac{-x}{x+y+4}\right)z^{-2}}{1-\left(\dfrac{2(4-y)}{x+y+4}\right)z^{-1}-\left(\dfrac{x-y-4}{x+y+4}\right)z^{-2}} \qquad (9)$$

Substituting $\begin{cases} b_0 = \dfrac{x}{x+y+4} \\ b_2 = \dfrac{-x}{x+y+4} = -b_0 \end{cases}$ and $\begin{cases} a_1 = \dfrac{2(4-y)}{x+y+4} \\ a_2 = \dfrac{x-y-4}{x+y+4} \end{cases}$,

a simple discrete form of (2) is obtained:

$$H_d(z) = \frac{b_0 + b_2 z^{-2}}{1-a_1 z^{-1} - a_2 z^{-2}} \qquad (10)$$

Furthermore, (9) can be represented as follows:

$$H_d(z) = b_0 \cdot \frac{1-z^{-2}}{1-a_1 z^{-1} - a_2 z^{-2}} \qquad (11)$$

The implementation of the Trapezoidal method using (11) is depicted in Fig. 7, where $w = 2T_s\omega$.
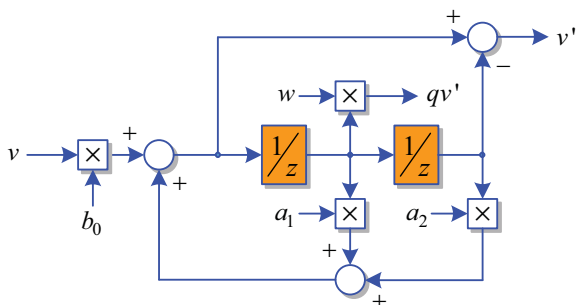
Fig. 7. Trapezoidal method implementation

B. Second order integrator

The equation of the second order integrator is presented below [12]:

$$y(n) = y(n-1) + \frac{T_s}{2}\left[3u(n-1)-u(n-2)\right]$$

For this method, $\dfrac{1}{s}$ is approximated by:

$$\frac{T_s}{2}\frac{3z^{-1}-z^{-2}}{1-z^{-1}} \qquad (12)$$

The implementation of the second order using (12) integrator is presented in Fig. 8.
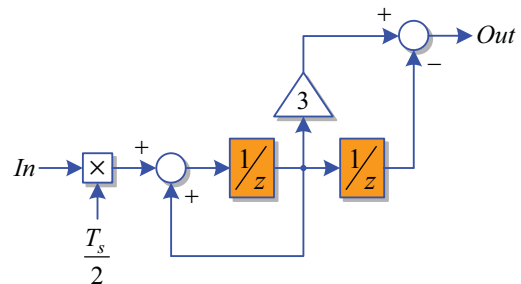
Fig. 8. Second order integrator implementation

C. Third order integrator

The equation of the third order integrator is given in the following [12]:

$$y(n) = y(n-1) + \frac{T_s}{12}\left[23u(n-1)-16u(n-2)+5u(n-3)\right]$$

For this method, $\dfrac{1}{s}$ is approximated by:

$$\frac{T_s}{12}\frac{23z^{-1}-16z^{-2}+5z^{-3}}{1-z^{-1}} \qquad (13)$$

Fig. 9 shows the implementation of the third order integrator.
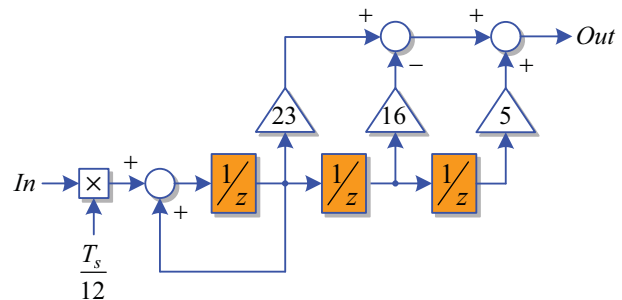
Fig. 9. Third order integrator implementation

In Fig. 10, a comparison between the Trapezoidal Method *(T)*, second order integrator *(2)* and third order integrator *(3)* is made. As it can be noticed, the best results are obtained when the third order integrator is used. Anyway, the all three proposed solutions give very good results compared to the Euler method.
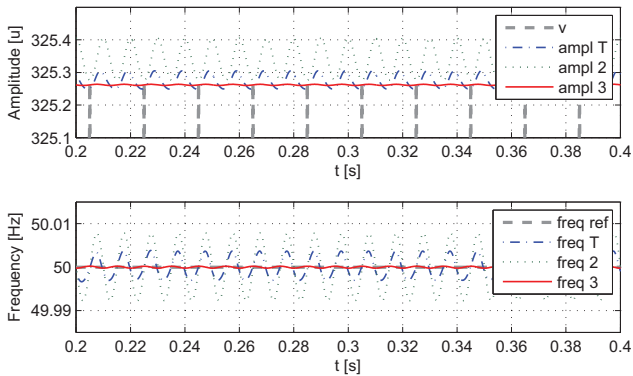
Fig. 10. Estimated amplitude and frequency of the input signal when Second order integrator, Third order integrator and Trapezoidal method are used

IV. EXPERIMENTAL RESULTS

An experimental system using a grid simulator (5kVA AC Power Source – model 5001 ix - California Instruments) has been built in order to test the proposed structure. The control structure was implemented using dSPACE 1103 platform.

The proposed PLL structure based on second order generalized integrator is experimentally validated in the following.
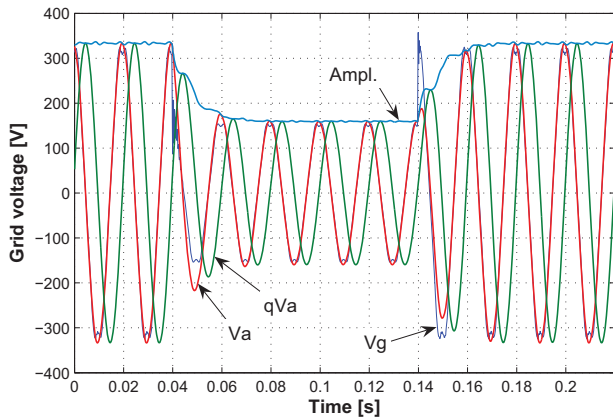
Fig. 11. Grid voltage sag of 50% - 10% THD (k=0.8)
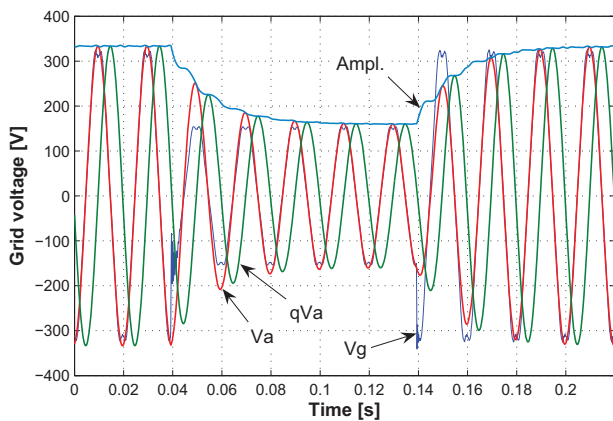
Fig. 12. Grid voltage sag of 50% - 10% THD (k=0.4)
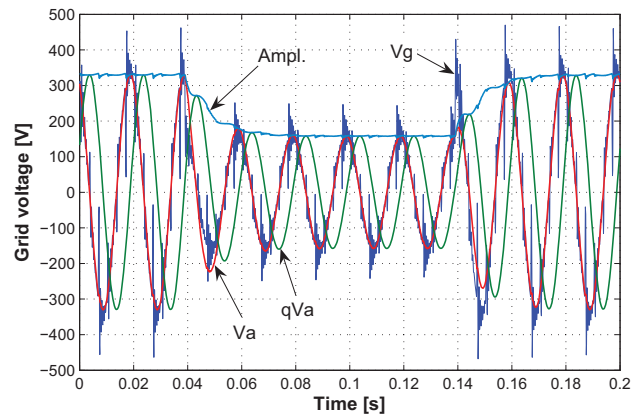
Fig. 13. Grid voltage sag of 50% - Notches (k=0.8)

All the experimental results were obtained using the PLL structure presented in Fig. 1. The block *"Orthogonal system generation"* was replaced with the structure presented in Fig. 2. For all experimental results presented in this paper, the PI controller parameters of the PLL structure were set as follows: - the settling time T_{set}=0.06 s; - dumping factor ξ=1. All the measurements have been done without using additional filters.

Fig. 11, 12 and 13 show the behaviour of the PLL system based on SOGI under grid voltage sag of 50%. The effect of the gain k (Fig. 2) at two different values is depicted in Fig. 11 and 12 for a grid voltage THD of 10%. It can be noticed that a smaller value of the gain gives a better filtering but slows the dynamic of the system. In Fig. 13 the proposed PLL structure is tested under a high content of notches in the grid voltage.

Fig. 14 and 15 show a frequency step and sweep response from 50 up to 51 Hz. It can be observed a fast estimation of the grid frequency. The grid voltage THD was set to 3% for this experiment.

The PLL behaviour under a phase jump of 60 degrees and voltage sag of 25% is presented in Fig. 16. It can be noticed that the PLL system responds according to its settling time (T_{set}=0.06 s).
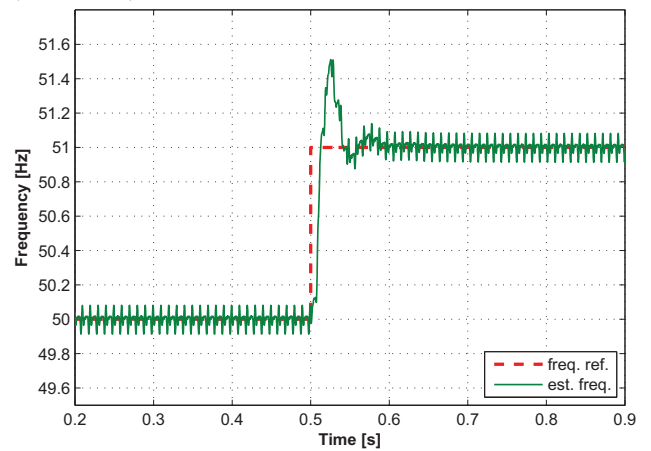
Fig. 14. Grid frequency step from 50 to 51 Hz (k=0.8)
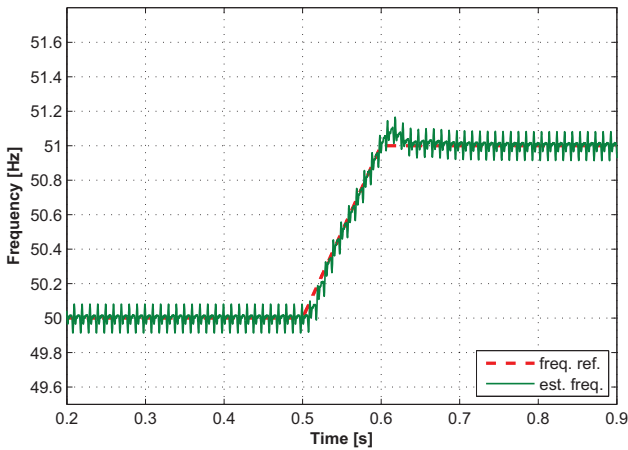
Fig. 15. Grid frequency sweep from 50 to 51 Hz (k=0.8)
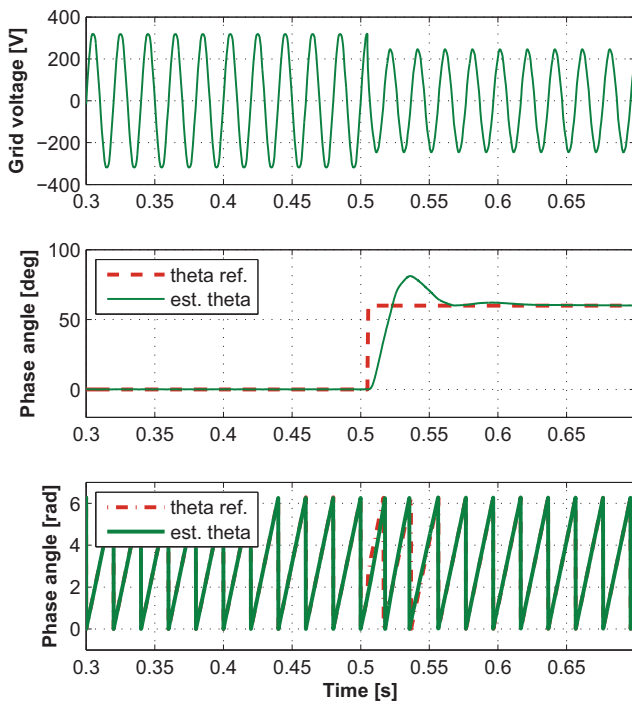

Fig. 16. Phase jump of 60 degrees and voltage sag of 25%

V. CONCLUSIONS

In this paper, a new single-phase PLL structure based on second order generalised integrator is presented. Using the known vectorial approach for the three phase systems, a new algorithm for single-phase systems was derived. The proposed structure has the following advantages: - it has a simple implementation; - the generated orthogonal system is filtered without delay by the same structure due to its resonance at the fundamental frequency, - the proposed structure is not affected by the frequency changes. The solutions for the discrete implementation of the new proposed structure are also presented. The effectiveness of the proposed method has been validated by the experimental results.

VI. REFERENCES

[1] L.N. Arruda, S.M. Silva, B.J.C. Filho, "PLL structures for utility connected systems", *Industry Applications Conference IAS*, 2001, vol. 4, pp. 2655 – 2660.

[2] N. Saitou, M. Matsui, and T. Shimizu, "A Control Strategy of Single-phase Active Filter using a Novel d-q Transformation", *Industry Applications Society IAS*, 2003, pp. 1222-1227.

[3] S.M. Silva, B.M. Lopes, B.J.C. Filho, R.P. Campana, "Performance evaluation of PLL algorithms for single-phase grid-connected systems", *Industry Applications Conference*, 2004, vol.4, pp. 2259 - 2263.

[4] S.M. Silva, L.N. Arruda, and B.J.C. Filho, , "Wide Bandwidth Single and Three-Phase PLL Structures for Utility Connected Systems", *9th. European Conference on Power Electronics and Applications EPE*, 2001, pp. 1660-1663.

[5] M. Ciobotaru, R. Teodorescu , F. Blaabjerg, "Improved PLL structures for single-phase grid inverters", *Proc. of PELINCEC'05*, 6 pages, paper ID 106.

[6] M. Ciobotaru, R. Teodorescu , F. Blaabjerg, "Control of single-stage single-phase PV inverter", *Proc. of EPE'05*, 10 pages, ISBN : 90-75815-08-5.

[7] B. Burger and A. Engler, "Fast signal conditioning in single phase systems" – *Proc. of European Conference on Power Electronics and Applications*, 2001.

[8] X. Yuan, W. Merk, H. Stemmler and J. Allmeling, "Stationary-Frame Generalized Integrators for Current Control of Active Power Filters with Zero Steady-State Error for Current Harmonics of Concern Under Unbalanced and Distorted Operating Conditions" *IEEE Trans. on Ind. App.*, Vol. 38, No. 2, 2002, pp. 523 – 532.

[9] R. Teodorescu, F. Blaabjerg, M. Liserre and U. Borup, "A New Control Structure for Grid-Connected PV Inverters with Zero Steady-State Error and Selective Harmonic Compensation", *Proc. of APEC'04*, Vol. 1, 2004, pp. 580-586.

[10] S. Fukuda and T. Yoda, "A novel current-tracking method for active filters based on a sinusoidal internal mode", *IEEE Trans. on Ind. App.*, Vol.37, No. 3, 2001, pp. 888 – 895.

[11] D. N. Zmood and D. G. Holmes, "Stationary Frame Current Regulation of PWM Inverters with Zero Steady-State Error", *IEEE Trans. on Power Electronics*, Vol. 18, No. 3, May 2003, pp. 814 – 822.

[12] E. Ceangă, C. Nichita, L. Protin and N. A. Cutululis, "*Théorie de la commande des systèmes*", *Editura Tehnică* Bucharest, 2001, ISBN 973- 31-2103-7.

[V]   **PV inverter simulation using MATLAB-Simulink graphical environment and PLECS blockset**

M. Ciobotaru, T. Kerekes, R. Teodorescu, and A. Bouscayrol,
Article published in Proceedings of IECON, 2006, pp. 5313-5318.

PV inverter simulation using MATLAB/Simulink graphical environment and PLECS blockset

M. Ciobotaru[(1)], T. Kerekes[(2)], R. Teodorescu[(3)], *Senior Member*, IEEE and
A. Bouscayrol[(4)], *Member*, IEEE

[(1)(2)(3)] Institute of Energy Technology, Aalborg University
Pontoppidanstraede 101, 9220 Aalborg
DENMARK
[(1)]*mpc@iet.aau.dk*   [(2)]*tak@iet.aau.dk*   [(3)]*ret@iet.aau.dk*

[(4)] University of Lille, L2EP,
L2EP, USTL, 59 655 Villeneuve d'Ascq cedex
FRANCE
[(4)] *Alain.Bouscayrol@univ-lille1.fr*

Abstract – In this paper a photovoltaic (PV) energy conversion system is simulated jointly with its control. The simulation of the system is developed for testing control algorithm before a real-time implementation. The control part is developed using MATLAB/Simulink in order to ensure a direct generation of the real-time code for the dSPACE control board. The simulation of the power system is first realized using MATLAB/Simulink. In a second step, the simulation of the power system is realized using the PLECS toolbox. Both simulation models are tested and selective simulation results are provided for a comparative study.

I. INTRODUCTION

Simulation of modern electrical systems using power electronics has always been a challenge because of the non-linear behavior of power switches, their connection to continuous sub-systems and the design of discrete-time control [1]. Nowadays, more and more complex systems are studied for designing efficient control strategies, such as renewable energy conversion systems [2], whole traction systems [3] and so on. In theses cases efficient simulations before practical control implantation are required.

A lot of simulation software has been developed in the past. Some of them has been dedicated to simulation of detailed behavior of power electronics based on specific circuit library, such as PSCAD (Professional's tool for Power Systems Simulation), CASPOC (Power Electronics and Electrical Drives Modeling and Simulation Software), PSPICE (Design and simulate analog and digital circuits), PSIM (simulation software designed for power electronics, motor control, and dynamic system simulation) and so on. Other software enables an efficient control development based on specific system libraries or toolboxes such as MATLAB/Simulink. Using this kind of software could be valuable for a direct generation of real-time control algorithm such as obtained for dSPACE controller boards.

Thus, using single software requires adaptations to ensure efficient simulations of the whole system taken into account non-linear behavior of power electronics and direct implementation of control laws [4], [5], [6].

This paper investigates the interest of combination of MATLAB/Simulink toolbox and PLECS [7] for simulation control of systems using power electronics. A photovoltaic (PV) energy conversion system is taken as an example.

In section II, both graphical environments are described. Section III is devoted to the simulation of the PV application. Finally, comparisons of the simulation results are presented in section IV.

II. GRAPHICAL ENVIRONMENT

Two kinds of graphical software are considered for studying control of system with power electronics. The first one is more appropriated in describing the power system as it is physically composed. The second one is more appropriated in describing the signal flow of digital control.

Circuit simulation programs are based on libraries of physical components to connect using lines representing physical connections. A system is then built by association of its physical components. The software has to internally solve association problem using several numerical methods. For instance, if two inductors are connected in series, only one state variable is calculated, because both currents are equals. This kind of software is very useful for systems design and analysis.

System simulation programs are based on libraries of functions. The system is described by a combination of basic functions connected using lines representing common variables. Several components can thus be depicted by a global function. For instance, two inductors connected in series can be described by a single transfer function with a single time constant. As a lot of analysis and automatic tools are often provided, such software is very useful for control design.

New possibilities are more and more offered to combine both graphical environments in order to describe the system as it can be viewed and to organize the control as it has to be designed. However, their philosophy is quiet different. Sometimes, there are difficulties to have a uniform simulation, and moreover some mistakes could be done by non-experimented users.

In this paper, the association of the well-known MATLAB/Simulink environment (system simulation program containing powerful libraries and toolboxes for automatic control) and the new PLECS (circuit simulation program including power electronics libraries) is tested. The objective is to develop digital control for power electronics, from the simulation to the practical implementation. Therefore, MATLAB/Simulink environment is well adapted for control development and contains automatic code generator. PLECS toolbox is used to provide a simulation model of the Plant, before the implementation on an actual process.

A. MATLAB/Simulink environment

To effectively design an embedded control system and accurately predict its performance, designers must understand the behavior of the entire system in which the control system will reside. MATLAB and Simulink form the core environment for Model-Based Design for creating accurate, mathematical models of physical system behavior. The graphical, block-diagram paradigm of the MATLAB/Simulink environment lets the user drag-and-drop predefined modeling elements, connect them together, and create models of dynamic systems. These dynamic systems can be continuous-time, multi-rate discrete-time, or any combination of the three.
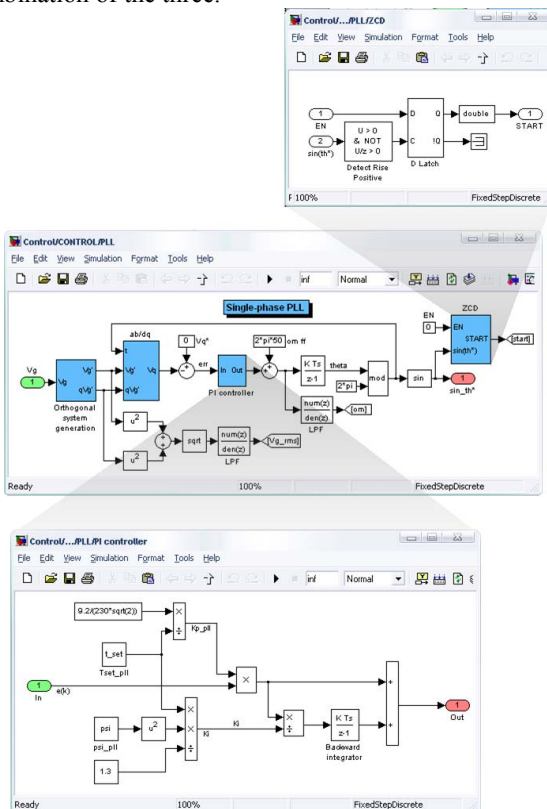
Fig. 1 Hierarchical models of complex control systems using Simulink

The modeling environment is hierarchical and self-documenting as presented in Fig. 1. System structure and function can be expressed by grouping model.

B. PLECS blockset

PLECS is a Simulink toolbox used for simulation of electrical circuits within the Simulink environment. Simulations are fast, due to the fact that components are taken to be ideal.

As shown on Fig. 2, circuits made with PLECS include resistors, inductors, capacitors, switches, and voltage and current sources all taken as ideal components. Voltages and currents can be measured using probes. These measurements can be used as feedback for the control within the Simulink environment or just viewed online using scopes.
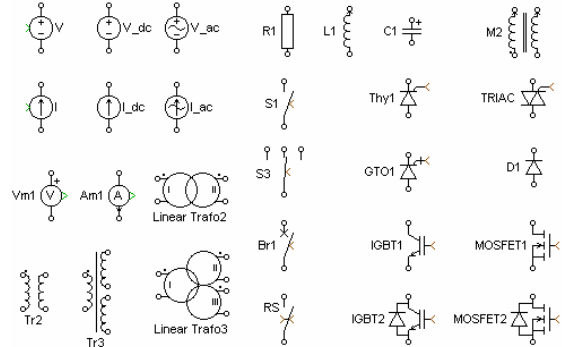
Fig. 2 Some of PLECS components used for circuit simulation

Voltages and currents can only be viewed in graph windows using special probes. Matlab Simulink is very good in post processing of simulation results. Actually most of the simulation tools provide an interface for Simulink.

Using this toolbox it is possible to implement the power converter and other electrical circuits as a PLECS subsystem and the control as standard Simulink subsystem.

C. Final step for a real-time implementation of the control

Using the system model and Real-Time Workshop, real-time code for testing, validation, and embedded implementation on the production target processor can be automatically generated using for example dSPACE hardware [8]. As it is created, the code is automatically optimized for fast execution and efficient use of memory. Automatically generating code from the system model avoids errors due to manual translation of the model into code, and saves time, allowing software developers to focus on more demanding tasks.

A typical example of using the dSPACE system for electrical drives simulations is described in [9] and for wind energy conversion systems (WECS) in [10].

However, before the real-time implementation, the Control part has to be validated by simulation using a plant model. This model could be developed using either the Simulink transfer functions or the PLECS toolbox.

III. SIMULATION OF PV INVERTER

A. Studied system and control

The general structure of a single-stage single-phase grid-connected PV inverter system, depicted in Fig. 3, contains two main parts: - the Plant part (hardware components) such as the PV arrays, PV inverter, filter and the grid utility; – and

the Control part composed by algorithms such as the Maximum-Power-Point-Tracker (MPPT), phase-locked-loop (PLL), dc voltage controller, current controller, etc.
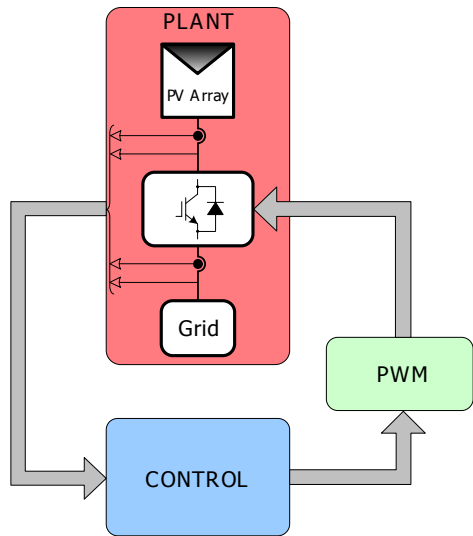

Fig. 3 Power electronic system with the grid, source (PV array), power converter, control and PWM

Using the advantage of the graphical representation of the Simulink environment, a simulation model has been built as presented in Fig. 4. The simulation model is divided in the Control part and the Plant part in such a way that the Control part can be directly implemented in a real-time application using dSPACE for experimental validation. Using the control system model and Real-Time Workshop, real-time code for testing, validation, and embedded implementation on the dSPACE system can be automatically generated (see Fig. 5).
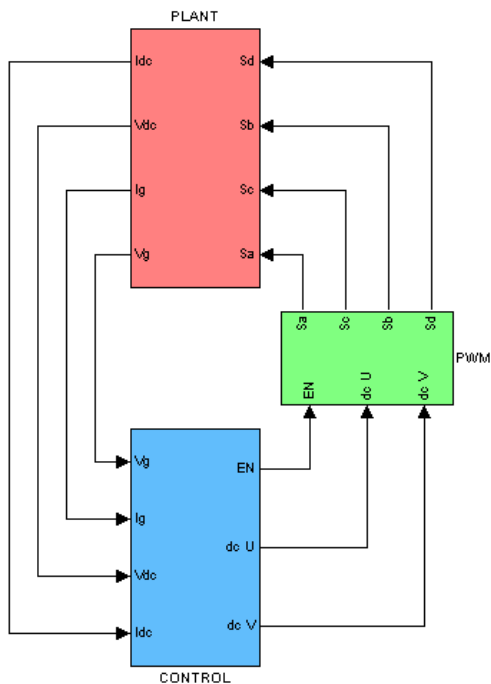
Fig. 4 Simulink model of the PV inverter

Therefore, the Control block in Fig. 4 and Fig. 5 is identical and can be first simulated off-line using a Plant and PWM model as presented in Fig. 4 and then tested on-line by removing the Plant model and adding interfaces towards the real Plant as shown in Fig. 5. This way the control development time can be reduced considerably.
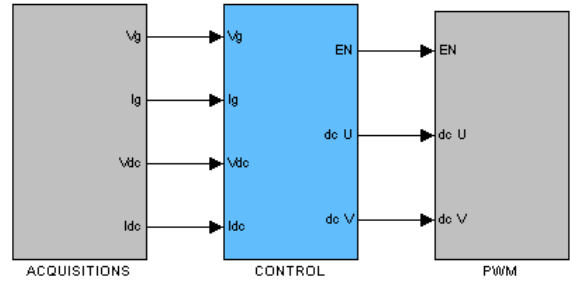
Fig. 5 Control system model for dSPACE implementation

The Control structure of the single-stage single-phase PV inverter system is shown in Fig. 6. The main elements of the Control structure are the synchronization algorithm based on PLL, the MPPT algorithm, the dc voltage controller and the current controller.
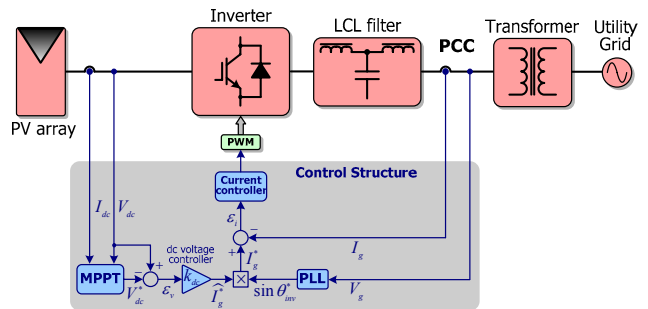
Fig. 6 Control diagram of the PV energy conversion system

The simulation model of the PV inverter Control structure was built based on a graphical intuitive way as it can be seen from Fig. 7.
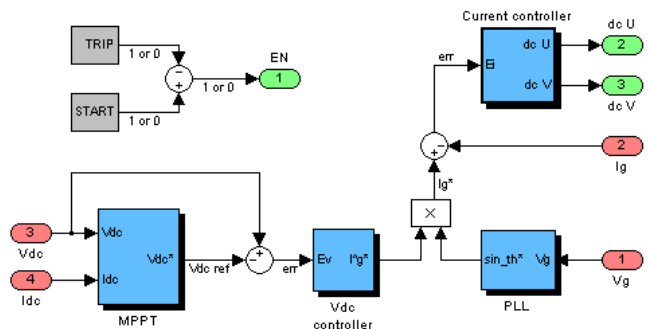
Fig. 7 Simulation model of the PV inverter Control structure

Fig. 8 presents the single-phase PLL structure including grid voltage monitoring [11]. The PLL is used to provide a unit power factor operation which involves synchronization of the inverter output current with the grid voltage and to give a clean sinusoidal current reference.
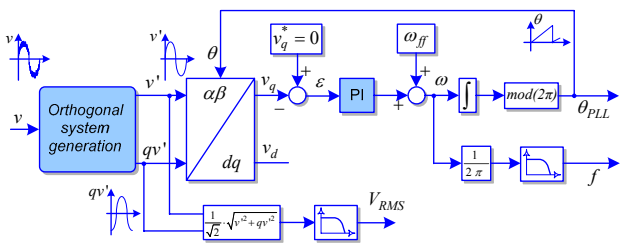
Fig. 8 General form of a single-phase PLL structure including grid voltage monitoring

The equivalent Simulink model for the single-phase PLL structure presented in Fig. 8 is shown in Fig. 9.
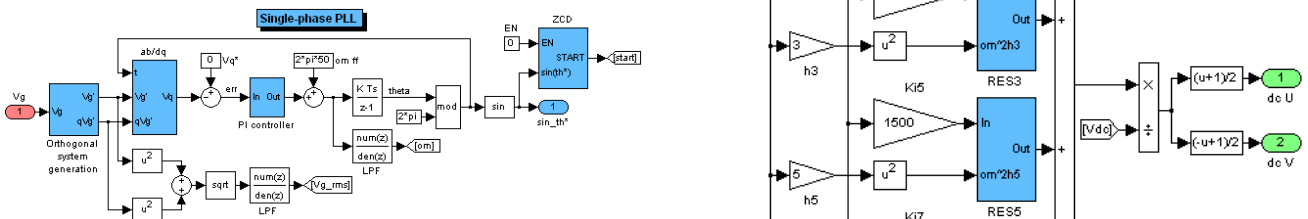

Fig. 9 Simulink model of the single-phase PLL structure

The grid current controller is implemented using the Proportional Resonant (PR) controller which is defined as [12]:

$$G_c(s) = K_p + K_i \frac{s}{s^2 + \omega_o^2} \qquad (1)$$

The PR controller can be associated with a harmonic compensator (HC) $G_h(s)$ which is defined as:

$$G_h(s) = \sum_{h=3,5,7,9} K_{ih} \frac{s}{s^2 + (\omega_o h)^2} \qquad (2)$$

The Simulink model of the grid current controller (PR+HC) is depicted in Fig. 10 where the same block for the double integrator is being reused for different resonance frequencies.

The tuning of the current controller has been done using the Sisotool toolbox provided in MATLAB/Simulink environment. The Root-locus and Bode diagram analysis of the PR+HC controller are presented in Fig. 11. This tool allows determining the gain of the controller manually imposing a certain bandwidth and in the same time the phase margin can be adjusted to ensure stability.

MATLAB/Simulink proves to be a good tool for control design, but modeling switching converters can be a challenge. Therefore, in order to test the performance of a power circuit simulation, the same Plant model has been developed using two different techniques: - one uses the transfer functions approach, and – the other makes use of PLECS toolbox.

B. Simulation of the Plant using MATLAB/Simulink

First the Plant model has been developed using transfer functions approach leading to high complexity and difficulty in monitoring signals at different nodes of the circuit.

The schematic for the power circuit is presented in Fig. 12. The Simulink model, using standard blocks, of the Voltage Source Inverter is shown in Fig. 13.
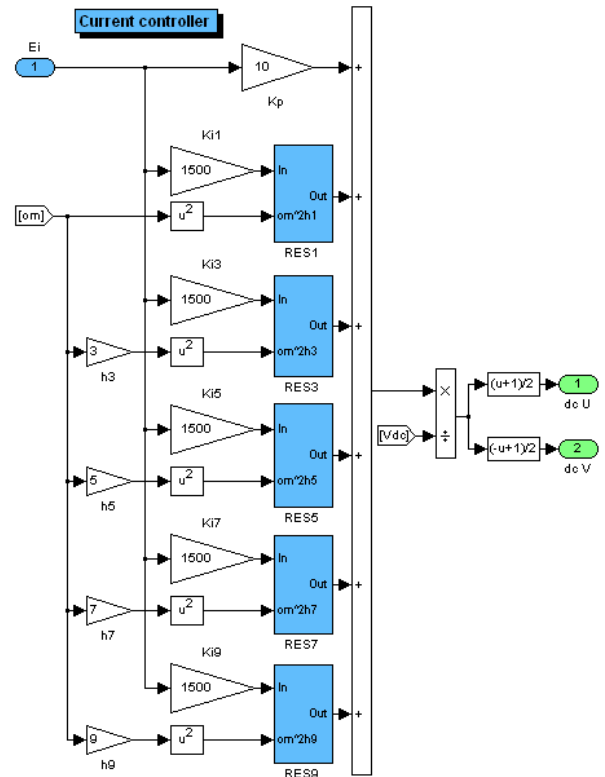

Fig. 10 Simulink model of the grid current controller
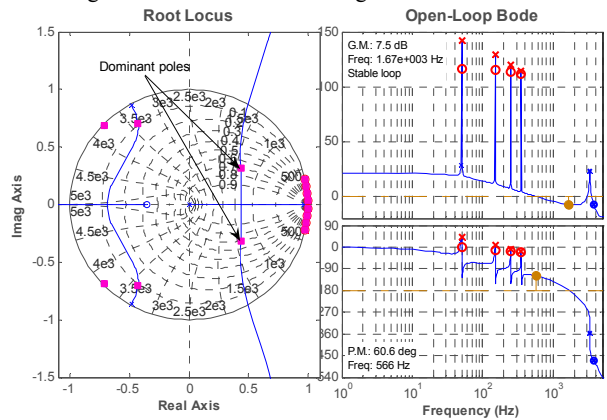

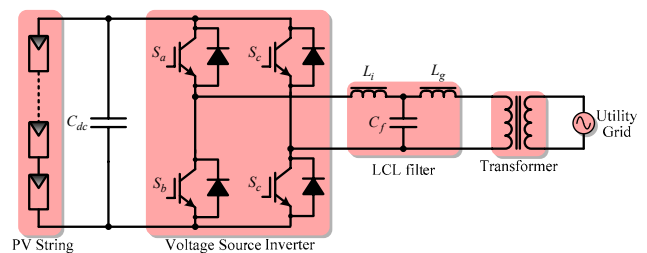Fig. 11 PR current controller – Root-locus and Bode diagram analysis
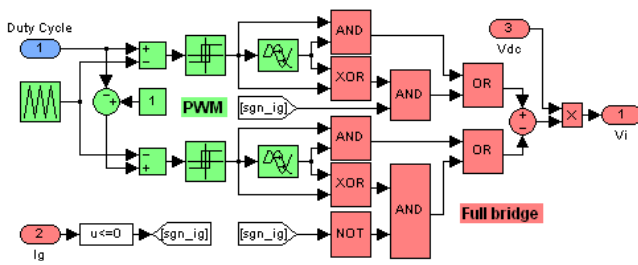

Fig. 12 Power circuit diagram

Fig. 13 Simulink model of the Voltage Source Inverter

Fig. 14 shows the Simulink transfer functions approach of the LCL filter and the grid utility. As it can be noticed, it is difficult to follow the signals at different nodes of the circuit especially if the complexity of the circuit becomes higher.
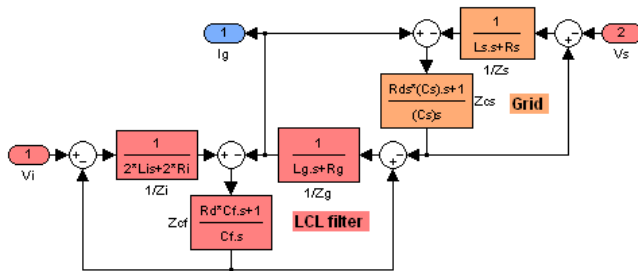

Fig. 14 Simulink transfer functions approach of the LCL filter and the grid utility

C. Simulation of the Plant using PLECS

Developing electrical circuits with PLECS is really easy and straightforward. One has just to drag and drop the components that are needed and connect them in order to make the desired electrical circuit.

The simulation model of the PV system using PLECS is similar to the one presented in Fig. 4, only the Plant subsystem has been changed using PLECS toolbox, the control strategy remaining the same as previously described in Fig. 7.

The Plant subsystem represents the electrical circuits modeled using PLECS. The power circuit includes models for the DC supply, inverter, LCL filter and utility grid. The detailed circuit for the Plant can be seen in Fig. 15. These models are made up of subsystems that are described below.

The DC supply is modeled by a voltage source. The inverter is based on the standard full bridge topology using 4 IGBTs with built-in anti-parallel diodes. These switches are controlled by the gate signals (*Sa-Sb-Sc-Sd*) which are forwarded to the PLECS circuit from the Simulink Control block using special gate signal ports. The electrical ports are used within the subsystem for the input and output of the electrical signals (DC+, DC-, L, N).
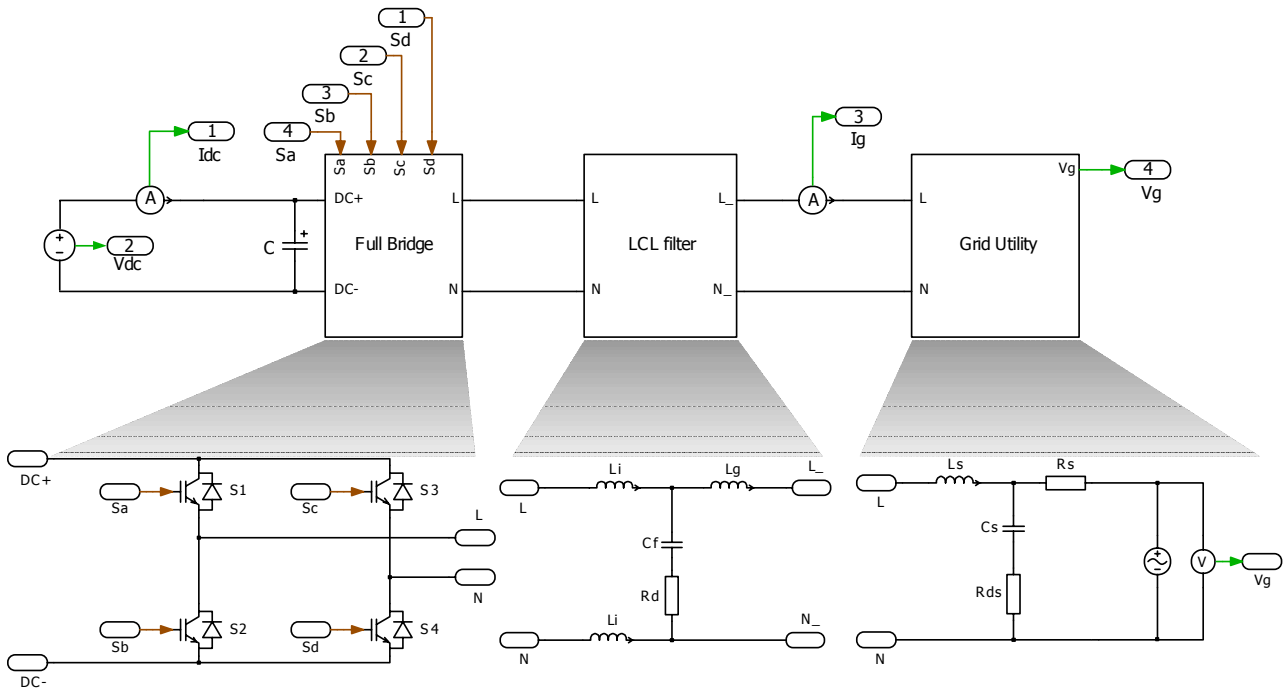

Fig. 15 PLECS circuit of the Full Bridge topology, connected to the Grid through an LCL filter

To filter the high frequency pulses of the inverter, an LCL filter is used. The inductance and capacitance values are set from the mask of the subsystems. For the electrical signals the before mentioned electrical ports are used.

The grid is modeled having inductive, resistive and capacitive components and the parameters are set through the mask of the subsystem.

Furthermore, as seen on Fig. 15, currents and voltages in any part of the circuit can be measured and then viewed on a scope or used as feedback in the control strategy within the Simulink environment.

IV. SIMULATION RESULTS

Fig. 16 shows a comparison between the simulation results obtained using two different techniques for modeling the Plant: – one makes use of PLECS toolbox (the first two subplots) - the other uses the Simulink transfer functions approach (the last two subplots). The simulation results were obtained using the same Control structure and the same parameters for the Plant. As it can be seen, there are almost no differences between the two different Plant implementations. However, the simulation time using PLECS model for the Plant was four times smaller than the simulation time using Simulink transfer functions approach. Thence, a real time of one second has been simulated in 59 seconds using PLECS and about 3 minutes 46 seconds using Simulink transfer functions.
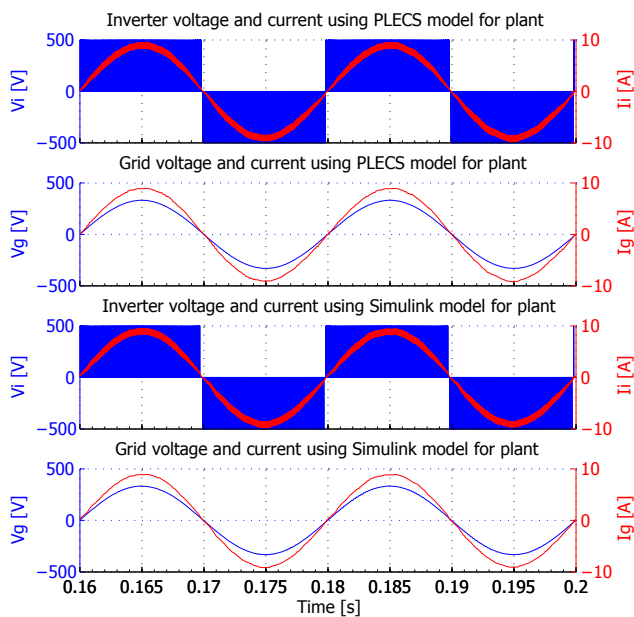
Fig. 16 Simulation results of the PV inverter

IV. CONCLUSION

This paper is focused on the simulation of the control of a power system before its real-time implementation.

First a particular case for simulation of single-phase PV inverter in Simulink is described focusing on the control design. The controller can be then automatically tested on-line using dSPACE system. Secondly PLECS, a new Simulink blockset implemented as a circuit simulator is introduced. The combination of the two tools provides a good environment for the switching power converter simulator.

PLECS is a well suited tool for modeling electrical circuits within MATLAB/Simulink environment. One of the major strength of combining PLECS with Simulink is not only the speed of the simulations, the simplicity of making the circuit, but also the advantage of simulating electrical circuits and controlling them within Control blocks built in standard Simulink environment. However, the combination of circuit software with system software could lead to confusion for novice users. Furthermore, the line connections between elements do not represent the same concept.

V. REFERENCES

[1] M. P. Kazmierkowski, R. Krishnan, F. Blaabjerg, *"Control in power electronics"*, Academic Press, Elesevier Science, 2002.
[2] J. T. Bialasiewicz and E. Muljadi, "Analysis of Renewable-Energy Systems Using RPM-SIM Simulator", *IEEE Trans. on Power Electronics*, vol. 53, no. 4, June 2006, p. 1137 – 1143.
[3] M. Eshani, Y. Gao, S. E. Gay, A. Emadi, "Modern electric, hybrid electric and fuel cell vehicles", *CRC Press, New York*, 2005.
[4] R. Teodorescu, D. P. Zelaya, K. Bresnahan and E. Rosu, "A Simulink Approach to Power Electronics Simulations", *Record of EPE 1995*, vol. 3, p. 954–958.
[5] S. Onoda and A. Emadi, "PSIM-based modeling of automatic power systems: conventional, electric and hybrid electric vehicles", *IEEE Trans. on Vehicular Technology*, vol. 53, no. 2, March 2004, p. 390-400.
[6] B. Kaminski, K. Werrzanowski and W. Koczara, "An application of PSIM simulation software for rapid prototyping of DSP based power electronics control systems", *Record of IEEE PESC 2004*, Germany, p. 336-341.
[7] J. H. Allmeling and W.P.Hammer, "PLECS – Piece-wise Linear Electrical Circuit Simulation for Simulink", *Record of IEEE PEDS 1999*, vol.1, p. 355-360.
[8] R. Otterbach, T. Pohlmann, A. Rukgauer and J. Vater, "DS1103 PPC controller board – rapid prototyping with combined RISC and DSP power for motion control" *Proc. of PCIM 1998*, Nürnberg.
[9] R. Teodorescu, M. Bech, F. Blaabjerg and J. K. Pedersen, "A new approach in teaching power electronics control of electrical drives using real-time systems"; *Record of COMPEL 2000*, p. 221 – 226.
[10] A. Bouscayrol, X. Guillaud and Ph. Delarue, "Hardware-in-the-loop simulation of a wind energy conversion system using energetic macroscopic representation"; *Record of. IEEE IECON 2005*, p. 2517 – 2522.
[11] M. Ciobotaru, R. Teodorescu and F. Blaabjerg, "A new single-phase PLL structure based on second order generalized integrator", *Record of IEEE PESC 2006*, Korea, p. 1511-1516.
[12] R. Teodorescu, F. Blaabjerg, U. Borup and M. Liserre, "A new control structure for grid-connected LCL PV inverters with zero steady-state error and selective harmonic compensation", *Record of IEEE APEC 2004*, United States, vol. 1, p. 580-586.

[VI] Advanced grid synchronization system for power converters under unbalanced and distorted operating conditions

by P. Rodriguez, A. Luna, M. Ciobotaru, R. Teodorescu, and F. Blaabjerg,
Article published in Proceedings of IECON, 2006, pp. 5173-5178.

Advanced Grid Synchronization System for Power Converters under Unbalanced and Distorted Operating Conditions

P. Rodríguez[⋆], A. Luna[⋆], M. Ciobotaru[★], R. Teodorescu[★], and F. Blaabjerg[★]

[⋆]Department of Electrical Engineering
Technical University of Catalonia
Barcelona - SPAIN
prodriguez@ee.upc.edu

[★]Institute of Energy Technology
Aalborg University
Aalborg - DENMARK
ret@iet.aau.dk

Abstract – **This paper proposes a new technique for grid synchronization under unbalanced and distorted conditions, i.e., the Dual Second Order Generalised Integrator – Frequency-Locked Loop (DSOGI-FLL). This grid synchronization system results from the application of the instantaneous symmetrical components method on the stationary and orthogonal $\alpha\beta$ reference frame. The second order generalized integrator concept (SOGI) is exploited to generate in-quadrature signals used on the $\alpha\beta$ reference frame. The frequency-adaptive characteristic is achieved by a simple control loop, without using either phase-angles or trigonometric functions. In this paper, the development of the DSOGI-FLL is plainly exposed and hypothesis and conclusions are verified by simulation and experimental results.**

I. INTRODUCTION

Increasing penetration of distributed power generation systems (DPGS) in recent years have made necessary to think again about the grid connection requirements (GCR). One relevant requisite resulting from the GCR review is that DPGS should ride through any grid disturbances –without tripping– as successfully as the conventional power plants they replace [1]. This requirement entails improving design and control of the power converters used in DPGS to avoid both over-current and over-/under-voltage tripping, even when the grid voltage is deteriorated as a result of transient short-circuits in the grid. Since most of the faults give rise to unbalanced voltages, the fast and accurate detection of the positive- and negative-sequence components of the grid voltage is a crucial issue in the design of control strategies for power converters that allow staying actively connected to the grid and keep generation up according to the GCR [2][3].

The grid frequency can show considerable fluctuations in power systems with large amount of DPGS during transient faults. This implies that the synchronization system should be insensitive to the grid frequency variations. The use of a phase-locked loop (PLL) is a conventional technique to make the synchronization system frequency-adaptive. In three-phase systems, the PLL usually employs a synchronous reference frame (SRF-PLL) [4]. In spite of its good behavior under ideal voltage conditions, the response of the SRF-PLL can become unacceptably deficient when the utility voltage is unbalanced. This drawback can be overcome by using a PLL based on the decoupled double synchronous reference frame (DSRF-PLL) [5], in which a decoupling network permits a proper isolation of the positive- and negative-sequence components. An alternative synchronization technique, based on the single-phase enhanced phase-locked loop (EPLL) and without using synchronous reference frames, is presented in

[6]. The EPLL allows independent frequency-adaptive synchronization with each phase-voltage of the three-phase system. The EPLL provides at its output a set of two orthogonal signals –in-phase/in-quadrature– synchronized with the phase-voltage applied to its input. To calculate the positive-sequence component of the grid voltage, the outputs of the three EPLLs –one per each phase– are processed according to the instantaneous symmetrical components (ISC) method. Eventually, a fourth single-phase EPLL is applied to one of the previously calculated positive-sequence voltages in order to estimate its phase-angle and amplitude. Although the EPLL-based positive-sequence detector constitutes a ingenious solution for grid synchronization in unbalanced three-phase systems, there are some features in this detector which are susceptible to be reviewed.

This work studies the structure of the single-phase EPLL and discusses about a new dual EPLL (DEPLL) for three-phase systems. Analysis of limitations in the DEPLL results in a new frequency-adaptive grid-synchronization system, namely the 'Dual Second Order Generalized Integrator' resting on a 'Frequency-Locked Loop' (DSOGI-FLL). The DSOGI-FLL translates the three-phase voltage from the *abc* to the $\alpha\beta$ reference frames. A DSOGI-based quadrature-signals generator (QSG) is used for filtering and obtaining the 90°-shifted versions from the $\alpha\beta$ voltages. These signals act as the inputs to the positive-/negative-sequence calculator (PSNC) which lies on the ISC method, formulated on the $\alpha\beta$ domain. In order to make the proposed synchronization system frequency-adaptive a very simple FLL is used.

II. POSITIVE- AND NEGATIVE-SEQUENCE CALCULATION ON THE $\alpha\beta$ REFERENCE FRAME

According to that stated by *Lyon* [7], instantaneous positive- and negative-sequence components, $\mathbf{v}_{abc}^{+}$ and $\mathbf{v}_{abc}^{-}$, of a generic voltage vector $\mathbf{v}_{abc} = \begin{bmatrix} v_a & v_b & v_c \end{bmatrix}^T$ are given by:

$$\mathbf{v}_{abc}^{+} = \begin{bmatrix} v_a^{+} & v_b^{+} & v_c^{+} \end{bmatrix}^T = [T_+]\mathbf{v}_{abc}, \qquad (1a)$$

$$\mathbf{v}_{abc}^{-} = \begin{bmatrix} v_a^{-} & v_b^{-} & v_c^{-} \end{bmatrix}^T = [T_-]\mathbf{v}_{abc}, \qquad (1b)$$

where $[T_+]$ and $[T_-]$ are defined as:

$$[T_+] = \frac{1}{3}\begin{bmatrix} 1 & a & a^2 \\ a^2 & 1 & a \\ a & a^2 & 1 \end{bmatrix} \quad ; \quad [T_-] = \frac{1}{3}\begin{bmatrix} 1 & a^2 & a \\ a & 1 & a^2 \\ a^2 & a & 1 \end{bmatrix}, \qquad (2)$$

with $a = e^{j\frac{2\pi}{3}} = -1/2 + e^{j\frac{\pi}{2}}\sqrt{3}/2$.

Regarding exclusively positive- and negative-sequence components, *Clarke* transformation allows voltage vector translation from the *abc* to the $\alpha\beta$ reference frames as follow:

$$\mathbf{v}_{\alpha\beta} = \left[T_{\alpha\beta} \right] \mathbf{v}_{abc} \;\;;\;\; \left[T_{\alpha\beta} \right] = \sqrt{\frac{2}{3}} \begin{bmatrix} 1 & -\frac{1}{2} & -\frac{1}{2} \\ 0 & \frac{\sqrt{3}}{2} & -\frac{\sqrt{3}}{2} \end{bmatrix}. \tag{3}$$

So instantaneous positive- and negative-sequence voltage components on the $\alpha\beta$ reference frame are calculated as:

$$\mathbf{v}_{\alpha\beta}^{+} = \left[T_{\alpha\beta} \right] \mathbf{v}_{abc}^{+} = \left[T_{\alpha\beta} \right] \left[T_{+} \right] \mathbf{v}_{abc}$$
$$= \left[T_{\alpha\beta} \right] \left[T_{+} \right] \left[T_{\alpha\beta} \right]^{T} \mathbf{v}_{\alpha\beta} = \frac{1}{2} \begin{bmatrix} 1 & -q \\ q & 1 \end{bmatrix} \mathbf{v}_{\alpha\beta}, \tag{4a}$$

$$\mathbf{v}_{\alpha\beta}^{-} = \left[T_{\alpha\beta} \right] \mathbf{v}_{abc}^{-} = \left[T_{\alpha\beta} \right] \left[T_{-} \right] \mathbf{v}_{abc}$$
$$= \left[T_{\alpha\beta} \right] \left[T_{-} \right] \left[T_{\alpha\beta} \right]^{T} \mathbf{v}_{\alpha\beta} = \frac{1}{2} \begin{bmatrix} 1 & q \\ -q & 1 \end{bmatrix} \mathbf{v}_{\alpha\beta}, \tag{4b}$$

where $q = e^{-j\frac{\pi}{2}}$ is a phase-shift time-domain operator to obtain in-quadrature version (90º-lagging) of an original waveform. Hence, the system of Fig. 1 is proposed, where the quadrature-signals generator (QSG) and the positive-/negative-sequence calculator (PNSC) blocks are highlighted.

III. QUADRATURE SIGNALS GENERATION BASED ON A DUAL EPLL

As explained in [6], the EPLL is actually an adaptive filter whose frequency moves based on the fundamental frequency of the grid. This adaptive filter can be understood as either a notch or a band-pass filter depending on the regarded node [8]. Fig. 2 shows the modular structure of the EPLL –slightly modified for a better visualization and understanding. In this figure, the EPLL has been split up into the band-pass adaptive filter (BPAF) and the standard PLL modules. Moreover, port symbols have been added because these two modules will act as independent blocks in the following. In the original EPLL [6], the in-quadrature output signal was 90º-leading the in-phase signal. This made possible to implement the time domain operator *a* and calculate (2) on the *abc* natural reference frame. The EPLL of Fig. 2 shows a small modification in relation to the original one: the quadrature output signal *qv'* is now 90º-lagging *v'*.
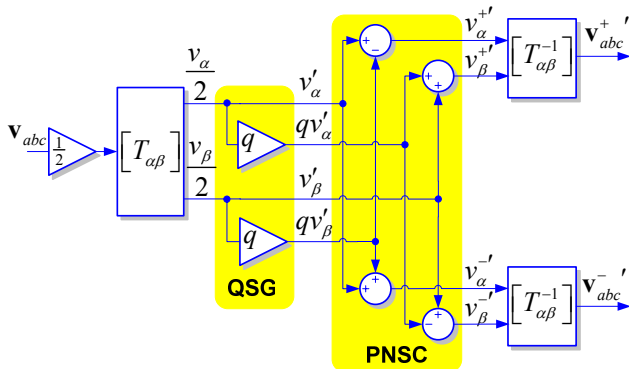
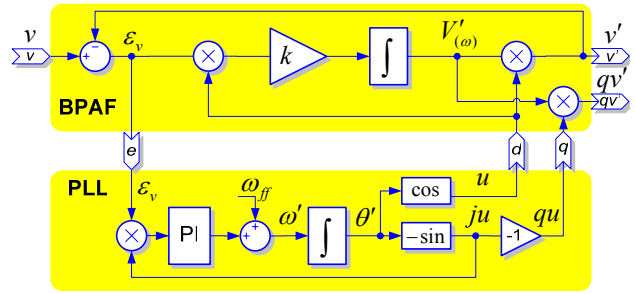Fig. 1. Positive-/negative-sequence calculation

Fig. 2. Modular EPLL structure

This change is due to the fact that the modified EPLL will be used to implement the *q* operator of (4). Transfer function of the BPAF is given by [8]:

$$D(s) = \frac{v'}{v}(s) = \frac{ks}{s^2 + ks + \omega'^2}, \tag{5}$$

where ω' is the grid frequency detected by the PLL.

As earlier mentioned, the EPLL concept results in a very interesting solution for synchronization with sinusoidal single-phase voltages because of: *i)* the band-pass filtering characteristic which attenuates undesired harmonics, *ii)* the capability to adapt ω' to the fundamental frequency of the grid, *iii)* the quadrature-signal generation which allows the application of the ISC method to calculate sequence components, *iv)* the competence identifying amplitude, phase-angle and frequency of the input signal.

In [6], the single-phase concept is directly extended toward the three-phase scenario by using three independent EPLLs – one per each phase– to implement positive-sequence calculation of (1a). This direct application of the EPLL to three-phase systems is prone to be improved since, as Fig. 1 shows, the two dimensional $\alpha\beta$ reference frame can be used instead of the *abc* natural reference frame, which entails: *i)* smaller computational burden because only two EPLL are used, *ii)* higher robustness because zero-sequence components are blocked in its input by *Clarke* transformation, *iii)* elimination of the fourth EPLL because amplitude and $\sin(\theta)/\cos(\theta)$ of the positive- and negative voltage vectors can be calculated by simple arithmetic operation on $\mathbf{v}_{\alpha\beta}^{+}$ and $\mathbf{v}_{\alpha\beta}^{-}$. Moreover, if it is accepted as true that α-β components of $\mathbf{v}_{\alpha\beta}$ are always in-quadrature, it is not necessary to detect the phase-angle in both α and β phases but only in one of them. Consequently, as Fig. 3 shows, two BPAFs and only one PLL are necessary to implement the QSG based on a dual EPLL (DEPLL-QSG). Letters identifying inputs and outputs in the blocks of Fig. 3 coincides with the ports name in Fig. 2. This nomenclature rule will be maintained from now on to designate block ports.

In most grids, positive- and negative-sequence impedances are equal and the synchronization system of Fig. 3 works well detecting positive- and negative-sequence components of the faulted voltage. However, effects of dynamic loads give rise to discrepancies between the positive- and negative-sequence impedances seen from the point of common coupling. This usually happens when big induction motors
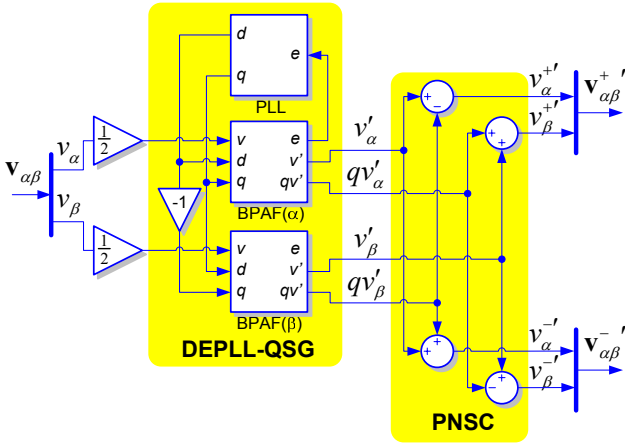
Fig. 3. Positive-/negative-sequence calculation based on the DEPLL

Fig. 4. (a) SOGI diagram, (b) SOGI-QSG diagram

are connected to the grid [9]. In such case, the DEPLL will make detection errors due to assumption about quadrature in the α-β components of $\mathbf{v}_{\alpha\beta}$ is not longer true. For this reason, a new frequency-adaptive phase-insensitive QSG is proposed in next section.

IV. SECOND ORDER GENERALIZED INTEGRATOR FOR QUADRATURE-SIGNALS GENERATION

To overcome drawbacks in the DEPLL-QSG, this work proposes the use of a second order generalized integrator (SOGI)[10] as a building block for the QSG. The SOGI diagram is shown in Fig. 4(a) and its transfer function is:

$$S(s) = \frac{d}{f}(s) = \frac{s\omega'}{s^2 + \omega'^2}. \tag{6}$$

Transfer function of (6) evidences that the SOGI acts as an infinite-gain integrator when input signal f is sinusoidal at ω' frequency. Intuitively, the system shown in Fig. 4(b) could be proposed for tracking the input signal v. Characteristics transfer functions of such system are given by:

$$D(s) = \frac{v'}{v}(s) = \frac{k\omega's}{s^2 + k\omega's + \omega'^2}, \tag{7a}$$

$$Q(s) = \frac{qv'}{v}(s) = \frac{k\omega'^2}{s^2 + k\omega's + \omega'^2}, \tag{7b}$$

where ω' and k set resonance frequency and damping factor respectively. Transfer functions of (7) reveal that tracking system of Fig. 4(b) provides band-pass and low-pass filtering characteristic to v' and qv' outputs respectively, which is interesting to attenuate harmonics of the input v. It is also evident from (7) that if v is a sinusoidal signal, v' and qv' will be sinusoidal as well. Moreover, qv' will be always 90º-lagging v', independently of both the frequency of v and the values of ω' and k. Consequently, the tracking system of Fig. 4(b) is actually a QSG insensitive to variation of either the tuning parameters or the input frequency (SOGI-QSG). Moreover, the SOGI-QSG has not to be synchronized with any additional sinusoidal reference signal which also makes it insensitive to phase variations in the input signal.
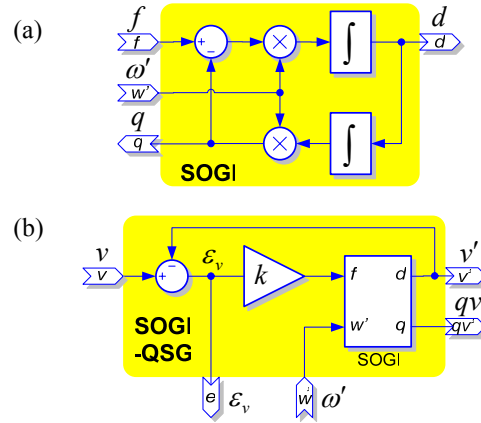
V. FREQUENCY-LOCKED LOOP

Once presented the structure of the SOGI-QSG it is now necessary to render it frequency-adaptive. This goal can be achieved by using the conventional PLL structure shown in Fig. 2. In such case, the error signal ε_v is provided to the PLL as an input and the estimated frequency ω' is returned back to the SOGI-QSG. Now, ju continues to be the feedback signal of the PLL control loop, whereas signals u and qu are no longer used. Feed-forward signal ω_{ff} is presetting the detected frequency around its nominal value to reduce the residual error controlled by the PI. Although a trigonometric function is used to obtain ju, this signal is not connected to the SOGI-QSG, so the system keeps insensitive to changes of the phase-angle of v. Consequently, a unit consisting of two SOGI-QSGs and only one PLL could be used in the structure of Fig. 3 for proper positive- and negative-sequence voltage components detection under generic grid conditions.

In the SOGI-QSG-PLL set-up, it is worth to realise that signal ju is 90º-leading v' when the PLL is synchronized in steady state. Taking into account that $ju = -qu$ and $qu \propto qv'$, it seems intuitive to use $-qv'$ (instead ju) as the feedback signal of the PLL control loop. Obviously, this change entails to modify the parameters of the PI controller as well. The subsystem resulting from these changes is simpler than the conventional PLL and neither phase-angle nor trigonometric functions are used for frequency estimation, being possible to talk about a frequency-locked loop (FLL) instead of a PLL. Fig. 5 shows the diagram of the proposed FLL, in which the product of $-qv'$ and ε_v is processed by an integrator controller with gain γ to obtain the estimated center grid frequency.
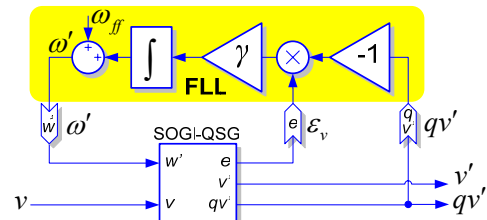

Fig. 5. FLL diagram

VI. GRID SYNCHRONIZATION SYSTEM BASED ON THE DSOGI-FLL

The structure of the grid synchronization system proposed in this paper is shown in Fig. 6. In this case, a set-up consisting of two SOGI-QSGs and only one FLL (DSOGI-FLL) provides the input signals to the PNSC on the $\alpha\beta$ reference frame. The DSOGI-FLL is extremely simple, and overcomes the drawbacks of earlier set-ups achieving proper positive- and negative-sequence components identification under generic grid operating conditions. Transfer functions from $\mathbf{v}_{\alpha\beta}$ to $\mathbf{v}_{\alpha\beta}^{+'}$ and $\mathbf{v}_{\alpha\beta}^{-'}$ is studied in the following.

When $\mathbf{v}_{\alpha\beta}$ is a positive-sequence balanced sinusoidal voltage at frequency ω, its α-β components keep the following relationship:

$$v_\beta(s) = -\frac{s}{\omega} v_\alpha(s) . \tag{8}$$

Taking into account that:

$$v_\alpha^{+'}(s) = \frac{1}{2}\left(v_\alpha'(s) - qv_\beta'(s)\right) = \frac{1}{2}\left(D(s) + \frac{s}{\omega}Q(s)\right)v_\alpha(s), \tag{9}$$

the transfer function from v_α to $v_\alpha^{+'}$ in the complex frequency domain is given by:

$$P(j\omega) = \frac{v_\alpha^{+'}}{v_\alpha}(j\omega) = \frac{1}{2}\frac{k\omega'(\omega+\omega')}{k\omega'\omega + j(\omega^2 - \omega'^2)}, \tag{10}$$

where ω', the frequency detected by the FLL, is supposed to be in steady-state. Conducting a similar reasoning on the β signal, it can be concluded that $v_\beta^{+'}$ has equal amplitude than $v_\alpha^{+'}$ but is 90°-lagging it. To know how $\mathbf{v}_{\alpha\beta}'$ will be when $\mathbf{v}_{\alpha\beta}$ is a negative-sequence vector it is only necessary to substitute ω by $-\omega$ in (10). Fig. 7 plots the amplitude of the transfer function of (10) for positive-sequence (ω>0 – continuous line) and negative-sequence (ω<0 –dashed line) voltages at the input of the DSOGI-FLL. Fig. 7 reveals that, in steady-state and regarding positive-sequence detection, the DSOGI-FLL acts as both a low-pass filter for positive-sequence and a notch filter for the negative-sequence.
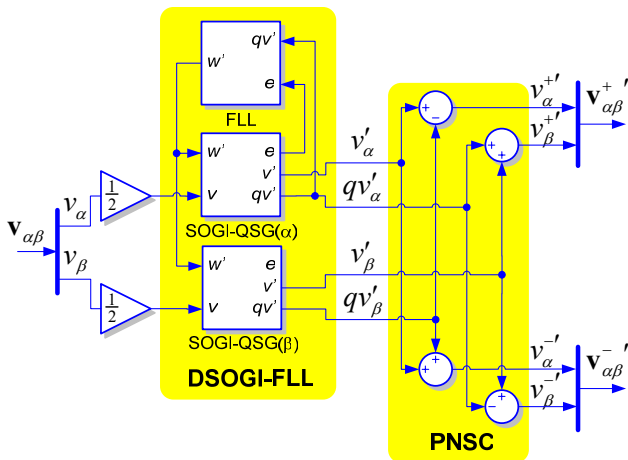

Fig. 6. Positive-/negative-sequence calculation based on the DSOGI-FLL
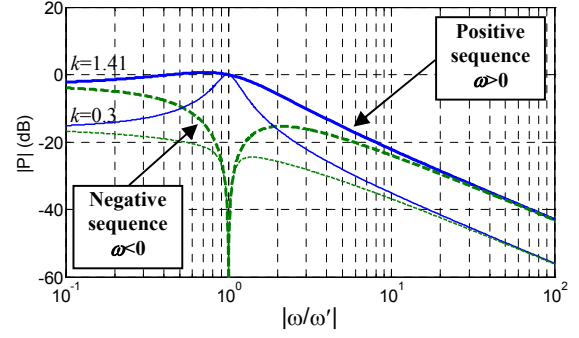

Fig. 7. Frequency response from v_α to $v_\alpha^{+'}$ with $\omega' = $ constant

Fig. 7 also shows that the smaller value for the gain k the more selective response of the system, which is interesting for harmonics rejection. However, this high selectivity entails higher oscillations in the response and longer stabilization time. Consequently, a trade-off between frequency selectivity and response speed should be adopted. Conclusions obtained for the detection of $\mathbf{v}_{\alpha\beta}^{+'}$ are directly applicable to the detection of $\mathbf{v}_{\alpha\beta}^{-'}$, being only necessary to swap the roll of the positive- and negative-sequence components.

VII. SIMULATION RESULTS

To evidence the high performances of the DSOGI-FLL, a case detecting positive- and negative-sequence components in an extremely adverse grid situation is simulated using MATLAB. The grid voltage is simultaneously affected by imbalance, distortion and frequency variation. The positive- and negative-sequence phasors of the faulty voltage are $\vec{V}^+ = 0.733\underline{|5°}$pu and $\vec{V}^- = 0.210\underline{|50,4°}$pu ; with $\vec{V}_{pf} = 1\underline{|0°}$pu for the pre-fault phase-voltage (220Vrms). The THD of the faulty voltage is set to 5%, being 3.7%, 3.1% and 1% the amplitudes for the 5th, 7th and 9th characteristic harmonics, respectively. The grid frequency jumps from 50Hz to 60Hz.

Fig. 8 shows the waveforms resulting from the previously mentioned simulation. The DSOGI-FLL parameters were set to $k = \gamma = 1.41$. Fig. 8(a) shows the unbalanced and distorted grid voltage resulting from applying all earlier disturbances in one go at t=100ms. Fig. 8(b) shows the detected amplitudes for the positive- and negative-sequence voltage vectors, whereas Fig. 8(c) and Fig. 8(d) show their phase-angles, respectively. These waveforms are given by:

$$\left|\mathbf{v}^{\pm'}\right| = \sqrt{\left(v_\alpha^\pm\right)^2 + \left(v_\beta^\pm\right)^2} \quad ; \quad \theta^{\pm'} = \tan^{-1}\frac{v_\beta^\pm}{v_\alpha^\pm} . \tag{11}$$

Fig. 8(e) and Fig. 8(f) show the detected positive- and negative-sequence voltages expressed on the *abc* natural reference frame and Fig. 8(g) shows the evolution of the frequency detected by the FLL. These plots reveal the excellent behavior of the DSOGI-FLL under such severe operating conditions. The proposed synchronization system is detecting the amplitude and phase-angle of the positive- and negative-sequence components after about 20ms from the grid fault occurrence.
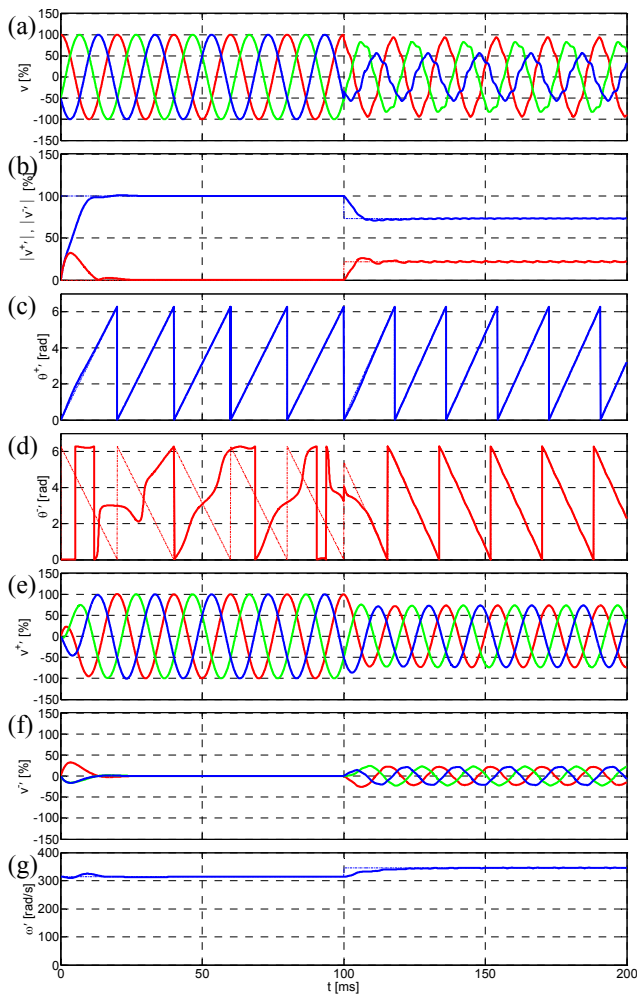
Fig. 8. Response of the DSOGI-PSC in presence of multiple disturbances.

It is worth to stress how 'clean' the positive-sequence waveforms of Fig. 8(e) are, THD of 0.5%. The negative-sequence waveforms of Fig. 8(f) have a THD of 2%. This distortion arises because the 5th harmonic of the grid voltage has negative-sequence and so the negative-sequence calculator does not act as a notch filter but as a low-pass filter, achieving a lower attenuation of the 5th harmonic. Phase-angles of Fig. 8(c) and Fig. 8(d) denote that $\alpha-\beta$ components of $\mathbf{v}_{\alpha\beta}$ are not in-quadrature. Nevertheless, the DSOGI-FLL is successful detecting the positive-and negative-sequence components of the grid voltage.

VIII. EXPERIMENTAL RESULTS

The DSOGI-FLL has been evaluated in an experimental set-up in which the faulty grid is replaced by a programmable three-phase ac-power source (California Instruments 5001IX) connected through a Δy transformer. In the y winding of this transformer, a VSI supplies energy from a dc power-supply to the grid. The DSOGI-FLL is the grid synchronization system used in the VSI control. The DSOGI-FLL algorithm, together the rest of controllers, is implemented in a DSP card (dSpace 1103). The sampling frequency is set to 15 kHz.

In a first experiment the ac-power source suddenly decreases the rms voltage of one phase from 220V to 100V. This fault is propagated to the y winding of the transformer as a dip type C, being $\vec{V}^{+} = 0.818\underline{|0°}$pu and $\vec{V}^{-} = 0.182\underline{|0°}$pu the positive- and negative-sequence phasors during the fault. Fig. 9 shows the waveforms from this first experiment, where it is remarkable the high speed in the detection, achieving precise results in less than one grid cycle. It is worth to notice that the detected phase-angles for both the positive- and negative-sequence voltages show a coherent evolution before the grid fault happens. It is because of the nonidealities of the experimental plant, which are giving rise to a very faint but steady imbalance in the grid voltage. The high sensibility of the DSOGI-FLL allows detecting this tiny negative-sequence component before the grid fault ocurrence. In a second experiment the grid frequency varies from 50Hz to 60Hz. Waveforms of Fig. 10 validate the frequency-adaptive characteristic of the DSOGI-FLL which is able to overcome this big jump of frequency without oscillations in about 40ms. A third experiment is devoted to evaluate the immunity of the DSOGI-FLL to distortion in the grid voltage. A distorted waveform with a THD of 5% and equal harmonic composition that earlier described in §VII is programmed in the ac-power source. In this case it is notable the high quality of the positive-sequence detected voltage. Since the insignificant amplitude of the negative-sequence component, there exists high distortion in the phase-angle calculated by (11) for this component. As fast as the negative-sequence component amplitude rises to higher levels, distortion in its phase-angle calculation decreases.

IX. CONCLUSION

A new concept in grid-synchronization, the DSOGI-FLL, has been introduced in this paper. This system consists of three fundamental blocks, i.e., *i)* the dual QSG, which uses the SOGI as a building block, *ii)* the FLL, which truly achieves grid frequency adaptation without involving phase-angle, and *iii)* the PNSC, which implements the ISC method on the $\alpha\beta$ reference frame. The DSOGI-FLL:

a) Exploits the ISC method on the stationary and orthogonal $\alpha\beta$ reference frame.
b) Does not need any trigonometric function since neither synchronous reference frame nor voltage controlled oscillator are used in its algorithm.
c) Is frequency-adaptive by using a FLL and not a PLL.
d) Is highly robust in front of transient events since grid frequency is more stable than voltage phase-angle.
e) Acts as either a low-pass or a notch filter depending on the relationship between input and detected sequences.
f) Attenuates high-order harmonics of the grid voltage.
g) Entails light computational burden, using only five integrators for detection of both sequence components.

Simulations together with an experimental evaluation were presented in order to demonstrate that DSOGI-FLL is a very suitable solution to the detection of fundamental-frequency positive- and negative-sequence components of unbalanced and distorted grid voltages.
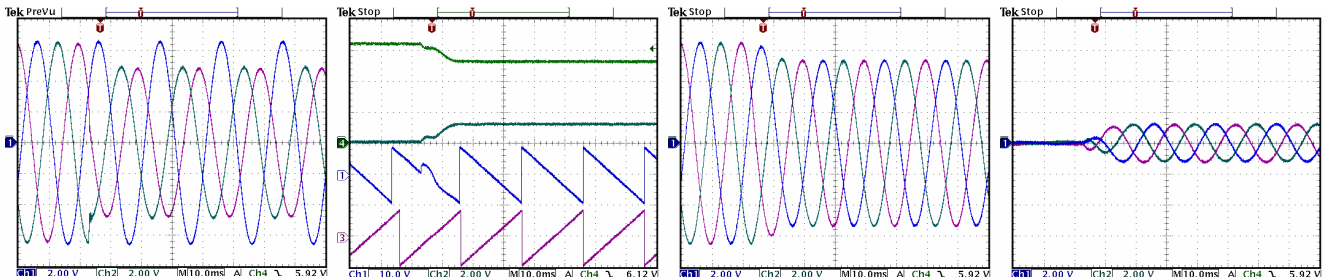
Fig. 9. Experimental evaluation of the DSOGI-FLL in presence of voltage sags type C. Plots from left to right:
faulty grid voltage; amplitudes and phase-angles detected; detected positive-sequence signals; detected negative-sequence signals
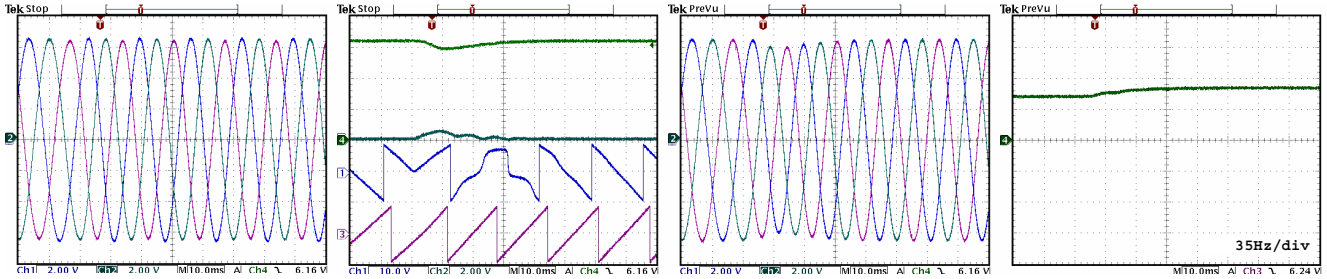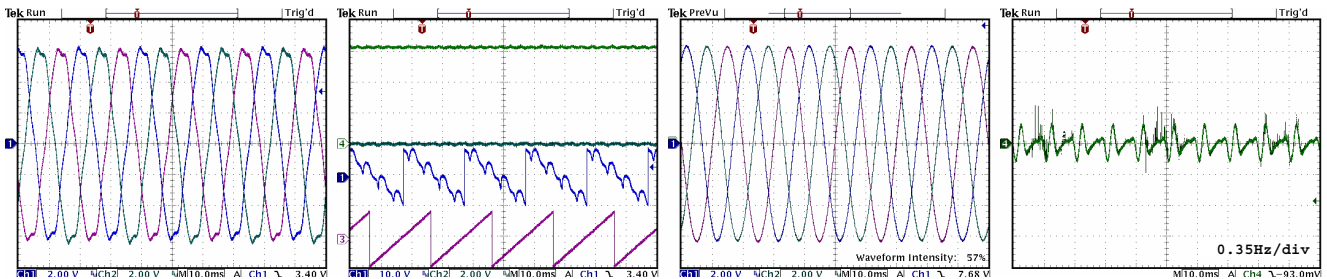

Fig. 10. Experimental evaluation of the DSOGI-FLL in presence of frequency variation (from 50Hz to 60Hz). Plots from left to right:
faulty grid voltage; amplitudes and phase-angles detected; detected positive-sequence signals; detected frequency

Fig. 11. Experimental evaluation of the DSOGI-FLL in presence of harmonics (THD=5%). Plots from left to right:
distorted grid voltage; amplitudes and phase-angles detected; detected positive-sequence signals; ripple in the detected frequency (magnified)

X. ACKNOWLEDGMENT

XI.- REFERENCES

[1] C. Jauch, J. Matevosyan, T. Ackermann, and S. Bolik, "International comparison of requirements for connection of wind turbines to power systems," *Wind Energy*, vol. 8, pp. 295-306, Jul. 2005.

[2] F.A. Magueed, A. Sannino, J. Svensson, "Transient performance of voltage source converter under unbalanced voltage dips," *in Proc. IEEE Power Electron. Spec. Conf. (PESC'04)*, 2004, pp. 1163-1168.

[3] A. Timbus, P. Rodríguez, R. Teodorescu, M. Liserre and F. Blaabjerg, "Control strategies for distributed power generation systems operating on faulty grid," *in Proc. IEEE Int. Symp. Ind. Electron. (ISIE'06)*, 2006.

[4] S. Chung, "A phase tracking system for three phase utility interface inverters," *IEEE Trans. Power Electron.*, vol. 15, pp. 431-438, May 2000.

[5] P. Rodríguez, J. Pou, J. Bergas, I. Candela, R. Burgos, and D. Boroyevich, "Double synchronous reference frame PLL for power converters," *in Proc. IEEE Power Electron. Spec. Conf. (PESC'05)*, 2005, pp. 1415-1421.

[6] M. Karimi-Ghartemani and M.R. Iravani, "A method for synchronization of power electronic converters in polluted and variable-frequency environments," *IEEE Trans. Power Systems*, vol. 19, pp. 1263-1270, Aug. 2004.

[7] W. V. Lyon, *Application of the Method of Symmetrical Components*, New York: McGraw-Hill, 1937.

[8] S. Luo and Z. Hou, "An adaptive detecting method for harmonic and reactive currents," *IEEE Trans. on Ind. Electron.*, vol. 42, pp. 85-89, Feb. 1995.

[9] A. Sannino, M.H.J. Bollen, J. Svensson, "Voltage tolerance testing of three-phase voltage source converters," *IEEE Trans. Power Delivery*, vol. 20, Apr. 2005, pp. 1633-1639.

[10] X. Yuan, W. Merk, H. Stemmler, J. Allmeling, "Stationary-frame generalized integrators for current control of active power filters with zero steady-state error for current harmonics of concern under unbalanced and distorted operating conditions," *IEEE Trans. on Ind Applicat.*, vol. 38, pp.523 – 532, Mar./Apr. 2002.

[VII] Control of single-stage single-phase PV inverter

Mihai Ciobotaru, Remus Teodorescu, Frede Blaabjerg

Control of Single-Stage Single-Phase PV Inverter

Mihai Ciobotaru, Remus Teodorescu and Frede Blaabjerg, Institute of Energy Technology, Aalborg University, Aalborg, Denmark

Abstract

In this paper the issue of control strategies for single-stage photovoltaic (PV) inverter is addressed. Two different current controllers (the classical proportional-integral (PI) and the novel proportional-resonant (PR) controllers) have been implemented and an experimental comparison between them has been made. A complete control structure for the single-phase PV system is also presented. The superiority of the PR controller is demonstrated with respect to the PI controller in terms of harmonic current rejection and the capability to remove the steady-state error without using the voltage feed-forward (VFF). The control strategy was successfully tested on a real 1.5 kW PV inverter.

Introduction

The market for PV power applications continues to develop at a high rate [1]. Between 2002 and 2003 the total installed capacity in the International Energy Agency (IEA) PhotoVoltaic Power Systems (PVPS) countries grew by 36 %, reaching 1 809 MW. Moreover, the price level of the PV modules and the system costs (inverter included) has decreased significantly [2]. The use of PV systems connected in parallel with the mains was simplified and is often supported by incentives from utilities and/or governmental bodies. Before connecting a PV system to the power network, the d.c. voltage of the solar modules must be converted into an a.c. voltage. Some protection systems are required to prevent damage in the PV system caused by the utility network and vice versa. The PV systems require standards addressing the use and the performance of grid-connected PV inverters, thus ensuring the safety and quality of the products.

The purpose of the power electronics in PVPS is to convert the d.c. current from the PV panels into an a.c. current to the grid, with the highest possible efficiency, the lowest cost and keep a superior performance. The basic interfacing is shown in Fig. 1.

A controversial issue for PV inverters is the current harmonics level. The IEEE 929 standard permits a limit of 5 % for the current total harmonic distortion (THD) factor with individual limits of 4 % for each odd harmonic from 3rd to 9th and 2 % for 11th to 15th while a recent draft of European IEC61727 suggests almost the same thing as previously mentioned. These levels are far more stringent than other domestic appliances, like IEC61000-3-2, as PV systems are viewed as generation sources and so are subject to higher standards than load systems.

For current-controlled PV inverters in most of the cases a PI controller with grid voltage feed-forward (VFF) is used [3], [4], but this solution exhibits two well known drawbacks (due to the poor performance of the integral action): inability of the PI controller to track a sinusoidal reference without steady-state error and poor disturbance rejection capability. An alternative solution in order to alleviate the PI's drawbacks is presented in [5], where a second order generalized integrator (GI) can be used. The GI is a double integrator that achieves an "infinite" gain at a certain frequency (resonance frequency), and almost no attenuation exists outside this frequency. Thus, it can be used as a notch filter in order to compensate the harmonics in a very selective way. Another approach reported in [6] where a new type of stationary-frame regulators called Proportional Resonant (PR) is introduced. In this approach the classical PI d.c.-compensator is transformed into an
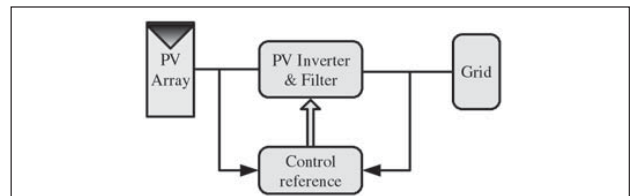

Fig. 1: Power electronic system with the grid, source (PV array), power converter and control
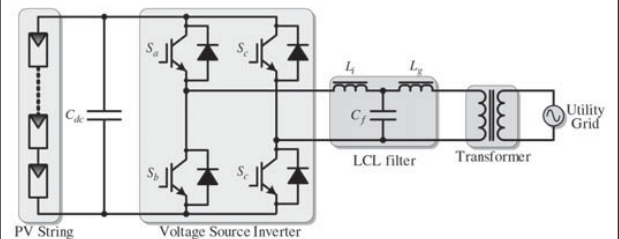

Fig. 2: The voltage source PV inverter connected to the grid through an LCL filter

equivalent a.c.-compensator having the same frequency response characteristics in the bandwidth of concern.

This paper is aimed at presenting a single-stage converter for single-phase PV systems. Two different current controllers have been implemented and an experimental comparison between them has been made. A complete control structure for the single-phase PV system is also presented. An incremental conductance method has been used in order to track the Maximum Power Point Tracker (MPPT) of the PV characteristic. In order to get a clean sinusoidal current reference (synchronized with the grid voltage) a phase-locked loop (PLL) based on a delay structure is used. The conclusions are presented in the final part of the paper.

System description

Usually the power converter interface from the d.c. source to the load and/or to the grid consists of a two stage converter: the d.c.-d.c. converter and the d.c.-a.c. converter. An alternative solution could be the use of a single-stage converter where the d.c.-d.c. converter is avoided and in order to ensure the necessary d.c. volt-
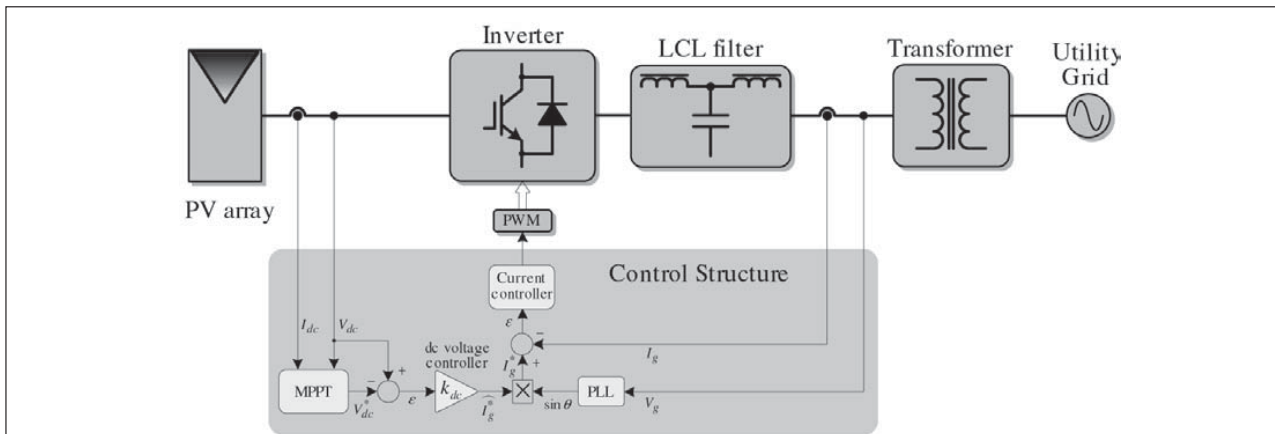
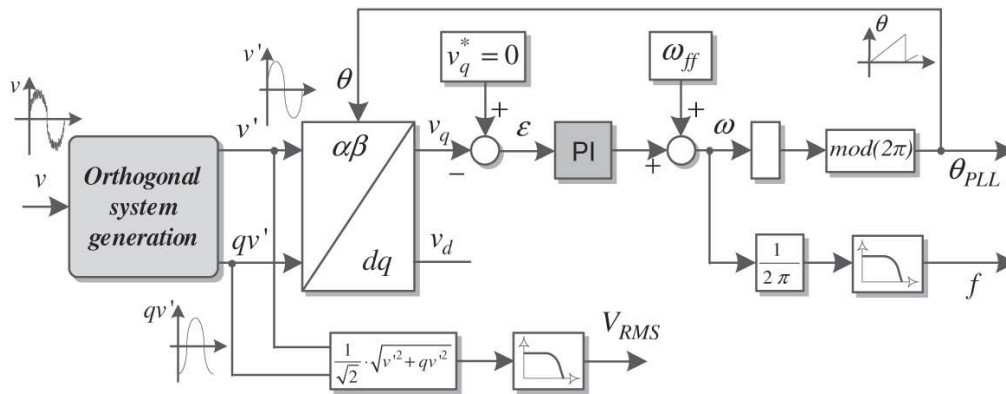Fig. 3: Control diagram of the PV energy conversion system

Fig. 4: General structure of a single phase PLL including grid voltage monitoring

age level the PV array can be a string of PV panels or a multitude of parallel strings of PV panels. In the classical solution with two-stage converter, the d.c.-d.c. converter requires several additional devices producing a large amount of conduction losses, sluggish transient response and high cost while the advantages of the single-stage converters are: good efficiency, a lower price and easier implementation. The disadvantages of the single-stage converter are the fact that the PV panels are in series and if shading occurs on one or several PV panels then the efficiency of the whole system is reduced.

As shown in Fig. 2, the PV inverter system consists of a solar panel string and a d.c. link capacitor C_{dc} on the d.c. side with an output a.c. filter (LCL), insulation transformer and grid connection on the a.c. side. The number of panels in the string has to ensure a d.c. voltage higher than the a.c. peak voltage at all time. The energy conversion from d.c. to a.c. side is made by a single-phase voltage source inverter. The used solar panel string consists of sixteen uniserial PV panels (120 W for each panel).

Control strategy

For the grid-connected PV inverters in the power range of 1-5 kW, the most common control structure for the d.c.-a.c. grid converter is a current-controlled H-bridge PWM inverter having a low-pass output filter. Typically L filters are used but the new trend is to use LCL filters that have a higher order (3rd) which leads to more compact design. The drawback is its resonance frequency which

can produce stability problems and special control design is required [7]. The control structure of the PV power conversion system is shown in Fig. 3.

The main elements of the control structure are the synchronization algorithm based on PLL, the MPPT, the input power control, the grid current controller including PWM.

PLL structure

The PLL is used to provide a unity power factor operation which involves synchronization of the inverter output current with the grid voltage and to give a clean sinusoidal current reference. The PI controller parameters of the PLL structure are calculated in such a way that the settling time and the damping factor of this PLL structure can be set directly. The PLL structure is also used for grid voltage monitoring in order to get the amplitude and the frequency values of the grid voltage. The general form of the PLL structure including grid voltage monitoring is presented in Fig. 4 [8].

MPPT algorithm

The task of the MPPT in a PV energy conversion system is to tune continuously the system so that it draws maximum power from the solar array regardless of weather or load conditions. Since the solar array has a non-ideal voltage-current characteristics and the

Mihai Ciobotaru, Remus Teodorescu, Frede Blaabjerg

conditions such as irradiance, ambient temperature, and wind that affect the output of the solar array are unpredictable, the tracker should deal with a nonlinear and time-varying system. The conventional MPPT algorithms are using $dP/dV = 0$ to obtain the maximum power point output. Several algorithms can be used in order to implement the MPPT as follows [9]: perturb & observe, incremental conductance, parasitic capacitance and constant voltage, but only the first two are the most frequently used.

The incremental conductance algorithm has been chosen as a MPPT strategy in this paper. This algorithm has advantages compared to perturb & observe as it can determine when the MPPT has reached the MPP, where perturb and observe oscillates around the MPP. Also, incremental conductance can track rapidly the increase and decrease of irradiance conditions with higher accuracy than perturb & observe. One disadvantage of this algorithm is the increased complexity when compared to perturb & observe. This increases the computational time and slows down the sampling frequency of the array voltage and current.

The flowcharts of the perturb & observe and of the incremental conductance algorithm are shown in Fig. 5 [10], where V_k and I_k are the momentary voltage and current of the PV array and V_{k-1}, I_{k-1} are the previous sampled voltage and current, respectively. The dP/dV term can be replaced by $I + (\Delta I/\Delta V) \cdot V$. The output of the MPPT is the d.c. voltage reference (V_{pv}^*).

Input power control

The control strategies of input power in the case of a power configuration of PV system without d.c.-d.c. converter are presented in the following section. In Fig. 6 a new control strategy of input power is proposed. The new element introduced is the power feed-forward. The computed value of the current amplitude reference using the PV Power and the RMS value of the a.c. voltage ($V_{ac\,RMS}$) is added to the output value of the d.c. voltage controller ($\hat{I}_r$) resulting in the a.c. current amplitude reference ($\hat{I}_{ref}$). Using the input power feed-forward the dynamic of the PV system is improved being known the fact that the MPPT is rather slow. The d.c. voltage controller ensures a quick response of the PV system at a sudden change of the input power.

Grid current controller

Classical PI control with grid voltage feed-forward (V_{ff}) as depicted in Fig. 7a, is commonly used for current-controlled PV inverters.

The PI current controller $G_{PI}(s)$ is defined as:

$$G_{PI}(s) = K_p + \frac{K_i}{s} \qquad (1)$$

In order to get a good dynamic response, a grid voltage feed-forward is used, as depicted in Fig. 7a. This leads in turn to stability problems related to the delay introduced in the system by the voltage feedback filter. In order to alleviate this problem an advanced filtering method for the grid voltage feed-forward should be considered. The Root-locus and Bode diagram analysis of the PI controller is presented in Fig. 8.

As it has been mentioned in the introduction of this paper, an alternative solution for the poor performances of the PI controller is the PR controller. The current loop of the PV inverter with PR controller is shown in Fig. 7b.

The PR current controller $G_c(s)$ is defined as [5, 7]:
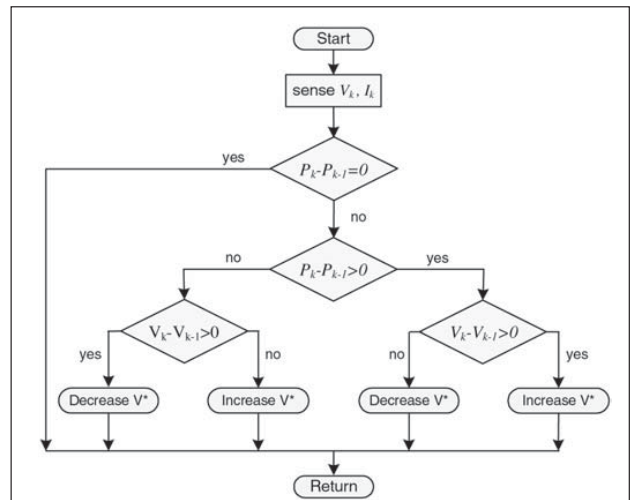
a)
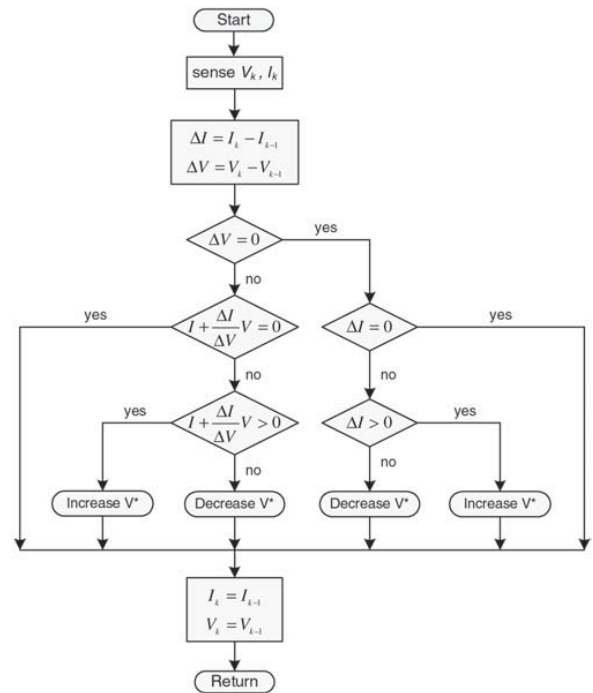
b)

Fig. 5: Flowcharts of the perturb & observe a) and incremental conductance algorithms b)
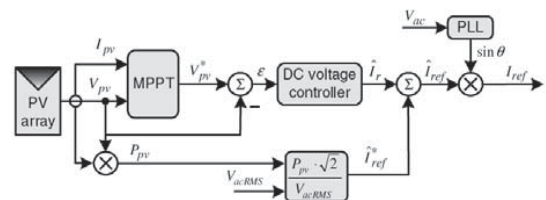

Fig. 6: New control structure of controlling the input power. A feed-forward of input power is used
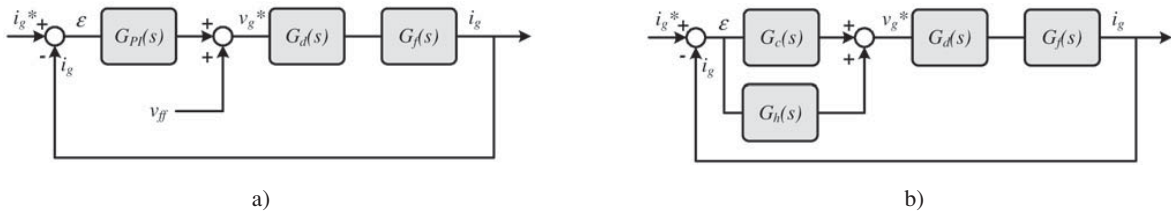
Fig. 7: The current loop of PV inverter: a) with PI controller; b) with PR controller
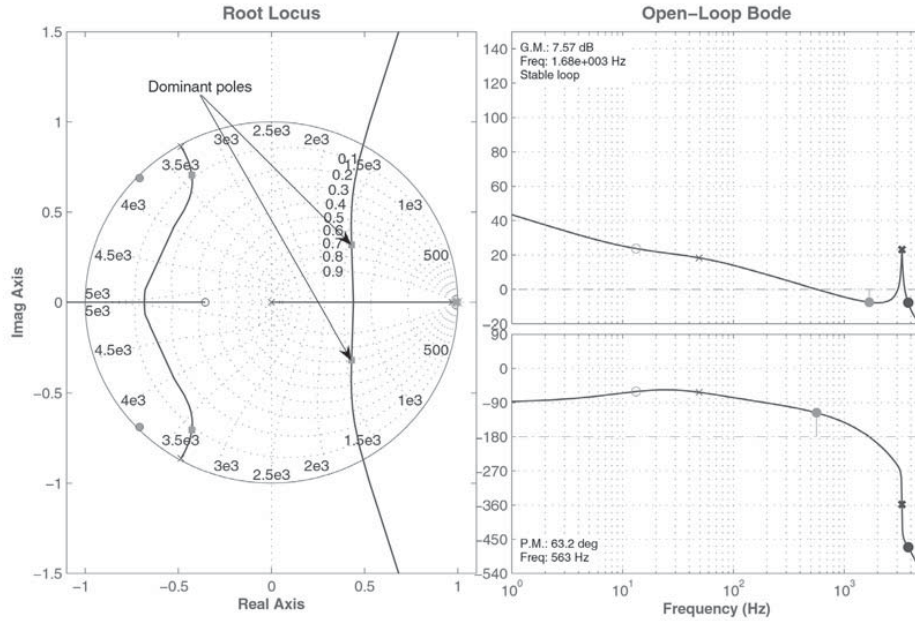

Fig. 8: PI current controller – Root-locus and Bode diagram analysis

$$G_c(s) = K_p + K_i \frac{s}{s^2 + \omega_o^2} \qquad (2)$$

The harmonic compensator (HC) $G_h(s)$ is defined as [7]:

$$G_h(s) = \sum_{h=3,5,7} K_{ih} \frac{s}{s^2 + (\omega_o h)^2} \qquad (3)$$

The HC is designed to out compensate the selected harmonics 3rd, 5th and 7th as they are the most predominant harmonics in the current spectrum.

A processing delay, usually equal to T_s for the PWM inverters [4], is introduced in $G_d(s)$. The filter transfer function $G_f(s)$ is expressed in (4) [11].

$$G_f(s) = \frac{i_i(s)}{v_i(s)} = \frac{1}{L_i s} \frac{\left(s^2 + z_{LC}^2\right)}{\left(s^2 + \omega_{res}^2\right)} \qquad (4)$$

where $z_{LC}^2 = \left[L_g C_f\right]^{-1}$ and, $\omega_{res}^2 = \frac{\left(L_i + L_g\right) \cdot z_{LC}^2}{L_i}$

where L_i, L_g and C_f are shown in Fig. 2. L_g includes the grid impedance due to the transformer and the grid lines.

The current error-disturbance ratio rejection capability at null reference is defined as:

$$\left.\frac{\varepsilon(s)}{v_g(s)}\right|_{i_i^*=0} = \frac{G_f(s)}{1 + (G_c(s) + G_h(s)) \cdot G_d(s) \cdot G_f(s)} \qquad (5)$$

where: ε is the current error and the grid voltage v_g is considered as the disturbance for the system.

In Fig. 9 is presented the Bode diagram of the disturbance rejection for the PI and PR controllers. It can very easily be noticed that the PI rejection capability is worse in comparison with the PR. Thus, it is demonstrated the superiority of the PR controller with respect to the PI in terms of harmonic current rejection.

The Root-locus and Bode diagram analysis of the PR+HC controller are presented in Fig. 10.

The size of the proportional gain K_p from PR controller determines the bandwidth and stability phase margin [5], in the same way as for the PI controller. As it can be observed from the open-loop Bode diagram (Fig. 10) the phase margin (PM) is determined to be equal with 60.6 degrees, indicating a good stability of the system. Also, the dominant poles of the controller are well damped as it can be seen in Fig. 10 exhibiting a damping factor equal with 0.7.
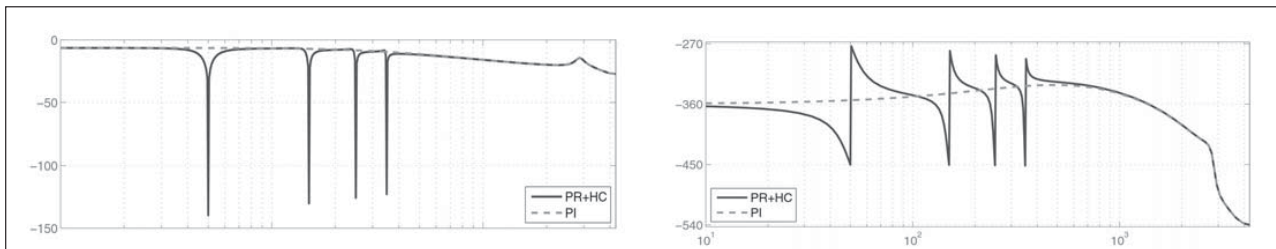
Fig. 9: Bode diagram of the disturbance rejection (current error ratio disturbance) of the PR+HC (3rd, 5th and 7th) and PI current controllers
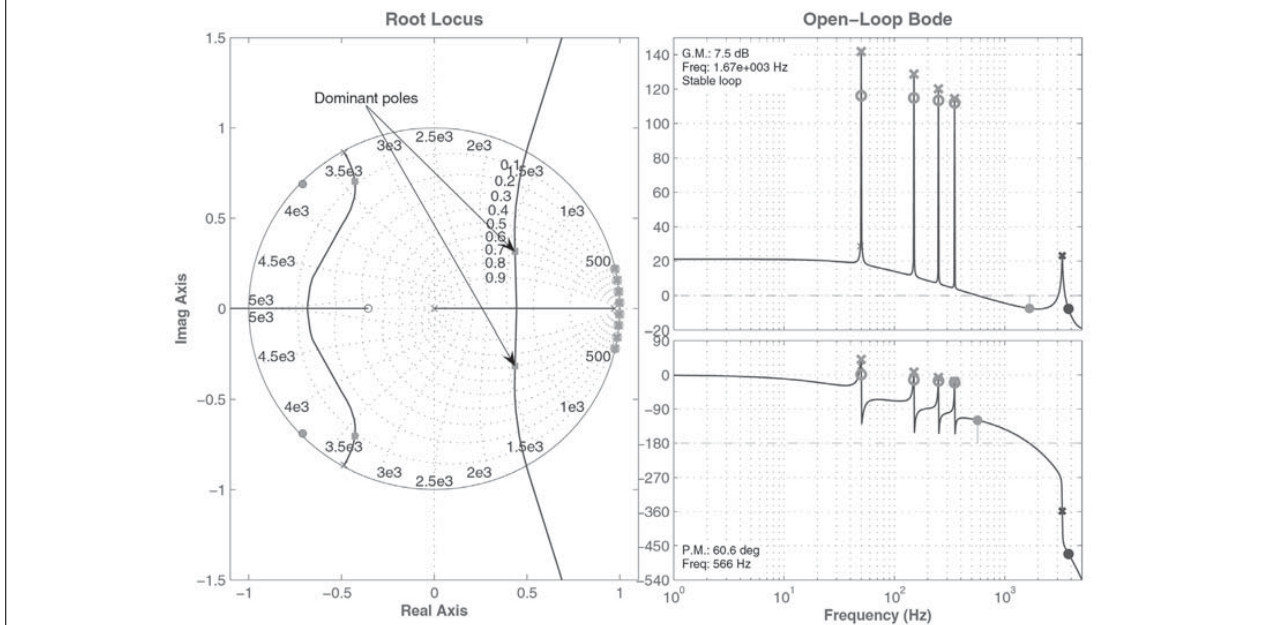

Fig. 10: PR current controller – Root-locus and Bode diagram analysis

Experimental results

A single-stage grid-connected PV inverter (1.5 kW power range) has been built in order to analyze the PV system performance, as depicted in Fig. 11a. The system is dSPACE based and voltage source inverter (VSI) is controlled using a unipolar PWM to place the harmonics on the high frequency side making them easier to filter. The parameters of the LCL filter were: L_i = 1426 µH, C_{ac} = 2.2 µF, L_g = 713 µH. The power stage of a Danfoss VLT 5004 rated 400 V/10A was used. The switching frequency of the inverter was 10 kHz. The control algorithm shown in Fig. 3 was implemented using the dSPACE DS1103 platform. For higher power, the LCL filter needs to be redesigned.

The system was tested in the following condition: the open circuit d.c. voltage provided by the uniserial sixteen PV panels was around 660 V, the RMS value of the grid voltage was V_g = 225 V with a THD of 2.2 % voltage background distortion. The grid impedance was measured to 1.2 Ω with a series inductance of 2.1 mH due to the insulation transformer, used in order to connect the PV system to the grid, and the grid inductance was measured to 50 µH. The total L_g will be 0.713 mH + 2.1 mH = 2.813 mH.

For small variations of L_g the PR controller behavior is not affected, but for large variations of L_g the stability of the current controller decreases and an adaptive tuning of the PR controller can be considered.

The plotted results have been captured using the graphical interface of the dSPACE system (Control Desk) and then exported to Matlab workspace for plotting.
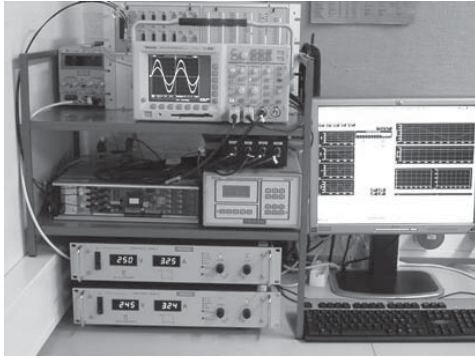
The solar panels string mounted on the roof of the laboratory are presented in the Fig. 11b [12].

The grid current and grid voltage at 1.5 kW for PI, PR and PR+HC controllers are presented in Fig. 12 a), b) and c). As it can be seen a much lower THD is obtained with the PR+HC controller. The grid current response at a 5 A step in the current reference is presented for the PI (Fig. 12d), PR (Fig. 12e) and PR+HC (Fig. 12f).

As it can be observed the PR and PR+HC controller yields a smaller overshoot than the PI controller.

In Fig. 13, a comparison of the spectrum for PI, PR and PR+HC in the lower frequency region is presented.

Using PI controller with VFF a current THD of 5.8% has been obtained while in the case of the PR controller the measured current THD was 9.7 %. Adding the HC for the PR controller a drastic attenuation of the current THD can be observed, decreasing to 0.5 %.
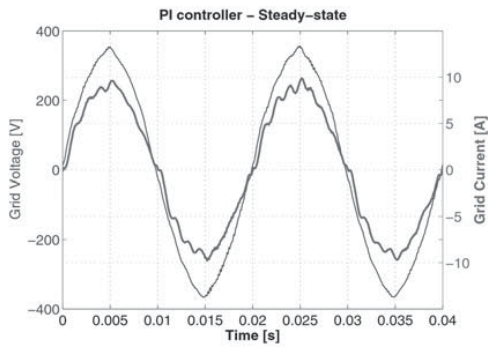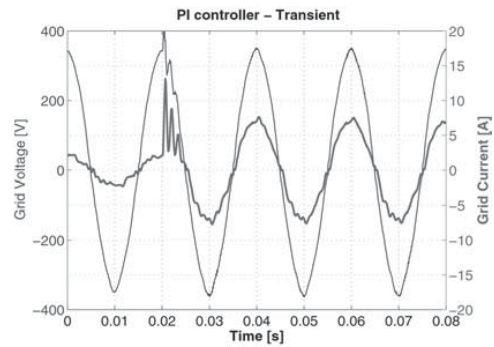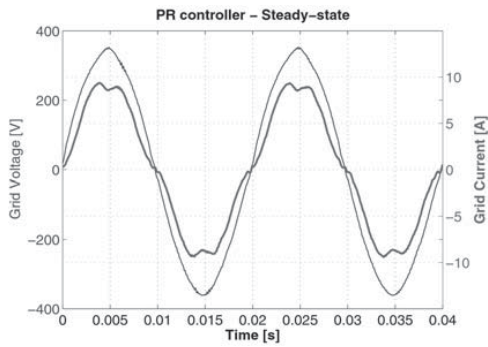
a)

b)

Fig. 11: a) Test setup for 1.5 kW PV inverter; b) The solar panels string mounted on the roof of the laboratory.
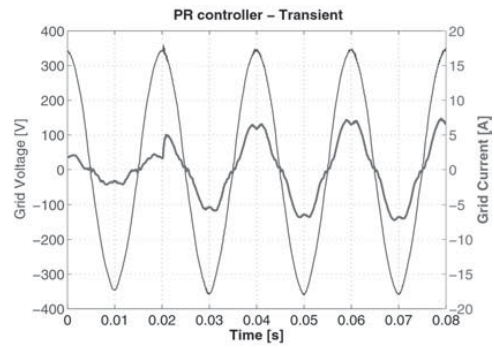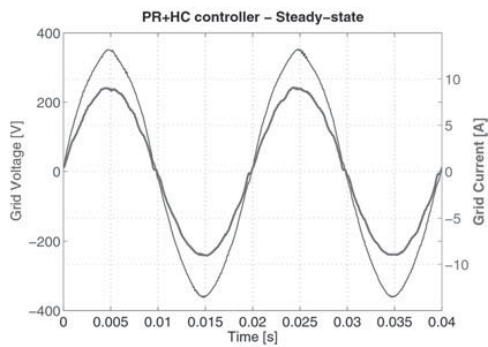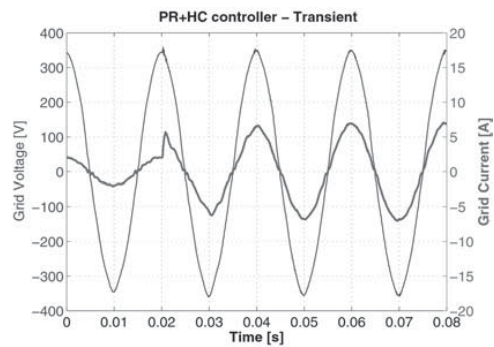

a)

d)

b)

e)

c)

f)

Fig. 12: Grid current (marked) and grid voltage at 1.5 kW for PI a), PR b) and PR+HC c) controllers. Grid current response (marked) at a 5 A step in the current reference for PI d), PR e) and PR+HC f) controllers
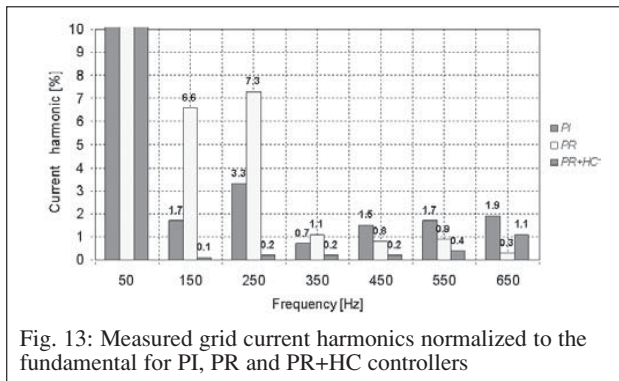
Mihai Ciobotaru, Remus Teodorescu, Frede Blaabjerg

Fig. 13: Measured grid current harmonics normalized to the fundamental for PI, PR and PR+HC controllers

Conclusion

An alternative solution using a single-stage converter, where the d.c.-d.c. converter is avoided, has been developed and successfully tested on a dSPACE controlled 1.5kW single-phase PV inverter. The advantages of the single-stage converters are: good efficiency, a lower price and easier implementation, while the main disadvantage is the fact that the PV panels are in series and if the shading occurs on one or several PV panels then the efficiency of the whole system is reduced.

It has been demonstrated that the PR+HC controller gives better performances then the classical PI controller for the grid current loop. The two well known drawbacks of the PI controller are: - steady-state error; and - poor harmonics rejection capability. The steady-state error can be overcome by the PR controller. The PR controller is able to remove the steady-state error without using VFF, which makes it more reliable. By adding the selective HC to the PR controller, a very good rejection for the dominant harmonics can be obtained.

References

[1] F. Blaabjerg, Zhe Chen and S.B.Kjaer. Power electronics as efficient interface in dispersed power generation systems, IEEE Transactions on Power Electronics, Vol. 19, Issue 5, 2004, pp. 1184 - 1194 .

[2] S.B. Kjaer, J.K. Pedersen and F. Blaabjerg. A review of single-phase grid-connected inverters for photovoltaic modules, IEEE Transactions on Industry Applications, Vol. 41, Issue 5, 2005, pp. 1292 - 1306 .

[3] M. Kazmierkovski, R. Krishnan, F. Blaabjerg. Control in Power Electronics, Selected Problems, Academic Press 2002, ISBN 0-12-402772-5.

[4] C. Cecati, A. Dell'Aquila, M. Liserre and V. G. Monopoli. Design of H-bridge multilevel active rectifier for traction systems, IEEE Trans. on Ind. App., Vol. 39, Sept./Oct. 2003, pp. 1541-1550.

[5] X. Yuan, W. Merk, H. Stemmler, J. Allmeling. Stationary-Frame Generalized Integrators for Current Control of Active Power Filters with Zero Steady-State Error for Current Harmonics of Concern Under Unbalanced and Distorted Operating Conditions, IEEE Trans. on Ind. App., Vol. 38, No. 2, Mar./Apr. 2002, pp. 523 – 532.

[6] D. N. Zmood and D. G. Holmes. Stationary Frame Current Regulation of PWM Inverters with Zero Steady-State Error, IEEE Trans. on Power Electronics, Vol. 18, No. 3, May 2003, pp. 814 – 822.

[7] R. Teodorescu, F. Blaabjerg, M. Liserre, U. Borup. A New Control Structure for Grid-Connected PV Inverters with Zero Steady-State Error and Selective Harmonic Compensation, Proc. of APEC'04, Vol. 1, pp. 580-586.

[8] M. Ciobotaru, R. Teodorescu and F. Blaabjerg, A new single-phase PLL structure based on second order generalized integrator, Record of IEEE PESC 2006, Korea, p. 1511-1516.

[9] D.P. Hohm and M.E. Ropp. Comparative Study of Maximum Power Point Tracking Algorithms Using an Experimental, Programmable, Maximum Power Point Tracking Test Bed, Proc. of Photovoltaic Specialists Conference, 2000, pp.1699 – 1702.

[10] Y.C. Kuo and T.J. Liang. Novel Maximum-Power-Point-Tracking Controller For Photovoltaic Energy Conversion System, IEEE Transactions on Industrial Electronics, Vol. 48, No. 3 , 2001 pp. 594 – 601.

[11] M. Liserre, F. Blaabjerg and S. Hansen. Design and Control of an LCL-filter Based Active Rectifier, Proc. of IAS'01, Vol. 1, pp. 299-307.

[12] R. Teodorescu and F. Blaabjerg. Photovoltaic Systems Are With Power Electronics, IEEE Power Electronics Society Newsletter, Forth Quarter 2005, Vol. 17, No. 4, ISSN 1054-7231.

The Authors

Frede Blaabjerg, (S'86-M'88-SM'97-F'03) received the M.Sc.EE. from Aalborg University, Denmark in 1987, and the PhD. degree from the Institute of Energy Technology, Aalborg University, in 1995. He was employed at ABB-Scandia, Randers, from 1987-1988. During 1988-1992 he was a PhD student at Aalborg University. He became an Assistant Professor in 1992 at Aalborg University, in 1996 Associate Professor and in 1998 full professor in power electronics and drives the same place. In 2006 he became the Dean of Faculty of Engineering and Science at Aalborg University. His research areas are in power electronics, static power converters, ac drives, switched reluctance drives, modeling, characterization of power semiconductor devices and simulation, wind turbines and green power inverter. He is the author or co-author of more than 300 publications in his research fields.

Mihai Ciobotaru was born in 1979 in Galati, Romania. He received his B.Sc. and M.Sc. degrees both in Electrical Engineering from "Dunarea de Jos" University of Galati in 2002 and 2003 respectively. From 2003 to 2004 he was employed as a teaching assistant at the Department of Electrotechnics, Electrical Machinery and Drives at the same institution. In February 2004, he joined the Institute of Energy Technology, Aalborg University, Denmark as a guest researcher working on single-phase grid connected inverter systems and since June 2004 he has been enrolled in a Ph.D. program with a provisional thesis title: "Reliable Grid Condition Detection and Control for Single-Phase Distributed Power Generation Systems".

Remus Teodorescu received the Dipl.Ing. degree in electrical engineering from Polytechnical University of Bucharest in 1989, and PhD.degree from University of Galati, Romania, in 1994. From 1989 to 1990, he worked for Iron and Steel Plant Galati and then he moved to Galati University where he worked as an assistant professor with Electrical Engineering Department. In 1998, he joined Aalborg University, Institute of Energy Technology, Power Electronics Section where he currently works as an Associate Professor. His research areas include power converters for renewable energy systems (PV, wind turbines), electrical drives. He has coauthored more than 100 technical papers, 12 of them published in journals. He is coauthor of 2 books and 5 patents. He received the Technical Committee Prize Paper Awards, IEEEIAS, 98 and OPTIM-ABB Prize paper Award at OPTIM 2002. He is a Senior Member of IEEE, Associate Editor for IEEE Transactions of Power Electronics Letters and chair of IEEE Danish IAS/IES/PELS chapter.

[VIII] **On-line grid impedance estimation based on harmonic injection for grid-connected PV inverter**

by M. Ciobotaru, R. Teodorescu, and F. Blaabjerg,
Article published in Proceedings of ISIE, 2007, pp. 2437-2442.

On-line grid impedance estimation based on harmonic injection for grid-connected PV inverter

Mihai Ciobotaru[(1)], Remus Teodorescu[(2)] and Frede Blaabjerg[(3)]

Institute of Energy Technology, Aalborg University
Pontoppidanstraede 101, 9220 Aalbborg, DENMARK
[(1)]*mpc@iet.aau.dk,* [(2)]*ret@iet.aau.dk and* [(3)]*fbl@iet.aau.dk*

Abstract – **The paper presents an on-line software method for impedance estimation of the energized impedances such as power system grid. The proposed method is based on producing a perturbation on the output of the power converter that is in the form of periodical injection of one or two voltage harmonic signals. The single harmonic injection uses a 600 Hz signal and the double harmonic injection uses a 400 Hz and 600 Hz signals, respectively. During the perturbation, the current response(s) at the same frequency as the injected signal(s) is/are measured. The value of the grid impedance is estimated using two different signal processing algorithms. The DFT technique is used for the single harmonic injection and the statistic technique is used for the double harmonic injection.**

The grid impedance estimation is used for compliance with the anti-islanding requirements of the German standard (VDE0126) and for robust control of the distributed power generation systems (DPGS).

Selected results are presented to confirm the performances of the proposed method.

Keywords **– impedance estimation, grid-connected systems, anti-islanding, adaptive current controller.**

I. INTRODUCTION

The increased penetration of the electrical grid with Distributed Power Generation Systems (DPGS) based on alternative sources such as photovoltaics (PVs), fuel cells and wind has been enabled by inverter technology developments [1]. The evolution of the recommended guidelines and standards has streamed manufacturing and shaped inverter design and control [2]-[3]. However, this necessitates continuous harmonization of standards at international level [4]. Integrating extra functions into the operation of the inverter such as harmonic filtering and distortion elimination have added another progress dimension [5]-[6].

In order to comply with certain stringent standard requirements for islanding detection such as the German standard VDE0126 for grid-connected PV systems, it is important to estimate the impedance of the distribution line (grid). Moreover, the estimation of the grid impedance can also be used in order to increase the stability of the current controller by adjusting its parameters on-line.

Several passive and active methods for estimating the grid impedance are reported in the technical literature [7], [8], [9], [10], [11], [12] and [13] using different techniques (e.g. identification techniques, harmonic(s) injection, current spike injection, voltage transient, etc.).

The objective of the paper is to propose an on-line grid impedance estimation method suitable for single-phase grid-connected systems (such as PV systems).

The proposed method is based on producing a perturbation on the output of the power converter that is in the form of periodical injection of one or two voltage harmonic signals. The single harmonic injection uses a 500 Hz signal and the double harmonic injection uses a 500 Hz and 600 Hz signals, respectively. During the perturbation, the current response(s) at the same frequency as the injected signal(s) is/are measured. The value of the grid impedance is estimated using two different signal processing algorithms. The DFT technique is used for the single harmonic injection and the statistic technique is used for the double harmonic injection.

The paper is organized as follows. First, two applications requiring on-line grid impedance estimation are presented. Next the proposed grid impedance estimation method based on voltage harmonic injection is described. Finally, results are presented to confirm that the proposed method performs in a satisfactory way.

A. Anti-islanding

The islanding problem is defined as a continuation of operation of a grid-connected converter after the grid has been turned off. As shown in Fig. 1, the grid-connected inverter can actually continue to run especially if there is a resonant RLC local load that cancels the grid current and that poses serious safety problems.
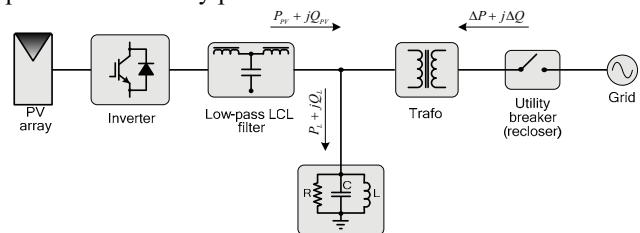

Fig. 1: Islanding operation phenomenon

There are anti-islanding standard requirements for photovoltaic inverters that require the detection of the increase of grid impedance within a determined time (ex. VDE0126 1 ohms jump in 5 seconds).

There are a number of passive and active methods to prevent islanding. The passive methods are monitoring the grid voltage, phase or frequency and impedance in order to detect islanding and the active methods are doing slight changes in the inverter output phase or frequency and measure the response of the grid to these changes. If the grid goes off, the response will be different and islanding can thus be detectable.

In order to measure the grid impedance on-line, several methods can be considered. The classical short-circuit current method can not be applied, while the inverter is running, this can only be applied off-line. The principle is to short-circuit the grid with low impedance and measure the voltage drop which can be used to calculate the grid impedance. This method is used by stand-alone grid impedance measuring instruments, but can not be implemented on-line.

New proposed active methods are based on producing some small disturbances, like applying a voltage pulse and measure the grid current response or injecting a non-characteristic harmonic current signal and measure the grid current response, which can be used on-line. Especially the latter one is now being researched very intense recently and the referenced patent US 6,933,714 B2 [14] is describing such a method where two different frequency current signals (ex. 40Hz and 60 Hz) are injected in the grid for a short period and based on DFT algorithm, the frequency components for these frequencies are extracted from the measured grid voltage and current and by dividing the voltage to the current the grid impedance at these frequency is determined. By linear interpolation, the grid impedance at 50 Hz is determined. The shortcomings of this method are that the disturbance in the current is rather important leading to power quality degradation to some extent.

The new proposed method will have the advantage with respect to patent US 6,933,714 B2 including: reduced disturbance at the output of the grid converter by using higher frequencies for shorter time period.

B. *Adaptive control of grid converters*

The grid impedance will also have impact on the current control of the grid converters in order to adapt it to large variations. As mentioned, the knowledge of the grid impedance is important for safe operation of a grid connected converter. The performance of the converter also depends on the grid impedance (Z_{grid}) and the voltage at the Point of Common Coupling (V_{PCC}) which in most cases is highly distorted due other nonlinear loads connected to PCC. See Fig. 2.

The current controller regulates the current to the grid and it is designed in accordance with the output filter impedance of the converter Z_{conv} and some assumed value of the grid impedance. A linear current controller for AC reference tracking with zero steady state error (zero phase shift and zero amplitude error) can be constructed either by transforming the control system into an equivalent DC system and using a DC controller or by using an AC controller (proportional resonant controller). In both cases the stability of the controllers depends upon the grid impedance as the grid impedance is a serial addition to the output filter of the converter.

Also the non-linear current controllers including hysteresis and predictive control are relying on a good knowledge of the grid impedance.
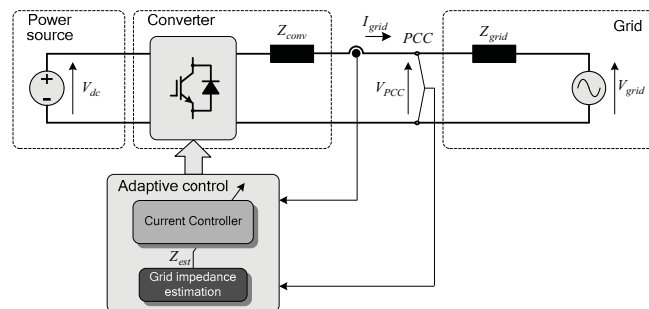

Fig. 2: Adaptive control of the grid-connected inverter

With the increased penetration of the distributed power generation systems, the value of the grid impedance in different points of common coupling can vary substantially, mainly due to the grid interface filters. The large variation in the grid impedance highly decreases the robustness of the current controller and can lead to instability. When the grid impedance is unknown, the design of the current controller is a trade off between performance and stability and selecting the controller parameters with a given stability margin provides poor performance when the grid impedance differs from the design background. Hence, the verge of stability can easily be reached or crossed by a realistic variation in the grid impedance or if the grid impedance changes suddenly. Thus, the variation of the grid impedance deteriorates both safety, the stability of the current controller and the performance of the current controller. By detecting the grid impedance on-line the current controller can be adjusted on-line so that the controller parameters match the actual grid impedance and, hence, both stability and good performance is achieved regardless of the grid impedance value.

II. ON-LINE IMPEDANCE ESTIMATION USING HARMONIC INJECTION

A. *Perturbation*

The principle of the harmonic injection is presented in Fig. 3. The grid-connected inverter is used directly to inject the harmonic current by adding a harmonic voltage to the inverter voltage reference as it can be seen in Fig. 5. The harmonic is injected in the zero voltage crossing moment. Therefore, the active power produced by the grid-connected

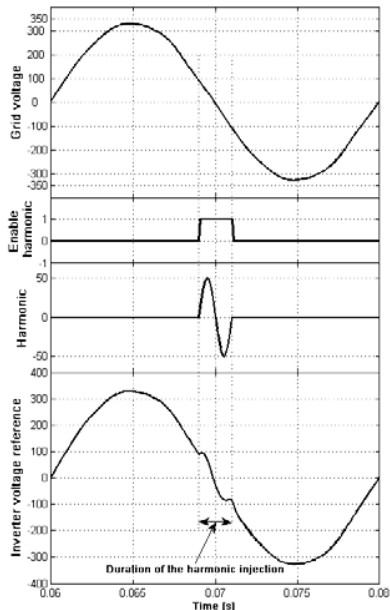inverter will be less affected compared to already known methods.

Fig. 3: Principle of the voltage harmonic injection

In Fig. 3 the first subplot shows a period of the grid voltage waveform. Then, in the second and the third subplots are shown the enable harmonic signal and the harmonic waveform respectively which are synchronized with the grid voltage angle provided by the phase-locked loop (PLL) to ensure the zero voltage crossing harmonic injection. The last subplot shows the waveform of the inverter voltage reference with the injected harmonic.

The frequency of the injected harmonic has been chosen ten times higher than the grid voltage frequency. There are some limitations by choosing the harmonic frequency. A lower chosen frequency can interact with the resonance of the current controller in the case of the proportional resonant current controller with harmonics compensation is used (see Fig. 4). On the opposite, the higher chosen frequency can be near the grid resonance frequency as presented in [15], which again negatively affects the final result. By linear interpolation, the grid impedance at 50 Hz is determined.
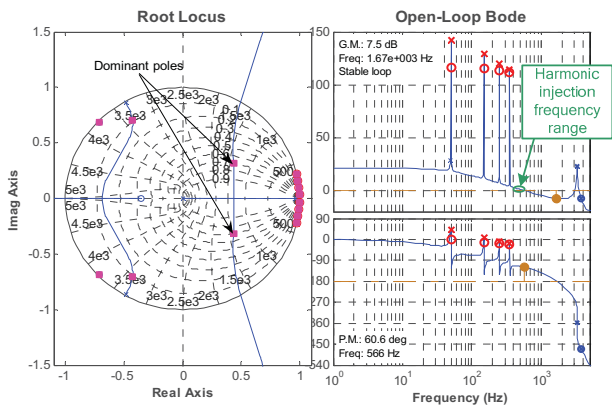

Fig. 4 Harmonic injection frequency range

By implementing the presented methods it is possible to estimate, at any instant, the grid impedance with good accuracy.

The proposed method uses periodical injection of one or two voltage harmonics. The single harmonic injection uses a 600 Hz signal as presented in Fig. 5a and the double harmonic injection uses a 400 Hz and 600 Hz signals, respectively (see Fig. 5b), where:

- θ_{PLL} – represents the grid phase angle provided by the PLL structure. It is used in order to synchronize the injection with the zero crossing of the grid voltage as shown in Fig. 3.
- I_g – the actual grid current
- I_g^* – the grid current reference
- V_h – the injected voltage harmonic
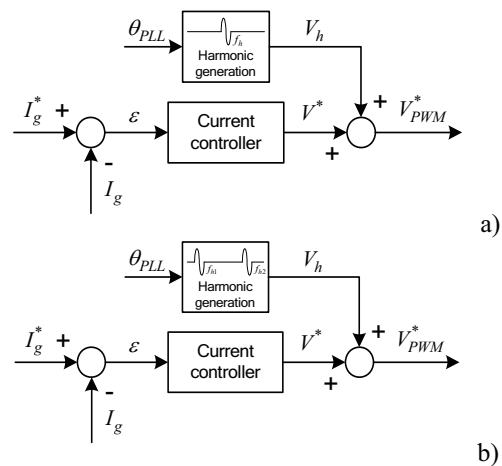- V_{PWM}^* – the inverter voltage reference

Fig. 5: Harmonic injection methods: a) single harmonic injection; b) double harmonic injection

B. Calculations

The estimation of the grid impedance using two different numerical methods is explained in the following.

Single harmonic injection

One of the methods is to inject into the grid a single frequency harmonic having one period time in a cycle (Fig 5a). The cycle time can be half or one second. In this case, the grid-connected inverter injects the single harmonic into the grid and measures the response of the injection using the current and voltage sensors. The signals are further derived in the way of Discrete Fourier Transformation (DFT) analysis and finally the amplitude and phase are obtained. The DFT uses equation (1) for coefficients calculation of the voltage and current harmonic.

$$\overline{\Lambda}_h = \sum_{n=0}^{N-1} v(n) \cdot \cos\left(\frac{2\pi \cdot h \cdot n}{N}\right) - j \cdot \sum_{n=0}^{N-1} v(n) \cdot \sin\left(\frac{2\pi \cdot h \cdot n}{N}\right) \quad (1)$$

$$\overline{\Lambda}_h = \lambda_{hr} + j \cdot \lambda_{hi}$$

where:

- N is the number of samples per fundamental period;

- $v(n)$ is the input signal (voltage or current) at point n;
- Λ_h is the complex Fourier vector of the hth harmonic of the input signal;
- λ_{hr} is the real part of Λ_h;
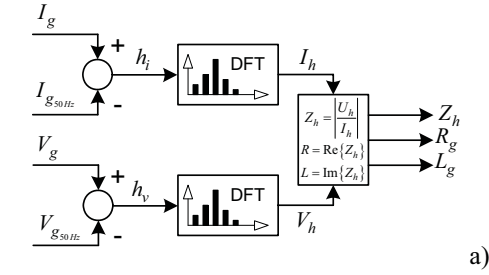- λ_{hi} is the imaginary part of Λ_h.

In the following, using the relations (2), (3) and (4) it is possible to measure the grid impedance $Z(h)$ and the resistive (R_g) and inductive (L_g) part of it. Fig. 6a shows the measurement structure used for this method.

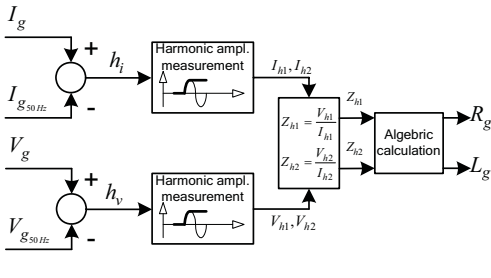$$\underline{Z}(h) = R_g + j \cdot \omega_h \cdot L_g \qquad (2)$$

$$Z(h) = \left| \frac{\underline{V}(h)}{\underline{I}(h)} \right| \qquad (3)$$

$$R_g = \mathrm{Re}\{\underline{Z}(h)\}$$
$$L_g = \mathrm{Im}\{\underline{Z}(h)\} \qquad (4)$$

a)

b)

Fig. 6: Grid impedance estimation algorithms: a) single harmonic injection; b) double harmonic injection

Double harmonic injection

The second method is explained as injecting two different frequency harmonics followed by harmonic response amplitude analyses for those two particular injected harmonics (Fig. 5b). This approach provides an alternative of being involved with phase angle calculation, which could be difficult to implement if the DSP operates in fixed-point numerical format. This method uses the absolute values mean of the current response at the frequency of the injected harmonic (Fig 6b). Thus, by computing the grid impedance in two different points (meaning two injected harmonics at different frequencies) the grid parameters are calculated by solving following set of equations:

$$\begin{cases} Z_1^2 = R_g^2 + \omega_1^2 \cdot L_g^2 \\ Z_2^2 = R_g^2 + \omega_2^2 \cdot L_g^2 \end{cases} \qquad (5)$$

$$L_g = \sqrt{\frac{Z_1^2 - Z_2^2}{\omega_1^2 - \omega_2^2}} \qquad (6)$$

$$R_g = \sqrt{\frac{\omega_1^2 \cdot Z_2^2 - \omega_2^2 \cdot Z_1^2}{\omega_1^2 - \omega_2^2}} \qquad (7)$$

where: - ω_1, ω_2 denote injected harmonic frequencies;
- $Z1$, $Z2$ are the impedances calculated on ω_1, ω_2;
- R_g, L_g are grid resistance and inductance.

Fig. 7 illustrates the waveforms of the voltage harmonics (h_v) and current harmonics (h_i) (see Fig. 6). These waveforms were obtained after removing the fundamental from the grid voltage and current.
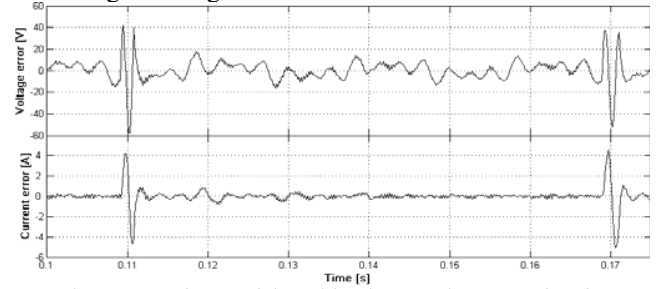

Fig. 7: Waveforms of the grid voltage and current after the fundamental was extracted

III. IMPLEMENTED TEST SETUP AND RESULTS

The proposed method for the grid impedance estimation has been tested on a single-phase grid-connected PV system. The power circuit and its afferent control diagram are presented in Fig. 8.
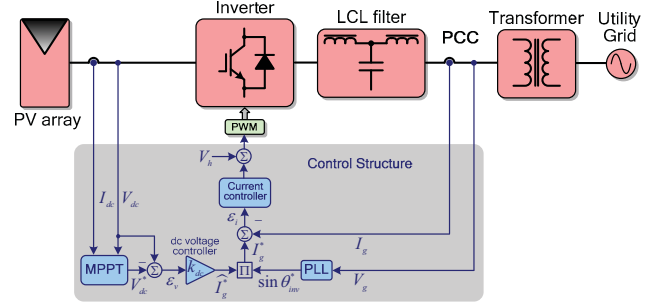

Fig. 8 The Control diagram of the PV system

The grid current controller is implemented using the Proportional Resonant (PR) controller which is defined as:

$$G_c(s) = K_p + K_i \frac{s}{s^2 + \omega_o^2} \qquad (8)$$

The PR controller has been associated with a harmonic compensator (HC) $G_h(s)$ which is defined as:

$$G_h(s) = \sum_{h=3,5,7,9} K_{ih} \frac{s}{s^2 + (\omega_o h)^2} \qquad (9)$$

The parameters of the LCL filter were set to L_1=0.7 mH, C=2.2 μF and L_2=1.4 mH.

Fig. 9 presents the grid impedance estimations for ten different values (between 0.05 mH and 2.5 mH) of the grid

inductance L_g on a grid resistance R_g of 0.5 Ω. The solid line represents the actual grid impedances Z_{h1} and Z_{h2} at the harmonic frequencies (where h_1 is the first injected harmonic having the frequency equal with 400Hz and h_2 is the second injected harmonic having the frequency equal with 600Hz). The dashed line represents the estimated grid impedance using (1) and (3) of the DFT algorithm (Fig. 6a). The estimated grid impedance, using the harmonic amplitude estimation method (STQ) (Fig. 6b), is represented with dashdot line. It can be seen that both methods presented in Fig. 6 give good results in terms of real grid impedance estimation, providing less than 15% error.
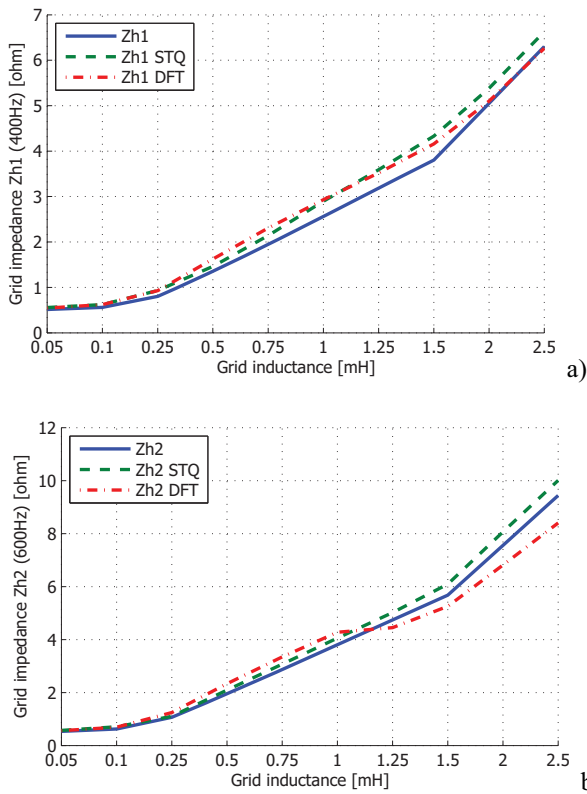

Fig. 9: Grid impedance estimation using harmonics injection a) h1 – 400Hz; b) h2 – 600Hz (R_g = 0.5 Ω and L_g – varies between 0.05 and 2.5 mH)

The grid impedance estimation on step variation in both grid inductance and resistance are presented in Fig. 10 (R_g step from 0.5 to 1 Ω and L_g step from 0.25 and 0.5 mH). The solid line represents the actual grid impedance at the harmonic frequencies. The dashed line represents the estimated grid impedance using DFT algorithm, and the dashdot line represents the estimated grid impedance using the harmonic amplitude estimation method (STQ). The grid inductance and resistance are finally obtained using (4), (6) and (7), as shown in Fig. 11. Both methods based on DFT and STQ perform satisfactorily.
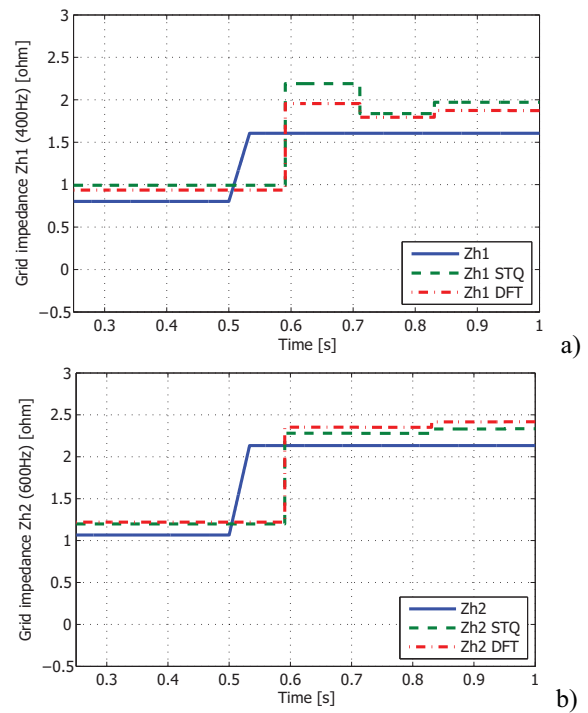

Fig. 10: Grid impedance estimation using harmonics injection a) h1 – 400Hz; b) h2 – 600Hz (R_g step from 0.5 to 1 Ω and L_g step from 0.25 and 0.5 mH)
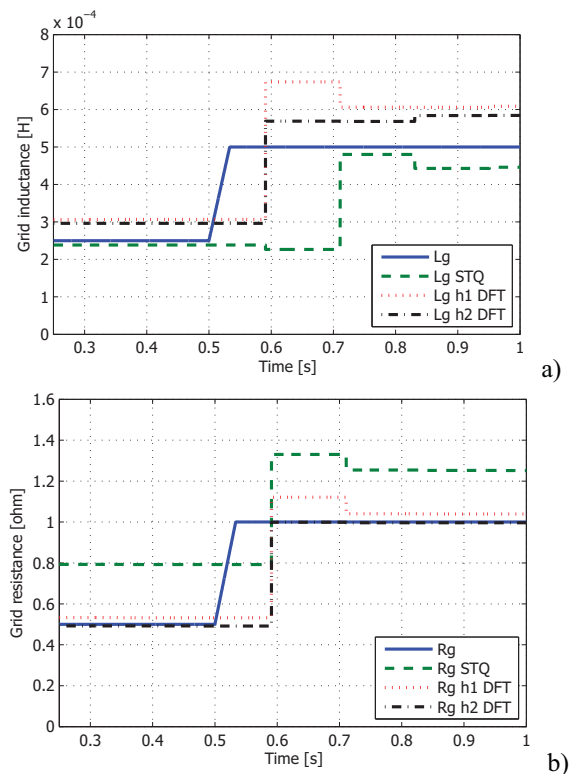

Fig. 11: a) Grid inductance estimation (L_g step from 0.25 and 0.5 mH); b) Grid resistance estimation (R_g step from 0.5 to 1 Ω)
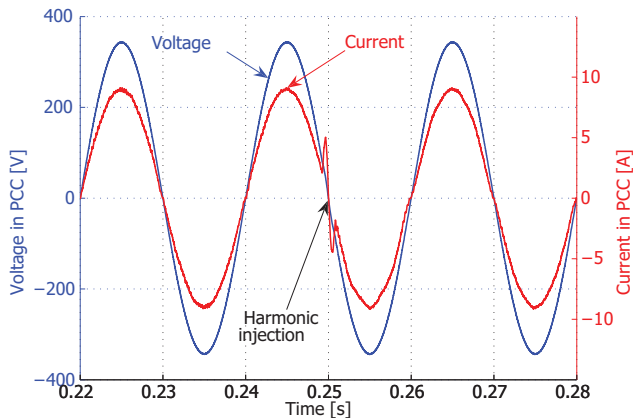
Fig. 12: The grid current and voltage during the harmonic injection

Fig. 12 presents the measured grid voltage and current at point of common couple (PCC) during the harmonic injection. A small disturbance of the grid current can be noticed compare to some similar known methods that make use of a low harmonic injection (e.g. 40, 60, 75 Hz). Of course that using a higher frequency injection implies an assumption that the grid impedance is linear on this frequency range. However, the estimation error caused by this assumption does not affect significantly the estimation of the grid impedance.

IV.   CONCLUSION

The grid impedance estimation using voltage harmonic injection is well suited for both, anti-islanding standard requirements (such as VDE0126) and robust control for distributed power generation systems (DPGS).

Using the harmonic signal injection at a higher frequency (e.g. 400 - 600Hz) the output power of the inverter is less disturbed compare to know similar methods. Moreover, the calculation algorithm based on statistic method (STQ), used in order to get the injected harmonic signal magnitude feedback, is less complicated in contrast with some of the known used algorithms based on more advanced mathematics such as DFT method, Prony extrapolation.

The use of a higher frequency injection implies an assumption that the grid impedance is linear on this frequency range. However, the estimation error caused by this assumption does not affect significantly the estimation of the grid impedance.

V. REFERENCES

[1]   F. Blaabjerg, Z. Chen, and S.B. Kjaer, "Power electronics as efficient interface in dispersed power generation systems", *IEEE Trans. on Power Electronics,* Vol. 19, No. 5, September 2004, pp. 1184-1194.

[2]   *IEEE Standard 929-2000:* IEEE Recommended practice for utility interface of photovoltaic (PV) systems.

[3]   *IEEE Standard 1547-2003:* IEEE Standard for interconnecting distributed resources with electric power systems.

[4]   A. Woyte, K. De Brabandere, D.V. Dommelen, R. Belmans, and J. Nijs, "International harmonization of grid connection guidelines: adequate requirements for the prevention of unintentional islanding", *Progress in Photovoltaics: Research and Applications 2003,* Vol. 11, pp. 407-424.

[5]   T.F. Wu, H.S. Nien, C.L. Shen and T.M. Chen, "A single-phase inverter system for PV power injection and active power filtering with non-linear inductor consideration", *IEEE Trans. on Industry Applications,* Vol. 41, No. 4, July/August 2005, pp. 1075-1083.

[6]   T.F. Wu, C.L. Shen, C.H. Chang, J. Chiu, "1~3W grid-connection PV power inverter with partial active power filter", *IEEE Trans. on Aerospace and Electronic Systems,* Vol. 39, No. 2, April 2003, pp. 635-646.

[7]   Sumner, M.; Palethorpe, B.; Thomas, D.; Zanchetta, P.; Di Piazza, M.C., "Estimation of power supply harmonic impedance using a controlled voltage disturbance," Power Electronics Specialists Conference, 2001. PESC. 2001 IEEE 32nd Annual, vol.2, pp. 522-527.

[8]   Di Piazza, M.C.; Zanchetta, P.; Sumner, M.; Thomas, D.W.P., "Estimation of load impedance in a power system," Harmonics and Quality of Power, 2000. Proceedings. Ninth International Conference on, vol.2, pp. 520-525.

[9]   Sumner, M.; Palethorpe, B.; Thomas, D.W.P.; Zanchetta, P.; Di Piazza, M.C., "A technique for power supply harmonic impedance estimation using a controlled voltage disturbance," Power Electronics, IEEE Transactions on , vol.17, no.2, pp. 207-215.

[10]   Rhode, J.P.; Kelley, A.W.; Baran, M.E., "Line impedance measurement: a nondisruptive wideband technique," Industry Applications Conference, 1995. Thirtieth IAS Annual Meeting, IAS '95., Conference Record of the 1995 IEEE , vol.3, pp. 2233-2240.

[11]   Ishigure, N.; Matsui, K.; Ueda, F., "Development of an on-line impedance meter to measure the impedance of a distribution line," Industrial Electronics, 2001. Proceedings. ISIE 2001. IEEE International Symposium on, vol.1, pp. 549-554.

[12]   Tsukamoto, M.; Ogawa, S.; Natsuda, Y.; Minowa, Y.; Nishimura, S., "Advanced technology to identify harmonics characteristics and results of measuring," Harmonics and Quality of Power, 2000. Proceedings. Ninth International Conference on, vol.1, pp., 341-346.

[13]   Asiminoaei, L.; Teodorescu, R.; Blaabjerg, F.; Borup, U., "Implementation and Test of an Online Embedded Grid Impedance Estimation Technique for PV Inverters," Industrial Electronics, IEEE Transactions on, vol.52, no.4, pp. 1136-1144.

[14]   United States Patent, "Method and apparatus for measuring the impedance of an electrical energy supply system", Patent No. US 6,933,714 B2, Aug. 23, 2005.

[15]   Enslin, J.H.R.; Heskes, P.J.M., "Harmonic interaction between a large number of distributed power inverters and the distribution network," Power Electronics, IEEE Transactions on, vol.19, no.6, p. 1586- 1593.

[IX]   Online grid impedance estimation for single-phase grid-connected systems using PQ variations

by M. Ciobotaru, R. Teodorescu, P. Rodriguez, A. Timbus, and F. Blaabjerg,
Article published in Proceedings of PESC, 2007, pp. 2306-2312.

Online grid impedance estimation for single-phase grid-connected systems using PQ variations

Mihai Ciobotaru[(1)]   Remus Teodorescu[(2)]   Pedro Rodriguez[(3)]   Adrian Timbus[(4)]   Frede Blaabjerg[(5)]

[(1) (2) (4) (5)] Institute of Energy Technology, Aalborg University
Pontoppidanstraede 101, 9220 Aalborg
DENMARK
Tel: +45-9635-9252, Fax: +45-4142-7949
[(1)] **mpc@iet.aau.dk** [(2)] ret@iet.aau.dk [(4)] avt@iet.aau.dk [(5)] fbl@iet.aau.dk

[(3)] Department of Electrical Engineering
Technical University of Catalonia,
SPAIN
+34 (93) 739 8036
[(3)] prodriguez@ee.upc.edu

Abstract- **This paper presents an online grid impedance estimation method for single-phase grid-connected systems, such as photovoltaic systems, small wind turbines, fuel-cells power systems. The method is based on producing a small perturbation on the output of the power converter that is in the form of periodical variations of active and reactive power (PQ variations). The main idea is to make the power converter working in two operation points in order to solve the equation of the equivalent grid impedance. During the perturbation, measurements of voltage and current are performed and signal processing algorithms are used in order to estimate the value of the grid impedance. The online grid impedance estimation method can be used for compliance with the anti-islanding standard requirements (IEEE1574, IEEE929 and VDE0126) and for adaptive control of the grid-connected converters. The proposed method is embedded in the existing power converter control. The selected results validate the effectiveness of the proposed method.**

Keywords- **Grid impedance estimation, Distributed generation, Grid-connected systems, Islanding detection, Adaptive control.**

I.   INTRODUCTION

The increased penetration of the electrical grid with Distributed Power Generation Systems (DPGS) based on alternative sources such as photovoltaics (PVs), fuel cells and wind has been enabled by inverter technology developments [1]. The evolution of the recommended guidelines and standards has streamed manufacturing and shaped inverter design and control [2], [3]. However, this necessitates continuous harmonization of standards at international level [4]. Integrating extra functions into the operation of the inverter such as harmonic filtering and distortion elimination have added another progress dimension [5], [6].

In order to comply with certain stringent standard requirements for islanding detection such as the German standard VDE0126 for grid-connected PV systems, it is important to estimate the impedance of the distribution line (grid). The standard requirement is to isolate the supply within 5 s after an impedance change of 1 ohm. Therefore, the PV inverters should make use of an online measurement technique in order to meet these regulation requirements. Moreover, the estimation of the grid impedance can also be used in order to increase the stability of the current controller by adjusting its

parameters online. If the variation is mainly resistive then the damping of the line filter is significant and makes the PV inverter control more stable. If the variation is mainly inductive, then the bandwidth of the controller decreases [15]. Also, in this case, due to the additional inductance of the grid, the tuning order of the line filter becomes lower and the filter will not fulfill the initial design purpose. Therefore, besides the standard requirement the knowledge about the grid impedance value is an added feature for the PV inverter [13].

The objective of the paper is to propose an online grid impedance estimation method suitable for single-phase grid-connected systems. The method relies on the variations of active and reactive power.

The paper is organized as follows. First, the known impedance estimation techniques are summarized. Secondly, two applications requiring on-line grid impedance estimation are presented. Next, the proposed grid impedance estimation method based on PQ variations is described. Finally, selected results are presented to validate the effectiveness of the proposed method.

II.   GRID IMPEDANCE ESTIMATION TECHNIQUES

According to [13] different techniques, as presented in [7], [8], [9], [10], [11] and [12] can be used for line impedance measurements. It is noticeable that, usually, these methods use special hardware devices. Once the inputs are acquired by voltage and current measurement, the processing part follows, typically involving large mathematical calculations in order to obtain the impedance value.

The state of the art divides the measuring solutions into two major categories: the passive and the active methods.

The passive method uses the non characteristic signals (line voltages and currents) that are already present in the system. This method depends on the existing background distortion of the voltage [16] and, in numerous cases, the distortion has neither the amplitude nor the repetition rate to be properly measured. This will not be interesting for implementing it in a PV inverter.

Active methods make use of deliberately "disturbing" the power supply network followed by acquisition and signal processing [7], [8], [9] and [11]. The way of "disturbing" the network can vary, therefore, active methods are also divided into two major categories: transient methods and steady-state methods, as briefly described in the following.

A. *Transient Active Methods*

It is worth mentioning that the transient methods are well suited for obtaining fast results, due to the limited time of the disturbing effect on the network. Quickly, by this technique, the impedance measuring device generates a transient current in the network (e.g., a resistive short circuit), and then measures the grid voltage and current at two different time instants, before and after the impulse occurrence. The impulse will bring in a large harmonic spectrum that afterwards should be analyzed. The results obtained show the network response over a large frequency domain, making this method well suited in applications where the impedance must be known at different frequencies. However, this method may involve high performance in A/D acquisition devices and must also use special numerical techniques to eliminate noise and random errors [17]. These requirements are difficult to achieve on a non dedicated harmonic analyzer platform like a PV inverter, even if a DSP controller is used.

B. *Steady-State Active Methods*

Steady-state methods typically inject a periodically known distortion into the grid and then make the analyses in the steady-state period. One of these techniques proposes the development of a dedicated inverter topology [11] and by measuring the phase difference between supply and inverter voltage the computation of line impedance. Another technique, which is easy to implement [18], repetitively connects a capacitive load to the network and measures the difference in phase shift of the voltage to the current.

The technique proposed in [13] is a steady-state technique that injects a non characteristic harmonic current into the grid and records the voltage change response. Results are processed by means of a Fourier analysis at the particular injected harmonic. In this way, the method has the entire control of the injected current. Thus, the calculation resumes only at the specific Fourier terms that give the final result. It is worth mentioning that the same technique can be used to obtain the frequency characteristic of the grid impedance, if the method repeats the measurements at different frequencies [19].

III. APPLICATIONS SUITED FOR GRID IMPEDANCE ESTIMATION

Two applications requiring on-line grid impedance estimation are briefly presented in the following.

A. *Anti-islanding method using grid impedance estimation*

The islanding problem is defined as a continuation of operation of a grid-connected converter after the grid has been turned off. As shown in Fig. 1, the grid-connected inverter can actually continue to run especially if there is a resonant RLC local load (where the resonant frequency is close to the line

frequency value and the value of the resistor R matches with the inverter output power). This worst case scenario poses serious safety problems.
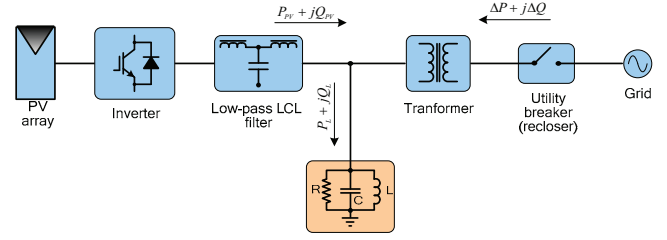

Figure 1. Islanding operation phenomenon

The German standard VDE0126 for PV inverters requires the detection of the increase of grid impedance within a determined time (1 ohm jump in the grid impedance has to be detected in 5 seconds). Therefore, the on-line grid impedance estimation is well suited for this particular standard requirement.

B. *Adaptive control for grid converters based on grid impedance estimation*

The grid impedance also has impact on the control of the grid converters. A large variation on the grid impedance highly decreases the stability and the performance of the current controller. As mentioned, the knowledge of the grid impedance is important for safe operation of a grid connected converter. The performance of the converter also depends on the grid impedance (Z_g) and the voltage at the Point of Common Coupling (V_{PCC}) which in most of the cases is distorted due to other nonlinear loads connected to PCC. See Fig. 2.
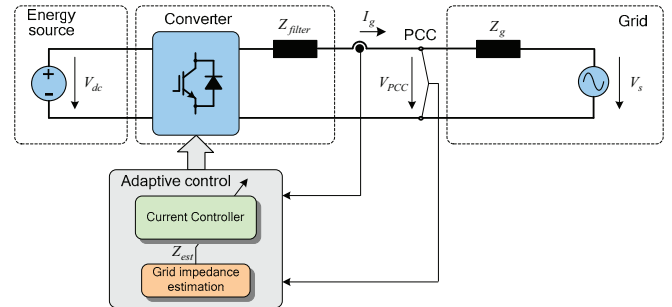

Figure 2. Adaptive control of the grid-connected inverter

The current controller parameters are tuned in accordance with the output filter impedance of the converter Z_{filter} and some assumed value of the grid impedance Z_g. A linear current controller for AC reference tracking with zero steady state error (zero phase shift and zero amplitude error) can be constructed either by transforming the control system into an equivalent DC system and using a DC controller or by using an AC controller (e.g. the proportional resonant controller). In both cases the stability of the controllers depends upon the grid impedance value as the grid impedance is a serial addition to the output filter of the converter. If the variation is mainly inductive, then the bandwidth of the controller decreases as it can be noticed from Fig. 3. In order to alleviate this problem,

the gain scheduling method can be used for adjusting online the current controller parameters, as presented in Fig. 4.
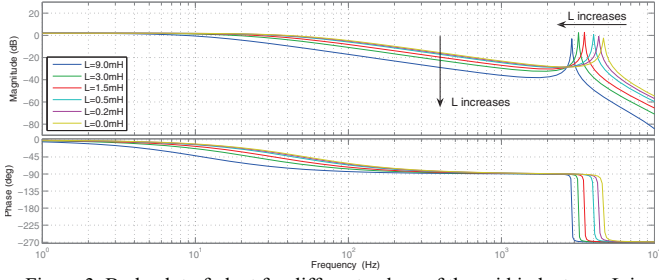

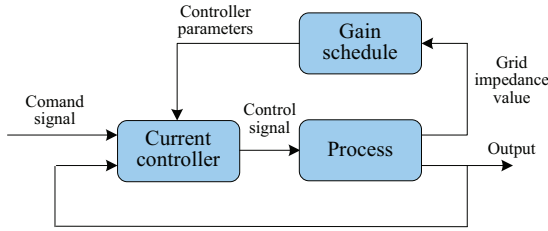Figure 3. Bode plot of plant for different values of the grid inductance L in case of using an LCL filter

Figure 4. Gain scheduling method

IV. GRID IMPEDANCE ESTIMATION - METHOD DESCRIPTION

The method relies on the variation of active and reactive power of the grid-connected converter. The principle of the variation of active and reactive power is presented in Fig. 5. A PQ control strategy is required in order to implement this method for a single-phase grid-connected system, as presented in [14].
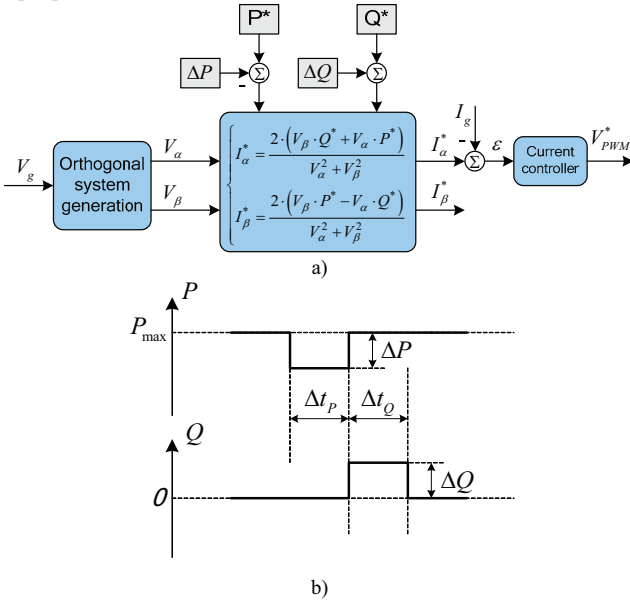

a)

b)

Figure 5. The principle for the variation of active (P) and reactive (Q) power

The PQ control structure is depicted in Fig. 5a. The Orthogonal System Generation (OSG) block is required in order to implement a PQ control in single-phase systems. The orthogonal voltage system is generated by a Second Order Generalized Integrator (SOGI) structure, as shown in [20]. For three-phase systems, this is not longer required, being replaced by the Clarke transformation block (abc-$\alpha\beta$).

The accuracy of this method depends of the PQ variation values (ΔP – variation value of active power P and ΔQ – variation value of reactive power Q) and the duration of the perturbation (ΔtP – variation period of active power P and ΔtQ – variation period of reactive power Q), as shown in Fig. 5b.

The PQ control principle is based on the relations presented in (1) and (2) according to [14].

$$\begin{cases} P = \dfrac{1}{2}\left(V_\alpha \cdot I_\alpha + V_\beta \cdot I_\beta\right) \\ Q = \dfrac{1}{2}\left(V_\beta \cdot I_\alpha - V_\alpha \cdot I_\beta\right) \end{cases} \tag{1}$$

$$\begin{cases} I_\alpha^* = \dfrac{2\cdot\left(V_\beta \cdot Q^* + V_\alpha \cdot P^*\right)}{V_\alpha^2 + V_\beta^2} \\ I_\beta^* = \dfrac{2\cdot\left(V_\beta \cdot P^* - V_\alpha \cdot Q^*\right)}{V_\alpha^2 + V_\beta^2} \end{cases} \tag{2}$$

Fig. 6 shows the principle of how the method using PQ variations works. The estimation of the grid impedance using PQ variations is explained in the following.

$$\overline{V}_{PCC} = \overline{I}_g \cdot \overline{Z}_g + \overline{V}_s \tag{3}$$

The equation of the grid voltage measured at the Point of Common Coupling (V_{PCC}) is given in (3), where I_g represents the current injected into the grid by the grid-connected converter, Z_g is the grid impedance and V_s represents the voltage source of the grid. The difficulty in the estimation of Z_g using (3) is that the voltage source of the grid (V_s) is immeasurable. Therefore, the main idea is to make the power converter working in two operation points (1 and 2), as presented in Fig. 6, in order to avoid the unknown variable V_s from (3).
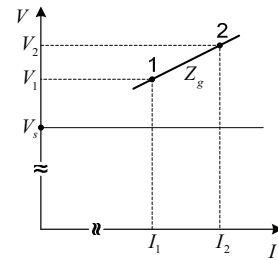

Figure 6. Power converter working in two operation points

It is assumed that the grid impedance is linear between these two nearby working points. In (4), the equations of the grid voltage in these two working points are presented. V_1 and V_2 represent the V_{PCC} for the working points 1 and 2. By subtracting V_2 from V_1 (5), the unknown variable V_s is avoided.

$$\begin{cases} \overline{V}_1 = \overline{I}_1 \cdot \overline{Z}_g + \overline{V}_s \\ \overline{V}_2 = \overline{I}_2 \cdot \overline{Z}_g + \overline{V}_s \end{cases} \tag{4}$$

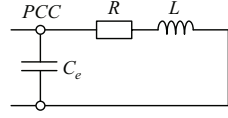$$\overline{V}_1 - \overline{V}_2 = \overline{Z}_g\left(\overline{I}_1 - \overline{I}_2\right) \tag{5}$$

Figure 7. Equivalent grid impedance

Fig. 7 shows the equivalent grid impedance, where R and L are the resistive and the inductive part of the grid impedance. At the fundamental frequency the influence of EMI capacitance C_e over the grid impedance can be neglected: Thus, the relation of the grid impedance Z_g can be written as shown in (6).

$$\overline{Z}_g = R + j\cdot\omega L = \frac{\overline{V}_1 - \overline{V}_2}{\overline{I}_1 - \overline{I}_2} \tag{6}$$

Furthermore, the expressions of the resistance R and inductance L are given in (7) and (8).

The ΔV_q from (8) is considered equal to 0, as the orthogonal voltage system is created artificially for a single-phase system.

$$\begin{cases} R = \mathrm{Re}\left(\dfrac{\overline{V}_1 - \overline{V}_2}{\overline{I}_1 - \overline{I}_2}\right) \\ L = \dfrac{1}{\omega}\cdot\mathrm{Im}\left(\dfrac{\overline{V}_1 - \overline{V}_2}{\overline{I}_1 - \overline{I}_2}\right) \end{cases} \tag{7}$$

$$\begin{cases} R = \dfrac{\Delta V_d\cdot\Delta I_d + \Delta V_q\cdot\Delta I_q}{\Delta I_d^2 + \Delta I_q^2} \\ L = \dfrac{\Delta V_q\cdot\Delta I_d - \Delta V_d\cdot\Delta I_q}{\left[\Delta I_d^2 + \Delta I_q^2\right]\cdot\omega} \end{cases} \tag{8}$$

As it can be seen from (8), the calculation algorithm for the grid impedance is less complicated in contrast with some of the known used algorithms based on more advanced mathematics such as DFT method [13], Prony extrapolation [7].

V. RESULTS

A single-stage grid-connected PV inverter (1.5 kW power range) has been modeled in order to analyze the proposed method performances, as depicted in Fig. 8. The system has been modeled using MATLAB/Simulink. The plant including the LCL filter and the grid impedance has been developed using Simulink transfer functions as shown in Fig. 9. The voltage source inverter (VSI) is controlled using a unipolar PWM to place the harmonics on the high frequency side making them easier to filter. The parameters of the LCL filter are: $L_1 = 1426$ µH, $C_f = 2.2$ µF, $L_2 = 713$ µH. The EMI capacitance C_e is equal to 1uF. The switching frequency of the inverter is 10 kHz. For higher power, the LCL filter needs to be redesigned.

The Proportional Resonant (PR) plus Harmonic Compensator (HC) current controller, as defined in [15], has been used to control the grid current.
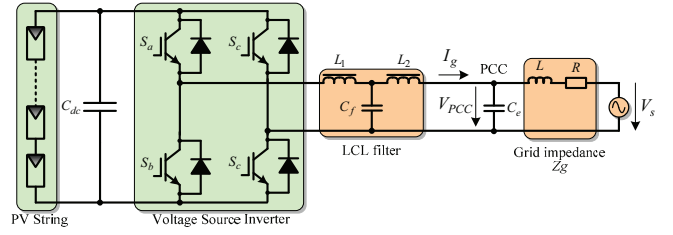

Figure 8. The voltage source PV inverter connected to the grid through an LCL filter
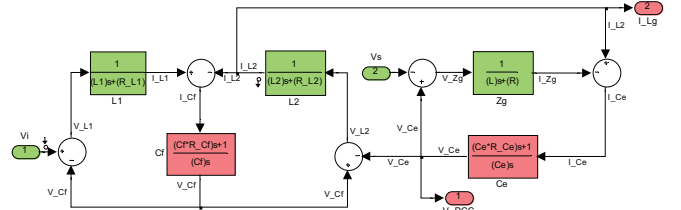

Figure 9. LCL filter and grid impedance modeling

The following parameters were used for the PQ variations: $\Delta P = 100$ W (6.6 % of nominal P), $\Delta Q = 100$ var, $\Delta tP = \Delta tQ = 60$ ms.

A resonant filter has been used (to filter the V_d, I_d, and I_q) in order to get accurate values for the R and L according to (8). The Bode plot and the step response of the resonant filter are presented in Fig. 10a and Fig. 10b. The resonant filter has been designed for a very good filtering without affecting to much the dynamics.
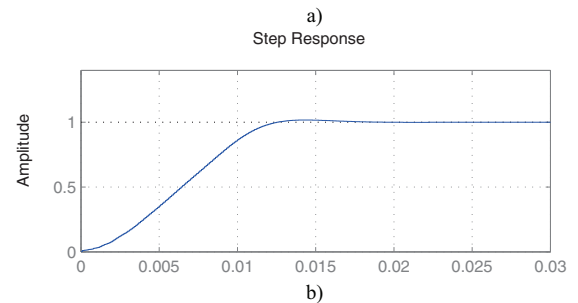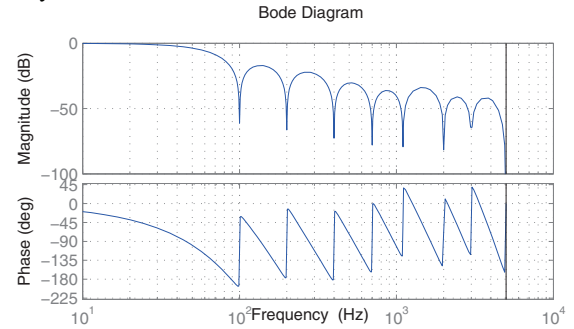

a)

b)
Figure 10. Resonant filter: a) Bode plot and b) Step response

In the following, selected results are presented to validate the proposed method.

The first set of results is obtained for a simultaneous resistive step of 0.1 ohm and an inductive step of 100 uH, in the case of a grid voltage THD equal to 0% (Fig. 11).

a)

b)

c)

d)

e)

f)

g)

h)
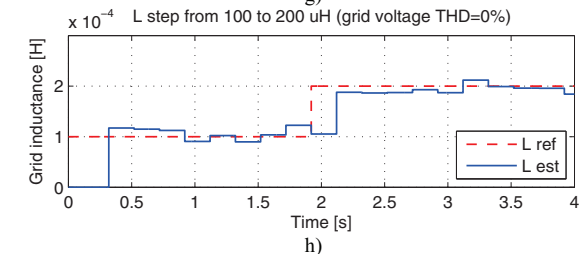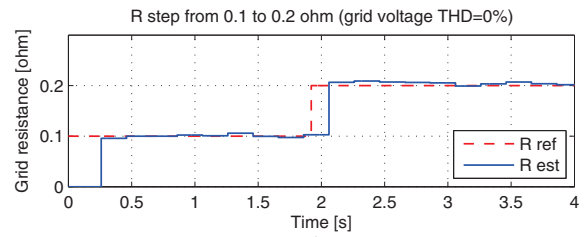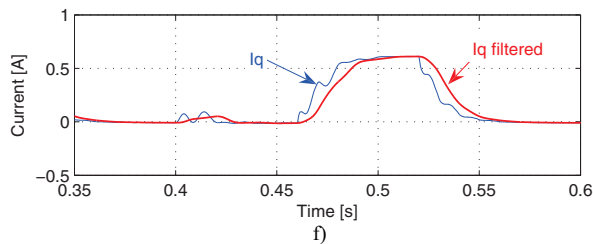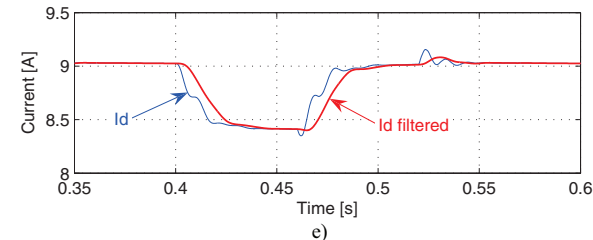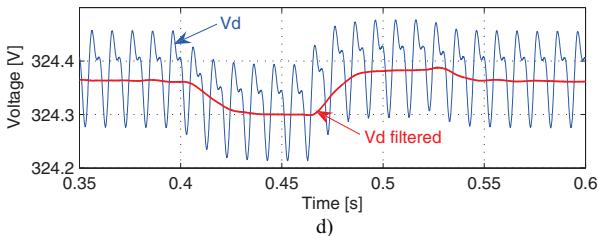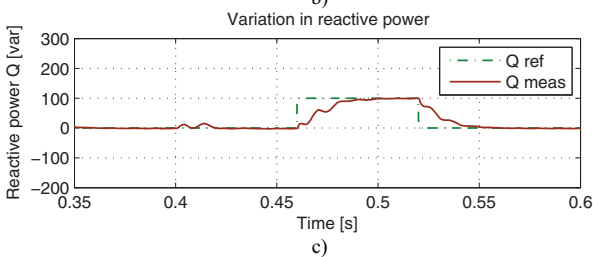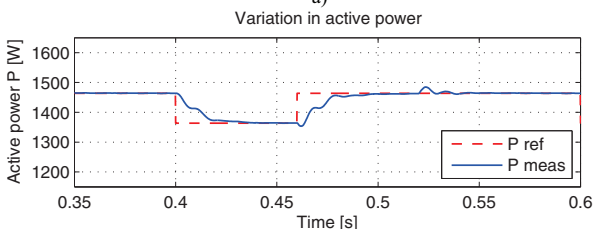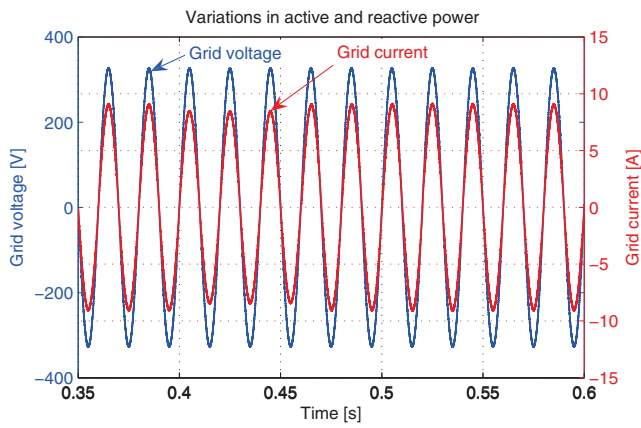
Figure 11. Simultaneous R and L steps (R step from 0.1 to 0.2 ohm and L step from 100 to 200uH, grid voltage THD = 0%)

Fig. 11a shows the behavior of the grid voltage (V_{PCC}) and the grid current (I_g) under PQ variations. The references and the measured values of the active and reactive power are shown in Fig. 11b and Fig.11c. The filtered values of V_d, I_d, and I_q, as shown in Fig. 11d, Fig. 11e and Fig. 11f, are used for solving (8). The estimated values of the resistive and inductive part (R est and L est) of the grid impedance are presented in Fig. 11g and Fig. 11h.

The second set of results is obtained for a simultaneous resistive step of 0.1 ohm and an inductive step of 100 uH, in the case of a grid voltage THD equal to 2.5% (Fig. 12). This is just to show that the harmonics have a minimal impact on the obtained results using the proposed method.

a)

b)

c)

2310

Figure 12. Simultaneous *R* and *L* steps (*R* step from 0.1 to 0.2 ohm and *L* step from 100 to 200uH, grid voltage THD = 2.5%)

Fig. 12a and Fig.12b show the references and the measured values of the active and reactive power. The filtered values of V_d, I_d, and I_q, as shown in Fig. 12c, Fig. 12d and Fig. 12e, are used for solving (8). Comparing the estimated values of the resistive and inductive part (*R est* and *L est*) of the grid impedance (comparing Fig. 11g with Fig. 12f, and Fig 11h with Fig 12g), similar results are obtained.
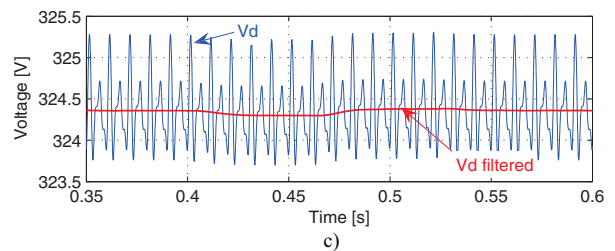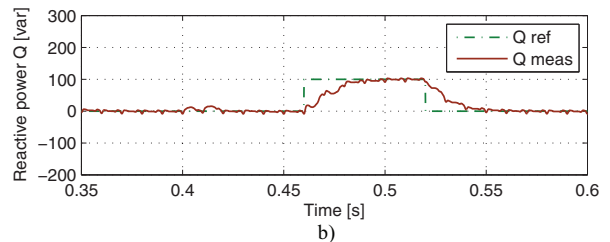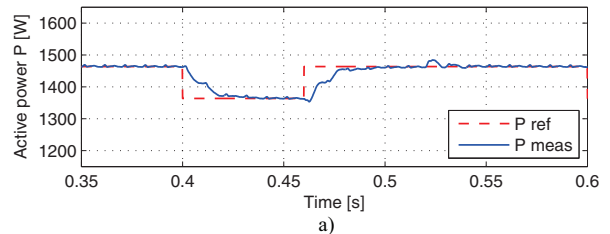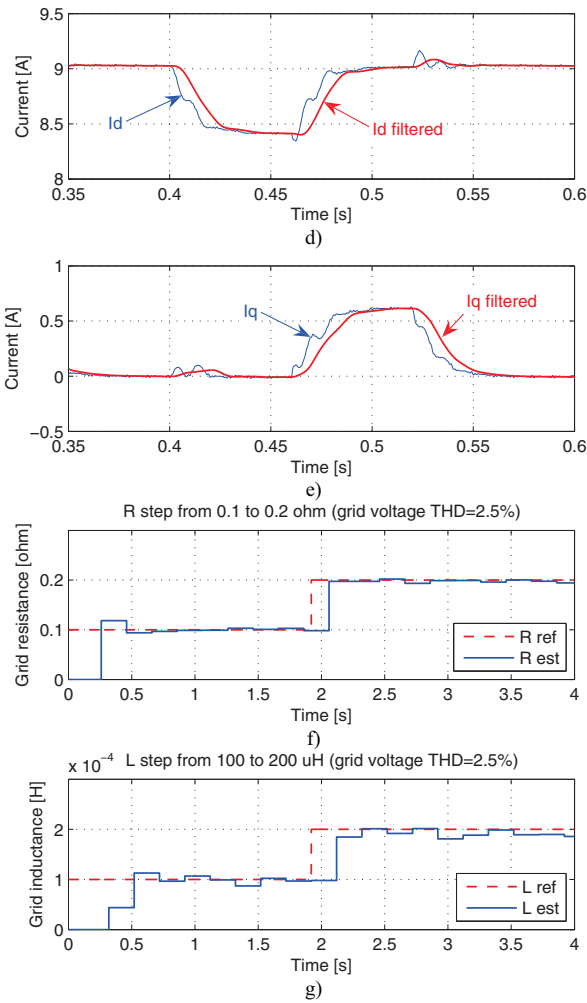
The results presented in Fig. 11 and Fig 12 are obtained using small values of the resistive and inductive part of the grid impedance. This can be the case when the grid converter is connected to the grid without an AC isolation transformer.

Fig. 13 shows the results for the case when the grid converter is connected to the grid through an AC transformer. For this particular case, the following test has been performed: - simultaneous *R* and *L* steps (*R* step from 1 to 2 ohm and *L* step from 2.5 to 5mH, grid voltage THD = 2.5%).

For the compliance with the German standard VDE0126, a resistive step of 1ohm has been performed in the both cases, with (L=100uH) and without (L=2.5mH) an AC isolation transformer. As it can be seen from Fig. 14, the proposed

method using PQ variations successfully fulfill the requirement of the standard VDE0126.
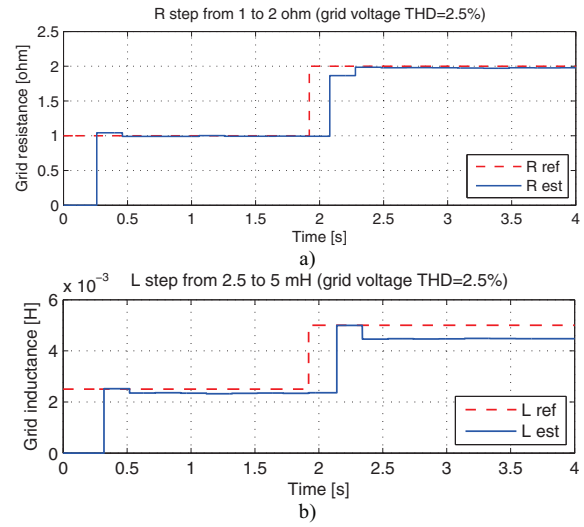
Figure 13. Simultaneous *R* and *L* steps (*R* step from 1 to 2 ohm and *L* step from 2.5 to 5mH, grid voltage THD = 2.5%)
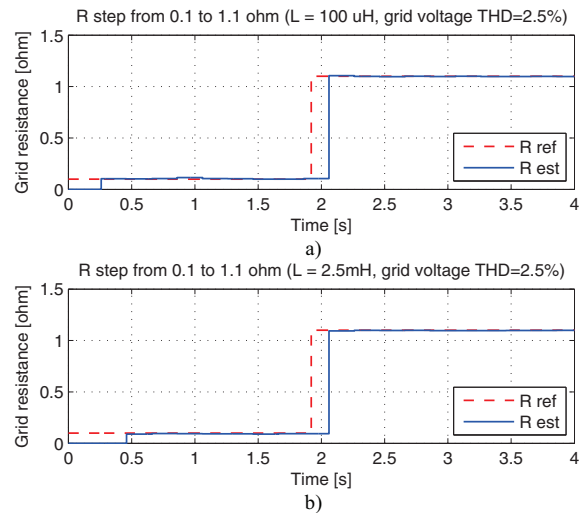
Figure 14. Resistive step of 1ohm (*R* step from 0.1 to 1.1 ohm, grid voltage THD = 2.5%): a) *L*=100uH and b) *L*=2.5mH

VI. CONCLUSIONS

The grid impedance estimation using PQ variations is well suited for both, anti-islanding standard requirements such as the German standard VDE0126 and adaptive control for grid converters due to the fact that the output power of the inverter is less disturbed compare to known active methods.

Moreover, the calculation algorithm for the grid impedance is less complicated in contrast with some of the known used algorithms based on more advanced mathematics such as DFT method, Prony extrapolation. Also, the PQ variation method proved to be robust under harmonics conditions.

However, the implementation of the proposed method necessitates the usage of the PQ control for a single-phase system which can be troublesome in the case of using an inappropriate orthogonal system generation method.

REFERENCES

[1] F. Blaabjerg, Z. Chen, and S.B. Kjaer, "Power electronics as efficient interface in dispersed power generation systems", *IEEE Trans. on Power Electronics,* Vol. 19, No. 5, September 2004, pp. 1184-1194.
[2] *IEEE Standard 929-2000:* IEEE Recommended practice for utility interface of photovoltaic (PV) systems.
[3] *IEEE Standard 1547-2003:* IEEE Standard for interconnecting distributed resources with electric power systems.
[4] A. Woyte, K. De Brabandere, D.V. Dommelen, R. Belmans, and J. Nijs, "International harmonization of grid connection guidelines: adequate requirements for the prevention of unintentional islanding", *Progress in Photovoltaics: Research and Applications 2003,* Vol. 11, pp. 407-424.
[5] T.F. Wu, H.S. Nien, C.L. Shen and T.M. Chen, "A single-phase inverter system for PV power injection and active power filtering with non-linear inductor consideration", *IEEE Trans. on Industry Applications,* Vol. 41, No. 4, July/August 2005, pp. 1075-1083.
[6] T.F. Wu, C.L. Shen, C.H. Chang, J. Chiu, "1~3W grid-connection PV power inverter with partial active power filter", *IEEE Trans. on Aerospace and Electronic Systems,* Vol. 39, No. 2, April 2003, pp. 635-646.
[7] Sumner, M.; Palethorpe, B.; Thomas, D.; Zanchetta, P.; Di Piazza, M.C., "Estimation of power supply harmonic impedance using a controlled voltage disturbance," Power Electronics Specialists Conference, 2001. PESC. 2001 IEEE 32nd Annual, vol.2, pp. 522-527.
[8] Di Piazza, M.C.; Zanchetta, P.; Sumner, M.; Thomas, D.W.P., "Estimation of load impedance in a power system," Harmonics and Quality of Power, 2000. Proceedings. Ninth International Conference on, vol.2, pp. 520-525.
[9] Sumner, M.; Palethorpe, B.; Thomas, D.W.P.; Zanchetta, P.; Di Piazza, M.C., "A technique for power supply harmonic impedance estimation using a controlled voltage disturbance," Power Electronics, IEEE Transactions on , vol.17, no.2, pp. 207-215.
[10] Rhode, J.P.; Kelley, A.W.; Baran, M.E., "Line impedance measurement: a nondisruptive wideband technique," Industry Applications Conference, 1995. Thirtieth IAS Annual Meeting, IAS '95., Conference Record of the 1995 IEEE , vol.3, pp. 2233-2240.
[11] Ishigure, N.; Matsui, K.; Ueda, F., "Development of an on-line impedance meter to measure the impedance of a distribution line," Industrial Electronics, 2001. Proceedings. ISIE 2001. IEEE International Symposium on, vol.1, pp. 549-554.
[12] Tsukamoto, M.; Ogawa, S.; Natsuda, Y.; Minowa, Y.; Nishimura, S., "Advanced technology to identify harmonics characteristics and results of measuring," Harmonics and Quality of Power, 2000. Proceedings. Ninth International Conference on, vol.1, pp., 341-346.
[13] Asiminoaei, L.; Teodorescu, R.; Blaabjerg, F.; Borup, U., "Implementation and Test of an Online Embedded Grid Impedance Estimation Technique for PV Inverters," Industrial Electronics, IEEE Transactions on , vol.52, no.4, pp. 1136- 1144.
[14] Georgakis, D.; Papathanassiou, S.; Hatziargyriou, N.; Engler, A.; Hardt, C., "Operation of a prototype microgrid system based on micro-sources quipped with fast-acting power electronics interfaces," Power Electronics Specialists Conference, 2004. PESC 04. 2004 IEEE 35th Annual , vol.4, pp. 2521- 2526.
[15] M. Liserre, R. Teodorescu, and F. Blaabjerg, "Stability of grid-connected PV inverters with large grid impedance variation," in Proc. IEEE PESC'04, 2004, pp. 4773–4779.
[16] K. O. H. Pedersen, A. H. Nielsen, and N. K. Poulsen, "Short-circuit impedance measurement," Proc. IEE—Generation, Transmission, Distrib., vol. 150, no. 2, pp. 169–174.
[17] B. Palethorpe, M. Sumner, and D. W. P. Thomas, "Power system impedance measurement using a power electronic converter," in Proc. Harmonics and Quality of Power Conf., vol. 1, 2000, pp. 208–213.
[18] K. Klaus-Wilhelm, "Process and Device for Impedance Measuring in AC Networks as Well as Process and Device for Prevention of Separate Networks," German Patent DE19504271 C1/1996.
[19] J.P. Rhode; A.W. Kelley and M.E. Baran, "Complete characterization of utilization-voltage power system impedance using wideband measurement," IEEE Trans. Ind. Appl., vol. 33, no. 6, pp. 1472–1479, Nov./Dec. 1997.
[20] M. Ciobotaru, R. Teodorescu and F. Blaabjerg, "A new single-phase PLL structure based on second order generalized integrator", in Record of IEEE PESC 2006, Jeju, Korea, p. 1511-1516.

[X] Line impedance estimation using active and reactive power variations

by A. V. Timbus, P. Rodriguez, R. Teodorescu, and M. Ciobotaru,
Article published in Proceedings of PESC, 2007, pp. 1273-1279.

Line Impedance Estimation Using Active and Reactive Power Variations

Adrian V. Timbus*, Pedro Rodriguez†, Remus Teodorescu* and Mihai Ciobotaru*

*Aalborg University, Institute of Energy Technology,
DK-9220 Aalborg, Denmark, Email: avt@iet.aau.dk, ret@iet.aau.dk
†Technical University of Catalonia, Electrical Engineering Department,
Colom 1, 08222 - Terrassa-Barcelona, Spain, Email: prodriguez@ee.upc.edu

Abstract— This paper proposes an estimation method of power system impedance based on power variations caused by a distributed power generation system (DPGS) at the point of common coupling (PCC). The proposed algorithm is computationally simple and uses the voltage variations at the point of common coupling (PCC) caused by the variations of the power delivered to utility network to derive the value of grid impedance. Accurate estimation of both resistive and inductive part of the impedance is obtained, as the results presented show.

Index Terms— Line impedance, power variations, distributed generation, grid converter control.

I. INTRODUCTION

THE value of grid impedance is a beneficial information for simulation and prediction of harmonic propagation into the power system. Moreover, with continuous connection and disconnection of loads in utility network, the line impedance value becomes vital for power system management.

Additionally, active filter control can be improved with the knowledge of line impedance value [1]–[3]. Better harmonic rejection as well as improved current controller response are obtained if the value of grid impedance is used in control [1]. Similarly, the gain of controllers for grid tied converters could be adjusted according to the value of the grid impedance ensuring system stability over a broad range of line impedance values.

Estimation of grid impedance is one of the demands for photovoltaic (PV) systems connected into the power system of some European countries for islanding detection purposes [4]. This fact was leading to an intensive research towards grid impedance identification [5]–[11]. Moreover, information about grid impedance would be useful for detection of grid faults and grid unbalance [12]. Additionally, grid impedance information can lead to identification of grid source voltage, hence the power system can be completely characterized.

As grid impedance information could be a valuable information for the control of grid connected systems, this paper proposes a simple method for accurate estimation of both resistive and inductive part of grid impedance. Due to the simplicity of the proposed algorithm and its necessity of using power variations, this method is suitable for embedding in distribution power generation systems based on variable input power, like wind turbines (WT) and photovoltaic (PV) systems.

Next section gives a short classification of existing methods to estimate the value of grid impedance. The method proposed in this work is analyzed in § III, where the equations for calculating the grid impedance as well as the methodology of applying this algorithm are discussed. Further on, the considered system comprising a grid tied converter and its control is discussed, followed by the results obtained in case of grid impedance variation. Different power variations are considered and their affect on the accuracy of detection the impedance value is discussed. Finally, the conclusions are presented in the last section.

II. OVERVIEW OF METHODS

Generally, the methods for grid impedance detection can be classified in two main groups, i.e. passive and active methods.

A. Passive methods

Passive methods are based on monitoring and measurements of grid distortions and based on these variations, the value of grid impedance is estimated. A major drawback of the passive methods is that the grid variations might not be sufficiently large to be accurately measured, hence failing to give an exact estimation of the grid impedance.

B. Active methods

Active methods are deliberately creating a disturbance at the point of common coupling (PCC) and the grid impedance calculation is based on grid response to the distortion. The most common disturbances can be summarized as consisting of [8]:

- *current pulse transient* usually applied at zero crossing of the voltage and produces a voltage transient in the grid based on which the grid impedance can be estimated.
- *noncharacteristic subharmonics (inter-harmonics)* injected into the utility network which give the possibility of calculating the line impedance at a particular frequency.
- *power variations* of both active and reactive power produce grid voltage variations based on which the line impedance can be estimated.

In [13], [14] a current spike of 60-100 A is deliberately injected at the point of common coupling by a grid tied power converter. Based on the voltage response to this disturbance,

the grid impedance value is determined using Fourier transform. The influence of non-linear loads connected close to the point of common coupling (PCC) is also addressed and as a consequence additional signal processing method is necessary in order to obtain accurate results.

In [5]–[8], [15] injection of inter-harmonic current is used to derived the grid impedance at that particular frequency. The value of inter-harmonic has to be chosen close to the fundamental grid frequency in order to state that the identified value of grid impedance can be approximated for fundamental frequency too. Due to the fact that the selected inter-harmonic is unique in the power system and is generated by the power generation system, this particular method would allow the connection of more than one generation unit on the same grid because their synchronization in respect to the inter-harmonic injection is possible [8], [16].

III. PROPOSED METHOD

This work proposes a method for detecting the grid impedance using variations of both active and reactive power generated by a grid connected generation system. The references for active and reactive power are intentionally varied in order to allow detection of both resistive and inductive parts of the line impedance. The proposed algorithm is detailed in the following.

A. Algorithm analysis

Unlike the method presented in [5] and [15], the proposed method works at a 50 Hz frequency, i.e. the fundamental component of the power is varying. Varying both active and/or reactive power it is possible to estimate the resistive and inductive parts of the impedance. The proposed method is based on the detection of dq components of grid voltage and current respectively, which are further reported to an arbitrary rotating reference frame synchronized with the grid angular frequency.

Considering a distributed generation system connected to the power grid as Fig. 1 illustrates, the phase angle of the arbitrary reference frame can be derived from the grid frequency information:

$$\theta = \int \omega \, dt \tag{1}$$

Because the voltage at the point of common coupling in two operating points can be written as:

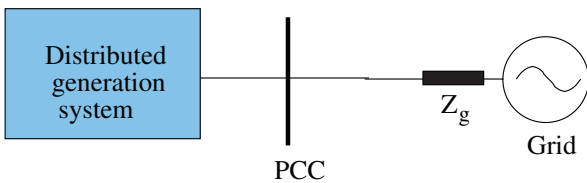$$\vec{V}_{pcc1} = \vec{V}_s(1) - Z \cdot \vec{i}_{pcc1} \tag{2a}$$

Fig. 1.   Distributed power generation system connected to utility grid.

$$\vec{V}_{pcc2} = \vec{V}_s(2) - Z \cdot \vec{i}_{pcc2} \tag{2b}$$

where *1* and *2* are representing the two different sampling instants, the line impedance can be calculated using the variations in both current and voltage at the point of common coupling:

$$Z = \frac{\Delta \vec{V}_{pcc}}{\Delta \vec{i}_{pcc}} \tag{3}$$

where:

$$\Delta \vec{V}_{pcc} = \vec{V}_{pcc}(1) - \vec{V}_{pcc}(2) \tag{4a}$$

$$\Delta \vec{i}_{pcc} = \vec{i}_{pcc}(1) - \vec{i}_{pcc}(2) \tag{4b}$$

are the voltage and current variation respectively at the point of common coupling. It should be noted that the above equations are valid only if the source voltage and grid impedance are not changing between the two sample instants, e.g. $\vec{V}_s(1) = \vec{V}_s(2)$.

The module and phase angle of the voltage at the PCC can be calculated from its $\alpha\beta$ components:

$$|V_{pcc1,2}| = \sqrt{V_\alpha^2 + V_\beta^2} \tag{5a}$$

$$\theta_{v_{pcc1,2}} = tan^{-1}\frac{V_\beta}{V_\alpha} \tag{5b}$$

Further on, the dq components of the grid voltage for both sampling instants can be derived as:

$$V_{d1,2} = |V_{pcc1,2}| \, cos(\theta_{V_{pcc1,2}} - \theta) \tag{6a}$$

$$V_{q1,2} = |V_{pcc1,2}| \, sin(\theta_{V_{pcc1,2}} - \theta) \tag{6b}$$

In this way, the voltage at the point of common coupling is always referring to a general rotating reference frame provided by θ. Based on the dq components of both voltage and current, the resistive and inductive part of the impedance can be calculated like:

$$R = \frac{(V_{q1} - V_{q2}) \cdot (I_{q1} - I_{q2}) + (V_{d1} - V_{d2}) \cdot (I_{d1} - I_{d2})}{(I_{q1} - I_{q2})^2 + (I_{d1} - I_{d2})^2} \tag{7a}$$

$$\omega L = \frac{(V_{d1} - V_{d2}) \cdot (I_{q1} - I_{q2}) - (V_{q1} - V_{q2}) \cdot (I_{d1} - I_{d2})}{(I_{q1} - I_{q2})^2 + (I_{d1} - I_{d2})^2} \tag{7b}$$
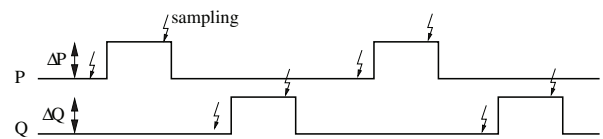

Fig. 2.   Active and reactive power variations used for line impedance detection.

Fig. 3. Plant model developed using PLECS toolbox within MATLAB®/Simulink®

B. Power variations

As (3) shows, grid voltage and current variations are necessary to estimate the value of the impedance. This is convenient for power generation systems based on renewable energies such as wind or photovoltaic systems which have variable input power. Considering that the variations of input power are reflected into the power delivered to the utility grid, these could be used to derive the necessary voltages and currents in two different operating conditions. However, with the introduction of variable speed wind turbine technology, the wind power variations are very much attenuated at the output of the turbine, hence deliberately power variations in dc-link might be necessary in order to obtain the two working points at the point of common coupling.

As the proposed method shows, variations of reactive power are necessary in order to create phase angle deviation $\Delta\theta$ at the point of common coupling. According to interconnection demands for power generation systems, wind turbine (WT) systems are allowed to have reactive power variation at PCC

of about 10% of nominal active power under normal operation conditions [17]. On the contrary, the photovoltaic (PV) systems should operate at unity power factor all the time, hence the reactive power oscillations necessary for line impedance detections should be small and for a short period of time. Therefore, this algorithm is more suited for wind power applications rather then photovoltaic, but using short term power variations would allow for implementation in PV systems as well.

In this work, only the grid side converter of a WT system having full scale power converter as grid interface is considered and both active and reactive power variations are made intentionally in periodical steps. Fig. 2 illustrates a possible way to vary the generated output power of the system and the sampling instants for both voltage and currents. The difference between the samplings at the instant when $P^* = P$ and at the instant when $P^* = P + \Delta P$ (and similarly for Q) yields $\Delta\vec{V}_{pcc}$ and $\Delta\vec{i}_{pcc}$ necessary for calculating the resistive and inductive part of the impedance.

Fig. 4. Control structure of the grid side converter having an algorithm for line impedance estimation.

1275

C. Discussion

Setting a proper ΔP and ΔQ and an accurate sampling interval between samples, the proposed algorithm is capable to estimate the value for both R and L with a good precision, as later seen in the § IV. However, should be noticed here that periodical oscillations of grid voltage at the PCC is subject to flicker, hence further considerations are necessary to avoid this.

In case of large wind power installations, the voltage variations at the point of common coupling ΔV_{pcc} might produce flicker, hence the entire installation is not complying with the power quality standards [18]. Because the proposed algorithm does not simply calculate the d and q components of both voltage and currents but uses an arbitrary rotating reference frame to refer to, it is possible to control the reactive power in a way that the magnitude of the voltage vector at PCC will not change. In this case, the voltage variation are mitigated to phase angle variation $\Delta\theta_{V_{pcc}}$:

$$V_{d1,2} = |V_{pcc1,2}| \cos(\theta_{V_{pcc1,2}} - \theta) \quad (8a)$$

$$|V_{pcc1}| = |V_{pcc2}| \quad (8b)$$

$$\theta_{V_{pcc1}} \neq \theta_{V_{pcc2}} \Longrightarrow V_{d1} \neq V_{d2} \quad (8c)$$

The scope of this work is to present and validate the basic method, hence the extra feature of having droop control on top of reactive power control will be discussed in another work.

IV. RESULTS AND VALIDATION

A. Simulation system

In order to validate the working principle of the proposed method, a simulation model was created in MATLAB®/Simulink. The model comprises two main parts, one containing the DPGS grid side power converter control and another containing the plant denoted by an LCL filter attached to the power converter, the grid impedance and the grid voltage source. For a better modeling of the plant, PLECS Toolbox [19] has been adopted in this work. This is a special Simulink toolbox which comprises models for electrical components such as resistor, inductance, capacitance or power switches, etc. hence being easier to modify the grid impedance and test the proposed method. Fig. 3 shows the model of the plant realized using PLECS and one can notice the easiness of adding or removing impedance in the grid.

The simulation model emulates the physical system available in the laboratory. In this case, the power converter is connected to a low voltage network (400 V) through a three phase Δy transformer having the resistance $R_t = 1\ \Omega$ and inductance $L_t = 2\ mH$. Using a Norma-Unilap 100 XE device with an accuracy of 5%, the grid impedance has been measured to be $Z_g = 0.22\ \Omega$ pure resistive. Since the PCC is defined on the secondary side of the transformer, the total impedance to be detected by the proposed method is comprising the grid and the transformer impedance.
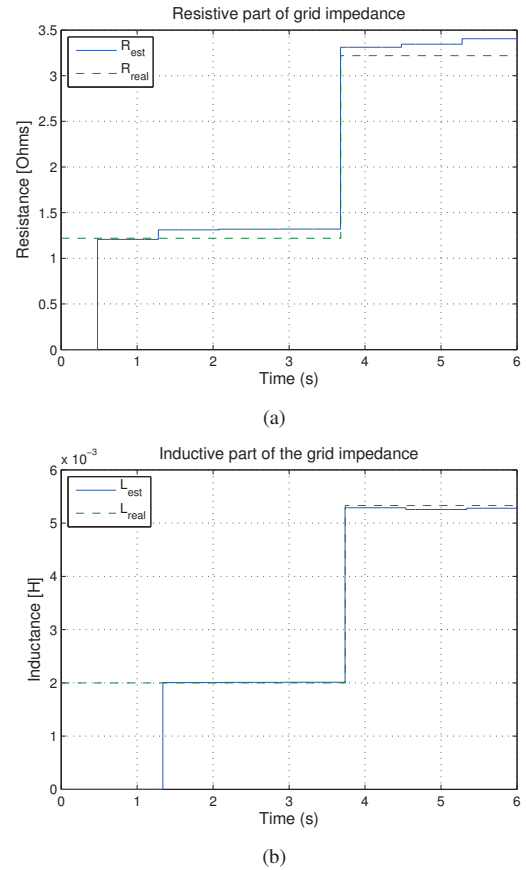

(a)

(b)

Fig. 5. Estimation of both resistive (a) and inductive (b) parts of the grid impedance in the situation of 10% active power variations at PCC.

B. Control structure

The control of grid side converter considered here is a traditional cascaded two loops control for PWM VSI converters, as depicted in Fig. 4. The outer loop comprises a controller for the dc-link voltage (and hence the active power
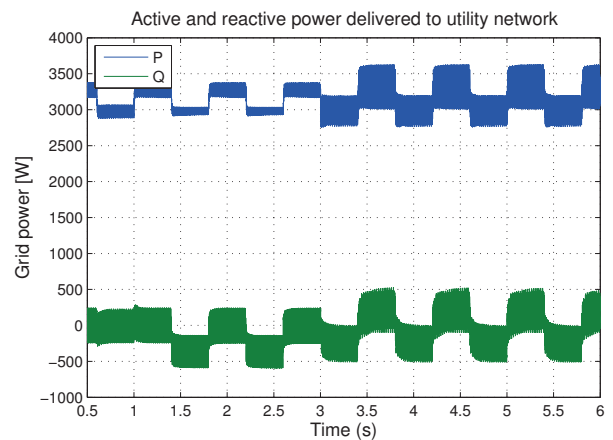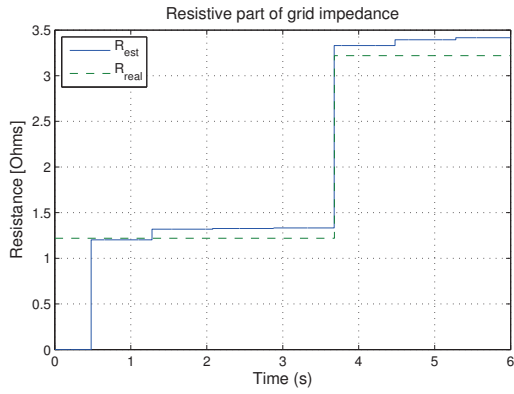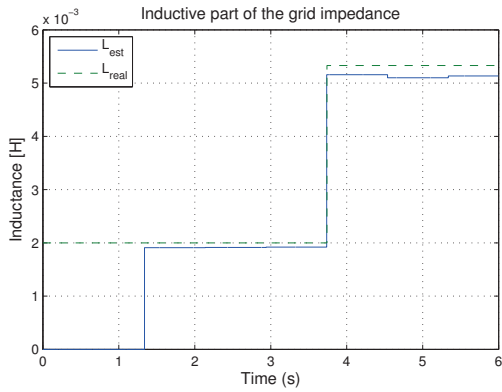

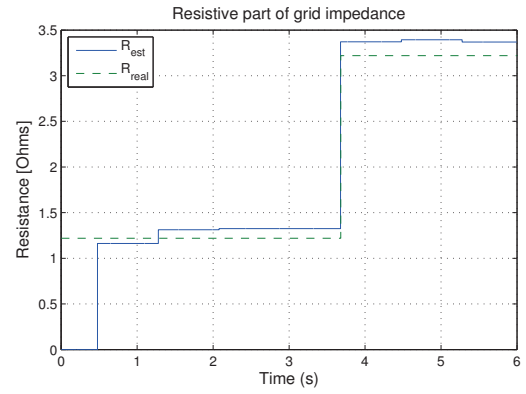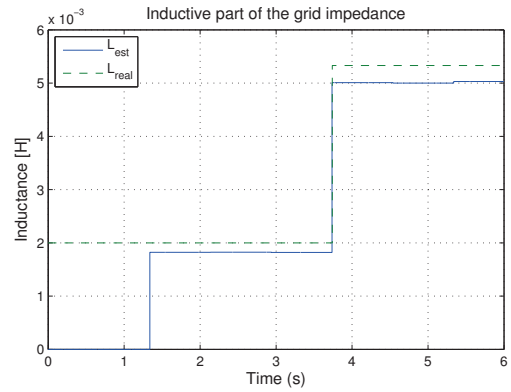Fig. 6. Active and reactive power delivered to utility network in case of 10% active power variation.

Fig. 7. Estimation of both resistive (a) and inductive (b) parts of the grid impedance in the situation of 5% active power variations at PCC.

Fig. 8. Estimation of both resistive (a) and inductive (b) parts of the grid impedance in the situation of 1% active power variations at PCC.

P) and a controller for the reactive power Q. The inner loop employs two proportional-resonant (PR) controllers for current regulation and it is implemented in $\alpha\beta$ stationary reference frame. Additionally to the controller for fundamental current (50 Hz), harmonic compensator (HC) for 5th and 7th harmonics are used. A phase-locked loop (PLL) system implemented in $\alpha\beta$ frame [20] is used to obtain the phase angle of the grid. The proposed algorithm for line impedance detection is based on (7a) and (7b) and has as inputs the dq components of both grid voltage and currents.

The reactive power oscillations are simply added to the reactive power reference while the active power oscillations are created by oscillating the power in dc-link.

C. Validation of method by simulation results

Simulation results in case of line impedance variations (both resistive and inductive) are presented in the following. To test the effectiveness of the proposed algorithm, large variations in both R and L have been made. An additional series impedance of $Z_a = 2 + j1.03 \ \Omega$ is connected into the circuit. The identification accuracy related to four different levels of active power variations is pursued. The reactive power variations are set to 300 VARs in each of the cases. The duration of power variation is kept long enough to give the system the possibility

to reach steady-state conditions.

1) Active power variation of 10%: Fig. 5 depicts the estimation of both active and reactive parts of grid impedance in situation when $\Delta P = 10\%$. As can be observed, there is a good agreement between the real impedance in the grid and the one identified using the proposed algorithm.

2) Active power variation of 5%: As illustrated in Fig. 7, the accuracy in detecting the exact value of grid impedance drops when $\Delta P = 5\%$. Small discrepancy can be observed between the estimated and the real signal for both resistive and inductive part of impedance. Table I shows the actual value of accuracy for both R and L in case of considered power variations.

3) Active power variation of 1%: Similar behavior as for previous case is noted also in situation when active power variations are down to 1% of the nominal power of the converter. In this case, the method estimates the resistive part of the impedance with an accuracy of less than 6% while the inductive part is estimated with an accuracy of about 5%.

4) Active power variation of 0.1%: If just 0.1% of nominal power is varied at the point of common coupling, the estimation of resistive and inductive parts of grid impedance is as illustrated in Fig. 9. According to data in Table I, the accuracy does not drop considerably, hence small power variations can
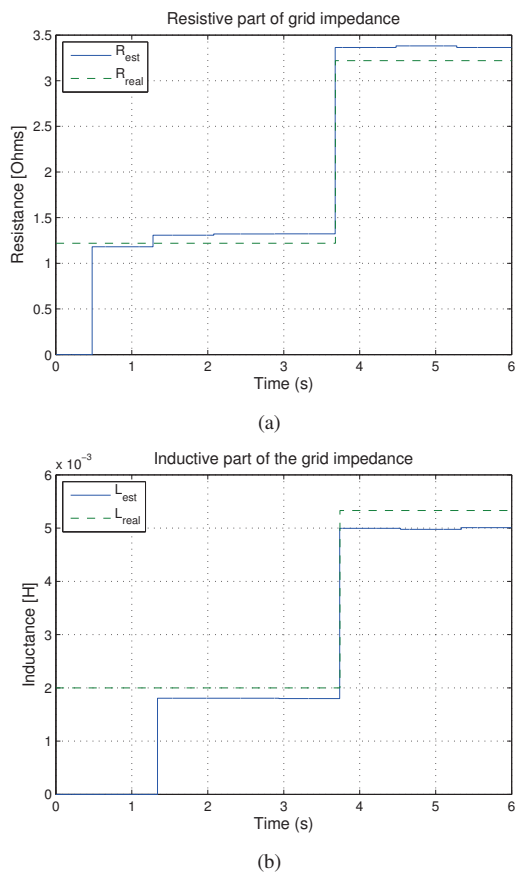
(a)

(b)

Fig. 9. Estimation of both resistive (a) and inductive (b) parts of the grid impedance in the situation of 0.1% active power variations at PCC.

ΔP	Accuracy R	Accuracy L
10 %	3.89 %	1.32 %
5 %	5.30 %	6.40 %
1 %	5.84 %	5.01 %
0.1 %	4.80 %	6.20 %

power generation systems based on variable input power such as wind turbines or photovoltaic systems. The presented results validate the effectiveness of the proposed method when large variations on both resistive and inductive part of grid impedance occur. The accuracy of this method is comparable with that of commercial products for measuring impedance available on the market today.

also be used to obtain accurate enough results.

V. CONCLUSION

This paper proposes a method for estimating the resistive and inductive part of the grid impedance based on variation of the delivered power into the network. The proposed algorithm is computationally simple and fits well into the control of
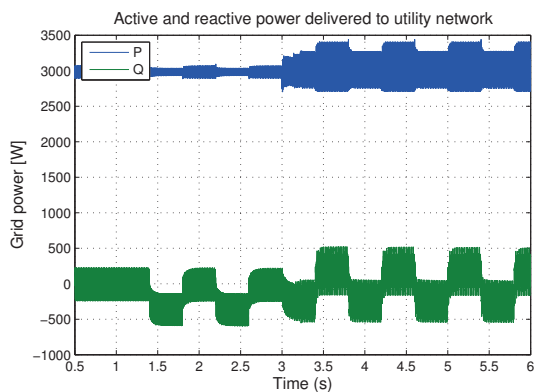

Fig. 10. Active and reactive power delivered to utility network in case of 0.1% active power variation.

REFERENCES

[1] A. Tarkiainen, R. Pollanen, M. Niemela, and J. Pyrhonen, "Identification of grid impedance for purposes of voltage feedback active filtering," *IEEE Power Electronics Letters*, vol. 2, no. 1, pp. 6–10, 2004.

[2] M. Sumner, B. Palethorpe, and D. Thomas, "Impedance measurement for improved power quality-part 2: a new technique for stand-alone active shunt filter control," *IEEE Trans. on Power Delivery*, vol. 19, no. 3, pp. 1457–1463, 2004.

[3] V. Diana, M. Sumner, P. Zanchetta, and M. Marinelli, "Non-invasive power system impedance monitoring for improved power quality," in *Power Electronics, Machines and Drives, 2004. (PEMD 2004). Second International Conference on (Conf. Publ. No. 498)*, vol. 1, 31 March-2 April 2004, pp. 265–268Vol.1.

[4] DIN and VDE, "Automatic disconnection device between a generator and the public low-voltage grid," Standard, 2005.

[5] L. Asiminoaei, R. Teodorescu, F. Blaabjerg, and U. Borup, "A new method of on-line grid impedance estimation for PV inverters," in *Proc. of APEC'04*, vol. 3, 2004, pp. 1527–1533.

[6] ——, "A digital controlled PV-inverter with grid impedance estimation for ENS detection," *IEEE Trans. on Power Electronics*, vol. 20, no. 6, pp. 1480–1490, 2005.

[7] A. V. Timbus, R. Teodorescu, F. Blaabjerg, and U. Borup, "Online grid measurement and ENS detection for PV inverter running on highly inductive grid," *IEEE Power Electronics Letters*, vol. 2, no. 3, pp. 77–82, 2004.

[8] F. Bertling and S. Soter, "A novel converter integrable impedance measuring method for islanding detection in grids with widespread use of decentral generation," in *Power Electronics, Electrical Drives, Automation and Motion, 2006. SPEEDAM 2006. International Symposium on*, May, 23rd - 26th, 2006, pp. 503–507.

[9] IEA-PVPS, "Evaluation of islanding detection methods for photovoltaic utility interactive power systems," IEA-PVPS, http://www.iea-pvps.org, Online report T5-09, March 2002. [Online]. Available: http://www.oja-services.nl/iea-pvps/products/download/rep5_09.pdf

[10] F. De Mango, M. Liserre, A. Dell'Aquila, and A. Pigazo, "Overview of anti-islanding algorithms for pv systems. part i: Passive methods," in *12th International Power Electronics and Motion Control Conference*, Aug. 2006, pp. 1878–1883.

[11] F. De Mango, M. Liserre, and A. Dell'Aquila, "Overview of Anti-Islanding Algorithms for PV Systems. Part II: ActiveMethods," in *12th International Power Electronics and Motion Control Conference*, Aug. 2006, pp. 1884–1889.

[12] M. H. J. Bollen, *Understanding Power Quality Problems: Voltage Sags and Interruptions*. IEEE Press, 2002.

[13] B. Palethorpe, M. Sumner, and D. Thomas, "Power system impedance measurement using a power electronic converter," in *Proc. of Harmonics and Quality of Power, 2000*, vol. 1, Orlando, FL, 2000, pp. 208–213.

[14] ——, "System impedance measurement for use with active filter control," in *Power Electronics and Variable Speed Drives, 2000*, London, 2000, pp. 24–28.

[15] A. V. Timbus, R. Teodorescu, F. Blaabjerg, and U. Borup, "ENS detection algorithm and its implementation for PV inverters," *IEE Proceedings- Electric Power Applications*, vol. 153, no. 2, pp. 206–212, 2006.

[16] A. Timbus, R. Teodorescu, F. Blaabjerg, and U. Borup, "Online grid impedance measurement suitable for multiple PV inverters running in parallel," in *Proc. of APEC '06*, 19-23 March 2006, p. 5pp.

[17] Eltra and Elkraft, "Wind turbines connected to grids with voltage below 100 kV," http://www.eltra.dk, 2004.

[18] IEC, "Electromagnetic compatibility (EMC) - Part 4: Testing and measurement techniques, Section 15: Flickermeter - Functional and design specifications," International Electrotechnical Commission, Tech. Rep. 61000-4-15, 1997.

[19] Plexim GmbH, "PLECS Toolbox," http://www.plexim.com, 2007. [Online]. Available: http://www.plexim.com

[20] P. Rodriguez, R. Teodorescu, I. Candela, A. V. Timbus, and F. Blaabjerg, "New positive-sequence voltage detector for grid synchronization of power converters under faulty grid conditions," in *Proc. of PESC'06*, 2006.

[XI] Power electronics and control of renewable energy systems

Power Electronics and Control of Renewable Energy Systems

F. Iov, M. Ciobotaru, D. Sera, R. Teodorescu, F. Blaabjerg

Aalborg University, Institute of Energy Technology
Pontoppidanstraede 101, DK-9220 Aalborg East, Denmark
fi@iet.aau.dk, mpc@iet.aau.dk, des@iet.aau.dk, ret@iet.aau.dk, fbl@iet.aau.dk

Abstract – **The global electrical energy consumption is still rising and there is a demand to double the power capacity within 20 years. The production, distribution and use of energy should be as technological efficient as possible and incentives to save energy at the end-user should also be set up. Deregulation of energy has in the past lowered the investment in larger power plants, which means the need for new electrical power sources may be very high in the near future. Two major technologies will play important roles to solve the future problems. One is to change the electrical power production sources from the conventional, fossil (and short term) based energy sources to renewable energy resources. Another is to use high efficient power electronics in power generation, power transmission/distribution and end-user application. This paper discuss some of the most emerging renewable energy sources, wind energy and photovoltaics, which by means of power electronics are changing from being minor energy sources to be acting as important power sources in the energy system.**

I. INTRODUCTION

In classical power systems, large power generation plants located at adequate geographical places produce most of the power, which is then transferred towards large consumption centers over long distance transmission lines. The system control centers monitor and regulate the power system continuously to ensure the quality of the power, namely frequency and voltage. However, now the overall power system is changing, a large number of dispersed generation (DG) units, including both renewable and non-renewable sources such as wind turbines, wave generators, photovoltaic (PV) generators, small hydro, fuel cells and gas/steam powered Combined Heat and Power (CHP) stations, are being developed [1], [2] and installed. A wide-spread use of renewable energy sources in distribution networks and a high penetration level will be seen in the near future many places. E.g. Denmark has a high power capacity penetration (> 20%) of wind energy in major areas of the country and today 18% of the whole electrical energy consumption is covered by wind energy. The main advantages of using renewable energy sources are the elimination of harmful emissions and inexhaustible resources of the primary energy. However, the main disadvantage, apart from the higher costs, e.g. photovoltaic, is the uncontrollability. The availability of renewable energy sources has strong daily and seasonal patterns and the power demand by the consumers could have a very different characteristic. Therefore, it is difficult to operate a power system installed with only renewable generation units due to the characteristic differences and the high uncertainty in the availability of the renewable energy sources. This is further strengthened as no real large energy storage systems exist.

The wind turbine technology is one of the most emerging renewable energy technologies. It started in the 1980'es with a few tens of kW production power to today with multi-MW size wind turbines that are being installed. It also means that wind power production in the beginning did not have any impact on the power system control but now due to their size they have to play an active part in the grid. The technology used in wind turbines was in the beginning based on a squirrel-cage induction generator connected directly to the grid. By that power pulsations in the wind are almost directly transferred to the electrical grid. Furthermore there is no control of the active and reactive power, which typically are important control parameters to regulate the frequency and the voltage. As the power range of the turbines increases those control parameters become more important and it is necessary to introduce power electronics [3] as an interface between the wind turbine and the grid. The power electronics is changing the basic characteristic of the wind turbine from being an energy source to be an active power source. The electrical technology used in wind turbine is not new. It has been discussed for several years [6]-[50] but now the price pr. produced kWh is so low, that solutions with power electronics are very attractive.

This paper will first discuss the basic development in power electronics and power electronic conversion. Then different wind turbine configurations will be explained both aerodynamically and electrically. Also different control methods will be shown for a wind turbine. They are now also installed in remote areas with good wind conditions (off-shore, on-shore) and different possible configurations are shown and compared. Next the PV-technology is discussed including the necessary basic power electronic conversion. Power converters are given and more advanced control features described. Finally, a general technology status of the wind power and the PV technology is presented demonstrating still more efficient and attractive power sources for the future.

II. Modern Power Electronics

Power electronics has changed rapidly during the last thirty years and the number of applications has been increasing, mainly due to the developments of the semiconductor devices and the microprocessor technology. For both cases higher performance is steadily given for the same area of silicon, and at the same time they are continuously reducing in price. A typical power electronic system, consisting of a power converter, a load/source and a control unit, is shown in Fig. 1.
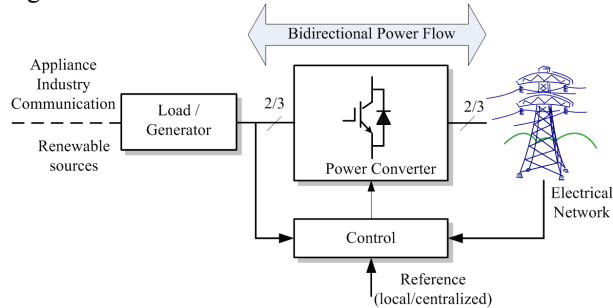

Fig. 1. Power electronic system with the grid, load/source, power converter and control.

The power converter is the interface between the load/generator and the grid. The power may flow in both directions, of course, dependent on topology and applications.

Three important issues are of concern using such a system. The first one is reliability; the second is efficiency and the third one is cost. For the moment the cost of power semiconductor devices is decreasing 1÷5 % every year for the same output performance and the price pr. kW for a power electronic system is also decreasing. An example of a mass-produced and high competitive power electronic system is an adjustable speed drive (ASD). The trend of weight, size, number of components and functions in a standard Danfoss Drives A/S frequency converter can be seen in Fig. 2. It clearly shows that power electronic conversion is shrinking in volume and weight. It also shows that more integration is an important key to be competitive as well as more functions become available in such a product.
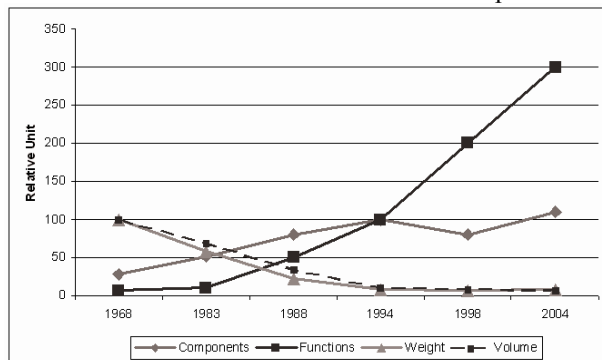

Fig. 2. Development of standard adjustable speed drives for the last four decades.

The key driver of this development is that the power electronic device technology is still undergoing important progress.

Fig. 3 shows different power devices and the areas where the development is still going on.
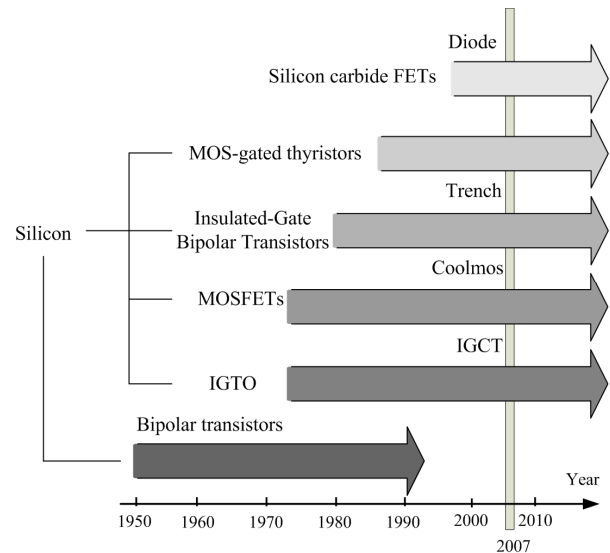

Fig. 3. Development of power semiconductor devices in the past and in the future [36].

The only power device which is not under development any more is the silicon-based power bipolar transistor because MOS-gated devices are preferable in the sense of easy control. The breakdown voltage and/or current carrying capability of the components are also continuously increasing. Important research is going on to change the material from silicon to silicon carbide, which may dramatically increase the power density of power converters.

III. Wind Energy conversion

Wind turbines capture power from the wind by means of aerodynamically designed blades and convert it to rotating mechanical power. The number of blades is normally three. As the blade tip-speed should be lower than half the speed of sound the rotational speed will decrease as the radius of the blade increases. For multi-MW wind turbines the rotational speed will be 10-15 rpm. The most weight efficient way to convert the low-speed, high-torque power to electrical power is to use a gear-box and a standard fixed speed generator as illustrated in Fig. 4.
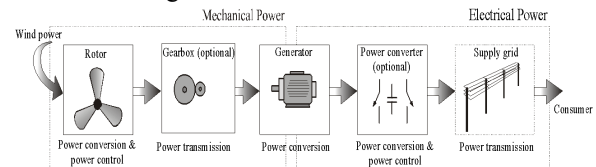

Fig. 4. Converting wind power to electrical power in a wind turbine [19].

The gear-box is optional as multi-pole generator systems are possible solutions. Between the grid and the generator a power converter can be inserted.

The possible technical solutions are many and a technological roadmap starting with wind energy/power and converting the mechanical power into electrical power is shown in Fig. 5. The electrical output can either be ac or dc. In the last case a power converter will be used as interface to the grid.
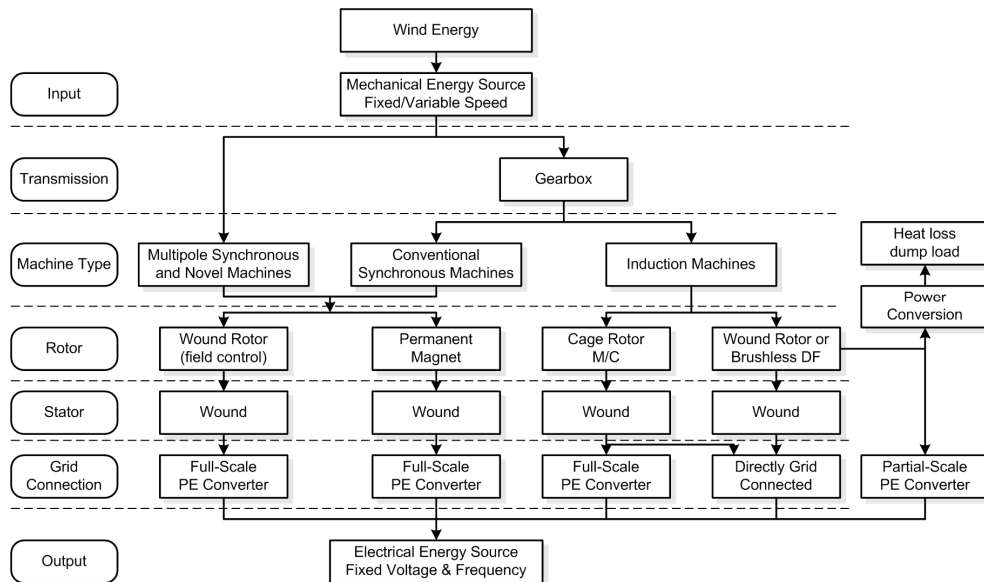
Fig. 5. Technological roadmap for wind turbine's technology [3].

A. Control methods for wind turbines

The development in wind turbine systems has been steady for the last 25 years and four to five generations of wind turbines exist and it is now proven technology. It is important to be able to control and limit the converted mechanical power at higher wind speed, as the power in the wind is a cube of the wind speed. The power limitation may be done either by stall control (the blade position is fixed but stall of the wind appears along the blade at higher wind speed), active stall (the blade angle is adjusted in order to create stall along the blades) or pitch control (the blades are turned out of the wind at higher wind speed) [6], [7]. The basic output characteristics of these three methods of controlling the power are summarized in Fig. 6.
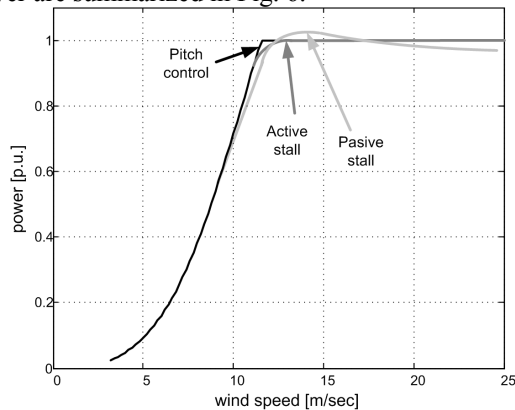

Fig. 6. Power characteristics of different fixed speed wind turbine systems.

Another control variable in wind turbine system is the speed. Based on this criterion the wind turbines are classified into two main categories [6], [7]; namely fixed speed and variable speed wind turbines respectively.

A fixed speed wind turbine has the advantages of being simple, robust, reliable, well proven and with low cost of the electrical parts. Its direct drawbacks are the uncontrollable reactive power consumption, mechanical stress and limited power quality control. Due to its fixed speed operation, wind speed fluctuations are converted to mechanical torque fluctuations,

beneficially reduced slightly by small changes in generator slip, and transmitted as fluctuations into electrical power to the grid. The power fluctuations can also yield large voltage fluctuations in the case of a weak grid and thus, significant line losses [6], [7].

The variable speed wind turbines are designed to achieve maximum aerodynamic efficiency over a wide range of wind speed. By introducing the variable speed operation, it is possible to continuously adapt (accelerate or decelerate) the rotational speed of the wind turbine to the wind speed v, in such a way that tip speed ratio is kept constant to a predefined value corresponding to the maximum power coefficient. Contrary to a fixed speed system, a variable speed system keeps the generator torque nearly constant, the variations in wind being absorbed by the generator speed changes.

Seen from the wind turbine point of view, the most important advantages of the variable speed operation compared to the conventional fixed speed operation are: reduced mechanical stress on the mechanical components such as shaft and gearbox, increased power capture and reduced acoustical.

Additionally, the presence of power converters in wind turbines also provides high potential control capabilities for both large modern wind turbines and wind farms to fulfill the high technical demands imposed by the grid operators [6], [7], [8] and [23], such as: controllable active and reactive power (frequency and voltage control); quick response under transient and dynamic power system situations, influence on network stability and improved power quality.

B. Wind Turbine Concepts

The most commonly applied wind turbine designs can be categorized into four wind turbine concepts. The main differences between these concepts concern the generating system and the way in which the aerodynamic efficiency of the rotor is limited during above the rated value in order to prevent overloading. These concepts are presented in detail in the following paragraphs.

1) Fixed Speed Wind Turbines (WT Type A)

This configuration corresponds to the so called Danish concept that was very popular in 80's. This wind turbine is fixed speed controlled machine, with asynchronous squirrel cage induction generator (SCIG) directly connected to the grid via a transformer as shown in Fig. 7.
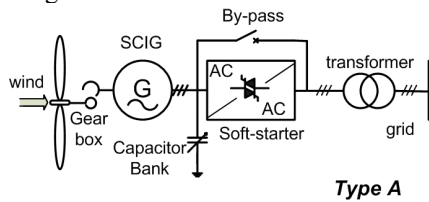

Type A

Fig. 7. Fixed speed wind turbine with directly grid connected squirrel-cage induction generator.

This concept needs a reactive power compensator to reduce (almost eliminate) the reactive power demand from the turbine generators to the grid. It is usually done by continuously switching capacitor banks following the production variation (5-25 steps) Smoother grid connection occurs by incorporating a soft-starter. Regardless the power control principle in a fixed speed wind turbine, the wind fluctuations are converted into mechanical fluctuations and further into electrical power fluctuations. These can yield to voltage fluctuations at the point of connection in the case of a weak grid. Because of these voltage fluctuations, the fixed speed wind turbine draws varying amounts of reactive power from the utility grid (in the case of no capacitor bank), which increases both the voltage fluctuations and the line losses.

Thus, the main drawbacks of this concept are: does not support any speed control, requires a stiff grid and its mechanical construction must be able to support high mechanical stress caused by wind gusts.

2) Partial Variable Speed Wind Turbine with Variable Rotor Resistance (WT Type B)

This configuration corresponds to the limited variable speed controlled wind turbine with variable rotor resistance, known as OptiSlip (Vestas^TM) as presented in Fig. 8.

It uses a wound rotor induction generator (WRIG) and it has been used by the Danish manufacturer Vestas Wind Systems since the mid 1990's.
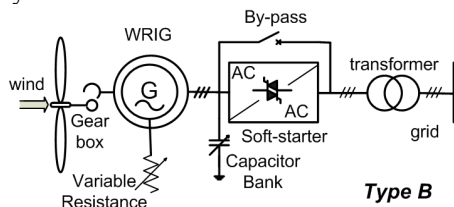

Type B

Fig. 8. Partial variable speed wind turbine with variable rotor resistance.

The generator is directly connected to the grid. The rotor winding of the generator is connected in series with a controlled resistance, whose size defines the range of the variable speed (typically 0-10% above synchronous speed). A capacitor bank performs the reactive power compensation and smooth grid connection occurs by means of a soft-starter. An extra resistance is added in the rotor circuit, which can be controlled by power electronics Thus, the total rotor

resistance is controllable and the slip and thus the power output in the system are controlled. The dynamic speed control range depends on the size of the variable rotor resistance. Typically the speed range is 0-10% above synchronous speed. The energy coming from the external power conversion unit is dumped as heat loss. In [24] an alternative concept using passive component instead of a power electronic converter is described. This concept achieves 10% slip, but it does not support controllable slip.

3) Variable Speed WT with partial-scale frequency converter (WT Type C)

This configuration, known as the doubly-fed induction generator (DFIG) concept, corresponds to the variable speed controlled wind turbine with a wound rotor induction generator (WRIG) and partial-scale frequency converter (rated to approx. 30% of nominal generator power) on the rotor circuit as shown in Fig. 9.
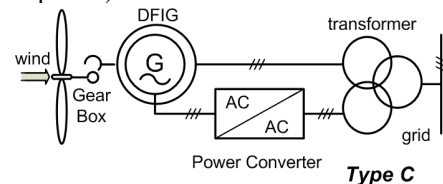

Type C

Fig. 9. Variable speed wind turbine with partial scale power converter.

The stator is directly connected to the grid, while a partial-scale power converter controls the rotor frequency and thus the rotor speed. The power rating of this partial-scale frequency converter defines the speed range (typically ±30% around synchronous speed). Moreover, this converter performs the reactive power compensation and a smooth grid connection. The control range of the rotor speed is wide compared to that of OptiSlip. Moreover, it captures the energy, which in the OptiSlip concept is burned off in the controllable rotor resistance. The smaller frequency converter makes this concept attractive from an economical point of view. Moreover, the power electronics is enabling the wind turbine to act as a more dynamic power source to the grid. However, its main drawbacks are the use of slip-rings and the protection schemes in the case of grid faults.

4) Variable Speed Wind Turbine with Full-scale Power Converter (WT Type D)

This configuration corresponds to the full variable speed controlled wind turbine, with the generator connected to the grid through a full-scale frequency converter as shown in Fig. 10.
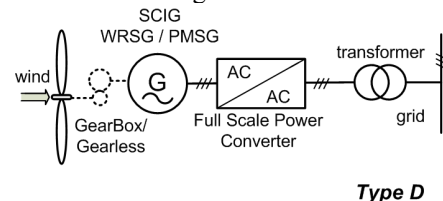

Type D

Fig. 10. Variable speed wind turbine with full-scale power converter.

The frequency converter performs the reactive power compensation and a smooth grid connection for the entire speed range. The generator can be electrically excited (wound rotor synchronous generator WRSG) or

permanent magnet excited type (permanent magnet synchronous generator PMSG). The stator windings are connected to the grid through a full-scale power converter.

Some variable speed wind turbines systems are gearless – see dotted gearbox in Fig. 10. In these cases, a bulky direct driven multi-pole generator is used. The wind turbine companies Enercon, Siemens Wind Power, Made and Lagerwey are examples of manufacturers using this configuration.

C. System comparison of wind turbines.

Comparing the different wind turbine topologies in respect to their performances will reveal a contradiction between cost and performance to the grid [5], [7]. A technical comparison of the main wind turbine concepts, where issues on grid control, cost, maintenance, internal turbine performance is given in Table 1.

Table 1. System comparison of wind turbine configurations.

System	Type A	Type B	Type C	Type D
Variable speed	No	No	Yes	Yes
Control active power	Limited	Limited	Yes	Yes
Control reactive power	No	No	Yes	Yes
Short circuit (fault-active)	No	No	No/Yes	Yes
Short circuit power	contribute	contribute	contribute	limit
Control bandwidth	1-10 s	100 ms	1 ms	0.5-1 ms
Standby function	No	No	Yes +	Yes ++
Flicker (sensitive)	Yes	Yes	No	No
Softstarter needed	Yes	Yes	No	No
Rolling capacity on grid	Yes, partly	Yes, partly	Yes	Yes
Reactive compensator (C)	Yes	Yes	No	No
Island operation	No	No	Yes/No	Yes
Investment	++	++	+	0
Maintenance	++	++	0	+

D. Control of Wind Turbines

Controlling a wind turbine involves both fast and slow control dynamics. Overall the power has to be controlled by means of the aerodynamic system and has to react based on a set-point given by a dispatched center or locally with the goal to maximize the power production based on the available wind power. The power controller should also be able to limit the power. An example of an overall control scheme of a wind turbine with a doubly-fed generator system is shown in Fig. 11 [5], [37].

Below maximum power production the wind turbine will typically vary the speed proportional with the wind speed and keep the pitch angle θ fixed. At very low wind the speed of the turbine will be fixed at the maximum allowable slip in order not to have over voltage. A pitch angle controller limits the power when the turbine reaches nominal power. The generated electrical power is done by controlling the doubly-fed generator through the rotor-side converter. The control of the grid-side converter is simply just keeping the dc-link voltage fixed. Internal current loops in both converters are used which typically are linear PI-controllers, as it is illustrated in Fig. 11. The power converters to the grid-side and the rotor-side are voltage source converters.
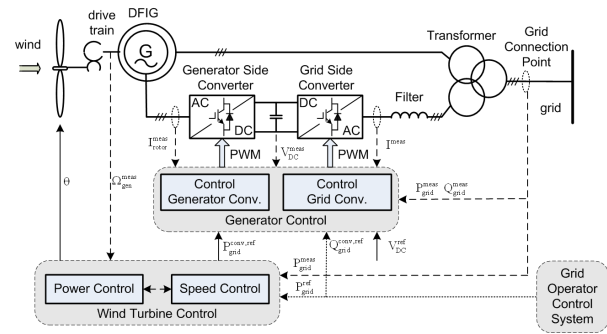

Fig. 11. Control of a wind turbine with doubly-fed induction generator (WT Type C).

Another solution for the electrical power control is to use the multi-pole synchronous generator. A passive rectifier and a boost converter are used in order to boost the voltage at low speed. The system is industrially used today and it is shown in Fig. 12.
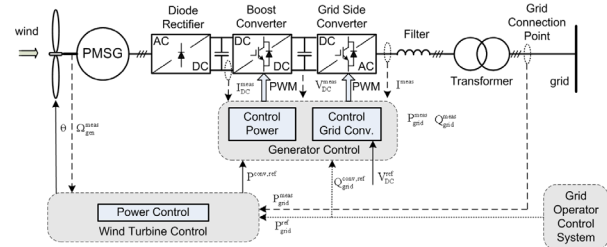

Fig. 12. Control of active and reactive power in a wind turbine with multi-pole synchronous generator (WT Type D).

A grid-side inverter is interfacing the dc-link to the grid. Common for both systems are they are able to control active and reactive power to the grid with high dynamics

E. Wind Farm Configurations

In many countries energy planning is going on with a high penetration of wind energy, which will be covered by large offshore wind farms. These wind farms may in the future present a significant power contribution to the national grid, and therefore, play an important role on the power quality and the control of complex power systems. Consequently, very high technical demands are expected to be met by these generation units, such as to perform frequency and voltage control, regulation of active and reactive power, quick responses under power system transient and dynamic situations, for example, to reduce the power from the nominal power to 20 % power within 2 seconds. The power electronic technology is again an important part in both the system configurations and the control of the offshore wind farms in order to fulfill the future demands.

One off-shore wind farm equipped with power electronic converters can perform both active and reactive power control and also operate the wind turbines in variable speed to maximize the energy captured and reduce the mechanical stress and acoustical noise. This solution is shown in Fig. 13 and it is in operation in Denmark as a 160 MW off-shore wind power station.

The active stall wind farms based on wind turbine Type A (see Fig. 7) are directly connected to the grid. A reactive power compensation unit is used in the connection point as shown in Fig. 14.
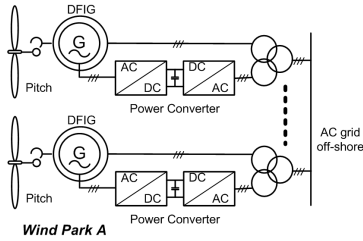
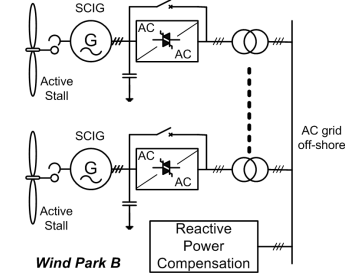Fig. 13. DFIG based wind farm with an AC grid connection.

Fig. 14. Active stall wind farm with an AC grid connection.

For long distance power transmission from off-shore wind farm, HVDC may be an interesting option. In an HVDC transmission system, the low or medium AC voltage at the wind farm is converted into a high dc voltage on the transmission side and the dc power is transferred to the on-shore system where the DC voltage is converted back into AC voltage as shown in Fig. 15. The topology may even be able to vary the speed on the wind turbines in the complete wind farm [47], [48].
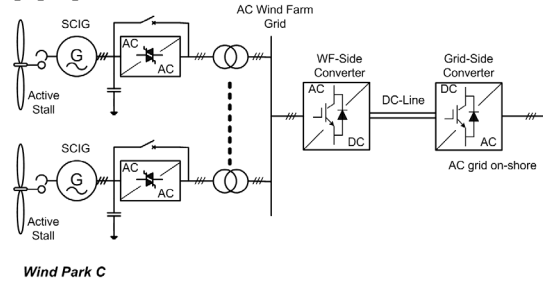

Fig. 15. Active stall wind farm with a DC-link grid connection.

Another possible DC transmission system configuration is shown in Fig. 16, where each wind turbine has its own power electronic converter, so it is possible to operate each wind turbine at an individual optimal speed. A common DC grid is present on the wind farm while a full scale power converter is used for the on-shore grid connection.
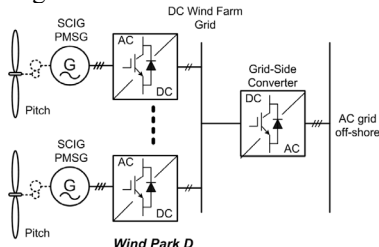

Fig. 16. Wind farm with common DC grid based on variable speed wind turbines with full scale power converter.

A comparison of these possible wind farm topologies is given in Table 2.

As it can be seen the wind farms have interesting features in order to act as a power source to the grid. Some have better abilities than others. Bottom-line will always be a total cost scenario including production,

investment, maintenance and reliability. This may be different depending on the planned site.

Table 2. Comparison of wind farm topologies.

	Wind Park A	Wind Park B	Wind Park C	Wind Park D
Individual speed control	Yes	No	Yes	No
Control active power electronically	Yes	No	Yes	Yes
Control reactive power	Yes	Centralized	Yes	Yes
Short circuit (active)	Partly	Partly	Yes	Yes
Short circuit power	Contribute	Contribute	No	No
Control bandwidth	10-100 ms	200ms - 2s	10 -100 ms	10 ms – 10 s
Stand by-function	Yes	No	Yes	Yes
Soft-starter needed	No	Yes	No	No
Rolling capacity on grid	Yes	Partly	Yes	Yes
Redundancy	Yes	Yes	No	No
Investment	+	++	+	+
Maintenance	+	++	+	+

F. Grid connection requirements

Some European countries have at this moment dedicated grid codes for wind power. These requirements reflect, in most of the cases, the penetration of wind power into the electrical network or a future development is prepared.

The requirements for wind power cover a wide range of voltage levels from medium voltage to very high voltage. The grid codes for wind power address issues that make the wind farms to act as a conventional power plant into the electrical network. These requirements have focus on power controllability, power quality, fault ride-through capability and grid support during network disturbances. According to several references [6] and [8] in some of the cases these requirements are very stringent.

1) Active power control

According to this demand the wind turbines must be able to control the active in the Point-of-Common-Coupling (PCC) in a given power range. The active power is typically controlled based on the system frequency e.g. Denmark, Ireland, Germany [51]-[57] so that the power delivered to the grid is decreased when the grid frequency rise above 50 Hz. A typical characteristic for the frequency control in the Danish grid code is shown in Fig. 17.
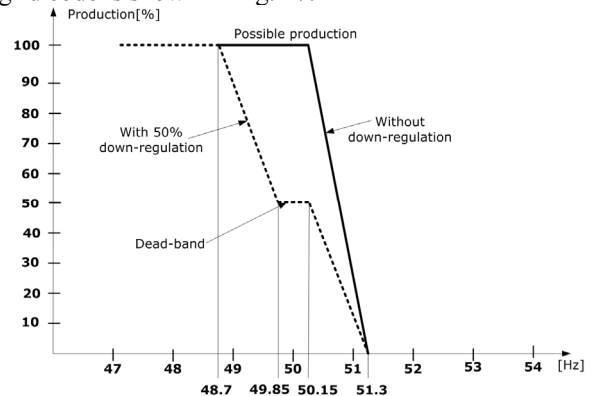

Fig. 17. Frequency control characteristic for the wind turbines connected to the Danish grid [52].

On the contrary other grid codes, e.g. Great Britain [58] specifies that the active power output must be kept constant for the frequency range 49.5 to 50.5 Hz, and a drop of maximum 5% in the delivered power is allowed when frequency drops to 47 Hz.

Curtailment of produced power based on system operator demands is required in Denmark, Ireland, Germany and Great Britain.

Currently, Denmark has the most demanding requirements regarding the controllability of the produced power. Wind farms connected at the transmission level shall act as a conventional power plant providing a wide range of controlling the output power based on Transmission System Operator's (TSO) demands and also participation in primary and secondary control [52]. Seven regulation functions are required in the wind farm control. Among these control functions, each one prioritized, the following must be mentioned: delta control, balance control, absolute production and system protection as shown in Fig. 18.
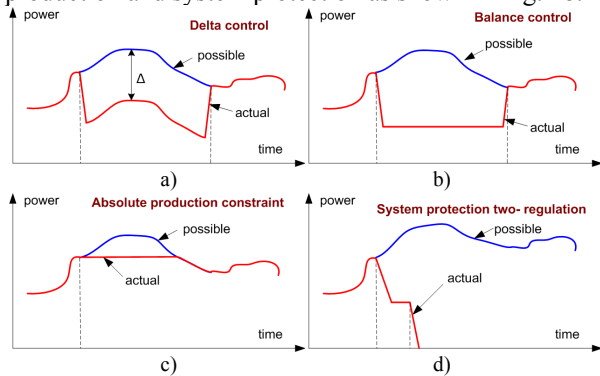

Fig. 18. Regulation function for active power implemented in wind farm controller required by the Danish grid codes: a) delta control, b) balance control, c) absolute production constraint and d) system protection.

2) Reactive power control and voltage stability

Reactive power is typically controlled in a given range. The grid codes specify in different ways this control capability. The Danish grid code gives a band for controlling the reactive power based on the active power output as shown in Fig. 19.
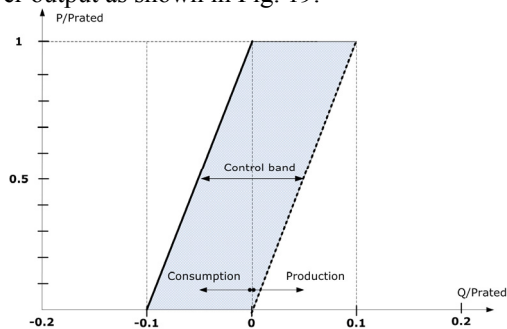

Fig. 19. Danish grid code demands for the reactive power exchange in the PCC [51], [52].

The Irish grid code specifies e.g. the reactive power capability in terms of power factor as shown in Fig. 20.
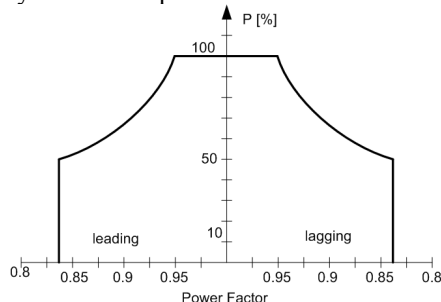

Fig. 20. Requirements for reactive power control in the Irish grid code for wind turbines [54].

The German transmission grid code for wind power specifies that the wind power units must provide a reactive power provision in the connection point without limiting the active power output as shown in Fig. 21.
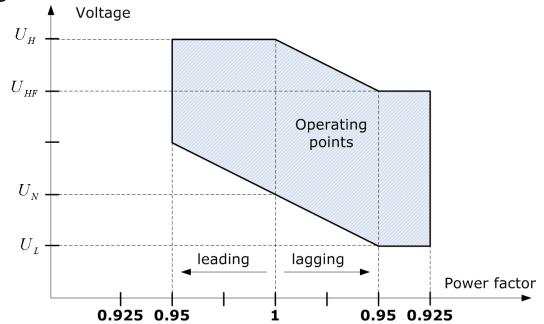

Fig. 21. Requirements for reactive power provision of generating units without limiting the active power output in the German transmission grid code [55], [56].

3) Power Quality

Power quality issues are addressed especially for wind turbines connected to the medium voltage networks. However, some grid codes, e.g. in Denmark and Ireland have also requirements at the transmission level.

Mainly two standards are used for defining the power quality parameters namely: IEC 61000-x-x and EN 50160. Specific values are given for fast variations in voltage, short term flicker severity, long term flicker severity and the total harmonic distortion. A schedule of individual harmonics distortion limits for voltage are also given based on standards or in some cases e.g. Denmark custom harmonic compatibility levels are defined. Interharmonics may also be considered [51].

4) Ride through capability

All considered grid codes requires fault ride-through capabilities for wind turbines. Voltage profiles are given specifying the depth of the voltage dip and the clearance time as well. One of the problems is that the calculation of the voltage during all types of unsymmetrical faults is not very well defined in some grid codes. The voltage profile for ride-through capability can be summarized as shown in Fig. 22.

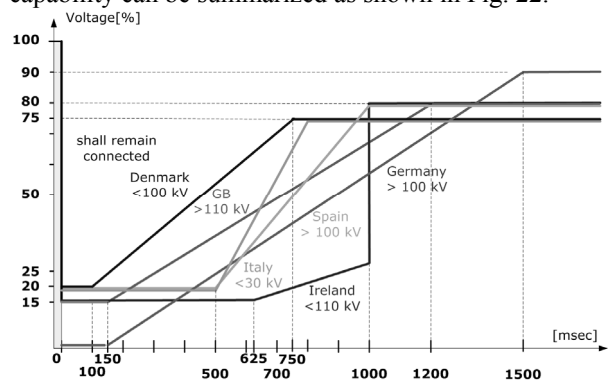Fig. 22. Voltage profile for fault ride-through capability in European grid codes for wind power [7].

Ireland's grid code is very demanding in respect with the fault duration while Denmark has the lowest short circuit time duration with only 100 msec. However, Denmark's grid code requires that the wind turbine shall remain connected to the electrical network during successive faults which is a technical challenge.

On the other hand Germany and Spain requires grid support during faults by reactive current injection up to 100% from the rated current [55], [56] and [59] as shown in Fig. 23.
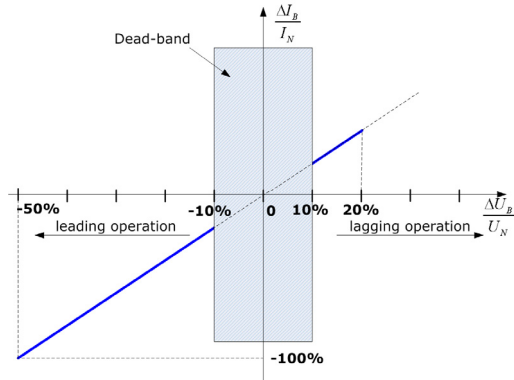

Fig. 23. Reactive current support during faults as specified in the German grid code [55].

This demand is relative difficult to meet by some of the wind turbine concepts e.g. active stall wind turbine with directly grid connected squirrel cage induction generator (WT Type A).

A summary regarding the interconnection requirements for wind power in Europe is given in detail in Appendix I.

IV. SOLAR ENERGY POWER CONVERSION

Photovoltaic (PV) power supplied to the utility grid is gaining more and more visibility due to many national incentives [65]. With a continuous reduction in system cost (PV modules, DC/AC inverters, cables, fittings and man-power), the PV technology has the potential to become one of the main renewable energy sources for the future electricity supply.

The PV cell is an all-electrical device, which produces electrical power when exposed to sunlight and connected to a suitable load. Without any moving parts inside the PV module, the tear-and-wear is very low. Thus, lifetimes of more than 25 years for modules are easily reached. However, the power generation capability may be reduced to 75% ~ 80% of nominal value due to ageing. A typical PV module is made up of around 36 or 72 cells connected in series, encapsulated in a structure made of e.g. aluminum and tedlar. An electrical model of PV cell is shown in Fig. 24.
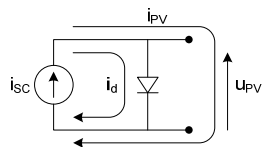

Fig. 24. Electrical model and characteristics of a PV cell.

Several types of proven PV technologies exist, where the crystalline (PV module light-to-electricity efficiency: η = 10% - 15%) and multi-crystalline (η = 9% - 12%) silicon cells are based on standard microelectronic manufacturing processes.

Other types are: thin-film amorphous silicon (η = 10%), thin-film copper indium diselenide (η = 12%), and thin-film cadmium telluride (η = 9%). Novel technologies such as the thin-layer silicon (η = 8%) and the dye-sensitised nano-structured materials (η = 9%) are in their early development. The reason to maintain a high level of research and development within these technologies is to decrease the cost of the PV-cells, perhaps on the expense of a somewhat lower efficiency. This is mainly due to the fact that cells based on today's microelectronic processes are rather costly, when compared to other renewable energy sources.

The series connection of the cells benefit from a high voltage (around 25 V ~ 45 V) across the terminals, but the weakest cell determines the current seen at the terminals.

This causes reduction in the available power, which to some extent can be mitigated by the use of bypass diodes, in parallel with the cells. The parallel connection of the cells solves the 'weakest-link' problem, but the voltage seen at the terminals is rather low.

Typical curves of a PV cell current-voltage and power-voltage characteristics are plotted in Fig. 25a and Fig. 25b respectively, with insolation and cell temperature as parameters.
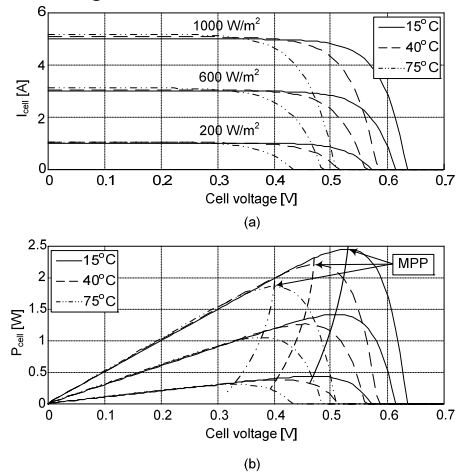

Fig. 25. Characteristics of a PV cell. Model based on the British Petroleum BP5170 crystalline silicon PV module. Power at standard test condition (1000 W/m2 irradiation, and a cell temperature of 25°C): 170 W @ 36.0 V [4].

The graph reveals that the captured power is determined by the loading conditions (terminal voltage and current). This leads to a few basic requirements for the power electronics used to interface the PV module(s) to the utility grid.

An overview of the power converter topologies for PV systems including their control techniques is given in the following sections. Next grid monitoring methods including grid voltage monitoring, grid impedance estimation and islanding detection are presented.

A. Structures for PV systems

The general block diagram of a grid connected photovoltaic system is similar with the one shown in Fig. 1. It consists of a PV array, a power converter with a filter, a controller and the grid utility.

The PV array can be a single panel, a string of PV panels or a multitude of parallel strings of PV panels. Centralized or decentralized PV systems can be used as depicted in Fig. 26.

1) Central inverters

In this topology the PV plant (typical > 10 kW) is arranged in many parallel strings that are connected to a single central inverter on the DC-side (Fig. 26a). These

inverters are characterized by high efficiency and low cost pr. kW. However, the energy yield of the PV plant decreases due to module mismatching and potential partial shading conditions. Also, the reliability of the plant may be limited due to the dependence of power generation on a single component: a failure of the central inverter results in that the whole PV plant is out of operation.
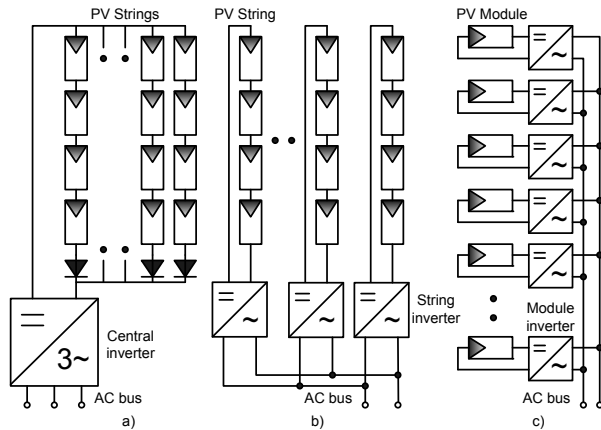

Fig. 26 Structures for PV systems: a) Central inverter, b) String inverter and c) Module integrated inverter [71].

2) String inverters

Similar to the central inverter, the PV plant is divided into several parallel strings. Each of the PV strings is assigned to a designated inverter, the so-called "string inverter" (see Fig. 26b). String inverters have the capability of separate Maximum Power Point (MPP) tracking of each PV string. This increases the energy yield by the reduction of mismatching and partial shading losses. These superior technical characteristics increase the energy yield and enhance the supply reliability. String inverters have evolved as a standard in PV system technology for grid connected PV plants.

An evolution of the string technology applicable for higher power levels is the multi-string inverter. It allows the connection of several strings with separate MPP tracking systems (via DC-DC converter) to a common DC-AC inverter. Accordingly, a compact and cost-effective solution, which combines the advantages of central and string technologies, is achieved. This multi-string topology allows the integration of PV strings of different technologies and of various orientations (south, north, west and east). These characteristics allow time-shifted solar power, which optimizes the operation efficiencies of each string separately. The application area of the multi-string inverter covers PV plants of 3-10 kW.

3) Module integrated inverter

This system uses one inverter for each module (Fig. 26c). This topology optimizes the adaptability of the inverter to the PV characteristics, since each module has its own Maximum Power Point (MPP) tracker. Although the module-integrated inverter optimizes the energy yield, it has a lower efficiency than the string inverter. Module integrated inverters are characterized by a more extended AC-side cabling, since each module of the PV plant has to be connected to the available AC grid (e.g. 230 V/ 50 Hz). Also, the maintenance processes are quite complicated, especially for facade-

integrated PV systems. This concept can be implemented for PV plants of about 50- 400 W peak.

B. Topologies for PV inverters

The PV inverter technology has evolved quite a lot during the last years towards maturity [66]. Still there are different power configurations possible as shown in Fig. 27.
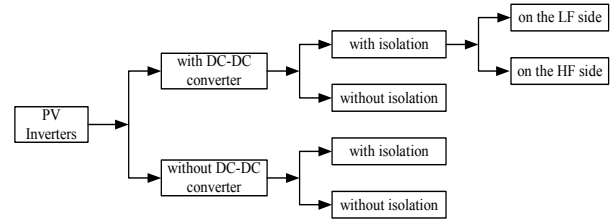

Fig. 27. Power configurations for PV inverters.

The question of having a dc-dc converter or not is first of all related to the PV string configuration. Having more panels in series and lower grid voltage, like in US and Japan, it is possible to avoid the boost function with a dc-dc converter. Thus a single stage PV inverter can be used leading to higher efficiencies.

The issue of isolation is mainly related to safety standards and is for the moment only required in US. The drawback of having so many panels in series is that MPPT is harder to achieve especially during partial shading, as demonstrated in [67]. In the following, the different PV inverter power configurations are described in more details.

1) PV inverters with DC-DC converter and isolation

The isolation is typically acquired using a transformer that can be placed on either the grid frequency side (LF) as shown in Fig. 28a or on the high-frequency (HF) side in the dc-dc converter as shown in Fig. 28b. The HF transformer leads to more compact solutions but high care should be taken in the transformer design in order to keep the losses low.
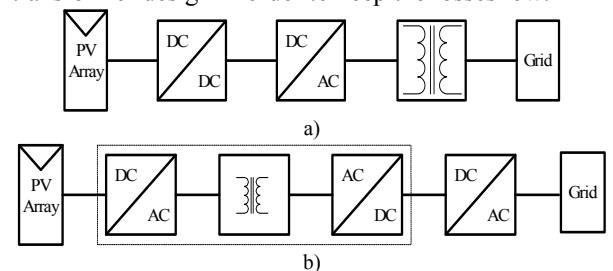
Fig. 28. PV inverter system with DC-DC converter and isolation transformer: a) on the Low Frequency (LF) side and b) on the High Frequency (HF) side.

In Fig. 29 a PV inverter with an HF transformer using an isolated push-pull boost converter is presented [68].

In this solution the dc-ac inverter is a low cost inverter switched at the line frequency. The new solutions on the market are using PWM dc-ac inverters with IGBT's switched typically at 10-20 kHz leading to a better power quality performance.

Other solutions for high frequency dc-dc converters with isolation include: full-bridge isolated converter, Single-Inductor push-pull Converter (SIC) and Double-Inductor Converter (DIC) [69].

Fig. 29. PV inverter with a high frequency transformer in the dc-dc converter.

In order to keep the magnetic components small high switching frequencies in the range of 20 – 100 kHz are typically employed. The full-bridge converter is usually utilized at power levels above 750 W. The advantages of this topology are: good transformer utilization – bipolar m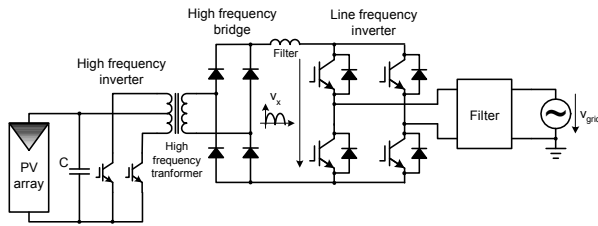agnetization of the core, good performance with current programmed control – reduced DC magnetization of transformer. The main disadvantages in comparison with push-pull topology are the higher active part count and the higher transformer ratio needed for boosting the dc voltage to the grid level.

The single inductor push-pull converter can provide boosting function on both the boosting inductor and transformer, reducing the transformer ratio. Thus higher efficiency can be achieved together with smoother input current. On the negative side higher blocking voltage switches are required and the transformer with tap point puts some construction and reliability problems.

Those shortcomings can be alleviated using the double inductor push-pull converter (DIC) where the boost inductor has been split into two. Actually this topology is equivalent with two inter-leaved boost converters leading to lower ripple in the input current. The transformer construction is simpler not requiring a tap point. The single disadvantage of this topology remains the need for an extra inductor.

2) PV inverters with DC-DC converter without isolation

In some countries as the grid-isolation is not mandatory, more simplified PV inverter design can be used, like shown in Fig. 30a.
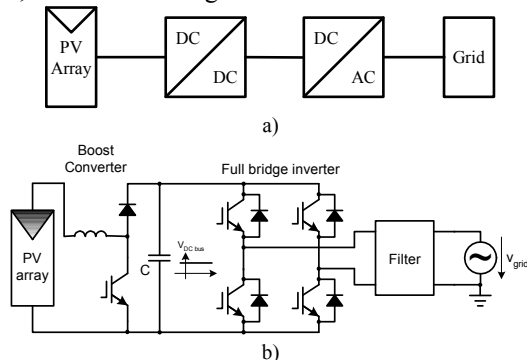

Fig. 30. PV inverter system with DC-DC converter without isolation transformer a) General diagram and b) Practical example with boost converter and full-bridge inverter.

In Fig. 30b a practical example [70] using a simple boost converter is shown.

3) PV inverters without DC-DC converter and with isolation

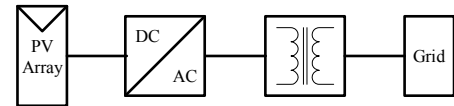The block diagram of this topology is shown in Fig. 31.

Fig. 31. General diagram of a PV system without DC-DC converter and with isolation transformer.
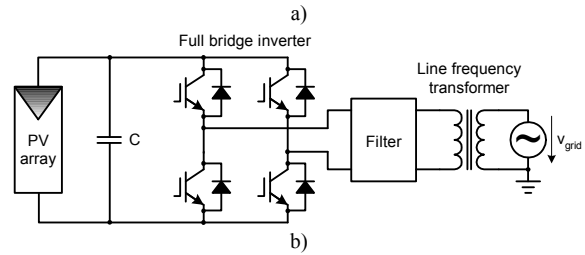
Fig. 32. Practical example of a PV system without DC-DC converter and with a full-bridge converter and isolation grid side transformer.

A PV inverter topology is presented in Fig. 32, in which a line frequency transformer is used. For higher power levels, self-commutated inverters using thyristors may be used [70].

4) PV inverters without DC-DC converter and without isolation

This topology is shown in Fig. 33a.
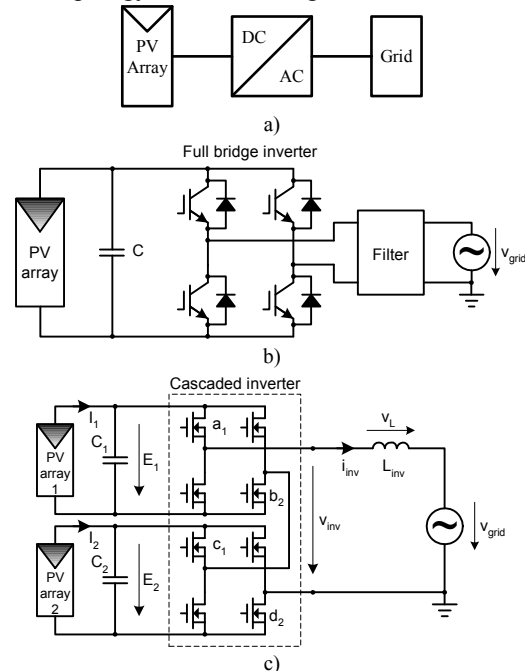
Fig. 33. Transformer-less PV inverter system without DC-DC converter: a) general diagram, b) typical example with full-bridge inverter and c) multilevel inverter.

In Fig. 33b, a typical transformer-less topology is shown using PWM IGBT inverters. This topology can be used when a large number of PV panels are available connected in series producing in excess of the grid voltage peak at all times.

Another interesting PV inverter topology without boost and isolation can be achieved using a multilevel concept. Grid connected photovoltaic systems with a five level cascaded inverter is presented in Fig. 33c [68]. The redundant inverter states of the five level cascaded inverter allow for a cyclic switching scheme which minimizes the switching frequency, equalizes stress evenly on all switches and minimizes the voltage ripple on the DC capacitors.

C. Control of PV inverters

Based on the above presented power converter topologies it can be concluded that two main structures are used in PV applications namely the double-stage conversion (DC to DC plus DC to AC) and the single stage conversion (DC to AC only). Therefore, the next sections present the control techniques used for these topologies.

1) Control of DC-DC boost converter

In order to control the output dc-voltage to a desired value, a control system is needed which automatically can adjust the duty cycle, regardless of the load current or input changes. There are at least two types of control for the dc-dc converters: the direct duty-cycle control and the current control [71].

Direct duty cycle - The output voltage is measured and then compared to the reference. The error signal is used as input in the compensator, which will calculate it from the duty-cycle reference for the pulse-width modulator as shown in Fig. 34a.

Current control - The converter output is controlled by the choice of the transistor peak current. The control signal is a current and a simple control network switches on and off the transistor such its peak current follows the control input. The current control (Fig. 34b), in the case of an isolated boost push-pull converter has some advantages against the duty-cycle control e.g. simpler dynamics (removes one pole from the control to output transfer function). Also as it uses a current sensor it can provide a better protection of the switch by limiting the current to acceptable levels.
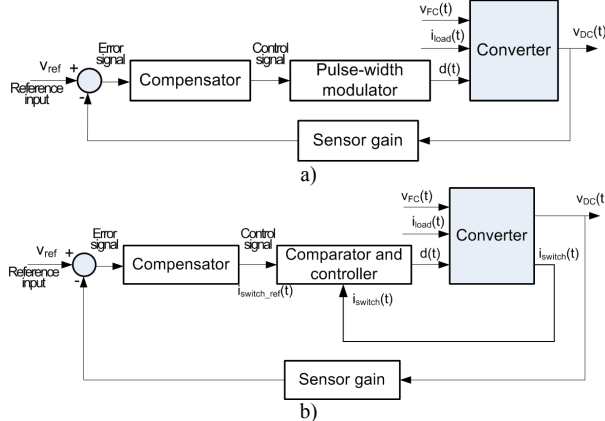

Fig. 34. Control strategies for switched dc-dc converters a) direct duty-cycle control and b) current control.

Among the drawbacks of the current control it can be mentioned that it requires an extra current sensor and it has a susceptibility to noise and thus light filtering of the feedback signals is required.

2) Control of DC-AC converter

For the grid-connected PV inverters in the range of 1-5 kW, the most common control structure for the DC-AC grid converter is using a current-controlled H-bridge PWM inverter which has a low-pass output filter. Typically L-filters are used but the new trend is to use LCL filters that have a higher order filter (3rd) which leads to a more compact design. The drawback is that due to its own resonance frequency it can produce stability problems and special control design is required

[72]. A typical single-stage PV grid-connected converter with an LCL filter is shown in Fig. 35.
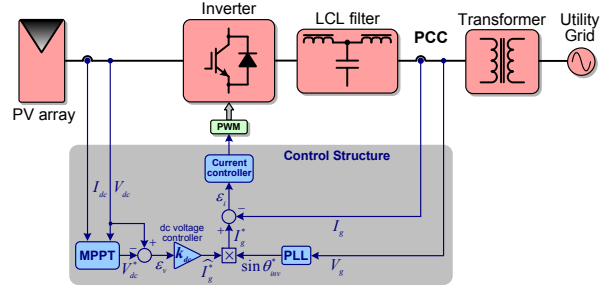

Fig. 35. Single-stage PV grid-connected system.

The main elements of the control structure are the synchronization algorithm based on PLL, the MPPT, the input power control, the grid current controller including the PWM generator.

The harmonics level in the grid current is still a controversial issue for PV inverters. The IEEE 929 standard from year 2000 allows a limit of 5% for the current Total Harmonic Distortion (THD) factor with individual limits of 4% for each odd harmonic from 3rd to 9th and 2% for 11th to 15th while a recent draft of European IEC61727 suggests something similar. These levels are far more stringent than other domestic appliances such as IEC61000-3-2 as PV systems are viewed as generation sources and so they are subject to higher standards than load systems.

Classical PI control with grid voltage feed-forward (v_{ff}) [13], as depicted in Fig. 36a, is commonly used for current-controlled PV inverters, but this solution exhibits two well known drawbacks: inability of the PI controller to track a sinusoidal reference without steady-state error and poor disturbance rejection capability. This is due to the poor performance of the integral action.
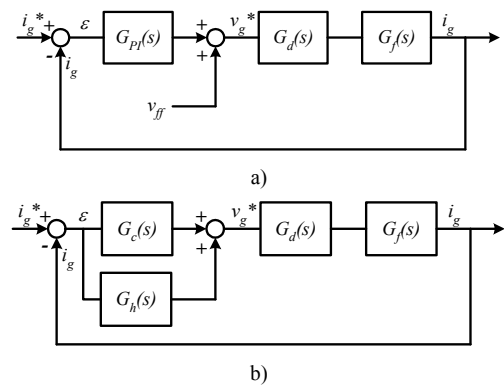
Fig. 36. The current loop of a PV inverter: a) with PI controller and b) with P+Resonant (PR) controller.

In order to get a good dynamic response, a grid voltage feed-forward (v_{ff}) is used, as depicted in Fig. 26a. This leads in turn to stability problems related to the delay introduced in the system by the voltage feedback filter.

In order to alleviate these problems, a second order generalized integrator (GI) as reported in [72], [73] and [74] can be used. The GI is a double integrator that achieves an infinite gain at a certain frequency, also called resonance frequency, and almost no gain exists outside this frequency. Thus, it can be used as a notch filter in order to compensate the harmonics in a very selective way. This technique has been primarily used

in three-phase active filter applications as reported in [73]. Another approach reported in [72] where a new type of stationary-frame regulators called P+Resonant (PR) is introduced and applied to three-phase PWM inverter control. In this approach the PI dc-compensator is transformed into an equivalent ac-compensator, so that it has the same frequency response characteristics in the bandwidth of concern. The current loop of the PV inverter with PR controller is depicted in Fig. 36b.

The harmonic compensator (HC) $G_h(s)$ as defined in [75] is designed to compensate the selected harmonics 3rd, 5th and 7th as they are the most prominent harmonics in the current spectrum. A processing delay typical equal to sampling time for the PWM inverters is introduced in [72].

Thus it is demonstrated the superiority of the PR controller in respect to the PI controller in terms of harmonic current rejection.

The issue of stability when several PV inverters run in parallel on the same grid becomes more and more important, especially when LCL filters are used. Thus, special attention is required when designing the current control.

3) Maximum Power Point Tracking (MPPT)

In order to capture the maximum power available from the PV array, a Maximum Power Point Tracker (MPPT) is required. The maximum power point of PV panels is a function of solar irradiance and temperature as depicted in Fig. 25. This function can be implemented either in the dc-dc converter or in the DC-AC converter. Several algorithms can be used in order to implement the MPPT like:

a) Perturb and Observe method

The most commonly used MPPT algorithm is the Perturb and Observe (P&O), due to its ease of implementation in its basic form. Fig. 25 shows the characteristic of a PV array, which has a global maximum at the MPP. Thus, if the operating voltage of the PV array is perturbed in a given direction and dP/dV > 0, it is known that the perturbation is moving the operating point towards the MPP. The P&O algorithm would then continue to perturb the PV array voltage in the same direction. If dP/dV < 0, then the change in operating point moved the PV array away from the MPP, and the P&O algorithm reverses the direction of the perturbation. [76] A problem with P&O is that it oscillates around the MPP in steady state operation. It can also track into the wrong direction, away from the MPP, under rapidly increasing or decreasing irradiance levels [77]-[79]. There are several variations of the basic P&O that have been proposed to minimize these drawbacks. These include using an average of several samples of the array power and dynamically adjusting the magnitude of the perturbation of the PV operating point.

b) Improved P&O method for rapidly changing irradiance

The method performs an additional measurement of power in the middle of the MPPT sampling period without any perturbation, and based on these measurements, it calculates the change of power due to the varying irradiation, [80] according to Fig. 37.
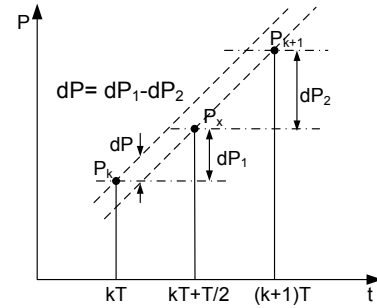
Fig. 37. Measurement of the power between two MPPT sampling instances.

Assuming that the rate of change in the irradiation is constant over one sampling period of the MPPT, the dP caused purely by the MPPT command can be calculated as:

$$dP = dP_1 - dP_2 = \left(P_x - P_k\right) - \left(P_{k+1} - P_x\right) = 2P_x - P_{k+1} - P_k \quad (1)$$

The resulting 'dP' reflects the changes due to the perturbation of the MPPT method.

Using the above calculation in the flowchart of the dp-P&O method, (see Fig. 38) can be avoided the confusion of the MPPT due to the rapidly changing irradiation.
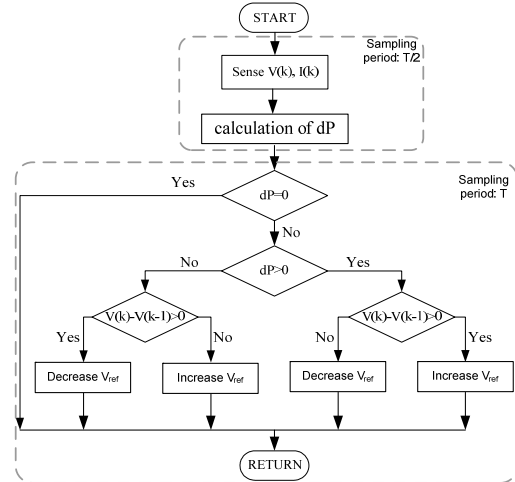
Fig. 38. The flowchart of the dp-P&O method.

The experimental results show that the dP-P&O method performs superior to the traditional P&O during rapidly changing irradiance, resulting in higher dynamic efficiency, see Fig. 39.
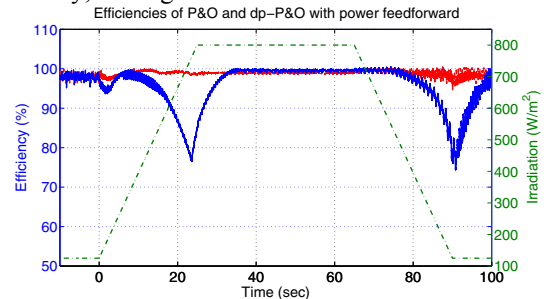
Fig. 39. The instantaneous efficiency of the traditional P&O method can decrease to below 80% during rapidly increasing and decreasing irradiation, while the efficiency of dP-P&O is not affected.

c) Incremental conductance method

The incremental conductance algorithm seeks to overcome the limitations of the P&O algorithm by using the PV array's incremental conductance to compute the sign of dP/dV without a perturbation. It does this using an expression derived from the

condition that, at the MPP, dP/dV = 0. Beginning with this condition, it is possible to show that, at the MPP dI/dV = -I/V [76] and [81]. Thus, incremental conductance can determine that the MPPT has reached the MPP and stop perturbing the operating point. If this condition is not met, the direction in which the MPPT operating point must be perturbed can be calculated using the relationship between dI/dV and -I/V. This relationship is derived from the fact that dP/dV is negative when the MPPT is to the right of the MPP and positive when it is to the left of the MPP. This algorithm has advantages over perturb and observe in that it can determine when the MPPT has reached the MPP, where perturb and observe oscillates around the MPP. Also, incremental conductance can track rapidly increasing and decreasing irradiance conditions with higher accuracy than perturb and observe [76]. However, because of noise and errors due to measurement and quantization, this method can also produce oscillations around the MPP; and it can also be confused in rapidly changing atmospheric conditions [77]. One disadvantage of this algorithm is the increased complexity when compared to perturb and observe. This increases real-time computational time, and slows down the sampling frequency of the array voltage and current.

d) Parasitic capacitance method

The parasitic capacitance method is a refinement of the incremental conductance method that takes into account the parasitic capacitances of the solar cells in the PV array. Parasitic capacitance uses the switching ripple of the MPPT to perturb the array. To account for the parasitic capacitance, the average ripple in the array power and voltage, generated by the switching frequency, are measured using a series of filters and multipliers and then used to calculate the array conductance. The incremental conductance algorithm is then used to determine the direction to move the operating point of the MPPT. One disadvantage of this algorithm is that the parasitic capacitance in each module is very small, and will only come into play in large PV arrays where several module strings are connected in parallel. Also, the DC-DC converter has a sizable input capacitor used to filter out the small ripple in the array power. This capacitor may mask the overall effects of the parasitic capacitance of the PV array.

e) Constant voltage method

This algorithm makes use of the fact that the MPP voltage changes only slightly with varying irradiances, as depicted in Fig. 25. The ratio of VMP/VOC depends on the solar cell parameters, but a commonly used value is 76% [76] and [82]. In this algorithm, the MPPT momentarily sets the PV array current to zero to allow a measurement of the array's open circuit voltage. The array's operating voltage is then set to 76% of this measured value. This operating point is maintained for a set amount of time, and then the cycle is repeated. A problem with this algorithm is that the available energy is wasted when the load is disconnected from the PV array; also the MPP is not always located at 76% of the array's open circuit voltage [76].

4) Input power control for PV applications

For PV applications, the input power control can be realized through the use of either DC-DC converter or DC-AC converters. The control strategies of the input power in the case of a power configuration of PV system without DC-DC converter (single-stage PV converter) are presented in the following. The implementation of the MPPT could be realized in two different ways in this case:

– the output of the MPPT is the AC current amplitude reference;

– the output of the MPPT is the DC voltage reference.

In the first case the MPPT block has I_{pv} and V_{pv} as inputs and the output variable is the AC current amplitude reference ($\hat{I}_{ref}$) as depicted in Fig. 40a [83].

In the second case the MPPT block has the same inputs (I_{pv} and V_{pv}) but the output variable of the algorithm is the dc voltage reference (V^*_{pv}). The dc voltage controller (P or PI controller) is used to control the DC voltage loop to produce the AC current amplitude reference ($\hat{I}_{ref}$). Then the AC current amplitude reference is multiplied by $sin(\theta)$, which is captured from a phase-looked-loop (PLL) circuit to produce the output current reference command I_{ref} of the inverter. This topology is described in Fig. 40b [84] and [85].
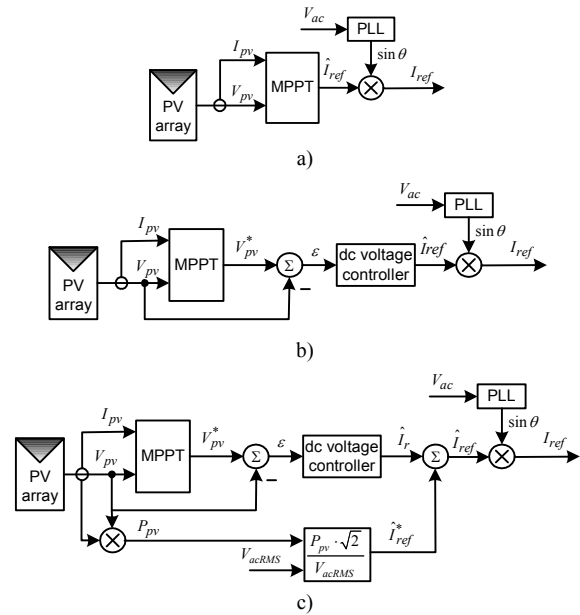
Fig. 40. Control structures of the input power. a) the output of MPPT is the ac current amplitude reference ($\hat{I}_{ref}$), b) the output of the MPPT is the dc voltage reference (V^*_{pv}) and a dc voltage controller is used, c) new control structure where a feed-forward of the input power is used.

In Fig. 40c a new control strategy of input power is proposed. The new element introduced is a power feed-forward. The computed value of the current amplitude reference using the PV power (P_{pv}) and the RMS value of the ac voltage (V_{acRMS}) is added to the output value of the dc voltage controller ($\hat{I}_r$) resulting in an ac-current amplitude reference ($\hat{I}_{ref}$). Using the input power feed-forward the dynamic of the PV system is improved being known the fact that the MPPT is rather slow.

D. PV systems - Grid monitoring

1) Grid voltage monitoring

The increased penetration of DPGS connected to the electrical grid based on sources such as PV necessitates better grid condition detection in order to meet standard specifications in terms of power quality and safety.

Grid-connected converter systems rely on accurate and fast detection of the phase angle, amplitude and frequency of the utility voltage to guarantee the correct generation of the reference signals. This is also required by the relevant grid codes which are country specific and can vary also in respect to the generation system (e.g. PV systems, wind turbines, fuel cell, etc). The grid codes may refer to different standards for distributed generation systems. These standards impose the operation conditions of the grid-connected converter systems in terms of grid voltage amplitude and frequency. Considering grid voltage monitoring requirements for interconnection of PV systems to the grid, the standard IEC61727 [86] and IEEE 929 [87] are given as examples. These standards apply to utility-interconnected PV power systems operating in parallel with the utility and utilizing static (solid-state) non-islanding inverters for the conversation of DC to AC.
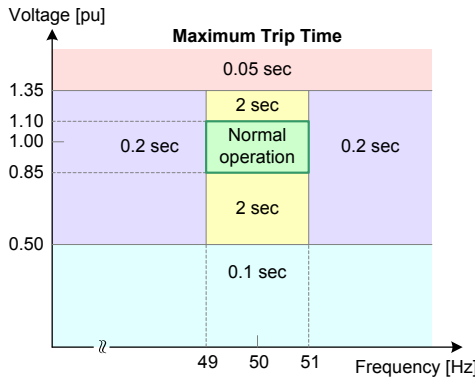

Fig. 41. Maximum trip times for both voltage amplitude and frequency according to the standard IEC61727 [86].

Fig. 41 shows the boundaries of operation in respect to grid voltage amplitude and frequency. A continuous operation area between 0.85 and 1.10 pu and ± 1 Hz around the nominal frequency is defined. Abnormal conditions can arise on the utility system that requires a response from the grid-connected PV system. This response is to ensure the safety of utility maintenance personnel and the general public, as well as to avoid damage to connected equipment, including the PV system. The abnormal utility conditions of concern are the grid voltage amplitude and frequency excursions above or below the values stated in Fig. 41. If the voltage amplitude or frequency exceeds the predefined limits, the grid-connected PV system has to cease to energize the utility line within the specified time interval. As it can be noticed from Fig. 41, the most restrictive requirement is when the maximum trip time is 0.05 seconds for a grid voltage amplitude excursion above 1.35 pu. An accurate and fast grid voltage monitoring algorithm is required in order to comply with these requirements.

Fig. 42 presents the principle of the grid voltage monitoring which consists in obtaining the parameters of the grid voltage as presented in (2).
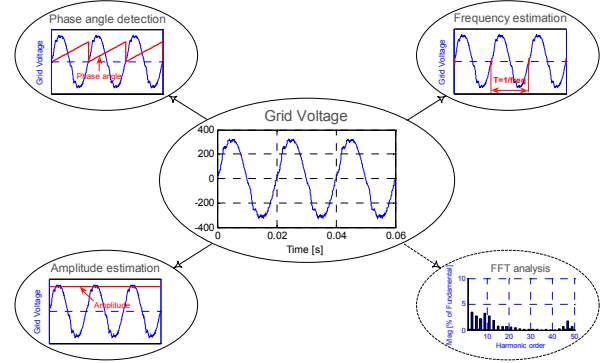

Fig. 42. Grid voltage monitoring principles.

$$v(t) = \underbrace{\widehat{V} \cdot \sin(\omega \cdot t)}_{Fundamental} + \underbrace{\sum \widehat{V}_h \cdot \sin(\omega_h \cdot t + \theta_h)}_{Harmonics} \qquad (2)$$

The voltage equation is divided in two main parts: the fundamental and the harmonics. The grid phase angle ($\omega \cdot t$) is mostly used for synchronization. Moreover, the detection of the grid phase angle can also be used for anti-islanding detection algorithms [88]. The frequency of the grid voltage (ω) is used for over/under frequency detection algorithms but also to provide information to the control system (such as resonant controllers or filters which need to adjust the resonance frequency). The amplitude of the grid voltage ($\widehat{V}$) is required for over/under voltage and to provide information to the control system (such as power feed forward loop). Additional information such as harmonic content of the grid voltage can be required for some algorithms (e.g. harmonics monitoring for the passive anti-islanding methods [88] or active power filters applications.

a) Grid voltage monitoring techniques – Overview

Different algorithms are used in order to monitor the grid voltage. In the technical literature numerous methods using different techniques are presented. These methods can be organized in three main categories:

- methods based on Zero-Crossing Detection (ZCD),
- methods based on Phase-Locked Loop (PLL)
- methods based on arctangent function ($\tan^{-1}$).

A simple method of obtaining the phase and frequency information is to detect the zero-crossing point of the grid voltage [89]-[91]. This method has two major drawbacks as described in the following.

Since the zero crossing point can be detected only at every half cycle of the utility frequency, the phase tracking action is impossible between the detecting points and thus the fast dynamic performance can not be obtained [92]. Some work has been done in order to alleviate this problem using multiple level crossing detection as presented in [93].

Significant line voltage distortion due to notches caused by power device switching and/or low frequency harmonic content can easily corrupt the output of a conventional zero-crossing detector [94]. Therefore, the zero-crossing detection of the grid voltage needs to obtain its fundamental component at the line frequency. This task is usually made by a digital filter. In order to avoid the delay introduced by this filter numerous techniques are used in the technical literature. Methods based on advanced filtering techniques are presented in

[94]-[98]. Other methods use Neural Networks for detection of the true zero-crossing of the grid voltage waveform [99]-[101]. An improved accuracy in the integrity of the zero-crossing can also be obtained by reconstructing a voltage representing the grid voltage [102]-[105].

However, starting from its simplicity, when the two major drawbacks are alleviated by using advanced techniques, the zero-crossing method proves to be rather complex and unsuitable for applications which require accurate and fast tracking of the grid voltage.

The arctangent function technique is another solution for detecting the phase angle and frequency of the grid voltage. An orthogonal voltage system is required in order to implement this technique. This method is used in adjustable speed drives applications in order to transform the feedback signals to a reference frame suitable for control purposes [19]. However, this method has the drawback that requires additional filtering in order to obtain an accurate detection of the phase angle and frequency in the case of a distorted grid voltage. Therefore, this technique is not suitable for grid-connected converter applications.

Recently, there has been an increasing interest in PLL techniques for grid-connected converter systems [106]. Usually, the PLL technique is mainly applied in communication technologies. Though, it has been proven that its application in the grid-connected converter systems was a success [91], [92], [106]-[126]. Used for such systems, the PLL is a grid voltage phase detection algorithm. The main task of the PLL algorithm is to provide a unitary power factor operation of a grid-connected converter system. This task involves synchronization of the converter output current with the grid voltage, and to provide a clean sinusoidal current reference to the current controller. Moreover, using the PLL, the grid voltage parameters such as amplitude and frequency, can be easily monitored.

Like in the case of the arctangent function technique, an orthogonal voltage system is required for the PLL algorithm. In a three-phase system, the grid voltage information can easily be obtained through the Clarke Transformation. However, for a single-phase system, the grid voltage is much more difficult to acquire [91]. Therefore, more attention should be paid for the generation of the orthogonal voltage system.

The general structures of a single-phase and three-phase PLL including the grid voltage monitoring are presented in Fig. 43a and Fig. 43b respectively. Usually, the main difference among different single-phase PLL methods is the orthogonal voltage system generation structure.
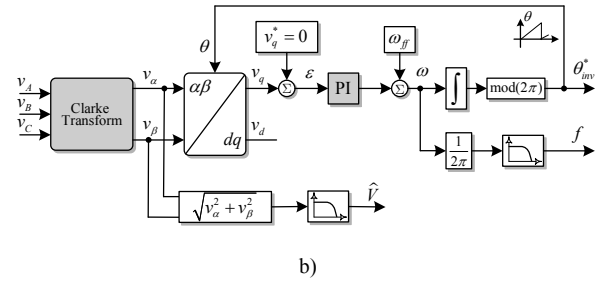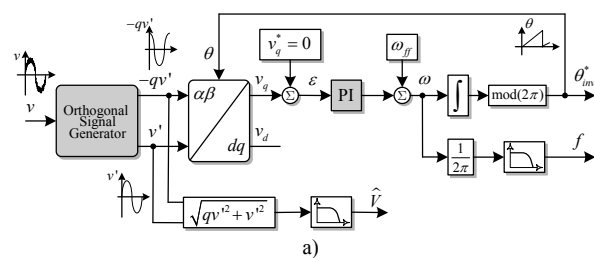

a)

b)

Fig. 43. General structure of a: a) single-phase PLL and b) three-phase PLL.

Next paragraph discusses about techniques used for generating the orthogonal voltage systems. The structure responsible for generating the orthogonal voltage system is called orthogonal signal generator.

b) Orthogonal signal generators

In the technical literature, some techniques for generating the orthogonal voltage components from a single-phase input signal are described, some of which are compared in [106] and [127]. An easy technique of generating the orthogonal voltage system in a single-phase system incorporates a transport delay function, which is responsible for introducing a phase shift of 90 degrees with respect to the fundamental frequency of the input signal [115]. A related method, but more complex of creating a phase shift of 90 degrees, uses the Hilbert Transformation [106] and [110]. Other methods of generating the orthogonal voltage system are based on inverse Park Transformation [106], [115], [122] and [126], using resonant structures such as Second Order Generalized Integrator (SOGI) [117] or Kalman estimator-based filter [112].

2) Grid impedance estimation

In order to comply with certain stringent standard requirements for islanding detection such as the German standard VDE 0126-1-1 [128] for grid-connected PV systems, it is important to estimate the impedance of the distribution line (grid). The standard requirement is to isolate the supply within 5 s after an impedance change of 1 ohm. Therefore, the PV inverters should make use of an online estimation technique in order to meet these regulation requirements. Moreover, the estimation of the grid impedance can also be used in order to increase the stability of the current controller by adjusting its parameters online (see Fig. 46). If the variation is mainly resistive then the damping of the line filter is significant and makes the PV inverter control more stable. As it can be noticed from Fig. 45, if the variation is mainly inductive, then the bandwidth of the controller decreases [129]. Also, in this case, due to the additional inductance of the grid, the tuning order of the line filter becomes lower and the filter will not fulfill the initial design purpose. In order to alleviate this problem, the gain scheduling method can be used for adjusting online the current controller parameters, as presented in Fig. 46. Therefore, besides the standard requirements the knowledge about the grid impedance value is an added feature for the PV inverter [130].
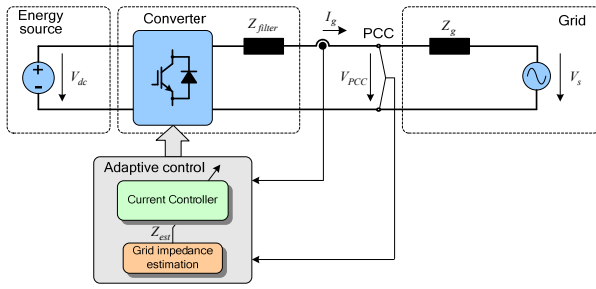
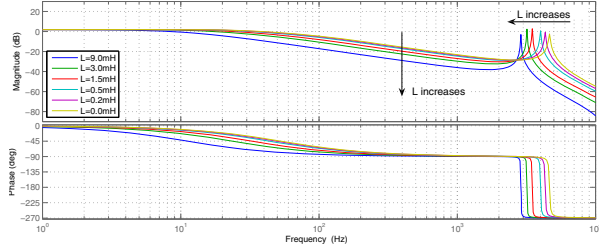Fig. 44. Adaptive control of the grid-connected inverter [138].

Fig. 45. Bode plot of plant for different values of the grid inductance L in case of using an LCL filter.
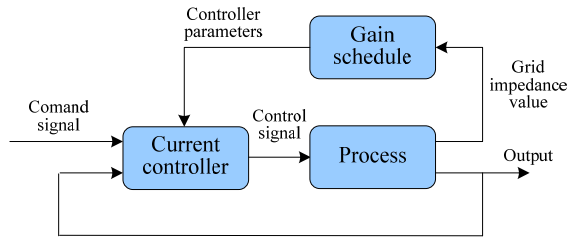

Fig. 46.Gain scheduling method [138].

According to [130] different techniques, as presented in [131]-[136] can be used for line impedance measurements. It is noticeable that, usually, these methods use special hardware devices. Once the inputs are acquired by voltage and current measurement, the processing part follows, typically involving large mathematical calculations in order to obtain the impedance value.

The state of the art divides the measuring solutions into two major categories: the passive and the active methods.

The passive method uses the non characteristic signals (line voltages and currents) that are already present in the system. This method depends on the existing background distortion of the voltage [137] and, in numerous cases, the distortion has neither the amplitude nor the repetition rate to be properly measured. This will not be interesting for implementing it in a PV inverter.

Active methods make use of deliberately "disturbing" the power supply network followed by acquisition and signal processing [131], [132], [133] and [135]. The way of "disturbing" the network can vary, therefore, active methods are also divided into two major categories: transient methods and steady-state methods.

Other two new active methods for estimating the grid impedance are presented in [138] and [139]. The method presented in [138] is based on producing a small perturbation on the output of the power converter that is in the form of periodical variations of active and reactive power (PQ variations). The control diagram for

the implementation of this technique is shown in Fig. 47.
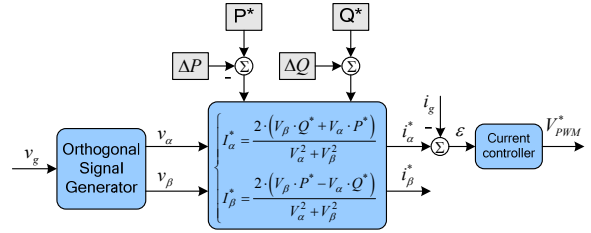
Fig. 47. Control diagram of the PQ control technique [138].

The main idea is to make the power converter working in two operation points (see Fig. 48) in order to solve the equation of the equivalent grid impedance.
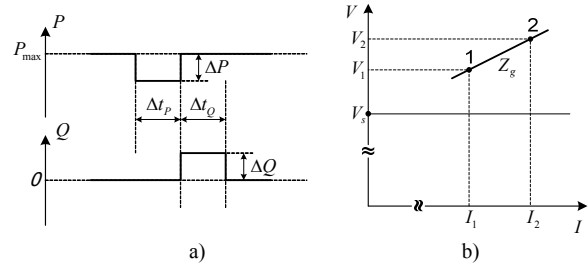
Fig. 48. a) Principle for the variation of active (P) and reactive (Q) power; b) Power converter working in two operation points [138].

During the perturbation, measurements of voltage and current are performed and signal processing algorithms are used in order to estimate the value of the grid impedance.

The method proposed in [139] is based on producing a perturbation on the output of the power converter that is in the form of periodical injection of one or two voltage harmonic signals (see Fig. 49). The single harmonic injection uses a 600 Hz signal and the double harmonic injection uses a 400 Hz and 600 Hz signals, respectively. During the perturbation, the current response(s) at the same frequency as the injected signal(s) is/are measured. The value of the grid impedance is estimated using two different signal processing algorithms. The DFT technique is used for the single harmonic injection and the statistic technique is used for the double harmonic injection (see Fig. 50).
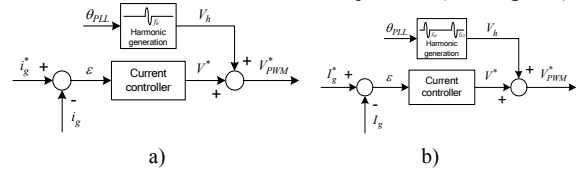
Fig. 49. Harmonic injection methods [139]: a) single harmonic injection; b) double harmonic injection.
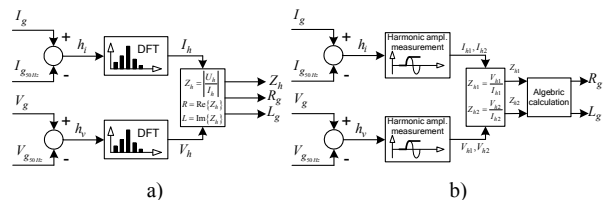
Fig. 50. Grid impedance estimation algorithms [139]: a) single harmonic injection; b) double harmonic injection.

3) Islanding detection

A grid-connected PV system shall cease to energize the utility line from a de-energized distribution line irrespective of connected loads or other generators

within specified time limits. This is to prevent back-feeding to the line, also called islanding, which could create hazardous situation for utility maintenance personnel and the general public. Although the probability of islanding occurrence is extremely low [158], standards dealing with the interconnection of inverter based photovoltaic system with the grid require that an effective anti-islanding method is incorporated into the operation of the inverter [87], [140], [141].

The German standard VDE 0126-1-1 [128] for grid-connected PV systems requires isolating the supply within 5 s after an impedance change of 1 ohm. The test setup proposed by this standard is shown in Fig. 51.

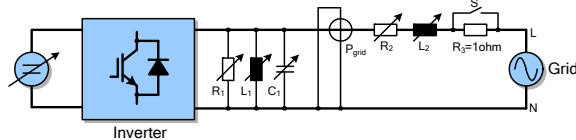Fig. 51. Test setup for the German standard VDE 0126-1-1 [128].

According to IEEE 929-2000 standard, a PV inverter shall cease to energize the utility line in ten cycles or less when subjected to a typical islanded load in which either of the following is true:

• There is at least a 50% mismatch in real power load to inverter output (that is, real power load is <50% or >150% of inverter power output).

• The islanded-load power factor is <0.95 (lead or lag).

If the real-power-generation-to-load match is within 50% and the islanded-load power factor is >0.95, then a PV inverter will cease to energize the utility line within 2 seconds whenever the connected line has a quality factor of 2.5 or less.

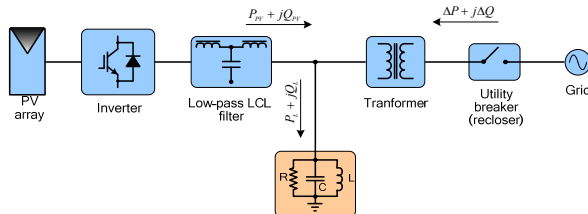The test setup for the IEEE 929-2000 is depicted in Fig. 52.

Fig. 52. Islanding operation test setup for IEEE 929-2000 standard [87].

There are numerous islanding detection methods for grid-connected PV systems reported in the technical literature [142]-[157] and their development has been summarized in a number of recent technical papers [147] and reports [142], [143]. They can be classified into two broad categories, namely, passive and active which can be inverter built or utility supported. The passive methods are based on the detection of the following:

• Over-voltage/under-voltage protection (OVP/UVP) [142], [144].

• Over-frequency/under-frequency protection (OFP /UFP) [142], [144].

• Voltage phase jump [142], [144], [147].

• Voltage harmonic monitoring [144], [147].

• Current harmonic monitoring.

However, passive methods have a number of weaknesses and inability to detect islanding. The use of non-detection zones (NDZs) is used as a measure of performance for both these techniques as well as the active ones in a number of papers [152], [154]. An evaluation of different but most widely-used passive anti-islanding methods is offered for passive methods in [136] and an excellent overview report for both passive and active methods is available in [142].

Active methods have been developed in order to overcome the limitations of the passive methods. In simple terms, active methods introduce perturbations in the inverter output power for a number of parameters as follows:

• Output power variation either real or reactive [144], [155].

• Active frequency drift or frequency shift up/down [142], [147]-[151].

• Sliding mode or slip-mode frequency shift [142], [147], [151].

• Sandia frequency shift or accelerated frequency drift or active frequency drift with positive feedback [147], [150].

• Impedance estimation [138], [139].

• Detection of impedance at a specific frequency or monitoring of harmonic distortion [142], [157].

• Sandia voltage shift [142].

• Frequency jump [142].

In a recent paper, it has been shown that although the effectiveness of passive methods can be established by non-detection zones [146] as represented by the power mismatch space (ΔP vs. ΔQ), in active frequency drifting methods their performance can be evaluated by using load parameter space based on the values of the quality factor and resonant frequency of the local load [154].

Although most of the papers have been concentrated on PV inverters, islanding detection is also needed for all other inverter based systems using different sources such as fuel cells [140], [155]. The algorithm proposed in [155] is an active method and continuously perturbs the reactive power supplied by the inverter by as much as $\pm 5\%$ while monitoring the utility voltage and frequency simultaneously. When islanding occurs, the deviation of the frequency taking place results in a real power reduced to 80%. A drop in voltage positively confirms islanding which in turn results in the inverter being successfully disconnected.

Many papers have concentrated on single-phase inverters and others also address three-phase technology [143], using DQ implementation [156]. Recently, the power mismatch for the 3rd and 5th harmonics and the implementation of an active anti-islanding method using resonant controllers was reported in [157].

Although numerous techniques exist and their implementation varies as it has been discussed so far, it is important to note that a recommendation for robust software based algorithms would simplify matters for the easier adoption of the most robust and simplest technique of all, and this should be kept as a guide for the further development of the anti-islanding technology [158].

A. Wind power

The wind turbine market was dominated in the last years by ten major companies [6], [48] and [50]. At the end of 2005 the wind turbine market share by manufacturer was as shown in Fig. 53.

The Danish company VESTAS Wind Systems A/S was still on the top position among the largest manufacturers of wind turbines in the world, followed by GE Wind, as the second largest in the world. German manufacturers ENERCON, Gamesa and Suzlon are in third, fourth and fifth positions, respectively. Notice that, the first four largest suppliers (Vestas, Gamesa, Enercon, GE Wind) had much larger markets with the first leading positions, compared to the others.
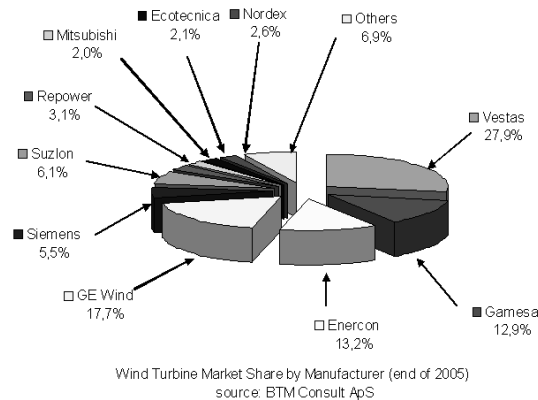

Fig. 53. Wind turbine market share by manufacturer (end of 2005).

Nowadays, the most attractive concept seemed to be the variable speed wind turbine with pitch control. Out of the Top Five-suppliers, only Siemens Wind Power (ex Bonus) used the 'traditional' active stall fixed speed concept, while the other manufacturers had at least one of their two largest wind turbines with the variable speed concept.

However, recently Siemens Wind Power has released the multi-megawatt class variable speed full-scale power converter wind turbine based on the squirrel-cage induction generator. The most used generator type was the induction generator (WRIG and SCIG). Only ENERCON and GE wind used the synchronous generator (WRSG). Only one manufacturer, ENERCON, offered a gearless variable speed wind turbine. All wind turbines manufacturers used a step-up transformer for connection of the generator to the grid.

A trend towards the configuration using a doubly-fed induction generator concept (Type C) with variable speed and variable pitch control, can be identified. In order to illustrate this trend, a dedicated investigation of the market penetration for the different wind turbine concepts is presented in [6]. The analysis cover approximately 75% of the accumulated world power installed at the end of 2004 as shown in Fig. 54.

Full-scale power converter based wind turbines have a relative constant market share over the years, while the interest for the variable-rotor resistance wind turbines (Type B) have fall down in the considered period.
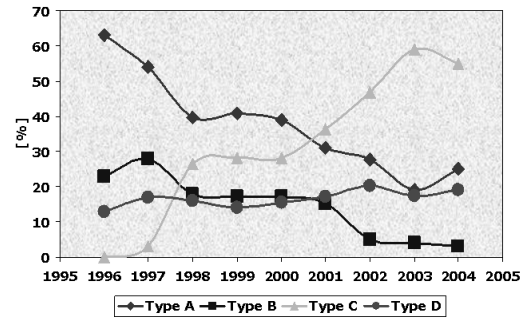
Fig. 54. Wind World share of yearly installed power for the considered wind turbine concepts (see Fig. 7 to Fig. 10).

B. Solar power

PV solar electricity is also a booming industry; since 1980, when terrestrial applications began, annual installation of photovoltaic power has increased to above 750 MWp, the cumulative installed PV power in 2004 reaching approximately 2.6 GWp [159] and [160].
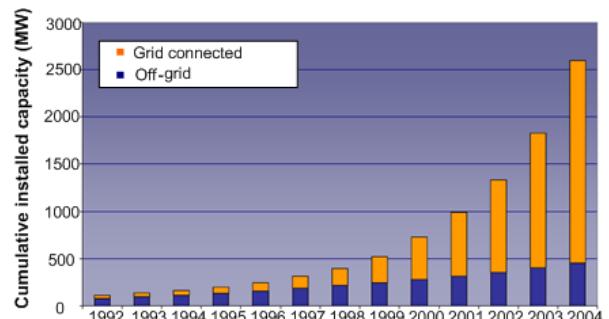
Fig. 55. Cumulative installed capacity from 1992 to 2004 in the IEA-PVPS reporting countries (source: IEA-PVPS, http://www.iea-pvps.org).

The annual rate of growth has varied between 20% in 1994 to over 40% in 2000, but the growth between 2002 and 2003 of 36% has been similar to the latest three years. As in the previous years the vast majority of new capacity was installed in Japan, Germany, and USA, with these three countries accounting for about 88% of the total installed in the year [160].

Historically the main market segments for PV were the remote industrial and developing country applications where PV power over long term is often more cost-effective than alternative power options such as diesel generator or mains grid extension. According to the IEA-PVPS, since 1997, the proportion of new grid-connected PV installed in the reporting countries rose from 42% to more than 93% in 2004 [160] (see Fig. 55).

According to [161], the prices for PV modules are around €5.7/Wp in Europe, with the lowest prices of: €3.10/Wp for monocrystalline modules, €3.02/Wp for polycrystalline modules and €2.96/Wp for thin film modules.

The prices for PV modules in the recent years are shown in Fig. 56.

In addition to the PV module cost, the cost and reliability of PV inverters are basic issues if market competitive PV supply systems are the aim. The inverter cost share represents about 10-15% of the total investment cost of a grid connected system.
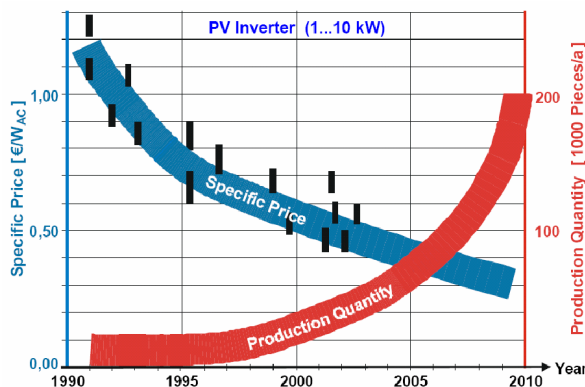
Fig. 56. Development and prognoses of specific cost and production quantity for the PV inverter of nominal powers between 1 and 10 kW during two decades (¦ indicates specific prices of products on the market [162].

The development of PV inverter specific cost (€/WAC) in small to medium power range (1-10 kW) is illustrated in Fig. 56. It can be seen that the inverter cost of this power class has decreased by more than 50% during the last decade. The main reasons for this reduction are the increase of the production quantities and the implementation of new system technologies (e.g. string-inverters). A further 50 % reduction of the specific cost is anticipated during the coming decade. The corresponding specific cost is expected to achieve about 0.3 €/WAC by the year 2010, which requires the implementation of specific measures for the development and the manufacturing processes [162].

VI. Conclusion

The paper discusses the applications of power electronic for both wind turbine and photovoltaic technologies. The development of modern power electronics has been briefly reviewed. The applications of power electronics in various kinds of wind turbine generation systems and offshore wind farms are also illustrated, showing that the wind turbine behavior/performance is significantly improved by using power electronics. They are able to act as a contributor to the frequency and voltage control by means of active and reactive power control.

Furthermore, PV systems are discussed including technology, inverters and their control methods.

Finally, a status of the wind turbine and PV market is given and some future trends are highlighted. Both wind and PV will be important power sources for the future energy system.

VII. References

[1] S. Heier, "Grid integration of wind energy conversion systems", translated by Rachel Waddington, John Wiley, 1998. ISBN-10: 0-47-197143X.

[2] E. Bossanyi, "Wind Energy Handbook", John Wiley, 2000.

[3] L.H. Hansen, L. Helle, F. Blaabjerg, E. Ritchie, S. Munk-Nielsen, H. Bindner, P. Sørensen and B. Bak-Jensen, "Conceptual survey of Generators and Power Electronics for Wind Turbines", Risø-R-1205(EN), 2001.

[4] F. Blaabjerg, and Z. Chen, "Power electronics as an enabling technology for renewable energy integration", Journal of Power Electronics, vol. 3, no.2, 2003, pp. 81-89.

[5] F. Blaabjerg, F. Iov, R. Teodorescu, Z. Chen, "Power Electronics in Renewable Energy Systems", keynote paper presented at EPE-PEMC Conference, 2006, Portoroz, Slovenia, pp. 1-17.

[6] A.D. Hansen, F. Iov, F. Blaabjerg, L.H. Hansen, "Review of contemporary wind turbine concepts and their market penetration", Journal of Wind Engineering, 28(3), 2004, pp. 247-263.

[7] F. Iov, F. Blaabjerg, "UNIFLEX-PM. Advanced power converters for universal and flexible power management in future electricity network – Converter applications in future European electricity network". Deliverable D2.1, EC Contract no. 019794(SES6), February 2007, p. 171, (available on line www.eee.nott.ac.uk/uniflex/Deliverables.htm).

[8] D. Milborrow, "Going mainstream at the grid face. Examining grid codes for wind", Windpower Monthly, September 2005, ISSN 109-7318.

[9] F. Iov, A.D. Hansen, P. Sørensen, N.A. Cutululis, "Mapping of grid faults and grid codes". Risø-R-1617(EN) (2007) 41 p. (available online at www.risoe.dk).

[10] Z. Chen, E. Spooner, "Grid Power Quality with Variable-Speed Wind Turbines", IEEE Trans. on Energy Conversion, Vol. 16, No.2, June 2001, pp. 148-154.

[11] F. Iov, Z. Chen, F. Blaabjerg, A. Hansen, P. Sorensen, "A New Simulation Platform to Model, Optimize and Design Wind Turbine", Proc. of IECON, 2002, Vol. 1, pp. 561-566.

[12] S. Bolik, "Grid Requirements Challenges for Wind Turbines", Proc. of Fourth International Workshop on Large-Scale Integration of Wind Power and Transmission Networks for Offshore Windfarms, 2003.

[13] E. Bogalecka, "Power control of a doubly fed induction generator without speed or position sensor", Proc. of EPE, 1993, Vol.8, pp. 224-228.

[14] O. Carlson, J. Hylander, K. Thorborg, "Survey of variable speed operation of wind turbines", Proc. of European Union Wind Energy Conference, Sweden, 1996, pp. 406-409.

[15] M. Dahlgren, H. Frank, M. Leijon, F. Owman, L. Walfridsson, "Wind power goes large scale", ABB Review, 2000, Vol.3, pp. 31-37.

[16] M.R. Dubois, H. Polinder, J.A. Ferreira, "Comparison of Generator Topologies for Direct-Drive Wind Turbines", IEEE Nordic Workshop on Power and Industrial Electronics (Norpie 2000), Aalborg-Denmark, pp. 22-26.

[17] L.H. Hansen, P.H. Madsen, F. Blaabjerg, H.C. Christensen, U. Lindhard, K. Eskildsen, "Generators and power electronics technology for wind turbines", Proc. of IECON '01, Vol. 3, 2001, pp. 2000-2005.

[18] Z. Chen, E. Spooner, "Wind turbine power converters: a comparative study", Proc. of PEVD, 1998, pp. 471-476.

[19] M.P. Kazmierkowski, R. Krishnan, F. Blaabjerg,"Control in Power Electronics-Selected problems", Academic Press, 2002. ISBN 0-12-402772-5.

[20] Å. Larsson, "The Power quality of Wind Turbines", Ph.D. report, Chalmers University of Technology, Göteborg, Sweden, 2000.

[21] R. Pena, J.C. Clare, G.M. Asher, "Doubly fed induction generator using back-to-back PWM converters and its application to variable speed wind-energy generation". IEE proceedings on Electronic Power application, 1996, pp. 231-241.

[22] J. Rodriguez, L. Moran, A. Gonzalez, C. Silva, "High voltage multilevel converter with regeneration capability", Proc. of PESC, 1999, Vol.2, pp.1077-1082.

[23] P. Sørensen, B. Bak-Jensen, J. Kristian, A.D. Hansen, L. Janosi, J. Bech, " Power Plant Characteristics of Wind Farms", Proc. of the Int. Conf. in Wind Power for the 21st Century, 2000.

[24] K. Wallace, J.A. Oliver, "Variable-Speed Generation Controlled by Passive Elements", Proc. of ICEM, 1998, pp. 1554-1559.

[25] S. Bhowmik, R. Spee, J.H.R. Enslin, "Performance optimization for doubly fed wind power generation systems", IEEE Trans. on Industry Applications, Vol. 35, No. 4 , July-Aug. 1999, pp. 949-958.

[26] Z. Saad-Saoud, N. Jenkins, "The application of advanced static VAr compensators to wind farms", IEE Colloquium on Power Electronics for Renewable Energy, 1997, pp. 6/1 - 6/5.

[27] J.B. Ekanayake, L. Holdsworth, W. XueGuang, N. Jenkins, "Dynamic modelling of doubly fed induction generator wind turbines", IEEE Trans. on Power Systems, Vol. 18 , No. 2 , May 2003 , pp.803-809.

[28] D. Arsudis, "Doppeltgespeister Drehstromgenerator mit Spannungszwischenkreis Umrichter in Rotorkreis für Wind Kraftanlagen, Ph.D. Thesis, 1998, T.U. Braunschweig, Germany.

[29] D. Arsudis, "Sensorlose Regelung einer doppelt-gespeisten Asynchronmaschine mit geringen Netzrückwirkungen", Archiv für Elektrotechnik, Vol. 74, 1990, pp. 89-97.

[30] T. Matsuzaka, K. Trusliga, S. Yamada, H. Kitahara, "A variable speed wind generating system and its test results". Proc. of EWEC '89, Part Two, 1989, pp. 608-612.

[31] R.S. Barton, T.J. Horp, G.P. Schanzenback, "Control System Design for the MOD-5A 7.3 MW wind turbine generator". Proc. of DOE/NASA workshop on Horizontal-Axis Wind Turbine Technology Workshop, 1984, pp. 157-174.

[32] O. Warneke, "Einsatz einer doppeltgespeisten Asynchronmaschine in der Großen Windenergie-anlage Growian", Siemens-Energietechnik 5, Heft 6, 1983, pp. 364-367.

[33] L. Gertmar, "Power Electronics and Wind Power", Proc. of EPE 2003, paper 1205.

[34] F. Blaabjerg, Z. Chen, S.B. Kjær, "Power Electronics as Efficient Interface in Dispersed Power Generation Systems", IEEE Trans. on PE, Vol. 19, No. 4, 2004, pp. 1184-1194.

[35] E.N. Hinrichsen, "Controls for variable pitch wind turbine generators", IEEE Trans. on Power Apparatus and Systems, Vol. 103, No. 4, 1984, pp. 886-892.

[36] B.J. Baliga, "Power IC's in the saddle", IEEE Spectrum, July 1995, pp. 34-49.

[37] A.D. Hansen, C. Jauch, P. Soerensen, F. Iov, F. Blaabjerg. "Dynamic Wind Turbine Models in Power System Simulation Tool DigSilent", Report Risoe-R-1400 (EN), Dec. 2003, ISBN 87-550-3198-6 (80 pages).

[38] T. A. Lipo, "Variable Speed Generator Technology Options for Wind Turbine Generators", NASA Workshop on HAWTT Technology, May 1984, pp. 214-220.

[39] K. Thorborg, "Asynchronous Machine with Variable Speed", Appendix G, Power Electronics, 1988, ISBN 0-13-686593-3, pp. G1.

[40] D. Arsudis, W. Vollstedt, "Sensorless Power control of a Double-Fed AC-Machine with nearly Sinusoidal Line Currents", Proc. of EPE, 1989, pp. 899-904.

[41] M. Yamamoto, O. Motoyoshi, "Active and Reactive Power control for Doubly-Fed Wound Rotor Induction Generator", Proc. of PESC, 1990, Vol. 1, pp. 455-460.

[42] O. Carlson, J. Hylander, S. Tsiolis, "Variable Speed AC-Generators Applied in WECS", European Wind Energy Association Conference and Exhibition, October 1986, pp. 685-690.

[43] J.D. van Wyk, J.H.R. Enslin, "A Study of Wind Power Converter with Microcomputer Based Maximal Power Control Utilising an Oversynchronous Electronic Schertives Cascade", Proc. of IPEC, 1983, Vol. I, pp. 766-777.

[44] T. Sun, Z. Chen, F. Blaabjerg, "Flicker Study on Variable Speed Wind Turbines With Doubly Fed Induction Generators". IEEE Trans. on Energy Conversion, Vol. 20, No. 4, 2005, pp. 896-905.

[45] T. Sun, Z. Chen, F. Blaabjerg, "Transient Stability of DFIG Wind Turbines at an External Short-circuit-Fault". Wind Energy, 2005, Vol. 8, pp. 345-360.

[46] L. Mihet-Popa, F. Blaabjerg, I. Boldea, "Wind Turbine Generator Modeling and Simulation Where Rotational Speed is the Controlled Variable". IEEE Transactions on Industry Applications, 2004, Vol. 40, No. 1. pp. 3-10.

[47] F. Iov, P. Soerensen, A. Hansen, F. Blaabjerg, "Modelling, Analysis and Control of DC-connected Wind Farms to Grid", International Review of Electrical Engineering, Praise Worthy Prize, February 2006, pp.10, ISSN 1827-6600.

[48] F. Iov, P. Soerensen, A. Hansen, F. Blaabjerg, "Modelling and Control of VSC based DC Connection for Active Stall Wind Farms to Grid", IEE Japan Trans. on Industry Applications, April 2006, Vol. 126-D, No. 5.

[49] A. Cameron, E. de Vries, "Top of the list", Renewable Energy World, James & James, January-February 2006, Vol. 9, No. 1, pp. 56-66, ISSN 1462-6381.

[50] A. Cameron, "Changing winds", BTM's world market update, Renewable Energy World, Pennwell Co., July-August 2006, Vol. 9, No. 4, pp. 28-41, ISSN 1462-6381.

[51] EnergiNet – Grid connection of wind turbines to networks with voltages below 100 kV, Regulation TF 3.2.6, May 2004, p. 29.

[52] Energinet - Grid connection of wind turbines to networks with voltages above 100 kV, Regulation TF 3.2.5, December 2004, p. 25.

[53] ESB Networks – Distribution Code, version 1.4, February 2005.

[54] CER – Wind Farm Transmission Grid Code Provisions, July 2004.

[55] E.ON-Netz – Grid Code. High and extra high voltage, April 2006.

[56] VDN – Transmission Code 2003. Network and System Rules of the German Transmission System Operators, August 2003.

[57] VDN – Distribution Code 2003. Rules on access to distribution networks, August 2003.

[58] National Grid Electricity Transmission plc – The grid code, Issue 3, Revision 17, September 2006.

[59] Gambica Technical Guide - Managing Harmonics. A guide to ENA Engineering Recommendation G5/4-1, 4th Edition, 2006, The Energy Networks Association.

[60] REE – Requisitos de respuesta frente a huecos de tension de las instalaciones de produccion de regimen especial, PO 12.3, November 2005.

[61] ENEL – DK 5400 - Criteri di allacciamento di clienti alla rete AT della distribuzione, October 2004.

[62] ENEL - – DK 5740 - Criteri di allacciamento di impianti di produzione alla rete MT di ENEL distribuzione, February 2005.

[63] TERNA - Codice di trasmissione, dispacciamento, sviluppo e sicurezza della rete, 2006.

[64] CEI 11/32, Appendice N.6 – Normativa impianti di produzione eolica, February 2006 (draft).

[65] IEA International Energy Agency: Trends in Photovoltaic Applications. Survey report of selected IEA countries between 1992 and 2003. Source: http://www.oja-services.nl/iea-pvps/products/download/rep1_13.pdf.

[66] H. Haeberlin, "Evolution of Inverters for Grid connected PV systems from 1989 to 2000", Proc. of Photovoltaic Solar Energy Conference, 2001.

[67] T. Shimizu, M. Hirakata, T. Kamezawa, H. Watanabe, "Generation Control Circuit for Photovoltaic Modules", IEEE Trans. On Power Electronics, Vol. 16, No. 3, May, 2001, pp. 293-300.

[68] M. Calais, V.G. Agelidis, L.J. Borle, M.S. Dymond, "A transformerless five level cascaded inverter based single phase photovoltaic system", Proc. of PESC, 2000, Vol. 3, pp. 1173-1178.

[69] R.W. Erickson, D. Maksimovic, "Fundamentals of Power Electronics", Kluwer Academic Pub; March 1, 1997, ISBN: 0-412-08541-0, 773 pages.

[70] M. Calais, J. Myrzik, T. Spooner, V.G. Agelidis, "Inverters for single-phase grid connected photovoltaic systems - An overview", Proc. of PESC '02, 2002, Vol. 4, pp. 1995 – 2000.

[71] F. Blaabjerg, R. Teodorescu, Z. Chen, M. Liserre, "Power Converters and Control of Renewable Energy Systems", Proc. of ICPE, 2004, pp. 1-19.

[72] R. Teodorescu, F. Blaabjerg, M. Liserre, U. Borup, " A New Control Structure for Grid-Connected PV Inverters with Zero Steady-State Error and Selective Harmonic Compensation", Proc. of APEC, 2004, Vol. 1, pp. 580-586.

[73] S. Fukuda and T. Yoda, "A novel current-tracking method for active filters based on a sinusoidal internal mode", IEEE Trans. on Ind. App., 2001, Vol.37, No. 3, pp. 888-895.

[74] X. Yuan, W. Merk, H. Stemmler and J. Allmeling, "Stationary-Frame Generalized Integrators for Current Control of Active Power Filters with Zero Steady-State Error for Current Harmonics of Concern Under Unbalanced and Distorted Operating Conditions", IEEE Trans. on Ind. App., Vol. 38, No. 2, 2002, pp. 523-532.

[75] M. Ciobotaru, R. Teodorescu, F. Blaabjerg, "Control of single-stage single-phase PV inverter", Proc. of EPE'05, 10 pages, ISBN : 90-75815-08-5.

[76] D.P. Hohm, M.E. Ropp, "Comparative Study of Maximum Power Point Tracking Algorithms Using an Experimental, Programmable, Maximum Power Point Tracking Test Bed". IEEE Proc. of Photovoltaic Specialists Conference, 2000, Pages:1699-1702.

[77] N. Femia, G. Petrone, G. Spagnuolo, M. Vitelli, "Optimizing sampling rate of P&O MPPT technique", Proc. of PESC, 2004, Vol. 3, pp. 1945-1949.

[78] A. Brambilla, M. Gambarara, A. Garutti, F. Ronchi, "New approach to photovoltaic arrays maximum power point tracking", Proc. of PESC, 1999, Vol. 2, pp. 632-637.

[79] X. Liu, L.A.C. Lopes, "An improved perturbation and observation maximum power point tracking algorithm for PV arrays", Proc. of PESC, 2004, Vol. 3, Pages: 2005 - 2010.

[80] D. Sera, T. Kerekes, R. Teodorescu, and F. Blaabjerg, "Improved MPPT method for rapidly changing environmental conditions," in Industrial Electronics, 2006 IEEE International Symposium on, Vol. 2, 2006, pp.1420-1425.

[81] K.H. Hussein, I. Muta, T. Hoshino, M. Osakada, "Maximum photovoltaic power tracking: an algorithm for rapidly changing atmospheric conditions". IEE Trans. on Generation, Transmission and Distribution, Jan. 1995, Vol. 142, No. 1, pp. 59-64.

[82] W. Swiegers, Enslin J.H.R.: "An integrated maximum power point tracker for photovoltaic panels", Proc. of ISIE, 1998, Vol. 1, pp. 40-44.

[83] T.J. Liang, Y.C. Kuo and J.F. Chen, "Single-stage photovoltaic energy conversion system", IEE Proceedings Electric Power Applications, 2001, Vol. 148, No. 4, pp. 339-344.

[84] Y.C. Kuo and T.J. Liang, "Novel Maximum-Power-Point-Tracking Controller for Photovoltaic Energy Conversion System", IEEE Trans. on Industrial Electronics, 2001, Vol. 48, No. 3, pp. 594-601.

[85] M. Nikraz, H. Dehbonei, C.V.N. Curtin, "Digital control of a voltage source inverter in photovoltaic applications", Proc. of PESC, 2004, Vol. 5, 2004, pp. 3266-3271.

[86] "Characteristics of the utility interface for photovoltaic (PV) systems," IEC 61727-2002, 2002.

[87] IEEE Standard 929-2000: IEEE Recommended practice for utility interface of photovoltaic (PV) systems.

[88] M. Francesco De, L. Marco, D.A. Antonio, and P. Alberto, "Overview of Anti-Islanding Algorithms for PV Systems. Part I: Passive Methods," Proc. of EPE-PEMC, 2006, pp. 1878-1883.

[89] F. M. Gardner, "Phaselock Techniques", Publisher: Wiley-Interscience, 1979, Vol. 2nd edition, ISBN-10: 0471042943, 304 pages.

[90] F. Mur, V. Cardenas, J. Vaquero, and S. Martinez, "Phase synchronization and measurement digital systems of AC mains for power converters", Proc. of CIEP, 1998, pp. 188-194.

[91] J. W. Choi, Y.K. Kim, and H.G. Kim, "Digital PLL control for single-phase photovoltaic system", IEE Trans. on Electric Power Applications, 2006, Vol. 153, pp. 40-46.

[92] S.K. Chung, "A phase tracking system for three phase utility interface inverters", IEEE Trans. on Power Electronics, 2000, Vol. 15, pp. 431-438.

[93] C. T. Nguyen and K. Srinivasan, "A New Technique for Rapid Tracking of Frequency Deviations Based on Level Crossings," IEEE Trans. on Power Apparatus and Systems, 1984, Vol. PAS-103, pp. 2230-2236.

[94] B.P. McGrath, D.G. Holmes, J.J.H. Galloway, "Power converter line synchronization using a discrete Fourier transform (DFT) based on a variable sample rate", IEEE Trans. on Power Electronics, 2005, Vol. 20, pp. 877-884.

[95] O. Vainio, S. J. Ovaska, and M. Polla, "Adaptive filtering using multiplicative general parameters for zero-crossing detection", IEEE Trans. on Industrial Electronics, 2003, vol. 50, pp. 1340-1342.

[96] S. Valiviita, S. J. Ovaska, and J. Kyyra, "Adaptive signal processing system for accurate zero-crossing detection of cycloconverter phase currents", Proc. of PCC, 1997, Vol.1, pp. 467-472

[97] O. Vainio and S. J. Ovaska, "Noise reduction in zero crossing detection by predictive digital filtering," IEEE Trans. on Industrial Electronics, 1995, vol. 42, pp. 58-62.

[98] R.W. Wall, "Simple methods for detecting zero crossing", Proc. of IECON, 2003, Vol.3, pp. 2477-2481.

[99] S. Valiviita, "Neural network for zero-crossing detection of distorted line voltages in weak AC-systems", Proc. of IMTC, 1998, Vol.1, pp. 280-285.

[100] S. Das, P. Syam, G. Bandyopadhyay, and A.K. Chattopadhyay, "Wavelet transform application for zero-crossing detection of distorted line voltages in weak AC-systems", Proc. of INDICON, 2004, pp. 464-467.

[101] S. Valiviita, "Zero-crossing detection of distorted line voltages using 1-b measurements", IEEE Trans. on Industrial Electronics, 1999, Vol. 46, pp. 917-922.

[102] R. Weidenbrug, F. P. Dawson, and R. Bonert, "New synchronization method for thyristor power converters to weak", IEEE Trans. on Industrial Electronics, 1993, Vol. 40, pp. 505-511.

[103] D.M. Baker and V.G. Agelidis, "Phase-locked loop for microprocessor with reduced complexity voltage controlled oscillator suitable for inverters," Proc. of PEDES, 1998, pp. 464-469 Vol.1.

[104] D. Nedeljkovic, J. Nastran, D. Voncina, and V. Ambrozic, "Synchronization of active power filter current reference to the network", IEEE Trans. on Industrial Electronics, 1999, vol. 46, pp. 333-339.

[105] D. Nedeljkovic, V. Ambrozic, J. Nastran, and D. Hudnik, "Synchronization to the network without voltage zero-cross detection", Proc. of MELECON, 1998, Vol. 2, pp. 1228-1232.

[106] S. M. Silva, B. M. Lopes, B. J. C. Filho, R. P. Campana, and W. C. Bosventura, "Performance evaluation of PLL algorithms for single-phase grid-connected systems," Proc. of IAS, 2004, Vol.4, pp. 2259-2263.

[107] W. Tsai-Fu, S. Chih-Lung, N. Hung-Shou, and L. Guang-Feng, "A 1phi-3W inverter with grid connection and active power filtering based on nonlinear programming and fast-zero-phase detection algorithm", IEEE Trans. on Power Electronics, 2005, Vol. 20, pp. 218-226.

[108] P. Rodriguez, A. Luna, M. Ciobotaru, R. Teodorescu, F. Blaabjerg, "Advanced Grid Synchronization System for Power Converters under Unbalanced and Distorted Operating Conditions", Proc. of IECON, 2006, pp. 5173-5178.

[109] L. R. Limongi, R. Bojoi, C. Pica, F. Profumo, and A. Tenconi, "Analysis and Comparison of Phase Locked Loop Techniques for Grid Utility Applications", Proc. of PCC, 2007, pp. 674-681.

[110] M. Saitou, N. Matsui, and T. Shimizu, "A control strategy of single-phase active filter using a novel d-q transformation", Proc. of IAS, 2003, Vol. 2, pp. 1222-1227.

[111] P. Rodriguez, J. Pou, J. Bergas, J. I. Candela, R. P. Burgos, and D. Boroyevich, "Decoupled Double Synchronous Reference Frame PLL for Power Converters Control", IEEE Trans. on Power Electronics, 2007, vol. 22, pp. 584-592.

[112] K. De Brabandere, T. Loix, K. Engelen, B. Bolsens, J. Van den Keybus, J. Driesen, and R. Belmans, "Design and Operation of a Phase-Locked Loop with Kalman Estimator-Based Filter for Single-Phase Applications", Proc. of IECON, 2006, pp. 525-530.

[113] P. Rodriguez, J. Pou, J. Bergas, I. Candela, R. Burgos, and D. Boroyevic, "Double Synchronous Reference Frame PLL for Power Converters Control", Proc. of PESC, 2005, pp. 1415-1421.

[114] T. Ostrem, W. Sulkowski, L. E. Norum, and C. Wang, "Grid Connected Photovoltaic (PV) Inverter with Robust Phase-Locked Loop (PLL)", Proc. of TDC, 2006, pp. 1-7.

[115] M. Ciobotaru, R. Teodorescu, and F. Blaabjerg, "Improved PLL structures for single-phase grid inverters", Proc. of PELINCEC, 2005, pp. 1-6.

[116] S. Shinnaka, "A New Frequency-Adaptive Phase-Estimation Method Based on a New PLL Structure for Single-Phase Signals", Proc. of PCC, 2007, pp. 191-198.

[117] M. Ciobotaru, R. Teodorescu, and F. Blaabjerg, "A New Single-Phase PLL Structure Based on Second Order Generalized Integrator", Proc. of PESC, 2006, pp. 1-6.

[118] V. Kaura and V. Blasko, "Operation of a phase locked loop system under distorted utility conditions", Proc. of APEC, 1996, Vol.2, pp. 703-708.

[119] S. K. Chung, "Phase-locked loop for grid-connected three-phase power conversion systems", IEE Trans. on Electric Power Applications, 2000, vol. 147, pp. 213-219.

[120] A. W. Krieger and J. C. Salmon, "Phase-locked loop synchronization with gated control," Proc. of CCECE, 2005, pp. 523-526.

[121] A. V. Timbus, R. Teodorescu, F. Blaabjerg, M. Liserre, and P. Rodriguez, "PLL Algorithm for Power Generation Systems Robust to Grid Voltage Faults", Proc. of PESC, 2006. pp. 1-7.

[122] L. N. Arruda, S. M. Silva, and B. J. C. Filho, "PLL structures for utility connected systems", Proc. of IAS, 2001, Vol. 4, pp. 2655-2660.

[123] E. S. Sreeraj and K. Chatterjee, "Power Factor Improvement in One Cycle Controlled Converter", Proc. of ISIE, 2006, pp. 1454-1460.

[124] S. K. Chung, H. B. Shin, and H. W. Lee, "Precision control of single-phase PWM inverter using PLL compensation", IEE Trans. on Electric Power Applications, 2005, Vol. 152, pp. 429-436.

[125] A. Timbus, M. Liserre, R. Teodorescu, and F. Blaabjerg, "Synchronization Methods for Three Phase Distributed Power Generation Systems. An Overview and Evaluation", Proc. of PESC, 2005, pp. 2474-2481.

[126] L. N. Arruda, B. J. Cardoso Filho, S. M. Silva, S. R. Silva, and A. S. A. C. Diniz, "Wide bandwidth single and three-phase PLL structures for grid-tied", Proc. of Photovoltaic Specialists Conference, 2000, pp. 1660-1663.

[127] J. Salaet, S. Alepuz, A. Gilabert, and J. Bordonau, "Comparison between two methods of DQ transformation for single phase converters control. Application to a 3-level boost rectifier", Proc. of PESC, 2004, Vol.1, pp. 214-220.

[128] DIN VDE 0126-1-1, "Automatic disconnection device between a generator and the public low-voltage grid", June 2005.

[129] M. Liserre, R. Teodorescu, and F. Blaabjerg, "Stability of grid-connected PV inverters with large grid impedance variation", in Proc. of PESC, 2004, pp. 4773–4779.

[130] L. Asiminoaei, R. Teodorescu, F. Blaabjerg, U. Borup, "Implementation and Test of an Online Embedded Grid Impedance Estimation Technique for PV Inverters", IEEE Trans. on Industrial Electronics, 2005, vol.52, no.4, pp. 1136-1144.

[131] M. Sumner, B. Palethorpe, D. Thomas, P. Zanchetta, M.C. Di Piazza, "Estimation of power supply harmonic impedance using a controlled voltage disturbance", Proc. of PESC, 2001, vol.2, pp. 522-527.

[132] M.C. Di Piazza, P. Zanchetta, M. Sumner, D.W.P. Thomas, "Estimation of load impedance in a power system", Proc. of Harmonics and Quality of Power Conference, 2000, vol.2, pp. 520-525.

[133] M. Sumner, B. Palethorpe, D.W.P. Thomas, P. Zanchetta, M.C. Di Piazza, "A technique for power supply harmonic impedance estimation using a controlled voltage disturbance", IEEE Trans. on Power Electronics, 2002, vol.17, no.2, pp. 207-215.

[134] J.P. Rhode, A.W. Kelley, M.E. Baran, "Line impedance measurement: a nondisruptive wideband technique", Proc. of IAS, 1995, vol.3, pp. 2233-2240.

[135] N. Ishigure, K. Matsui, F. Ueda, "Development of an on-line impedance meter to measure the impedance of a distribution line", Proc. of ISIE, 2001, vol.1, pp. 549-554.

[136] Tsukamoto, M.; Ogawa, S.; Natsuda, Y.; Minowa, Y.; Nishimura, S., "Advanced technology to identify harmonics characteristics and results of measuring," Harmonics and Quality of Power, 2000. Proceedings. Ninth International Conference on, vol.1, pp., 341-346.

[137] K.O.H. Pedersen, A.H. Nielsen, and N.K. Poulsen, "Short-circuit impedance measurement," IEE Trans. on Generation, Transmission and Distribution, 2003, vol. 150, no. 2, pp. 169–174.

[138] M. Ciobotaru, R. Teodorescu, P. Rodriguez, A. Timbus and F. Blaabjerg, "Online grid impedance estimation for single-phase grid-connected systems using PQ variations", Proc. of PESC, 2007, pp. 2306-2312.

[139] M. Ciobotaru, R. Teodorescu and F. Blaabjerg, "On-line grid impedance estimation based on harmonic injection for grid-connected PV inverter", Proc. of ISIE, 2007, pp. 2437-2442.

[140] IEEE Standard 1547-2003: IEEE Standard for interconnecting distributed resources with electric power systems.

[141] A. Woyte, K. De Brabandere, D.V. Dommelen, R. Belmans, and J. Nijs, "International harmonization of grid connection guidelines: adequate requirements for the prevention of unintentional islanding", Progress in Photovoltaics: Research and Applications, 2003, Vol. 11, pp. 407-424.

[142] W. Bower and M Ropp, "Evaluation of islanding detection methods for photovoltaic utility-interactive power systems", IEA Task V Report IEA-PVPS T5-09, March 2002.

[143] Z. Ye, R. Walling, L. Garces, R. Zhou, L. Li and T. Wang, "Study and development of anti-islanding control for grid-connected inverters", National Renewable Energy Laboratory, NREL/SR-560-36243, May 2004.

[144] H. Kobayashi, K. Takigawa and E. Hashimoto, "Method for preventing islanding phenomenon on utility grid with a number of small scale PV systems", Proc. of Photovoltaic Specialists Conference, 1991, pp. 695-700.

[145] A. Kitamura, M. Okamoto, F. Yamamoto, K. Nakaji, H. Matsuda, K. Hotta, "Islanding phenomenon elimination study at Rokko test center", Proc. of Photovoltaic Specialists Conference, 1994, Vol. 1, p. 759-762.

[146] Z. Ye, A. Kolwalkar, Y. Zhang, P. Du and R. Walling, "Evaluation of anti-islanding schemes based on non-detection zone concept", IEEE Trans. on Power Electronics, 2004, Vol. 19, No. 5, pp. 1171-1176.

[147] M.E. Ropp, M. Begovic and A. Rohatgi, "Prevention of islanding in grid-connected photovoltaic systems", Progress in Photovoltaics: Research and Applications, 1999, Vol. 7, pp. 39-59.

[148] M.E. Ropp, M. Begovic and A. Rohatgi, "Analysis and performance assessment of the active frequency drift method of islanding prevention", IEEE Trans. on Energy Conversion, 1999, Vol. 14, No. 3, pp. 810-816.

[149] S. Yuyama, T. Ichinose, K. Kimoto, T. Itami, T. Ambo, C. Okado, K. Nakajima. S. Hojo, H. Shinohara, S. Ioka and M. Kuniyoshi, "A high-speed frequency shift method as a protection for islanding phenomena of utility interactive PV systems", Solar Energy Materials and Solar Cells, 1994, Vol. 35, pp. 477-486.

[150] P. Sanchis, L. Marroyo and J. Coloma, "Design methodology for the frequency shift method of islanding prevention and analysis of its detection capability", Progress in Photovoltaics: Research and Applications, 2005, Vol. 13, pp. 409-428.

[151] G.A. Smith, P.A. Onions and D.G. Infield, "Predicting islanding operation of grid connected PV inverters", IEE Trans. Electrical Power Applications, 2000, Vol. 147, No 1, pp. 1-5.

[152] M.E. Ropp, M. Begovic, A. Rohatgi, G.A. Kern, H. Bonn and S. Gonzalez, "Determining the relative effectiveness of islanding detection methods using phase criteria and non-detection zones", IEEE Trans. on Energy Conversion, 2000, Vol. 15, No. 3, pp. 290-296.

[153] G.K. Hung, C.C. Chang and C.L. Chen, "Automatic phase-shift method for islanding detection of grid-connected photovoltaic inverters", IEEE Trans. on Energy Conversion, 2003, Vol. 18, No. 1, pp. 169-173.

[154] V. John, Z. Ye and A. Kolwalkar, "Investigation of anti-islanding protection of power converter based distributed generators using frequency domain analysis", IEEE Trans. on Power Electronics, 2004, Vol. 19, No. 5, pp. 1177-1183.

[155] L.A.C. Lopes and H. Sun, "Performance assessment of active frequency drifting islanding detection methods", IEEE Trans. on Energy Conversion, 2006, Vol. 21, No. 1, pp. 171-180.

[156] C. Jeraputra and P.N. Enjeti, "Development of a robust anti-islanding algorithm for utility interconnection of distributed fuel cell powered generation", IEEE Trans. on Power Electronics, 2004, Vol. 19, No. 5, pp. 1163-1170.

[157] Z. Ye, L. Li, L. Garces, C. Wang, R. Zhang, M. Dame, R. Walling and N. Miller, "A new family of active anti-islanding schemes based on DQ implementation for grid-connected inverters", Proc. of PESC, 2004, pp. 235-241.

[158] N. Cullen, J. Thornycroft and A. Collinson, "Risk analysis of islanding of photovoltaic power systems within low voltage distribution networks", IEA Report PVPS T5-08, March 2002.

[159] European Photovoltaic Industry Association: EPIA Roadmap. Source: http://www.epia.org/04events/docs/EPIAroadmap.pdf.

[160] IEA International Energy Agency: Trends in Photovoltaic Applications. Survey report of selected IEA countries between 1992 and 2003. Source: http://www.oja-services.nl/iea-pvps/products/download/rep1_13.pdf.

[161] G. Cramer , M. Ibrahim and W. Kleinkauf, "PV System Technologies: State-of-the-art and Trends in Decentralized Electrification." Science Direct-Refocus, Vol. 5, pp. 38-42. source: www.sciencedirect.com, www.re-focus.net.

[162] Mohammad Shahidehpour, Fred Schwartz, "Don't Let the Sun Go Down on PV". IEEE Power and Energy Magazine, 2004, Vol. 2, No. 3, pp. 40-48.

Appendix I. Review of connection requirements for wind power in European grid codes [7].

		Denmark		Ireland	Germany	Great Britain	Spain	Italy (draft)
		DS	TS					
Voltage Level		DS	TS	DS(TS)	TS(DS)	TS(DS)	TS	> 35 kV
Power Level		all	all	≥5MW	all	all	all	> 10 MW
Tolerance over frequency range		yes	yes	yes	yes	yes	-	yes
Frequency	Frequency control	all	all	all	all	all	-	> 25 MW
	MW Curtailment	20-100% P_r	20-100% P_r	yes	yes	-	-	-
	Maximum Ramp Rates	10-100% P_r/min	10-100% P_r/min	1-30 MW/min	yes	-	-	<20% P_r/min
Voltage	Voltage Control	no	no	yes	no	no	-	no
	Reactive Power Control	yes	yes	yes	yes	yes	-	yes
Voltage quality	Fast voltage variations	≤ 3%	≤ 3%	-	≤ 2%	≤ 3%-	-	EN 50160
	Short Term Flicker Severity	-	≤ 0.3	≤ 0.35	-	≤0.8	-	EN 50160
	Long Term Flicker Severity	≤ 0.35	≤ 0.2	≤ 0.35	≤ 0.46	≤0.6	-	EN 50160
	Harmonic Compatibility Levels	Specific levels	-	Specific Levels[1]	EN 50160	IEC 61000-3-2	-	EN 50160
	THD	-	≤ 1.5%	≤ 1.5%	≤ 8%	N/A	-	EN 50160
Fault ride-through	Fault duration	100 msec	100 msec	625 msec	150 msec	140 msec	500 msec	500 msec
	Min voltage	25%U_r	25%U_r	15%U_r	0%U_r	15%U_r	20%U_r	20% U_r
	Recovery time	1 sec	1 sec	3 sec	1.5 sec	1.2 sec	1 sec	0.3 sec
	Voltage profile	2, 3-ph	1, 2, 3- ph	1, 2, 3- ph	generic	generic	generic	generic
	Reactive current injection	no	no	no	Up to 100%	no	Up to 100%	no
Island operation		not required	not required	not required	not required	not required	not required	not required
Black start capability		not required	not required	may	if required	not required	not required	not required
Signals, Communication and Control	Availability	yes	yes	yes	yes	yes	-	yes
	Active power output	yes	yes	yes	yes	yes	-	yes
	Reactive power output	yes	yes	yes	yes	yes	-	yes
	MW Curtailment	yes	yes	yes	yes	yes	-	-
	Frequency control	yes	yes	yes	yes	yes	-	-
	Circuit breaker status	yes	yes	yes	yes	yes	-	yes
	Meteorological data: Wind speed, wind direction, air pressure and temperature	yes	yes	yes	-	-	-	yes

1) Harmonic compatibility levels are given in general for loads and installations. DSO shall provide a schedule of individual limits where appropriate.

[XII] Offset rejection for PLL based synchronization in grid-connected converters

by M. Ciobotaru, R. Teodorescu, and V. G. Agelidis,
Article published in Proceedings of APEC, 2008, pp. 1611-1617.

Offset rejection for PLL based synchronization in grid-connected converters

Mihai Ciobotaru[1]

Remus Teodorescu[2]

Vassilios G Agelidis[3]

[1] [2] Institute of Energy Technology, Aalborg University
Pontoppidanstraede 101, 9220 Aalborg, DENMARK
Tel: +45-9635-9252, Fax: +45-9815-1411

[3] School of Electrical and Information Engineering,
University of Sydney, NSW 2006 Australia
Tel: +(612) 9351 3446, Fax: +(612) 9351 3847

[1] mpc@iet.aau.dk   [2] ret@iet.aau.dk

[3] v.agelidis@ee.usyd.edu.au

Abstract - **Grid-connected converters rely on fast and accurate detection of the phase angle, amplitude and frequency of the utility voltage to guarantee the correct generation of the reference signals. An important issue associated with accurate grid voltage monitoring is the presence of an offset in the measured grid voltage. This voltage offset is typically introduced by the measurements and data conversion processes and causes errors for the estimated parameters of the grid voltage. Accordingly, this paper presents an offset rejection method for grid-connected converters based on a Phase-Locked-Loop (PLL) technique. The offset rejection method relies on the Second Order Generalized Integrator (SOGI) having the advantages of a simple implementation independent of the grid frequency and avoidance of filtering delays due to its resonance at the fundamental frequency. Selected experimental results validate the performance and robustness of the proposed offset rejection method.**

Keywords - **Offset Rejection, PLL, Inverters, Grid Connected Systems, Distributed Generation, Grid Voltage Monitoring.**

I. INTRODUCTION

Phase, amplitude and frequency of the utility voltage are critical information for the operation of the grid-connected inverter systems. In such applications, an accurate and fast detection of the phase angle, amplitude and frequency of the utility voltage is essential to assure the correct generation of the reference signals and to cope with the standard requirements for the grid-connected converters, such as [1] and [2].

An important issue associated with accurate grid voltage monitoring is the presence of an offset in the measured grid voltage. This voltage offset is typically introduced by the measurements and data conversion processes and causes errors for the estimated parameters of the grid voltage. For instance,

the grid-connected converters based on fixed-point DSP require a manual setting of an offset before the Analogue to Digital (A/D) conversion in order to deliver a positive signal (e.g. 0 to +3V signal) to the A/D converter input of the fixed-point DSP. After the A/D conversion the signal data type is `uint` (unsigned integer) and has to be converted to `int` (integer) in accordance with the offset applied before the A/D conversion. Therefore, a perfect matching between the offset value applied before the A/D conversion and the signal data type conversion from `uint` to `int` is difficult to obtain.

As concluded in [3], the error caused by the voltage offset has the same frequency as the utility voltage. Since the frequency of the error is relatively low, the low pass filtering effect of the loop filter cannot be expected. The extremely low band-width can provide the filtering effect. However, this degrades the dynamic performances and is not acceptable. Therefore, more attention has to be considered for the voltage offset.

This paper presents an effective offset rejection method for grid-connected converters based on a PLL technique. The proposed method is suitable for both, grid-connected systems (e.g. Photovoltaics, Wind Turbines, etc) and power condition equipments (e.g. Uninterruptible Power Supply (UPS), active filters, etc) which rely on PLL based synchronization.

II. SYSTEM DESCRIPTION

A single-phase Distributed Power Generation System (DPGS) based on a PLL technique has been chosen in order to test the proposed method. The general structure of the single-phase DPGS including the power circuit and the control diagram is presented in Fig. 1.
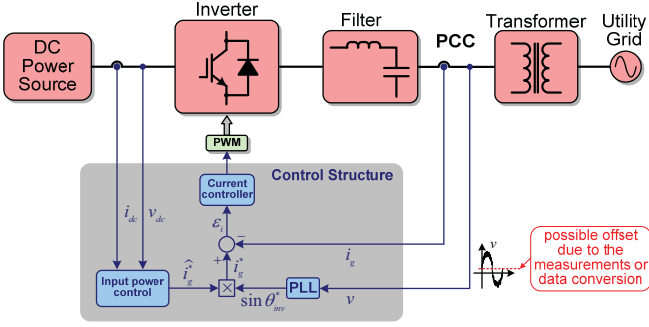
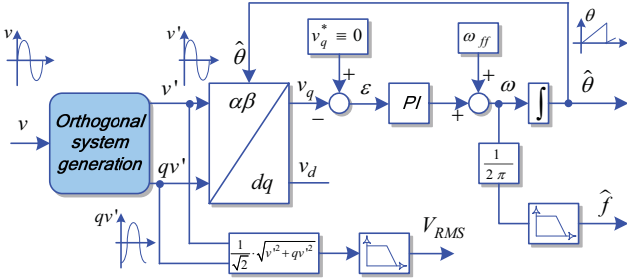Fig. 1. Single-phase DPGS based on PLL technique.

Fig. 2. General structure of a single-phase PLL.

Fig. 2 shows the general structure of a single-phase PLL including the grid voltage monitoring. Usually, the main difference among different single-phase PLL topologies is the orthogonal voltage system generation technique.

There are different ways of generating the orthogonal voltage system for a single-phase system. The common methods used in the technical literature make use of the transport delay block, Hilbert transformation, inverse Park transformation as presented in [4]-[9]. However, these methods have one or more of the following shortcomings: frequency dependency, high complexity, nonlinearity, poor or no filtering. Therefore, more attention should be paid on single-phase PLL systems.

III. OFFSET REJECTION METHOD

An alternative of creating an orthogonal voltage system for a single-phase PLL is presented in [10]. The proposed Orthogonal Signal Generator (OSG) method relies on the Second Order Generalized Integrator (SOGI). The advantages of the proposed approach include simple implementation independent of the grid frequency and avoidance of filtering delays due to its resonance at the fundamental frequency.

The offset rejection method presented in this paper is based on the OSG-SOGI (OSG based on SOGI) structure. The method of creating the orthogonal voltage system for a single-phase PLL including the offset rejection feature is further presented.

A. Orthogonal system generation

The OSG-SOGI structure is depicted in Fig. 3. The input signal v is the grid voltage. As output signals, two sine waves (v' and qv') with a phase shift of 90° are generated. The component v' has the same phase and magnitude as the fundamental of the input signal (v) [11].
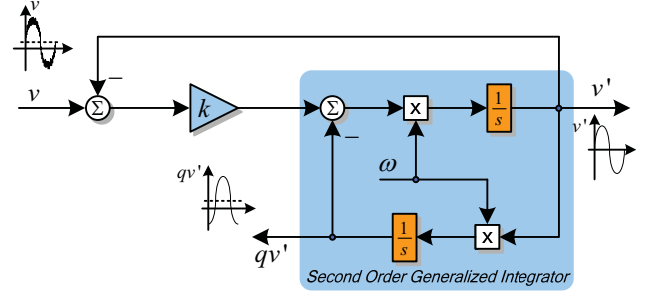

Fig. 3. Standard OSG-SOGI structure [10].

The SOGI structure is defined in (1) [10]-[14]. The closed-loop transfer functions ($H_d = \dfrac{v'}{v}$ and $H_q = \dfrac{qv'}{v}$) of the structure presented in Fig. 3 are defined in (2) and (3).

$$H_{SOGI}(s) = \frac{\omega s}{s^2 + \omega^2} \tag{1}$$

$$H_d(s) = \frac{v'}{v}(s) = \frac{k\omega s}{s^2 + k\omega s + \omega^2} \tag{2}$$

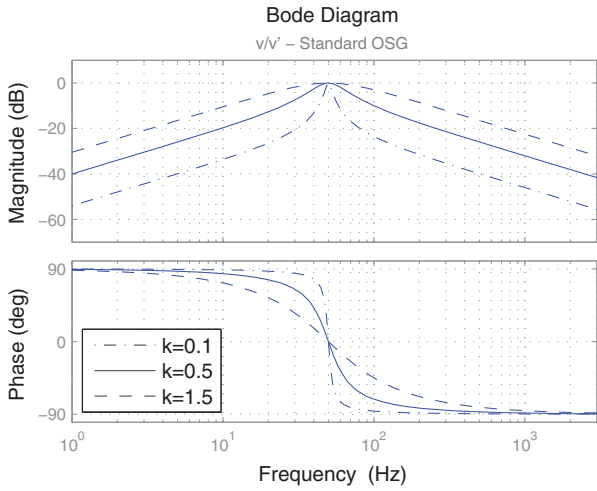$$H_q(s) = \frac{qv'}{v}(s) = \frac{k\omega^2}{s^2 + k\omega s + \omega^2} \tag{3}$$

- where ω represents the resonance frequency of the SOGI;
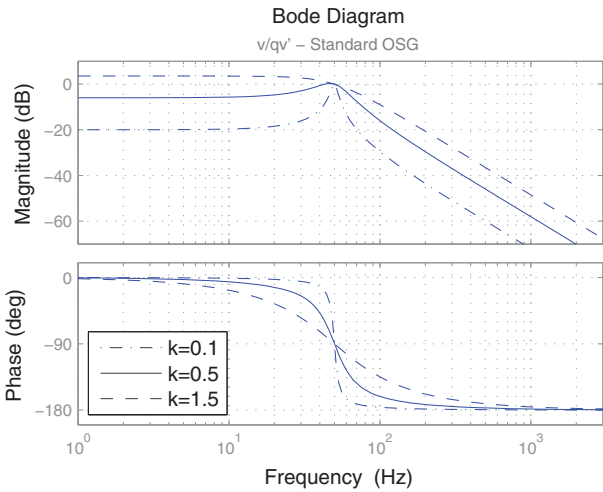- k is the gain which affects the bandwidth of the OSG-SOGI structure.

The Bode representations of the closed-loop transfer functions $H_d = \dfrac{v}{v'}$ and $H_q = \dfrac{qv'}{v}$, for the proposed OSG-SOGI at different values of gain k, are shown in Fig. 4a and Fig. 4b. The tuning of the proposed structure is frequency dependent, thus problems can occur when grid frequency has fluctuations. As a consequence, an adaptive tuning of the structure with respect to its resonance frequency is required. Therefore, the resonance frequency of the SOGI is adjusted online using the frequency provided by the PLL structure.

Using the OSG-SOGI structure the input signal v (grid voltage) is filtered resulting two clean orthogonal voltage waveforms v' and qv', due to the resonance frequency of the SOGI at ω (grid frequency).

The single-phase PLL based on the SOGI combines all the advantages of other known methods such as Transport-Delay, Hilbert Transformation, and Inverse Park Transformation [4]-[8]. Specifically, by using the OSG-SOGI structure shown in Fig. 3, the following three main tasks can be accomplished: - generation of the orthogonal voltage system; - filtering of the orthogonal voltage system without delay; - making the OSG structure frequency adaptive. However, the OSG-SOGI structure, as it is presented in Fig. 3, has a common drawback specific to all methods presented in [4]-[8]. Namely, all OSG methods are sensible at voltage offset. As it can be seen from Fig. 4, the OSG-SOGI structure rejects the DC component only for the component v' . The orthogonal component qv' is directly affected by the presence of any voltage offset. Therefore, an improved OSG-SOGI structure is proposed and presented in the next section.
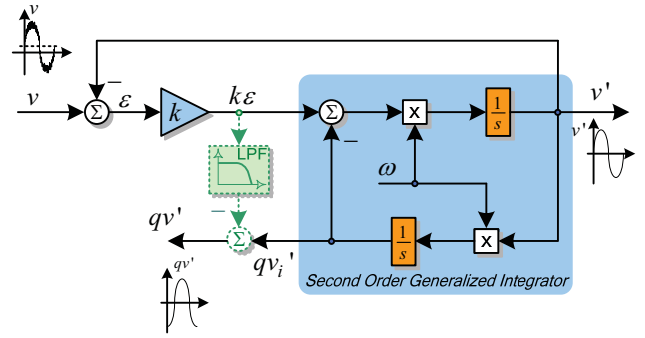
Fig. 5. Improved OSG-SOGI structure.

a)

b)

Fig. 6. Bode plot (a) and step response (b) of the closed-loop transfer function $H_d = \dfrac{v}{qv}'$, for k=0.7.

a)

b)

Fig. 4. Bode plots of the closed-loop transfer functions: a) $H_d = \dfrac{v}{v}'$ and b) $H_d = \dfrac{v}{qv}'$, for different values of gain k.

B. Offset rejection of the measured voltage

The improved OSG-SOGI structure is shown in Fig. 5. As it can be seen from Fig. 4a, the component v' does not contain any DC component. In the case of any offset in the voltage signal v, the signal ε will contain that offset due to the subtraction $v - v' = \varepsilon$. Therefore, the improvement over the structure presented in Fig. 3 consists in subtracting $k\varepsilon$ from qv_i' (green dotted [----] structure including the Low Pass Filter (LPF) from Fig. 5). Furthermore, a LPF is required in order to filter out the harmonics which can be present in the voltage signal (v). From Fig. 6a and Fig. 6b it can be noticed the effectiveness of the proposed method for the offset rejection. The solid lines are obtained using the standard OSG-SOGI presented in Fig. 3 and the dashed, dotted and dashdot lines are obtained for three different cut-off frequencies of the LPF using the improved structure presented in Fig. 5. A gain k of 0.7 has been used for the plots presented in Fig. 6a and Fig. 6b.
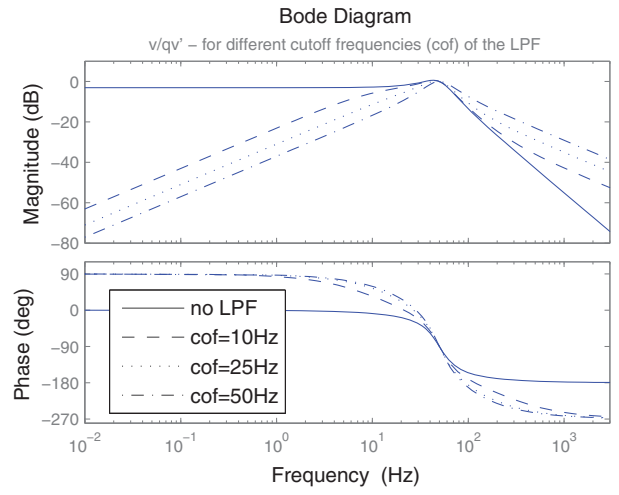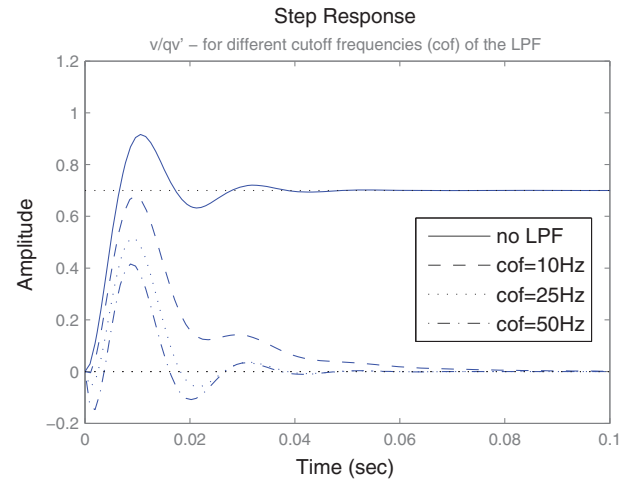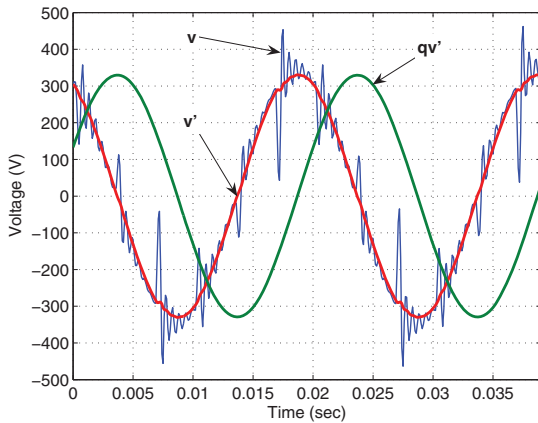
IV. RESULTS

The PLL structure based on OSG-SOGI has been implemented using a setup based on dSPACE 1103 (Fig. 7a). The voltage waveforms were generated by an AC source. Fig. 7b shows how the OSG-SOGI structure is able to generate a

clean orthogonal voltage system (represented by v' and qv') using a highly distorted grid voltage waveform (v) containing notches.
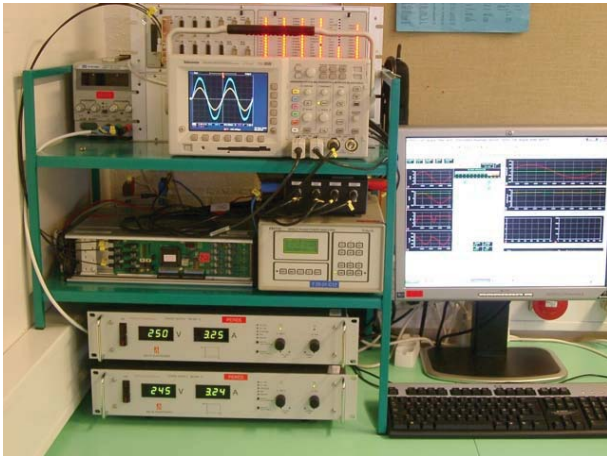

a)

b)

Fig. 7. a) Experimental setup; b) Distorted grid voltage v and the generated orthogonal voltage system (v' and its quadrature qv').

Two cases have been analyzed in order to test the effectiveness of the proposed method for offset rejection. In the first case a 5% (of voltage amplitude) offset has been introduced in the measured voltage (Fig. 8 and Fig. 9). For the second case a 25% offset has been introduced in order to test the robustness of the proposed method (Fig. 10 and Fig. 11). The plots (a) of the Fig. 8 - Fig. 11 show the voltage waveform and its amplitude, estimated by the OSG-SOGI. The plots (b) of the Fig. 8 - Fig. 11 contain the orthogonal voltage system (v' and qv'), generated by the OSG-SOGI. The plots (c) of the Fig. 8 - Fig. 11 represent the estimated frequency of the voltage signal using the PLL based on OSG-SOGI.

The Fig. 8 and Fig. 10 show the results obtained using standard OSG-SOGI structure presented in Fig. 3, while the Fig. 9 and Fig. 11 show the results obtained using the improved OSG-SOGI structure as drown in Fig. 5. As it can be noticed from Fig. 8 (standard OSG-SOGI), a 5% offset in the voltage highly affects the estimation of the frequency and amplitude of the voltage (2 Hz ripple in the estimated

frequency and 25 V ripple in the estimated amplitude). On the contrary, using the offset rejection method as presented in Fig. 5, the estimated frequency and amplitude of the voltage is not affected by the 5% voltage offset (Fig. 9). Moreover, the offset rejection method proved to be very efficient and robust even when using a 25% offset in the voltage as presented in Fig. 11.
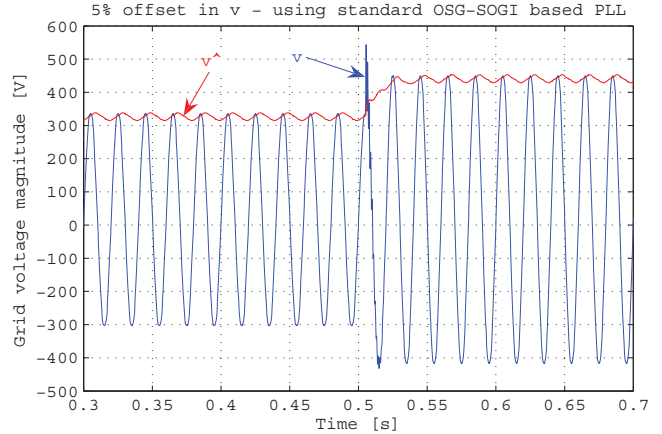
a)
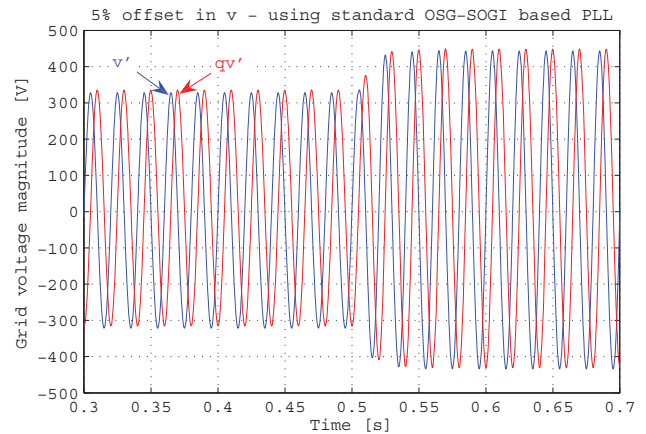
b)
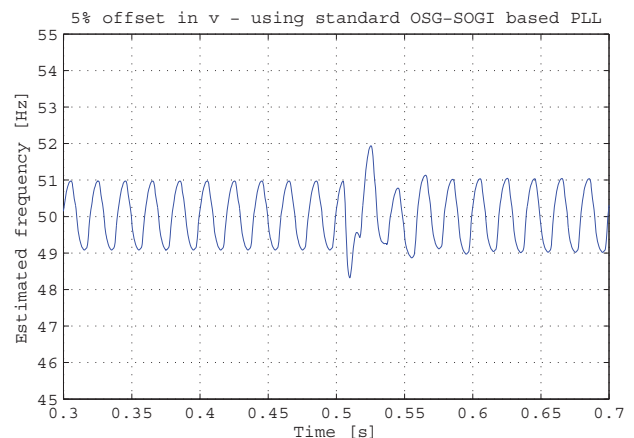
c)

Fig. 8. Obtained results using standard OSG-SOGI structure (Fig. 3) under a 5% voltage offset: a) amplitude estimation; b) generated orthogonal voltage system; c) frequency estimation.
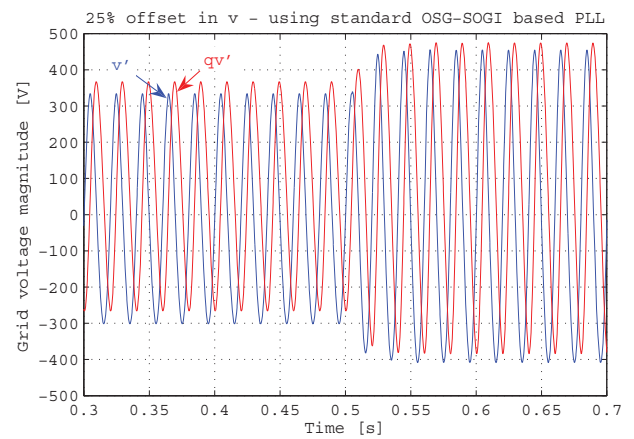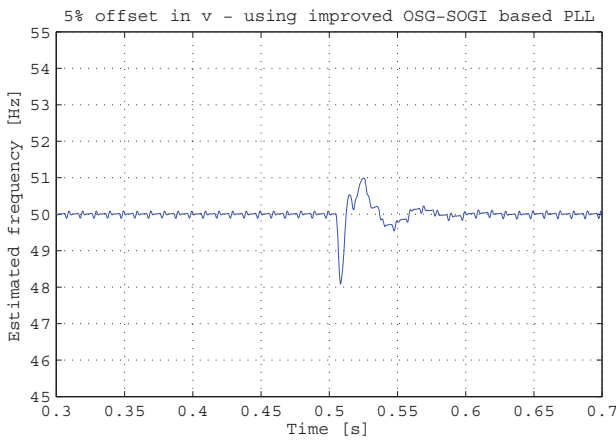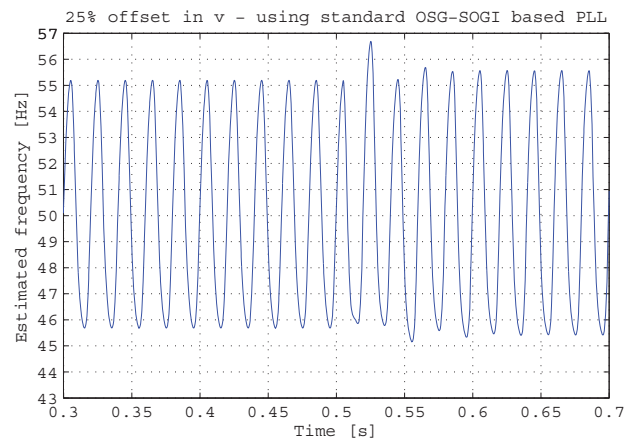
Fig. 9. Obtained results using improved OSG-SOGI structure (Fig. 5) under a 5% voltage offset: a) amplitude estimation; b) generated orthogonal voltage system; c) frequency estimation.

Fig. 10. Obtained results using standard OSG-SOGI structure (Fig. 3) under a 25% voltage offset: a) amplitude estimation; b) generated orthogonal voltage system; c) frequency estimation.

As it can clearly be seen from Fig. 10, the error generated by the voltage offset has the same frequency with the fundamental frequency of the voltage, thus being very difficult to filter it out using an extremely low band-width PI controller for the PLL, as mentioned in [3].

A voltage swell of 35% has been deliberately created in order to show that the dynamic of the OSG-SOGI structure is not affected by the offset rejection method proposed in Fig. 5. A 2.5% voltage Total Harmonic Distortion (THD) was used for the experimental results presented in Fig. 8 - Fig. 11.
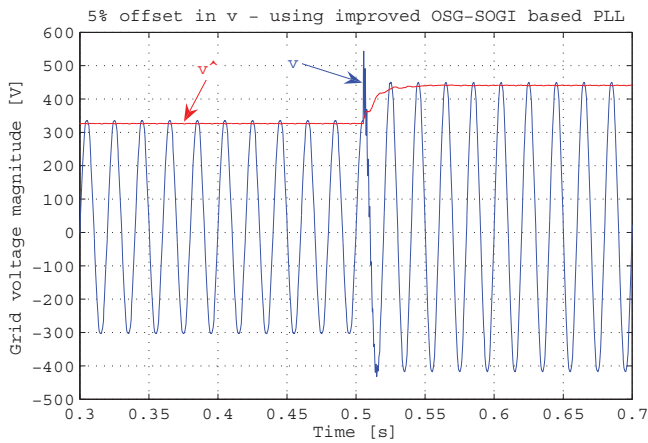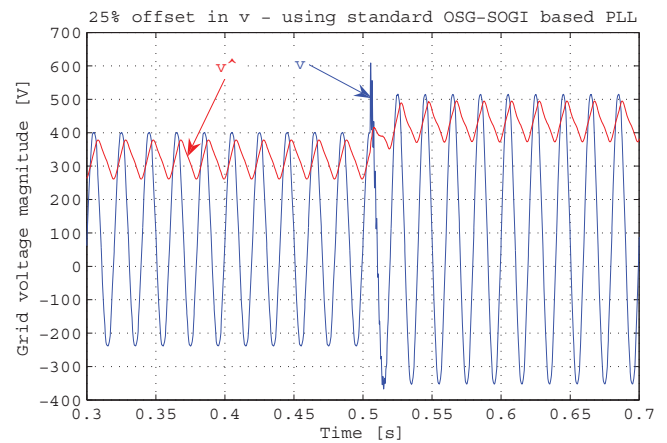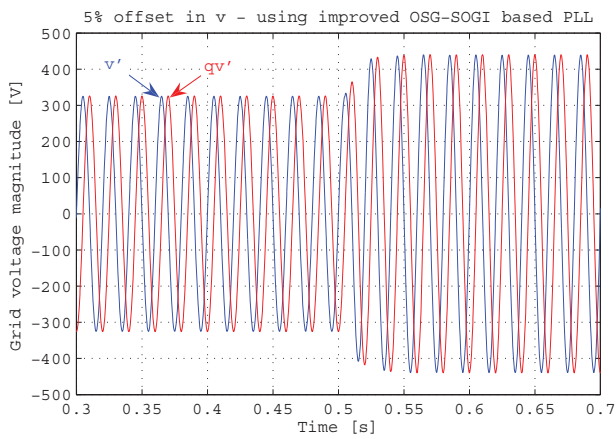
a)

b)

c)

Fig. 11. Obtained results using improved OSG-SOGI structure (Fig. 5) under a 25% voltage offset: a) amplitude estimation; b) generated orthogonal voltage system; c) frequency estimation.
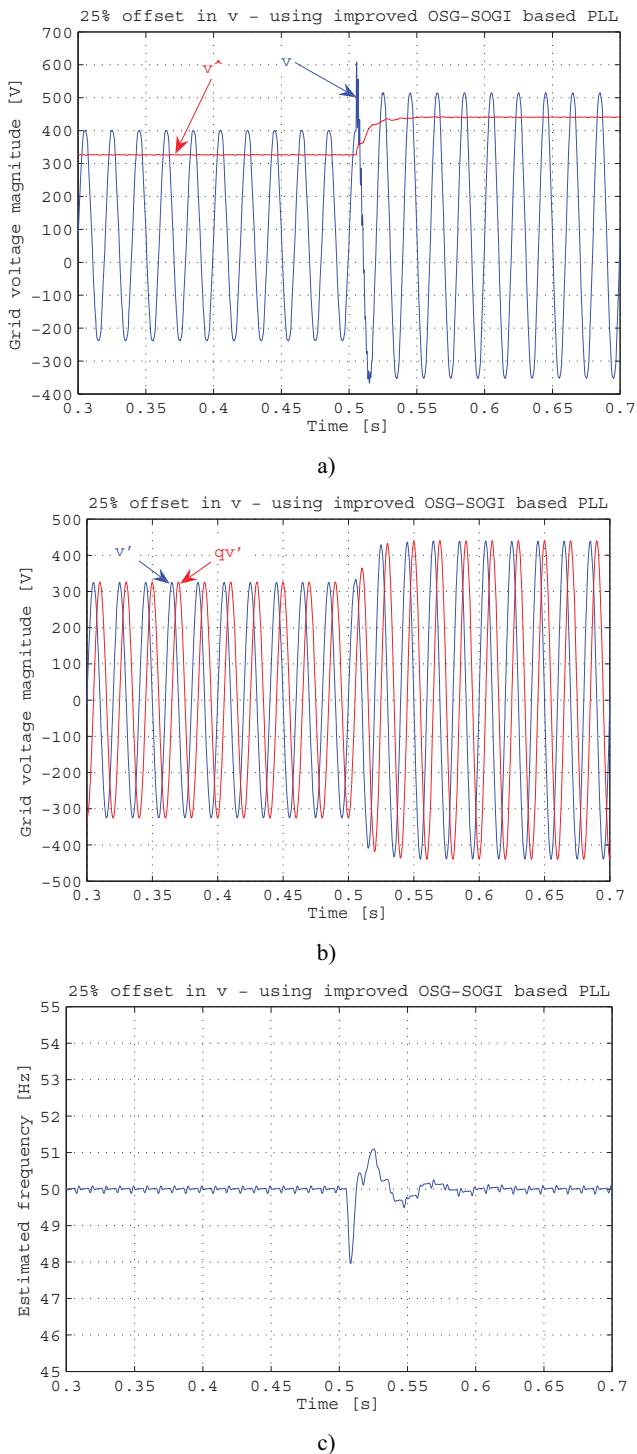
V. CONCLUSIONS

An important issue associated with accurate grid voltage monitoring is the presence of an offset in the measured grid voltage. The majority of the PLL based synchronization systems are not able to reject the voltage offset which is typically introduced by the measurements and data conversion processes. Therefore, this paper presents an effective offset rejection method for grid-connected converters based on a Phase-Locked-Loop (PLL) technique. The proposed method is suitable for both, grid-connected systems (e.g. Photovoltaics, Wind Turbines) and power condition equipments (e.g. Uninterruptible Power Supply (UPS), active filters) which rely on PLL based synchronization.

The presented results proved the performances and robustness of the proposed offset rejection method.

VI. REFERENCES

[1] IEEE Standard 929-2000: IEEE Recommended practice for utility interface of photovoltaic (PV) systems.

[2] IEEE Standard 1547-2003: IEEE Standard for interconnecting distributed resources with electric power systems.

[3] S.-K. Chung, "Phase-locked loop for grid-connected three-phase power conversion systems", Electric Power Applications - IEE Proceedings, Volume 147, Issue 3, 2000, pp. 213 – 219.

[4] L.N. Arruda, S.M. Silva, B.J.C. Filho, "PLL structures for utility connected systems", IEEE Industry Applications Conference IAS, 2001, vol. 4, pp. 2655 – 2660.

[5] N. Saitou, M. Matsui, and T. Shimizu, "A Control Strategy of Single-phase Active Filter using a Novel d-q Transformation", IEEE Industry Applications Society IAS, 2003, pp. 1222-1227.

[6] S.M. Silva, B.M. Lopes, B.J.C. Filho, R.P. Campana, "Performance evaluation of PLL algorithms for single-phase grid-connected systems", IEEE Industry Applications Conference, 2004, vol.4, pp. 2259 - 2263.

[7] S.M. Silva, L.N. Arruda, and B.J.C. Filho, "Wide Bandwidth Single and Three-Phase PLL Structures for Utility Connected Systems", 9th. European Conference on Power Electronics and Applications EPE, 2001, pp. 1660-1663.

[8] M. Ciobotaru, R. Teodorescu, F. Blaabjerg, "Improved PLL structures for single-phase grid inverters", Proc. of PELINCEC'05, 6 pages, paper ID 106.

[9] M. Ciobotaru, R. Teodorescu, F. Blaabjerg, "Control of single-stage single-phase PV inverter", Proc. of EPE'05, 10 pages, ISBN : 90-75815-08-5.

[10] M. Ciobotaru, R. Teodorescu and F. Blaabjerg, "A new single-phase PLL structure based on second order generalized integrator", in Record of IEEE PESC 2006, Jeju, Korea, p. 1511-1516.B.

[11] Burger and A. Engler, "Fast signal conditioning in single phase systems" – Proc. of European Conference on Power Electronics and Applications, 2001.

[12] X. Yuan, W. Merk, H. Stemmler and J. Allmeling, "Stationary-Frame Generalized Integrators for Current Control of Active Power Filters with Zero Steady-State Error for Current Harmonics of Concern Under Unbalanced and Distorted Operating Conditions" IEEE Trans. on Ind. App., Vol. 38, No. 2, 2002, pp. 523 – 532.

[13] R. Teodorescu, F. Blaabjerg, M. Liserre and U. Borup, "A New Control Structure for Grid-Connected PV Inverters with Zero Steady-State Error and Selective Harmonic Compensation", Proc. of IEEE APEC'04, Vol. 1, 2004, pp. 580-586.

[14] S. Fukuda and T. Yoda, "A novel current-tracking method for active filters based on a sinusoidal internal mode", IEEE Trans. on Ind. App., Vol.37, No. 3, 2001, pp. 888 – 895.

[15] D. N. Zmood and D. G. Holmes, "Stationary Frame Current Regulation of PWM Inverters with Zero Steady-State Error", IEEE Trans. on Power Electronics, Vol. 18, No. 3, May 2003, pp. 814 – 822.

[XIII] Accurate and less-disturbing active anti-islanding method based on PLL for grid-connected PV inverters

by M. Ciobotaru, V. G. Agelidis, and R. Teodorescu,
Article published in Proceedings of PESC, 2008, pp. 4569 – 4576.

Accurate and Less-Disturbing Active Anti-Islanding Method based on PLL for Grid-Connected PV Inverters

M. Ciobotaru[*], V. Agelidis[**] and R. Teodorescu[*]

[*] Institute of Energy Technology, Aalborg University, Aalborg, Denmark

[**] Power Engineering School of Electrical and Information Engineering, University of Sydney, NSW 2006, Australia

Abstract - **Islanding prediction is a necessary feature of inverter-based Photovoltaic (PV) system in order to meet stringent standard requirements for interconnection with the electrical grid. Both passive and active anti-islanding methods exist. Typically, active methods modify a given parameter, which also affects the shape and quality of the injected current. In this paper, an accurate and less-disturbing active method suitable for Phase-Locked Loop (PLL) based controllers is proposed. The PLL structure is built using a Second Order Generalized Integrator (SOGI). Each output cycle the inverter current reference is slightly modified by an injected signal thus affecting the generated current in a negligible way. Therefore, a feedback signal can be extracted from the voltage of the Point of Common Coupling (PCC) as a consequence of the injected signal. When the grid becomes unavailable, the feedback signal extracted from the voltage at PCC moves outside of a pre-set threshold value. This new active anti-islanding method meets both standard requirements IEEE 929-2000, IEEE 1547.1 and VDE 0126.1.1. The disturbance used by this method is small compared to other active anti-islanding methods, such as active frequency drift or frequency shift up/down. Moreover, this method does not present Non-Detection-Zones (NDZ), it does not affect the zero-crossing of the injected current and it can also estimate the grid impedance. In addition, the method is highly robust to different grid disturbances and stiffness, and is effective for multiple inverters running in parallel. The performance of the proposed method has been studied through extensive simulations using MATLAB/Simulink for several operating conditions and load types and then successfully tested on an experimental setup. Selected results are presented in order to confirm the validity of the proposed method[*].**

Keywords - **Islanding Detection, Grid Connected Systems, PV Inverters, Distributed Generation Systems, Renewable Energy, Power Quality and Safety.**

I. INTRODUCTION

The ever increasing penetration of the electrical grid with distributed generation (DG) based on alternative sources such as photovoltaics (PVs), fuel cells and wind has been enabled by inverter technology developments [1]. The evolution of the recommended guidelines and standards has streamed manufacturing and shaped inverter design and control [2], [3], [5] and [6]. However, this necessitates continuous harmonization of standards at international level [4]. Recently, there have been a number of overview papers on single-phase PV grid-connected systems. Integrating extra functions into the operation of the inverter such as harmonic filtering and distortion elimination have added another progress dimension.

Islanding phenomenon for a distributed power generation system (DPGS) is defined when the DPGS continues to operate with local loads when the grid is disconnected [3]. Islanding can be intentional and unintentional [3]. In this paper, the unintentional islanding is considered, in which the Distributed Resource (DR) energizes a portion of the area electric power system (EPS) through the Point of Common Coupling (*PCC*), the DR interconnection system shall detect the island and cease to energize the area EPS within two seconds of the formation of an island [3], [4] and [6]. As an issue, it applies for all DG systems including PV systems [2]. Although the probability of islanding occurrence is extremely low [9], standards dealing with the interconnection of inverter based photovoltaic system with the grid require that an effective anti-islanding method is incorporated into the operation of the inverter [2]-[4] and [6].

There are numerous islanding detection methods for grid-connected PV systems reported in the technical literature [10]-[25] and their development has been summarized in a number of recent technical papers [7], [8], [15], and reports [10], [11]. They can be classified into two broad categories, namely, passive and active which can be inverter built or utility supported. The passive methods are based on the detection of the following:

- Over-voltage/under-voltage protection (OVP / UVP) [10], [12].
- Over-frequency/under-frequency protection (OFP / UFP) [10], [12].
- Voltage phase jump [10], [12], [15].
- Voltage harmonic monitoring [12], [15].
- Current harmonic monitoring [7].

However, passive methods have a number of weaknesses and inability to detect islanding. The use of non-detection zones (NDZs) is used as a measure of performance for both these techniques as well as the active ones in a number of papers [20], [22]. An evaluation of different but most widely-used passive anti-islanding methods is offered for passive methods in [7] and [14] and an excellent overview report for both passive and active methods is available in [10].

Active methods have been developed in order to overcome the limitations of the passive methods. In simple terms, active methods introduce perturbations in the inverter output power for a number of parameters as follows:

---

[*] *The proposed method is under patent pending.*

- Output power variation either real or reactive [12], [23].
- Active frequency drift or frequency shift up/down [10], [15]-[19].
- Sliding mode or slip-mode frequency shift [10], [15], [19].
- Sandia frequency shift or accelerated frequency drift or active frequency drift with positive feedback [15], [18].
- Impedance measurement [10], [12], [15].
- Detection of impedance at a specific frequency or monitoring of harmonic distortion [10], [25].
- Sandia voltage shift [10].
- Frequency jump [10].

In a recent paper, it has been shown that although the effectiveness of passive methods can be established by non-detection zones [14] as represented by the power mismatch space (ΔP vs. ΔQ), in active frequency drifting methods their performance can be evaluated by using load parameter space based on the values of the quality factor and resonant frequency of the local load (Q_f vs. f_o) [22].

Although most of the papers have been concentrated on PV inverters, islanding detection is also needed for all other inverter based systems using different sources such as fuel cells [3], [23]. The algorithm proposed in [23] is an active method and continuously perturbs the reactive power supplied by the inverter by as much as ±5% while monitoring the utility voltage and frequency simultaneously. When islanding occurs, the deviation of the frequency taking place results in a real power reduced to 80%. A drop in voltage positively confirms islanding which in turn results in the inverter being successfully disconnected.

Many papers have concentrated on single-phase inverters and others also address three-phase technology [11], using DQ implementation [24]. Recently, the power mismatch for the 3rd and 5th harmonics and the implementation of an active anti-islanding method using resonant controllers was reported in [25].

Although numerous techniques exist and their implementation varies as it has been discussed so far, it is important to note that a recommendation for robust software based algorithms would simplify matters for the easier adoption of the most robust and simplest technique of all, and this should be kept as a guide for the further development of the anti-islanding technology [9].

Moreover, there is a little technical information available for anti-islanding methods operating with controllers based on phase-locked loop (PLL) for single-phase systems as most of them rely on the zero-crossing of the voltage to get information in order for the anti-islanding method to operate.

The objective of the paper is to propose a simple non-invasive active anti-islanding method suitable for single-phase grid-connected PV systems. The method relies on the current angle being the monitored variable which is derived from a PLL structure built with a second-order generalized integrator [26]. Prior to deriving the angle reference signal for the current controller, this angle signal is slightly distorted by a sinusoidal signal having a very low amplitude and the same frequency as the one obtained from the PLL fully synchronized at the same time. Every cycle this distortion is corrected as long as the grid voltage is available. When the grid is disconnected, the distortion through a loop of either positive or negative injection will continue to distort the angle reference eventually pushing the feedback signal from the inverter to cross the selected boundary and therefore causing the inverter to trip and prevent islanding.

The paper is organized as follows. First the grid-connected PV system is described. Next the proposed anti-islanding method is presented. Finally, results are presented for both resistive load as well as parallel *RCL* load to confirm that the proposed methods performs in a satisfactory way and meets the requirements of the *IEEE 929-2000* standard.

II. GRID-CONNECTED PV SYSTEM AND ITS CONTROL

A. Power Circuit

Figure 1 shows the power circuit of the PV inverter system consisting of a solar panel string and a DC link capacitor C_{DC} on the DC side with an output AC filter (LC), a local parallel RLC load, an isolation transformer and the grid connected on the AC side through the utility's breaker circuit. It is important in this configuration that the number of panels making up the string has to ensure that the input DC voltage is higher than the AC peak voltage at all times so that the energy can be transferred from the DC-side to the AC-side. The energy conversion from DC type to the sinusoidal form is achieved through a single-phase voltage source inverter operating at a relatively high switching frequency, e.g. 10 kHz.
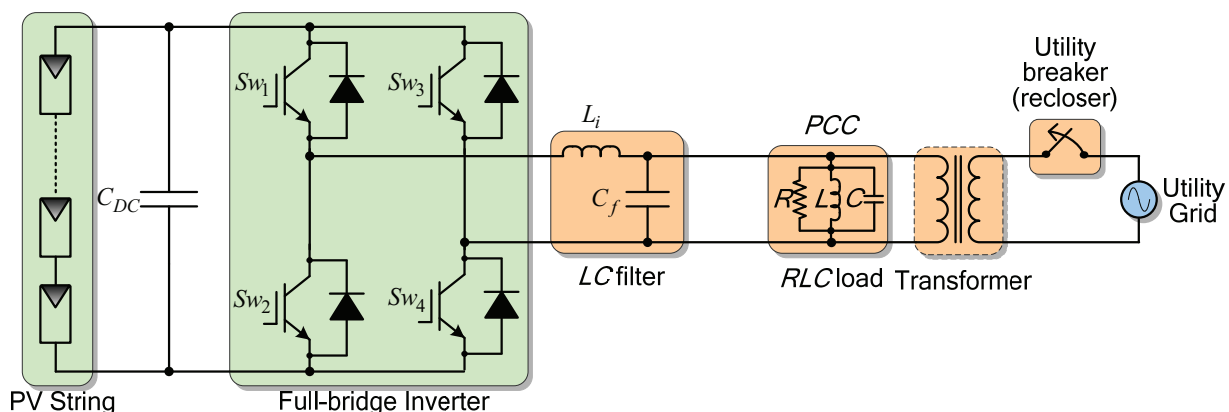

Figure 1. The PV inverter system connected to the utility grid.

Figure 2. Grid-connected PV system and its associated control.

Figure 3. Second Order Generalized Integrator based PLL and proposed anti-islanding method.

B. Control Structure

The main elements of the control structure are presented in Figure 2. The control circuit of the PV inverter consists of the following parts: - the synchronization algorithm based on a PLL; - the maximum power point tracker (MPPT); - the DC voltage controller and; - the grid current controller including the generator of the PWM control signals.

III. PROPOSED ANTI-ISLANDING METHOD

The proposed anti-islanding method and the PLL implementation are both shown in Figure 3. The main task of a PLL structure is to provide a unit power factor operation, which involves synchronization of the inverter output current with the grid voltage, and to give a pure sinusoidal current reference. Specifically, the orthogonal signal generator and the PLL structure for a single-phase system have been described in more details in [27] and [28].

The method is based on the modification of the derived angle of the inverter current angle (θ_{PLL}). In particular, a sinusoidal signal (σ_{inj}) synchronized with the cycle is injected to slightly modify the inverter current angle (θ_{PLL}). A feedback signal is then extracted from the voltage at the PCC (namely from v_q) as a consequence of the injected signal σ_{inj}. The signal injection can be done with either positive or negative sign as shown in Figure 3.

The principle of the proposed signal injection method is described as follows. The injected signal σ_{inj} is defined by (1):

$$\sigma_{inj} = k \cdot \sin \theta_{PLL} \tag{1}$$

- where the gain k is used to choose the amount of disturbance needed for the islanding detection.

The resulting phase angle reference of the inverter, as shown in Figure 3, becomes:

$$\sin \theta_{inv}^* = \sin(\theta_{PLL} + \sigma_{inj}) = \sin(\theta_{PLL} + k \cdot \sin \theta_{PLL}) \tag{2}$$

It is known that:

$$\sin(a+b) = \sin a \cdot \cos b + \cos a \cdot \sin b \tag{3}$$

From (2) and (3) (by replacing $a = \theta_{PLL}$ and $b = k \cdot \sin \theta_{PLL}$) it results:

$$\sin \theta_{inv}^* = \sin \theta_{PLL} \cdot \cos(k \cdot \sin \theta_{PLL}) + \cos \theta_{PLL} \cdot \sin(k \cdot \sin \theta_{PLL}) \tag{4}$$

The approximations presented in (5) are made in order to show the analogy of the proposed method compare to a second-harmonic signal injection.

$$\begin{cases} \sin(k \cdot \sin \theta_{PLL}) \simeq k \cdot \sin \theta_{PLL}, \text{ for k} \ll \\ \cos(k \cdot \sin \theta_{PLL}) \simeq 1, \text{ for k} \ll \end{cases} \tag{5}$$

Applying the approximations from (5) to (4) it results:

$$\sin \theta_{inv}^* \simeq \sin \theta_{PLL} + k \cdot \sin \theta_{PLL} \cdot \cos \theta_{PLL} \qquad (6)$$

Being known that:

$$\sin 2\theta = 2 \cdot \sin \theta \cdot \cos \theta \qquad (7)$$

and writing (6) as:

$$\sin \theta_{inv}^* \simeq \sin \theta_{PLL} + \frac{k}{2} \cdot (2 \cdot \sin \theta_{PLL} \cdot \cos \theta_{PLL}) \qquad (8)$$

It results:

$$\sin \theta_{inv}^* \simeq \sin \theta_{PLL} + \frac{k}{2} \cdot \sin 2\theta_{PLL} \qquad (9)$$

For small values of k (e.g. for $k<0.05$), the addition of $k \cdot \sin \theta_{PLL}$ to θ_{PLL}, as provided by the PLL, it is similar to the addition of a second-harmonic signal ($\hat{A} \cdot \sin 2\theta_{PLL}$) to $\sin \theta_{PLL}$, the only difference being that the amplitude of the signal as expressed in (9) can be slightly different (app. 0.05%) than the amplitude of the signal as expressed in (2).

The addition of $k \cdot \sin \theta_{PLL}$ to θ_{PLL} has been chosen over the addition of a second-harmonic signal due to the fact that the signal expressed in (2) is unitary unlike the signal expressed in (9), thus not affecting the current reference amplitude. In other words, by adding $k \cdot \sin \theta_{PLL}$ to θ_{PLL}, the current reference will contain a small sinusoidal signal with a frequency twice the fundamental frequency, according to (9).

When the inverter supplies power to the grid, the consequence of adding $k \cdot \sin \theta_{PLL}$ to θ_{PLL} is observed as a feedback signal in the voltage at the PCC. The feedback signal has the double of the fundamental frequency and its amplitude is related to the grid impedance value. The feedback signal can be extracted from the voltage at PCC after the Park Transform (from v_q). After the transformation, the feedback signal frequency will become half of the frequency, as it is demonstrated below.

The Park Transform is presented as:

$$v_q = -\sin \theta \cdot v_\beta + \cos \theta \cdot v_\alpha \qquad (10)$$

Considering the orthogonal voltage system of the feedback voltage (v_α' and v_β') due to the signal injection as shown in (2) and removing the fundamental components, the expression shown in (10) becomes:

$$v_q' = -\sin \theta \cdot v_\beta' + \cos \theta \cdot v_\alpha' \qquad (11)$$

- where v_α' and v_β' are considered normalized and represented as:

$$\begin{cases} v_\alpha' = \sin(2\theta) \\ v_\beta' = \sin\left(2\theta + \pi/2\right) = \cos(2\theta) \end{cases} \qquad (12)$$

From (11) and (12) it results:

$$v_q' = -\sin \theta \cdot \cos(2\theta) + \cos \theta \cdot \sin(2\theta) \qquad (13)$$

Knowing that:

$$\begin{cases} \sin(2\theta) = 2 \cdot \sin \theta \cdot \cos \theta \\ \cos(2\theta) = \cos^2 \theta - \sin^2 \theta \end{cases} \qquad (14)$$

It results:

$$v_q' = -\sin \theta \cdot (\cos^2 \theta - \sin^2 \theta) + \cos \theta \cdot 2 \cdot \sin \theta \cdot \cos \theta \qquad (15)$$

Solving the expression shown in (15), it results:

$$\begin{aligned} v_q' &= \sin \theta \cdot \left[-(\cos^2 \theta - \sin^2 \theta) + 2 \cdot \cos^2 \theta \right] \Leftrightarrow \\ v_q' &= \sin \theta \cdot \underbrace{\left[\sin^2 \theta + \cos^2 \theta \right]}_{=1} \Leftrightarrow \\ v_q' &= \sin \theta \end{aligned} \qquad (16)$$

Thus, the feedback voltage signal can by easily extracted after the Park Transform by using a resonant filter tuned on the fundamental frequency.

The proposed islanding detection method is based on the detection of the grid impedance changes. The relation between the feedback signal due to the injection and the grid impedance is given in Figure 4. As it can be noticed, the relation between the feedback signal and the grid resistance is nonlinear, while the relation with the grid inductance is linear.

One of the main advantages of the proposed anti-islanding method is that it does not affect the zero crossing of the current. Very small amplitude of the injected signal (σ_{inj}) is required to be injected at all times for the method to be successful when needed.
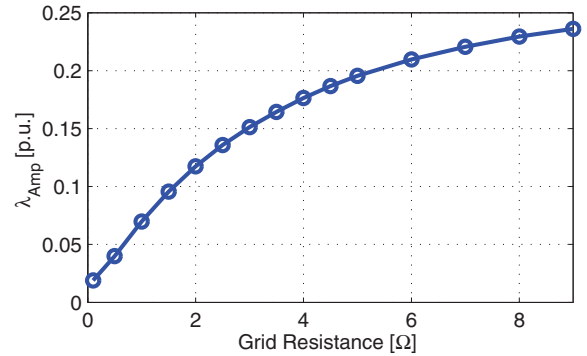
(a)
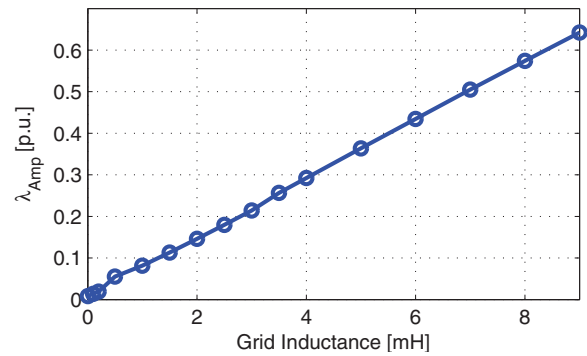
(b)

Figure 4. The relation between the feedback signal and the grid impedance: a) grid resistance R_g; b) grid inductance L_g
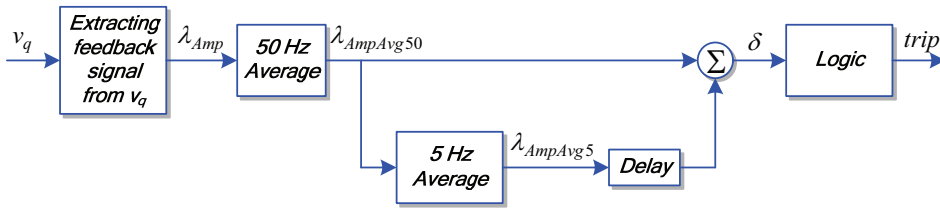
Figure 5. Signal processing for islanding detection.

The structure presented in Figure 5 assists with the monitoring of the anti-islanding condition, where: - λ_{Amp} is the amplitude of the feedback signal extracted from v_q; - $\lambda_{AmpAvg50}$ is the 50 Hz average of the signal λ_{Amp}; - $\lambda_{AmpAvg5}$ is the 5 Hz average of the signal $\lambda_{AmpAvg50}$; - δ represents the difference between the actual value of $\lambda_{AmpAvg50}$ and the delayed value of $\lambda_{AmpAvg5}$. When the islanding occurs, this is also reflected in the grid impedance value. The change in the grid impedance value is then detected in the feedback signal in the form of δ. Then, following the algorithm shown in Figure 6, a trip signal is generated.

The flowchart of the islanding detection algorithm (the "Logic" block from Figure 5) is presented in Figure 6. The algorithm is described as follows:

- the component δ is compared to a threshold value;

- when δ is bigger than the threshold value a timer is started. The time value of the timer is named t_t and its initial condition is 0 s. If the δ remains larger than the threshold value for more than 0.2 s the PV inverter is tripped. Otherwise, if δ becomes smaller than the threshold value within 0.2 s, the timer is reset to 0 s. The threshold value and the tripping time can be chosen in accordance with one of the standards IEEE 929-2000, IEEE 1547.1-2005 and VDE 0126.1.1.
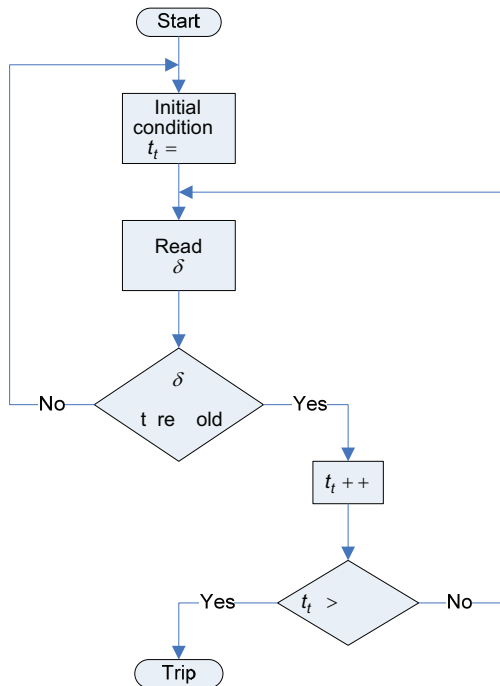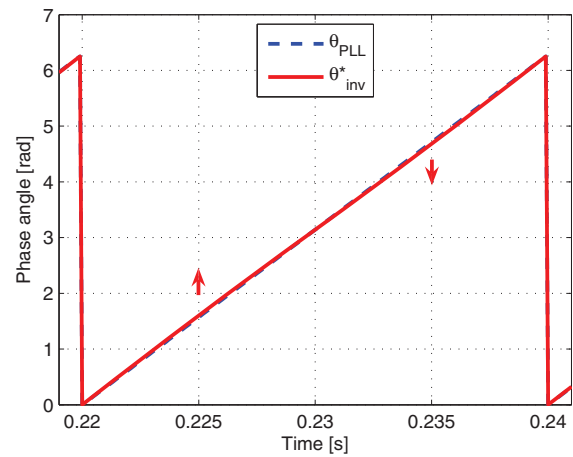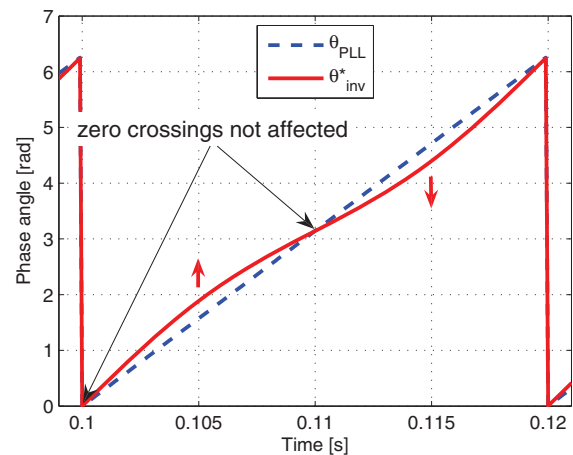
Figure 7b and Figure 8b show the effect of the injected signal (σ_{inj}) for the inverter phase angle reference (θ_{inv}^{*}) and for the grid current reference in p.u. ($\sin\theta_{inv}^{*}$) respectively, when the amplitude of the injected signal is 10 times larger than necessary in order to illustrate in a clear manner the effect of the signal injection and for clarity purposes. As it can be seen from Figure 8, the zero crossings of the grid current reference are not affected.
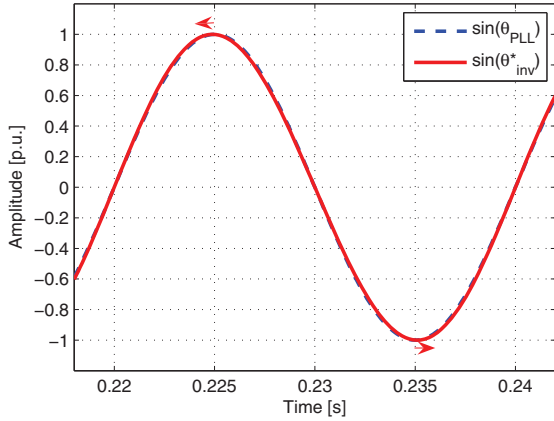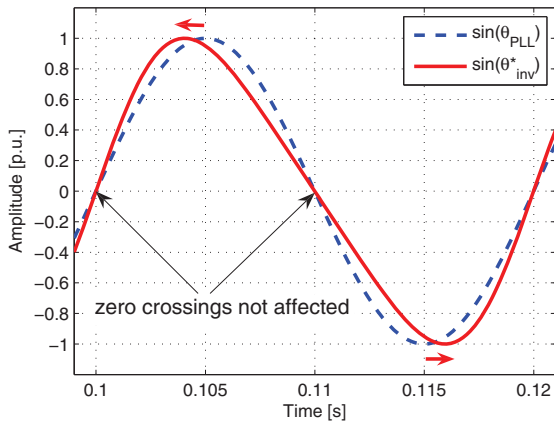

(a)

(b)

Figure 7. The effect of the injected signal (σ_{inj}) for the inverter phase angle reference (θ_{inv}^{*}) at normal operation (a) and when the amplitude of the injected signal is 10 times larger than necessary (b).

Figure 6. The islanding detection algorithm.

(a)

(b)

Figure 8. The effect of the injected signal (σ_{inj}) for the grid current reference in p.u. ($sin\,\theta^*_{inv}$) at normal operation (a) and when the amplitude of the injected signal is 10 times larger than necessary (b).

IV. Selected Results

The proposed anti-islanding method described previously has been implemented using a setup based on dSPACE 1103 setup.

Based on the requirements of the IEEE Standard 929-2000, it is imperative that any method of anti-islanding is tested to establish its performance when a parallel *RLC* load with a specific quality factor Q is used.

Figure 9 shows a comparison of the grid current and the inverter phase angle reference with and without signal injection. As it can be seen, the grid current is insignificantly affected by the injected signal (σ_{inj}). The gain k, as presented in Figure 3, represents the injection ratio and it was set to 0.03 for all of the results presented in the following. Very small amplitude of the injected signal (σ_{inj}) was required to be injected at all times in order to detect the islanding even for an RLC load with a quality factor of 10. The grid voltage THD was about 2.5% for all of the results.

Four cases were investigated in order to validate the proposed method. In the Case 1 only a parallel resistive load of 36.14 Ω was used. The islanding detection and the grid current and the voltage in the PCC for the Case 1 are presented in Figure 10. As it can be seen, it is confirmed that the islanding is detected within the time frame required by the standards [2] and [6].
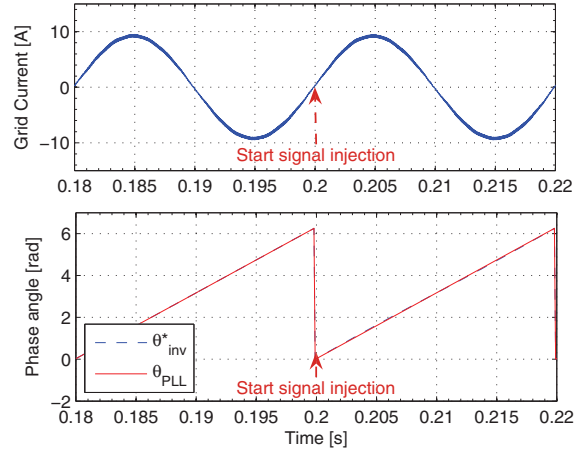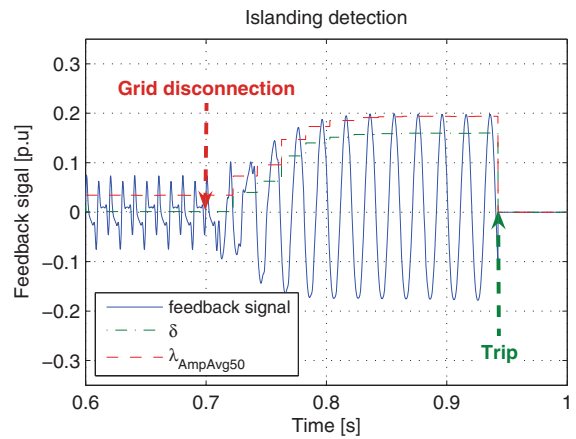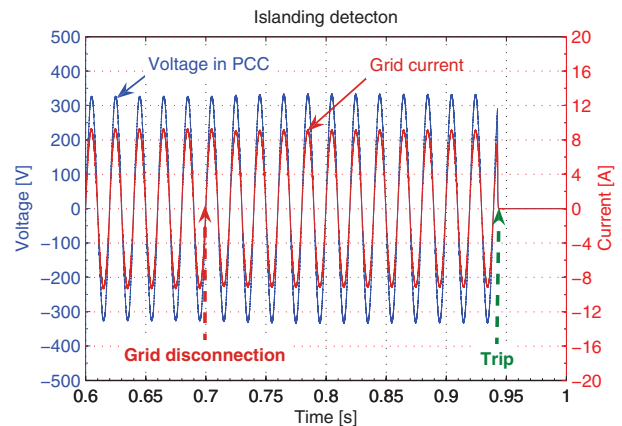

Figure 9. Comparison of the grid current and the phase angle reference with/without signal injection.
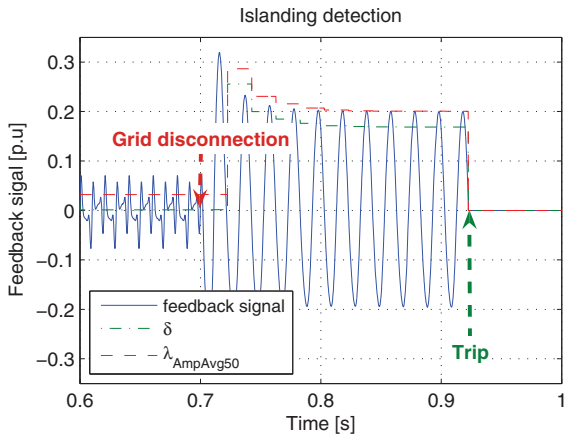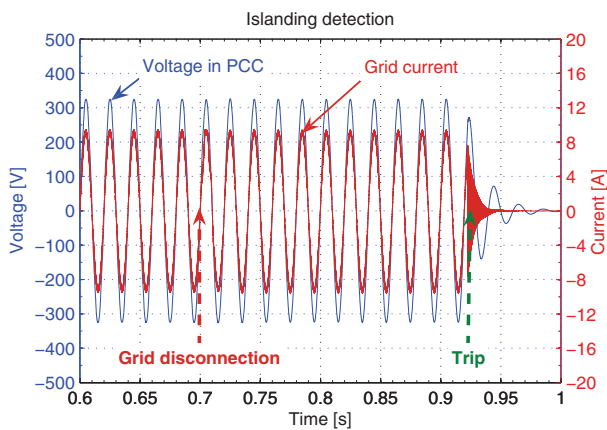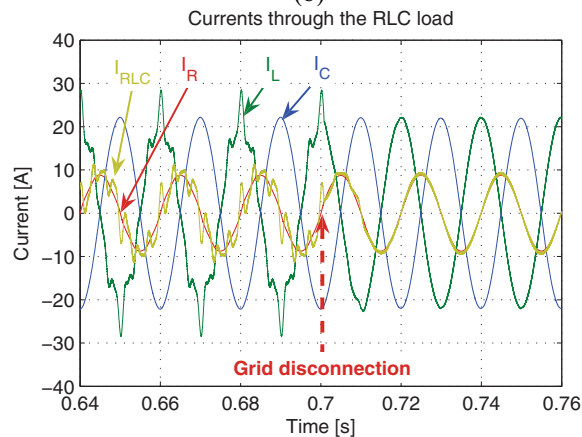

(a)

(b)

Figure 10. Islanding detection in the case of a parallel R load only: a) the islanding detection based on the feedback signal; b) the grid current and voltage in the PCC.

(a)

(b)

(c)

Figure 11. Islanding detection in the case of a parallel RLC load with a Q=2.5: a) the islanding detection; b) the grid current and voltage in the PCC; c) the currents through the RLC load.

Figure 11 represents the Case 2 where a parallel RLC load with a quality factor of 2.5 in accordance with the IEEE Standard 929-2000 was used. As it can be noticed, the islanding detection does not pose any difficulties. The currents through the RLC load are shown in Figure 11c. A significant change in the harmonic content can be seen when the grid is disconnected. This is due to the harmonic background of the voltage in the PCC.
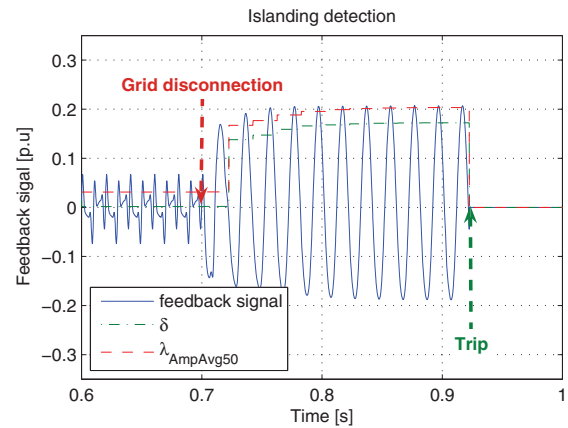

Figure 12. Islanding detection in the case of a parallel RLC load with a Q=1.

Figure 12 shows the Case 3 where a parallel RLC load with a quality factor of 1 in accordance with the IEEE Standard 1547.1 was used. As it can be seen, the islanding detection performs very well.
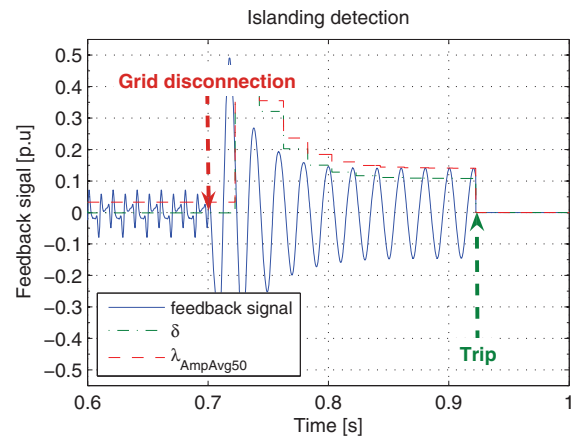

Figure 13. Islanding detection in the case of a parallel RLC load with a Q=10.

Figure 13 presents the Case 4 where a parallel RLC load with a quality factor of 10 was used. This was to show that the proposed method can perform well even under higher quality factors. The proposed method proved to be robust and effectiveness.

V. CONCLUSIONS

In this paper a new simple and effective anti-islanding method suitable for a single-phase grid-connected inverter system based on a PLL controller is proposed. The islanding detection method is based on the detection of the grid impedance changes. The proposed method relies on a continuous injection of a signal to the inverter angle being used as a modified reference for the inverter current to be generated. This affects the inverter in a negligible way when the grid is available. However, the method is able to detect grid failure by detecting the changes in the grid impedance. Namely, the feedback signal extracted from the voltage gives the information about the grid impedance changes, thus resulting in an effective islanding detection. Selected results are presented to confirm the effectiveness of the proposed method for a typical RLC load.

REFERENCES

[1] F. Blaabjerg, Z. Chen, and S.B. Kjaer, "Power electronics as efficient interface in dispersed power generation systems", IEEE Trans. on Power Electronics, Vol. 19, No. 5, September 2004, p. 1184-1194.

[2] IEEE Standard 929-2000: IEEE Recommended practice for utility interface of photovoltaic (PV) systems.

[3] IEEE Standard 1547-2003: IEEE Standard for interconnecting distributed resources with electric power systems.

[4] A. Woyte, K. De Brabandere, D.V. Dommelen, R. Belmans, and J. Nijs, "International harmonization of grid connection guidelines: adequate requirements for the prevention of unintentional islanding", Progress in Photovoltaics: Research and Applications 2003, Vol. 11, p. 407-424.

[5] M. Calais, J. Myrzik, T. Spooner and V.G. Agelidis, "Inverters for single-phase grid connected photovoltaic systems – an overview", in Record of IEEE PESC 2002, 23-27 June, Cairns, Australia, p. 1995-2000.

[6] IEEE Standard 1547.1-2005: IEEE Standard conformance test procedures for equipment interconnecting distributed resources with electric power systems.

[7] M. Francesco De, L. Marco, D. A. Antonio, and P. Alberto, "Overview of Anti-Islanding Algorithms for PV Systems. Part I: Passive Methods", Proc. of EPE-PEMC, 2006, pp. 1878-1883.

[8] M. Francesco De, L. Marco, and D. A. Antonio, "Overview of Anti-Islanding Algorithms for PV Systems. Part II: Active Methods", Proc. of EPE-PEMC , 2006, pp. 1884-1889.

[9] N. Cullen, J. Thornycroft and A. Collinson, "Risk analysis of islanding of photovoltaic power systems within low voltage distribution networks", IEA Report PVPS T5-08, March 2002.

[10] W. Bower and M Ropp, "Evaluation of islanding detection methods for photovoltaic utility-interactive power systems", IEA Task V Report IEA-PVPS T5-09, March 2002.

[11] Z. Ye, R. Walling, L. Garces, R. Zhou, L. Li and T. Wang, "Study and development of anti-islanding control for grid-connected inverters", National Renewable Energy Laboratory, NREL/SR-560-36243, May 2004.

[12] H. Kobayashi, K. Takigawa and E. Hashimoto, "Method for preventing islanding phenomenon on utility grid with a number of small scale PV systems", Record of. IEEE Photovoltaic Specialists Conference 1991, p. 695-700.

[13] A. Kitamura, M. Okamoto, F. Yamamoto, K. Nakaji, H. Matsuda, K. Hotta, "Islanding phenomenon elimination study at Rokko test center", Record of IEEE Photovoltaic Specialists Conference 1994, vol. 1, p. 759-762.

[14] Z. Ye, A. Kolwalkar, Y. Zhang, P. Du and R. Walling, "Evaluation of anti-islanding schemes based on non-detection zone concept", IEEE Trans. on Power Electronics, Vol. 19, No. 5, September 2004, p. 1171-1176.

[15] M.E. Ropp, M. Begovic and A. Rohatgi, "Prevention of islanding in grid-connected photovoltaic systems", Progress in Photovoltaics: Research and Applications, 7, 39-59, 1999.

[16] M.E. Ropp, M. Begovic and A. Rohatgi, "Analysis and performance assessment of the active frequency drift method of islanding prevention", IEEE Trans. on Energy Conversion, Vol. 14, No. 3, September 1999, p. 810-816.

[17] S. Yuyama, T. Ichinose, K. Kimoto, T. Itami, T. Ambo, C. Okado, K. Nakajima. S. Hojo, H. Shinohara, S. Ioka and M. Kuniyoshi, "A high-speed frequency shift method as a protection fro islanding phenomena of utility interactive PV systems", Solar Energy Materials and Solar Cells, Vol. 35, 1994, p. 477-486.

[18] [P. Sanchis, L. Marroyo and J. Coloma, "Design methodology for the frequency shift method of islanding prevention and analysis of its detection capability", Progress in Photovoltaics: Research and Applications 2005, Vol. 13, p. 409-428.

[19] G.A. Smith, P.A. Onions and D.G. Infield, "Predicting islanding operation of grid connected PV inverters", IEE Proceedings-Electrical Power Applications, Vol. 147, No 1, January 2000, p. 1-5.

[20] M.E. Ropp, M. Begovic, A. Rohatgi, G.A. Kern, H. Bonn and S. Gonzalez, "Determining the relative effectiveness of islanding detection methods using phase criteria and non-detection zones", IEEE Trans. on Energy Conversion, Vol. 15, No. 3, September 2000, p. 290-296.

[21] G.K. Hung, C.C. Chang and C.L. Chen, "Automatic phase-shift method for islanding detection of grid-connected photovoltaic inverters", IEEE Trans. on Energy Conversion, Vol. 18, No. 1, March 2003, p. 169-173.

[22] V. John, Z. Ye and A. Kolwalkar, "Investigation of anti-islanding protection of power converter based distributed generators using frequency domain analysis", IEEE Trans. On Power Electronics, Vol. 19, No. 5, September 2004, p. 1177-1183.

[23] L.A.C. Lopes and H. Sun, "Performance assessment of active frequency drifting islanding detection methods", IEEE Trans. on Energy Conversion, Vol. 21, No. 1, March 2006, p. 171-180.

[24] C. Jeraputra and P.N. Enjeti, "Development of a robust anti-islanding algorithm for utility interconnection of distributed fuel cell powered generation", IEEE Trans. on Power Electronics, Vol. 19, No. 5, September 2004, p. 1163-1170.

[25] Z. Ye, L. Li, L. Garces, C. Wang, R. Zhang, M. Dame, R. Walling and N. Miller, "A new family of active anti-islanding schemes based on DQ implementation for grid-connected inverters", in Record of IEEE PESC 2004, Aachen, Germany, p. 235-241.

[26] M. Liserre, A. Pigazo, A. Dell'Aquila and V.M. Moreno, "Islanding detection method for single-phase distributed generation systems based on inverters", Record of IEEE IECON 2005, p. 2505-2510.

[27] M. Ciobotaru, R. Teodorescu and F. Blaabjerg, "A new single-phase PLL structure based on second order generalized integrator", in Record of IEEE PESC 2006, Jeju, Korea, p. 1511-1516.

[28] M. Ciobotaru, R. Teodorescu and V. G. Agelidis, 'Offset rejection for PLL based synchronization in grid-connected converters', *Proc. of APEC'08*, pp. 1611-1617;